



TECHNISCHE UNIVERSITÄT BERGAKADEMIE FREIBERG

Institut für Mineralogie

Lehrstuhl für Lagerstättenlehre und Leibniz-Labor für Angewandte Meeresforschung

Brennhausgasse 14

09596 Freiberg

Abschlußbericht zum Vorhaben

" Detailuntersuchung der magmatisch-hydrothermalen
Goldvererzung des Conical Seamount (Papua-Neuguinea)
mit Flachbohrungen "

BMBF 03G0166

(01.06.2002 - 30.11.2004)

Inhaltsverzeichnis

I.	Aufgabenstellung und Voraussetzung zur Durchführung des Projektes.....	3
I. 1.	Aufgabenstellung	3
I. 2.	Voraussetzungen, unter denen das Vorhaben durchgeführt wurde	3
I. 3.	Planung und Ablauf des Vorhabens	3
I. 4.	wissenschaftlicher und technischer Stand, an den angeknüpft wurde	4
II.	Ergebnisse, Verwertung und Veröffentlichungen	6
II. 1.	Ergebnisse	6
II. 2.	Verwertung der Ergebnisse	23
II. 3.	Fortschritt auf dem Gebiet des Vorhabens bei anderen Stellen	23
II. 4.	Geplante Veröffentlichungen	23
III.	Erfolgskontrollbericht	26
III. 1.	Beitrag zu den förderpolitischen Zielen.....	26
III. 2.	Wissenschaftlicher und technischer Erfolg	26
III. 3.	Fortschreibung des Verwertungsplans / Erfindungen und Schutzrechtanmeldungen ..	26
III. 4.	Arbeiten, die zu keiner Lösung geführt haben	26
III. 5.	Präsentationsmöglichkeiten	26
III. 6.	Einhaltung der Ausgaben- und Zeitplanung.....	26

Anhang

Publikationen (4x)

Kurzfassungen (8x)

Bericht Dr. R. Binns

Auszüge aus Diplomarbeiten (2x)

Publikationen, die nach Abschluss des Vorgängerprojektes BMBF 03G0133 erschienen sind (3x)

- SO166 CONDRILL -

**" Detailuntersuchung der magmatisch-hydrothermalen
Goldvererzung des Conical Seamount (Papua-Neuguinea)
mit Flachbohrungen "**

Prof. Dr. Peter M. Herzig*

Dr. Sven Petersen*

Technische Universität Bergakademie Freiberg

Institut für Mineralogie

Lehrstuhl für Lagerstättenlehre und Leibniz-Labor für Angewandte Meeresforschung

Brennhausgasse 14

09596 Freiberg

Tel. +49-3731-2662

Fax +49-3731-2610

email pherzig@ifm-geomar.de*
spetersen@ifm-geomar.de*

www <http://www.mineral.tu-freiberg.de/econgeology/index.html>

UNTER ZUARBEIT VON DR. THOMAS MONECKE, DR. THOMAS KUHN*, DIPL.-MIN. KLAUS-PETER
BECKER, DIPL.-GEOL. THOMAS IHLE, DIPL.-MIN. DIRK SANDMANN, DIPL.-MIN. OLAF
SCHOLTYSEK, DIPL.-MIN. ARON GABRIEL UND DIPL.-ING. TOBIAS WAGNER

sowie

Dr. Mark Hannington, University of Ottawa, Canada

Dr. J. Pasava und Dr. A. Vymazalova, Czech Geological Survey, Prague

Dr. Ray Binns, CSIRO, North Ryde, Australia

* Der Projektleiter sowie die Bearbeiter Dr. S. Petersen und Dr. T. Kuhn sind während der Laufzeit des Projektes von der TU Bergakademie Freiberg an das Leibniz-Institut für Meereswissenschaften (IFM-GEOMAR) Kiel gewechselt.

- SO166 CONDRILL -

" Detailuntersuchung der magmatisch-hydrothermalen Goldvererzung des Conical Seamount (Papua-Neuguinea) mit Flachbohrungen "

Die Forschungsfahrt SO166 vom 22. August bis 11. Oktober 2002 untersuchte geologische und lagerstättenkundliche Fragestellungen in dem Seegebiet südlich der Insel Lihir sowie im östlichen Manus Becken (Papua-Neuguinea). Die Hydrothermalsysteme des flachmarinen Vulkans Conical Seamount und die Massivsulfidvorkommen PACMANUS, Desmos Caldera und Susu Knolls wurden durch Flachbohrungen (5 m) untersucht. Größere Bereiche des Meeresbodens in der Umgebung der Insel Lihir wurden bathymetrisch vermessen, um die strukturellen Besonderheiten dieses Seegebietes aufzunehmen und ihre Auswirkungen auf den Vulkanismus und die damit verbundenen Mineralisationsprozesse zu untersuchen.

Für die Flachbohrungen wurde der so genannte "Rockdrill" des British Geological Survey eingesetzt, der bis zu 5 m lange Bohrkern aus Wassertiefen bis zu 2000 m bergen kann. Dieser Einsatz war der Erste seiner Art auf der Sonne und hat in besonderer Weise gezeigt, dass der Einsatz beweglicher Bohrgeräte von dem Forschungsschiff SONNE aus möglich ist.

Als wichtigste Ergebnisse des gesamten wissenschaftlichen Programms sind hervorzuheben:

- die Hinweise auf eine flächenmäßig größere Ausdehnung der bekannten Goldmineralisation am Conical Seamount
- die Beprobung alterierter Gesteine unterhalb frischer ankaramitischer Basalte, die Hinweise auf eine mögliche größere Goldvererzung in der Tiefe des Conical Seamount bieten.
- die Beprobung extrem Cu-, Zn- und Au-reicher Massivsulfide unterhalb des Meeresbodens im Bereich des Pacmanus Hydrothermalfeldes
- Hinweise auf episodische hydrothermale Aktivität und Umlagerungsprozesse im Bereich des PACMANUS Hydrothermalfeldes.
- Hinweise auf lokale Unterschiede (z.B. magmatischer Eintrag von Metallen) in den verschiedenen Bereichen des PACMANUS Hydrothermalfeldes

I. Aufgabenstellung und Voraussetzung zur Durchführung des Projektes

I. 1. Aufgabenstellung

Im Rahmen der Forschungsfahrt SO166 sollte die Ausbildung der Alteration und Goldmineralisation des flachmarinen Vulkans Conical Seamount mit Flachbohrungen systematisch untersucht werden. Für die Flachbohrungen wurde der sogenannte "Rockdrill" des British Geological Survey eingesetzt, der bis zu 5 m lange Bohrkern aus Wassertiefen bis zu 2000 m bergen kann. Dabei sollten erstmals Aufschlüsse über die 3. Dimension dieses neuen Vererzungstyps erhalten werden. Insbesondere sollte geklärt werden, ob und wie sich die Mineralisation und Alteration mit der Tiefe fortsetzen. Im Rahmen der Forschungsfahrt wurde darüber hinaus das PACMANUS Hydrothermalfeld im Bereich des östlichen Manus Beckens untersucht, das eines der goldreichsten submarinen Hydrothermalvorkommen überhaupt ist. Aufgrund hoher Gas-, Fluor- und SO₂-Gehalte in den Fluiden sowie aufgrund des Auftretens metallreicher Glaseinschlüsse in den Nebengesteinen wurde eine Beteiligung magmatischer Lösungen an der Bildung dieses Vorkommens postuliert (Douville et al., 1999; Yang und Scott, 1996).

Die Untersuchungen der TU Bergakademie Freiberg konzentrieren sich im Wesentlichen auf lagerstättenkundliche Fragestellungen. Das Hauptinteresse liegt dabei auf der Untersuchung der Alterations- und Mineralisationsprozesse am Conical Seamount sowie in der Untersuchung der Anreicherungsprozesse von Bunt- und Edelmetallen im Bereich des PACMANUS Hydrothermalfeldes. Darüber hinaus wurden frische Gesteine aus beiden Hydrothermalvorkommen mineralogisch und geochemisch bearbeitet. In Zusammenarbeit mit dem Institut für Geowissenschaften der Universität Kiel wurden ausgewählte Proben datiert. Geochemische Untersuchungen sowie Isotopenuntersuchungen an Sulfiden (S) und Sulfaten (S, Sr) des PACMANUS Hydrothermalsystems sollten klären, welche Prozesse zur Goldanreicherung in diesem Hydrothermalsystem führen, und ob sich ein magmatischer Eintrag in den Sulfiden selbst nachweisen lässt.

Literatur

- Douville, E., Bienvu, P., Charlou, J.-L., Donval, J.P., Fouquet, Y., Appriou, P., and Gamo, T., 1999, Yttrium and rare earth elements in fluids from various deep-sea hydrothermal systems: *Geochimica et Cosmochimica Acta*, v. 63, p. 627-643.
- Yang, K., and Scott, S.D., 1996, Possible contribution of a metal-rich magmatic fluid to a sea-floor hydrothermal system: *Nature*, v. 383, p. 420-423.

I. 2. Voraussetzungen, unter denen das Vorhaben durchgeführt wurde

Die durchgeführte Forschungsfahrt beruhte im Wesentlichen auf den intensiven Untersuchungen die im Vorfeld mit den Forschungsfahrten SO94 (1994) und SO133 durchgeführt wurden. Die guten Beziehungen zur Regierung und insbesondere dem Geologischen Dienst von Papua-Neuguinea erlaubten einen reibungslosen Ablauf des Genehmigungsprozesses und der Durchführung der Fahrt. Die Bohrungen im Bereich des PACMANUS Hydrothermalfeldes sind von der Firma Nautilus Minerals Cooperation unterstützt worden, die für dieses Gebiet die Explorationsrechte besitzt.

I. 3. Planung und Ablauf des Vorhabens

Die Beprobung des Untergrundes von submarinen Hydrothermalsystemen im Seegebiet von Papua-Neuguinea konzentrierte sich im Wesentlichen auf zwei

Untersuchungsgebiete: a) den Topbereich des 1994 entdeckten Conical Seamount und b) die massivsulfidführenden Strukturen des PACMANUS Hydrothermalfeldes. Insgesamt wurden im Bereich von Conical Seamount 39 Bohrungen niedergebracht, von denen 37 einen Kerngewinn von insgesamt 20.8 m erzielten. Der Kerngewinn von durchschnittlich 31% liegt deutlich höher als derjenige von ODP-Bohrungen in vergleichbaren Lithologien. Nach Beendigung der Arbeiten am Conical Seamount konnten innerhalb weniger Tage 10 Bohrungen im östlichen Manusbecken abgeteuft werden, die spektakuläre Ergebnisse aus einem aktiven submarinen Hydrothermalsystem erbrachten. Hier konnten insgesamt 9 m Massivsulfide erbohrt werden. Darüber hinaus wurde der fernsehgesteuerte TV-Greifer eingesetzt um umfangreiches Probenmaterial von aktiven und inaktiven Sulfidschornsteinen zu bergen.

I. 4. *wissenschaftlicher und technischer Stand, an den angeknüpft wurde*

a) Stand der Wissenschaft

Unser Verständnis submariner Hydrothermalsysteme wurde in den letzten 20 Jahren von der Tatsache beeinflusst, dass nur die Oberfläche dieser Vorkommen für die Wissenschaft erreichbar waren. Erst mit dem Einsatz der „Joides Resolution“ im Rahmen des Ocean Drilling Programs (ODP) bestand die Möglichkeit Informationen aus dem Untergrund dieser Vorkommen zu bekommen. In den letzten Jahren wurden Tiefbohrungen im Bereich des Atlantik (TAG Hydrothermalfeld, Humphris et al., 1995) und Nordwestpazifik (Middle Valley und Escanaba Trog, Davis et al., 1992; Zierenberg et al., 1998) niedergebracht, um ein besseres Verständnis dieser Vorkommen entlang Mittelozeanischer Rücken zu bekommen. Im Jahre 2002 wurde mit den Bohrungen im Manus Becken erstmals auch ein Back-Arc Becken erbohrt (Binns et al., 2002). Bei allen diesen Bohrungen hat sich gezeigt, dass die oberflächennahen Bereiche aus technischen Gründen oft nicht gekernt werden können. Die Benutzung mobiler Bohrsysteme und ihr Absatz am Meeresboden erlaubt neben einem kontrollierteren Bohrvorgang auch einen erhöhten Kerngewinn. Darüber hinaus sind diese Systeme von einer Vielzahl von Schiffen einsetzbar und daher für die Wissenschaft zugänglicher als die Bohrschiffe des Ocean Drilling Programs.

Conical Seamount ist ein inaktiver Fore-Arc-Vulkan zwischen der Manus-Kilinau-Subduktionszone und dem Neu Irland-Inselbogen in den Gewässern von Papua-Neuguinea. Conical Seamount befindet sich in einem seismisch, tektonisch und thermisch aktiven, NE-SW streichenden Korridor zwischen der etwa 10 km entfernten Südspitze der Insel Lihir und dem Neu Irland-Inselbogen (Herzig et al., 1994). Während der Sonne-Fahrt SO94 wurden 1994 insgesamt 12 bis dahin unbekannte Seamounts südlich von Lihir Island entdeckt, kartiert und beprobt. Conical Seamount ist der größte Seamount der Region südlich von Lihir und besitzt einen Basisdurchmesser von 2.5 km in 1.650 m Wassertiefe und ein etwa 150 x 200 m großes Gipfelplateau in 1.050 m Wassertiefe. Die Beprobung des Gipfelplateaus während SO94 und SO133 (1998) zeigte das Auftreten einer gangförmigen, sulfidische Goldvererzungen in Trachybasalten an, die sich von bisher bekannten submarinen Hydrothermalvorkommen deutlich unterschied. Die Vererzung ist durch erhöhte Konzentrationen der typisch epithermalen (d.h. magmatisch-hydrothermalen) Elemente Au, As, Sb, Hg, und Ag gekennzeichnet, wobei Goldgehalte bis zu 230 ppm gemessen wurden (Petersen et al., 2002). Die Vererzung ist teilweise mit Alterationsmineralen wie z.B. Alunit assoziiert, die für konventionelle marine Hydrothermalvorkommen (Meerwasserzirkulationssysteme) ungewöhnlich sind und darauf hinweisen, dass zumindest ein Teil des Goldes offenbar direkt durch magmatisch-hydrothermale bzw. juvenile Fluide eingetragen wurde (Herzig et al., 1999).

Abschlussbericht CONDRILL (03G0166)
 Detailuntersuchung der magmatisch-hydrothermalen Goldvererzung des Conical Seamount
 (Papua-Neuguinea) mit Flachbohrungen

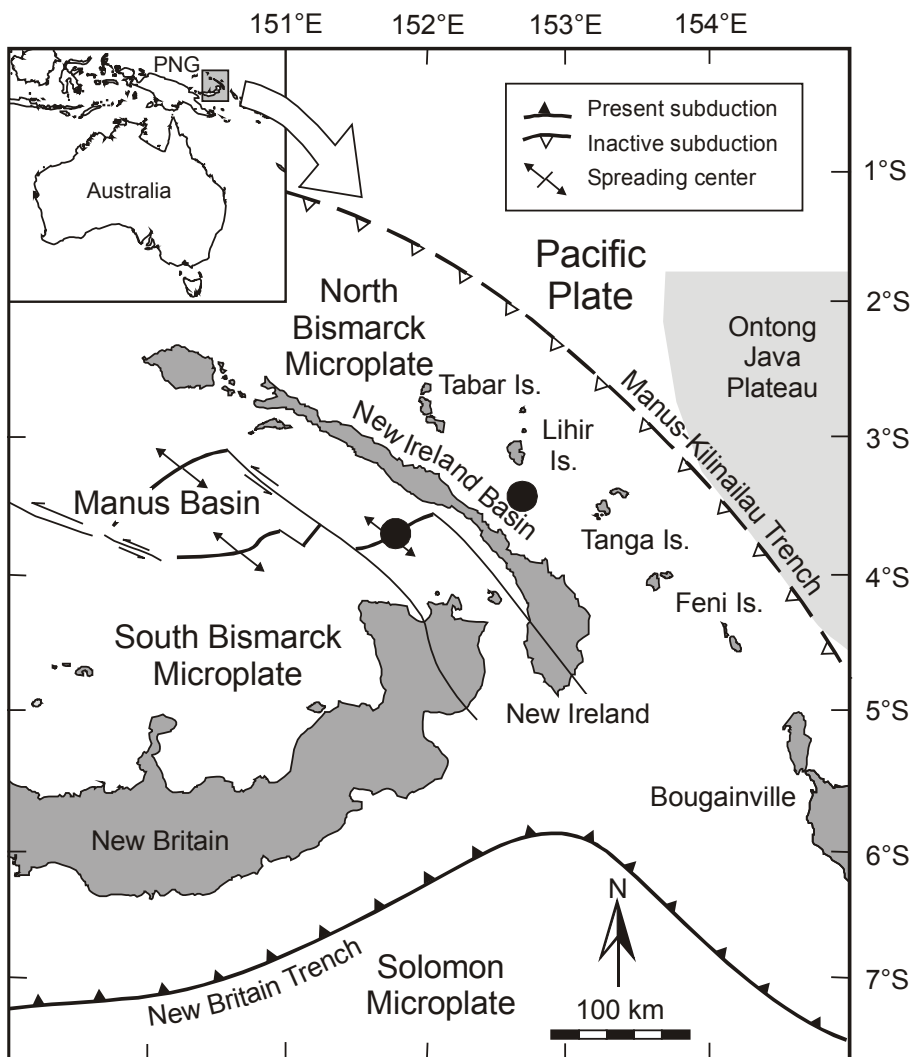


Abb. 1: Lagekarte der während SO166 aufgesuchten Arbeitsgebiete im Bereich des Neu Irland Inselbogens.

Dieser Zusammenhang ist insofern von Bedeutung, als dass Conical Seamount sich nur etwa 25 km südlich der in dem Krater des Luise Volcano liegenden Goldlagerstätte Ladolam auf der Insel Lihir befindet. Bei Ladolam handelt es sich um die größte durch magmatische Fluide gebildete (epithermale) Goldlagerstätte weltweit. Aufgrund der Nähe zu Lihir und der Ähnlichkeiten in Mineralisation und Gesteinsalteration sowie des Auftretens beider Vererzungen im Bereich von Vulkangebäuden wurde von uns schon 1994 vermutet, dass Conical Seamount möglicherweise ein submarines Gegenstück der Goldlagerstätte sein könnte.

Literatur

Binns, R.A., Barriga, F., and Miller, D.J., 2002, Leg 193 summary, in Binns, R.A., Barriga, F.J.A.S., and Miller, D.J., eds., Proceedings of the Ocean Drilling Program, Initial Reports, Volume 193, College Station, TX, p. 1-84.

Davis, E.E., Mottl, M.J., and Fisher, A.T., et al., 1992, Proceedings of the Ocean Drilling Program, Initial Reports, 139, College Station, TX, 1026 p.

Herzig, P.M., Hannington, M.D., McInnes, B., Stoffers, P., Villinger, H.W., Seifert, R., Binns, R.A., Liebe, T., and Shipboard_Scientific_Party, 1994, Submarine volcanism and hydrothermal venting studied in Papua, New Guinea: Eos, Transactions, American Geophysical Union, v. 75, p. 513, 515-516.

Herzig, P.M., Petersen, S., and Hannington, M.D., 1999, Epithermal-type gold mineralization at Conical Seamount: a shallow submarine volcano south of Lihir Island, Papua New Guinea, in Stanley, C.J., ed., Mineral Deposits: Processes to Processing, Proceedings of the fifth biennial SGA meeting and the tenth Quadrennial IAGOD symposium London, p. 527-530.

- Humphris, S.E., Herzig, P.M., Miller, D.J., Alt, J.C., Becker, K., Brown, D., Brüggmann, G., Chiba, H., Fouquet, Y., Gemell, J.B., Guerin, G., Hannington, M.D., Holm, N.G., Honnorez, J.J., Itturino, G.J., Knott, R., Ludwig, R., Nakamura, K., Petersen, S., Reysenbach, A.-L., Rona, P.A., Smith, S., Sturz, A.A., Tivey, M.K., and Zhao, X., 1995, The internal structure of an active sea-floor massive sulphide deposit: *Nature*, v. 377, p. 713-716.
- Petersen, S., Herzig, P.M., Hannington, M.D., Jonasson, I.R., and Arribas, A.j., 2002, Submarine vein-type gold mineralization near Lihir island, New Ireland fore-arc, Papua New Guinea: *Economic Geology*, v. 97, p. 1795-1813.
- Zierenberg, R.A., Fouquet, Y., Miller, D.J., Bahr, J.M., Baker, P.A., Bjerkgard, T., Brunner, C.A., Duckworth, R.C., Gable, R., Gieskes, J., Goodfellow, W.D., Gröschel-Becker, H.M., Guerin, G., Ishibashi, J., Itturino, G., James, R.H., Lackschewitz, K.S., Marquez, L.L., Nehlig, P., Peter, J.P., Rigsby, C.A., Schultheiss, P., Shanks, W.C., Simoneit, B.R.T., Summit, M., Teagle, D.A.H., Urvat, M., and Zuffa, G.G., 1998, The deep structure of a sea-floor hydrothermal deposit: *Nature*, v. 392, p. 485-488.

b) technischer Stand / Vorarbeiten

Sämtliche Methoden der isotopengeochemischen, mineralogischen und geochemischen Analytik, die zum Einsatz gekommen sind, sind in der Arbeitsgruppe seit Jahren etabliert. Darüber hinaus wurde in Freiberg die Rietveld-Methode, eine nichtlineare Optimierungsmethode zur quantitativen Röntgenphasenanalytik, entscheidend mitentwickelt. Dieses Verfahren wurde an den Proben des Conical Seamount zur Bestimmung des Phasenbestands eingesetzt. Untersuchungen der Platingruppenelementanalytik werden seit Jahren vom Tschechischen Geologischen Dienst entwickelt und hier erstmals für Proben aus dem submarinen Bereich eingesetzt.

II. Ergebnisse, Verwertung und Veröffentlichungen

II. 1. Ergebnisse

Conical Seamount

Durch den Einsatz des Rockdrill konnten an 39 Lokationen im Bereich des Gipfelplateaus des Conical Seamount Bohrkerne gezogen werden. Neben frischen ankaramitischen Basalten konnten eine Reihe alterierter und mineralisierter Proben gewonnen werden. Von Bedeutung ist dabei insbesondere die deutliche Ausweitung des bisher bekannten hydrothermal beeinflussten Bereiches nach Westen (Stationen 40RD, 42RD und 43RD; siehe Abb. 1). Darüber hinaus konnten alterierte Proben unterhalb von frischen Basalten (Station 47RD; Tiefe: 4,5 Meter) geborgen werden. Dies wird als wichtiger Hinweis auf eine mögliche, größere Tiefenerstreckung der Mineralisation angesehen.

Insgesamt wurden 50 Teilproben für die geochemischen sowie röntgenographischen Analysen aufbereitet. Besonderer Wert wurde bei den Untersuchungen auf die quantitative Röntgenphasenanalytik gelegt, die eine bessere Unterscheidung der verschiedenen Alterationsprozesse erlaubt. Parallel dazu wurden geochemische Analysen durchgeführt, um geochemische Trends während der Alteration aufzuzeigen und Hinweise auf die chemischen Charakteristika der beteiligten Fluide zu geben.

Die Gesteine des Conical Seamount sind als alkalische bis subalkalische, ankaramitische Basalte, Trachybasalte bis basaltische Trachyandesite anzusprechen (Abb. 3a) und zeigen für fast alle Proben eine geringe Variation in der geochemischen Zusammensetzung. Nur ein Teil der mineralisierten Proben ist im TAS-Diagramm auffällig. Die Zr-TiO₂-Verhältnisse von Proben des Conical Seamount sind nahezu konstant,

während die Nb/Y-Verhältnisse bei nahezu konstanten Nb-Gehalten variabel sind und auf eine Mobilisierung von Y während der hydrothermalen Alteration hindeuten (Abb. 3b). Auch sind in den bisher untersuchten Proben in unterschiedlichen Alterationsgruppen deutliche Variationen von z.B. MgO bzw. K₂O zu beobachten (Abb. 4). Die vollständigen geochemischen Analysen der Gesteine sind im Appendix 1 wiedergegeben.

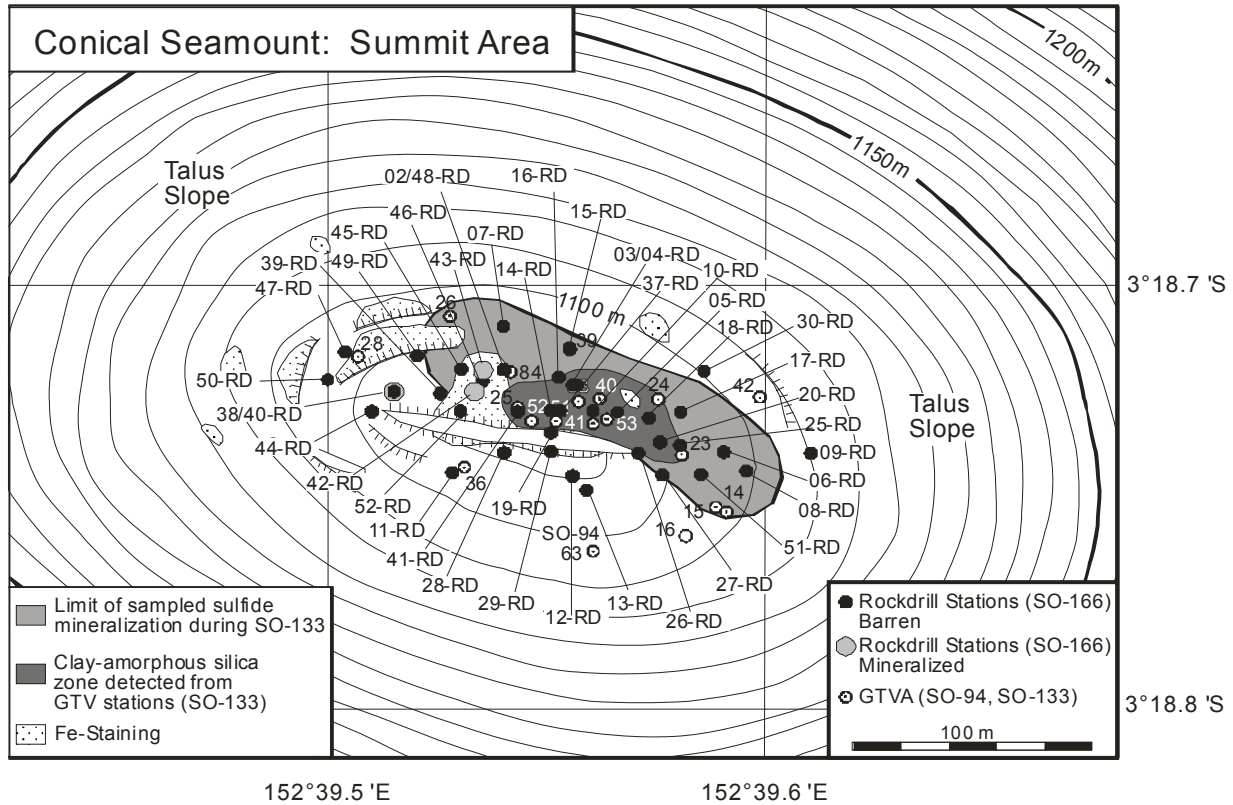


Abb. 2: Vereinfachte Lagekarte der Bohrlokationen im Gipfelbereich des Conical Seamount.

Abschlussbericht CONDRILL (03G0166)
 Detailuntersuchung der magmatisch-hydrothermalen Goldvererzung des Conical Seamount
 (Papua-Neuguinea) mit Flachbohrungen

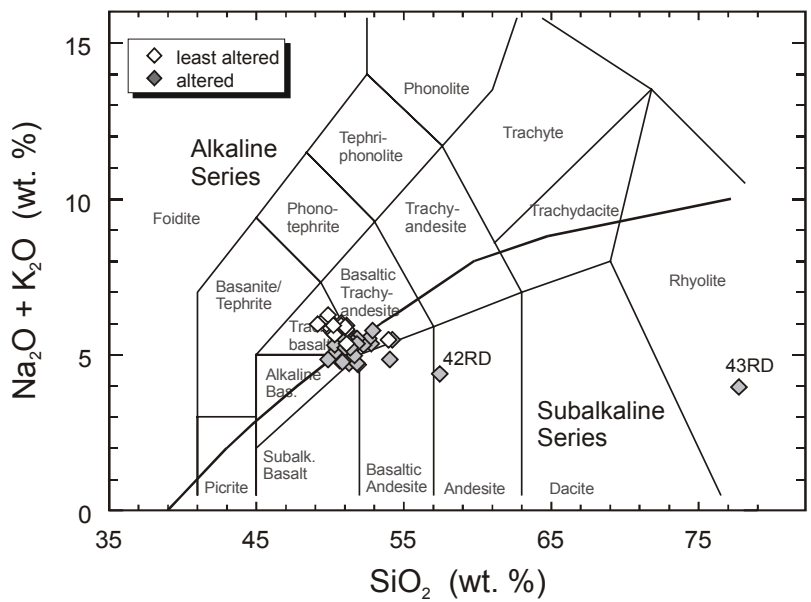


Abb. 3: Geochemische Charakterisierung des Probenmaterials vom Conical Seamount im a) TAS-Diagramm (nach Le Maitre, 1989) b) Zr/TiO₂-Diagramm (nach Winchester und Floyd, 1977). Zum Vergleich sind in das Zr/TiO₂-Diagramm Analysen von stark alterierten Proben früherer Forschungsfahrten (SO94 und SO133; Symbol: X) eingetragen.

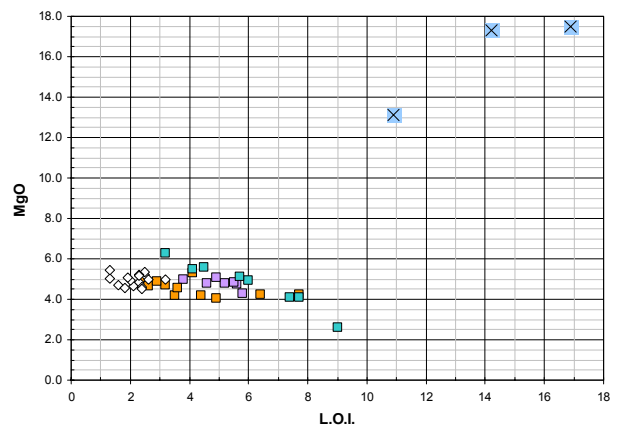
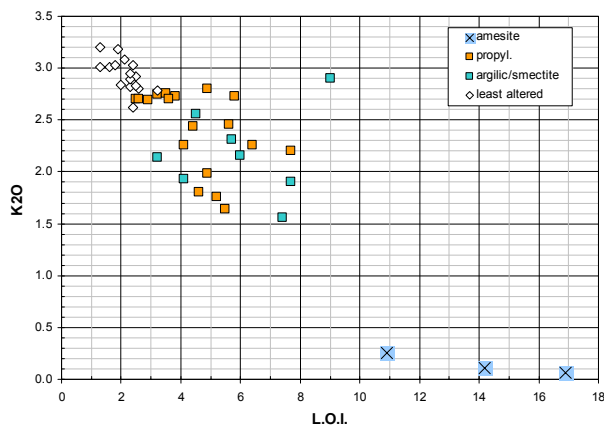
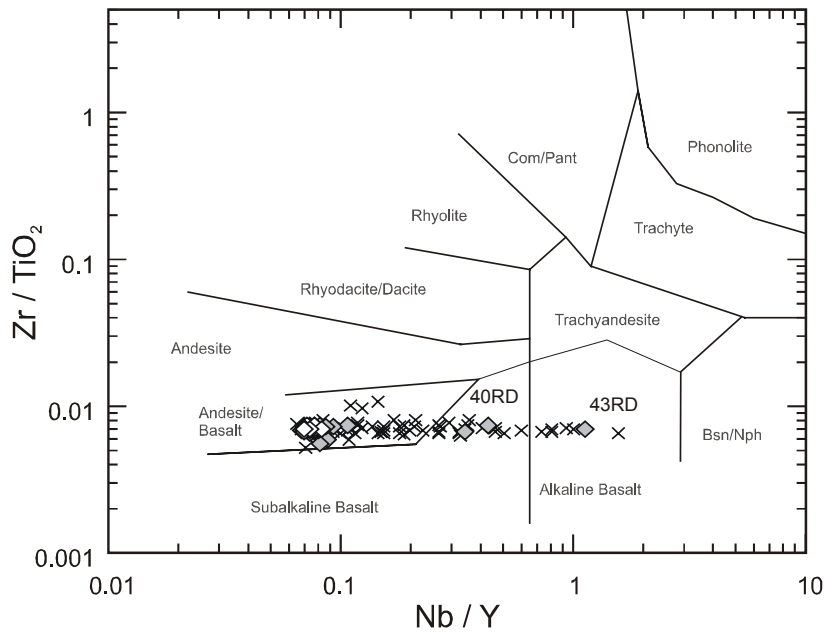


Abb. 4: Einfluss des Alterationsgrades auf die Hauptelementgeochemie (K₂O und MgO) und den Glühverlust (L.O.I.; alle Angaben in Gew.%) sowie die Alterationsmineralogie.

Die mineralogischen Untersuchungen der polymetallischen Mineralisation selbst haben kaum Unterschiede zu dem Probenmaterial ergeben, das bei vorherigen Fahrten mit Hilfe des TV-Greifers von der Oberfläche gewonnen werden konnte. Neben den für Conical Seamount typischen Erzmineralen (Chalkopyrit, Sphalerit, Galenit und Pyrit) konnte allerdings das vermehrte Auftreten der Arsensulfide Auripigment, Realgar und des Antimonsulfides Stibnit beobachtet werden (Abb. 4). In einer Probe konnte darüber hinaus das seltene Ag-Sb-Sulfid Stephanit (Ag_5SbS_4) erstmals für den Conical Seamount nachgewiesen werden (Abb. 4b, c).

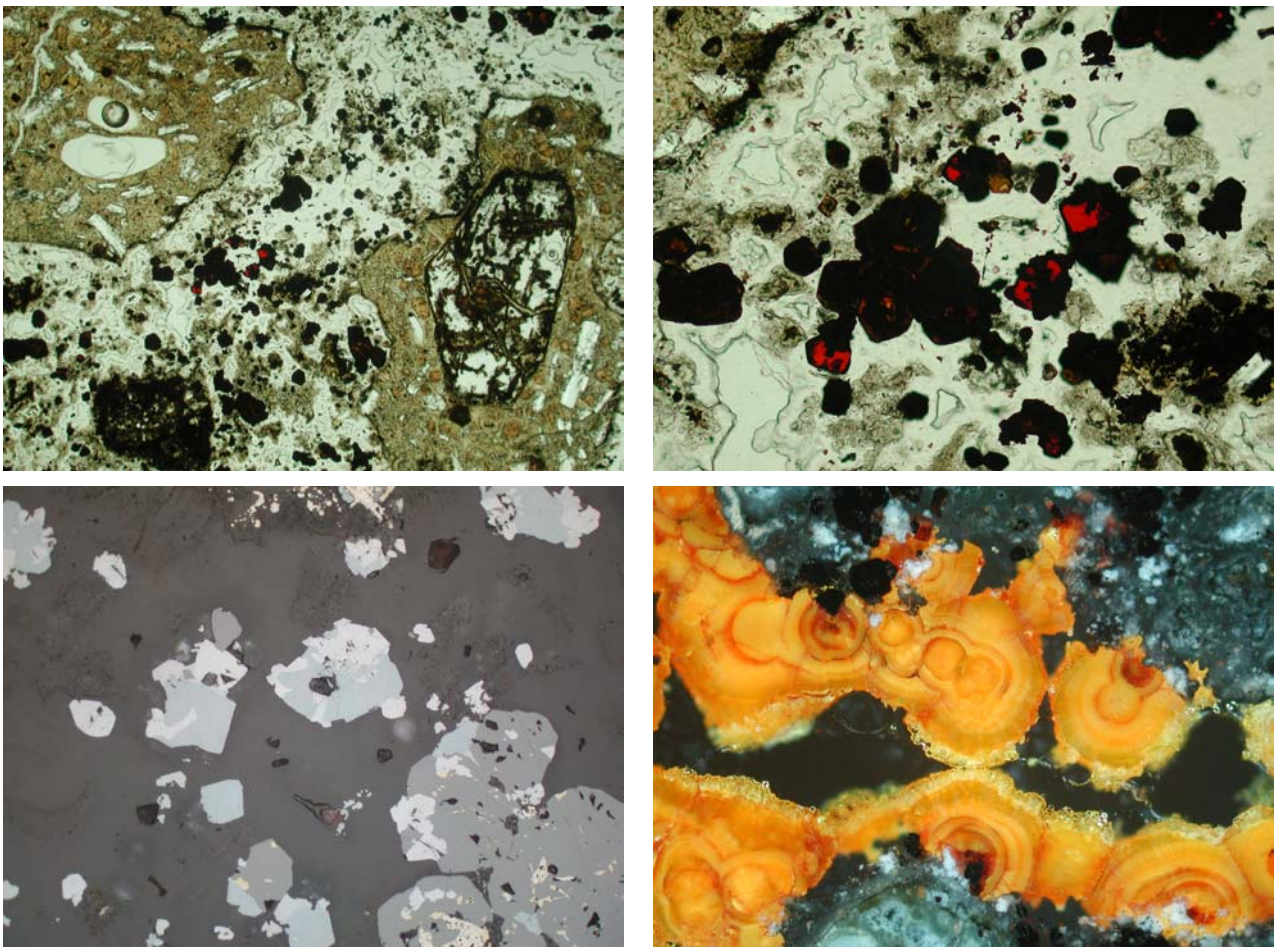


Abb. 5: Dünnschliffotos der polymetallischen Probe SO166-40RD(0-6). a) Nebengesteinsbrekzie mit kiesel-säurerreicher Matrix und disseminiert auftretenden Sulfiden (Durchlicht; Bildbreite= 3,2mm). b) Ausschnitt von A, der die feinverteilt auftretenden Sulfide in amorpher Kieselsäure zeigt. Die durchscheinenden roten Kristalle sind Stephanit (Ag_5SbS_4 ; Durchlicht; Bildbreite= 1,6mm). c) Verwachsung von Stephanit (blaugrau) mit Sphalerit, Galenit und Chalkopyrit (Auflicht; Bildbreite= 800 μm). d) Collomorpher Auripigment in einer späten Rissfüllung (Auflicht; gekreuzte Nicols; Bildbreite= 1,6mm).

Hauptaugenmerk der Freiburger Untersuchungen lag auf der mineralogisch orientierten **Alterationsstudie** des Probenmaterials vom Conical Seamount. Dafür wurden Röntgenbeugungsexperimente an insgesamt 50 gepulverten Gesamtgesteinsproben durchgeführt. Zunächst wurde der Phasenbestand der Bohrkernproben mittels Röntgenpulverdiffraktometrie qualitativ und quantitativ bestimmt. Die quantitativen Untersuchungen erfolgten mit Hilfe der Rietveld-Methode, einer nichtlinearen

Optimierungsmethode (Kleeberg und Bergman, 2002, Monecke et al., 2001). Basierend auf den Ergebnissen der quantitativen Phasenanalyse wurde eine Unterteilung der Proben in Gruppen mit ähnlichem Phasenbestand mittels hierarchischer Clusteranalyse vorgenommen. Diese statistische Analyse zeigte, dass vier Gruppen von Proben mit jeweils ähnlichem Phasenbestand unterschieden werden können (Abb. 6).

Die erste Gruppe besteht aus Diopsid, Ca-reichen Plagioklas, Na-reichen Sanidin, Biotit, Magnetit und vulkanischem Glas. Die quantitativen Phasenanalysen zeigen, dass das vulkanische Glas zwischen 10 und 35 Gew.-% der Proben entspricht. Diopsid kommt in Konzentrationen von 30 bis 35 Gew.-% vor, während die Feldspatgehalte von 30 bis 45 Gew.-% schwanken. Die Gehalte an Biotit und Magnetit liegen meist unter 6 Gew.-%. Dünnschliffbeobachtungen legen nahe, dass der Phasenbestand der Proben nicht wesentlich durch die Prozesse der hydrothermalen Alteration modifiziert worden ist. Die häufig auftretenden Klinopyroxen- und Plagioklaseinsprenglinge erscheinen im optischen Mikroskop weitgehend unalteriert. Klinopyroxen bildet idiomorphe Kristalle, die Größen von bis zu 5 mm erreichen. Fast alle Klinopyroxeneinsprenglinge weisen oszillierende Zonierungen sowie eine deutliche Sektorzonierung auf. Die leistenförmigen Plagioklaseinsprenglinge sind bis zu 1 mm groß. Die Grundmasse der Trachybasalte besteht weitgehend aus vulkanischem Glas, in dem Pyroxen-, Biotit-, Plagioklas- und Sanidinmikrolithe auftreten. Magnetit kommt sowohl in Form kleiner Einsprenglinge als auch feinverteilt in der Grundmasse vor. Akzessorisch auftretender Apatit bildet kleine Kristalle, die meist von den Klinopyroxeneinsprenglingen beherbergt werden.

Trachybasaltproben der zweiten Gruppe bestehen zu 10 bis 35 Gew.-% aus vulkanischem Glas und beinhalten 25 bis 35 Gew.-% Diopsid, 30 bis 40 Gew.-% Feldspat und unter 6 % Biotit. Die Proben enthalten bis zu 10 Gew.-% Analcim und bis zu 4 Gew.-% K-reichen monoklinen Feldspat. Pyrit und Markasit erreichen bis zu 6 Gew.-%. Im Vergleich zu den nicht alterierten Gesteinen enthalten die Proben dieser Gruppe einen niedrigeren Anteil an Magnetit (unter 4 Gew.-%). Petrographische Untersuchungen zeigen, dass Pyrit und Markasit in den Trachybasalten dieser Gruppe häufig als Füllung von Gasblasen auftreten oder kleine Körner bilden, die fein in der Grundmasse verteilt sind. Primäre Magnetite sind teilweise oder vollständig von diesen Sulfiden verdrängt worden. Die gefügekundlichen Beobachtungen zeigen, dass die Proben dieser Gruppe leicht hydrothermal alteriert wurden. Von besonderem Interesse ist das Vorkommen von Analcim, ein sekundäres Mineral, das sich häufig auch in modernen Geothermalsystemen an Land bildet.

Die dritte Probengruppe enthält neben vulkanischem Glas einen hohen Anteil an Tonmineralen. Der Diopsidgehalt schwankt zwischen 15 und 30 Gew.-%. Zusätzlich zu primärem Plagioklas und Sanidin (35 bis 50 Gew.-%) wurden in einigen Proben bis zu 5 Gew.-% eines K-reichen monoklinen Feldspates beobachtet. Es handelt sich hierbei vermutlich um ein Produkt der hydrothermalen Alteration. Der Biotitgehalt dieser Proben ist variabel. Magnetit konnte mit Hilfe der Röntgenbeugung nicht beobachtet werden. Die Gesamtgesteinsproben enthalten bis zu 10 Gew.-% Pyrit und Markasit. Röntgendiffraktometrische Untersuchungen an Tonmineralfraktionen zeigten, dass die alterierten Gesteine hohe Gehalte an Smektit aufweisen. Durch die Anpassung von modellierten Röntgendiffraktogrammen an die gemessenen Beugungsbilder der Tonmineralfraktionen konnte demonstriert werden, dass sowohl dioktaedrische als auch trioktaedrische Smektite auftreten. Darüber hinaus wurde in den Tonmineralfraktionen Vermikulit angetroffen. Dünnschliffuntersuchungen haben gezeigt, dass in erster Linie das vulkanische Glas in der Grundmasse durch die Smektite verdrängt wird. Smektit tritt in Säumen rund um alterierte

Klinopyroxeneinsprenglinge auf oder bildet die Füllung von Rissen, die reliktsche Klinopyroxenkristalle durchziehen. Primärer Magnetit ist vollständig durch feine Verwachsungen von Sulfiden und vermutlich amorphen Phasen ersetzt. Die in den Proben enthaltenen Plagioklaseinsprenglinge erscheinen unter dem optischen Mikroskop weitgehend unalteriert. Rückstreuелеktronenstrahlbilder zeigen jedoch, dass diese Phasen durch die hydrothermale Alteration chemisch verändert wurden. In vielen Fällen kam es durch die Überlagerung sekundärer chemischer Gradienten mit primären Zonierungen zur Bildung komplizierter Internstrukturen.

Die mineralisierten Proben sind durch stark erhöhte Gehalte an amorpher Kieselsäure und durch das Auftreten buntmetallhaltiger Sulfide (Cu, Zn, Pb) deutlich von den anderen Probengruppen abgesetzt.

Interpretation der Ergebnisse

Die Bohrkampagne im Rahmen der Forschungsfahrt SO166 zeigte, dass im Gipfelbereich des Conical Seamount sowohl frische, scheinbar nicht hydrothermal alterierte Trachybasalte als auch stark alterierte Äquivalente auftreten. Hydrothermal alterierte Proben kommen in erster Linie in dem nördlichen und östlichen Teil des Gipfelbereichs vor, während der südliche Bereich von frischen Trachybasalten dominiert wird. Meeresbodenbeobachtungen legen die Vermutung nahe, dass die Zone intensiver hydrothermaler Alteration von den im Süden auftretenden frischen Gesteine durch eine etwa 100 m lange vulkanische Struktur getrennt wird. Es handelt sich möglicherweise um die Aufstiegszone frischer Lava, die in den südlichen Teil des Gipfelbereiches abgefließen ist und die dort eventuell auftretenden hydrothermal alterierten Gesteine bedeckt hat. Eine solche Vermutung wird durch Beobachtungen an Bohrkernen gestützt, in denen intensiv hydrothermal alterierte Gesteine unterhalb frischer Trachybasalte auftreten.

Eine Rekonstruktion der physikochemischen Bedingungen, die während der Bildung der Pyrit- und Markasitmineralisation und der damit verbundenen Nebengesteinsalteration vorherrschte, kann anhand der relativen Stabilitäten der in den Proben auftretenden Minerale vorgenommen werden. Detaillierte Untersuchungen an aktiven Geothermalsystemen an Land haben gezeigt, dass di- und trioktaedrische Smektiten nur bei relativ niedrigen Temperaturen stabil sind. In einem Temperaturbereich von 150 bis 200°C kommt es zu einer Umwandlung dieser Phasen in Illit bzw. Chlorit (Simmons und Browne, 2000). Aufgrund der Stabilitätsgrenze von Smektit muss daher davon ausgegangen werden, dass die in großen Teilen des Gipfelbereiches des Conical Seamount auftretende hydrothermale Alteration bei relativ niedrigen Temperaturen abgelaufen ist. Die Alteration scheint in einem leicht sauren bis alkalischen Milieu erfolgt zu sein, da Indikatorminerale für extrem saure Bedingungen wie Alunit, Kaolinit und Zunyit [13] in den Bohrproben nicht angetroffen wurden (White und Hedenquist, 1995). Das gehäufte Auftreten von Sulfiden und das Fehlen sekundärer Sulfate und Oxide zeigt, dass die hydrothermale Alteration in einem relativ reduzierenden Umfeld stattgefunden hat.



Abb. 6: Dendrogramm der verschiedenen Alterationsgruppen als Ergebnis der röntgenographischen Untersuchungen. Sulfidführende, propylitisch alterierte Proben sind durch das Auftreten von Pyrit und Markasit gekennzeichnet, während die argillischen Proben vermehrt Smektit führen.

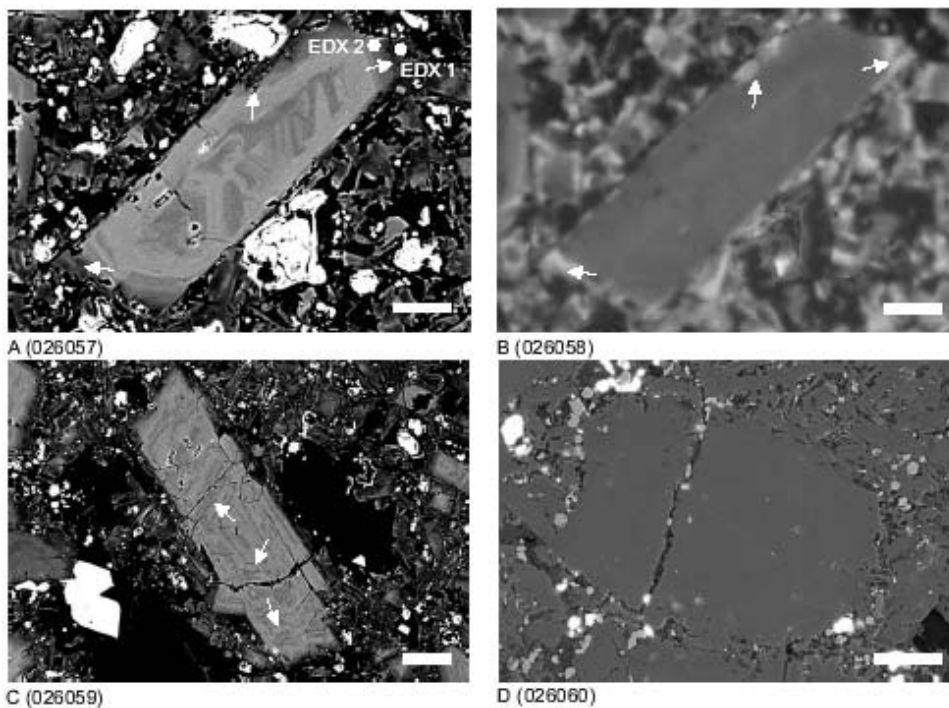


Abb. 7: REM-Aufnahmen von Alterationserscheinungen an Feldspat der Probe 08RD70-80. A) Alterierter Plagioklas mit interner Zonierung. Die randliche Alteration geht mit einer Albitisierung des Feldspats einher. (BSE; Maßstab= 30µm). B) Kathodolumineszenzbild des Plagioklaskristalls in A. Die alterierten Bereiche (Pfeile) zeigen eine deutliche Lumineszenz (CL; Maßstab=30µm). C) Ungewöhnlich gebogene Zonierungen (Pfeile) in Plagioklas (BSE; Maßstab=50µm). D) Alterierter Plagioklas mit irregulärer Kornform in einer Matrix aus Glas, Sanidin und Plagioklas (SE; Maßstab=50µm).

Abschlussbericht CONDRILL (03G0166)
 Detailuntersuchung der magmatisch-hydrothermalen Goldvererzung des Conical Seamount
 (Papua-Neuguinea) mit Flachbohrungen

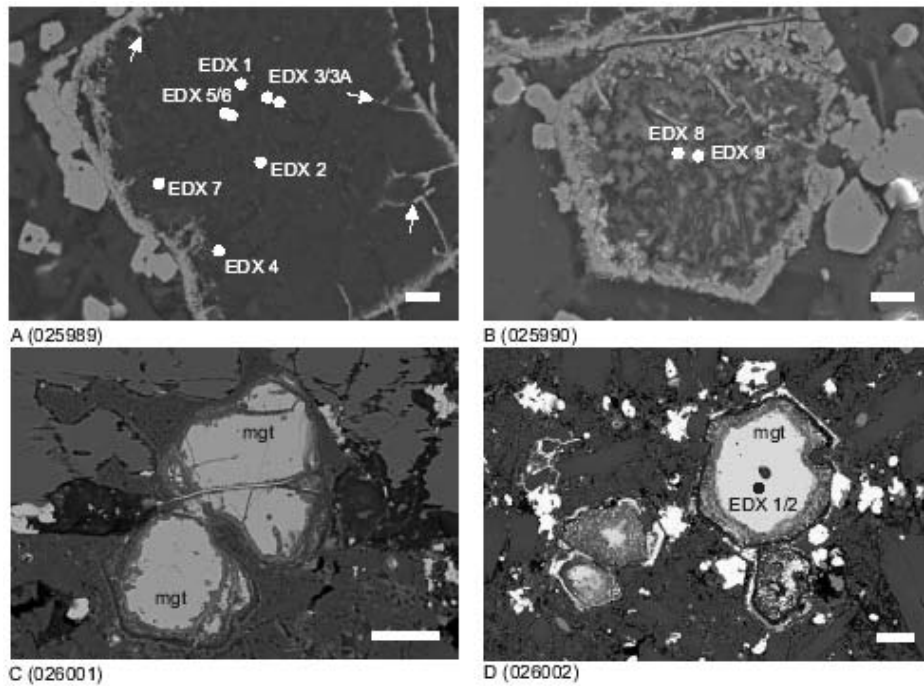


Abb. 8: REM-Aufnahmen von Alterationserscheinungen an Magnetit. A) Pyrit verdrängt Magnetit entlang von Rissen (Pfeile). Der Kernbereich dieser Magnetitkristalle ist in TiO_2 angereichert (BSE; Probe 08RD70-80; Maßstab= 10 μ m). B) Komplett zersetzter Magnetit (BSE; Probe 08RD70-80; Maßstab=10 μ m) C) Magnetit wird entlang von Rissen ersetzt (BSE; Probe 18RD45-55; Maßstab=50 μ m). D) Teilweise ersetzter Magnetit mit Anreicherung von TiO_2 , Al_2O_3 und MgO (BSE; Probe 18RD45-55; Maßstab=30 μ m).

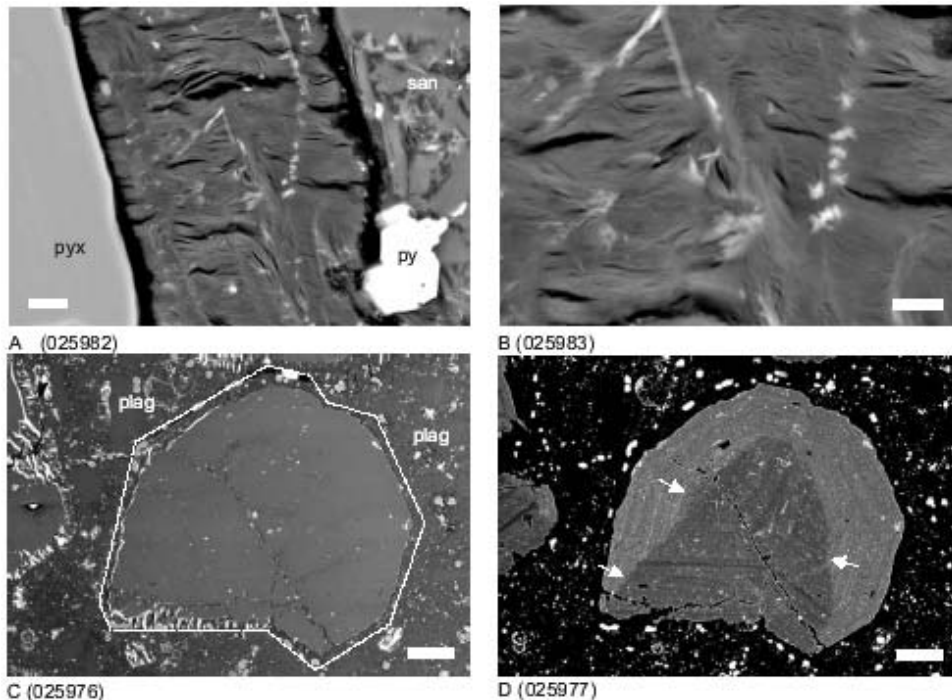


Abb. 9: REM-Aufnahmen von Alterationserscheinungen an Pyroxenen der Probe 08RD70-80. A) Oberflächenveränderung von Pyroxenen (pyx) in Smektit. Die Matrix zeigt Pyrit (py) und Sanidin (san). (BSE; Maßstab= 10 μ m). B) Detailaufnahme des Smektit (BSE; Maßstab=5 μ m) C) Partiiell alterierter Pyroxen in einer Matrix mit Plagioklas (plag). (SE; Maßstab=50 μ m). D) Gleicher Kristall. Auffällig sind die ausgeprägte Oszillationszonierung und die Sektorzonierung, die von der Alteration beeinflusst werden (BSE; Pfeile; Maßstab=30 μ m).

PACMANUS Hydrothermalfeld

Zweiter Schwerpunkt der Arbeiten der Freiburger Arbeitsgruppe war die Bearbeitung der geborgenen Kerne aus dem PACMANUS Gebiet (Abb. 10). Insgesamt konnten während der Forschungsfahrt 8,8 m Massivsulfide aus dem Bereich des Roman Ruins Hydrothermalfeldes beprobt werden (Abb. 11). Die Proben aus dem Untergrund des Hydrothermalfeldes unterscheiden sich deutlich von den bisher bekannten Massivsulfiden, wie sie mit TV-Greifern und Tauchbooten vom Meeresboden gewonnen wurden (Moss und Scott, 2001). Zwar werden die Proben ebenfalls von Chalkopyrit und Sphalerit dominiert, jedoch treten Fahlerze und Bornit in den Bohrproben mengenmäßig deutlich zurück. Das Auftreten von Anhydrit in mehreren Bohrkernen zeigt eine deutliche Zumischung von Meerwasser im oberflächennahen Bereich an. Die Untersuchung der Sr- und S-Isotopenverhältnisse dieser sulfatreichen Proben zeigt neben einer Beteiligung von Sulfat aus dem Meerwasser auch eine Zumischung von oxidiertem Schwefel oder magmatische SO_2 an (siehe unten). Ein Teil der Bohrkerne zeigt Texturen, die für die Resedimentation der Sulfide sprechen und ein deutliches Indiz für mehrere Episoden hydrothermalen Aktivität sind. Diesem Hinweis wurde, in Zusammenarbeit mit Dr. Jan Scholten (Institut für Geowissenschaften, Universität Kiel) durch Altersdatierungen an ausgewählten Proben nachgegangen (siehe hierzu Auszug aus der Diplomarbeit T. Ihle). Dabei hat sich gezeigt, dass die Massivsulfide über einen Zeitraum von ca. 2000 Jahren abgesetzt wurden. Die geringen Konzentrationen an Uran in einigen der Proben ermöglichten jedoch nur Altersabschätzungen mit einem relativ großen Fehler (siehe Ausschnitt Diplomarbeit T. Ihle).

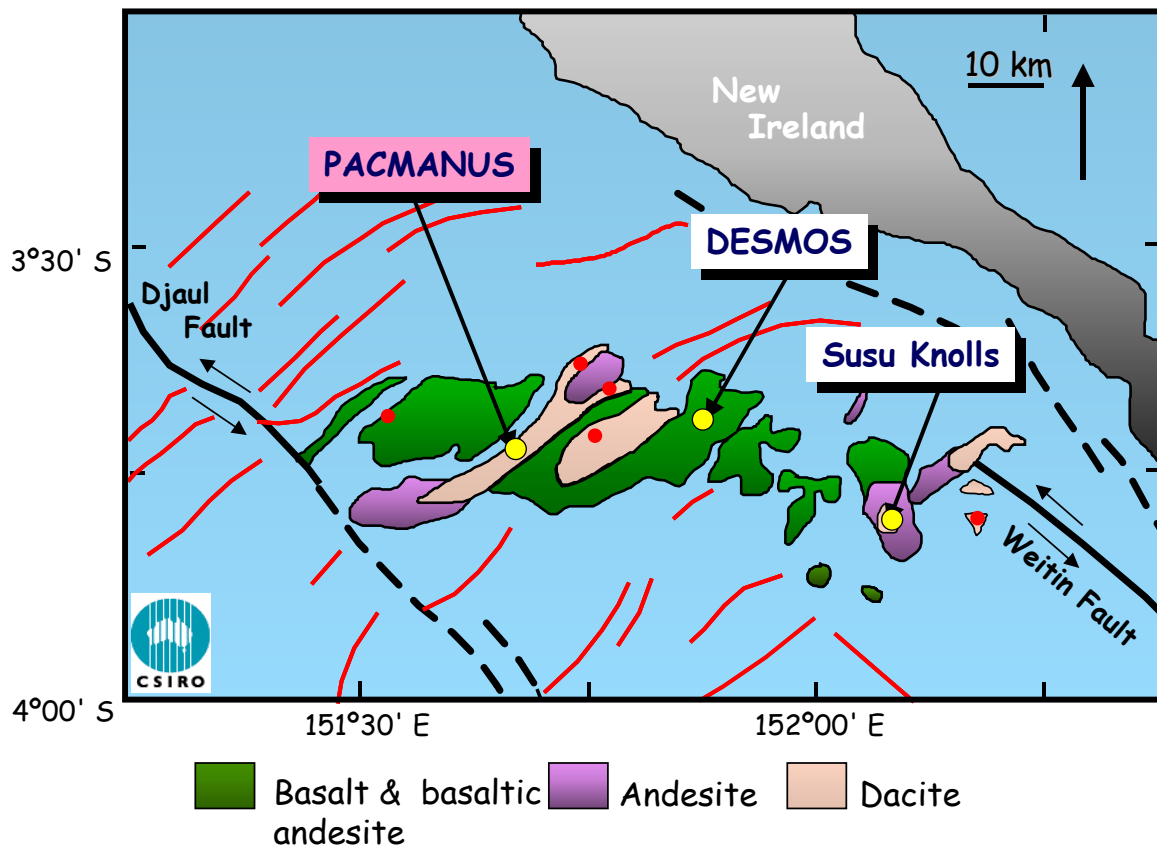


Abb. 10: Submarine Hydrothermalsysteme im östlichen Manus Becken. All 3 Felder wurden während SO166 mindestens mit einer Kernbohrung untersucht, allerdings konnten nur im Bereich des PACMANUS Hydrothermalfeldes Sulfide erbohrt werden (verändert nach Binns et al., 2002).

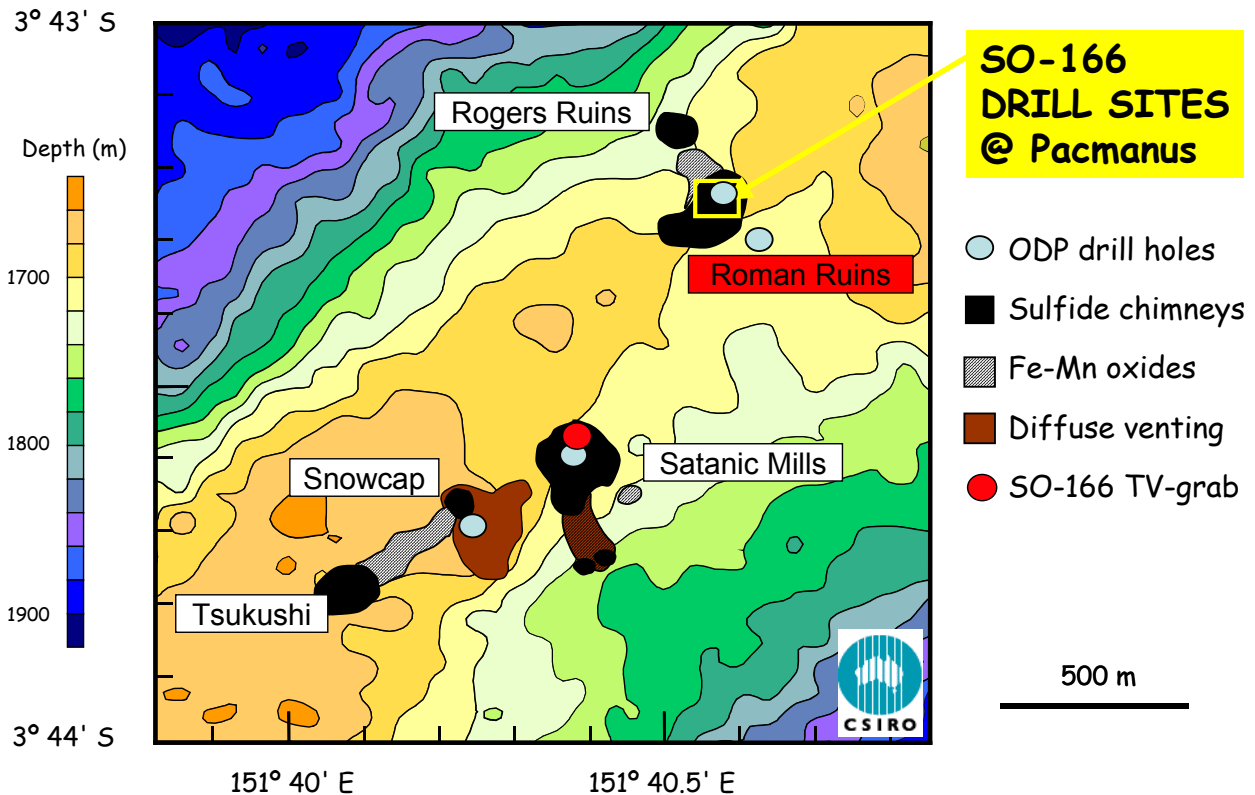


Abb. 11: Detaillierte Bathymetrie des PACMANUS Hydrothermalfeldes mit der Lage der verschiedenen Hydrothermalgebiete und dem Bohrgebiet innerhalb von Roman Ruins (verändert nach Binns et al., 2002).

Die geochemischen Analysen der Massivsulfidkerne zeigen insgesamt sehr hohe Gehalte an Kupfer, Zink, Blei, Gold und Silber, aber auch Arsen und Antimon sind deutlich angereichert. Die höchsten Bunt- und Edelmetallgehalte wurden im Kern 65RD gemessen, der, bei einer Kernlänge von 0,4 Metern, durchschnittlich 35 ppm Au, 240 ppm Ag, 7,1 Gew.% Cu, 26,6 Gew.% Zn und 0,6 Gew.% Pb aufweist (siehe Petersen et al im Anhang; Tabelle 1 und 2). Eine 20 cm mächtige Lage aus Chalkopyrit im Bereich von 10-30 cm Teufe ist sogar durch Gehalte von 57 ppm Au gekennzeichnet. Auch der längste Kern (69RD) weist, bei einer Kernlänge von insgesamt 2,2 Metern, hohe Bunt- und Edelmetallgehalte auf. Die Durchschnittsgehalte für diesen Kern liegen bei 11,3 ppm Au, 160 ppm Ag, 2,4 Gew.% Cu, 26,0 Gew.% Zn und 0,9 Gew.% Pb. Im Gegensatz zu publizierten Daten, die eine positive Korrelation von Gold mit Kupfer aufweisen, zeigen die Bohrkernproben eine positive Korrelation von Gold mit Zink. In einigen Kernen konnte eine Änderung in der Sulfidzusammensetzung mit der Tiefe beobachtet werden. So nehmen die Konzentrationen der Elemente Au, Ag, As, Cd, Ga, Pb, Sb und Zn mit der Tiefe ab. Diese Elementanreicherung im oberflächennahen Bereich ist vermutlich das Ergebnis episodischer hydrothermalen Aktivität, die zur Remobilisation dieser Elemente, zum Transport an die Oberfläche und dort zum Widerabsatz führt. Dieser Prozess des "zone refining" wurde auch bei den Untersuchungen des TAG Hydrothermalfeldes nachgewiesen (Petersen et al., 2000) und scheint ein verbreiteter Prozess zu sein, der die Geochemie solcher Hydrothermalvorkommen noch während ihrer Bildung beeinflusst.

Die Beprobung von hochtemperierten Austrittsstellen im Bereich des PACMANUS Hydrothermalfeldes (Satanic Mills und Roman Ruins) durch den TV-Greifer erlaubt zusätzlich einen Vergleich zwischen diesen beiden Vorkommen. Dazu wurden neben den geochemischen Untersuchungen an Gesamtsulfiden auch Mikrosondenmessungen und

Abschlussbericht CONDRILL (03G0166)
Detailuntersuchung der magmatisch-hydrothermalen Goldvererzung des Conical Seamount
(Papua-Neuguinea) mit Flachbohrungen

die Schwefelisotopenwerte der Sulfide herangezogen. Die Sulfide von Satanic Mills sind durch niedrigere Schwefelisotopenverhältnisse gekennzeichnet ($-1,1$ bis $0,2$ ‰ $\delta^{34}\text{S}$, $N=9$), als diejenigen von Roman Ruins ($0,0$ bis $3,0$ ‰ $\delta^{34}\text{S}$, $N=10$; Abb. 12) und scheinen einen erhöhten Eintrag an magmatischem Schwefel (Disproportionierung von SO_2) in Satanic Mills anzudeuten. Dies steht im Einklang mit den erhöhten Gehalten an typisch "magmatogenen" Elementen wie As, Bi, Hg, In, Sb, Sn und Te in den Erzen von Satanic Mills im Vergleich zu den Proben von Roman Ruins (bis zu $6,2$ Gew. % As, 145 ppm Bi, 78 ppm Hg, 341 ppm In, 9500 ppm Sb, 432 ppm Sn und 39 ppm Te in den Sulfiden von Satanic Mills).

Tabelle. 1: Geochemie von Massivsulfidbohrkernen aus dem Roman Ruins Gebiet, PACMANUS.

core	section	Cu	Zn	Pb	Fe	Ca	Ba	SiO ₂	Au	Ag	As	Bi	Cd	Co	Ga	Hg	In	Mo	Ni	Sb	Se	Sn	Te	Tl		
		wt.%								ppm																
SO166-60RD	0-30 cm	4.6	18.1	0.56	21.9	0.1	6.6	6.1	12.35	112	2655	1.0	636	4	99	2	28	73	16	421	<3	3	<0.2	97		
	30-60 cm	8.3	1.5	0.08	26.1	7.6	1.3	<0.5	1.46	5	1855	16.0	23	35	3	<1	7	103	14	24	24	3	2.5	73		
	60-90 cm	6.2	0.7	0.03	25.3	10.1	0.5	<0.5	1.15	6	1950	11.0	11	35	3	<1	6	98	13	36	28	3	3.2	97		
SO166-61RD	0-45 cm	1.3	22.4	0.78	4.7	0.1	19.5	12.3	8.26	188	1615	0.7	759	1	50	<1	7	29	<10	600	<3	1	<0.2	71		
	45-90 cm	3.1	14.5	0.50	6.4	0.1	28.5	7.8	7.89	100	964	4.4	561	3	46	3	10	32	<10	396	<3	3	<0.2	44		
	90-140 cm	0.2	32.1	2.31	2.3	0.1	20.0	5.7	6.10	542	2140	<0.2	762	6	11	14	0.1	6	<10	943	<3	<0.5	<0.2	38		
SO166-63RD	0-50 cm	8.8	12.4	0.54	22.3	4.9	3.0	<0.5	8.05	106	2350	9.2	384	2	33	<1	15	64	<10	362	9	2	0.2	79		
SO166-65RD	0-10 cm	1.6	38.4	0.85	4.1	<0.1	15.0	2.4	16.45	264	2525	<0.2	1100	4	116	6	64	19	<10	764	<3	3	<0.2	37		
	10-30 cm	12.9	12.2	0.13	12.9	<0.1	21.0	1.1	57.15	135	1505	<0.2	550	4	113	<1	109	73	<10	472	<3	7	<0.2	5		
	30-40 cm	1.1	44.7	1.14	3.3	<0.1	9.1	4.5	9.20	410	4715	<0.2	1300	2	101	<1	28	10	<10	1067	<3	1	<0.2	60		
	40-45 cm	9.8	0.1	0.02	<0.1	<0.1	<0.1	0.9	1.07	4	783	1.8	3	6	4	<1	9	46	11	8	6	6	<0.2	36		
SO166-66RD	0-10 cm	0.6	33.1	0.26	6.5	<0.1	14.5	4.9	11.60	394	1825	<0.2	1040	1	39	<1	4	20	<10	855	<3	1	<0.2	30		
	10-30 cm	28.3	0.9	0.02	26.6	<0.1	3.3	0.5	2.39	41	383	5.8	30	2	11	<1	44	55	<10	28	<3	10	<0.2	5		
	30-55 cm	1.2	33.1	0.13	4.6	<0.1	18.0	6.6	28.8	192	766	<0.2	1120	3	148	<1	57	18	17	538	<3	21	<0.2	14		
	55-80 cm	0.5	33.5	0.30	3.8	<0.1	15.0	14.2	27.25	258	810	<0.2	1010	3	77	<1	22	13	<10	613	<3	3	<0.2	10		
SO166-67RD	0-20 cm	0.7	46.6	1.22	3.3	0.5	7.8	1.6	35.80	584	2380	<0.2	1570	1	119	14	4	<5	12	1100	<3	3	<0.2	57		
	20-45 cm	2.7	10.5	1.04	12.7	9.3	5.9	<0.5	8.96	140	1300	0.8	344	2	51	<1	17	36	<10	233	<3	9	<0.2	61		
	45-70 cm,a	2.6	12.4	0.16	8.7	10.7	6.6	<0.5	15.10	233	1100	0.7	457	3	62	<1	16	36	12	219	<3	4	<0.2	52		
	45-70 cm,b	0.5	35.2	0.86	2.3	5.5	11.0	<0.5	15.70	468	1110	<0.2	1050	4	27	<1	0.1	<5	12	707	<3	4	<0.2	19		
	70-80 cm	1.6	14.7	0.07	10.1	11.5	2.4	0.8	10.80	41	761	0.5	555	1	96	<1	22	20	<10	137	<3	5	<0.2	24		
	80-110 cm	5.8	0.4	0.03	23.9	9.4	0.1	<0.5	1.56	6	880	16.0	6	50	4	<1	6	57	<10	16	27	3	1.9	38		
	110-125 cm	4.1	0.2	0.02	28.6	6.9	0.1	0.5	3.11	8	1340	15.0	5	57	7	<1	4	62	<10	16	36	2	2.5	39		
	125-145 cm	3.8	0.2	0.03	22.5	11.6	<0.1	<0.5	1.35	5	759	8.3	4	23	2	<1	4	39	<10	13	19	6	0.6	25		
	145-160 cm	5.0	0.1	0.01	27.3	7.7	<0.1	<0.5	1.75	6	1180	17.0	2	85	3	<1	3	78	<10	10	58	2	1.3	58		
	160-180 cm	3.8	0.1	0.01	31.8	5.4	<0.1	<0.5	2.00	5	1390	23.0	3	120	3	<1	3	110	<10	11	59	2	2.2	66		
180-190 cm	2.7	0.3	0.03	24.8	10.6	<0.1	<0.5	2.20	6	1280	7.3	5	16	3	<1	4	40	<10	17	14	1	0.3	37			
SO166-68RD	0-34 cm	9.2	7.9	0.31	28.2	0.2	2.4	9.6	4.66	72	1915	16.0	243	23	36	<1	18	250	19	207	26	5	4.5	73		
	34-42 cm	0.2	0.2	0.01	32.1	7.0	0.1	<0.5	1.41	2	660	19.0	6	31	1	<1	1	64	22	13	26	1	7.4	31		
SO166-69RD	0-20 cm	0.1	40.2	1.92	5.1	0.1	13.0	<0.5	0.94	32	4960	<0.2	866	<1	38	4	0.2	15	<10	924	<3	<0.5	<0.2	128		
	20-50 cm	5.1	12.1	0.11	25.9	<0.1	10.0	<0.5	11.55	35	2270	3.9	400	4	66	1	22	66	16	273	7	4	<0.2	63		
	50-85 cm	5.9	17.6	1.15	18.3	<0.1	7.2	7.1	13.65	41	2725	1.9	619	2	93	2	40	58	15	548	4	23	<0.2	110		
	85-120 cm	0.4	44.7	0.99	3.8	<0.1	8.2	7.6	30.40	403	1225	<0.2	1520	<1	135	4	7	8	<10	812	<3	7	<0.2	26		
	120-150 cm	0.3	32.3	0.96	2.9	4.2	15.5	<0.5	11.90	216	502	<0.2	1030	2	125	5	24	8	<10	408	<3	24	<0.2	7		
	150-180 cm	3.8	4.2	0.04	10.7	16.4	3.5	1.3	2.44	17	488	1.9	110	6	10	6	10	<1	9	23	<10	44	7	1	<0.2	16
	180-220 cm	0.2	30.0	1.01	2.4	2.8	16.5	5.2	4.05	68	150	<0.2	581	2	6	3	0.3	2	<10	120	<3	5	<0.2	2		

Tabelle. 2: Vergleich der Durchschnittszusammensetzung von Satanic Mills (Oberflächenproben) mit Roman Ruins (Kernproben und Oberflächenproben).

	Cu	Zn	Pb	Fe	Ca	Ba	SiO ₂	Au	Ag	As	Bi	Cd	Co	Ga	Hg	In	Mo	Ni	Sb	Se	Sn	Te	Tl
	wt.%							ppm															
Satanic Mills																							
surface samples																							
N=101 (this study)	10.8	21.1	1.0	8.4	0.2	15.2	5.2	14.64	254	10200	9	694	7	127	19	84	9	<10	1345	6	11	0.7	83
Roman Ruins																							
cores (N=35, this study)																							
	4.2	17.4	0.5	15.1	4.1	8.2	3.0	10.81	156	1580	5	533	15	50	2	18	43	<10	363	11	5	0.8	46
surface samples																							
N=46 (this study)	3.3	19.6	1.0	12.5	3.2	8.4	8.6	10.46	171	1640	4	571	25	44	3	17	35	<10	410	9	5	0.7	52
PACMANUS																							
(N=252)																							
	7.4	22.6	1.2	10.5	0.9	10.3	8.0	13.4	257	6300	7	785	6	99	13	62	22	<10	1010	8	19	3	73

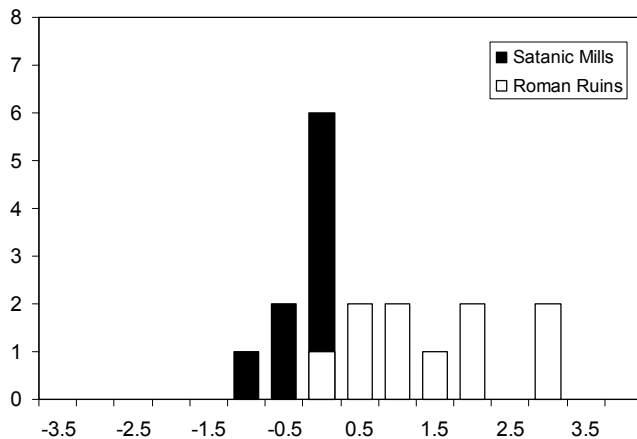


Abb. 12: Schwefelisotopenverhältnisse von Massivsulfiden des PACMANUS Hydrothermalfeldes zeigen deutliche Unterschiede zwischen den beiden hoch-temperierten Massivsulfidlokationen Satanic Mills und Roman Ruins an (n=19).

Verteilung, Mineralogie und Mineralchemie von gediegen Gold

Die mineralogischen Untersuchungen zeigen, dass das Auftreten von Gold im Bereich des PACMANUS Hydrothermalfeldes sehr variabel ist. Deutliche Unterschiede bestehen zwischen den Oberflächenproben von Satanic Mills und den Proben (sowohl Kerne als auch Oberflächenproben) von Roman Ruins (Abb. 13). Während in Oberflächenproben gediegen Gold überwiegend an Cu-As-reiche Mineralparagenesen gebunden ist und als Einschluss in Chalkopyrit aber auch in Fahlerz, Bornit bzw. Digenit auftritt (Abb. 14) liegt das Gold in den Bohrkernproben überwiegend als Einschluss in Sphalerit und seltener in Chalkopyrit, Galenit und auch amorpher Kieselsäure vor (siehe Auszug Diplomarbeit T. Ihle). Dies trifft sowohl auf die Cu-reichen Proben in den Bohrkernen zu, als auch auf die Zn- und Ba-reichen Kernproben zu. Letztere Paragenese ist mit dem Auftreten von Gold in anderen Back-Arc Bereichen des SW-Pazifik (z.B. dem Lau Becken; Herzig et al., 1993) vergleichbar. Unterschiede zwischen Roman Ruins und Satanic Mills spiegeln sich ebenfalls in der Mineralchemie des Goldes wider. Bisherige Untersuchungen waren davon ausgegangen, das gediegen Gold im PACMANUS Hydrothermalfeld sehr rein ist und nur geringe Variationen zwischen den verschiedenen Lokationen vorliegen (Moss und Scott, 2001; Abb. 15a).

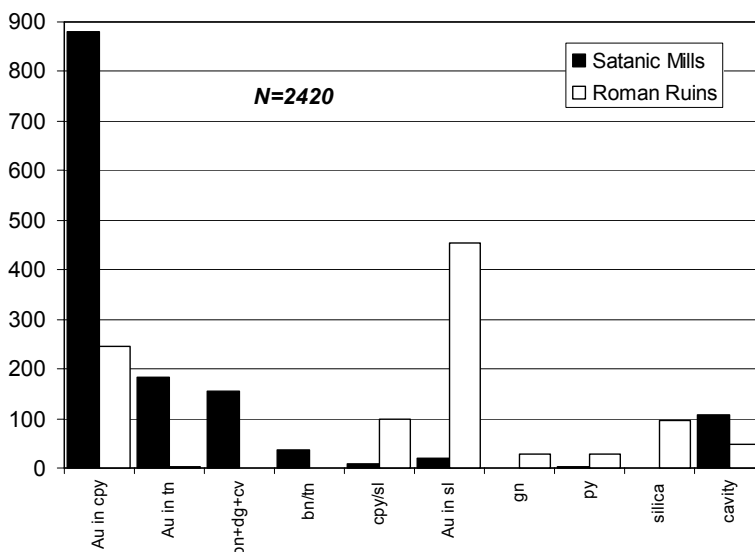


Abb. 13: Häufigkeitsverteilung der Wirtminerale für Gold-Einschlüsse vom PACMANUS Hydrothermalfeld gegliedert nach Hydrothermalgebiet.

Abkürzungen: bn=Bornit, cpy=Chalkopyrit, cv=Covellin, dg=Digenit, gn=Galenit, py=Pyrit, silica=amorphe Kieselsäure, si=Sphalerit, tn=Tennantit.

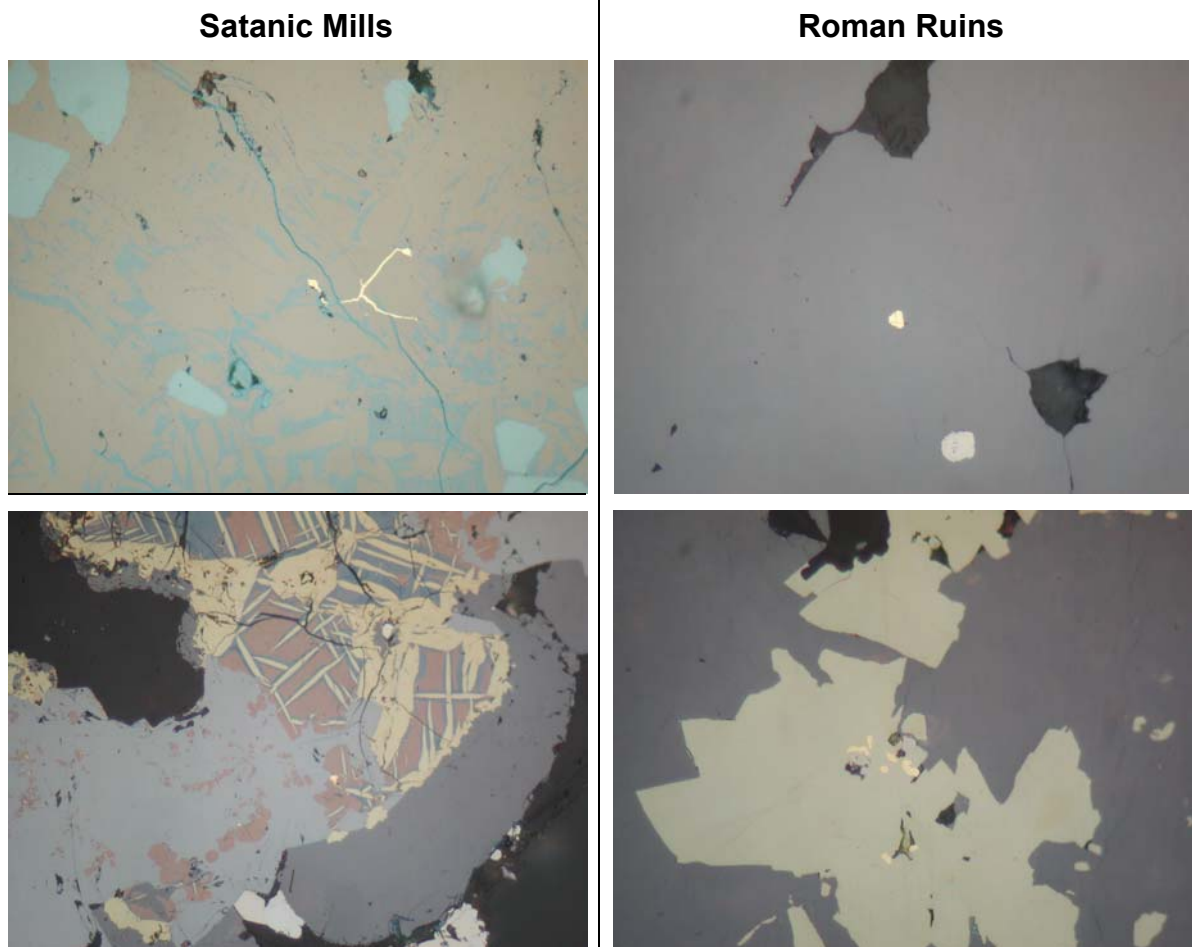


Abb. 14: Unterschiede im Auftreten von gediegen Gold (hellgelb) in Proben aus Satanic Mills und Roman Ruins. In Satanic Mills liegt das Gold überwiegend als Einschluss in Fahlerzen (Cu-As-Sb-Sulfiden), Chalkopyrit oder Cu-reichen Sulfiden wie Bornit und Digenit vor, während Gold in den Proben von Roman Ruins mit Sphalerit (dunkelgrau) und seltener mit Chalkopyrit (gelb) assoziiert ist. Bildbreite ist 150µm in allen Abbildungen.

Mikrosondenanalysen der Bohrkern- und Oberflächenproben der Forschungsfahrt SO166 zeigen dagegen ein viel breiteres Spektrum und deutlich höhere Silbergehalte, wie sie bisher von keiner anderen submarinen Massivsulfidlagerstätte beschrieben worden sind. Darüber hinaus ist gediegen Gold von Roman Ruins im Vergleich zu Gold von Satanic Mills durch deutlich höhere Silbergehalte gekennzeichnet. Während der Silbergehalt in den Proben von Roman Ruins zwischen 1,6 und 16,4 Gew. % Ag liegen (Normiert auf 100%Au+Ag; Mittelwert 8,2 Gew. % Ag, N=107) liegen, weisen die Proben von Satanic Mills eine engeres Spektrum auf (1,1 bis 9,4 Gew. % Ag; Mittelwert 4,0 Gew. % Ag, N=110). Goldanreicherungen in Zn-reichen Mineralparagenesen wurden bisher oft mit Remobilisationprozessen erklärt, bei denen Gold aus früher gebildeten Mineralisationsphasen gelöst, transportiert und wieder abgesetzt wird. Dieser Prozess führt jedoch im Allgemeinen, aufgrund der unterschiedlichen Löslichkeiten von Au und Ag, zu einer Trennung von Ag und Au und einer Erhöhung der Goldreinheit in den sekundären Goldkörnern (Hannington et al., 1991). Dies konnte für eine ganze Reihe von Vorkommen gezeigt werden. Die hier gemessenen stark erhöhten Silbergehalte in den Goldkörnern der Zn-reichen Paragenese sprechen aber deutlich gegen diesen Prozess als Anreicherungs- und Transportprozess für das Gold im Bereich von Roman Ruins.

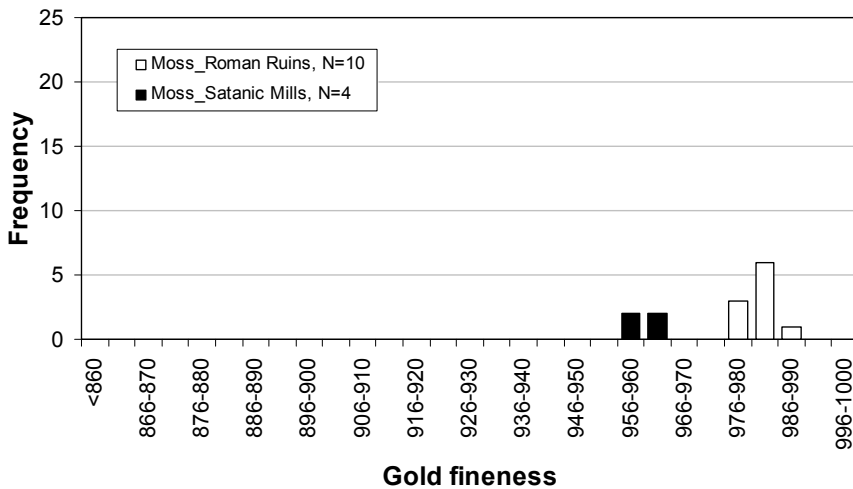


Abb. 15a: Publierte Häufigkeitsverteilung der Goldreinheit in Proben aus dem PACMANUS Hydrothermalfeld (Oberflächenproben, Moss and Scott, 2001; N=14).

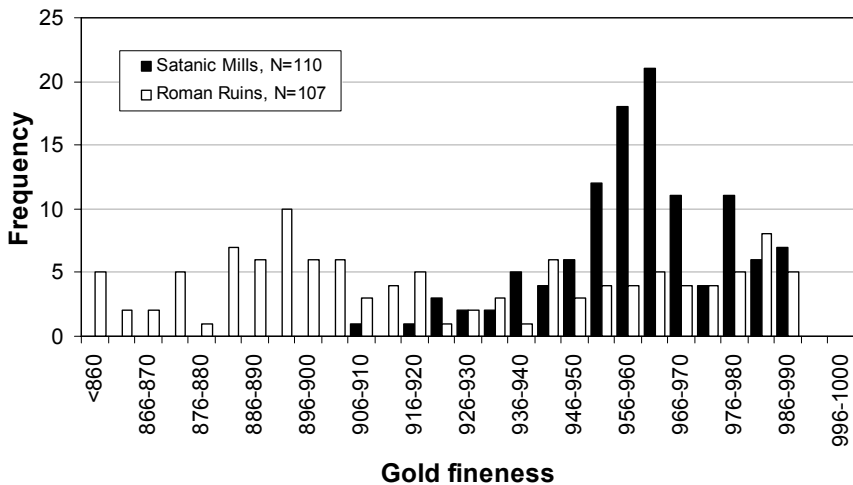


Abb. 15b: Häufigkeitsverteilung der Goldreinheit in Proben aus dem PACMANUS Hydrothermalfeld (Bohrkerne und Oberflächenproben, N=217). Deutlich wird die reduzierte Aussagekraft der publizierten Daten (oben) im Hinblick auf die tatsächlichen Gegebenheiten.

Die konduktive Abkühlung primär an Gold angereicherter Fluide scheint daher der wahrscheinlichste Absatzmechanismus zu sein. Die Reinheit des Goldes in den Cu-reichen Proben und die gleichzeitig niedrigen Fe-Gehalte im Sphalerit zeigen hohe Schwefelaktivitäten in diesen Fluiden an. Diese Fluide müssen auf Temperaturen unterhalb von 150°C abgekühlt worden sein, um das Löslichkeitsmaximum zwischen 250°C und 150°C in sauren, reduzierten Lösungen zu umgehen, wie sie für das Pacmanus Hydrothermalfeld vorliegen. Durch die Abnahme der Temperatur wird die Schwefelaktivität gesenkt, was sich wiederum in den erhöhten Ag-Gehalten des Goldes und in den gleichzeitig erhöhten Fe-Gehalten des assoziierten Sphalerit widerspiegelt.

Die lokale Zumischung von Meerwasser kann ebenfalls zur Destabilisierung der Au-Komplexe beitragen und dieser Prozess wird auch durch das Auftreten von Baryt in einigen Proben angedeutet.

Die detaillierten geochemischen Untersuchungen an einer großen Massivsulfidscheibe (50 x 40 cm) eines inaktiven Schwarzen Rauchers von Satanic Mills erlauben erstmals die Dokumentation der Spurenelementverteilung innerhalb eines gesamten Chimneys und geben Einblicke in die Transportprozesse einzelner Spurenmetalle, wie z.B. In, Bi und andere (Abb. 16; siehe auch Auszug Diplomarbeit A. Gabriel). So zeigt sich hier, dass

Gold im Bereich von Satanic Mills oft an die fokussierten Lösungsbahnen kleinerer Schlotstrukturen gebunden ist (Pfeile in Abb. 15). Allerdings wird hier auch deutlich, dass Abkühlung und/oder eine Zumischung von Meerwasser notwendig sind, um das Gold zu fällen, da die ehemals heißesten Bereiche im Inneren des Schlotes durch „niedrige“ Au-Konzentrationen gekennzeichnet sind. Diese „niedrigen“ Gehalte bewegen sich immer noch im Bereich von 5 bis 10 ppm Au!

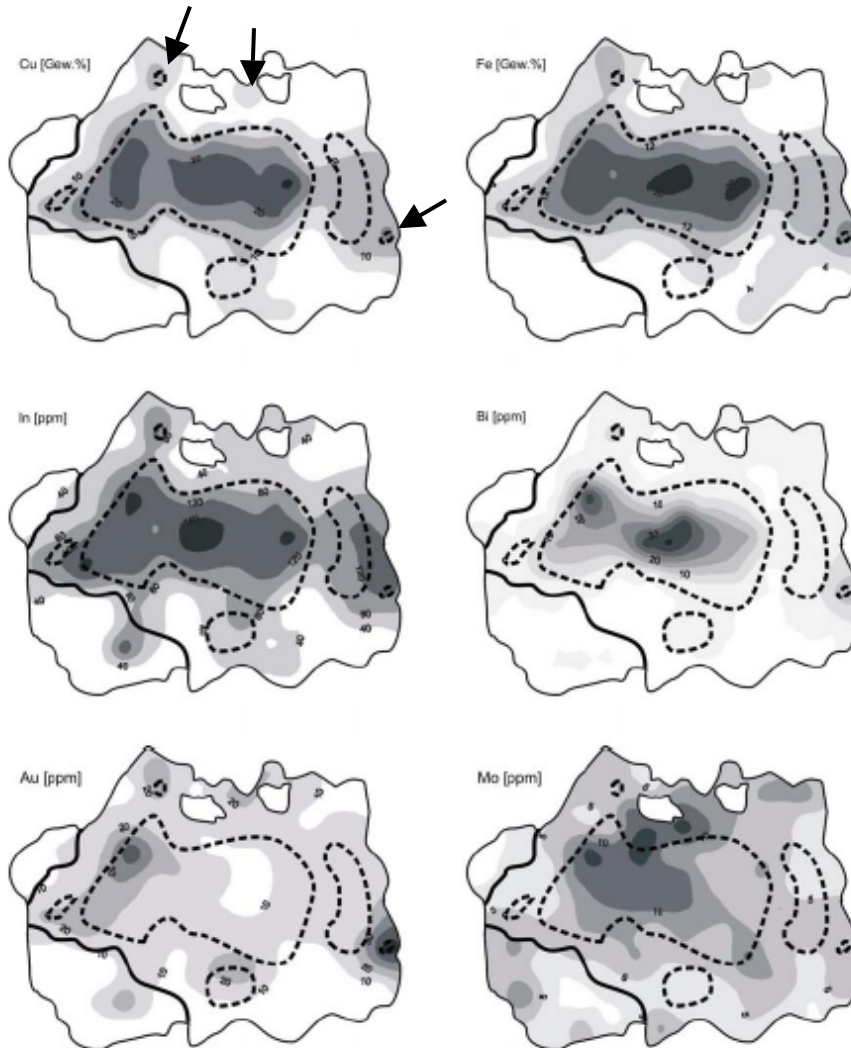


Abb. 16: Ausgewählte Haupt- und Spurenelementverteilung innerhalb einer 50 x 40 cm messenden Massivsulfid-schale eines inaktiven schwarzen Rauchers. Die Karten basieren auf der geochemischen Untersuchung von 85 Bohrkernen (3,2 cm Ø).

Die hier beschriebenen Unterschiede zwischen Satanic Mills und Roman Ruins deuten eventuell auf Unterschiede in den Fluidwegsamkeiten im Untergrund hin. Die Wärmequelle des Pacmanus Hydrothermalfeldes könnte z.B. im Bereich von Snowcap liegen, welches durch das Auftreten von extrem sauren Fluiden gekennzeichnet ist. Vermutlich wird ein Teil der aufsteigenden Lösungen im Untergrund abgelenkt und speist die mehrere hundert Meter auseinander liegenden Raucher von Satanic Mills und Roman Ruins (Abb. 17). Dabei könnte die Nähe des Satanic Mills Feldes zu Snowcap und der postulierten Wärmequelle einen erhöhten Eintrag magmatischer Komponenten erklären, wohingegen Roman Ruins zu weit entfernt ist und überwiegend durch konventionelle Fluide geprägt wird. Permeable Schichten (z.B. resedimentierte Hyaloklastite; Paulick et al., 2004) könnten dabei die bevorzugten Wegsamkeiten für die hydrothermalen Lösungen in diesem Hydrothermalfeld sein (siehe Abb. 17). Diese permeablen Schichten werden lokal von

nichtpermeablen frischem Dazit überdeckt, der möglicherweise für die vermindert auftretende hydrothermale Aktivität im Bereich von Snowcap verantwortlich ist.

Die vorläufigen Altersbestimmungen zeigen, dass Teile des Systems seit ca. 2000 Jahren aktiv sind und während dieser Zeit können sowohl Au und Ag als auch Cu und Zn durch unterschiedliche Prozesse angereichert worden sein. Detaillierte Untersuchungen und eine größere Anzahl an Proben sind notwendig, um die Altersstellung der Sulfide zueinander besser zu verstehen.

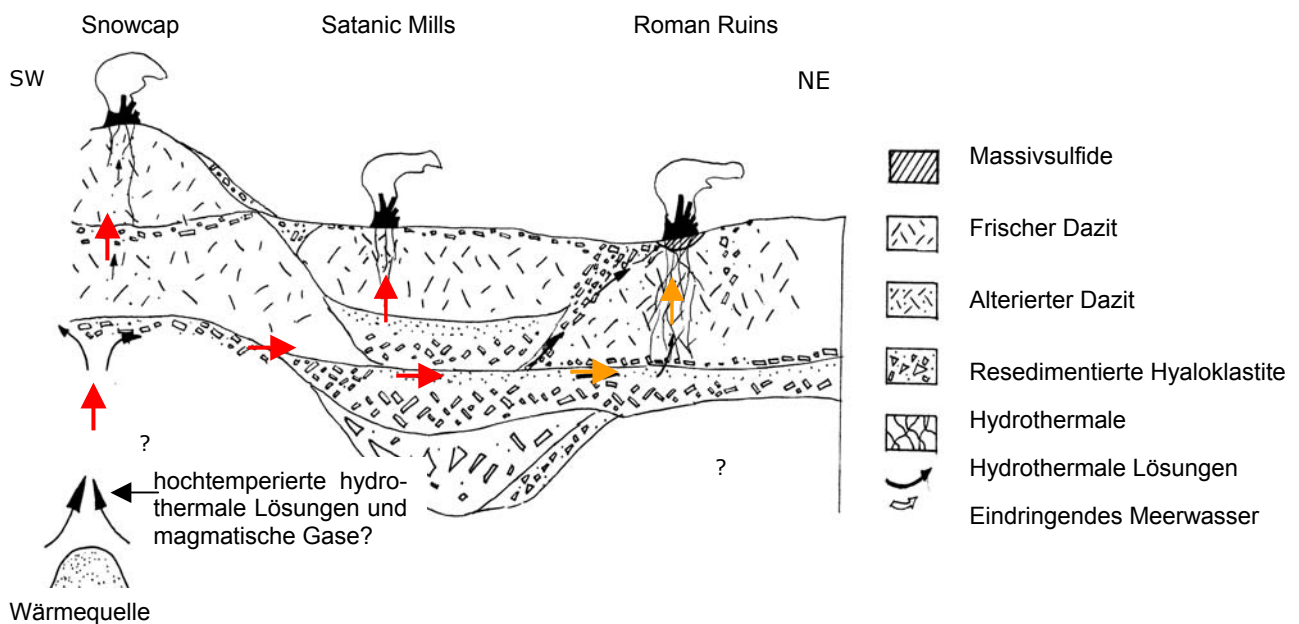


Abb. 17: Vereinfachte Darstellung des Roman Ruins Hydrothermalfeldes mit den unmittelbar benachbarten Hydrothermalfeldern Snowcap und Satanic Mills. Die von den hydrothermalen Lösungen bevorzugten Weggamkeiten befinden sich inmitten der resedimentierten Hyaloklastite. Nebengesteine sind meist alterierte Dazite. Die Wärmequelle wird aufgrund geophysikalischer Daten unterhalb von Snowcap vermutet. Modifiziert nach Paulick et al. (2004) und Lackschewitz et al. (2004). Darstellung ist ohne Maßstab.

Neben den Untersuchungen der Freiburger Arbeitsgruppe wurden durch Dr. R. Binns (CSIRO, North Ryde, Australien) und Dr. J. Pasava (Czech Geological Survey, Prague, Tschechische Republik) weitere Spezialuntersuchungen durchgeführt.

Strontium- und Schwefelisotopenverhältnisse in Sulfaten des PACMANUS Hydrothermalfeldes (Beitrag Dr. R. Binns, siehe Anhang)

Die Untersuchung der Sulfate (Baryt und Anhydrit) aus den Bohrkernen schließt die Lücke zwischen Oberflächenproben und Proben aus dem tieferen Untergrund, die im Rahmen des ODP Leg 193 genommen wurden. Es konnte gezeigt werden, dass die Sr-Isotopenverhältnisse der SO166 Barytproben deutlich weniger radiogen sind als die später gebildeten Anhydrite und auch niedriger sind als die von rezent austretenden hochtemperierten Lösungen (siehe Beitrag Dr. R. Binns, CSIRO). Damit konnte erstmals gezeigt werden, dass sich hydrothermale Lösungen mit der Zeit von weniger radiogenen Fluiden zu Fluiden mit einer deutlichen Meerwassersignatur entwickeln können. Der Anhydrit zeigt darüber hinaus eine deutliche Mischsignatur zwischen hydrothermalen Lösung und Meerwasser.

Die Schwefelisotopenverhältnisse des Anhydrit aus dem Kern 60RD reichen von +20.6 bis +21.1 ‰ $\delta^{34}\text{S}$ und liegen damit nahe der Meerwasserzusammensetzung (+21.0 ‰; Rees et al., 1978). Lediglich die Probe 69RD(148-152) hat leicht erniedrigte $\delta^{34}\text{S}$ -Werte (+20.3‰) gegenüber Meerwasser. Dies könnte auf die Beteiligung von Sulfat hindeuten, das bei der Oxidation von H_2S oder durch die Disproportionierung von magmatischem SO_2 entstanden ist. Da kein isotopisch leichtes Sulfid in diesem Kern beobachtet worden ist, wie es bei der Disproportionierung von SO_2 zu erwarten wäre, erscheint die erste Alternative wahrscheinlicher.

Platingruppenelemente (PGE) in Massivsulfiden des PACMANUS Hydrothermalfeldes (Beitrag Dr. J. Pasava, siehe Manuskript im Anhang)

In Zusammenarbeit mit dem Geologischen Dienst der Tschechischen Republik (Dr. Jan Pasava und Dr. Anna Vymazalova) wurde anhand des vorliegenden Probenmaterials erstmals versucht, die Platingruppenelementführung von Massivsulfiden aus einem Back-Arc Becken zu untersuchen. Auch hier lag die Dokumentation etwaiger Unterschiede zwischen den Massivsulfiden von Satanic Mills und Roman Ruins im Vordergrund. Die Untersuchungen haben zum Einen gezeigt, dass die Massivsulfide des PACMANUS Hydrothermalfeldes insgesamt relativ hohe PGE-Gehalte aufweisen und das zum Anderen Cu-reiche Proben gegenüber Zn-reichen Proben und Sulfide aus dem Satanic Mills Gebiet gegenüber den Proben von Roman Ruins deutlich an Pd und Rh angereichert sind (siehe Publikation Pasava et al 2004; im Anhang). Letzteres wird mit einem eventuellen Eintrag magmatischer Komponenten in das Hydrothermalsystem von Satanic Mills erklärt. Das Fehlen von Pt und Ir in diesen Proben weist auf unterschiedliche Fraktionierungen der PGE's beim Absatz der Sulfide hin, wobei Pd und Rh in den hoch-temperiert gebildeten Chalkopyrit eingebaut werden und das Pt zusammen mit Ir an die Wassersäule verloren gehen.

Literatur

- Binns, R.A., Barriga, F., and Miller, D.J., 2002, Leg 193 summary, in Binns, R.A., Barriga, F.J.A.S., and Miller, D.J., eds., Proceedings of the Ocean Drilling Program, Initial Reports, Volume 193, College Station, TX, p. 1-84.
- Hannington, M.D., Herzig, P.M., and Scott, S.D., 1991, Auriferous hydrothermal precipitates on the modern seafloor, in Foster, R.P., ed., Gold Metallogeny and Exploration: Glasgow, Blackie and Son Ltd, p. 249-282.
- Herzig, P.M., Hannington, M.D., Fouquet, Y., von Stackelberg, U., and Petersen, S., 1993, Gold-rich polymetallic sulfides from the Lau back-arc and implications for the geochemistry of gold in sea-floor hydrothermal systems in the Southwest Pacific: Economic Geology, v. 88, p. 2182-2209.
- Kleeberg, R. und Bergmann, J. (2002) In: Powder diffraction. Proceedings of the II International School on Powder Diffraction (eds. S.P.S. Gupta & P. Chatterjee) 63-76 (Allied Publ., New Delhi, 2002).
- Lackschewitz, K.S., Devey, C.W., Stoffers, P., Botz, R., Eisenhauer, A., Kummert, M., Schmidt, M., and Singer, A., 2004, Mineralogical, geochemical and isotopic characteristics of hydrothermal alteration processes in the active, submarine, felsic-hosted PACMANUS field, Manus Basin, Papua New Guinea: Geochimica et Cosmochimica Acta, v. 68, p. 4405-4427.
- Monecke, T., Köhler, S., Kleeberg, R., Herzig, P.M., Gemmell, J.B. (2001) Quantitative phase-analysis by the Rietveld method using X-ray powder-diffraction data: Application to the study of alteration halos associated with volcanic-rock-hosted massive sulfide deposits. Canadian Mineralogist 39: 1617-1633.
- Moss, R., and Scott, S.D., 2001, Geochemistry and mineralogy of gold-rich hydrothermal precipitates from the Eastern Manus Basin, Papua New Guinea: Canadian Mineralogist, v. 39, p. 957-978.
- Paulick, H., Vanko, D.A., and Yeats, C.J., 2004, Drill core-based facies reconstruction of a deep-marine felsic volcano hosting an active hydrothermal system (Pual Ridge, Papua New Guinea, ODP Leg 193): Journal of Volcanology and Geothermal Research, v. 130, p. 31-50.
- Petersen, S., Herzig, P.M., and Hannington, M.D., 2000, Third dimension of a presently forming VMS deposit: TAG hydrothermal mound, Mid-Atlantic Ridge, 26°N: Mineralium Deposita, v. 35, p. 233-259.

Rees, C.E., Jenkins, W.J., and Monster, J., 1978, The sulphur isotopic composition of ocean water sulphate: *Geochimica et Cosmochimica Acta*, v. 42, p. 377-381. Simmons, S.F., Browne, P.R.L. (2000) Hydrothermal minerals and precious metals in the Broadlands-Ohaaki Geothermal System: Implications for understanding low-sulfidation epithermal environments. *Economic Geology* 95: 971-999.
White, N.C., Hedenquist, J.W. (1995) Epithermal gold deposits: Styles, characteristics and exploration. *Society of Economic Geologists Newsletters* 23: 1-13.

II. 2. Verwertung der Ergebnisse

Eine unmittelbare wirtschaftliche Verwertungsmöglichkeit der erzielten Ergebnisse ist nicht gegeben.

II. 3. Fortschritt auf dem Gebiet des Vorhabens bei anderen Stellen

Für das Vorhaben relevante Ergebnisse von dritter Seite sind in der Zwischenzeit nicht bekannt geworden.

II. 4. Geplante Veröffentlichungen

Neben den unten angeführten Publikationen und Kurzfassungen sind folgende weitere Publikationen in Vorbereitung.

- Alterationsbedingungen im Bereich des Conical Seamount (in Zusammenarbeit mit Dr. T. Monecke; Geological Survey of Canada)
- Geochemie frischer und alterierte Gesteine des Conical Seamount
- Die Ergebnisse zur Verteilung von Gold in Satanic Mills und Roman Ruins sowie Untersuchungen zu den möglichen Transportprozessen
- Haupt- und Spurenelementkartierung eine inaktiven Chimneystruktur von Satanic Mills
- Altersdatierung der Massivsulfide von PACMANUS (in Zusammenarbeit mit Dr. J. Scholten; Universität Kiel)

Liste der im Rahmen des Projektes CONDRILL bisher entstandenen Publikationen (siehe Anhang)

Referierte Manuskripte

Monecke, T., Giorgetti, G., Scholtysek, O., Kleeberg, R., Götze, J., Hannington, M.D., Petersen, S. und Herzig, P.M. (submitted) Textural and mineralogical changes associated with the incipient hydrothermal alteration of glassy dacite at the submarine PACMANUS hydrothermal system, Eastern Manus Basin.

Petersen, S., Herzig, P.M., Kuhn, T., Monecke, T., Franz, L., Hannington, M.D. und Gemmill, J.B. (accepted Marine Georesource and Geotechnology) Shallow drilling of seafloor hydrothermal systems using the BGS Rockdrill: Conical Seamount (New Ireland Fore-Arc) and PACMANUS (Eastern Manus Basin), Papua New Guinea. *Marine Georesources and Geotechnology*.

Pasava, J., Vymazalova, A., Petersen, S. und Herzig, P. (2004) PGE distribution in massive sulfides from the PACMANUS hydrothermal field, eastern Manus basin, Papua New Guinea: implications for PGE enrichment in some ancient volcanogenic massive sulfide deposits. *Mineralium Deposita*, 39(7):784-792.

Andere

Freiberg University and Geological Survey of Canada (2004) Colour-shaded bathymetry, Lihir Island Group, New Ireland Basin, Papua New Guinea (compilation of data from SO-94, SO-133 and SO-166 bathymetric mapping). Geological Survey of Canada, Open File 3831, Map, 1 sheet.

Herzig, P.M., Petersen, S., Kuhn, T., Hannington, M.D., Gemmill, J.B., Skinner, A.C. und Shipboard Scientific Party (2003) Shallow drilling of seafloor hydrothermal systems using R/V SONNE and the BGS

Abschlussbericht CONDRILL (03G0166)
Detailuntersuchung der magmatisch-hydrothermalen Goldvererzung des Conical Seamount
(Papua-Neuguinea) mit Flachbohrungen

Rockdrill: Conical Seamount (New Ireland Fore-Arc) and PACMANUS (Eastern Manus Basin), Papua New Guinea, InterRidge News, 12(1): p. 22-25.

Kurzfassungen

- Monecke, T., Hannington, M.D., Petersen, S., Herzig, P.M., and Kleeberg, R. (2005) Low-temperature hydrothermal alteration at Conical Seamount, Papua New Guinea. GAC-MAC-CSPG-CSSS Joint Meeting, 15.-18. May 2005, Halifax, Nova Scotia, Canada: p. 133.
- Ihle, T., Petersen, S., Herzig, P.M. und Hannington, M.D. (2005) Siting of gold and characteristics of gold-bearing massive sulfides from the interior of the felsic-hosted PACMANUS massive sulfide deposit, Eastern Manus basin (PNG). Proceedings of the 8th biennial SGA meeting Beijing, China: (accepted).
- Petersen, S., Kuhn, T., Scholten, J., Hannington, M.D. und Herzig, P. (2005). Hydrothermale Prozesse und magmatische Einträge im PACMANUS Hydrothermalfeld, östliches Manus Becken (PNG). BMBF Statusseminar, Meeresforschung mit FS Sonne: p. 151-154.
- Monecke, T., Petersen, S., Kleeberg, R., Hannington, M.D. und Herzig, P.M. (2005). Mineralogische Untersuchungen an den hydrothermal alterierten Nebengesteinen der flachmarinen Goldvererzung des Conical Seamount, Papua Neuguinea. BMBF Statusseminar, Meeresforschung mit FS Sonne: p. 139-142.
- Petersen, S., Herzig, P.M., Hannington, M.D. und Gemmill, J.B. (2003) Gold-rich massive sulfides from the interior of the felsic-hosted PACMANUS massive sulfide deposit, Eastern Manus Basin (PNG). In Eliopoulos, D.G. et al., Mineral Exploration and Sustainable Development, Proceedings of the 7th biennial SGA meeting Athens, Greece: 171-174.
- Monecke, T., Petersen, S., Petzold, R., Kleeberg, R. und Herzig, P.M. (2003) Shallow submarine gold mineralization at Conical Seamount, Papua New Guinea: Initial results of an alteration study. In Eliopoulos, D.G. et al., Mineral Exploration and Sustainable Development, Proceedings of the 7th biennial SGA meeting Athens, Greece: 155-158.
- Herzig, P.M., Petersen, S., Kuhn, T., Hannington, M.D., Gemmill, J.B. und Skinner, A.C. (2003) Shallow drilling of seafloor hydrothermal systems: the missing link. In Eliopoulos, D.G. et al., Mineral Exploration and Sustainable Development, Proceedings of the 7th biennial SGA meeting Athens, Greece: 103-105.
- Petersen, S., Herzig, P.M., Hannington, M.D. und Kelley, D.S. (2003) Diversity of seafloor hydrothermal systems on sediment-free mid-ocean ridges. Geological Society of America Annual Meeting 2003, Seattle, Abstracts with Program, v.35(6), paper 1-2.
- Hannington, M.D., de Ronde, C. und Petersen, S. (2003) The spectrum of ore-forming fluids in the VMS environment: modern and ancient. Geological Society of America Annual Meeting 2003, Seattle, Abstracts with Program, v.35(6), paper 1-1.
- Kuhn, T., Hannington, M., Petersen, S. und Herzig, P. (2003) Meeresbodenkartierung in der Umgebung von Lihir Island (Papua-Neuguinea) mit der Fächerecholotanlage auf FS Sonne während der Fahrten SO-94, SO-133 und SO-166: 3D-Modellierung der bathymetrischen Daten und tektonische Interpretation. BMBF Statusseminar, Meeresforschung mit FS Sonne: p. 281-284.
- Herzig, P.M., Hannington, M.D., Petersen, S. und Kuhn, T. (2003) Shallow drilling of seafloor hydrothermal systems: the missing link. BMBF Statusseminar, Meeresforschung mit FS Sonne: p.143-144.
- Herzig, P.M., Hannington, M.D., Petersen, S. und Kuhn, T. (2002) Shallow drilling of seafloor hydrothermal systems: the missing link. Underwater Mining Institute, Auckland, Newzealand.

Öffentlichkeitsarbeit

Die Forschungsfahrt wurde in verschiedenen regionalen und überregionalen Zeitungen der breiten Öffentlichkeit vorgestellt.

Sächsische Zeitung vom 13.09.2002
Freie Presse vom 17.09.2002
Wochenspiegel vom 18.09.2002
Leipziger Volkszeitung vom 20.09.2002
Wochenspiegel vom 09.10.2002
Sächsische Zeitung vom 24.10.2002
Wochenspiegel vom 30.10.2002

Abschlussbericht CONDRILL (03G0166)
Detailuntersuchung der magmatisch-hydrothermalen Goldvererzung des Conical Seamount
(Papua-Neuguinea) mit Flachbohrungen

Wochenspiegel vom 03.01.2003
Stern vom 03.02.2003
Kieler Nachrichten vom 04.02.2003
Vogtlandanzeiger vom 04.02.2003
Rheinische Post vom 05.02.2003
Dresdener Neueste Nachrichten vom 05.02.2003
Financial Times Deutschland vom 13.02.2003
Züricher Sonntagszeitung vom 03.03.2003
Westdeutsche Allgemeine Zeitung vom 08.03.2003

Darüber hinaus wurden ein 45-minütiger bzw. ein 5-minütiger Fernsehbeitrag von der Deutschen Welle ausgestrahlt.

Dem Anhang sind 3 Publikationen beigelegt, die Ergebnisse der vorherigen Forschungsfahrten SO94 und SO133 berücksichtigen und seit der Abgabe des Abschlussberichtes von SO133 (03G0133) erschienen sind.

- Gemmell, J.B., Sharpe, R., Jonasson, I.R., and Herzig, P.M. (2004) Sulfur isotope evidence for magmatic contributions to submarine and subaerial gold mineralization: Conical Seamount and the Ladolam gold deposit, Papua New Guinea: *Economic Geology*, v. 99, p. 1711-1725.
- Müller, D., Franz, L., Petersen, S., Herzig, P.M., and Hannington, M.D. (2003) Comparison between magmatic activity and gold mineralization at Conical Seamount and Lihir Island, Papua New Guinea: *Mineralogy and Petrology*, v. 79, p. 259-283.
- Petersen, S., Herzig, P.M., Hannington, M.D., Jonasson, I.R., and Arribas, A.J. (2002) Submarine vein-type gold mineralization near Lihir island, New Ireland fore-arc, Papua New Guinea: *Economic Geology*, v. 97, p. 1795-1813.

III. Erfolgskontrollbericht

III. 1. Beitrag zu den förderpolitischen Zielen

In den Programmen zur Meeresforschung der Bundesregierung ist das „Meer als Ressourcenquelle“ ausdrücklich hervorgehoben. Dabei wird insbesondere auf die Verbesserung der Grundlagenkenntnisse und die Erforschung und Bewertung mariner Ressourcen hingewiesen. Darüber hinaus dienen die Untersuchungen der dritten Dimension von Hydrothermalsystemen dem besseren Verständnis der Wechselwirkungen zwischen Erdkruste, Hydrosphäre und Atmosphäre.

III. 2. Wissenschaftlicher und technischer Erfolg

- Erstmaliger Einsatz des mobilen BGS-Rockdrill auf einen deutschen Forschungsschiff.
- Hinweise auf eine flächenmäßig größere und in die Tiefe reichende Ausdehnung der bekannten Goldmineralisation am Conical Seamount.
- die Beprobung extrem bunt- (Cu, Zn) und edelmetallreicher (Au, Ag) Massivsulfide unterhalb des Meeresbodens im Bereich des PACMANUS Hydrothermalfeldes, die dieses Vorkommen auch aus wirtschaftlicher Sicht interessant machen können.
- Hinweise auf episodische hydrothermale Aktivität und Umlagerungsprozesse im PACMANUS Hydrothermalfeld.
- Differenzen in Geochemie, Mineralogie und Isotopie der PACMANUS Vererzung die auf kleinräumig wechselnde Fluidzusammensetzungen hindeuten (z.B. durch einen unterschiedlichen magmatischen Eintrag von Metallen in den verschiedenen Bereichen des PACMANUS Hydrothermalfeldes).

III. 3. Fortschreibung des Verwertungsplans / Erfindungen und Schutzrechtanmeldungen

Keine

III. 4. Arbeiten, die zu keiner Lösung geführt haben

Keine

III. 5. Präsentationsmöglichkeiten

Keine

III. 6. Einhaltung der Ausgaben- und Zeitplanung

Der Finanzierungs- und Zeitplan wurde eingehalten. Für die Beschaffung wurden die Richtlinien des Landes Sachsen beachtet. Der Verwendungsnachweis und die Schlussrechnung sind dem Projektträger zugegangen.

Beitrag
Dr. Ray Binns

Strontium and Sulfur Isotopes in Anhydrite and Barite from CONDRILL cores at PACMANUS, Eastern Manus Basin, Papua New Guinea

R. A. Binns

Commonwealth Scientific and Industrial Research Organisation (CSIRO), Division of Exploration and Mining, PO Box 136, North Ryde NSW 1670, Australia
and
Department of Earth and Marine Sciences, Australian National University, Canberra ACT 0200, Australia

Methods

The eight samples provided as small slices or fillets of core (Table 1) were first examined by stereomicroscope, and various portions were crushed and mounted in refractive index oils to determine the relative distribution of barite and anhydrite. Five representative samples were used to prepare concentrates for isotope analysis, and polished thin sections were prepared from four of these in order to assess paragenetic relationships. Anhydrite concentrates were obtained by initial hand picking followed by gentle grinding under acetone, then further hand picking to remove remaining sulfides, and finally by brief treatment in boiling water to remove any secondary gypsum. Fractions essentially free from sulfide inclusions (<0.5%) were used for sulfur and strontium isotope analysis, except for 148516A-2 where ~15% of tiny sulfide inclusions remained in the Sr isotope fraction. Concentrates were examined optically to check for presence of other sulfates. Only 148517A (99% anhydrite, 1% barite) was significantly contaminated in this way.

Barite concentrates were prepared by first picking and grinding portions of the samples rich in this mineral, followed by prolonged dissolution of anhydrite in refrigerated distilled water then removal of gypsum in boiling distilled water, and finally by chemical attack in a boiling 10% HCl-HNO₃ solution to partially remove sulfides and micropanning to remove clay and silica. All barite concentrates were examined in oil mounts under a petrological microscope to ensure suitability and absence of anhydrite. The proportions of barite in fractions used for Sr isotope analysis were ~10% in 148511B, ~35% in 148513B, and ~90% in 148517B, the contaminants being sulfides and only a trace of clay. No other sulfates or Sr-bearing minerals were observed, and the resultant Sr data are considered to truly represent barite.

For strontium isotope measurements, Sr was extracted from anhydrite and barite concentrates by leaching in HCl, and separated by cation exchange chromatography with AG50W-X8 resin for loading with H₃PO₄ onto Ta filaments. Isotope ratios were measured on a VG 354 thermal ionization mass spectrometer at CSIRO, North Ryde. Measured blanks were negligible. Raw data from 54 ratio determinations were filtered using a 2 σ rejection criterion. Internal precisions calculated as two standard errors of the mean are cited in Table 2. Simultaneous ratio measurements of the NBS-SRM987 standard averaged 0.710276 (2 σ =0.0015%, n=14) for anhydrite runs, and 0.710279 (2 σ =0.0014%, n=19) for barite runs.

Sulfur isotope ratios in anhydrite were determined by direct combustion of the sample with a small amount of V₂O₅ in a tin cup, using a modified Roboprep elemental analyser attached to a Finnigan 252 mass spectrometer at CSIRO, North Ryde. Samples were analysed relative to an internal gas standard and calibrated using international standards IAEA-S1 ($\delta^{34}\text{S}=-0.3\text{‰}$) and NBS-127 ($\delta^{34}\text{S}=+20.3\text{‰}$). Results are reported in Table 2 using the δ notation relative to Canon Diablo

troilite (CDT). Replicate analyses of standards were better than $\pm 0.2\%$. Barite concentrates and one anhydrite concentrate were insufficiently free of sulfide for analysis by this method.

Results

Structure and Paragenesis

Petrological and mineragraphic studies were not a prime objective of this study, but were carried out on four samples in order to establish temporal relationships between the sulfates and other minerals as an aid to interpretation of isotope data. Descriptions are presented in Table 1. The six samples from Hole 60-RD (148511 to 148516) all come from a single lithologic unit, described in Fig. 6.3b of Cruise Report SO-166 CONDRILL as “nodular pyrite-chalcopyrite-anhydrite breccia”, and in Appendix C as containing rounded clasts of semi-massive chalcopyrite-pyrite set in a matrix of “white” anhydrite (here termed “grey”, reflecting presence of some sulfides), with 1-2 cm wide, irregular anhydrite veins running the length of the core. On the small samples provided, the latter veins may only appear as isolated pods, but they clearly constitute the final stage of mineral development.

The overall structure of samples 148511 to 148515 from Hole 60-RD is illustrated in Figure 1. Whereas their “wallrock” material is referred to in Table 1 as a “breccia”, with “nodules” of massive sulfide enclosed in a grey “matrix” of granular anhydrite with barite and disseminated sulfides, the structures are not those of typical “jigsaw fit” hydrothermal breccias. The sulfide nodules (and smaller equivalents scattered through the matrix) are highly irregular in shape and tend to exhibit euhedral crystal outgrowths at their borders, with no clear evidence of having been fractured from a larger body of massive sulfide. Nevertheless, these sulfide nodules represent the first-formed hydrothermal precipitates. A possible clue regarding their formation is provided by the scattered presence of mm- to cm-size fragments of altered dacite within the “breccia matrix”. In some of these, fine grained disseminated sulfides (principally pyrite) are evenly distributed throughout, but in others coarser grains of pyrite and chalcopyrite are concentrated at fragment margins, commonly with euhedral outer faces resembling those of the massive sulfide nodules. Several porous sulfide nodules in 148513 have cavities lined by clay material resembling the groundmass of the altered dacite fragments but which, if correctly so identified, has been partly dissolved.

It is tentatively suggested that many, if not all of the sulfide nodules nucleated on altered dacite fragments derived from the true wallrock disrupted in the early stages of hydrothermal fracturing, and that further growth of sulfides, then of the grey “matrix”, and finally of the white bladed anhydrite took place during progressive hydraulic dilation in what is essentially a continuous event but with changing composition of the responsible fluid. Similar processes, including hydrothermal corrosion or dissolution of altered wallrock, have been proposed by Barriga et al. (2001) for the deeper stockwork zone below Roman Ruins drilled by ODP Leg 193 (Hole 1189B).

The paragenetic sequence in samples 148511 to 148515 is early pyrite-chalcopyrite-(sphalerite)-barite-granular anhydrite-late bladed anhydrite. Overlap occurs of decreasingly abundant sulfides with granular anhydrite, and between barite and granular anhydrite. Apart from scarce translucent sphalerite rims (Fe-poor) on sulfide nodules that corrode chalcopyrite in particular, there is no clear evidence for replacement. As a complication, dendritic trails of opaque sphalerite (Fe-bearing) granules cut through granular anhydrite of the grey matrix in sample 148513, with marginal outgrowths of relatively late barite and coarse pyrite.

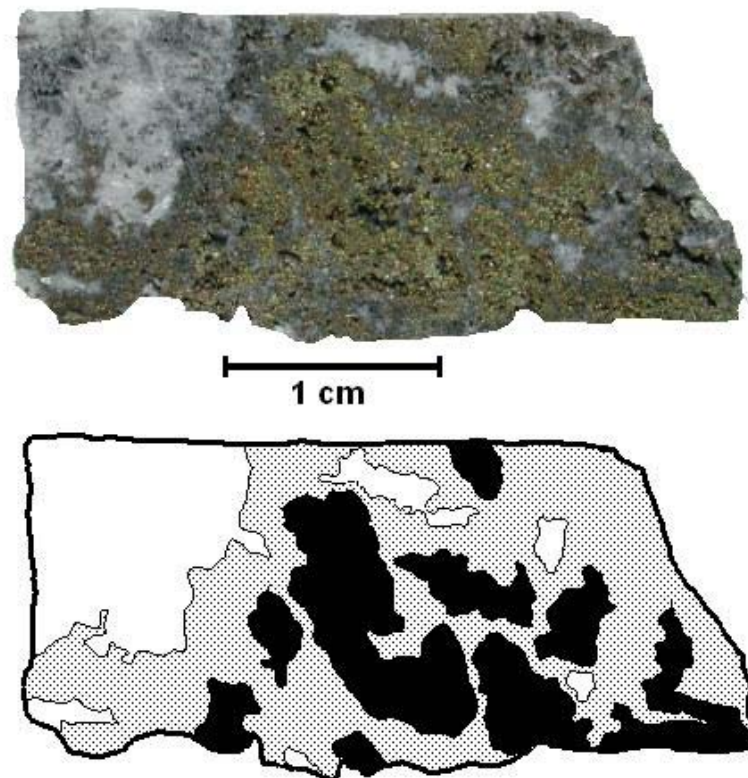


Fig. 1. Photograph and sketch of sample 148512 (60-RD, 49-53 cm). White = late-stage bladed anhydrite pods; black = early massive sulfide nodules; grey = anhydrite-barite-sulfide “matrix” of “breccia”. The matrix also contains numerous smaller particles equivalent to the massive sulfide nodules.

Sample 148516 differs from the other samples from Hole 60-RD in that a white anhydrite vein (with fanlike bundles of narrow blades containing numerous fluid inclusions) abuts directly against a large sulfide nodule, without development of the grey barite-bearing “matrix” although the anhydrite becomes more granular at the contact. This sample has a grey sliver of earlier granular anhydrite, with disseminated sulfides and also cut by dendritic sphalerite trails, on the opposite side of the white vein. Although it is difficult to be certain in the tiny sample, the grey sliver is likely to be paragenetically equivalent to matrix anhydrite in the other samples.

Apart from the presence of lamellate growths of chalcopyrite on one side of the sulfide nodule in sample 148516, which (probably coincidentally) bears some textural similarity with conduit linings typical of PACMANUS chimneys, the fabrics of the CONDRILL Hole 60-RD samples do not resemble those of chimneys. Rather, there are close similarities with the <20 cm intersection of semi-massive sulfide cored at 31.0 mbsf immediately below the casing of ODP Hole 1189B at Roman Ruins (Shipboard Scientific Party, 2002; Binns, 2005). This contains irregular massive aggregates or nodules of coarse pyrite with chalcopyrite overgrowths set in a dark grey matrix of bladed to granular anhydrite with disseminated pyrite-chalcopyrite, and late pale grey patches and veinlets of bladed anhydrite (partly altered to gypsum) largely devoid of sulfides. Like the CONDRILL Hole 60-RD samples, it contains scattered fragments of altered dacite with disseminated sulfides, but barite is lacking. Sphalerite is rare. Collectively, these “nodular breccias” are considered to represent an upper zone (Cu-Au rich) of the stockwork that underlies Roman

Ruins. In the deeper stockwork from ~40 to ~100 mbsf in ODP Hole 1189B, chalcopyrite is scarce and altered wallrock fragments are more abundant, in structures ranging from pyrite-quartz-(anhydrite) veining to jigsaw-fit hydrothermal breccias with pyrite-quartz-(anhydrite) matrices. Quartz is absent from the upper stockwork zone.

The two samples from CONDRILL Hole 69-RD derive from an intersection containing two adjacent lithologies as logged in Appendix C, Cruise Report SO-166 CONDRILL. Lithology A is described in that report as “massive sphalerite with barite, disseminated pyrite and chalcopyrite”, and is cut by Lithology B “anhydrite-pyrite-chalcopyrite breccia with a 2-3 mm wide anhydrite band at the contact with lithology A, and with minor clasts of altered dacite”.

Sample 148517 from Hole 69-RD is dominated by a dark grey wallrock (Lithology A) composed of zoned, botryoidal sphalerite with inclusions of pyrite and chalcopyrite, overgrowing early barite blades. An irregular 1-cm white pod of bladed anhydrite with internal drusy cavities and diffuse borders itself appears to have filled a dilational opening or former large cavity. This is probably an offshoot from the anhydrite vein at the contact of lithologies A and B described in the Cruise Report. The border zone, marked by large barite blades intergrown with coarse anhydrite and botryoidal sphalerite, shows evidence of barite replacement by anhydrite. The paragenetic sequence is early barite-sphalerite-(pyrite, chalcopyrite)-late anhydrite. The wallrock component of this sample resembles in mineralogy and fabric the outer walls of many PACMANUS chimneys.

Sample 148518 from Hole 69-RD represents Lithology B, and contains veins of white anhydrite (with drusy cavities) cutting a finer grey material composed of anhydrite with disseminated pyrite and chalcopyrite, with small inclusion of altered dacite. The grey portion resembles the “matrix” material of samples from Hole 60-RD, but lacks barite. Overall, the sample is similar to the semi-massive sulfide from the upper stockwork zone (31.0 mbsf) in ODP Hole 1189B, described above. Sample 148518 was not used for isotope analyses.

Strontium Isotopes

The analysed anhydrite concentrates from Holes 60-RD and 69-RD, apart from sample 148516A-2, represent the late-stage white, bladed anhydrite veins or pods. Sample 148516A-2 is an earlier anhydrite possibly equivalent to granular “matrix” anhydrite of other Hole 60-RD samples. Barites 148511B and 148513B are dominated by fine euhedral blades derived from the earlier pockets of this mineral near the margins of sulfide nodules, but contain a small proportion of larger blades such as are intergrown with anhydrite in the grey “matrix” zones of Hole 60-RD “stockwork” samples. Barite concentrate 148517B from Hole 69-RD was prepared from sphalerite-rich wallrock (Lithology A) remote from the anhydrite pod and its baritic border zone, and represents the paragenetically earliest occurrence of this mineral, possibly in what was possibly a buried chimney fragment rather than stockwork material.

The strontium isotope ratios of the late-stage bladed anhydrite veins or pods are relatively radiogenic, $^{87}\text{Sr}/^{86}\text{Sr}$ ranging from 0.7068 to 0.7080. The earlier anhydrite 148516A-2 ($^{87}\text{Sr}/^{86}\text{Sr}$ = 0.7067) falls close to the lower end of this range, and is slightly less radiogenic than its accompanying bladed vein 148516A-1 ($^{87}\text{Sr}/^{86}\text{Sr}$ = 0.7071). By contrast, the paragenetically earlier barites are distinctly less radiogenic, with $^{87}\text{Sr}/^{86}\text{Sr}$ ranging from 0.7046 for 148517B intergrown with wallrock sphalerite (possible chimney fragment) in Hole 69-RD, to 0.7058 and 0.7059 in the two matrix barites from Hole 60-RD considered more related to the stockwork below Roman Ruins. Clearly the Sr isotopic constitution of hydrothermal fluids from which the sulfate minerals were deposited has changed with time towards more radiogenic values. Using Sr as a tracer following

Roberts et al. (2003) and Bach et al. (2005), the data may be interpreted to denote increasing admixture of recirculated seawater into the hydrothermal fluid.

Eastern Manus Basin seawater has $^{87}\text{Sr}/^{86}\text{Sr} = 0.70916$ and contains 7.2 ppm Sr (Roberts et al., 2003; Binns et al., 2004). Fresh volcanic glasses (andesite-dacite-rhyodacite) from Pual Ridge (the edifice hosting the PACMANUS hydrothermal field) have $^{87}\text{Sr}/^{86}\text{Sr} = 0.70359$ ($n = 18$, $\sigma = 0.00002$; Binns, unpublished data). The end-member hydrothermal components of two high-temperature vent fluids collected at the Satanic Mills site, PACMANUS (Douville, 1999), recalculated by extrapolation to zero Mg content to remove seawater admixed within the chimney or during sampling, have $^{87}\text{Sr}/^{86}\text{Sr} = 0.70500$ and 0.70537 and Sr contents of 10.2 and 8.8 ppm respectively (Binns et al., 2004). These end-member values, when compared with the data for fresh Pual Ridge lavas which can be taken to represent either Sr leached from wallrocks during hydrothermal alteration or Sr contained in magmatic fluids derived from a cogenetic intrusion, suggest that the vent fluids were already mixed (by 25% and 32% respectively) with more deeply recirculated seawater before reaching the seafloor.

Relative to the average vent fluid end member, the proportion of additional seawater mixed into the fluids from which the CONDRILL anhydrites crystallised is estimated from the data above to range from 45% to 75%, while for fluids from which CONDRILL barites crystallised the proportion is distinctly lower, from zero to 25%. Barite 148517B from Hole 69-RD ($^{87}\text{Sr}/^{86}\text{Sr} = 0.70461$) is actually less radiogenic than either of the two end-member vent fluids, implying its formation from an even more primitive hydrothermal fluid that was less contaminated at depth (with ~20% of deeply recirculated seawater) than the vent end-member fluids. This is a characteristic also of some chimney barites, as indicated below.

Sulfur Isotopes

Sulfur isotope ratios in bladed anhydrite from late-stage veins in Hole 60-RD range from +20.6 to +21.1 $\delta^{34}\text{S}$, close to the value for seawater sulfate (+21.0; Rees et al., 1978) and indicating this to be the virtually exclusive anion source. Late stage anhydrite 148517A from Hole 69-RD has $\delta^{34}\text{S}$ of +20.3, slightly lighter than seawater considering analytical uncertainty. This suggests a small component of sulfate derived from oxidation of hydrothermal H_2S or disproportionation of magmatic SO_2 .

Individual $\delta^{34}\text{S}$ values do not correlate with $^{87}\text{Sr}/^{86}\text{Sr}$ in the CONDRILL anhydrites, so there is no hint of a systematic component of non-seawater sulfate. Extrapolated hydrothermal end-member components of the two PACMANUS vent fluids contain 146 and 148 ppm S as H_2S , respectively, and zero sulfate (Binns et al., 2004, from data of Douville, 1999, and Gamo et al., 1996). Eastern Manus Basin seawater contains 963 ppm S as sulfate (Binns et al., 2004), so contributions derived by partial oxidation or disproportionation of the hydrothermal component will be heavily masked by seawater. Regrettably, this issue cannot be assessed for the earlier anhydrite or barite concentrates from CONDRILL cores, which were unsuitable for S isotope analysis.

Comparisons with PACMANUS Chimneys

Barite is by far the dominant sulfate mineral in PACMANUS chimneys, occurring both as early blades intergrown with sphalerite particularly in chimney walls, and as late euhedral crystals lining the inner surfaces of conduits. Irrespective of paragenetic status, $^{87}\text{Sr}/^{86}\text{Sr}$ varies from 0.7046 to 0.7054 (Fig. 2), and $\delta^{34}\text{S}$ from 19.3 to 21.1 in chimney barites from Roman Ruins and Satanic Mills (Binns, unpublished data). Like sample 148517B, many chimney barites have less radiogenic

$^{87}\text{Sr}/^{86}\text{Sr}$ than in end-member components of vent fluids, so they evidently formed from more primitive hydrothermal fluids with a greater “igneous” character.

CONDRILL barites span a similar overall range in $^{87}\text{Sr}/^{86}\text{Sr}$ to chimney barites (Fig. 2). Barite 148517B from chimney-like Lithology A in Hole 69-RD conforms to the least radiogenic chimney barites, while barites 148511B and 148513B from stockwork-like “matrices” in Hole 60-RD have slightly more radiogenic Sr than chimney barites indicating their crystallization from fluid with a higher proportion of admixed seawater.

Occasional anhydrite in PACMANUS chimneys is generally developed either as fine grained, earthy veinlets cutting across the main concentric structure or, in an unusually pyrite-rich chimney, as euhedral crystals lining conduits. Anhydrites of this late-stage character have $^{87}\text{Sr}/^{86}\text{Sr}$ ranging from 0.7071 to 0.7090 (Fig. 2), and $\delta^{34}\text{S}$ from 20.1 to 20.6. CONDRILL anhydrites overlap these ranges but have slightly less radiogenic $^{87}\text{Sr}/^{86}\text{Sr}$ (Fig. 2) and $\delta^{34}\text{S}$ values closer to seawater sulfate.

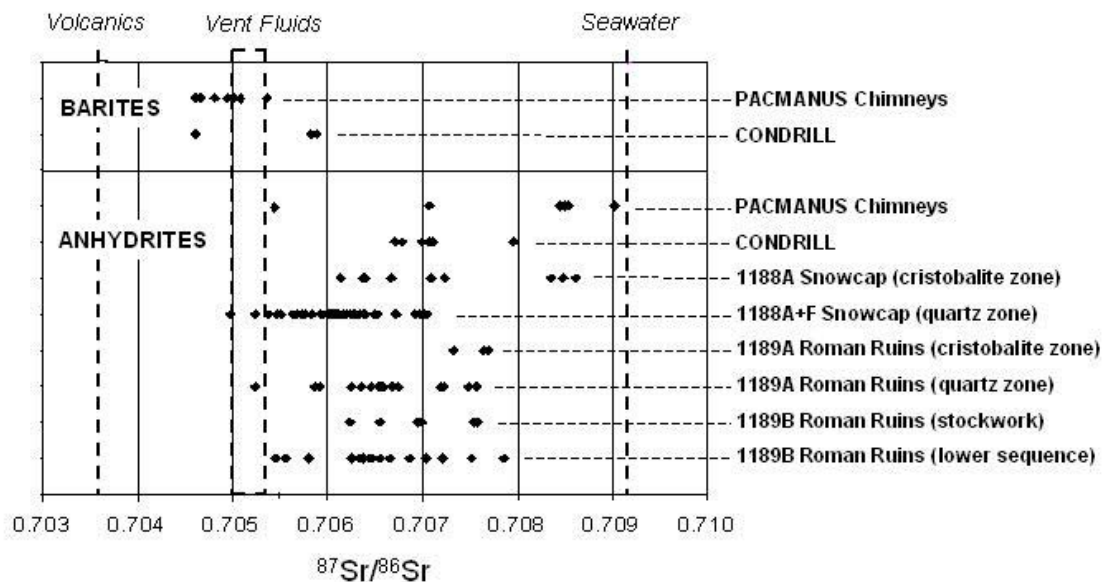


Fig. 2. $^{87}\text{Sr}/^{86}\text{Sr}$ ratios of CONDRILL anhydrites and barites, compared to ratios in sulfate minerals from PACMANUS chimneys (Binns, unpublished; Kim et al., 2003) and ODP drill cores (Roberts et al., 2003; Bach et al., 2005; see text for explanation of subgroups). Ratios used for interpretation in Pual Ridge volcanic glasses, seawater, and end-member vent fluids from two PACMANUS sites are indicated.

Two examples are known to me of chimney anhydrite with a possible early paragenetic character. One is in a sphalerite-pyrite chimney wall (close to a chalcopyrite conduit lining) containing internal rosettes of coarse, bladed anhydrite showing replacement by sulfides. Jonguk Kim (personal communication, 2003; see also Kim et al., 2003) determined $^{87}\text{Sr}/^{86}\text{Sr} = 0.7054$ (close to 0.7051 in barite from the adjoining outer wall) and $\delta^{34}\text{S} = 14.7$ (possibly affected by sulfide contaminant) for this anhydrite. This sample importantly shows that relatively primitive hydrothermal fluids (low seawater component) occasionally precipitate anhydrite rather than barite. The second example is a small fragment of coarse anhydrite intergrown with chalcopyrite reported

by Binns and Scott (1993), where the anhydrite, with $^{87}\text{Sr}/^{86}\text{Sr} = 0.7084$ and $\delta^{34}\text{S} = 17.7$, is contrarily quite radiogenic (high seawater component, similar to late-stage chimney anhydrites) but also possesses relatively light sulfur indicative of a hydrothermal fluid significantly influenced by disproportionation of magmatic SO_2 as argued by Kim et al (2003). It is conceivable that earlier granular anhydrites intergrown with barite in the “matrix” of CONDRILL Hole 60-RD cores, so far not analysed, share one or both of these characteristics.

Comparisons with Sub-Seafloor Sulfates

Barite is only a trace constituent in veins and altered wallrocks intersected by ODP drilling at PACMANUS during Leg 193, and no isotope data are available. Anhydrite, however, is very common in altered wallrocks as veins, breccia matrices, vesicle fillings, and disseminations. Roberts et al. (2003) and Bach et al. (2005) conducted an extensive Sr and S isotopic study of Leg 193 anhydrites. At Site 1188 (Snowcap site, characterized by low-temperature diffuse venting at seafloor outcrops of altered dacite/rhyodacite), a vertical profile with systematic downhole decrease in anhydrite $^{87}\text{Sr}/^{86}\text{Sr}$ was found. Drilling at this site penetrated a thin cap (~ 40 m) of unaltered rhyodacite in Hole 1188A before passing rapidly into extensively and pervasively altered lavas, which continued in adjacent Hole 1188F to 387 mbsf. At ~105 mbsf the principal silica phase in altered rocks changed from cristobalite to quartz. Anhydrites from the upper cristobalite-bearing alteration zone are relatively radiogenic, with $^{87}\text{Sr}/^{86}\text{Sr}$ falling quite regularly from ~0.7085 immediately beneath the unaltered dacite cap to ~0.7063 near the cristobalite-quartz transition (Fig. 2). Anhydrites from the lower quartz-bearing zone are less radiogenic overall, maintaining ratios mostly close to an average of 0.7061 (but spreading from 0.7050 to 0.7070; Fig. 2). Roberts et al. (2003) interpreted these data to indicate variable mixing between conductively heated seawater and a primary hydrothermal fluid comparable with the calculated end-member fluid at PACMANUS vent sites, the highest seawater proportions being achieved at the top of the alteration zone.

Similar interpretations were assigned to variations in anhydrite $^{87}\text{Sr}/^{86}\text{Sr}$ in two significantly differing ODP holes at Roman Ruins (Site 1189, characterised by high-temperature focused venting at seabed sulfide chimneys), although neither showed a systematic downhole trend. In Hole 1189A, drilled to 126 mbsf beside chimneys approximately 20 m southwest of the CONDRILL drilling footprint, a <10 m fresh dacite cap was underlain by pervasively altered lavas in which the cristobalite-quartz transition occurring at ~ 20 mbsf indicates a steeper thermal gradient during hydrothermal alteration. Anhydrites from the cristobalite bearing upper zone have radiogenic $^{87}\text{Sr}/^{86}\text{Sr}$ near 0.7076, whereas in the deeper quartz-bearing zone the ratios fall to an average of 0.7066 (range 0.7052 to 0.7076; Fig. 2).

ODP Hole 1189B slightly higher on the Roman Ruins mound lies centrally within the CONDRILL footprint. The hole was cased to 30 mbsf, and to ~100 mbsf intersected (with poor core recovery) an apparent stockwork zone (Shipboard Scientific Party, 2002) of altered dacites extensively veined and brecciated by quartz-pyrite-(anhydrite), the topmost core of which (at 31.0 mbsf) was semi-massive sulfide (described above) with significant Cu and Au contents. From ~100 mbsf to its termination at 206 mbsf, Hole 1189B passed through a distinctly different, less altered and sulfide-poor lower sequence with interleaved cristobalite and quartz-bearing intervals. Anhydrites from the upper stockwork zone have $^{87}\text{Sr}/^{86}\text{Sr}$ ranging from 0.7076 in the topmost semi-massive sulfide (structurally comparable with CONDRILL Hole 60-RD “nodular breccias”) to a less radiogenic average of 0.7067 (range 0.7062 to 0.7070) in the lower stockwork (Fig. 2). Anhydrites from veins in the lower sequence have a wide range in $^{87}\text{Sr}/^{86}\text{Sr}$, from 0.7055 to 0.7079, but the average ratio of 0.7065 is similar to that of the lower stockwork.

The CONDRILL anhydrites, mostly bladed varieties from the late stage veins or pods but including an earlier selvage of granular anhydrite, span the range in Hole 1189B stockwork anhydrites (Fig. 2) although notably all but one are less radiogenic than the semi-massive (nodular) sulfide at the top of the stockwork zone.

Anhydrites from ODP Holes 1188A and 1188F at Snowcap, and from Hole 1189A at Roman Ruins, exhibit a wider range in $\delta^{34}\text{S}$ (18.1 to 21.9) than anhydrites from late-stage chimney anhydrites (20.1 to 20.6) or the CONDRILL anhydrites (20.3 to 21.1). Ratios significantly exceeding seawater sulfate ($\delta^{34}\text{S} = 21$) occur at ~50 mbsf in the upper cristobalite-bearing alteration zone of Hole 1188A and from 11 to 59 mbsf in Hole 1189A (within both the cristobalite and quartz-bearing alteration zones), while at deeper levels $\delta^{34}\text{S}$ vary randomly with depth from 18 to 21. Roberts et al. (2003) and Bach et al. (2005) attribute the heavier $\delta^{34}\text{S}$ values (>21) to partial reduction of intermixed seawater sulfate by ferrous iron in the hydrothermal fluid, and lighter $\delta^{34}\text{S}$ (<21) to oxidation of H_2S or disproportionation of magmatic SO_2 .

In Hole 1189B at Roman Ruins, anhydrite $\delta^{34}\text{S}$ is relatively heavy overall, ranging from 20.7 to 22.3 in the stockwork zone and from 20.4 to 22.4 in the lower sequence, indicating a generally higher contribution from partially reduced seawater sulfate. Anhydrite and secondary gypsum in the semi-massive sulfide at 31.0 mbsf in this hole have $\delta^{34}\text{S} = 21.3$, close to seawater sulfate and comparable with the late-stage anhydrites of CONDRILL samples.

Discussion

Isotope data from shallow subsurface CONDRILL anhydrite and barite provide a valuable link between equivalent data for seafloor chimneys and for deeper subsurface ODP anhydrites, clarifying contrasted sulfate mineral relationships in the latter two settings. In particular, Sr isotope ratios of CONDRILL barites are distinctly less radiogenic than those in accompanying late-stage anhydrites, paralleling similar behaviour in the chimneys but with somewhat less overall contrast. This implies that the barites crystallised from a hydrothermal fluid comparable with computed end-member hydrothermal components of high temperature fluids sampled at PACMANUS chimneys or, in the case of many chimney barites and barite from a possible buried chimney fragment in CONDRILL Hole 69-RD, an even more primitive fluid with less admixed deeply recirculated seawater. Chimney and CONDRILL anhydrites, on the other hand, crystallised from fluids with a greater component of admixed seawater. The proportion of admixed seawater (relative to the end-member vent fluid component) is somewhat less overall in shallow subsurface CONDRILL anhydrites (45-75%) than in chimney anhydrites, but in Hole 60-RD this did not change systematically with depth.

Paragenetic and structural relationships in the CONDRILL stockwork-like samples confirm an early stage of barite crystallization followed with some overlap by anhydrite in an apparently continuously dilating fracture system. Thus, for the first time in a subsurface setting, Sr isotopes clearly establish that the hydrothermal fluid evolved with time towards compositions with higher seawater components. Hints of this are given by Sr isotope comparisons in samples showing several anhydrite generations, including CONDRILL sample 148516 and several ODP cores (Bach et al., 2005).

Barium is highly insoluble in sulfate-bearing fluids, hence it must necessarily have been transported upwards to the barite depositional sites within a reduced sulfide-bearing fluid like the sampled vent fluids, to deposit rapidly after mixing close to these sites with sulfate-bearing seawater. Seawater itself contains negligible Ba so this element is deeply sourced, either by

leaching from volcanic wallrocks during alteration or introduced in magmatic fluids from a chamber underlying the PACMANUS hydrothermal system.

Anhydrite in late-stage veins of these samples precipitated later, from a fluid now mixed with substantial seawater. Sulfur isotope ratios in CONDRILL anhydrites indicate that their sulfate anion derived virtually exclusively from this admixed seawater, which Roberts et al. (2003) consider was conductively heated prior to mixing since anhydrite is soluble in seawater-like compositions below 140-150 °C. Unlike many deeper anhydrites sampled by ODP drilling, there is no indication in CONDRILL anhydrites of isotopically heavy sulfate components derived by partial reduction of seawater sulfate, nor of isotopically light sulfate derived by oxidation of sulfide or disproportionation of magmatic SO₂, except that a minor amount of the latter may have been present in the case of an anhydrite vein in sample 148517 from Hole 69-RD. At 1.5 mbsf, this sample is deeper than the stockwork-like samples from Hole 60-RD (0.4 to 0.7 mbsf). Relative proximity to the sea floor may explain this slight difference, although the semi-massive sulfide at 31.0 mbsf in ODP Hole 1189B instead suggests a rather variable relationship with depth.

PACMANUS seawater contains 434 ppm Ca, and extrapolated end member hydrothermal fluids sampled at two PACMANUS chimney vents contain 583 and 410 ppm Ca respectively (Binns et al., 2004). The calcium cation in CONDRILL anhydrites would be subequally derived from both these components of their parental hydrothermal fluid.

Additional work is desirable to amplify this study. In particular, Sr and S isotope analyses of anhydrites from the matrix portions of the Hole 60-RD stockwork-like samples, and S isotope analyses of their associated barites, would further clarify the conclusions from this preliminary study regarding progressive mixing of seawater into the hydrothermal fluid. The samples provided were too small to successfully attempt this with the methods available, but microbeam methods (Craddock and Bach, 2004) could overcome this for Sr isotope analysis. Anhydrite and barite reported in other CONDRILL cores also merit further examination.

Mineragraphic and microstructural data reported here draw attention to the similarity between “nodular breccias” encountered in shallow CONDRILL cores and the semimassive sulfide sampled at 31.0 mbsf immediately below the cased interval of ODP Hole 1189B, both containing altered dacite fragments and being interpreted as representatives of an upper zone in the stockwork underlying the Roman Ruins hydrothermal chimney field. Rapid penetration rates during emplacement of casing by hammer-in drilling, and the nature of debris collected on the drill, suggest that the remaining “missing link” between CONDRILL and ODP samples consists of similar stockwork material, with a proportion of buried chimney fragments resembling those in CONDRILL Hole 69-RD (Binns, 2005). Formation of the stockwork by progressive mineralization involving increased seawater mixing within continuously expanding hydraulic dilational structures, and the general absence of evidence for mineral replacements, argue against a “zone refining” model to explain the high Cu, Zn, Au and Ag tenors of typical PACMANUS chimneys. An alternative suggestion is that fractional crystallization of hydrothermal fluids involving extensive subsurface precipitation of pyrite has removed much Fe from the ascending hydrothermal fluids that ultimately form chimneys at the sea floor.

Acknowledgements

Sven Petersen kindly selected the samples provided for this study. Heather Middleton and Anita Andrew are thanked for Sr and S isotope analyses, respectively, at CSIRO Minerals Research Laboratory, Sydney. Research funded by CSIRO, Australia.

References

- Bach, W., Roberts, S., and Binns, R.A., 2005. Data Report: Chemical and isotopic (S, Sr) composition of anhydrite from ODP Leg 193, PACMANUS hydrothermal system, Manus Basin, Papua New Guinea. In Barriga, F.J.A.S, Binns, R.A., Miller, D.J., and Herzig, P.M (Eds.). *Proceedings of the Ocean Drilling Program, Scientific Results*, v. 193, [Online: http://www-odp.tamu.edu/publications/193_SR/VOLUME/CHAPTERS/214.PDF].
- Barriga, F.J.A.S, Binns, R.A., Miller, D.J., and Shipboard Scientific Party, 2001. Hydrothermal corrosion: a major pre-ore forming process documented by ODP Leg 193 (PACMANUS, Manus basin, Papua New Guinea). *EOS, Transactions American Geophysical Union*, v. 82(47), Fall Meeting Supplement, Abstract OS11A-0339, p. F587.
- Binns, R.A., 2005. Data Report: Geochemistry of massive and semimassive sulfides from Site 1189, Ocean Drilling Program Leg 193. In Barriga, F.J.A.S, Binns, R.A., Miller, D.J., and Herzig, P.M (Eds.). *Proceedings of the Ocean Drilling Program, Scientific Results*, v. 193, [Online: http://www-odp.tamu.edu/publications/193_SR/VOLUME/CHAPTERS/206.PDF].
- Binns, R.A. and Scott, S.D., 1993. Actively forming polymetallic sulfide deposits associated with felsic volcanic rocks in the eastern Manus back-arc basin, Papua New Guinea. *Economic Geology*, v. 88, p. 2226-2236.
- Binns, R.A., Barriga, F.J.A.S., Miller, D.J., et al., 2002. Anatomy of an active felsic-hosted hydrothermal system, eastern Manus Basin. *Proceedings of the Ocean Drilling Program, Initial Reports*, v. 193, variously paginated.
- Binns, R.A., Dotter, L.E., and Blacklock, K.A., 2004. Chemistry of borehole fluids collected at PACMANUS, Papua New Guinea, ODP Leg 193. In Barriga, F.J.A.S, Binns, R.A., Miller, D.J., and Herzig, P.M (Eds.). *Proceedings of the Ocean Drilling Program, Scientific Results*, v. 193, [Online: http://www-odp.tamu.edu/publications/193_SR/VOLUME/CHAPTERS/210.PDF].
- Douville, E., 1999. Les fluides hydrothermaux oceaniques comportement geochimique des elements traces et des terres rares: Processus associes et modelisation thermodynamique [PhD Thesis]: Brest, (University of Brest, France).
- Gamo, T., Okamura, K., Kodama, Y., Charlou, J.-L., Urabe, T., Auzende, J.-M., Shipboard Scientific Party of the ManusFlux Cruise, and Ishibashi, J., 1996. Chemical characteristics of hydrothermal fluids from the Manus back-arc basin, Papua New Guinea, I. Major chemical components. *EOS, Transactions of the American Geophysical Union*, Western Pacific Geophysics Meeting Supplement 77: W116.
- Kim, J., Lee, K.-Y., and Lee, I., 2003. S, Sr, and Pb isotopic systematics of hydrothermal chimney from the eastern Manus back-arc basin, Western Pacific: Evaluation of magmatic contribution to hydrothermal system. *Geological Society of America, Abstracts with Programs*, v. 35(6), abstract 94-5.
- Rees, C. W., Jenkins, W. J., and Monster, J., 1978. The sulfur isotope geochemistry of ocean water sulfate. *Geochimica et Cosmochimica Acta*, v. 42, p. 377-382
- Roberts, S., Bach, W., Binns R.A., Vanko, D.A., Yeats C.J., Teagle, D.A.H., Blacklock K., Blusztajn, J.S., Boyce, A., Cooper, M., Holland N., and McDonald B., 2003. Contrasting evolution of hydrothermal fluids in the PACMANUS system, Manus basin: The Sr and S isotope evidence. *Geology*, v. 31, p. 805-808.
- Shipboard Scientific Party, 2002). Site 1189. In Binns, R.A., Barriga, F.J.A.S., Miller, D.J., et al., *Proceedings of the Ocean Drilling Program, Initial Reports*, v. 193, 259 pp. [CD-ROM, ODP, Texas A&M University, College Station TX USA]

Table Captions

Table 1. Descriptions of CONDRILL samples provided for isotopic studies of sulfates.

Table 2. Isotope analyses of sulfates from CONDRILL cores 60-RD and 69-RD, PACMANUS, Papua New Guinea.

Table 1. Descriptions of CONDRILL samples provided for isotopic studies of sulfates

Hole	Depth (cm)	CSIRO No.	Description	Samples analysed
60-RD	39-42	148511	<p>Slice cut along the core. The sample contains two cm-size and several smaller, irregular but sharply-demarcated pods of white bladed anhydrite (crystals 2-4 mm long) relatively free of sulfides, one with an anhydrite-lined drusy cavity. The pods appear to “invade” a “breccia” consisting of numerous highly irregular-shaped nodules of sulfide, 1 to 5 mm across, dispersed in a grey matrix of granular anhydrite (0.1-0.6 mm diameter) and barite blades (0.1-0.5 mm long) intergrown with finer grains and patches of sulfides. The matrix also contains cavities lined by anhydrite with lesser barite and sulfide. Rare fragments of clay-altered dacite 1mm or less across (with disseminated sulfides, and opaline silica at their rims) also occur in the “breccia” portion. Sulfide nodules vary in texture and mineral abundance: most contain pyrite and chalcopyrite, commonly euhedral or subhedral, and coarser at nodule margins. In many nodules small spheroidal pyrite cores outlined by dusty inclusions or cavities are overgrown by coarser, often subhedral pyrite. Chalcopyrite tends to concentrate at nodule margins or to poikilitically enclose pyrite in the interior, without clear evidence of replacement. Some but not all nodules have narrow rims of colourless translucent sphalerite that appear to have corroded the pyrite and chalcopyrite but which themselves display crystal faces against enclosing matrix anhydrite. In the grey “breccia” matrix, small anhedral or occasionally subhedral particles of pyrite-chalcopyrite occur interstitially between or as inclusions within anhydrite: most of these are rimmed by colourless sphalerite with common euhedral outer surfaces. As well as the larger blades intergrown with anhydrite, barite tends to form pockets ~200 µm across of finer blades, with or without anhydrite, that concentrate in positions where sulfide nodules abut. In these, very fine grained sphalerite dominates the interstitial and included sulfides. Within or at the margins of these pockets, barite blades are partly surrounded by or completely enclosed within larger anhydrite blades. Euhedral blades of barite also occur as inclusions within granular matrix anhydrite away from the pockets. At the borders of the large white anhydrite pods against the “breccia” matrix there is no definite textural evidence of two anhydrite generations although the fabric tends to change gradually from bladed to more granular. Earlier grey anhydrite (with barite and sulfides) of the “breccia” matrix and later bladed anhydrite of the white pods thus appear the products of a single infill event where fluid compositions changed</p>	<p>148511A: bladed anhydrite hand-picked from the largest white pod.</p> <p>148511B: barite separated chemically from the grey “breccia” matrix</p> <p>Polished thin section.</p>

Hole	Depth (cm)	CSIRO No.	Description	Samples analysed
60-RD	49-53	148512	<p>progressively. Traces of secondary gypsum occur at the margins or along cleavage fractures of some matrix anhydrite crystals.</p> <p>Edge fillet cut along the core (Fig. 1). Megascopically similar to 148511, but white bladed anhydrite (blades to 3 mm long) here forms an irregular, continuous vein with apophyses that wedge apart fragments of “breccia” consisting of close-packed, porous chalcopyrite-rich sulfide nodules set in a grey matrix of anhydrite, barite, and fine grained sulfides. Several small fragments (< 2 mm) of clay-altered dacite with disseminated sulfides occur within the grey matrix.</p>	
60-RD	53-56	148513	<p>Slice cut along the core. Also megascopically similar in appearance to 148511, with several irregular 1-2 cm pods of white bladed anhydrite (one vein-like with irregular borders) and a number of smaller equivalents invading or occupying former large cavities in a “breccia” consisting of numerous irregular massive sulfide nodules closely packed within a grey anhydrite-barite-sulfide matrix. The “breccia” also contains an 8 mm fragment of clay-altered dacite displaying a lobate (corroded?) border, and several smaller equivalents, with disseminated fine grained and clustered coarser grained pyrite-(chalcopyrite) and showing marginal concentrations of opaline silica. The sulfide nodules, here up to 1.5 cm across, contain a higher proportion of pyrite but are otherwise similar in mineralogy and microfabric (chalcopyrite is typically late-stage) to those in 148511. Their margins are highly irregular and show no evidence of cataclastic fracturing. Rims of pale translucent sphalerite are present but less common, mostly occurring where chalcopyrite rather than sphalerite abuts against matrix sulfates. Some cavities within certain porous nodules are lined with (but not filled by) clay aggregates, resembling the groundmass of altered dacite fragments. Smaller equivalents of the sulfide nodules, consisting of only a few grains, are also disseminated through the grey matrix, which is dominated by relatively coarse, granular to mildly bladed anhydrite (0.5-2 mm). Unlike in 148511, fracture-like trails or dendritic growths of fine grained opaque sphalerite locally cut across the matrix anhydrite. In places, tiny euhedral blades of barite (50-100 µm long) project outwards from these fractures, apparently replacing coarse anhydrite. Elsewhere, coarse pyrite euhedra surround the sphalerite fracture fillings or dendrites. Most barite, however, occurs as clusters of equally tiny blades radiating outwards from the sulfide nodules where the timing relationship to enclosing anhydrite is less clear.</p>	<p>148513A: bladed anhydrite hand-picked from the largest white pod.</p> <p>148513B: barite separated chemically from the grey “breccia” matrix.</p> <p>Polished thin section.</p>
60-RD	65-69	148514	<p>Edge fillet cut along the core. Basically similar to the above samples, although the white bladed anhydrite (1-2 mm blades, with drusy cavities) itself possesses the</p>	

Hole	Depth (cm)	CSIRO No.	Description	Samples analysed
60-RD	69	148515	<p>appearance of a semicontinuous “breccia” matrix enclosing large (to 3 cm) irregular “clasts” of chalcopyrite-rich sulfides, while the finer grained grey (anhydrite)-barite-sulfide material forms a 1 to 5 mm thick selvage between the two, evidently formed after the sulfide nodules but before the white anhydrite. The grey material consists mainly of subequal proportions of euhedral barite crystals (50-100 µm long) and sulfides, with minor anhydrite.</p> <p>Small chip from an edge fillet, possibly taken at a large drusy cavity. The sample consists mostly of glassy white anhydrite crystals, radiating outwards from two cm-size sulfide nodules and becoming coarser and more bladed (to 5 mm long) towards the possible drusy cavity. There is no intervening grey sulfate-sulfide selvage, but several rosettes of grey barite blades (0.5-1 mm long) projecting outwards from the sulfide nodules are intergrown with granular anhydrite at the margin of the white pod or vein.</p>	148515A: glassy anhydrite blades hand picked from the coarser end (centre?) of the vein or pod.
60-RD	73-75	148516	<p>Slice cut along core. A 5 mm-wide vein of milky white bladed anhydrite abuts directly against the curved edge of a >2 cm porous, pyritic sulfide nodule, with drusy cavities at the contact. A thin offshoot from the vein cuts the nodule, and similar anhydrite fills some but not all cavities within the porous nodule. On the wall of the white vein opposite the nodule there is a thin (2 mm) layer of grey anhydrite intergrown with fine sulfides. This resembles in megascopic appearance the “breccia matrix” of other samples from 60-RD, but the sample does not permit a definite comparison. No equivalent layer occurs at the boundary of the white vein with the sulfide nodule. In polished thin section, the grey layer consists of granular to mildly bladed anhydrite (0.5-1 mm) with scattered interstitial pyrite and fewer chalcopyrite grains (20-100 µm), cut by dendritic trails (compare 148513) of very fine-grained opaque sphalerite with traces of pyrite. The white vein, by contrast, has only rare sulfides and consists of narrow fan-like bundles of long anhydrite blades (to 2.5 mm long) that diverge away from a relatively sharp contact with the grey layer toward the vein centre. At the contact with the sulfide nodule, the vein anhydrite is partly granular and partly developed as fan-like bundles again diverging away from the contact toward the vein centre. Hence, the white anhydrite constitutes a largely filled crustiform vein earlier than both the grey anhydrite layer and the sulfide nodule. Unlike other samples, the anhydrite crystals of the white vein contain sectors clouded by numerous tiny fluid inclusions. Traces of secondary gypsum occur at anhydrite margins. The sulfide nodule is layered, with pyrite dominant in the outer layer and chalcopyrite in the interior. The pyritic exterior shows numerous small</p>	<p>148516A-1: milky bladed anhydrite (with fluid inclusions) hand picked from the white vein.</p> <p>148516A-2: granular anhydrite hand picked from the grey layer.</p> <p>Polished thin section.</p>

Hole	Depth (cm)	CSIRO No.	Description	Samples analysed
69-RD	148-152	148517	<p>anhedral cores overgrown by pyrite with euhedral outer faces against cavities, in places mantled by chalcopyrite. The chalcopyrite-rich interior ranges from crustiform aggregates of long, subparallel crystals, to granular with numerous, usually euhedral, pyrite inclusions. Translucent sphalerite rims on chalcopyrite within and at the margin of the nodule are present but very rare. Barite is absent from this sample.</p> <p>Fillet cut along core, evidently dominated by lithology A as logged in Appendix C, Cruise Report SO-166 CONDRILL. An irregular white pod of stout anhydrite blades (2 mm long) with internal drusy cavities, possibly an offshoot from lithology B, here appears to occupy a large irregular cavity within porous dark grey wallrock material (lithology A?) composed of barite blades (typically 0.2 to 0.4 mm long but varying markedly across the sample) overgrown by botryoidal sphalerite conspicuously and repeatedly zoned from deep red brown to pale brown or yellow in transmitted light. Inclusions of pyrite and chalcopyrite, up to 150 µm across but generally much finer, are sparsely distributed throughout the sphalerite. Margins of the white pod are diffuse and marked by large barite blades (1-2 mm long) intergrown with coarse anhydrite and botryoidal sphalerite, the former commonly interstitial to or overgrowing barite blades with evidence of replacement in the form of corroded crystal faces on barite.</p>	<p>148517A: anhydrite blades hand picked from the white pod.</p> <p>148517B: fine barite blades chemically separated from dark grey wallrock remote from the white pod and its surrounding diffuse margin of coarse barite-anhydrite-sphalerite.</p>
69-RD	174-177	148518	<p>Slice cut along core. Logged as lithology B in Appendix C, Cruise Report SO-166 CONDRILL. A wedge-shaped white vein 3 to 6 mm wide of coarse anhydrite (stout crystals 1-2 mm long) with disseminated sulfide (predominantly pyrite) cuts pale grey, finer material composed of anhydrite with a higher proportion of pyrite and chalcopyrite. Barite is lacking. A 5-mm inclusion of altered dacite occurs within the grey material.</p>	<p>Polished thin section.</p>

Table 2. Isotope analyses of sulfates from CONDRILL cores 60-RD and 69-RD, PACMANUS, Papua New Guinea

CONDRIIL	CSIRO No.	Description	$^{87}\text{Sr}/^{86}\text{Sr}$	2SE%	$\delta^{34}\text{S}$
<i>Anhydrites</i>					
60-RD, 39-42 cm	148511A	Coarse blades from white pod	0.706986	0.0012	21.1
60-RD, 53-56 cm	148513A	Coarse blades from white pod	0.707951	0.0012	20.9
60-RD, 69 cm	148515A	Coarse blades from white vein or pod	0.706782	0.0011	20.6
60-RD, 73-75 cm	148516A-1	Fanlike bundles from white vein	0.707061	0.0012	21.0
60-RD, 73-75 cm	148516A-2	Granules from earlier grey layer	0.706706	0.0009	
69-RD, 148-152 cm	148517A	Coarse blades from white vein/pod	0.707103	0.0013	20.3
<i>Barites</i>					
60-RD, 39-42 cm	148511B	Fine blades in grey "matrix" of sulfide "breccia"	0.705880	0.0009	
60-RD, 53-56 cm	148513B	Fine blades in grey "matrix" of sulfide "breccia"	0.705818	0.0013	
69-RD, 148-152 cm	148517B	Fine blades intergrown with wallrock sphalerite	0.704613	0.0015	

Appendix 1

Geochemische Daten der Gesteine
vom Conical Seamount

Cruise Station alteration	SO166 07RD (0-75) least altrd	SO166 08RD (0-50) smectite	SO166 08RD (50-100) smectite	SO166 09RD (0-50) smectite	SO166 09RD (50-80) smectite	SO166 10RD (0-50) analcim	SO166 10RD (50-80) analcim	SO166 11RD (0-50) least altrd	SO166 13RD (0-50) least altrd	SO166 13RD (50-100) least altrd
Lat°min	03°18.710'S	03°18.745'S	03°18.745'S	03°18.740'S	03°18.740'S	03°18.730'S	03°18.730'S	03°18.730'S	03°18.748'S	03°18.748'S
Long°min	152°39.540'E	152°39.595'E	152°39.595'E	152°39.610'E	152°39.610'E	152°39.560'E	152°39.560'E	152°39.543'E	152°39.558'E	152°39.558'E
depth	1066 m	1101 m	1101 m	1112 m	1112 m	1073 m	1073 m	1078 m	1082 m	1082 m
SiO ₂	47.50	46.80	47.80	48.30	49.60	47.40	47.30	49.50	48.50	47.90
TiO ₂	0.77	0.80	0.82	0.79	0.81	0.79	0.78	0.80	0.83	0.80
Al ₂ O ₃	15.70	16.30	16.60	16.00	16.90	16.30	15.60	16.00	15.70	15.50
Fe ₂ O ₃	9.49	10.20	10.10	8.21	8.66	8.39	9.29	8.60	9.40	9.50
FeO										
MnO	0.15	0.07	0.07	0.13	0.13	0.11	0.14	0.15	0.16	0.15
MgO	5.23	4.08	4.11	5.58	5.30	4.26	4.74	4.83	4.98	4.96
CaO	11.00	7.97	7.19	9.60	9.60	10.00	10.10	11.40	11.30	10.90
Na ₂ O	2.97	2.99	2.99	2.50	2.69	2.78	2.40	2.81	2.78	2.84
K ₂ O	2.92	1.56	1.90	2.56	2.73	2.73	2.46	2.82	2.80	2.78
P ₂ O ₅	0.37	0.34	0.33	0.39	0.38	0.39	0.38	0.40	0.40	0.38
LOI	2.5	7.4	7.7	4.5	3.4	5.8	5.6	2.3	2.6	3.2
Total	98.6	98.5	99.6	98.6	100.2	99.0	98.8	99.6	99.5	98.9
S (%)	0.34	5.66	5.95	1.93	1.99	2.70	1.61	0.54	0.23	0.25
CO ₂	0.5	0.2	0.2	0.5	0.4	0.2	0.4	0.2	0.4	0.3
Ag ppm	<0.1	<0.1	0.1	0.2	0.3	0.1	<0.1	0.4	<0.1	<0.1
As	na	na	na	na	na	na	na	na	na	na
Au	<0.02	<0.02	<0.02	<0.02	<0.02	<0.02	<0.02	<0.02	<0.02	<0.02
Ba	235	258	285	306	na	249	253	251	252	252
Be	1.1	0.8	0.9	0.9	1.0	0.8	0.9	1.1	1.1	1.1
Bi	<0.2	<0.2	0.2	0.3	0.6	<0.2	<0.2	<0.2	<0.2	<0.2
Cd	<0.2	<0.2	<0.2	0.6	0.5	<0.2	<0.2	0.3	<0.2	0.2
Co	32	35	35	33	36	27	30	28	31	30
Cr	159	127	104	145	160	121	145	139	204	173
Cs	1.20	1.10	1.00	0.50	0.49	11.00	6.30	1.50	1.30	1.10
Cu	123	111	131	151	164	133	137	106	112	139
Ga	17	17	17	17	18	17	17	47	31	18
Hf	1.5	1.5	1.5	1.4	1.30	1.50	1.50	1.50	1.60	1.50
In	0.06	0.06	0.06	0.07	0.35	0.07	0.06	0.05	0.06	0.07
Mo	4.4	2.4	1.8	3.8	5.2	2.9	3.5	4.4	5.9	4.9
Nb	1.40	1.40	1.40	1.40	1.40	1.40	1.40	1.40	1.40	1.40
Ni	50	39	31	46	51	34	45	42	65	55
Pb	6	9	7	12	17	6	5	46	9	5
Rb	54	15	16	45	40	42	39	56	53	52
Sb	0.2	0.6	0.3	2.9	0.7	0.4	0.4	1.6	0.6	0.5
Sc	36	36	36	36	38.0	35	34	35	37	35
Sn	1.0	1.9	0.9	1.5	1.3	1.0	0.8	0.8	0.9	1.0
Sr	1027	1096	1028	1082	1190	1193	1129	1027	1047	1029
Ta	0.08	0.10	0.10	0.09	0.10	0.09	0.08	0.09	0.09	0.09
Te	<0.2	1.1	1.3	<0.2	<0.2	<0.2	<0.2	<0.2	<0.2	<0.2
Th	0.90	0.88	0.89	0.78	0.73	0.92	0.86	0.92	0.97	0.88
Tl	0.32	0.56	0.62	3.20	3.20	0.25	0.21	1.10	0.54	0.43
U	0.96	2.60	3.80	1.80	1.90	2.50	0.79	1.40	1.50	1.50
V	312	321	324	310	326	306	309	285	285	296
Y	18	18	18	18	17.00	17	18	20	19	19
Zn	97	61	59	101	70	86	97	107	95	98
Zr	54	57	56	49	45.0	58	58	58	59	57
La	9.8	10.0	10.0	9.7	9.9	10.0	10.0	10.0	10.0	10.0
Ce	22	23	23	22	22	24	23	23	23	23
Pr	3.1	3.2	3.3	3.2	3.2	3.3	3.3	3.3	3.3	3.2
Nd	15	15	15	15	15	16	15	16	15	15
Sm	3.9	3.8	3.9	3.9	4.0	4.1	4.0	4.0	3.9	3.8
Eu	1.20	1.30	1.30	1.30	1.30	1.40	1.30	1.40	1.30	1.30
Gd	4.1	4.0	4.0	4.1	3.9	4.1	4.1	4.2	4.2	4.0
Tb	0.57	0.57	0.57	0.56	0.58	0.58	0.57	0.59	0.60	0.58
Dy	3.3	3.3	3.2	3.2	3.1	3.2	3.3	3.4	3.4	3.3
Ho	0.65	0.63	0.62	0.61	0.58	0.62	0.63	0.66	0.64	0.64
Er	1.70	1.70	1.60	1.60	1.50	1.60	1.70	1.70	1.70	1.70
Tm	0.25	0.24	0.24	0.25	0.22	0.24	0.25	0.26	0.26	0.26
Yb	1.60	1.60	1.60	1.50	1.40	1.50	1.60	1.70	1.70	1.60
Lu	0.27	0.26	0.25	0.24	0.22	0.24	0.26	0.27	0.28	0.26

Cruise Station alteration	SO166 13RD (100-150) least altrd	SO166 14RD (0-50) propylitic	SO166 15RD (0-50) K-spar	SO166 15RD (50-100) K-spar	SO166 15RD (100-125) K-spar	SO166 16RD (0-50) least altrd	SO166 17RD (0-65) smectite	SO166 18RD (0-50) smectite	SO166 18RD (50-85) smectite	SO166 19RD (0-35) propylitic
Lat°min	03°18.748'S	03°18.730'S	03°18.715'S	03°18.715'S	03°18.715'S	03°18.722'S	03°18.730'S	03°18.731'S	03°18.731'S	03°18.735'S
Long°min	152°39.558'E	152°39.550'E	152°39.550'E	152°39.550'E	152°39.550'E	152°39.552'E	152°39.580'E	152°39.572'E	152°39.572'E	152°39.550'E
depth	1082 m	1063 m	1071 m	1071 m	1071 m	1072 m	1086 m	1076 m	1076 m	1075 m
SiO ₂	47.90	47.50	48.60	47.70	48.80	49.70	49.20	47.95	49.70	48.80
TiO ₂	0.74	0.79	0.79	0.77	0.80	0.82	0.79	0.83	0.83	0.80
Al ₂ O ₃	15.20	15.50	15.60	15.40	15.70	16.20	15.90	17.15	17.20	15.50
Fe ₂ O ₃	9.60	10.00	8.51	8.94	8.11	10.20	10.40	9.27	9.70	9.21
FeO										
MnO	0.16	0.15	0.12	0.12	0.11	0.16	0.15	0.09	0.11	0.15
MgO	5.33	4.70	4.86	4.78	4.78	4.71	6.05	4.41	4.44	5.03
CaO	11.30	10.80	10.80	10.70	10.90	11.20	9.70	8.11	8.62	11.30
Na ₂ O	2.78	2.74	3.46	3.39	3.25	2.85	2.46	2.73	2.50	2.68
K ₂ O	2.83	2.75	1.64	1.76	1.80	3.01	2.17	2.43	2.80	2.70
P ₂ O ₅	0.38	0.38	0.35	0.36	0.35	0.40	0.38	0.40	0.41	0.40
LOI	2.5	3.2	5.5	5.2	4.6	1.6	4.2	6.6	5.2	2.5
Total	98.7	98.5	100.2	99.1	99.2	100.9	101.4	99.9	101.5	99.1
S (%)	0.14	1.17	2.80	3.56	2.95	0.28	1.98	3.79	3.38	0.65
CO ₂	0.4	0.4	0.3	0.3	0.3	0.4	1.3	0.2	0.4	0.2
Ag ppm	<0.1	0.1	<0.1	<0.1	0.1	<0.1	<0.1	0.4	0.1	0.4
As	na	na	na	na	na	na	na	na	na	na
Au	<0.02	<0.02	<0.02	<0.02	<0.02	<0.02	<0.02	<0.02	<0.02	<0.02
Ba	258	247	244	250	247	na	na	241	na	250
Be	1.1	1.1	0.8	0.8	0.8	1.2	1.1	1.3	1.3	1.0
Bi	<0.2	<0.2	<0.2	<0.2	<0.2	<0.2	<0.2	0.4	<0.2	<0.2
Cd	<0.2	<0.2	<0.2	<0.2	<0.2	<0.2	<0.2	<0.2	<0.2	0.2
Co	32	30	30	31	30	31	36	43	36	28
Cr	186	171	180	169	148	142	194	233	167	138
Cs	1.30	1.70	1.40	1.40	1.30	1.20	0.78	0.89	0.66	2.40
Cu	129	128	132	130	130	112	153	156.5	152	115
Ga	17	33	16	27	17	21	17	18	18	17
Hf	1.40	1.50	1.50	1.40	1.50	1.6	1.5	1.45	1.5	1.60
In	0.06	0.05	0.07	0.06	0.06	0.06	0.07	0.07	0.06	0.06
Mo	4.2	7.5	3.8	3.7	2.3	4.9	4.4	7.25	4.4	4.9
Nb	1.30	1.40	1.40	1.30	1.30	1.4	1.4	1.5	1.5	1.40
Ni	50	54	53	47	42	46	62	76	52	43
Pb	6	7	5	4	6	6	5	8	7	6
Rb	59	52	18	18	19	55	36	45	43	47
Sb	0.4	0.3	<0.2	<0.2	<0.2	0.6	0.2	0.35	0.8	0.4
Sc	38	34	37	36	38	37	37	32	33	37
Sn	1.0	1.3	1.1	0.8	0.9	1.0	0.9	1.6	1.2	1.0
Sr	990	1005	989	1003	1007	1090	1030	1063	1130	1012
Ta	0.09	0.09	0.09	0.08	0.09	0.09	0.09	0.12	0.10	0.09
Te	<0.2	<0.2	<0.2	<0.2	<0.2	<0.2	<0.2	<0.2	<0.2	<0.2
Th	0.85	0.88	0.83	0.83	0.82	0.94	0.84	0.92	0.95	0.89
Tl	0.33	0.32	0.14	0.21	0.25	0.47	0.83	0.72	0.53	0.35
U	1.40	1.90	0.78	0.75	0.66	1.30	0.63	0.69	0.69	1.90
V	285	294	302	301	311	324	328	332	340	272
Y	18	19	18	18	17	20	19	18.5	19	20.00
Zn	97	98	76	84	67	87	85	75.5	74	97
Zr	55	57	54	55	55	56	52	56	56	59.0
La	9.6	10.0	9.2	9.5	9.6	9.9	9.5	9.9	11.0	10.0
Ce	22	23	22	22	22	22	21	23	23	22
Pr	3.1	3.2	3.1	3.1	3.1	3.2	3.1	3.2	3.3	3.3
Nd	15	15	15	15	15	15	15	15	16	15
Sm	3.8	3.8	3.8	3.8	3.7	4.0	4.0	3.9	4.0	4.2
Eu	1.30	1.30	1.30	1.20	1.30	1.30	1.30	1.30	1.20	1.40
Gd	3.9	4.2	4.0	3.9	3.9	3.9	4.0	4.1	4.0	4.4
Tb	0.56	0.58	0.56	0.55	0.54	0.58	0.59	0.59	0.59	0.62
Dy	3.2	3.3	3.2	3.2	3.1	3.1	3.2	3.4	3.2	3.6
Ho	0.59	0.63	0.61	0.60	0.61	0.58	0.64	0.64	0.65	0.66
Er	1.60	1.70	1.60	1.60	1.60	1.50	1.70	1.65	1.70	1.80
Tm	0.24	0.25	0.25	0.24	0.24	0.22	0.25	0.25	0.25	0.27
Yb	1.60	1.70	1.50	1.60	1.50	1.40	1.70	1.65	1.60	1.70
Lu	0.26	0.27	0.26	0.25	0.24	0.22	0.26	0.26	0.26	0.28

Cruise Station alteration	SO166 25RD (0-25) analcim	SO166 26RD (0-30) propylitic	SO166 27RD (0-40) least altrd	SO166 28RD (0-35) propylitic	SO166 28RD (35-70) propylitic	SO166 29RD (0-15) least altrd	SO166 30RD (0-30) analcim	SO166 30RD (30-60) smectite	SO166 37RD (0-30) least altrd	SO166 39RD (0-40) propylitic
Lat°min	03°18.737'S	03°18.740'S	03°18.745'S	03°18.740'S	03°18.740'S	03°18.740'S	03°18.720'S	03°18.720'S	03°18.729'S	03°18.725'S
Long°min	152°39.580'E	152°39.570'E	152°39.575'E	152°39.540'E	152°39.540'E	152°39.550'E	152°39.585'E	152°39.585'E	152°39.551'E	152°39.525'E
depth	1089 m	1089 m	1078 m	1082 m	1082 m	1076 m	1115 m	1115 m	1057 m	1064 m
SiO ₂	49.80	48.60	49.90	51.80	49.40	49.20	50.00	47.80	50.30	47.10
TiO ₂	0.78	0.79	0.80	0.78	0.80	0.79	0.80	0.80	0.81	0.81
Al ₂ O ₃	15.90	15.70	16.30	14.90	15.80	16.10	16.20	15.40	16.40	15.20
Fe ₂ O ₃	9.31	9.26	9.80	8.58	9.50	10.60	9.60	10.10	9.50	9.90
FeO										
MnO	0.13	0.15	0.16	0.14	0.14	0.18	0.14	0.16	0.15	0.14
MgO	5.05	4.65	4.57	4.20	4.58	4.61	4.99	5.97	4.67	5.28
CaO	10.80	10.90	11.00	10.00	11.00	11.00	10.60	10.00	11.40	11.60
Na ₂ O	2.01	2.88	2.90	2.49	2.38	2.55	2.35	2.35	2.81	2.32
K ₂ O	2.80	2.70	3.03	2.76	2.70	3.03	2.73	2.45	3.08	2.26
P ₂ O ₅	0.33	0.38	0.42	0.36	0.40	0.41	0.39	0.36	0.41	0.35
LOI	4.9	2.6	1.8	3.5	3.6	2.4	3.8	4.1	2.1	4.1
Total	101.8	98.6	100.7	99.5	100.3	100.9	101.6	99.5	101.6	99.1
S (%)	1.99	0.79	0.46	1.50	1.15	0.08	1.65	2.25	0.13	2.00
CO ₂	0.4	0.2	0.2	0.3	0.6	1.0	0.4	0.7	0.7	0.2
Ag ppm	0.1	0.3	0.1	0.4	0.4	<0.1	0.3	0.5	0.2	0.9
As	na	na	na	na	na	na	na	na	na	na
Au	<0.02	<0.02	<0.02	<0.02	<0.02	<0.02	<0.02	<0.02	0.02	0.02
Ba	na	236	na	na	na	na	na	261	na	252
Be	1.1	1.1	1.2	1.1	1.2	1.2	1.2	1.1	1.2	0.9
Bi	<0.2	<0.2	<0.2	<0.2	<0.2	<0.2	<0.2	<0.2	<0.2	<0.2
Cd	<0.2	<0.2	<0.2	0.3	<0.2	<0.2	<0.2	0.2	<0.2	0.4
Co	34	28	29	28	33	33	35	35	30	33
Cr	158	238	157	126	166	211	137	150	142	157
Cs	1.10	1.10	0.92	2.00	4.10	1.10	1.20	0.34	1.40	0.96
Cu	148	121	109	138	139	135	144	241	135	137
Ga	19	17	17	16	17	37	18	17	17	17
Hf	1.4	1.60	1.6	1.5	1.5	1.5	1.5	1.50	1.6	1.60
In	<0.05	0.05	0.07	0.06	0.05	0.07	0.06	0.10	0.07	0.06
Mo	3.1	6.7	6.3	17.0	5.2	5.7	3.4	4.3	3.4	7.1
Nb	1.3	1.40	1.4	1.4	1.3	1.4	1.4	1.40	1.4	1.40
Ni	41	87	50	31	50	73	42	48	50	44
Pb	5	5	12	8	49	5	5	6	11	7
Rb	43	46	53	53	52	46	39	35	54	43
Sb	<0.2	0.4	1.1	6.0	3.5	0.5	0.2	0.2	1.5	1.6
Sc	41	33	36	36	38	36	37	35	38	40
Sn	0.9	0.9	3.8	0.8	1.0	1.1	1.0	1.2	1.0	0.9
Sr	1180	1028	1100	996	1120	1120	1120	1008	1050	1135
Ta	0.09	0.10	0.09	0.09	0.09	0.08	0.09	0.08	0.09	0.08
Te	<0.2	<0.2	<0.2	<0.2	<0.2	<0.2	<0.2	<0.2	<0.2	<0.2
Th	0.85	0.91	0.97	0.91	0.87	0.94	0.91	0.87	0.92	0.90
Tl	0.48	0.32	0.38	0.76	2.30	0.34	0.37	0.33	0.91	0.63
U	0.93	2.00	1.90	8.60	1.40	0.70	0.78	0.64	1.00	2.20
V	322	304	316	280	327	329	333	317	328	319
Y	18	19	20	17	19	20	20	18	20	18
Zn	59	99	81	70	74	83	85	123	79	95
Zr	53	58	57	54	54	56	54	56	56	56
La	8.8	10.0	10	8.8	9.9	9.9	9.9	9.9	10	10.0
Ce	20	23	23	20	22	22	22	22	22	23
Pr	2.9	3.2	3.4	2.9	3.2	3.3	3.2	3.2	3.3	3.3
Nd	14	15	16	13	15	15	15	15	15	16
Sm	3.6	4.0	4.1	3.6	4.0	4.1	4.1	3.9	4.2	4.0
Eu	1.20	1.30	1.30	1.20	1.30	1.30	1.30	1.30	1.30	1.40
Gd	3.9	4.2	4.2	3.8	4.1	4.2	4.2	4.1	4.4	4.2
Tb	0.54	0.59	0.62	0.54	0.60	0.60	0.62	0.57	0.62	0.58
Dy	3.1	3.4	3.5	3.0	3.3	3.4	3.3	3.3	3.4	3.4
Ho	0.63	0.68	0.68	0.57	0.65	0.66	0.67	0.61	0.67	0.63
Er	1.60	1.80	1.80	1.60	1.80	1.80	1.80	1.60	1.80	1.60
Tm	0.24	0.27	0.27	0.22	0.25	0.26	0.26	0.25	0.26	0.25
Yb	1.60	1.70	1.70	1.50	1.60	1.70	1.70	1.60	1.70	1.70
Lu	0.25	0.28	0.27	0.24	0.25	0.27	0.27	0.26	0.28	0.26

Cruise Station alteration	SO166	SO166	SO166	SO166	SO166	SO166	SO166	SO166	SO166	SO166
Lat°min	40RD (0-40)	40RD (outer)	41RD (0-30)	42RD (0-50)	42RD (50-90)	42RD (90-120)	42RD (120-160)	43RD (0-25)	44RD (0-55)	45RD (0-23)
Long°min	mineralized	mineralized	least altrd	least altrd	propylitic	propylitic	propylitic	mineralized	least altrd	least altrd
depth	03°18.725'S	03°18.725'S	03°18.745'S	03°18.725'S	03°18.725'S	03°18.725'S	03°18.725'S	03°18.720'S	03°18.730'S	03°18.720'S
	152°39.515'E	152°39.515'E	152°39.528'E	152°39.533'E	152°39.533'E	152°39.533'E	152°39.533'E	152°39.535'E	152°39.510'E	152°39.530'E
	1085 m	1085 m	1083 m	1094 m	1094 m	1094 m	1094 m	1084 m	1095 m	1057 m
SiO ₂	21.40	19.70	49.40	51.80	53.90	51.50	48.20	69.00	48.80	48.40
TiO ₂	0.80	0.73	0.80	0.77	0.78	0.76	0.76	0.55	0.78	0.80
Al ₂ O ₃	20.30	17.00	16.00	14.80	14.00	14.80	15.00	9.60	15.70	15.50
Fe ₂ O ₃	18.00	17.20	8.82	8.29	7.26	9.38	9.80	5.32	10.20	11.20
FeO										
MnO	0.21	0.19	0.15	0.14	0.11	0.15	0.12	0.02	0.16	0.18
MgO	17.50	13.10	4.94	4.53	4.04	4.18	4.24	0.42	5.02	5.44
CaO	0.07	0.19	11.10	10.40	9.70	9.90	10.50	0.27	11.10	11.10
Na ₂ O	0.04	0.04	2.88	2.63	2.13	2.20	2.11	0.51	2.95	2.88
K ₂ O	0.06	0.25	2.84	2.62	1.99	2.44	2.26	3.03	3.20	3.01
P ₂ O ₅	0.21	0.25	0.38	0.37	0.33	0.39	0.36	0.01	0.39	0.40
LOI	16.9	10.9	2.0	2.4	4.9	4.4	6.4	9.7	1.3	1.3
Total	95.9	94.6	99.3	98.8	99.1	100.1	99.8	99.2	99.6	100.2
S (%)	14.20	16.90	0.40	0.56	2.23	1.51	2.96	4.64	0.09	0.04
CO ₂	0.2	0.3	0.2	0.4	0.3	0.8	0.4	0.3	0.30	0.30
Ag ppm	40	132	0.3	0.3	0.3	0.1	0.1	27	0.2	0.2
As	1610	1570	na	na	na	na	na	3810	na	na
Au	1.01	14.2	0.15	<0.02	<0.02	0.04	0.03	3.05	0.03	<0.02
Ba	<20	<20	240	262	238	na	233	151	na	na
Be	0.8	0.9	1.1	1.1	0.8	1.1	1.0	0.5	1.2	1.1
Bi	<0.2	<0.2	<0.2	<0.2	<0.2	<0.2	<0.2	<0.2	<0.2	<0.2
Cd	38	319	0.3	<0.2	0.5	0.5	0.9	32	0.6	0.3
Co	40	37	32	25	27	30	31	19	33	35
Cr	120	111	158	235	154	182	166	70	159	169
Cs	0.40	0.67	1.30	1.40	3.20	2.70	4.80	7.90	0.92	0.80
Cu	161	2070	130	111	112	142	133	340	129	115
Ga	19	27	18	17	17	16	16	10	17	17
Hf	1.6	1.4	1.60	1.50	1.50	1.4	1.50	1.0	1.5	1.6
In	<0.05	0.18	0.05	0.06	<0.05	0.06	<0.05	<0.05	0.18	0.07
Mo	51.0	113.0	6.3	15.0	25.0	12.0	9.4	49.0	3.4	4.0
Nb	1.50	1.50	1.50	1.40	1.40	1.3	1.30	0.92	1.4	1.4
Ni	37	43	46	79	45	60	52	19	45	55
Pb	450	22130	15	8	6	8	14	2660	14	15
Rb	0.64	5.5	58	49	37	51	40	36	62	54
Sb	35.3	77.5	0.6	1.3	7.9	4.8	25.0	218	0.4	0.8
Sc	30	27	36	34	34	35	33	17	38	37
Sn	0.7	1.2	0.9	0.9	1.0	1.0	0.9	0.7	0.9	1.0
Sr	108	190	1037	980	1014	1030	1125	162	1040	997
Ta	0.09	0.09	0.12	0.09	0.09	0.08	0.08	0.06	0.09	0.08
Te	8.3	13.0	<0.2	<0.2	<0.2	<0.2	<0.2	<0.2	<0.2	<0.2
Th	0.91	0.77	0.89	0.86	0.88	0.89	0.85	0.61	0.93	0.90
Tl	5	12	0.51	0.50	6.20	6.60	12.00	54	0.54	0.36
U	37	65	1.90	2.90	10.00	4.20	2.10	17	0.80	0.69
V	453	487	297	263	254	296	292	157	326	335
Y	3.5	4.4	19	18	15	18	18	0.82	19	20
Zn	2180	66700	99	126	105	90	121	4440	92	105
Zr	59	49	57	57	56	52	55	38	53	53
La	16.0	17.0	10.0	9.6	8.6	9.6	10.0	3.4	10.0	9.9
Ce	30	31	22	21	19	21	23	6	22	22
Pr	3.9	4.0	3.2	3.1	2.7	3.1	3.2	0.7	3.2	3.3
Nd	16	16	15	14	13	15	15	3	15	15
Sm	2.5	2.7	4.1	3.7	3.3	4.0	4.0	0.4	4.1	4.1
Eu	0.53	0.74	1.40	1.30	1.20	1.30	1.30	0.13	1.30	1.30
Gd	1.4	1.8	4.3	4.0	3.6	4.1	4.2	0.2	4.2	4.1
Tb	0.17	0.22	0.61	0.55	0.49	0.58	0.60	0.04	0.61	0.61
Dy	0.8	1.1	3.5	3.2	2.9	3.1	3.3	0.2	3.3	3.4
Ho	0.14	0.18	0.66	0.62	0.54	0.64	0.64	0.04	0.66	0.66
Er	0.34	0.44	1.80	1.70	1.40	1.60	1.60	0.10	1.70	1.80
Tm	0.06	0.07	0.27	0.25	0.21	0.24	0.25	<0.02	0.25	0.26
Yb	0.40	0.46	1.70	1.60	1.30	1.60	1.60	0.12	1.70	1.70
Lu	0.07	0.07	0.27	0.26	0.21	0.25	0.25	<0.02	0.27	0.26

Cruise	SO166	SO166	SO166	SO166	SO166	SO166
Station	46RD (0-35)	47RD (0-27)	48RD (0-65)	49RD (0-55)	50RD (0-25)	51RD (0-30)
alteration	propylitic	least altrd	least altrd	propylitic	least altrd	smectite
Lat°min	03°18.723'S	03°18.715'S	03°18.720'S	03°18.718'S	03°18.722'S	03°18.745'S
Long°min	152°39.535'E	152°39.505'E	152°39.540'E	152°39.520'E	152°39.511'E	152°39.585'E
depth	1057 m	1061 m	1055 m	1086 m	1095 m	1073 m
SiO ₂	47.10	49.20	49.20	48.60	49.70	49.50
TiO ₂	0.78	0.78	0.76	0.80	0.79	0.81
Al ₂ O ₃	15.80	15.20	15.50	15.60	15.80	16.20
Fe ₂ O ₃	8.75	10.40	10.30	10.40	9.19	9.80
FeO						
MnO	0.11	0.15	0.16	0.15	0.14	0.13
MgO	4.22	5.19	5.09	4.90	5.15	5.74
CaO	9.90	11.40	11.20	11.10	11.30	8.84
Na ₂ O	2.11	2.66	2.63	2.47	2.25	2.44
K ₂ O	2.20	2.89	3.18	2.69	2.95	2.79
P ₂ O ₅	0.36	0.36	0.39	0.37	0.37	0.39
LOI	7.7	2.3	1.9	2.9	2.3	3.9
Total	99.0	100.5	100.3	100.0	99.9	100.5
S (%)	3.57	0.07	0.28	1.13	0.09	1.95
CO ₂	0.2	0.50	0.90	0.4	0.30	0.5
Ag ppm	0.2	0.3	<0.1	0.2	<0.1	0.1
As	na	na	na	na	na	na
Au	<0.02	<0.02	<0.02	0.03	<0.02	<0.02
Ba	255	na	na	na	na	na
Be	1.1	1.1	1.1	1.1	1.1	1.1
Bi	<0.2	<0.2	<0.2	<0.2	<0.2	<0.2
Cd	<0.2	<0.2	<0.2	0.2	<0.2	<0.2
Co	31	31	33	30	26	36
Cr	141	206	241	170	204	166
Cs	6.00	0.94	1.10	1.30	1.30	0.29
Cu	136	111	125	111	74	217
Ga	17	16	17	18	17	18
Hf	1.50	1.5	1.5	1.6	1.6	1.5
In	0.05	0.05	0.06	<0.05	0.07	0.08
Mo	3.0	4.8	5.6	8.5	4.6	4.5
Nb	1.40	1.5	1.4	1.4	1.4	1.4
Ni	36	62	76	48	60	58
Pb	10	58	6	16	85	5
Rb	43	50	51	50	48	39
Sb	0.8	5.6	0.6	0.6	4.7	0.5
Sc	35	40	39	39	40	37
Sn	1.1	1.0	1.2	0.9	1.0	1.0
Sr	1160	1020	1080	1130	1120	1020
Ta	0.09	0.09	0.09	0.11	0.09	0.09
Te	<0.2	<0.2	<0.2	<0.2	<0.2	<0.2
Th	0.91	0.89	0.92	0.93	0.91	0.94
Tl	0.22	0.56	0.38	0.68	0.31	0.82
U	0.85	1.10	1.00	2.10	1.10	1.70
V	302	315	316	302	300	329
Y	17	18	19	18	20	19
Zn	133	82	87	89	118	80
Zr	55	54	53	53	55	53
La	9.9	9.0	9.9	9.6	10.0	10.0
Ce	22	20	22	21	22	22
Pr	3.1	2.9	3.2	3.2	3.3	3.2
Nd	14	14	15	15	16	15
Sm	3.9	3.9	4.2	4.0	4.2	4.1
Eu	1.40	1.30	1.30	1.30	1.40	1.30
Gd	4.0	4.1	4.2	4.1	4.3	4.1
Tb	0.58	0.58	0.60	0.59	0.62	0.63
Dy	3.2	3.3	3.3	3.3	3.5	3.4
Ho	0.60	0.65	0.66	0.65	0.68	0.68
Er	1.60	1.70	1.80	1.70	1.70	1.80
Tm	0.24	0.25	0.25	0.24	0.26	0.26
Yb	1.50	1.60	1.70	1.60	1.70	1.70
Lu	0.24	0.26	0.25	0.25	0.27	0.26

Publikationen

Shallow Drilling of Seafloor Hydrothermal Systems Using the BGS Rockdrill: Conical Seamount (New Ireland Fore-Arc) and PACMANUS (Eastern Manus Basin), Papua New Guinea

SVEN PETERSEN, PETER M. HERZIG, THOMAS KUHN, THOMAS MONECKE, AND LEANDER FRANZ 5

Leibniz-Laboratory for Applied Marine Research, Freiberg University of Mining and Technology, Freiberg, Germany

MARK D. HANNINGTON

Geological Survey of Canada, Ottawa, Canada 10

J. BRUCE GEMMELL

Center of Ore Deposit Research, University of Tasmania, Hobart, Tasmania, Australia

From September to October 2002, shallow drilling, using the submersible (5 m) Rockdrill of the British Geological Survey and the German R/V Sonne revealed critical information on the subsurface nature of two distinct hydrothermal systems in the New Ireland fore-arc and the Manus Basin of Papua New Guinea. Drilling at Conical Seamount significantly extends the known surface extent of the previously discovered vein-style gold mineralization (up to 230 g/t Au) at this site. Drilling the conventional PACMANUS volcanic-hosted massive sulfide deposit recovered complexly textured massive sulfide with spectacular concentrations of gold in several core sections including 0.5 m@28 g/t Au, 0.35 m@30 g/t Au, and 0.20 m@57 g/t Au. Shallow drilling is a fast and cost efficient method that bridges the gap between surface sampling and deep (ODP) drilling and will become a standard practice in the future study of seafloor hydrothermal systems and massive sulfide deposits. 15 20 25

Q2 Received ■; accepted ■.

Cruise SO166 was funded by the German Federal Ministry for Education and Research through a grant to PMH (BMBF grant 03G0166A). Additional support through the Leibniz Program of the German Research Foundation is gratefully acknowledged. We thank Captain Martin Kull and his crew for their support during the entire drilling program, and Alistair Skinner, Neil Campbell, Eileen Gillespie, and David Smith for their professional handling of the British Geological Survey Rockdrill. TM gratefully acknowledges financial support by the Emmy Noether Program of the German Research Foundation. JBG thanks the Australian Research Council's Special Research Centers program and CODES. This is

Q1 GSC contribution No. xxxxx. This work is a contribution to the IGCP Project 502 "Global Comparison of Volcanic-hosted Massive Sulphide Districts."

Address correspondence to Sven Petersen, Institute of Mineralogy, Department of Economic Geology and Petrology and Leibniz-Laboratory for Applied Marine Research, Brennhausgasse 14, Freiberg 09596, Germany. E-mail: petersen@mineral.tu-freiberg.de

Q3 **Keywords**

Our knowledge of seafloor hydrothermal systems and massive sulfide deposits is largely based on surface sampling by dredges, TV-guided grabs, submersibles, and ROVs. For the larger deposits in particular, their characterization and evaluation is limited by the lack of sufficient data on their size and especially the three dimensional distribution of major and trace elements within the deposit. Drilling is necessary to obtain information about the subsurface nature of the deposits. Until recently, the scientific community has been relying on the Ocean Drilling Program (ODP) to drill hydrothermal sites. In the past decade, ODP has drilled a total of four different hydrothermal sites, including the sediment-hosted Middle Valley site at the Juan de Fuca Ridge, the sediment-sill complex at Escanaba Trough at the southern Gorda Ridge, the sediment-free, basalt-hosted TAG hydrothermal mound at the Mid-Atlantic Ridge, and the PACMANUS site in the eastern Manus back-arc basin.

Drilling the sediment-hosted Middle Valley site during ODP Legs 139 and 169 has shown that the mineralization is the result of a structurally focused, long-lived hydrothermal system that produced stratigraphically stacked massive sulfide lenses over a depth interval of 210 m (Zierenberg et al. 1998; Fouquet et al. 1998a). Silicification at depth resulted in the formation of a deep copper zone as replacement of a permeable sediment horizon (Zierenberg et al. 1998). Hydrothermal reworking at the Bent Hill site resulted in some zone refining with sphalerite enriched near the top of the deposit and chalcopyrite more common at deeper levels (Duckworth et al. 1994).

The sediment-sill complex at Escanaba Trough on the southern Gorda Ridge was also drilled during ODP Leg 169 (Fouquet et al. 1998a). Sulfide recovery was generally poor, with less than 1 m of in situ sulfides recovered in only the uppermost cores of two holes (Fouquet et al. 1998b). In contrast to Middle Valley, deep drilling indicated that massive sulfide formation is predominantly located at the sediment/seawater interface and forms a thin (5–15 m) veneer on top of the sediment (Zierenberg and Miller 2000), likely related to a recent hydrothermal event (Zierenberg et al. 1998).

The only sediment-free, basalt-hosted hydrothermal system drilled so far is the active Trans-Atlantic Geotraverse (TAG) hydrothermal mound at the base of the eastern valley wall of the Mid-Atlantic Ridge at 26°N (Humphris et al. 1995; Herzig et al. 1998b). Drilling up to 125 m deep indicated that the size of the mound-stockwork complex is approximately 3.9 million tonnes (Hannington et al. 1998). Comparisons of geochemical data with samples collected during earlier submersible dives confirm that surface samples are not representative of the bulk composition of the deposit and that zone refining has effectively stripped metals from the massive sulfides and concentrated them at the top of the deposit (Hannington et al. 1998; Peterson et al. 2000). Unexpectedly, the bulk of the mound is composed of breccias that, most likely, formed as a result of collapse of anhydrite-cemented portions of the mound following major episodes of hydrothermal activity and/or hydraulic fracturing due to fluid overpressure in the subseafloor (Humphris et al. 1995).

The Ocean Drilling Program targeted that felsic-hosted PACMANUS site in the eastern Manus Basin during Leg 193 (Binns et al. 2002). Poor core recovery in the sulfide-rich intervals, at least partially due to casing requirements for deep drilling, prevented an adequate assessment of the economic potential of the site, but indicated that massive sulfide formation may be restricted to a thin veneer at the top of the

extrusive rocks (Binns et al. 2002). Intense anhydrite veining and clay alteration at depth indicate the presence of a large hydrothermal system underneath a fresh volcanic carapace (Binns et al. 2002). 75

It is evident from the results of these ODP drilling operations that coring of the immediate subsurface is often not possible during ODP Legs, owing to the need to set casing for deep hard rock drilling, thus leaving a significant gap between surface sampling and deep drilling. Portable drilling devices that can be used from ships of opportunity are needed to obtain this vital information. 80

In 2002, we successfully deployed the British Geological Survey (BGS) Rockdrill from the German R/V *Sonne* and demonstrated that shallow drilling of seafloor hydrothermal systems with a lander-type system is feasible from a conventional research vessel, thereby significantly extending our knowledge of the 3rd dimension of the deposits. Here, we present the first results of this recent drilling and coring program at Conical Seamount (New Ireland fore-arc) and PACMANUS/Roman Ruins (Eastern Manus Basin) in the Bismarck Archipelago of Papua New Guinea. 85

Geological Setting of the Drill Sites

The Bismarck Archipelago is located in the northeastern province of Papua New Guinea and includes the islands of New Britain, New Ireland, Bougainville, and the Solomons. The region is dominated by the presently active north-northeast-facing New Britain Trench and back-arc spreading in the Manus basin to the north (Figure 1). The Manus Basin is a rapidly opening (~10 cm/yr) back-arc basin located north of the active New Britain subduction zone (Figure 1) within a complex zone of oblique convergence between the major Indo-Australian and Pacific plates. True seafloor spreading occurs in the Central and Western Manus Basins, whereas the Eastern Manus Basin is characterized by extensional rifting (Martinez and Taylor 1996). 90 95

The New Ireland region is well known for its gold potential including the giant Ladolam epithermal gold deposit (ca. 40 million oz. contained Au) located in the Luise Volcano on the island of Lihir (Moyle et al. 1990; Carman 2003). Gold-rich massive sulfides deposits are also presently forming in the submarine environment in the Central and Eastern Manus basins (Tufar 1990; Binns and Scott 1993; Lisitsyn et al. 1993; Gamo et al. 1997; Moss and Scott 2001). Additionally, gold-rich (up to 230 g/t Au) siliceous veins were discovered in 1994 at Conical Seamount, a small volcano between Lihir Island and the New Ireland arc and documented the presence of a new type of seafloor hydrothermal deposit with similarities to vein-style gold deposits on land (Herzig et al. 1994, 1998a, 1999; Petersen et al. 2002). 100 105

Conical Seamount belongs to the NW-SE trending Tabar-Lihir-Tanga-Feni volcanic chain that extends for approximately 260 km parallel to the coast line of New Ireland (Figure 1). Volcanic activity in the Tabar-Feni island chain, which began about 3.5 million years ago, appears to be related to extension along north-east-trending structures that cut across the New Ireland Basin (Stewart and Sandy 1988; McInnes and Cameron 1994). The volcanism in the area belongs to a high-K calc-alkaline magma series and includes alkali-olivine basalts, trachybasalts, and foid-bearing mafic rocks (Kennedy et al. 1990; Müller et al. 2001, 2003). 110 115

Conical Seamount (Figure 1b) was discovered in 1994 and is the largest of several young volcanic cones in the area south of Lihir Island (Herzig et al. 1994). It has a basal diameter of 2.5 km and rises about 600 m above the surrounding 120

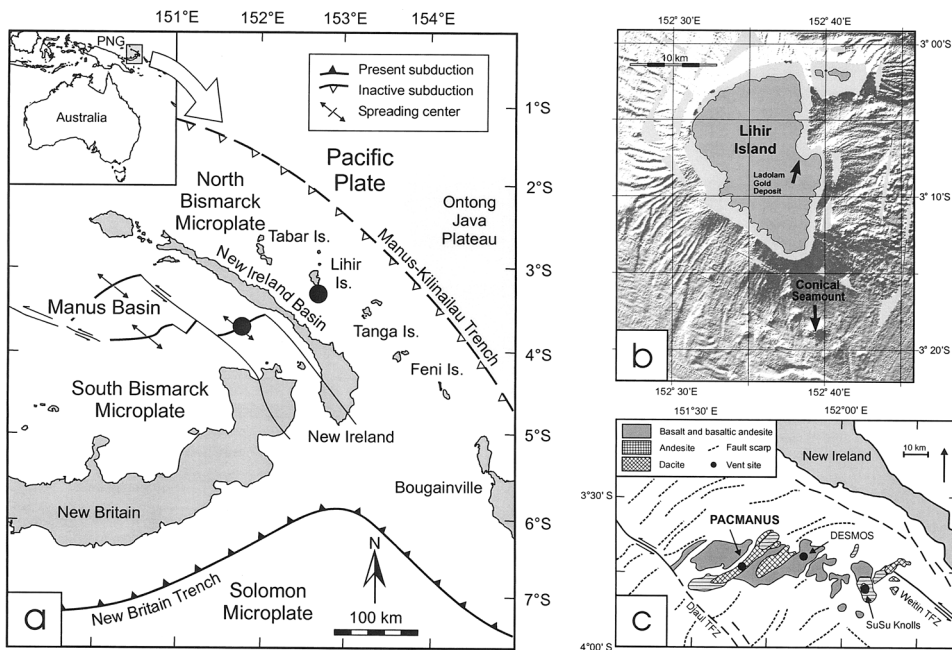


Figure 1. (a) Regional geological setting of the New Ireland fore-arc and the Manus Basin. Rockdrill sites (solid circles) at Conical Seamount (south of Lihir Island) and PACMANUS/Roman Ruins (Eastern Manus Basin) are indicated. (b) Shaded bathymetric relief of the area surrounding Lihir Island showing the location of Conical Seamount south of Lihir. The giant Ladolam epithermal gold deposit is located approximately 21 km north of Conical Seamount (modified from Petersen et al. 2002). (c) Regional geology of the Eastern Manus Basin and location of the PACMANUS hydrothermal field (modified from Binns et al. 2002).

seafloor to a minimum depth of 1,050 m. The seamount is characterized by a small summit plateau extending over 100×200 m and hosting an elongate, 100-m long, E-W-oriented volcanic feature that is interpreted to be an eruptive fissure (Herzig et al. 1999). The volcano consists of massive lava flows, pillows, and talus breccias comprising moderately vesicular fragments and scoria. The symmetrical shape of the volcano suggests a relatively young age although its flanks are covered by pelagic sediments (Herzig et al. 1999). The first indications of gold-rich epithermal-style vein mineralization at the summit plateau of Conical Seamount were found in 1994 (Herzig et al. 1994; Herzig and Hannington 1995) and confirmed in 1998 (Herzig et al. 1998a, 1999; Petersen et al. 2002).

The Eastern Manus Basin, which is host to several massive sulfide deposits including PACMANUS, DESMOS, and SuSu Knolls, is a pull-apart rift zone with east-west trending neovolcanic ridges composed of basaltic to rhyodacitic volcanic rocks (Binns and Scott 1993; Moss et al. 2001; Sinton et al. 2003). The basin is bounded by two sinistral transform faults, the Djual and Weitin Faults.

The PACMANUS hydrothermal field (Figure 1c) is situated on the crest of Pual Ridge, an elongate feature composed of dacite with subordinate basaltic andesite and rhyodacite which stands 500–700 m above the surrounding basin floor (Binns et al. 2002). The ridge itself is terraced and consists of stacked 5–30-m thick lava flows (Binns et al. 2002). Five principal areas of hydrothermal activity (Roman

Ruins, Satanic Mills, Tsukushi, Rogers Ruins, and Snowcap) have been delineated at the PACMANUS site. Except for Snowcap, they consist of active and inactive black smoker chimneys and spires on basal sulfide mounds. Hydrothermal fluids escape as acid (pH = 2.5–3.5 at 25°C) black to gray smoke with exit temperatures up to 276°C or as clear fluids vigorously venting from nearby sulfide structures (Binns et al. 2002). Surface samples contain up to 64 ppm Au and 2030 ppm Ag (average = 13 ppm Au and 295 ppm Ag) and an average of 5.9 wt.% Cu and 25 wt.% Zn (Scott and Binns 1995; Parr et al. 1996; Moss and Scott 2001; Lee 2000). Chimneys are composed predominantly of chalcopyrite, sphalerite, with subsidiary pyrite, bornite, tennantite, galena, and dufrenoyite (Binns et al. 2002). The gangue includes variable proportions of barite, anhydrite and amorphous silica.

The Snowcap site is somewhat different and characterized by outcrops of dacite-rhyodacite lava and hyaloclastite, which are altered by highly acidic, oxidized fluids to an assemblage of cristobalite, minor natroalunite, diaspore, and illite-montmorillonite and traces of pyrite, marcasite, chalcopyrite, enargite, and (formerly molten) globules of native sulfur (Binns et al. 2002).

Methods

The British Geological Survey (BGS) 5-meter “Rockdrill” is a portable drilling unit, comes in a soft top 40’ container and a flatbed 20’ container and consists of a 5-meter core barrel drill rig, a 2500 m winch, and a control cabin from which the drilling operation is run (Figure 2). The drill operates in water depths upto 2000 m and was deployed over the stern of the vessel, using the ship’s 35 t “A” frame gantry

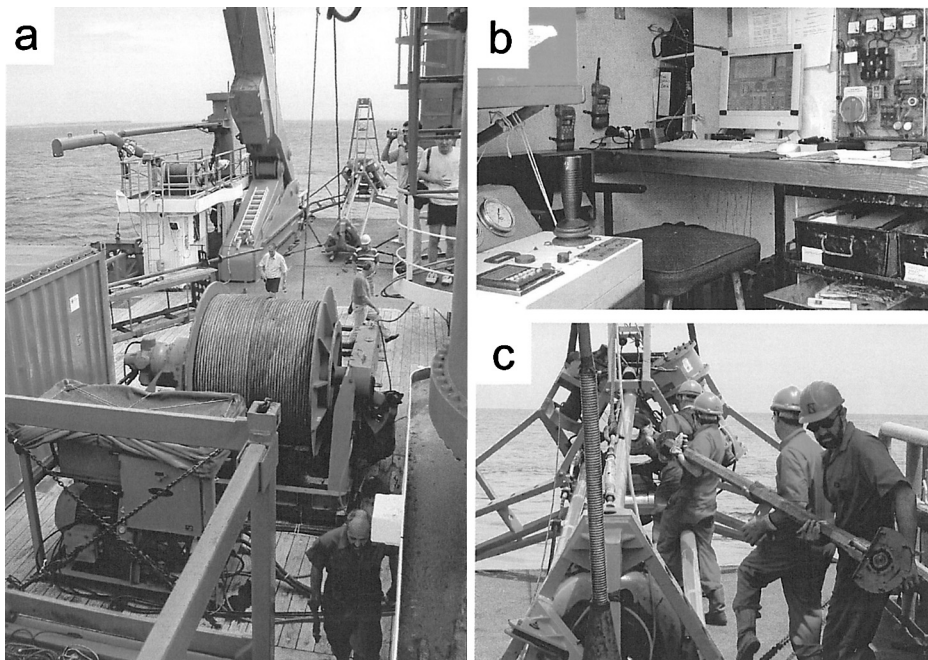


Figure 2. BGS Rockdrill during drilling operations with R/V Sonne in the New Ireland fore-arc and the Manus back-arc.

in conjunction with the BGS umbilical winch. The installed seabed camera system provides a black and white seafloor image close to the drill bit allowing an assessment of the position of the rig on the seabed prior to commencement of drilling. 165 The rugged topography at both sites caused problems in landing the rig at the desired drilling positions with sufficient stability to attempt drilling (less than 25 degrees of inclination). However, the use of the rig-installed, downward-looking echosounder and the integrated pitch/roll inclinometer allowed for controlled landing and slope monitoring before cable tension was finally released and the rig 170 allowed to sit on the seabed. The coring was carried out with two types of “off the shelf” drill bits (surface set stepped profile and grade 9 matrix impregnated diamond bits), both of which proved equally suitable for the rubbly and pebbly volcanic rocks at Conical Seamount and for cutting sulfides at PACMANUS.

The drill core material was initially logged on board. Representative thin sections 175 were prepared for petrographic inspection and 85 quarter core samples (10 to 50 cm of core length) were crushed to a grain size below 2 mm with an impact mill for whole-rock mineralogical and geochemical investigations. The crushed samples were repeatedly washed with distilled water to remove seawater salt. The washed material from Conical Seamount was then split with a riffle splitter and one split 180 was taken for geochemical analysis. For geochemical analysis the splits from Conical Seamount and the entire quarter core sections from the PACMANUS sulfides were milled using an agate mill. Gold analyses for whole rock samples from Conical Seamount were performed by the Lihir Management Company at Lihir by analyzing 185 20 g sample material in duplicate using a fire assay with an atomic absorption spectroscopy (AAS) finish. Massive sulfides from PACMANUS and selected mineralized samples from Conical Seamount were analyzed commercially at Activation Laboratories Limited (Canada) for their major and trace element composition using an assay with inductively coupled plasma optical emission spectrometry finish (ICP-OES) for Cu, Zn, and Pb, and instrumental neutron activation analyses (INAA) for 190 the trace elements presented here.

Results

Out of 41 attempts, 39 holes were drilled in various areas of the summit plateau of Conical Seamount with only two core barrels returning without recovery (Figure 3; Table 1). The cumulative penetration achieved in all holes was more than 91 m with 195 individual penetration varying between 0.95 and 5.0 m (avg. 2.3 m). With an average recovery of 31%, almost 21 m of core were recovered with individual core lengths of up to 1.5 m (avg. 0.51 m). The core recoveries were low due to the fractured nature of the rock and the presence of volcanic rubble at the surface of Conical Seamount that often blocked the bit. 200

Most of the core recovered from Conical Seamount consists of variably altered ankaramitic basalt (Figure 4). Least-altered rocks from Conical Seamount are vesicular ankaramitic pebbles, boulders and blocks that, judging from seafloor observation, reach up to 1 m in diameter. Fresh ankaramite is dark grey to black and shows porphyric to glomerophytic textures. Magmatic minerals are mm- to cm-sized, 205 black clinopyroxene and grey plagioclase phenocrysts, bluish magnetite octahedra, and very rare olivine xenocrysts and dark brown hornblende phenocrysts. The vesicles are of variable size (< 1 mm–4 cm), abundance (1–10 vol.-% of the whole rock) and shape (spherical, elliptical and elongated types).

Table 1. Drilling statistics for Conical Seamount (New Ireland fore-arc) and PACMANUS/Roman Ruins (Eastern Manus Basin)

Parameter	Conical Seamount	PACMANUS/Roman Ruins
Number of holes	41	10
Technical failures	2	0
Holes without recovery	2	0
Total penetration	91.1 m	35.6 m
Individual penetration	0.95–5.00 m	2.06–5.00 m
Average penetration	2.3 m	3.6 m
Total core length	20.8 m	11.1 m*
Individual core length	0–1.50 m	0.35–2.20 m
Average core length	0.5 m	1.1 m
Average recovery	31%**	31%
Individual recovery	0–100%	9–65%

*8.9 m of massive sulfide.

**Based on 37 holes drilled with recovery.

Alteration is mainly manifested by the modification of the groundmass and the 210 formation of varying amounts of disseminated pyrite. Pyroxene and plagioclase phenocrysts are mostly unaltered and magnetite in most cores is still intact. Moderate to intense clay-pyrite alteration has been observed in a number of cores (03RD, 05RD,

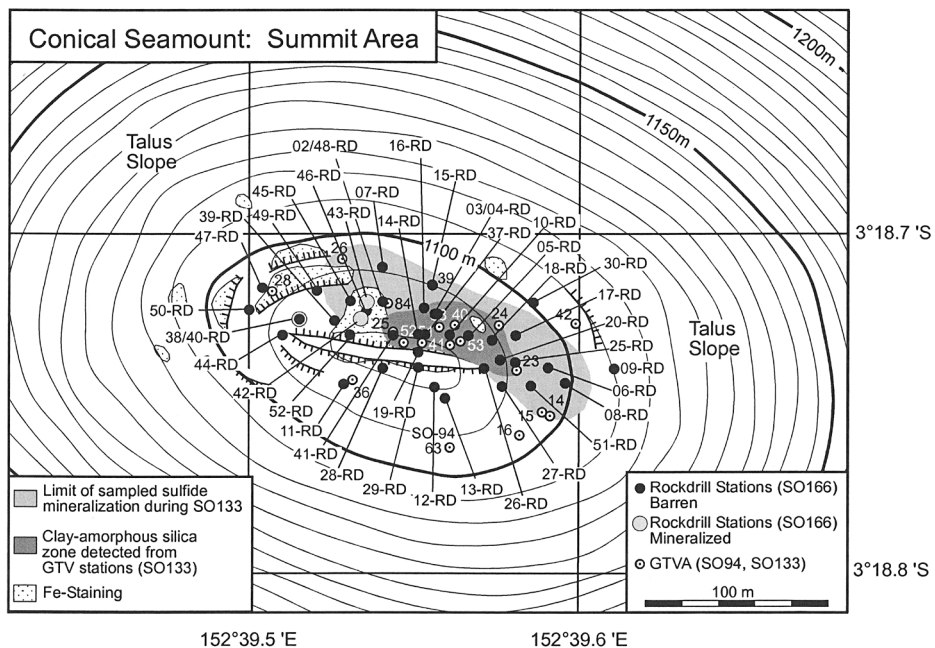


Figure 3. Conical Seamount summit plateau with drill holes from cruise SO166 as well as mineralized zones as interpreted from SO133 TV-grab stations (modified from Petersen et al. 2002).

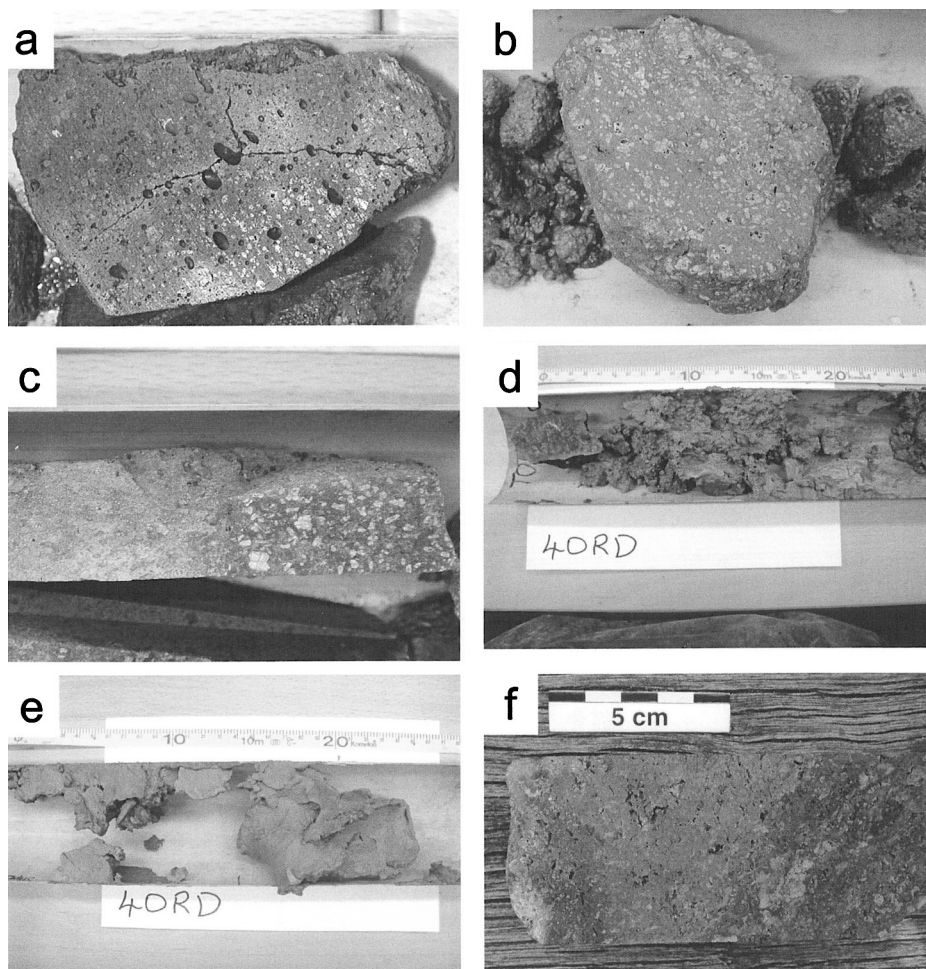


Figure 4. Drill core recovered from Conical Seamount using the BGS Rockdrill. (a) Least altered vesicular ankaramitic basalt (sample 19RD60-68). (b) Intense clay-pyrite alteration of dense ankaramite (sample 08RD27-33). (c) Clay-pyrite alteration of pyroxene with pinkish K-feldspar on fracture planes (sample 18RD42-48). Field of view is 6 cm. (d) Intensely mineralized basalt (left) with abundant clay-rich polymetallic ooze (sample 40RD0-40). (e) Clay-rich material recovered from the outside of the core barrel during station 40RD (sample 40RD OUT). (f) Silica flooding in basaltic sample with abundant fine-grained, disseminated sulfides. Vesicles are lined with realgar and orpiment (sample 43RD10-25).

08RD, 15RD, 17RD, 18RD, 40RD, and 43RD) and is characterized by partial to complete replacement of the matrix as well as pyroxene phenocrysts by a mixture 215 of white clays, amorphous silica, and trace pyrite. Intensely altered, soft, sand-sized material was recovered in only two holes (38RD and 52RD), and at the bottom of 47RD, underneath a cap of least altered basalt, highlighting the difficulty of sampling this material. However, these samples showed that alteration is laterally far 220 more widespread than previously documented and that for parts of Conical Seamount intensely altered lava flows are covered by younger, unmineralized lavas.

Polymetallic mineralization similar to the mineralization previously encountered in surface TV-grab samples during cruise SO 133 in 1998 was discovered in two holes (Figure 4d–f). These cores (40RD, penetration 3.6 m; 43RD, penetration 4.5 m) are located on the western side of the plateau, mainly in an area of increased Fe staining of the basalt which may derive from weathering of sulfides. Core 43RD and the uppermost sample of core 40RD show intense silicification and abundant disseminated sulfides including galena, sphalerite, some chalcopyrite, and minor pyrite, together with amorphous silica throughout the samples. Larger vesicles are filled or lined with realgar and orpiment. The lowermost part of core 40RD consists of soft, sand-sized and mineralized material containing abundant chlorite. In order to recover this material flushing of the core barrel was strongly reduced during the last few minutes of station 40RD. Most likely as a result of this procedure we recovered 300 gm of light grey mud at the outside of the core barrel (sample 40RD OUT) that was not flushed away.

Mineralized drill core samples contain up to 14.2 g/t Au (20 g fire assay; Lihir Gold Ltd., Table 2) and appear to be part of a more extensive gold zone located below a carapace of relatively fresh ankaramite and trachybasalt. In addition to high concentrations of gold, these samples contain high values of Pb (up to 2.2 wt.%; Table 3), As (up to 3810 ppm), and Sb (up to 218 ppm), and low contents of Cu (up to 0.2 wt.%) and Zn (up to 6.6 wt.%), which is distinct from typical submarine massive sulfide deposits. Since core 40RD had a penetration of 3.63 m and 43RD of 4.47 m, it seems likely that the gold-rich mineralization at Conical Seamount is not restricted to the surface but that there is potential for gold mineralization at depth.

In the PACMANUS hydrothermal field drilling was carried out over two days at the Snowcap (57RD) and Roman Ruins sites (stations 60RD to 69RD). At Roman Ruins 10 holes were drilled in the NE part of the hydrothermal field (Figure 5). A total penetration of 35.55 m and a total recovery of 11.07 m of mainly massive sulfides were achieved. Individual holes reached between 2.06 m and 5.00 m (average 3.56 m), with core lengths of 0.35 to 2.20 m (avg. 1.12 m) and a recovery rate between 9 and 65% (avg. 30%).

Station 57RD at Snowcap recovered 10 cm of dacite fragments and penetration proved difficult. Operations at Roman Ruins had far better results. Two out of the 10 holes attempted recovered least altered to weakly altered dacite (stations 62RD and 64RD); massive sulfides were recovered from the other eight holes (Figure 6). The longest sulfide intersections were 2.2 m (core 69RD, 4.9 m penetration), 1.9 m (core 67RD, 5.0 m penetration), and 1.4 m in length (core 61RD, 2.8 m penetration). Four of the holes drilled at Roman Ruins penetrated close to 5 m into the massive sulfide mound (60RD, 65RD, 67RD, and 69RD). One hole (61RD) terminated in weakly to intensely altered dacite possibly indicating that massive sulfide formation is limited to a thin veneer directly above and below the seafloor.

Least-altered volcanic rocks drilled from Roman Ruins are dacites displaying flow foliation. Fresh dacite is mainly aphyric with a glassy groundmass and numerous vesicles of different shapes and sizes, which often display an elongation into the direction of the lava flow. Rare plagioclase phenocrysts reach a length of 0.5–2 mm. The rocks are often distinctly fractured with multicolored joints and surfaces due to hydrothermal overprint or interaction with seawater.

The sulfide-bearing cores are dominated by light brown to brown sphalerite with varying proportions of barite, pyrite and chalcopyrite (Figure 6a and b). Anhydrite, amorphous silica, and rare, variably altered dacite fragments occur together with the

Table 2. Summary and preliminary results of Rockdrill operations at Conical Seamount

Station	Location	Depth	Penetration	Core Recovery	Alteration	Au (ppm)
02RD	03°18.720'S/152°39.540'E	1064 m	—	failure	—	—
03RD	03°18.724'S/152°39.555'E	1063 m	1.00 m	0.25 m	clay-pyrite	<0.02
04RD	03°18.724'S/152°39.555'E	1060 m	3.64 m	0.50 m	clay-pyrite	<0.02
05RD	03°18.730'S/152°39.565'E	1063 m	5.00 m	0.30 m	strong clay-pyrite	<0.02
06RD	03°18.740'S/152°39.590'E	1089 m	1.10 m	1.10 m	clay-pyrite	<0.02
07RD	03°18.710'S/152°39.540'E	1066 m	2.12 m	0.75 m	least altered	<0.02
08RD	03°18.745'S/152°39.595'E	1101 m	1.37 m	1.00 m	clay-pyrite	<0.02
09RD	03°18.740'S/152°39.610'E	1112 m	1.06 m	0.85 m	clay-pyrite	<0.02
10RD	03°18.730'S/152°39.560'E	1073 m	2.06 m	0.81 m	weak pyrite	<0.02
11RD	03°18.730'S/152°39.543'E	1078 m	2.09 m	0.50 m	least altered	<0.02
12RD	03°18.745'S/152°39.555'E	1096 m	1.05 m	0.23 m	least altered	<0.02
13RD	03°18.748'S/152°39.558'E	1082 m	2.33 m	1.45 m	least altered	<0.02
14RD	03°18.730'S/152°39.550'E	1063 m	1.70 m	0.50 m	weak pyrite	<0.02
15RD	03°18.715'S/152°39.550'E	1071 m	1.50 m	1.20 m	weak pyrite	<0.02
16RD	03°18.722'S/152°39.552'E	1072 m	1.29 m	0.65 m	least altered	<0.02
17RD	03°18.730'S/152°39.580'E	1086 m	3.48 m	0.65 m	clay-pyrite	<0.02
18RD	03°18.731'S/152°39.572'E	1076 m	1.51 m	0.85 m	clay-pyrite	<0.02
19RD	03°18.735'S/152°39.550'E	1075 m	1.49 m	0.35 m	least altered	<0.02
20RD	03°18.738'S/152°39.575'E	1099 m	—	failure	—	—

25RD	03°18.737'S/152°39.580'E	1089 m	0.95 m	0.30 m	weak pyrite	<0.02
26RD	03°18.740'S/152°39.570'E	1089 m	1.50 m	0.30 m	weak pyrite	<0.02
27RD	03°18.745'S/152°39.575'E	1078 m	1.11 m	0.40 m	weak pyrite	<0.02
28RD	03°18.740'S/152°39.540'E	1082 m	2.40 m	0.70 m	weak pyrite	<0.02
29RD	03°18.740'S/152°39.550'E	1076 m	1.00 m	0.15 m	least altered	<0.02
30RD	03°18.720'S/152°39.585'E	1115 m	3.14 m	0.60 m	weak clay-pyrite	<0.02
37RD	03°18.729'S/152°39.551'E	1057 m	1.50 m	0.30 m	least altered	<0.02
38RD	03°18.725'S/152°39.515'E	1110 m	4.50 m	scrapings	strong clay-pyrite	n.a.
39RD	03°18.725'S/152°39.525'E	1064 m	1.70 m	0.40 m	weak pyrite	<0.02
40RD	03°18.725'S/152°39.515'E	1085 m	3.63 m	0.40 m	mineralized + chlorite	1.01
40RDOUT					mineralized mud + chlorite	14.20
41RD	03°18.745'S/152°39.528'E	1083 m	1.03 m	0.30 m	least altered	<0.02
42RD	03°18.725'S/152°39.533'E	1094 m	3.00 m	1.50 m	weak pyrite	<0.02
43RD	03°18.720'S/152°39.535'E	1084 m	4.47 m	0.25 m	mineralized + silica	3.05
44RD	03°18.730'S/152°39.510'E	1095 m	2.67 m	0.55 m	least altered	<0.02
45RD	03°18.720'S/152°39.530'E	1057 m	5.00 m	0.30 m	least altered	<0.02
46RD	03°18.723'S/152°39.535'E	1057 m	4.05 m	0.35 m	weak pyrite	<0.02
47RD	03°18.715'S/152°39.505'E	1061 m	5.00 m	0.27 m	clay-pyrite at depth	<0.02
48RD	03°18.720'S/152°39.540'E	1055 m	1.25 m	0.65 m	least altered	<0.02
49RD	03°18.718'S/152°39.520'E	1086 m	1.33 m	0.55 m	weak pyrite	<0.02
50RD	03°18.722'S/152°39.511'E	1095 m	1.64 m	0.25 m	least altered	<0.02
51RD	03°18.745'S/152°39.585'E	1073 m	1.41 m	0.30 m	weak clay-pyrite	<0.02
52RD	03°18.730'S/152°39.530'E	1059 m	5.00 m	scrapings	strong clay-pyrite	n.a.

Table 3. Selected base metal and trace element contents of mineralized drill core from Conical Seamount

Station	Cu %	Zn %	Pb %	Au ppm	Ag ppm	As ppm	Sb ppm
40RD (0–40 cm)	0.03	0.28	0.07	1.01	40	1610	35
40RD (OUT)	0.21	6.62	2.20	14.20	132	1570	78
Q7 43RD (0–25 cm)	0.04	0.50	0.27	3.05	27	3810	218

sulfides. The textures, in most cases, resemble those of sulfides recovered from the surface of the PACMANUS field (Moss and Scott 2001). Ribbon-banded sphalerite as observed in “beehive” smokers at various other seafloor hydrothermal sites is common. Relics of chalcopyrite-lined chimney orifices and pyritized former worm tubes further indicate that part of the recovered massive sulfide was formed above the seafloor. 275

A 20-cm-thick layer of chalcopyrite intergrown with abundant black sphalerite was sampled in the upper part of 65RD (Figure 6c). Hole 66RD contains a section of massive dense chalcopyrite separating layers of porous massive sphalerite (Figure 6d). Drill site 60RD recovered a sphalerite ± chalcopyrite and barite assemblage underlain by a nodular breccia of rounded chalcopyrite + pyrite clasts set in a matrix of anhydrite (Figure 6e). The presence of abundant anhydrite within this and other 280

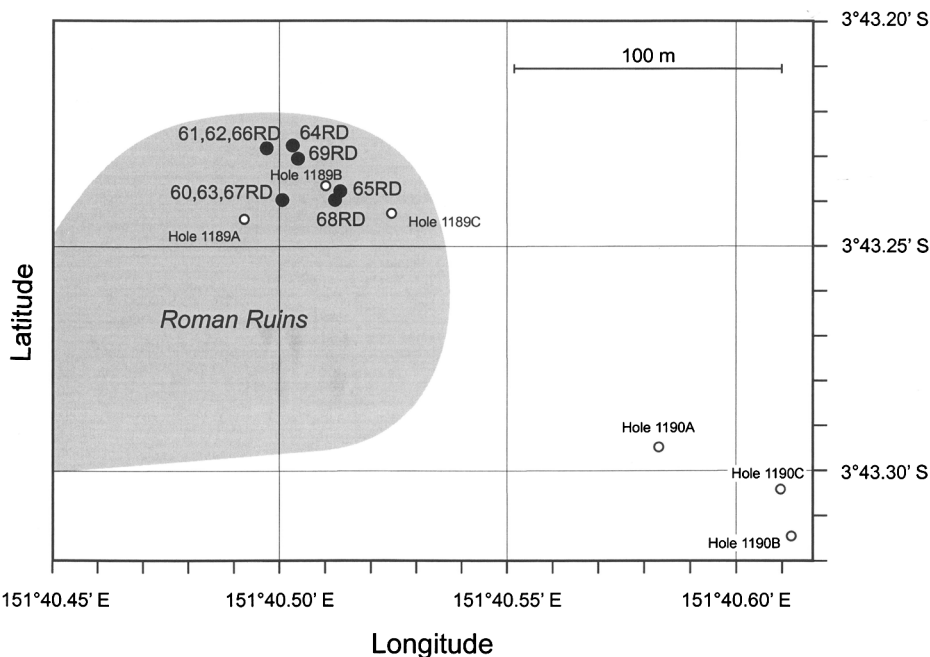


Figure 5. Location of BGS Rockdrill holes at PACMANUS (filled circles) drilled during the recent cruise SO166. Ocean Drilling Program (ODP) sites are also indicated (open symbols; Binns et al. 2002). The approximate area of sulfide outcrop at Roman Ruins is shaded (modified from Binns et al. 2002).

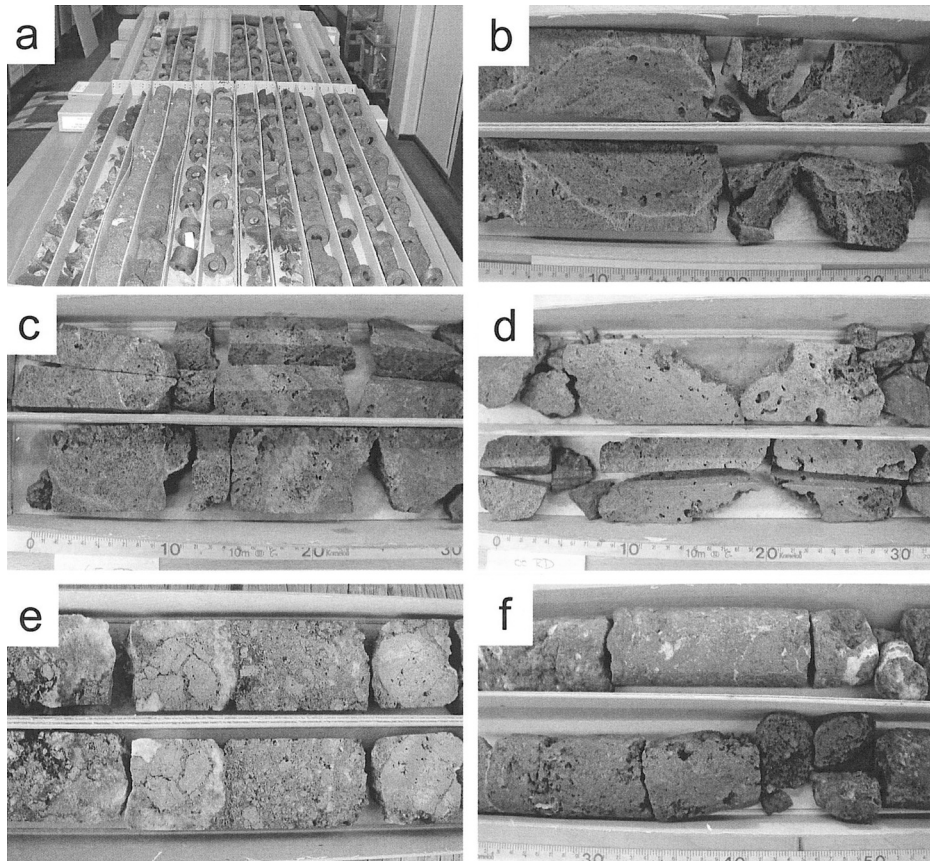


Figure 6. (a) Collection of drill core recovered from PACMANUS/Roman Ruins during two days of drilling with the BGS Rockdrill. (b) Massive porous sphalerite and barite showing evidence for multiple overgrowths. Section 61RD0-35. (c) Porous brownish sphalerite and barite interlayered with massive chalcopyrite intergrown with dark-brown sphalerite (center). Section 65RD0-30. (d) Massive dense chalcopyrite intercalated between porous sphalerite and barite. Section 66RD0-35. (e) Nodular pyrite-chalcopyrite-anhydrite breccia from the bottom of core 60RD. Section 60RD65-85. (f) Massive porous sphalerite (lower part of the image; section 67RD20-55) overlying nodular to sandy pyrite-chalcopyrite breccia in a matrix of anhydrite (upper part of the image; section 67RD 120-155).

cores is indicative of seawater penetrating into the massive sulfide mound and mixing with the hydrothermal fluid and/or conductively heating in the subsurface. The nodular appearance of the chalcopyrite + pyrite fragments suggests that massive sulfides have been mechanically reworked, likely due to the formation and dissolution of anhydrite and/or fluid overpressure. This is confirmed by several cores that contain fine-grained, clastic chalcopyrite + pyrite sand. 285

Preliminary analyses of quarter core sections, varying in length from 10 to 50 cm, indicate high base and precious metal contents (Table 4). The most impressive grades 290 come from hold 65RD (4.4 m penetration) which returned 0.45 m @ 31 g/t Au, 210 g/t Ag, 7.4 wt.% Cu, 23.9 wt.% Zn, and 0.5 wt.% Pb, including a section of 0.2 m with 57.2 g/t Au. Another exceptional result came from hold 66RD (3.7 m

Table 4. Geochemistry of entire massive sulfide drill cores from Roman Ruins (PACMANUS) as well as of selected gold-rich and gold-poor core sections

Core	Penetration	Core length	Description	N	Cu wt. %	Zn wt. %	Pb wt. %	Fe wt. %	Ba wt. %	Au ppm	Ag ppm
core 60RD	4.4 m	0.9 m	Sphalerite overlying nodular pyrite-chalcopyrite-anhydrite breccia	3	6.4	6.8	0.22	23.2	2.8	5.0	41
core 61RD	2.8 m	1.4 m	Porous sphalerite-barite with minor chalcopyrite	3	1.5	23.3	1.24	4.1	22.6	7.4	286
core 63RD	2.7 m	0.5 m	Resedimented fine-grained pyrite-chalcopyrite-sphalerite	1	8.8	12.4	0.54	22.1	3.0	8.1	106
core 65RD	4.4 m	0.4 m	Sphalerite-rich core with 20 cm thick interval of chalcopyrite-sphalerite	4	7.4	23.9	0.50	11.3	14.7	31.2	210
core 66RD	3.7 m	0.8 m	Porous sphalerite-barite with 20 cm thick interval of massive, dense chalcopyrite	4	7.7	25.2	0.17	10.4	12.9	19.6	200
core 67RD	5.0 m	1.9 m	Sphalerite-barite overlying nodular pyrite-chalcopyrite-anhydrite breccia	11	3.3	10.3	0.35	20.3	2.9	8.6	130
core 68RD	2.1 m	0.4 m	Pyrite-chalcopyrite breccia	2	7.5	6.5	0.25	27.4	1.9	4.0	58

core 69RD	4.9 m	2.2 m	Sphalerite-barite dominated core with minor alternating pyrite-chalcopyrite sections	7	2.3	25.6	0.85	9.0	10.6	11.4	163
Selected gold-rich sections											
core 65RD	(10–30 cm)		Chalcopyrite with dark-brown to black sphalerite and late barite	1	12.9	12.2	0.13	11.9	21.0	57.1	135
core 67RD	(0–20 cm)		Porous sphalerite with minor barite	1	0.7	46.6	1.22	3.3	7.8	35.8	584
core 69RD	(85–120 cm)		Porous dark-brown sphalerite with minor barite and amorphous silica	1	0.4	44.7	0.99	3.5	8.2	30.4	403
Selected gold-poor sections											
core 60RD	(30–90 cm)		Nodular pyrite-chalcopyrite-anhydrite breccia (lower part of core)	2	7.2	1.1	0.06	25.3	0.9	1.3	6
core 67RD	(80–190 cm)		Clastic pyrite-chalcopyrite in anhydrite matrix (lower part of core)	6	4.4	0.2	0.02	29.4	<0.1	1.9	<5

N = number of subsamples/core sections analyzed. All analyses are averages of two duplicate measurements with the exception of sections from core 67RD which were analyzed once. Methods: Cu, Zn, and Pb by assay with ICP-OES finish; Fe, Ba, Au, and Ag by INAA; Chemical analyses were carried out commercially at Activation Laboratories Limited (Canada). Cores 62RD and 64RD recovered least altered and weakly altered dactite.

penetration) which returned 0.8 m @ 19.6 g/t Au, 200 g/t Ag, 7.7 wt.% Cu, 25.2 wt.% Zn, and 0.2 wt.% Pb. The longest core (69RD, 4.9 m penetration) recovered 2.2 m @ 11.4 g/t Au, 163 g/t Ag, 2.3 wt.% Cu, 25.6 wt.% Zn, and 0.9 wt.% Pb.

Overall, the major and trace element distribution in most cores is very heterogeneous and follows the complicated mineralogical zonation. Gold enrichment throughout the cores is generally related to sphalerite-rich sections, yet the highest Au-grade occurs in a section of chalcopyrite associated with dark-brown to black sphalerite and abundant late barite (Table 4). The association of chalcopyrite and sphalerite in this section might indicate that this mineral assemblage was deposited at higher temperatures. However, core sections of other cores that contain light-to dark-brown sphalerite are also enriched in gold (Table 4).

Several cores show more or less distinct enrichments of Zn, Pb, Ba, Au, and Ag in the upper parts of the core, whereas low precious metal concentrations, despite elevated concentrations of Zn and/or Cu occur in the lower parts of cores 65RD and 69RD. Low gold contents in the reworked nodular chalcopyrite + pyrite + anhydrite breccias at the bottom of cores 60RD and 67RD possibly indicate that zone refining is responsible for some of the precious metal enrichment observed in PACMANUS massive sulfides. The reworking of sulfides and the overprinting with late barite is a consequence of multiple hydrothermal events and complicates the interpretation of the geochemical data. Gold enrichment with chalcopyrite ± sphalerite as well as with sphalerite ± barite results in low correlation coefficients for gold with most elements. Positive correlations exist for Au–Zn ($r = 0.49$; $N = 35$), Au–Ag ($r = 0.49$), and Au–Ba ($r = 0.48$), whereas correlation coefficients for Au–Cu ($r = -0.06$) and Au–Fe ($r = -0.49$) are low or negative. High positive correlation coefficients occur for Zn–Ag ($r = 0.86$), Zn–Pb ($r = 0.72$) and Pb–Ag ($r = 0.69$). Negative correlation coefficients for Fe/Ag ($r = -0.74$) indicate the preferred precipitation of Ag with Zn–Pb-sulfides. Arsenic shows no clear correlation with the major elements, except Pb ($r = 0.54$).

TV-guided surface grab sampling that accompanied the drilling program recovered massive sulfides as well as active and inactive chimneys from the Satanic Mills and Roman Ruins sites. Samples from the Satanic Mills site include chalcopyrite-bornite chimney conduits as well as Zn-rich samples and small tennantite-tetrahedrite-bornite chimneys. Some samples from the mound surface at Roman Ruins show a knife-edge contact between least altered, black dacitic hyaloclastite set in a matrix of porous sphalerite and intensely clay-altered white dacite fragments cemented by chalcopyrite, pyrite and sphalerite. This suggests the presence of a high-temperature fluid just below the seafloor. A strongly siliceous, black to dark brown layer occurs in several samples suggesting the presence of a siliceous cap in certain areas.

Discussion

Investigations of the third dimension of seafloor massive sulfide deposits has, until now, been possible only by deep drilling during operations of the Ocean Drilling Program. At PACMANUS, and previously at Middle Valley, Escanaba, and TAG coring in massive sulfides has proved extremely difficult, with very low core recoveries. The need to set casing for deep hard-rock drilling often prevented coring of the immediate subsurface, thus leaving a significant gap between surface sampling and deep core recovery. Drilling with a portable submersible drill such as the BGS

Rockdrill can bridge this sampling gap. Coring at Conical Seamount and Roman Ruins has provided information not previously available and has documented significant subsurface mineralization at both locations.

Drilling the upper five meters at the top of Conical Seamount has provided evidence for more widespread alteration and mineralization in the subsurface. The extension of mineralization to the western part of the summit plateau and the recovery of altered material below a carapace of least-altered volcanic rocks indicates the possibility of a larger Au-mineralized hydrothermal system at depth. At Conical Seamount deeper drilling is now required to fully assess the depth extent of the mineralization.

At Roman Ruins, drilling with the BGS Rockdrill revealed high base- and precious metal contents at depth, similar to those in chimneys collected from the surface. The mineralogy observed in drill core samples from Roman Ruins is also similar to those of surface samples, however, the amount of As-Sb-sulfosalts and galena seems to be lower at depth. The nodular texture observed in cores 60RD and 67RD strongly resembles cores from the central part of the TAG hydrothermal field that were recovered during Ocean Drilling Program Leg 158 (Humphris et al. 1995; Herzig et al. 1998b; Petersen et al. 2000). These textures were interpreted to be the result of multiple episodes of hydrothermal activity and associated zone refining of elements (Petersen et al. 2000). Although at a smaller scale, a similar decrease in the concentration of several elements down core is evident in the breccia sections at the Roman Ruins site, with enrichment of the precious metals Au and Ag, as well as Zn, Cu, and Pb at the seafloor. The abundance of anhydrite, the occurrence of reworked sulfides, and the complex intergrowths observed through the core sections at PACMANUS imply that seawater penetration, reworking of primary sulfide material and possibly multistaged hydrothermal activity are important processes during the near-seafloor evolution of the deposit.

The successful drilling and coring operations with the BGS Rockdrill and R/V *Sonne* indicate that shallow drilling of deep marine mineral deposits is feasible, a prerequisite for the economic evaluation of seafloor hydrothermal systems. Results obtained by drilling at the summit plateau of Conical Seamount indicate that even deeper drilling is required to assess the size of this unique deposit fully. Shallow drilling of seafloor mineral deposits will likely become a future standard practice in the evaluation of seafloor hydrothermal systems and portable drill rigs such as the BGS Rockdrill are already advancing to mission specific platform status within the new phase of ocean drilling (IODP).

References

- Binns, R. A. and S. D. Scott. 1993. Actively forming polymetallic sulfide deposits associated with felsic volcanic rocks in the eastern Manus back-arc basin, Papua New Guinea. *Economic Geology* 88: 2222–2232.
- Binns, R. A., F. J. A. S. Barriga, and D. J. Miller. 2002. Leg 193 Summary. In R. A. Binns, F. J. A. S. Barriga, and D. J. Miller, eds., *Proceedings of the Ocean Drilling Program, Initial Reports 193*: College Station, TX: pp. 1–84.
- Carman, G. D. 2003. Geology, mineralization, and hydrothermal evolution of the Ladolam gold deposit, Lihir Island, Papua New Guinea. Pp. 247–284 in S. F. Simmons and I. Graham (eds.), *Volcanic, Geothermal, and Ore-Forming Fluids: Rulers and Witnesses of Processes within the Earth*. Society of Economic Geologists, Special Publication 10.

- Duckworth, R. C., A. E. Fallick, and D. Rickard. 1994. Mineralogy and sulfur isotopic composition of the Middle Valley massive sulfide deposit, northern Juan de Fuca Ridge. Pp. 373–385 in M. J. Mottl, E. E. Davis, A. T. Fisher and J. F. Slack (eds.), *Proceedings of the Ocean Drilling Program, Scientific Results 139*. College Station, TX. 390
- Fouquet, Y., R. A. Zierenberg, D. J. Miller, and Shipboard Scientific Party. 1998a. Introduction: Investigation of hydrothermal circulation and genesis of massive sulfide deposits at sediment-covered spreading centers at Middle Valley and Escanaba Trough. Pp. 7–16 in Y. Fouquet, R. A. Zierenberg, and D. J. Miller (eds.), *Proceedings of the Ocean Drilling Program, Initial Reports 169*. College Station, TX. 395
- Fouquet, Y., R. A. Zierenberg, D. J. Miller, and Shipboard Scientific Party. 1998b. Chapter 6: Escanaba Trough: Central Hill (Site 1038). Pp. 253–298 in Y. Fouquet, R. A. Zierenberg, and D. J. Miller (eds.), *Proceedings of the Ocean Drilling Program, Initial Reports 169*. College Station, TX. 400
- Gamo, T., K. Okamura, J. L. Charlou, T. Urade, J. M. Auzende, J. Ishibashi, K. Shitashima, H. Chiba, R. A. Binns, K. Gena, K. Henry, O. Matsubayashi, R. Moss, Y. Nagaya, J. Naka, and E. Ruellan. 1997. Acidic and sulfate-rich hydrothermal fluids from the Manus back-arc basin, Papua New Guinea. *Geology* 25: 139–142.
- Hannington, M., A. G. Galley, P. M. Herzig, and S. Petersen. 1998. Comparison of the TAG mound and stockwork complex with Cyprus-type massive sulfide deposits. Pp. 389–415 in P. M. Herzig, S. E. Humphris, and D. J. Miller (eds.), *Proceedings of the Ocean Drilling Program, Scientific Results 158*. College Station, TX. 405
- Herzig, P. M., and M. D. Hannington. 1995. Hydrothermal activity, vent fauna, and submarine gold mineralization at alkaline fore-arc seamounts near Lihir Island, Papua New Guinea. *Proceedings of PACRIM '95*. Australasian Institute of Mining and Metallurgy, Melbourne: pp. 279–284. 410
- Herzig, P. M., M. D. Hannington, B. McInnes, P. Stoffers, H. W. Villinger, R. Seifert, R. A. Binns, T. Liebe, and Shipboard Scientific Party. 1994. Submarine volcanism and hydrothermal venting studied in Papua, New Guinea. *Eos, American Geophysical Union Transactions* 75: 513, 515–516. 415
- Herzig, P. M., M. D. Hannington, P. Stoffers, and Shipboard Scientific Party. 1998a. Petrology, gold mineralization and biological communities at shallow submarine volcanoes of the New Ireland Fore-Arc (Papua New Guinea). *InterRidge* 7: 34–38.
- Herzig, P. M., S. E. Humphris, D. J. Miller, and R. A. Zierenberg eds. 1998b. *Proceedings of the Ocean Drilling Program, Scientific Results 158*. College Station, TX. 420
- Herzig, P. M., S. Petersen, and M. D. Hannington. 1999. Epithermal-type gold mineralization at Conical Seamount: A shallow submarine volcano south of Lihir Island, Papua New Guinea. Pp. 527–530 in C. J. Stanley (ed.), *Mineral deposits: processes to processing. Proceedings of the fifth biennial SGA meeting and the tenth Quadrennial IAGOD symposium*. London. 425
- Humphris, S. E., P. M. Herzig, D. J. Miller, J. C. Alt, K. Becker, D. Brown, G. Brüggmann, H. Chiba, Y. Fouquet, J. B. Gemmel, G. Guerin, M. D. Hannington, N. G. Holm, J. J. Honnorez, G. J. Itturino, R. Knott, R. Ludwig, K. Nakamura, S. Petersen, A.-L. Reysenbach, P. A. Rona, S. Smith, A. A. Struz, M. K. Tivey, and X. Zhao. 1995. The internal structure of an active sea-floor massive sulphide deposit. *Nature* 377: 713–716. 430
- Kennedy, A. K., T. L. Grove, and R. W. Johnson. 1990. Experimental and major element constraints on the evolution of lavas from Lihir Island, Papua New Guinea. *Contributions to Mineralogy and Petrology* 104: 722–734. 435
- Lee, S. M. 2000. *A geochemical study for the submarine hydrothermal mineralization II*. Korea Ocean Research and Development Institute. Q5
- Lisitsyn, A. P., K. A. W. Crook, Y. A. Bogdanov, L. P. Zonenshayn, K. G. Muravyev, W. Tufar, Y. G. Gurvich, V. V. Gordeyev, and G. V. Ivanov. 1993. A hydrothermal field in the rift zone of the Manus Basin, Bismarck Sea. *International Geology Review* 35: 105–126. 440

- Martinez, F. and B. Taylor. 1996. Backarc spreading, rifting, and microplate rotation, between transform faults in the Manus Basin. Pp. 203–224 in J. M. Auzende and J. Y. Collot (eds.), *Seafloor Mapping in the West, Southwest and South Pacific; Results and Applications. Marine Geophysical Researches*. Dordrecht, Netherlands: D. Reidel Publishing.
- McInnes, B. I. A. and E. M. Cameron. 1994. Carbonated, alkaline metasomatic melts from a sub-arc environment: Mantle wedge samples from the Tabar-Lihir-Tanga-Feni arc, Papua New Guinea. *Earth and Planetary Science Letters* 122: 125–141. 445
- Moss, R. and S. D. Scott. 2001. Geochemistry and mineralogy of gold-rich hydrothermal precipitates from the Eastern Manus Basin, Papua New Guinea. *Canadian Mineralogist* 39: 957–978. 450
- Moss, R., S. D. Scott, and R. A. Binns. 2001. Gold content of Eastern Manus Basin volcanic rocks: Implications for enrichment in associated hydrothermal precipitates. *Economic Geology* 96: 91–107.
- Moyle, A. J., B. J. Doyle, H. Hoogvliet, and A. R. Ware. 1990. Ladolam gold deposit, Lihir Island. Pp. 1793–1805 in F. E. Hughes (ed.), *Geology of the Mineral Deposits of Australia and Papua New Guinea* 2. 455
- Müller, D., L. Franz, P. M. Herzig, and S. Hunt. 2001. Potassic igneous rocks from the vicinity of epithermal gold mineralization, Lihir Island, Papua New Guinea. *Lithos* 57: 163–186.
- Müller, D., L. Franz, S. Petersen, P. M. Herzig, and M. D. Hannington. 2003. Comparison between magmatic activity and gold mineralization at Conical Seamount and Lihir Island, Papua New Guinea. *Mineralogy and Petrology* 79: 259–283. 460
- Parr, J. M., R. A. Binns, and J. B. Gemmill. 1996. Sulfide chimneys from the Satanic Mills site in the PACMANUS hydrothermal field, eastern Manus Basin, Papua New Guinea. *EOS, American Geophysical Union Transactions* 77: W120.
- Petersen, S., P. M. Herzig, and M. D. Hannington, 2000. Third dimension of a presently forming VMS deposit: TAG hydrothermal mound, Mid-Atlantic Ridge, 26°N. *Mineralium Deposita* 35: 233–259. 465
- Petersen, S., P. M. Herzig, M. D. Hannington, I. R. Jonasson, and A. Jr. Arribas. 2002. Submarine vein-type gold mineralization near Lihir Island, New Ireland fore-arc, Papua New Guinea. *Economic Geology* 97: 1795–1813. 470
- Sinton, J. M., L. L. Ford, B. Chappell, and M. T. McCulloch. 2003. Magma genesis and mantle heterogeneity in the Manus Back-Arc basin, Papua New Guinea. *Journal of Petrology* 44: 159–195.
- Stewart, W. D. and M. J. Sandy. 1988. Geology of New Ireland and Djaul Islands, northeastern Papua New Guinea, Pp. 13–30 in M. S. Marlow, S. V. Dadisman, and N. F. Exon, (eds.), *Geology and offshore resources of Pacific island arcs – New Ireland and Manus region, Papua New Guinea. Circum-Pacific Council for Energy and Mineral Resources Earth Science Series 9*. Houston, Texas, Circum-Pacific Council for Energy and Mineral Resources. 475
- Tufar, W. 1990. Modern hydrothermal activity, formation of complex massive sulfide deposits and associated vent communities in the Manus back-arc basin (Bismarck Sea, Papua New Guinea). *Mitteilungen der Österreichischen Geologischen Gesellschaft* 82: 183–210. 480
- Zierenberg, R. A. and D. J. Miller. 2000. Overview of Ocean Drilling Program Leg 169: Sedimented ridges II. Pp. 1–39 in R. A. Zierenberg, Y. Fouquet, D. J. Miller, and W. R. Normark (eds.), *Proceedings of the Ocean Drilling Program, Scientific Results 169*. College Station TX. 485
- Zierenberg, R. A., Y. Fouquet, D. J. Miller, J. M. Bahr, P. A. Baker, T. Bjerkgard, C.-A. Brunner, R. C. Duckworth, R. Gable, J. Gieskes, W. D. Goodfellow, H. M. Gröschel-Becker, G. Guerin, J. Ishibashi, G. Iturino, R. H. James, K. S. Lackschewitz, L. L. Marquez, P. Nehlig, J. P. Peter, C. A. Rigsby, P. Schultheiss, W. C. Shanks, B. R. T. Simoneit, M. Summit, D. A. H. Teagle, M. Urvat, and G. G. Zuffa. 1998. The deep structure of a sea-floor hydrothermal deposit. *Nature* 392: 485–488. 490

Textural and mineralogical changes associated with the incipient hydrothermal alteration of glassy dacite at the submarine PASCAMANUS hydrothermal system, Eastern Manus Basin

Thomas Monecke · Giovanna Giorgetti · Olaf Scholtysek · Reinhard Kleeberg · Jens Götze · Mark D. Hannington · Sven Petersen · Peter M. Herzig

T. Monecke (✉)

Department of Earth Sciences, University of Ottawa
Marion Hall, 140 Louis Pasteur, Ottawa, ON, K1N 6N5, Canada
E-mail: thomas.monecke@science.uottawa.ca

G. Giorgetti

Dipartimento di Scienze della Terra
Via Laterina 8; 53100 Siena, Italy

O. Scholtysek · R. Kleeberg · Jens Götze

Institut für Mineralogie, TU Bergakademie Freiberg
Brennhausgasse 14, D-09596 Freiberg, Germany

M. D. Hannington

Department of Earth Sciences, University of Ottawa
Marion Hall, 140 Louis Pasteur, Ottawa, ON, K1N 6N5, Canada

S. Petersen · P. M. Herzig

Leibniz-Institut für Meereswissenschaften
Wischofstraße 1-3, D-24148 Kiel, Germany

ABSTRACT

Variably altered dacite from the PACMANUS vent field in the eastern Manus back-arc basin, Papua New Guinea, has been studied to determine the textural and mineralogical characteristics of hydrothermal alteration taking place in the immediate subsurface of this modern seafloor hydrothermal systems. Careful textural investigations show that fluid flow through the fresh and glassy dacite has been strongly controlled by the primary volcanic textures. Quench fractures as well as networks of interconnected perlitic cracks linking vesicles provided pathways for hydrothermal fluids flowing up to the seafloor. Hydrothermal alteration along these pathways resulted in the formation of pseudoclastic textures. Textural evidence as well as seafloor observations suggest that alteration of the glassy dacite has not been sustained, the samples have been affected by incipient hydrothermal alteration that is typically not preserved in ancient volcanic-rock-hosted massive sulfide deposits. Interaction of the glassy dacite with the hydrothermal fluids primarily resulted in the conversion of volcanic glass to dioctahedral smectite, only minor amounts of trioctahedral smectite were formed. Destruction of the volcanic glass and the formation of smectite caused pronounced changes in the chemistry of the dacite samples, in particular a decrease in the SiO_2 whole-rock content and the concentrations of Na_2O and K_2O . The two alkali elements behaved differently during hydrothermal alteration due to preferential incorporation of K into the interlayer position of the newly formed dioctahedral smectite. Smectite formation occurred under rock-dominated conditions although the addition of Mg was required to form trioctahedral smectite from the silicic volcanic glass. Primary plagioclase was resistant to hydrothermal alteration highlighting the fact that the destruction of volcanic glass and feldspar are not necessarily contemporaneous in massive sulfide forming hydrothermal systems. Incipient alteration of the glassy dacite close to the seafloor occurred at temperatures below 150 to 200°C in an environment that allowed the development of steep temperature gradients. Comparison to the findings of deep drilling during ODP Leg 193 suggests that the smectite-rich alteration in the immediate subsurface of the PACMANUS hydrothermal vent site represents the low-temperature equivalent of illite- and chlorite-rich alteration associations forming in the upflow zones of the hydrothermal fluids in the deeper portion of the volcanic sequence.

INTRODUCTION

In the past decades, hydrothermal alteration halos enveloping massive sulfide deposits have been studied extensively for both their genetic and exploration implications. Numerous studies have established that hydrothermal alteration halos show a pronounced mineralogical, geochemical and isotopic zonation (Urabe and Scott 1983; Schmidt 1988; Marquis et al. 1990; MacLean and Hoy 1991; Gemmell and Large 1992; Offler and Whitford 1992; Cagatay 1993; Large et al. 2001; Monecke et al. 2001). The observed zoning of the alteration halos has commonly be interpreted by a model in which hydrothermal fluids migrate outward from the center of discharge, gradually cool and convert the volcanic host rocks to different alteration mineral associations at decreasing temperatures. However, several studies have established that the development of the zonation is also related to the evolution of the thermal regime in time. At a given point in space, alteration typically commences with the formation of low-temperature mineral associations during the intensifying stage of the hydrothermal activity. The low-temperature alteration products are replaced by high-temperature phases during main stage mineralization (Pisutha-Arnond and Ohmoto 1983; Ohmoto 1996; Doyle 2001). In addition, waning of the hydrothermal activity may coincide with pronounced changes in the alteration conditions and the formation of retrograde alteration associations (Cagatay 1993; Giorgetti et al. 2003).

Among the currently least understood alteration processes are those taking place during the early intensifying stage where initial fluid pathways are established through unaltered volcanic rocks. In ancient massive sulfide forming systems, the textural and mineralogical characteristics of the incipient hydrothermal alteration are difficult to study due to the overprinting effects of alteration processes coinciding with the thermal maximum and the late temperature decline. In addition, it has to be taken into account that the original texture and mineralogy of the hydrothermally altered volcanic rocks are modified during diagenesis, compaction, metamorphism, and tectonic deformation. Mineralogical modifications occurring in response to low-grade regional metamorphism are substantial (Gustin 1990; Offler and Whitford 1992), and a high-grade metamorphic overprint may obliterate original alteration signatures to a large extent (Stanton 1983; Marquis et al. 1990; Roberts et al. 2003a). In addition, polyphase deformation and superposition of regional and contact metamorphic events may obscure the stratigraphic relationships between the massive sulfides, altered wall rocks, and least altered precursors (Lentz and Van Staal 1995).

Textural and mineralogical characteristics associated with the incipient stages of hydrothermal alteration are probably best constrained by the study of sulfide precipitating vent sites at the modern seafloor. These hydrothermal systems are known to represent close analogues to massive sulfide deposits located in ancient volcanic terrains, but are not affected by metamorphic recrystallization or

tectonic deformation (Francheteau et al. 1979; Halbach et al. 1989; Hannington et al. 1995; Humphris et al. 1995; Iizasa et al. 1999; Herzig and Hannington 2000).

The present contribution focuses on hydrothermally altered dacite that was sampled from an immature vent site at the submarine PACMANUS vent field in the Eastern Manus Basin, southwest Pacific. The texture of the siliceous volcanic rocks has been studied to determine the mechanisms by which fluid pathways form through glassy, coherent volcanic rocks during the incipient stage of alteration. Microscopic and microanalytical investigations were carried out to constrain the mineralogy of the dacite samples and to identify replacement textures that formed in response to the early hydrothermal alteration. The mineralogy of the fine-grained secondary phases were studied by X-ray diffraction analysis and transmission electron microscopy. Particular emphasis has been paid on the identification of the sheet silicates that formed during the alteration of the glassy lava. It is demonstrated that the results of these investigations provide important information on the physicochemical condition of hydrothermal alteration in the immediate subsurface of the PACMANUS vent field.

GEOLOGIC SETTING

The Manus Basin is situated in the western Pacific and occupies an area between the islands of New Hanover, New Ireland, New Britain, and Manus. It represents a back-arc extensional structure that lies at the eastern side of the Bismarck Sea, northeast of New Guinea (Fig. 1). The region has been located above subduction zones for at least the last 40 Ma. During the Oligocene and Miocene, the plate tectonic situation in this area was characterized by the southwestward subduction of the Pacific plate along the Manus-Kilinau Trench and the formation of an island arc as evidenced by exposures on New Hanover and New Ireland (Exon et al. 1986). In the late Miocene, subduction of the Pacific Plate was stopped due to the collision of the Ontong Java Plateau with the trench (Coleman and Kroenke 1981; Phinney et al. 1999). Stalling of the subduction zone was accompanied by plate rotation and subduction reversal resulting in the formation of the northeast-facing New Britain Trench, at which the Solomon Sea microplate is presently subducted in a northward direction under the Bismarck microplate. Current arc volcanism occurs along the concave northern side of New Britain and back-arc spreading takes place in the Manus Basin that separates the Bismarck microplate into northern and southern segments (Fig. 1).

The current configuration of spreading segments, extensional faults, and obliquely oriented transform faults in the Manus Basin is well constrained by data collected during numerous research cruises (Taylor 1979; Martinez and Taylor 1996; Binns et al. 2002). Creation of new oceanic crust in the

Manus Basin occurs mainly along the approximately 120 km long, SW-NE trending Manus spreading center. The spreading rate of the wedge-shaped spreading center decreases from 92 mm/a at the southwestern end to 0 mm/a in the northeast (Martinez and Taylor 1996). The Manus spreading center passes into an extensional transform zone at its southwestern tip that separates the spreading center from the Willaumez transform zone (Taylor et al. 1994). The northeastern end of the Manus spreading center terminates at the Djaul transform fault. The left-lateral Willaumez transform zone trends northwest towards Manus Island and forms the western boundary of the Manus basin. The Southern Rifts consist of a westward narrowing rift zone containing deep grabens that also terminate in the left-lateral Djaul transform fault in the northeast (Martinez and Taylor 1996, 2003).

The Eastern Manus Basin represents a complex pull-apart zone that is located between the Djaul transform fault in the southwest and the left-lateral Weitin fault in the northeast (Fig. 1). The Eastern Manus Basin is characterized by an east-west belt of en echelon neovolcanic structures that is referred to as the Eastern Manus volcanic zone. Individual volcanic edifices in this zone trend mainly northeast, normal to the inferred extension direction. Most edifices are constructional features ranging from central eruptions of basalt and basaltic andesite to linear ridges formed by fissure eruptions of andesite and dacite (Binns and Scott 1993; Binns et al. 1995, 2002; Martinez and Taylor 1996).

The PACMANUS hydrothermal field is situated on Pual Ridge, a northeast trending volcanic edifice in the Eastern Manus Basin (Fig. 2). Pual Ridge has an overall length of 15 km and a width of 1 to 1.5 km. It rises approximately 500 m above the surrounding seafloor to a minimum water depth of about 1655 m (Binns and Scott 1993; Waters and Binns 1998). Glassy dacite dominates the ridge crest. The surfaces of the dacitic lavas are typically extremely rough although some smooth sheet flows and lobate flows have been observed. The steep flanks of the ridge expose terraces of hummocky to blocky dacite lava, with some mass-wasted talus material. The deeper portions of the ridge largely consist of lobate tabular flows of vesicular andesite whereas the surrounding 2,200 m deep valley floor is dominated by lobate flows of basaltic andesite (Binns and Scott 1993; Binns et al. 1995; Waters et al. 1996; Waters and Binns 1998).

Several isolated hydrothermal deposits are scattered along the crest of Pual Ridge (Binns and Scott 1993; Binns et al. 1995). The main hydrothermal activities are restricted to a 2 km long section, referred to as the PACMANUS hydrothermal field. The vent field is located between two low knolls in the middle of the ridge crest that are composed of dacite. Seafloor observations revealed that the vent field comprises several discrete areas of hydrothermal activity (Fig. 2). Exit temperatures of the hydrothermal fluids range from 240 to 268 °C in areas of high-temperature discharge, but are as low as 6 °C in zones of diffuse low-temperature venting (Auzende et al. 1996; Gamo et al. 1996; Douville et al. 1999; Binns et al. 2002).

The Rogers Ruins area at the northern end of the PACMANUS vent field contains actively venting black smokers that are up to 7.5 m in height. Immediately to the east of this area, numerous small occurrences of Fe and Mn oxide mounds venting clear hydrothermal fluids have been observed. The Roman Ruins area is located approximately 250 m to the south of Rogers Ruins. It contains many simple columnar chimneys as well as some complex multispired chimneys that reach a maximum height of 20 m. Commonly, individual chimneys have coalesced into wall-like constructions. Although most chimneys are inactive, some black smokers and chimneys emitting clear hydrothermal fluid have been observed at Roman Ruins. High-temperature venting also occurs at Satanic Mills, a vent site that has a diameter of approximately 200 m. Satanic Mills contains scattered black to gray smoker chimneys as well as structures that vigorously vent clear hydrothermal fluid (Moss and Scott 2001; Binns et al. 2002).

The Marker 14 site represents a zone of altered dacite with diffuse venting and scattered Fe and Mn oxide deposits (Binns et al. 2002). The Snowcap site is located to the southwest of Satanic Mills (Fig. 2). It occupies the crest and the flanks of a knoll that is 10 to 15 m high and approximately 100 by 200 m in size. The vent site is dominated by altered dacite lava as well as associated hyaloclastite. Diffuse low-temperature venting is extensive across the crest of Snowcap. The diffuse vent sites are marked by conspicuous white bacterial mats or methane hydrate deposits. Several small fields of actively smoking and inactive chimneys have been located at the southwestern fringes of the Snowcap area (Binns and Scott 1993; Binns et al. 2002). The southwestern end of PACMANUS vent field is occupied by the Tsukushi site. It contains numerous actively venting chimneys that are up to 30 m in height and 10 m in diameter (Binns et al. 2002).

The subsurface geology of PACMANUS hydrothermal vent site has been constrained by Ocean Drilling Program (ODP) Leg 193. Deep drilling was successfully performed at Snowcap and Roman Ruins to a maximum penetration of 386.7 and 206 meters below seafloor (mbsf), respectively. Drilling operations at Satanic Mills were abandoned at a depth of 20.1 mbsf (Binns et al. 2002).

Coring during Leg 193 revealed that the Pacmanus vent field is capped by relatively unaltered dacite, ranging from < 10 to 40 m in thickness, with a rapid underlying transition to pervasively altered volcanic rocks. Alteration in the deep subsurface is complex and the alteration mineralogy varies with depth and between the two sites. Particular pronounced are variations in the phyllosilicate mineralogy. At Snowcap, chlorite and illite are the dominant phyllosilicates down to a depth of 120 mbsf (Lackschewitz et al. 2004). Locally, the chlorite- and illite-bearing alteration association is overprinted by pyrophyllite (Yeats et al. 2001; Binns et al. 2002; Roberts et al. 2003b; Lackschewitz et al. 2004). Below 120 mbsf, the pervasively altered rocks contain substantial amounts of mixed-layer phases. However, these phases disappear below 322 mbsf where chlorite and illite are abundant

(Lackschewitz et al. 2004). At Roman Ruins, the unaltered dacite cap is underlain by alternating intervals of altered coherent volcanic rocks and various breccia types (Paulick et al. 2004). These volcanic rocks contain substantial amounts of chlorite and illite down to the maximum penetration of 206 mbsf. Mixed-layer phases are only present between 125 and 190 mbsf (Lackschewitz et al. 2004).

MATERIALS AND METHODS

The samples used in the present study were collected from the immediate subsurface of an immature vent site at the fringe of the Satanic Mills area (Fig. 2) during cruise SO-166 of the German research vessel *Sonne* (Herzig et al. 2003). Seafloor observations prior to sampling showed that the sampling area was dominated by small and presumably young black smokers that were sited immediately on top of variably altered volcanic substrate. In addition to small, sphalerite-dominated black smoker chimneys and numerous chimney fragments, a large number of dacite specimens has been recovered during the TV grab station (station 58GTV at 3°43.62'S and 151°40.31'E; 1,682 meters below sea-level). The dacite samples were found to exhibit a surprising range of alteration intensities, apparently unaltered glassy dacite as well as intensely-altered equivalents were recovered.

The texture and mineralogy of representative dacite samples were initially studied in hand specimen and in thin section. In addition to conventional optical microscopy, cathodoluminescence (CL) microscopy was conducted using the hot cathode CL microscope HC1-LM (Neuser 1995) operated at 14 kV with a current density of $\sim 10 \mu\text{A}/\text{mm}^2$ and an operating vacuum of $< 1.3 \cdot 10^{-4}$ Pa. Scanning electron microscopy (SEM) was utilized to visualize small scale alteration features. A Jeol JSM 6400 microscope equipped with a Tracor (Noran) series II energy-dispersive X-ray spectrometer was used. Routine operating conditions were 20 kV with a beam current of 600 pA. High resolution back-scattered electron (BSE) images were collected at up to 25 kV and 6 nA.

The microscopy investigations were followed by whole-rock mineralogical and geochemical analyses. The samples were crushed and repeatedly washed with distilled water to remove any seawater salt. After centrifuging and drying, the samples were split. One half of the sample was taken for qualitative and quantitative phase analysis by X-ray powder diffraction (XRD) whereas the other split was used for whole-rock geochemical analysis.

The preparation of XRD samples involved a further crushing of the sample material to $< 400 \mu\text{m}$. The finely crushed samples were split and 1.80 g sample material were mixed with 0.20 g synthetic ZnO used as an internal standard for XRD analysis. Further grinding to a grain size below $10 \mu\text{m}$ was

performed under ethanol in a vibratory McCrone micronizing mill. After drying, the obtained fine powders were vibrated along with small steel balls for five minutes in a mixer mill to achieve homogeneous mixing. Standard random powder mounts were obtained by filling the powder into conventional top-loading sample holders. Step-scan XRD data (5 to 80 °2 θ , 0.03 °2 θ step width, 8 s/step) were collected with an URD 6 (Seifert-FPM, Germany) diffractometer. The diffractometer was equipped with a diffracted-beam graphite monochromator and a variable divergence slit that allowed the irradiation of a constant area of the rotated sample. A Co tube was used and operated at 40 kV and 30 mA. Qualitative phase analysis of the raw diffraction patterns was carried out by conventional search/match procedures using reference diffraction patterns stored in the ICDD PDF-2 (International Center for Diffraction Data). Subsequent quantitative phase analysis was performed using the fundamental-parameter Rietveld programs AutoQuan and BGMN (Taut et al. 1997; Bergmann et al. 1998). Details on the applied method of quantification are described in Monecke et al. (2001), Kleeberg and Bergmann (2002), as well as Ufer et al. (2004).

Information on the mineralogy of sheet silicates contained in intensely-altered samples were obtained from X-ray diffraction experiments after enriching these minerals in the < 2 μ m size fraction of the crushed whole-rock samples (< 400 μ m). Enrichment of the clay minerals was conducted because the whole-rock samples contained only moderate amounts of sheet silicates hampering accurate determination of crystallographic data in the multi-phase samples due to extensive peak overlap. The < 2 μ m size fraction was separated from the crushed material by gravity sedimentation and centrifuging. Random powder mounts were prepared and investigated by XRD using the measurement conditions described above. In addition, strongly oriented samples were prepared using the standard glass slide method. After air drying, step scan data (2 to 16 and 28 to 31 °2 θ , 0.05 °2 θ step width, 10 s/step) were collected on the strongly oriented samples. In addition, the enriched samples were analyzed in ethylene glycol solvated conditions and after heating at 550 °C for 2.4 hours (2 to 16 °2 θ , 0.05 °2 θ step width, 10 s/step).

The sheet silicates minerals contained in the intensely-altered equivalents were also studied by transmission and analytical electron microscopy (TEM-AEM). Initially, sticky wax-polished thin sections were prepared. Copper discs with a 600 μ m central opening were then attached to the areas of interest. Subsequent argon ion milling of the areas of interest was conducted using a Gatan Duall Ion Mill 600. A Jeol 2010 microscope at the University of Siena was used at routine operating conditions of 200 kV. Analytical electron microscopy was carried out using a Link Isis X-ray energy dispersive system (EDS). The obtained spectra were processed using K-values obtained from natural ion-milled standards as described by Li et al. (1994). The semi-quantitative analyses were obtained from samples areas that are approximately 20 to 30 nm in diameter.

The geochemical composition of the dacite samples was determined by inductively coupled plasma (ICP) spectroscopic techniques. Initially, the finally crushed whole-rock samples were pulverized with an agate mill to a grain size < 63 μm . 0.5 g of sample powder was then fused with a mixed lithium metaborate-tetraborate flux. The fusion melt was dissolved in 6 M nitric acid and then made up to a volume of 250 ml with ultrapure H₂O. The concentrations of the major elements were subsequently determined by optical emission spectrometry (ICP-OES) using a Perkin-Elmer OPTIMA 3000. Total S was analyzed by combustion followed by infrared spectrophotometry (LECO). The loss on ignition (LOI) was determined by gravimetry at 900 °C. Trace element analysis was performed on sample solutions obtained by total dissolution of 0.5 g of powder in a mixed-acid digestion of nitric, hydrochloric, perchloric, and hydrofluoric acids followed by a lithium metaborate fusion of any residual material. The dissolved samples and fusion melt were combined and diluted to a final volume of 100 ml in 4 % nitric acid. The concentrations of Sc, V, Cr, Co, Ni, Cu, Zn, and Sr were determined by ICP-OES whereas Rb, Y, Zr, Nb, Ag, Cd, Sb, Cs, Pb, Bi, Th, and U were analyzed by ICP mass spectrometry (ICP-MS). An externally calibrated Perkin-Elmer SCIEX ELAN 6100 quadrupole instrument was used. The analytical procedure was validated by repeated independent preparation and analysis of international reference materials. Relative standard deviations determined in this way are typically below 1 % for major elements and below 5 % for elements occurring in trace concentrations. Agreement of the observed element concentrations and certified values indicates that the accuracy of the element determinations is typically much better than ± 5 %.

RESULTS

Hand specimen

The variably altered dacite samples recovered from the Satanic Mill vent site show fractures having different orientations. Particular abundant are long fractures that transect the hand specimens. The orientation of the fractures with respect to the seafloor is constrained on the basis of Mn oxide/hydroxide coating on the sample surfaces. In most samples examined, the long fractures appear to be perpendicular to the former lava surface. This finding is consistent with the observation that the long fractures are perpendicular to the flow foliation of the lava as defined by the shapes of the vesicles. A second set of fractures is approximately parallel to the lava surface and perpendicular to the long fractures. These fractures are curved and sometimes only few centimeters long extending only between adjacent long fractures.

Least-altered dacite samples have polygonal shapes that are related to the occurrence of the two fractures sets described above and fracturing related to the sampling using the TV grab. The least-altered dacite is fresh in appearance, black, glassy, moderately vesicular (5 to 15 %), and aphyric in

hand specimen. The vesicles range up to several millimeters in size and are round to elongate, sometimes almost tabular. Elongated vesicles define a stretching direction that was presumably parallel to the flow direction of the lava. The glassy groundmass adjacent to fractures and vesicles intersected by fractures sometimes contains clay minerals (Fig. 3). In some cases, fracture and vesicle walls are lined by sulfides.

Hydrothermally altered dacite contains significant amounts of clay minerals and sulfides. Moderately-altered dacite is light brownish- to greenish-gray in color. Alteration is most pronounced in the groundmass surrounding vesicles that are linked by small cracks and fractures (Fig. 3). The walls of the vesicles and fractures are typically lined by sulfides. The most intensely-altered samples recovered are light grayish-green in color, very soft and friable due to the high content of clay minerals. In contrast to least-altered samples, perlitic cracks are abundant in the hydrothermally altered rocks. The intersecting cracks are delicate, arcuate or gently curved. The perlitic cracks surround round to subrounded cores of less intensely-altered dacite. Cores of comparably fresh material are several millimeters across, ranging in shape from spherical to almost tabular (Fig. 3).

Least-altered dacite

Thin section inspection revealed that the fresh and apparently unaltered dacite contains approximately 0.5 % microphenocrysts of plagioclase, clinopyroxene, and magnetite (Figs. 4a,b). The microphenocrysts are typically isolated and evenly distributed, but sometimes form clusters and glomerocrysts. The glassy groundmass contains approximately 30 % microlites. Most microlites are composed of plagioclase, but clinopyroxene and magnetite microlites are also common.

Plagioclase microphenocrysts are lath-shaped ranging up to 500 μm in size. Plagioclase crystal fragments and microphenocrysts having distinctly round shapes are also present. The plagioclase laths commonly exhibit oscillatory growth zoning and simple twinning. The CL colors of the microphenocrysts range from reddish-brown to greenish (Fig. 4a). The plagioclase microphenocrysts are relatively homogeneous in composition (An_{46} to An_{50}) with a low orthoclase component of 0.6 to 1.0 mol.% (Monecke et al. unpubl. EMP data). Skeletal plagioclase crystals are common that range in size from approximately 150 to 300 μm . The skeletal crystals have tabular to rectangular hollow cores or are characterized by swallow-tail terminations (Fig. 4c).

Clinopyroxene microphenocrysts are euhedral to subhedral and less than 500 μm in size (Fig. 4b). The crystals commonly enclose melt inclusions. The microphenocrysts exhibit complex zoning patterns. BSE imaging showed that oscillatory and sector zoning occurs in addition to pronounced compositional variations between the core and rim of individual microphenocrysts. Individual zones of the microphenocrysts correspond compositionally to magnesium-rich augite ($\text{Wo}_{38}\text{En}_{40}\text{Fs}_{22}$ -

Wo₄₂En₃₉Fs₁₉) and magnesium-rich clinoenstatite (Wo₀₃En₆₁Fs₃₆-Wo₀₄En₅₇Fs₃₉). The application of stoichiometric criteria (Droop 1987) indicates that clinopyroxene microphenocrysts contain a relatively low (typically < 10 % of total iron) amount of ferric iron (Monecke et al. unpubl. EMP data). Magnetite microphenocrysts are up to 120 µm in size, subhedral or skeletal and frequently enclose large inclusions of glass. The microphenocrysts have TiO₂ contents ranging from 13.2 to 14.3 wt.% and contain between 2.3 and 2.5 wt.% Al₂O₃ and 1.8 to 2.2 wt.% MgO (Monecke et al. unpubl. EMP data).

Plagioclase microlites distributed throughout the glassy matrix of the dacite samples show variable orientations. In most samples investigated, larger crystals (< 50 µm) show a preferred orientation that is interpreted to reflect the orientation of the lava flow. However, smaller plagioclase microlites are typically randomly oriented. The microlites are acicular to lath-shaped and frequently skeletal in nature (Figs. 5a,b). The plagioclase microlites exhibit a very weak violet to reddish-brown CL signal that is difficult to identify due to the low transparency of the volcanic glass (Fig. 4a). Semi-quantitative SEM-EDX measurements suggest that plagioclase microlites have compositions similar to the microphenocrysts (An₄₁ to An₅₂) although they typically exhibit a slightly higher orthoclase components (up to 2.5 mol.%). Clinopyroxene microlites occurring in the glassy matrix have a maximum size of approximately 40 µm. Most pyroxene microlites are distinctly acicular although elongate to stubby as well as rounded and marginally corroded crystals are also present (Figs. 5a,b). EDX measurements show that the clinopyroxene microlites contain higher relative clinoferrosilite components when compared to the microphenocrysts. The samples contain abundant titanomagnetite microlites that are usually smaller than 20 µm. These microlites are skeletal, dendritic, or euhedral in shape. Intergrowth with clinopyroxene is common. The titanomagnetite microlites exhibit compositions comparable to those observed for the microphenocrysts.

Apatite and pyrrhotite are the only accessory phases identified in the unaltered dacite samples. Apatite forms rare clusters of euhedral crystals that are < 5 to 10 µm in size. The apatite grains are enclosed in the glass matrix or form rare inclusions in plagioclase microphenocrysts (Fig. 5b). They possess a distinct yellow CL color and can, therefore, be readily identified under the CL microscope. SEM-EDX measurements revealed that the apatite crystals contain detectable amounts of Cl (up to 1.8 wt.%). Primary pyrrhotite is very rare in the unaltered dacite samples forming approximately 10 µm large grains that usually occur in contact with magnetite and clinopyroxene microlites and microphenocrysts.

Hydrothermally altered dacite

Samples affected by hydrothermal alteration are typified by the abundant presence of interconnected perlitic cracks. Thin section inspection confirmed that alteration intensity defined on the basis of hand specimen inspection is related to the number and density of perlitic cracks in the samples. The perlitic

cracks are enveloped by zones of intense hydrothermal alteration. The alteration halos are broadly parallel to the fractures (Fig. 4d). Vesicles linked by the perlitic cracks are surrounded by alteration halos (Fig. 4e). Hydrothermal alteration resulted in distinct change in the groundmass color. Zones of intense alteration have a grayish color in transmitted light whereas the groundmass is light to dark brown away from fractures and vesicles that acted as fluid pathways. Plagioclase and clinopyroxene microphenocrysts are apparently not affected by the hydrothermal alteration although fracturing of microphenocrysts intersected by perlitic cracks is common (Fig. 4f).

The SEM investigations show that alteration of the groundmass primarily caused a conversion of volcanic glass to secondary phases that are too fine grained to be resolved even with this electron microscopic method (Figs. 5c-e). Contacts between the intensely altered matrix and the apparently unaltered equivalent are relatively sharp, alteration produces concave surface into the least-altered matrix (Fig. 5c). Plagioclase microlites are apparently unaffected by the hydrothermal alteration and commonly cut across replacement fronts in the glass matrix. EDX measurements revealed no systematic changes in the plagioclase composition. Destruction of the poorly transparent volcanic glass in the alteration halos surrounding perlitic cracks and vesicles resulted in an accentuation of the plagioclase microlites under the CL microscope (Figs. 4d-g). In contrast to plagioclase, clinopyroxene and titanomagnetite microlites are less abundant in zones of intense hydrothermal alteration when compared to the unaltered glassy groundmass. Replacement of clinopyroxene by fine grained secondary minerals has been frequently observed under the SEM. Titanomagnetite appears to have been converted to pyrite as evidenced by the abundant presence of pyrite grains in zones of intense hydrothermal alteration. However, some large titanomagnetite grains are present adjacent to fluid pathways suggesting alteration primarily affected small microlites (Figs. 5c, d). The altered groundmass locally contains secondary apatite. The secondary apatite grains are typified by irregular grain shapes and low Cl contents (up to 0.5 wt.%). Due to their distinct yellow CL color and their abundant presence, the small (< 25 μm) apatite grains can be readily identified by CL microscopy (Fig. 4g). In addition to apatite, rare sphalerite, chalcopyrite, and bornite grains have been recognized in the altered groundmass.

In hydrothermally altered dacite, sulfides commonly precipitated along the fracture and vesicle walls. Particularly common are sphalerite, pyrite, chalcopyrite, and pyrrhotite (Figs. 5c,f). Semi-quantitative EDX analyses revealed that the sphalerite contains up to 20 wt.% FeO and approximately 0.7 wt.% Cd. In addition to these sulfides, rare marcasite, galena, bornite, and covellite have been recognized. Vesicles commonly contain barite laths (Fig. 5f). Barite shows a distinct dark blue CL color (Fig. 4e). Other sulfates including anhydrite have not been recognized in thin section.

Phase abundances

The XRD investigations on the whole-rock samples confirmed that least-altered dacite primarily consists of volcanic glass, plagioclase, clinopyroxene, and titanomagnetite (Table 1). The glass content of least-altered dacite varies from 70 to 75 wt.%. The rocks comprise approximately 20 wt.% plagioclase and 5 wt.% clinopyroxene. The samples were found to contain approximately 0.8 wt.% titanomagnetite. The quantitative phase analysis showed that moderately- to intensely-altered dacite contains substantial amounts of smectite (approximately 5 to 20 wt.%). The glass content of the hydrothermally altered samples is distinctly lower than that of the least-altered equivalents and ranges from only 50 to 65 wt.%. Plagioclase forms 19 to 27 wt.% of the rocks and clinopyroxene occurs in concentrations between 3 and 6 wt.%. Although magnetite is still present in the moderately- to intensely-altered rocks, the abundance of this mineral appears to decrease with increasing alteration intensity. Iron-rich sphalerite was detected in all samples in trace amounts (< 1.5 wt.%). Traces of barite, pyrite, and chalcopyrite were recognized by XRD in some intensely-altered samples (Table 1).

Clay mineralogy

Information on the clay mineralogy of the intensely-altered dacite samples were gathered by XRD analysis of the < 2 μm fractions of the whole-rock samples. The samples investigated are typified by a uniform clay mineralogy. A representative diffraction patterns of an intensely-altered samples that was enriched in the sheet silicates by gravity sedimentation and prepared on an oriented aggregate mount is given in Figure 6. In untreated condition, broad and overlapping reflections can be observed at 12.4 to 14.5 Å. In ethylene glycole solvated conditions, the peak positions increase to 17 Å (second order reflection at 8.5 Å) whereas heating at 550 °C resulted in a shift of the reflections to 9.6 Å. This behavior is characteristic for smectite whereby the broad first order peak is caused by non-uniform basal distances. The non-uniform basal spacing is related to different amounts of interlayer water molecules and/or variations in the interlayer cation occupancy.

The position of the 060 reflection of smectite present in the intensely-altered samples was determined in diffraction patterns collected on the random powder mounts. The diffraction patterns of all samples show a relatively intense 060 reflection that is located at approximately 1.49 Å suggesting that the smectite is dominantly dioctahedral in nature. However, an additional small peak can be observed at 1.53 Å implying that trioctahedral smectite is also present in subordinate amounts. The relative proportions of dioctahedral and trioctahedral smectite varies between samples as evidenced by the relative sizes of the 1.49 Å and 1.53 Å reflections (Fig. 7). The XRD patterns collected on the random powder mounts of the < 2 μm fraction also revealed the occurrence of anatase, a phase that was not detected in whole-rock diffraction patterns. This observation indicates that secondary anatase is present in trace amounts in smectite-bearing dacite samples.

The intensely-altered dacite samples have also been studied by TEM to determine the micro-textural characteristics of the clay minerals and their intergrowth relationships with other phases. The glassy groundmass of the dacite shows different degrees of hydrothermal alteration in areas that are only few micrometers apart.

Figure 8 is a representative low-magnification image of a dominantly glassy groundmass located away from fluid pathways. The glass is porous whereby some pores are coated by smectite layers. Small (up to 10 nm thick) smectite crystals are present that show lattice fringes with a spacing of approximately 1.0 to 1.3 nm. In addition to smectite, the glassy groundmass contains anhedral areas that are approximately 20 nm in size. These areas are typified by a low contrast, but lattice fringes can be observed. Based on the spacing of the lattice fringes and the large Ti peak noticeable in EDX spectra, this phase is interpreted to be anatase.

Figure 9 shows a representative image of an area located adjacent to a veinlet where glass is almost entirely converted into smectite and anatase. The nanometer-thick smectite crystals show random orientations and are frequently bent. The 00l lattice fringes have a variable spacing (1.0 to 1.3 nm) and are wavy in appearance, the termination of layers is common. Smectite present in the altered glass surrounding vesicles shows very similar textural characteristics as shown in Figure 10. In addition to smectite and anatase, the glassy groundmass contains prismatic apatite (20 by 100 nm in size) as well as plagioclase nanolites that are interpreted to be primary in origin.

AEM analyses were performed on areas dominated by smectite to constrain the composition of the clay minerals. Because most smectite crystals are smaller than 30 nm in diameter (resolution of the analytical method), pure analyses were difficult to obtain. Most EDX spectra collected showed that the smectite-rich areas consist of Si with lower amounts of Al and traces of K. Smectite with an elevated content of Mg was only locally observed. Representative AEM analyses performed on relatively large smectite crystals are given in Table 2. The analyses are given on the basis of 44 negative charges.

The AEM investigations revealed that smectite present in the three texturally distinct positions cannot be discriminated on the basis of their chemical composition. Dioctahedral smectite is present in the glassy matrix away from fluid pathways and occurs abundantly in the alteration halos surrounding vesicles and veinlets. Most trioctahedral smectite was observed in glass-rich areas of the altered dacite samples. Dioctahedral and trioctahedral smectite show very similar textural characteristics. They have similar sizes and shapes and primarily replace the glassy groundmass of the dacite. Replacement of primary phases such as plagioclase or pyroxene was not observed by transmission electron microscopy.

Chemical composition

The results of the geochemical analyses performed on the whole-rock samples are listed in Table 1. The composition of the dacite samples varies as function of alteration intensity, expressed by concentration of smectite as determined by Rietveld refinement of the XRD patterns. The SiO₂ whole-rock concentrations decrease from approximately 70 wt.% in unaltered dacite to 61 wt.% in the most intensely-altered equivalent (Fig. 11). In contrast, alteration caused an increase in the Al₂O₃ concentrations and a systematic change in the TiO₂ content. The content of MnO decreases with increasing alteration intensity. Anomalous MgO contents were only observed for the two most intensely-altered dacite samples recovered from Satanic Mills. Alteration of the glassy dacite resulted in a marked loss of the Na₂O and K₂O concentrations (Fig. 11). However, the Na₂O/K₂O ratio is not constant and decreases slightly from 2.4 in unaltered samples to a value of 2.1 in the most intensely-altered equivalent suggesting that these two alkali elements behave differently during hydrothermal alteration. The LOI and S whole-rock values are elevated in altered samples (Table 1).

The concentrations of Rb and Cs increase with increasing alteration intensity (Fig. 11), but no consistent trend can be observed for Sr. The Cu content of the samples investigated also increases with increasing smectite content. Hydrothermally altered dacite samples generally show higher Zn, Pb, Ag, and Cd concentrations than their least-altered equivalents. The Cd content correlates positively with Zn. The concentrations of the elements Sc, V, Nb, Zr, Y, Th, and U broadly increase from the least-altered dacite samples to the most intensely-altered equivalents. However, element ratios frequently used in petrogenetic studies such as the Ti/Zr and Nb/Y ratios are constant (Table 1). A significant change can only be observed for the U/Th ratio that increases from 0.6 in least-altered dacite to as high as 1.0 in the altered equivalents.

DISCUSSION

Formation of fluid pathways in the glassy dacite

The textural investigations carried out on the material recovered from Satanic Mills revealed that the incipient alteration of the dacite samples is strongly controlled by the primary volcanic textures.

Samples recovered from the immediate subsurface of the dacite lava typically show fractures that are approximately perpendicular and parallel to the lava surface, respectively. Both sets of fractures are interpreted to be quench fractures that resulted from the rapid cooling of the lava following its emplacement at the ocean floor (Yamagishi and Dimroth 1985; Yamagishi 1991; Davis and McPhie 1996). Sulfide lining of the fracture surfaces and associated minor alteration of the glassy

groundmass suggest that the quench fractures acted as fluid pathways for the upwelling hydrothermal fluids. However, the bulk of the polygonal dacite fragments enclosed by the quench fractures is fresh and unaltered. Alteration away from the fracture surfaces was found to be restricted to the walls of vesicles intersected by the quench fractures (Fig. 3).

In contrast to fresh and unaltered glassy dacite, intensely-altered samples are typified by a network of interconnected perlitic cracks. Perlitic cracks are known to form in response to the release of strain derived from rapid cooling of the lava (Marshall 1961) or hydration of the volcanic glass (Ross and Smith 1955; Friedman et al. 1966; Jezek and Noble 1978). The observed textural relationships suggest that the perlitic cracks formed subsequent to the quench fracturing of the lava, but prior to hydrothermal alteration. In the case of the samples investigated, alteration is most pronounced at the intersection of the perlitic cracks with the quench fractures and gradually decreases into the polygonal dacite fragments. Away from the quench fractures, the perlitic cracks commonly enclose cores of glassy groundmass that are apparently unaffected by the alteration (Fig. 3). The resultant pseudoclastic texture is similar to that described for ancient volcanic rocks showing relict perlitic cracks (Dimroth and Lichtblau 1979; Allen 1988; Noh and Boles 1989; Doyle 2001; Gifkins and Allen 2001).

The results of the present study suggest that fluid flow through the coherent dacite at Satanic Mills was focused along the different fracture sets. Percolation of the hydrothermal fluids away from these fracture sets was very limited. However, it is important to note that the linkage of the elongated vesicles during perlite formation enhanced the permeability of the coherent dacite substantially. The vesicularity of the samples investigated ranges up to 20 vol.%.

Processes of mineral formation and alteration

Hand specimen inspection suggested that the infiltration of the perlitic dacite by the upwelling hydrothermal fluids caused an extensive replacement of the dacite by secondary minerals. However, the more detailed textural observations at the thin section scale revealed that the mineralogical composition of the whole-rock samples has been modified by two different processes, namely the replacement of primary phases by secondary minerals and the precipitation of minerals into open space. Although both processes change the nature of the whole-rock samples, only the former process is directly related to the interaction of the volcanic rocks with the hydrothermal fluids.

The XRD investigations showed that the transformation of volcanic glass to dioctahedral smectite represented the quantitatively most important alteration process in the immediate subsurface of the Satanic Mills vent site. The dioctahedral smectite belongs to the montmorillonite-beidellite series,

compositions on the montmorillonite side prevail. TEM imaging showed that the dioctahedral smectite represents a pristine alteration products of the volcanic glass forming randomly oriented, bent crystal flakes that are only several tens of nanometer thick. In analogy to the observations of Banfield et al. (1991), it is suggested that the smectite flakes originated through a dissolution-recrystallization mechanism from the volcanic glass. Smectite growth at Satanic Mills did not involve the development of protocrystalline precursor phases as described by Kawano et al. (1993) and Masuda et al. (1996).

The formation of dioctahedral smectite at the expense of the volcanic glass was related to pronounced chemical changes, in particular a decrease in the SiO_2 whole rock content (Fig. 11). Pronounced SiO_2 loss into solution is a well documented effect occurring during the experimental alteration of volcanic glass and clay mineral formation (Caballero et al. 1991; Ghiara et al. 1993; De La Fuente et al. 2002). Alteration of the glass matrix of the dacite samples investigated also caused a decrease in the Na_2O and K_2O whole-rock concentrations (Fig. 11). This observation implies that a significant influx of alkali elements from the hydrothermal fluids was not required to convert volcanic glass into dioctahedral smectite. The observed shift of the whole-rock $\text{Na}_2\text{O}/\text{K}_2\text{O}$ ratio can be readily explained by the fact that the crystallizing smectite preferentially incorporated K into its interlayer position (Table 2). In contrast to these elements, alteration resulted in increasing Al_2O_3 whole-rock concentrations, presumably due to mass changes associated with the mobilization of SiO_2 and the alkali elements.

The dissolution of the volcanic glass was accompanied by an increase in the MgO concentrations (Table 1). Correlation of the MgO whole-rock content and the size of the 1.53 Å reflection in XRD patterns (Fig. 7) suggests that trioctahedral smectite represents the principal host of this element in the altered samples. The presence of trioctahedral smectite with compositions corresponding to saponite was confirmed by the TEM investigations. The formation of saponite during glass dissolution must have involved the influx of Mg from the hydrothermal fluids, unaltered dacite from Satanic Mills contains only low amounts of MgO (Table 1). Based on this observation, it is suggested that the fluid composition and the relative amount of fluids available during glass alteration controlled the overall ratio at which dioctahedral and trioctahedral smectite formed. Mg metasomatism was not pronounced in the case of the samples investigated because only minor amounts of trioctahedral smectite were formed.

In addition to the precipitation of smectite, alteration of the glass matrix resulted in the crystallization of anatase and apatite. Anatase is not present in the unaltered glassy groundmass and, therefore, clearly represents a product of hydrothermal alteration (Fig. 9). In contrast, primary as well as secondary apatite occurs in the glassy groundmass of the dacite samples recovered from Satanic Mills. Both types of apatite can be readily distinguished by cathodoluminescence and analytical

scanning electron microscopy. Secondary apatite is only present in the smectite-bearing groundmass surrounding fluid pathways and shows highly irregular grain shapes. Secondary apatite was found to be characterized by distinctly lower chlorine concentrations when compared to primary crystals. The formation of secondary anatase and apatite in the altered groundmass was probably related to processes of element redistribution within the glassy matrix, slightly elevated whole-rock concentrations of TiO_2 in the most intensely-altered rocks are probably related to overall mass change caused by the mobilization of SiO_2 and the alkali elements.

The microscopic investigations showed that primary minerals contained in the glassy groundmass are not readily altered during incipient alteration. In many cases, the microlites are texturally indistinguishable between areas affected by hydrothermal alteration and the glassy groundmass located away from fluid pathways. However, replacement of titanomagnetite and clinopyroxene by secondary phases has been observed. The former process appears to be responsible for the formation of abundant, finely dispersed pyrite in the alteration halos enveloping the fluid pathways. In contrast to titanomagnetite and clinopyroxene, alteration of the plagioclase has not been recognized. The chemical composition and cathodoluminescence properties of the plagioclase microphenocrysts and microlites were apparently not modified during alteration of the surrounding glass matrix. In particular the latter observation is remarkable because the structure of luminescence centers in feldspars is known to be very sensitive to processes of hydrothermal alteration (Mora and Ramseyer 1992; Vanko and Laverne 1998; Finch and Klein 1999; Götze et al. 1999).

In contrast to the alteration of the glassy groundmass, precipitation of secondary minerals within the network of interconnected fractures and vesicles took place in an environment dominated by the chemical influence of the hydrothermal fluids. Sphalerite, pyrrhotite, and pyrite are the most abundant secondary precipitates. However, coating of fracture and vesicle walls by secondary smectite has also been recognized. The precipitation of sulfides into open space clearly caused the observed increase in the whole-rock concentrations of Zn, Cu, Pb, Ag, and Cd. Whole-rock mass changes of these elements are not directly connected to mineral transformations occurring during hydrothermal alteration of the volcanic rocks whereas addition of sulfur to the whole-rock samples is related to the sulfidization of primary titanomagnetite as well as the precipitation of secondary sulfides and sulfates into open space. The calculation of whole-rock mass gains and losses is, therefore, only of limited value to characterize the chemical environment of alteration at Satanic Mills.

Thermal regime of alteration

The maximum temperature of hydrothermal alteration in the immediate subsurface of the Satanic Mills hydrothermal vent site can be determined on the basis of mineral stability constraints. In particular,

the abundant presence of smectite species in the hydrothermally altered rocks allows some important constraints on the thermal regime of alteration.

It is well known that alteration in geothermal systems produces a sequence of clay minerals similar to that occurring during the prograde diagenesis of pelitic sediments. Dioctahedral smectite converts to illite at elevated temperatures (Fig. 12). The exact nature of the pathway by which this transition occurs has been the focus of considerable debate (Altaner and Ylagan 1997). Most authors agree that the transition involves a continuous transformation of mixed-layer phases whereby the relative amount of illite layers increases with increasing temperature and reaction progress (Hower et al. 1976; Altaner et al. 1984; Brusewitz 1986; Inoue et al. 1990, 1992; Ylagan et al. 1996). However, several investigations have shown that mixed-layer illite/smectite with R1 ordering and an intermediate illite to smectite ratio is dominant in some systems with other kinds of mixed-layer phases occurring only in minor proportions, implying that discontinuous reaction pathways may also occur (Dong et al. 1997; Tillick et al. 2001; Yan et al. 2001). The existence of a direct smectite to illite transition has been proposed by Amouric and Olives (1991).

Trioctahedral smectite species are converted to chlorite at elevated temperatures. Proposed pathways involve either a continuous mixed-layer chlorite/smectite transformation series (Bettison and Schiffman 1988; Schiffman and Fridleifsson 1991; Robinson et al. 1993) that includes the formation of random mixed-layering (Bettison-Varga et al. 1991; Shau and Peacor 1992; Bettison-Varga and MacKinnon 1997), a discontinuous smectite-corrensite-chlorite sequence (Shau and Peacor 1992; Schiffman and Staudigel 1995; Schmidt and Robinson 1997) whereby corrensite is regarded to be a discrete phase rather than a R1 chlorite(0.5)/smectite mixed-layer phase (Shau et al. 1990; Shau and Peacor 1992), or a direct smectite to chlorite transition (Robinson and Santana de Zamora 1999).

Figure 12 shows a compilation of temperature ranges for which dioctahedral and trioctahedral smectite species have been reported in various geothermal systems. Inspection of the plot reveals that dioctahedral and trioctahedral smectite is present up to maximum temperatures of approximately 150 °C. However, the transition of smectite to illite and chlorite through one of the above mentioned reaction pathways occurs over broad temperature intervals that vary as function of kinetically controlled processes of reaction progress (Essene and Peacor 1995; Robinson et al. 2002). In some systems including the Wairakei geothermal field in New Zealand and the Sumikawa geothermal field in Japan, mixed-layer smectite/illite phases have been reported to occur at temperatures as low as 100 °C (Harvey and Browne 1991; Inoue et al. 1992). Corrensite and chlorite are typically present at temperatures in excess of 200 °C, but they have also been observed at temperatures of only 100 °C at the Chipilapa geothermal field in El Salvador (Robinson and Santana de Zamora 1999).

Assuming that the alteration conditions at Satanic Mills are comparable to those of geothermal systems occurring on land, it has to be concluded that incipient alteration of the glassy dacite samples investigated in the present study took place at temperatures below approximately 100 to 150 °C.

It is important to note that smectite represents a stable (or metastable) alteration product in the hydrothermally altered dacite samples recovered from Satanic Mills despite the fact that high-temperature fluids must have circulated through nearby open space fissures resulting in the construction of sphalerite-rich black smoker chimneys at the sampling site. This observation suggests that steep temperature gradients existed between the open fluid channels and the surrounding volcanic rock affected by the incipient hydrothermal alteration. Microphotographs such as those shown in Figures 4d and 5c imply that steep temperature gradients may have developed at the millimeter scale.

The development of steep temperature gradients in the immediate subsurface of the Satanic Mills vent site can be related to the dynamic environment of alteration that was dominated by two contrasting effects, namely heating of the volcanic rocks by the upwelling hydrothermal fluids and concomitant cooling of the dacite by the ambient seawater. The low-temperature alteration products forming in the immediate subsurface at Satanic Mills are expected to convert to high-temperature equivalents only during prolonged upflow of high-temperature fluids or once the volcanic rocks are concealed beneath an insulating cap of sulfide precipitates.

Implications to the understanding of multistage alteration

The present mineralogical investigations complement the results of ODP drilling Leg 193 because comparably little information is available on the alteration in the immediate subsurface. Deep drilling at Snowcap and Roman Ruins could only be achieved by setting casing strings to prevent the collapse of the upper bore hole walls and drilling operations at Satanic Mills were abandoned at a depth of 20.1 mbsf. The core recovery at this site was very poor (Binns et al. 2002) and negligible alteration of the core prevented further work on the alteration mineralogy (Lackschewitz et al. 2004).

Alteration in the deeper portion of the volcanic sequence (Yeats et al. 2001; Binns et al. 2002; Roberts et al. 2003b; Lackschewitz et al. 2004) is distinctly different to that observed in the dacite sampled in the immediate subsurface. The insulating effect of the relatively impermeable coherent dacite capping the volcanic sequence allowed the development of a steep geothermal gradient (Lackschewitz et al. 2004). High-temperature alteration at relatively shallow depth is indicated by the abundant presence of mixed-layer phases, illite, and chlorite immediately below the capping dacite.

The oxygen isotope compositions of these phases are indicative for alteration temperatures between approximately 220 and 300 °C (Lackschewitz et al. 2004).

Comparison of the results of the present study to those obtained by ODP drilling reveals that different alteration mineral associations form contemporaneously within the PACMANUS submarine geothermal system. At present, high-temperature alteration associations develop in the deep central upflow zones of the hydrothermal fluids whereas low-temperature alteration occurs close to the seafloor, and probably in the periphery of the upflow zones. However, temporal changes in the thermal regime and geometry of the upflow zones through time are likely to have resulted in overprinting relationships between the alteration mineral associations forming at different temperatures. Studies on ancient massive sulfide deposits suggest that high-temperature alteration zones migrate outwards during the lifetime of most hydrothermal systems (Pisutha-Arnond and Ohmoto 1983; Ohmoto 1996). At Pacmanus, a complex history of changing alteration conditions is indicated by the presence of mineralized mass flow deposits at depth that presumably formed during earlier mineralizing hydrothermal events (Paulick et al. 2004).

Based on textural investigations on drill core recovered during ODP Leg 193, Binns et al. (2002) suggested that early alteration at Pacmanus produces a pervasive green coloration of the dacite with silica polymorphs, illite, chlorite, and some pyrite being the principal alteration products. However, it is cautioned here that conclusive constraints on the relative timing of different alteration mineral associations cannot be obtained by hand specimen inspection or optical microscopy due to the small grain sizes of the alteration products.

The results of the present study suggest that pervasive alteration comprising illite and chlorite in the deep subsurface represents the high-temperature equivalent of the smectite dominated alteration association occurring in the immediate subsurface (Fig. 12). The high-temperature phases may have originated from previously formed smectite through continuous or discontinuous reaction pathways as described above, but may also have formed through replacement of previously unaltered volcanic glass and rock-forming minerals (Steiner 1968; De La Fuente et al. 2002), or direct precipitation from the hydrothermal fluids (Alt and Jiang 1991). These different modes of formation are difficult to distinguish, but important from a genetic point of view. Future mineralogical investigations on the drill core material recovered during ODP Leg 193 should, therefore, include textural studies at the micro- and nanometer scale.

CONCLUSIONS

The PACMANUS hydrothermal vent field represents a modern analogue of ancient seafloor hydrothermal systems forming massive sulfide deposits. Seafloor sampling revealed that the immediate substrate to sphalerite-rich black smoker chimneys at the Satanic Mills vent site is composed of coherent dacite. Careful textural investigations on variably altered samples recovered from this site show that hydrothermal fluid flow through the glassy dacite was initially focused along quench fractures and interconnected networks of perlitic cracks and vesicles. The primary volcanic textures represented a principal control on the permeability characteristics of the silicic host rocks of this massive sulfide mineralization.

Seafloor observations and the textural evidence suggests that alteration of the dacite has not been sustained. The sphalerite-rich black-smoker chimneys forming at the seafloor were small, and presumably young. Complex overprinting relationships between different alteration mineral associations have not been observed and dacite samples of different alteration intensity have been recovered from a comparably small sampling area. The mineralogy of the products of hydrothermal alteration are consistent with maximum alteration temperatures of approximately 150 to 200°C. The evidence suggests that the samples were affected by incipient hydrothermal alteration that occurred in an environment allowing the development of steep temperature gradients.

The mineralogical investigations showed that the different primary phases contained in the hydrothermally altered dacite samples show variable susceptibilities to hydrothermal alteration. The destruction of the volcanic glass was found to be the quantitatively most important alteration process modifying the composition of the volcanic rocks. In addition to the destruction of the volcanic glass, alteration of primary clinopyroxene and titanomagnetite has been observed. Primary plagioclase was apparently unaffected by the incipient hydrothermal alteration. Even in the most intensely altered samples, plagioclase microphenocrysts and microlites have chemical compositions and cathodoluminescence properties comparable to those contained in least-altered equivalents. This finding contradicts the commonly held perception that plagioclase alteration is a universal alteration characteristic of massive sulfide forming hydrothermal activities. The destruction of the volcanic glass and alteration of primary plagioclase is not necessarily contemporaneous and may occur under different physicochemical conditions of alteration.

Incipient alteration of the dacite samples recovered from the Satanic Mills vent site occurred in a rock-dominated environment. Chemical analysis of variably altered dacite samples shows that alteration did not involve a pronounced metasomatic overprint. The abundant dioctahedral smectite was mainly formed by chemical components supplied by the volcanic glass. Only the formation of trioctahedral

species required the addition of Mg to the silicic volcanic rocks. Alkali metasomatism did not occur during the incipient hydrothermal alteration of the samples investigated. However, Na and K behaved differently during hydrothermal alteration because K liberated during the destruction of the volcanic glass was preferentially incorporated into the interlayer position of the newly formed dioctahedral smectite. The findings of the present study imply that the pronounced potassium enrichment characteristic of alteration halos associated with ancient massive sulfide deposits is not a product of the initial, intensifying stage of hydrothermal alteration, but is probably associated with the alteration taking place at distinctly higher temperatures.

Comparison of the results of the present study with those of deep ODP drilling reveals that different alteration mineral associations form contemporaneously at different locations within the PACMANUS hydrothermal system. Low-temperature alteration appears to be restricted to the immediate subsurface and possibly to the periphery of the hydrothermal system whereas high-temperature alteration occurs in the upflow zones of the hydrothermal fluids. Complex overprinting relationships between these distinct types of hydrothermal alteration are predicted to form in response to changes in the regime of fluid flow throughout the lifetime of the hydrothermal system.

ACKNOWLEDGMENTS

We thank Captain M. Kull, his officers, and the crew onboard R/V Sonne cruise 166 for their expert help. We also gratefully acknowledge analytical efforts by U. Kempe, K. Venance, C. Grégoire, and A. Obst. We express our gratitude for fruitful discussions and comments on various geological and mineralogical aspects of the study to J.B. Gemmell and H. Paulick. We appreciate valuable comments on the mathematical description of turbostratic disorder in smectites by K. Ufer, J. Bergmann, and G. Roth. TM gratefully acknowledges funding by the Emmy Noether Program of the German Research Foundation. The Italian National Research Program in Antarctica (PNRA) supported the TEM facility used by GG. Sample acquisition was supported by the German Federal Ministry of Education and Research through a grant to PMH. The Leibniz Program of the German Research Foundation provided additional financial support to PMH. This work is a contribution to the IGCP Project 502 “Global comparison of volcanic-hosted massive sulfide districts”.

FIGURE CAPTION

- Fig. 1** Simplified geological map showing the major tectonic elements in the Manus Basin region and the location of hydrothermal vent fields (modified from Binns et al., 2002).
- Fig. 2** Distribution of hydrothermal deposits at the PACMANUS vent field. The map also gives the sampling location of the dacite samples investigated in present study and the drilling locations of Ocean Drilling Program Leg 193. The inset shows the seafloor geology of the Eastern Manus Basin (modified from Binns et al., 2002).
- Fig. 3:** Textural variations in samples of different alteration intensity. Intersecting, delicate, arcuate or gently curved perlitic cracks are only abundant in hydrothermally altered rocks. The textural sketches were directly drawn from photomicrographs.
- Fig. 4:** Microphotographs of variably altered dacite from the Satanic Mills vent site. A. Cathodoluminescence image of a plagioclase microphenocryst. The crystal is hosted by unaltered volcanic glass containing plagioclase microlites showing a weak violet CL color. Scale bar is 250 μm . B. Clinopyroxene microphenocryst hosting a glass inclusion. The crystal is contained in an unaltered glassy matrix containing abundant microlites. Transmitted light. Scale bar is 100 μm . C. Skeletal plagioclase crystal with swallow-tail terminations. Some of the larger plagioclase microlites show a preferred orientation whereas small microlites are randomly oriented. Transmitted light. Scale bar is 50 μm . D. Cathodoluminescence image of open space fractures that are surrounded by altered groundmass. Destruction of dark volcanic glass resulted in an accentuation of the weak violet CL color of plagioclase microlites. The open space fractures contain abundant sulfide precipitates. Scale bar is 250 μm . E. Cathodoluminescence image of altered groundmass surrounding a vesicle. The vesicle walls are coated by sulfides and some rare barite laths that are typified by a dark bluish CL color. Scale bar is 250 μm . F. Cathodoluminescence image of a plagioclase microphenocrysts contained in intensely altered groundmass. Although the plagioclase crystals are intersected by fractures that apparently acted as fluid pathways, the CL behavior of the crystals is identical to microphenocrysts contained in unaltered dacite. Scale bar is 250 μm . G. Cathodoluminescence image of altered groundmass surrounding an arcuate crack. The altered groundmass contains abundant secondary apatite that is typified by a bright yellowish CL color. Scale bar is 250 μm .
- Fig. 5:** Scanning electron microscope images obtained on variably altered dacite from the Satanic Mills vent site. A. BSE image of unaltered groundmass consisting of glass and randomly oriented plagioclase microlites. Clinopyroxene (cpx) and magnetite (mgt) are comparably rare. Scale bar is 20 μm . B. BSE image showing a cluster of euhedral apatite (ap) grains that are partially hosted by a plagioclase microphenocryst. Scale bar is 20 μm . C. SE image of an alteration halo surrounding an open space fracture. The volcanic glass is partially converted to fine grained secondary minerals close to the fracture. Plagioclase microlites and magnetite (mgt) are apparently unaltered. The fracture contains a pyrrhotite (po) lath. Scale bar is 100 μm . D. SE image of a perlitic crack in an altered dacite sample. The presence of a small central cavity, the symmetrical banding, and the absence of microlites suggests that the secondary smectite (sm) precipitated into open space. The alteration halo surrounding the crack contains randomly oriented plagioclase microlites and rare magnetite (mgt). Scale bar is 20 μm . E. SE image of a skeletal plagioclase crystals contained in the groundmass of an intensely-altered dacite sample. The formerly glass matrix is largely replaced by fine grained secondary minerals. Scale bar is 20 μm . F. BSE image of barite (brt), sphalerite (sp), and pyrite (py) precipitates in a vesicle contained in

an intensely-altered dacite sample. The formerly glassy matrix surrounding the vesicle is intensely-altered. Scale bar is 30 μm .

- Fig. 6:** XRD patterns of a representative dacite sample that contains substantial amounts of smectite. In untreated condition, broad and overlapping basal reflections can be observed that are caused by the non-uniform basal spacing of the smectite (12.6 to 14.5 \AA). The peak position increases to 17 \AA in ethylene glycole solvated conditions (second order reflection at 8.5 \AA) and shifts to 9.6 \AA in response to heating at 550 $^{\circ}\text{C}$. The diffraction patterns were collected on a strongly oriented mount of the < 2 μm fraction.
- Fig. 7:** XRD patterns of intensely-altered dacite samples containing substantial amounts of smectite. The diffraction patterns of all samples show an intense 060 reflection at approximately 1.49 \AA suggesting that the smectite is dominantly dioctahedral in nature. In two samples, an additional small peak at 1.53 \AA can be observed that indicates the presence of small amounts of trioctahedral smectite. The diffraction patterns were collected on random powder mounts of the < 2 μm fractions.
- Fig. 8:** Low-magnification TEM image of a partially altered glassy groundmass. The light gray and relatively round areas represent pores. Several smectite flakes are present (sm). The inset shows a high-resolution image with 1.1 nm spaced lattice fringes typical of collapsed smectite. The location of the high-magnification image is indicated by the arrow.
- Fig. 9:** Low-magnification TEM image of intensely-altered glassy groundmass adjacent to a fracture that acted as a fluid pathway. The altered glass contains abundant smectite flakes (sm) and anatase (anat). The white arrows indicate areas selected for high-resolution imaging. The inset on the right side shows wavy lattice fringes of collapsed smectite and regularly 0.37 nm-spaced lattice fringes of anatase. The inset on the left side illustrates the presence of wavy lattice fringes (1.1-1.3 nm) of smectite surrounding a 15 nm thick smectite crystal.
- Fig. 10:** Low-magnification TEM image of altered matrix surrounding a vesicle. The formerly glassy matrix contains bent smectite flakes (sm) and prismatic apatite crystals (ap). The arrow shows the position of the high-resolution image given as an inset. The enlarged area shows a smectitic flake that abuts against an apatite crystal.
- Fig. 11:** Variations of the geochemical composition of whole-rock samples as function of the smectite content. The total amount of smectite was determined by the Rietveld method using X-ray diffraction data.
- Fig. 12:** Comparison of well temperatures for which the occurrence of dioctahedral and trioctahedral phyllosilicates is reported in various geothermal systems (modified from Robinson et al., 2002). Thick lines indicate that the mineral is abundantly present, and thin lines indicate that the species is of minor occurrence.

REFERENCES

- Allen RL (1988) False pyroclastic textures in altered silicic lavas, with implications for volcanic-associated mineralization. *Econ Geol* 83: 1424-1446
- Alt JC, Jiang WT (1991) Hydrothermally precipitated mixed-layer illite-smectite in recent massive sulfide deposits from the sea floor. *Geology* 19: 570-573
- Altaner SP, Ylagan RF (1997) Comparison of structural models of mixed-layer illite/smectite and reaction mechanisms of smectite illitization. *Clays Clay Miner* 45: 517-533
- Altaner SP, Hower J, Whitney G, Aronson JL (1984) Model for K-bentonite formation: Evidence from zoned K-bentonites in the disturbed belt, Montana. *Geology* 12: 412-415
- Amouric M, Olives J (1991) Illitization of smectite as seen by high-resolution transmission electron microscopy. *Eur J Mineral* 3: 831-835
- Auzende JM, Urabe T, Binns RA, Charlou JL, Gena K, Gamo T, Henry K, Matsubayashi O, Matsumoto T, Moss R, Naka J, Nagaya Y, Okamura K, Ruellan E (1996) Cruise explores hydrothermal vents of the Manus Basin. *EOS Trans Amer Geophys Union* 77: 244
- Banfield JF, Jones BF, Veblen DR (1991) An AEM-TEM study of weathering and diagenesis, Albert Lake, Oregon: I. Weathering reactions in the volcanics. *Geochim Cosmochim Acta* 55: 2781-2793
- Bergmann J, Friedel P, Kleeberg R (1998) BGMN - A new fundamental parameters based Rietveld program for laboratory X-ray sources, its use in quantitative analysis and structure investigations. *CPD Newslett* 20: 5-8
- Bettison LA, Schiffman P (1988) Compositional and structural variations of phyllosilicates from the Point Sal ophiolite, California. *Amer Mineral* 73: 62-76
- Bettison-Varga L, MacKinnon IDR (1997) The role of randomly mixed-layered chlorite/smectite in the transformation of smectite to chlorite. *Clays Clay Miner* 45: 506-516
- Bettison-Varga L, MacKinnon IDR, Schiffman P (1991) Integrated TEM, XRD and electron microprobe investigation of mixed-layer chlorite-smectite from the Point Sal ophiolite, California. *J metamorphic Geol* 9: 697-710
- Binns RA, Scott SD (1993) Actively forming polymetallic sulfide deposits associated with felsic volcanic rocks in the eastern Manus back-arc basin, Papua New Guinea. *Econ Geol* 88: 2226-2236
- Binns RA, Parr JM, Scott SD, Gemmell JB, Herzig PM (1995) PACMANUS: An active, siliceous volcanic-hosted hydrothermal field in the eastern Manus Basin, Papua New Guinea. In: Mauk JL, St. George, JD (eds) *Proceedings of the 1995 Pacific Rim Congress. Exploring the Rim*. Australasian Institute of Mining and Metallurgy, Parkville, Australia, p. 49-54
- Binns RA, Barriga FJAS, Miller DJ, Shipboard Scientific Party (2002) Leg 193 summary. Anatomy of an active felsic-hosted hydrothermal system, Eastern Manus Basin. *Proceedings of the Ocean Drilling Program, Initial Reports 193*, pp 1-84
- Brusewitz AM (1986) Chemical and physical properties of Paleozoic potassium bentonites from Kinnekulle, Sweden. *Clays Clay Miner* 34: 442-454
- Caballero E, Reyes E, Huertas F, Linares J, Pozzuoli A (1991) Early-stage smectites from pyroclastic rocks of Almeria (Spain). *Chem Geol* 89: 353-358
- Cagatay MN (1993) Hydrothermal alteration associated with volcanogenic massive sulfide deposits: Examples from Turkey. *Econ Geol* 88: 606-621
- Coleman PJ, Kroenke LW (1981) Subduction without volcanism in the Solomon Island arc. *GeoMarine Lett* 1: 129-134
- Davis BK, McPhie J (1996) Spherulites, quench fractures and relict perlite in a Late Devonian rhyolite dyke, Queensland, Australia. *J Volcanol Geotherm Res* 71: 1-11
- De La Fuente S, Cuadros J, Linares J (2002) Early stages of volcanic tuff alteration in hydrothermal experiments: Formation of mixed-layer illite-smectite. *Clays Clay Miner* 50: 578-590
- Dimroth E, Lichtblau AP (1979) Metamorphic evolution of Archean hyaloclastites, Noranda area, Quebec, Canada. Part I: Comparison of Archean and Cenozoic sea-floor metamorphism. *Can J Earth Sci* 16: 1315-1340
- Dong H, Peacor DR, Freed RL (1997) Phase relations among smectite, R1 illite-smectite, and illite. *Amer Mineral* 82: 379-391

- Douville E, Bienvenu P, Charlou JL, Donval JP, Fouquet Y, Appriou P, Gamo T (1999) Yttrium and rare earth elements in fluids from various deep-sea hydrothermal systems. *Geochim Cosmochim Acta* 63: 627-643
- Doyle MG (2001) Volcanic influences on hydrothermal and diagenetic alteration: Evidence from Highway-Reward, Mount Windsor Subprovince, Australia. *Econ Geol* 96: 1133-1148
- Droop GTR (1987) A general equation for estimating Fe³⁺ concentrations in ferromagnesian silicates and oxides from microprobe analyses, using stoichiometric criteria. *Mineral Mag* 51: 431-435
- Essene EJ, Peacor DR (1995) Clay mineral thermometry - a critical perspective. *Clays Clay Miner* 43: 540-553
- Exon NF, Stewart WD, Sandy MJ, Tiffin DL (1986) Geology and offshore petroleum prospects of the New Ireland Basin, northeastern Papua New Guinea. *BMR J Austral Geol Geophys* 10: 39-51
- Finch AA, Klein J (1999) The causes and petrological significance of cathodoluminescence emission from alkali feldspars. *Contrib Mineral Petrol* 135: 234-343
- Francheteau J, Needham HD, Choukroune P, Juteau T, Séguret M, Ballard RD, Fox PJ, Normark W, Carranza A, Cordoba D, Guerrero J, Rangin C, Bougault H, Cambon P, Hekinian R (1979) Massive deep-sea sulphide ore deposits discovered on the East Pacific Rise. *Nature* 277: 523-528
- Friedman I, Smith RL, Long WD (1966) Hydration of natural glass and formation of perlite. *Geol Soc Amer Bull* 77: 323-328
- Gamo T, Okamura K, Kodama Y, Charlou JL, Urabe T, Auzende JM, Shipboard-Scientific-Party, Ishibashi J (1996) Chemical characteristics of hydrothermal fluids from the Manus back-arc Basin, Papua New Guinea, I. Major chemical components. *EOS Trans Amer Geophys Union* 77: W116
- Gemmell JB, Large RR (1992) Stringer system and alteration zones underlying the Hellyer volcanic-hosted massive sulfide deposit, Tasmania, Australia. *Econ Geol* 87: 620-649
- Ghiara MR, Franco E, Petti C, Stanzione D, Valentino GM (1993) Hydrothermal interaction between basaltic glass, deionized water and seawater. *Chem Geol* 104: 125-138
- Gifkins CC, Allen RL (2001) Textural and chemical characteristics of diagenetic and hydrothermal alteration in glassy volcanic rocks: Examples from the Mount Read Volcanics, Tasmania. *Econ Geol* 96: 973-1002
- Giorgetti G, Monecke T, Kleeberg R, Herzig PM (2003) Intermediate sodium-potassium mica in hydrothermally altered rocks of the Waterloo deposit, Australia: A combined SEM-EMP-XRD-TEM study. *Contrib Mineral Petrol* 146: 159-173
- Götze J, Habermann D, Neuser RD, Richter DK (1999) High-resolution spectrometric analysis of rare earth elements-activated cathodoluminescence in feldspar minerals. *Chem Geol* 153: 81-91
- Gustin MS (1990) Stratigraphy and alteration of the host rocks, United Verde massive sulfide deposit, Jerome, Arizona. *Econ Geol* 85: 29-49
- Halbach P, Nakamura K, Wahsner M, Lange J, Sakai H, Käselitz L, Hansen RD, Yamano M, Post J, Prause B, Seifert R, Michaelis W, Teichmann F, Kinoshita M, Märten A, Ishibashi J, Czerwinski S, Blum N (1989) Probable modern analogue of Kuroko-type massive sulphide deposits in the Okinawa Trough back-arc basin. *Nature* 338: 496-499
- Hannington MD, Jonasson IR, Herzig PM, Petersen S (1995) Physical and chemical processes of seafloor mineralization at mid-ocean ridges. In: Humphris SE, Zierenberg RA, Mullineaux LS, Thomson RE (eds) *Seafloor hydrothermal systems: Physical, chemical, biological and geological interactions*. *Geophys Monogr Ser* 91, pp 115-157
- Harvey CC, Browne PRL (1991) Mixed-layer clay geothermometry in the Wairakei geothermal field, New Zealand. *Clays Clay Miner* 39: 614-621
- Herzig PM, Hannington MD (2000) Polymetallic massive sulfides and gold mineralization at mid-ocean ridges and in subduction-related environments. In: Cronan DS (ed) *Handbook of marine minerals deposits*. CRC Press, Boca Raton, pp 347-368
- Herzig PM, Petersen S, Kuhn T, Hannington MD, Gemmell JB, Skinner AC, Shipboard Scientific Party (2003) Shallow drilling of seafloor hydrothermal systems using R/V Sonne and the BGS

- Rockdrill: Conical Seamount (New Ireland Fore-Arc) and Pacmanus (Eastern Manus Basin), Papua New Guinea. *InterRidge News* 12: 22-26
- Hower J, Eslinger EV, Hower ME, Perry EA (1976) Mechanism of burial metamorphism of argillaceous sediment: 1. Mineralogical and chemical evidence. *Geol Soc Amer Bull* 87: 725-737
- Humphris SE, Herzig PM, Miller DJ, Alt JC, Becker K, Brown D, Brüggemann G, Chiba H, Fouquet Y, Gemmell JB, Guerin G, Hannington MD, Holm NG, Honnorez JJ, Iturrino GJ, Knott R, Ludwig R, Nakamura K, Petersen S, Reysenbach AL, Rona PA, Smith S, Sturz AA, Tivey MK, Zhao X (1995) The internal structure of an active sea-floor massive sulphide deposit. *Nature* 377: 713-716
- Iizasa K, Fiske RS, Ishizuka O, Yuasa M, Hashimoto J, Ishibashi J, Naka J, Horii Y, Fujiwara Y, Imai A, Koyama S (1999) A Kuroko-type polymetallic sulfide deposit in a submarine silicic caldera. *Science* 283: 975-977
- Inoue A, Watanabe T, Kohyama N, Brusewitz AM (1990) Characterization of illitization of smectite in bentonite beds at Kinnekulle, Sweden. *Clays Clay Miner* 38: 241-249
- Inoue A, Utada M, Wakita K (1992) Smectite-to-illite conversion in natural hydrothermal systems. *Appl Clay Sci* 7: 131-145
- Jezek PA, Noble DC (1978) Natural hydration and ion exchange of obsidian: An electron microprobe study. *Amer Mineral* 63: 266-273
- Kawano M, Tomita K, Kamino Y (1993) Formation of clay minerals during low temperature experimental alteration of obsidian. *Clays Clay Miner* 41: 431-441
- Kleeberg R, Bergmann J (2002) Quantitative phase analysis using the Rietveld method and a fundamental parameter approach. In: Gupta SPS, Chatterjee P (eds) *Powder diffraction. Proceedings of the II international school on powder diffraction*. Allied Publishers, New Delhi, pp 63-76
- Kristmannsdottir H (1979) Alteration of basaltic rocks by hydrothermal activity at 100-300°C. In: Mortland M, Farmer V (eds) *Developments in Sedimentology* 27, pp 359-367
- Lackschewitz KS, Devey CW, Stoffers P, Botz R, Eisenhauer A, Kummert M, Schmidt M, Singer A (2004) Mineralogical, geochemical and isotopic characteristics of hydrothermal alteration processes in the active, submarine, felsic-hosted PACMANUS field, Manus Basin, Papua New Guinea. *Geochim Cosmochim Acta* 68: 4405-4427
- Large RR, Allen RL, Blake MD, Herrmann W (2001) Hydrothermal alteration and volatile element halos for the Rosebery K lens volcanic-hosted massive sulfide deposit, western Tasmania. *Econ Geol* 96: 1055-1072
- Lentz DR, Van Staal CR (1995) Predeformational origin of massive sulfide mineralization and associated footwall alteration at the Brunswick 12 Pb-Zn-Cu deposit, Bathurst, New Brunswick: Evidence from the porphyry dike. *Econ Geol* 90: 453-463
- Li G, Peacor DR, Merriman RJ, Roberts B (1994) The diagenetic to low-grade metamorphic evolution of matrix white micas in the system muscovite-paragonite in a mudrock from central Wales, United Kingdom. *Clays Clay Miner* 42: 369-381
- MacLean WH, Hoy LD (1991) Geochemistry of hydrothermally altered rocks at the Horne mine, Noranda, Quebec. *Econ Geol* 86: 506-528
- Marquis P, Brown AC, Hubert C, Rigg DM (1990) Progressive alteration associated with auriferous massive sulfide bodies at the Dumagami mine, Abitibi greenstone belt, Quebec. *Econ Geol* 85: 746-764
- Marshall RR (1961) Devitrification of natural glass. *Geol Soc Amer Bull* 72: 1493-1520
- Martinez F, Taylor B (1996) Backarc spreading, rifting, and microplate rotation, between transform faults in the Manus Basin. *Mar Geophys Res* 18: 203-224
- Martinez F, Taylor B (2003) Controls on back-arc accretion: Insights from the Lau, Manus and Mariana basins. In: Larter RD, Leat PT (eds) *Intra-oceanic subduction systems: Tectonic and magmatic processes*. *Geol Soc London Spec Pub* 219, pp 19-54
- Masuda H, O'Neil JR, Jiang WT, Peacor DR (1996) Relation between interlayer composition of authigenic smectite, mineral assemblages, I/S reaction rate and fluid composition in silicic ash of the Nankai Trough. *Clays Clay Miner* 44: 443-459
- Monecke T, Köhler S, Kleeberg R, Herzig PM, Gemmell JB (2001) Quantitative phase-analysis by the Rietveld method using X-ray powder-diffraction data: Application to the study of alteration

- halos associated with volcanic-rock-hosted massive sulfide deposits. *Can Mineral* 39: 1617-1633
- Moos R, Scott SD (2001) Geochemistry and mineralogy of gold-rich hydrothermal precipitates from the eastern Manus Basin, Papua New Guinea. *Can Mineral* 39: 957-978
- Mora CI, Ramseyer K (1992) Cathodoluminescence of coexisting plagioclases, Boehls Butte anorthosite: CL activators and fluid flow paths. *Amer Mineral* 77: 1258-1265
- Neuser RD (1995) A new high-intensity cathodoluminescence microscope and its application to weakly luminescing minerals. *Bochumer Geol Geotechn Arb* 44: 116-118
- Noh JH, Boles JR (1989) Diagenetic alteration of perlite in the Guryongpo area, Republic of Korea. *Clays Clay Miner* 37: 47-58
- Offler R, Whitford DJ (1992) Wall-rock alteration and metamorphism of a volcanic-hosted massive sulfide deposit at Que River, Tasmania: Petrology and mineralogy. *Econ Geol* 87: 686-705
- Ohmoto H (1996) Formation of volcanogenic massive sulfide deposits: The Kuroko perspective. *Ore Geol Rev* 10: 135-177
- Paulick H, Vanko DA, Yeats CJ (2004) Drill core-based facies reconstruction of a deep-marine felsic volcano hosting an active hydrothermal system (Pual Ridge, Papua New Guinea, ODP Leg 193). *J Volcanol Geotherm Res* 130: 31-50
- Patrier P, Papanagioulou P, Beaufort D, Traineau H, Brill H, Rojas J (1996) Role of permeability versus temperature in the distribution of the fine (<0.2 μm) clay fraction in the Chipilapa geothermal system (El Salvador, Central America). *J Volcanol Geotherm Res* 72: 101-120
- Phinney EJ, Mann P, Coffin MF, Shipley TH (1999) Sequence stratigraphy, structure, and tectonic history of the southwestern Ontong Java Plateau adjacent to the North Solomon Trench and Solomon Island arc. *J Geophys Res* 104: 20449-20466
- Pisutha-Arnond V, Ohmoto H (1983) Thermal history, and chemical and isotopic compositions of the ore-forming fluids responsible for the kuroko massive sulfide deposits in the Hokuroku District of Japan. *Econ Geol Monogr* 5: 523-558
- Roberts MD, Oliver NHS, Fairclough MC, Hölttä PS, Lahtinen R (2003a) Geochemical and oxygen isotope signature of sea-floor alteration associated with a polydeformed and highly metamorphosed massive sulfide deposit, Ruostesuo, Central Finland. *Econ Geol* 98: 535-556
- Roberts S, Bach W, Binns RA, Vanko DA, Yeats CJ, Teagle DAH, Blacklock K, Blusztajn JS, Boyce AJ, Cooper MJ, Holland N, McDonald B (2003b) Contrasting evolution of hydrothermal fluids in the PACMANUS system, Manus Basin: The Sr and S isotope evidence. *Geology* 31: 805-808
- Robinson D, Santana de Zamora A (1999) The smectite to chlorite transition in the Chipilapa geothermal system, El Salvador. *Amer Mineral* 84: 607-619
- Robinson D, Bevins RE, Rowbotham G (1993) The characterization of mafic phyllosilicates in low-grade metabasalts from eastern North Greenland. *Amer Mineral* 78: 377-390
- Robinson D, Schmidt ST, Santana de Zamora A (2002) Reaction pathways and reaction progress for smectite-to-chlorite transformation: Evidence from hydrothermal altered metabasites. *J metamorphic Geol* 20: 167-174
- Ross CS, Smith RL (1955) Water and other volatiles in volcanic glasses. *Amer Mineral* 40: 1071-1089
- Schiffman P, Fridleifsson GO (1991) The smectite-chlorite transition in drillhole NJ-15, Nesjavellir geothermal field, Iceland: XRD, BSE and electron microprobe investigations. *J metamorphic Geol* 9: 679-696
- Schiffman P, Staudigel H (1995) The smectite to chlorite transition in a fossil seamount hydrothermal system: The basement complex of La Palma, Canary islands. *J metamorphic Geol* 13: 487-498
- Schmidt JM (1988) Mineral and whole-rock compositions of seawater-dominated hydrothermal alteration at the Arctic volcanogenic massive sulfide prospect, Alaska. *Econ Geol* 83: 822-842
- Schmidt ST, Robinson D (1997) Metamorphic grade and porosity and permeability controls on mafic phyllosilicate distributions in a regional zeolite to greenschist facies transition of the North Shore Volcanic Group, Minnesota. *Geol Soc Amer Bull* 109: 683-697
- Shau YH, Peacor DR (1992) Phyllosilicates in hydrothermally altered basalts from DSDP Hole 504B, Leg 83 - a TEM and AEM study. *Contrib Mineral Petrol* 112: 119-133

- Shau YH, Peacor DR, Essene EJ (1990) Corrensite and mixed-layer chlorite/corrensite in metabasalt from northern Taiwan: TEM/AEM, EMPA, XRD, and optical studies. *Contrib Mineral Petrol* 105: 123-142
- Simmons SF, Browne PRL (2000) Hydrothermal minerals and precious metals in the Broadlands-Ohaaki Geothermal System: Implications for understanding low-sulfidation epithermal environments. *Econ Geol* 95: 971-999
- Stanton RL (1983) The direct derivation of sillimanite from a kaolinitic precursor: Evidence from the Geco Mine, Manitouwadge, Ontario. *Econ Geol* 78: 422-437
- Steiner A (1968) Clay minerals in hydrothermally altered rocks at Wairakei, New Zealand. *Clays Clay Miner* 16: 193-213
- Taut T, Kleeberg R, Bergmann J (1997) The new Seifert Rietveld program and its application to quantitative phase analysis. In: Morawiec H, Stróz D (eds) *Applied Crystallography. Proceedings of the XVII Conference*. World Scientific, Singapore, pp 87-92
- Taylor B (1979) Bismarck Sea: Evolution of a back-arc basin. *Geology* 7: 171-174
- Taylor B, Crook K, Sinton J (1994) Extensional transform zones and oblique spreading centers. *J Geophys Res* 99: 19707-19718
- Tillick DA, Peacor DR, Mauk JL (2001) Genesis of dioctahedral phyllosilicates during hydrothermal alteration of volcanic rocks: I. The Golden Cross epithermal ore deposit, New Zealand. *Clays Clay Miner* 49: 126-140
- Ufer K, Roth G, Kleeberg R, Stanjek H, Dohrmann R, Bergmann J (2004) Description of X-ray powder pattern of turbostratically disordered layer structures with a Rietveld compatible approach. *Z Kristallogr* 219: 519-527
- Urabe T, Scott SD (1983) Geology and footwall alteration of the South Bay massive sulphide deposit, northwestern Ontario, Canada. *Can J Earth Sci* 20: 1862-1879
- Vanko DA, Laverne C (1998) Hydrothermal anorthitization of plagioclase within the magmatic/hydrothermal transition at mid-ocean ridges: Examples from deep sheeted dikes (Hole 504B, Costa Rica Rift) and a sheeted dike root zone (Oman ophiolite). *Earth Planet Sci Lett* 162: 27-43
- Waters JC, Binns RA (1998) Contrasting styles of felsic submarine volcanism, eastern Manus Basin, Papua New Guinea. *Abstr Geol Soc Austral* 49: 459
- Waters JC, Binns RA, Naka J (1996) Morphology of Submarine Felsic Volcanic Rocks on Pual Ridge, Eastern Manus Basin, Papua New Guinea. *EOS Trans Amer Geophys Union* 77: W120
- Yamagishi H (1991) Morphological and sedimentological characteristics of the Neogene submarine coherent lavas and hyaloclastites in Southwest Hokkaido, Japan. *Sed Geol* 74: 5-23
- Yamagishi H, Dimroth E (1985) A comparison of Miocene and Archean rhyolite hyaloclastites: Evidence for a hot and fluid rhyolite lava. *J Volcanol Geotherm Res* 23: 337-355
- Yan Y, Tillick DA, Peacor DR, Simmons SF (2001) Genesis of dioctahedral phyllosilicates during hydrothermal alteration of volcanic rocks: II. The Broadland-Ohaaki hydrothermal system, New Zealand. *Clays Clay Miner* 49: 141-155
- Yeats C, Bach W, Vanko DA, Roberts S, Lackschewitz K, Paulick H (2001) Fluid-Dacite Interaction in the PACMANUS seafloor hydrothermal system - preliminary results from secondary mineral chemistry and geochemical modelling. *EOS Trans Amer Geophys Union* 82: OS11A-0346
- Ylagan RF, Altaner SP, Pozzuoli A (1996) Hydrothermal alteration of a rhyolitic hyaloclastite from Ponza Island, Italy. *J Volcanol Geotherm Res* 74: 215-231

Table 1 Quantitative phase analyses and geochemical composition of whole-rock samples from the PACMANUS hydrothermal field

	Least-altered			Moderately-altered		Intensely-altered		
	58GTV-1a	58GTV-1d	58GTV-2a	58GTV-3i	58GTV-3a	58GTV-4b	58GTV-4t	58GTV-4q
Phase abundances (wt. %):								
Glass	74.6±1.1	72.1±1.5	70.9±1.1	65.2±2.1	61.7±2.0	53.4±2.0	61.6±2.0	51.9±2.3
Plagioclase	20.0±0.9	19.7±1.3	22.2±1.0	22.7±1.1	24.5±1.0	27.3±1.0	18.6±1.0	19.8±1.1
Clinopyroxene	4.7±1.1	7.3±2.1	5.9±1.3	5.5±1.5	5.8±1.1	5.2±1.1	3.4±1.1	5.0±1.5
Magnetite	0.7±0.1	0.8±0.2	0.9±0.1	0.8±0.2	0.5±0.1	0.5±0.1	0.5±0.2	0.6±0.2
Smectite	-	-	-	4.7±1.6	6.4±1.7	12.1±1.7	15.1±1.6	21.3±2.0
Sphalerite	-	-	-	1.1±0.1	1.3±0.1	1.6±0.1	0.8±0.1	0.4±0.1
Barite	-	-	-	-	-	-	-	0.4±0.1
Chalcopyrite	-	-	-	-	-	-	-	0.2±0.1
Pyrite	-	-	-	-	-	-	-	0.3±0.1
Major element concentrations (wt. %):								
SiO ₂	70.10	69.90	69.20	68.00	67.50	62.80	63.50	60.70
TiO ₂	0.60	0.61	0.61	0.63	0.63	0.67	0.72	0.73
Al ₂ O ₃	13.70	13.90	13.70	14.10	14.10	14.90	16.00	15.90
Fe ₂ O ₃ ^T	4.69	4.69	4.82	4.72	4.75	4.95	4.78	4.95
MnO	0.12	0.12	0.12	0.11	0.11	0.09	0.09	0.09
MgO	0.82	0.81	0.83	0.82	0.79	0.85	1.48	1.89
CaO	2.79	2.83	2.84	2.80	2.82	2.74	2.83	2.45
Na ₂ O	4.66	4.66	4.66	4.49	4.35	3.65	3.52	3.00
K ₂ O	1.91	1.94	1.95	1.90	1.97	1.59	1.58	1.43
P ₂ O ₅	0.12	0.13	0.12	0.12	0.12	0.11	0.11	0.10
LOI	2.0	1.6	1.6	2.6	2.6	5.3	6.4	6.8
Total	101.51	101.19	100.45	100.29	99.74	97.65	101.01	98.04
S	<0.01	<0.01	0.03	0.40	0.38	1.15	0.84	0.79
Trace element abundances (ppm):								
Sc	11	11	11	12	12	12	13	13
V	19	19	19	22	19	20	23	22
Cr	35	<10	15	<10	25	13	88	<10
Co	6	5	5	5	6	6	6	6
Ni	13	<10	<10	<10	13	<10	26	<10
Cu	39	28	36	207	120	342	894	1570
Zn	102	91	506	5050	4700	11900	4750	2430
Rb	26	26	27	26	33	40	32	36
Sr	275	276	275	300	289	301	304	283
Y	34	36	36	35	36	40	39	44
Zr	129	128	127	134	133	142	149	152
Nb	1.8	1.8	1.8	1.9	1.9	2.0	2.1	2.1
Ag	0.2	<0.1	<0.1	0.6	0.4	1.0	0.6	0.2
Cd	0.4	<0.2	0.8	14	14	27	12	6.2
Cs	0.7	0.7	0.8	0.8	1.1	2.3	2.0	2.9
Pb	10	7	24	114	28	256	74	19
Bi	<0.5	<0.5	<0.5	<0.5	<0.5	<0.5	<0.5	<0.5
Th	1.2	1.2	1.2	1.2	1.2	1.3	1.4	1.4
U	0.7	0.7	0.7	1.2	0.9	1.2	1.2	1.3
Element ratios:								
Na ₂ O/K ₂ O	2.44	2.40	2.39	2.36	2.21	2.30	2.23	2.10
Ti/Zr	34.86	35.72	36.00	35.24	35.50	35.36	36.22	36.00
Nb/Y	0.05	0.05	0.05	0.05	0.05	0.05	0.05	0.05
U/Th	0.58	0.58	0.58	1.00	0.75	0.92	0.86	0.93

Table 2 Chemical composition of dioctahedral and trioctahedral smectite as constrained TEM-AEM

	Dioctahedral smectite		Trioctahedral smectite	
	\bar{x} (n=6)	σ (n=6)	\bar{x} (n=6)	σ (n=6)
Si	7.61	0.15	7.09	0.16
Al ^{IV}	0.39	0.15	0.91	0.16
Al ^{VI}	2.78	0.47	1.12	0.35
Ti	0.05	0.09	0.21	0.20
Mg	0.78	0.66	2.82	0.49
Fe	0.43	0.04	0.78	0.11
Na	0.28	0.15	0.27	0.27
Ca	0.12	0.11	0.10	0.06
K	0.52	0.27	0.24	0.10
Σ VI	4.04	0.21	4.92	0.17
Σ XII	0.91	0.30	0.62	0.24

Notes: The chemical formulae are calculated on the basis of 44 negative charges. All Fe is given as Fe³⁺. The mean values (\bar{x}) and standard deviations (σ) have been calculated on the basis of 6 independent analyses. Σ VI = total of octahedral cations, Σ XII = total of interlayer cations.

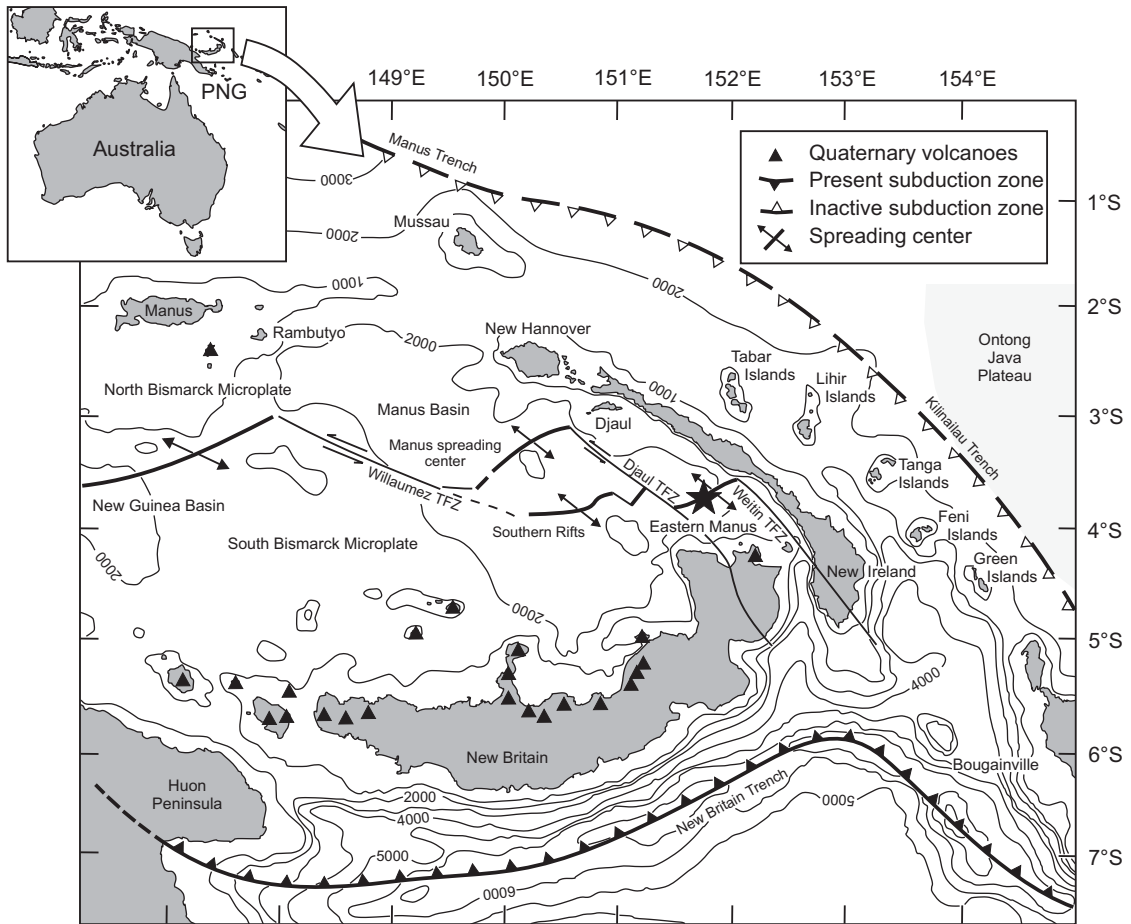


Figure 1 (Monecke et al.)

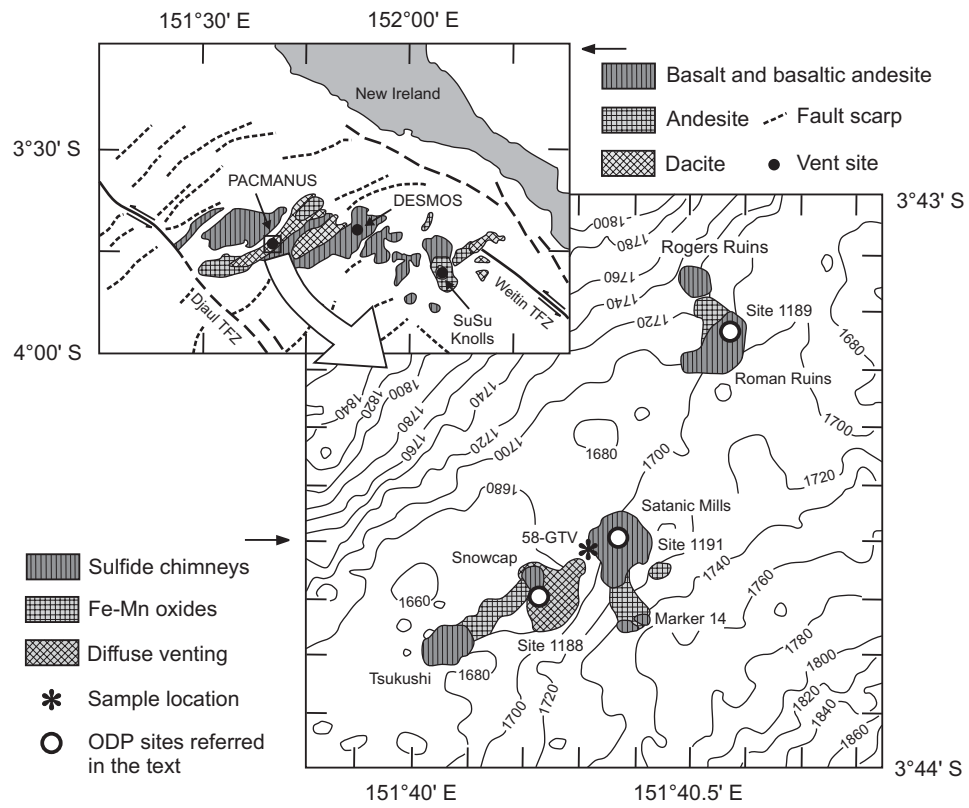


Figure 2 (Monecke et al.)

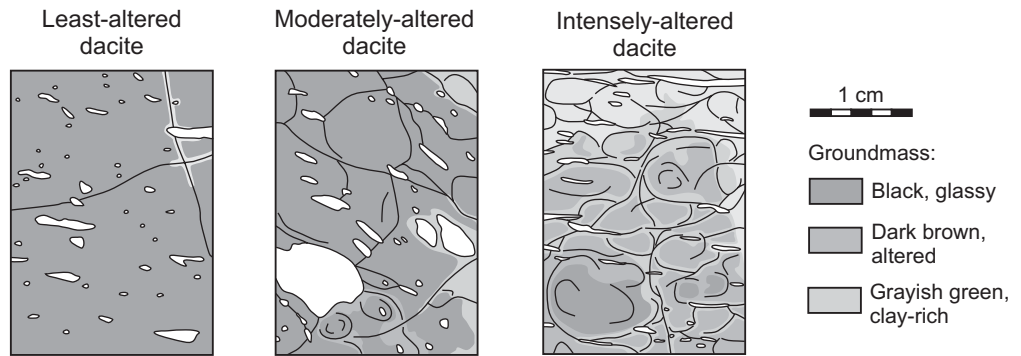


Figure 3 (Monecke et al.)

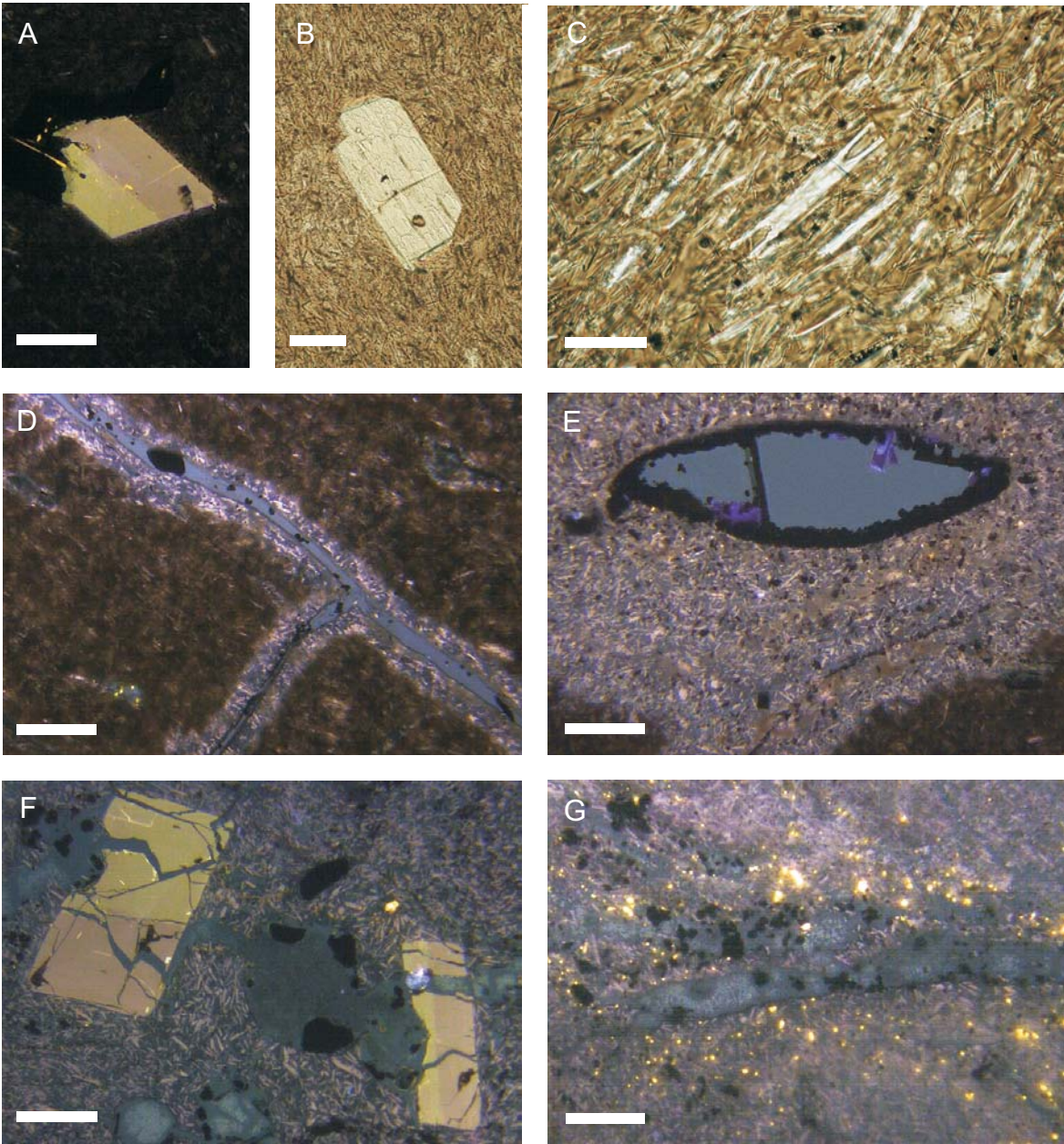


Figure 4 (Monecke et al.)

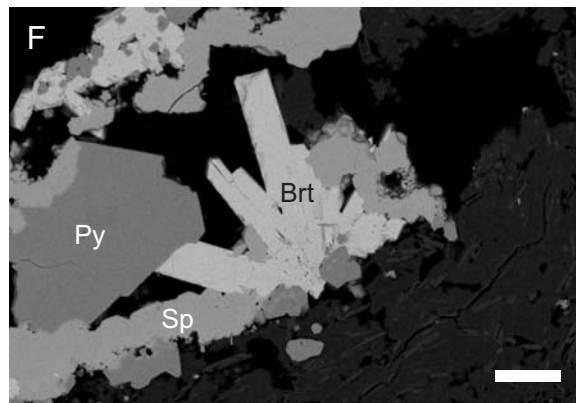
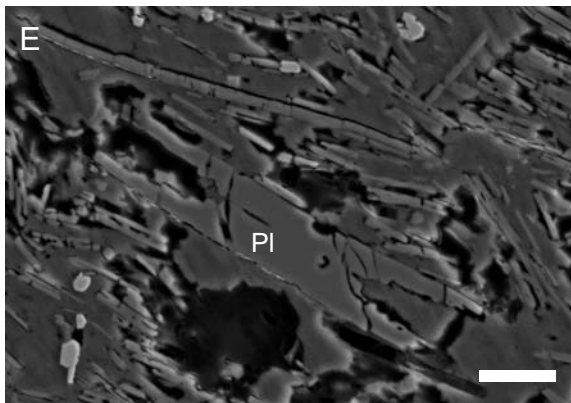
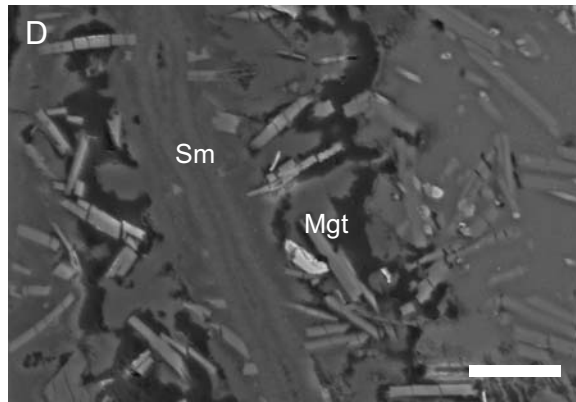
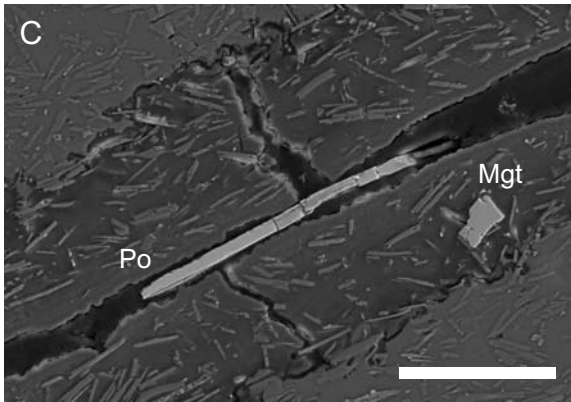
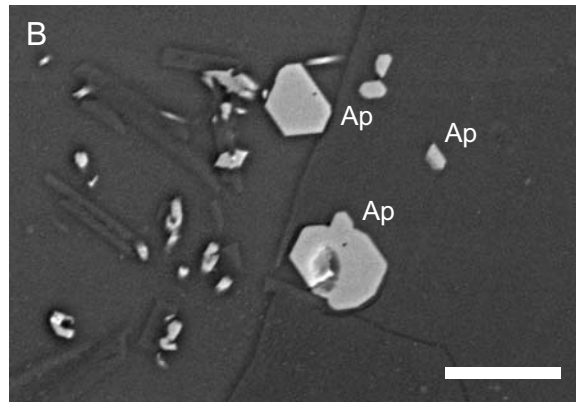
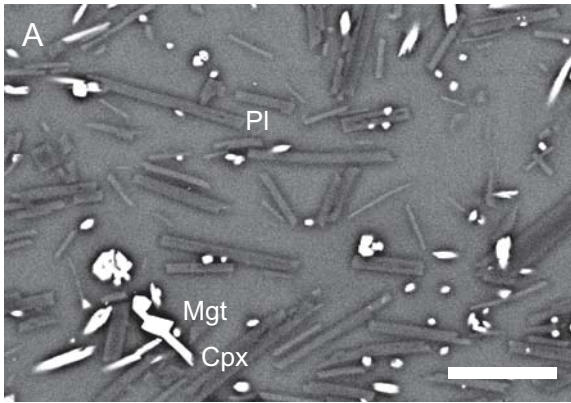


Figure 5 (Monecke et al.)

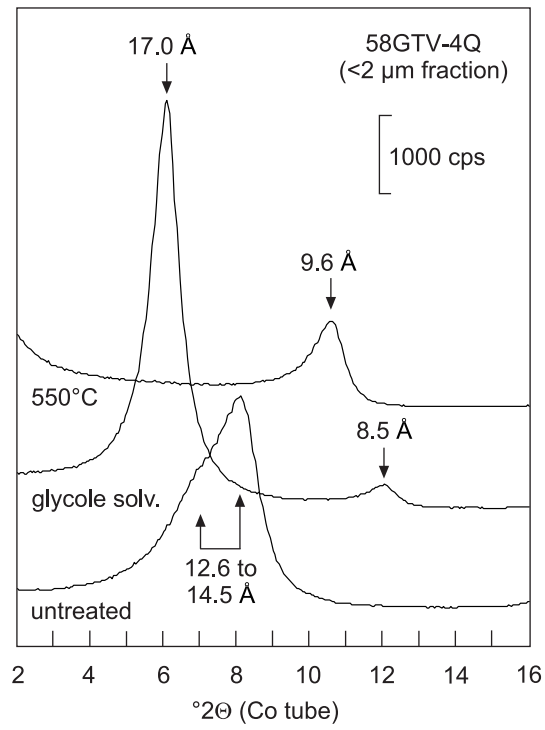


Figure 6 (Monecke et al.)

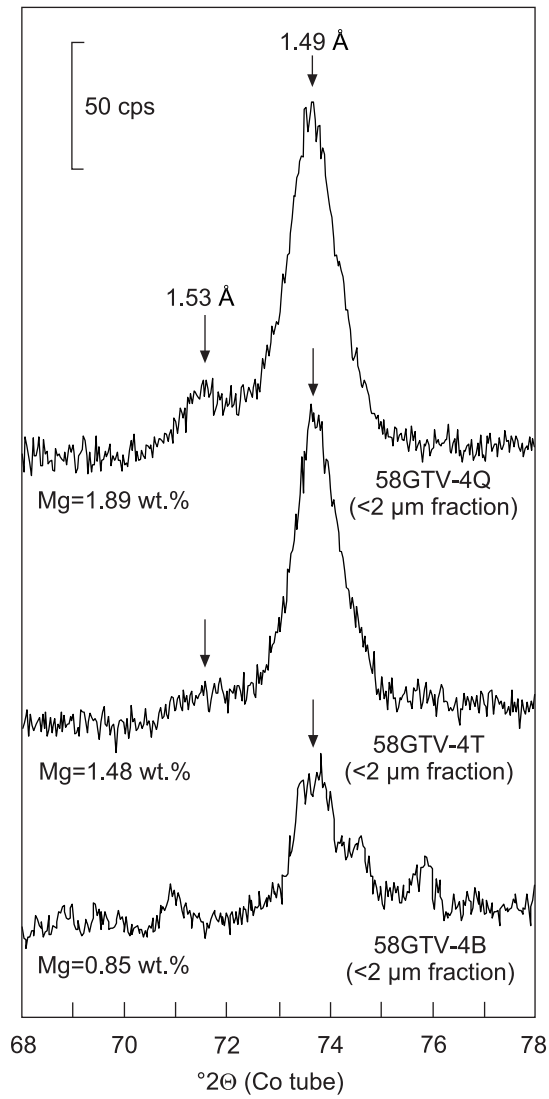


Figure 7 (Monecke et al.)

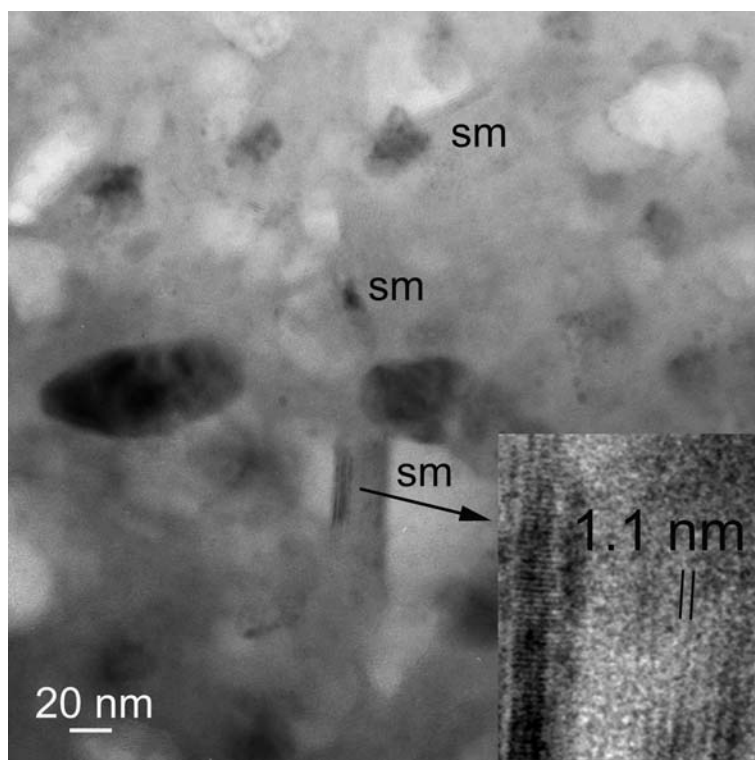


Figure 8 (Monecke et al.)

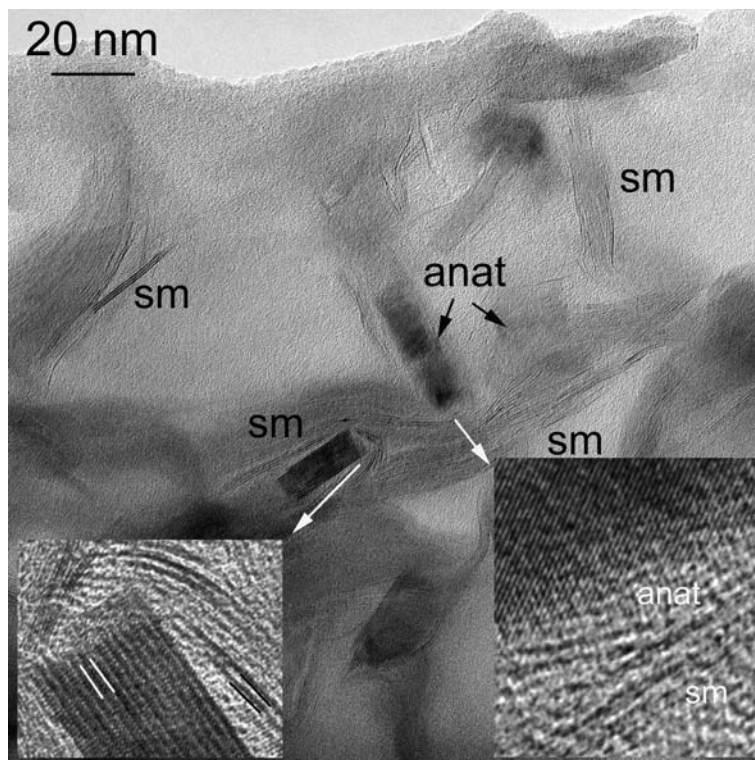


Figure 9 (Monecke et al.)

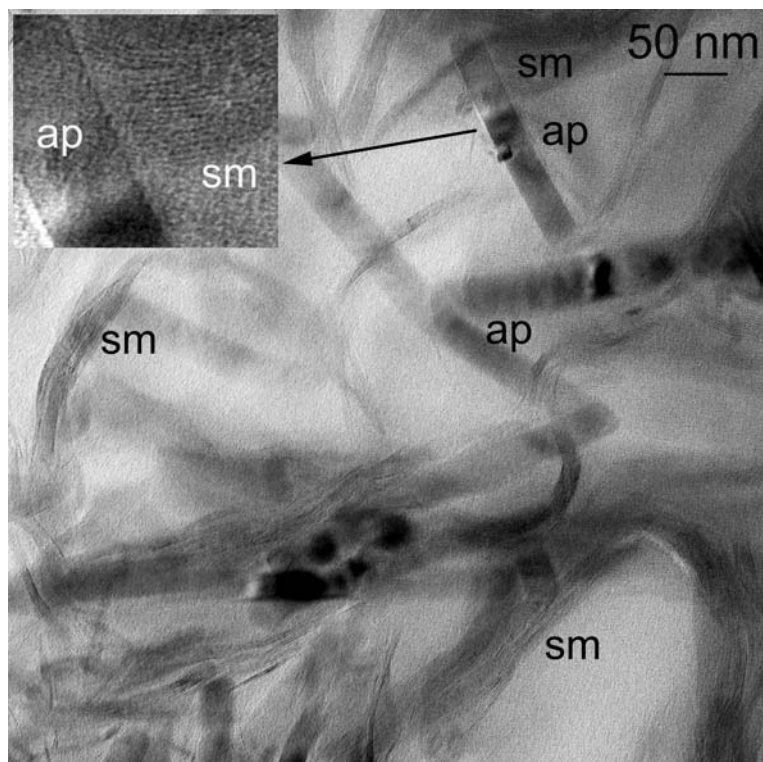


Figure 10 (Monecke et al.)

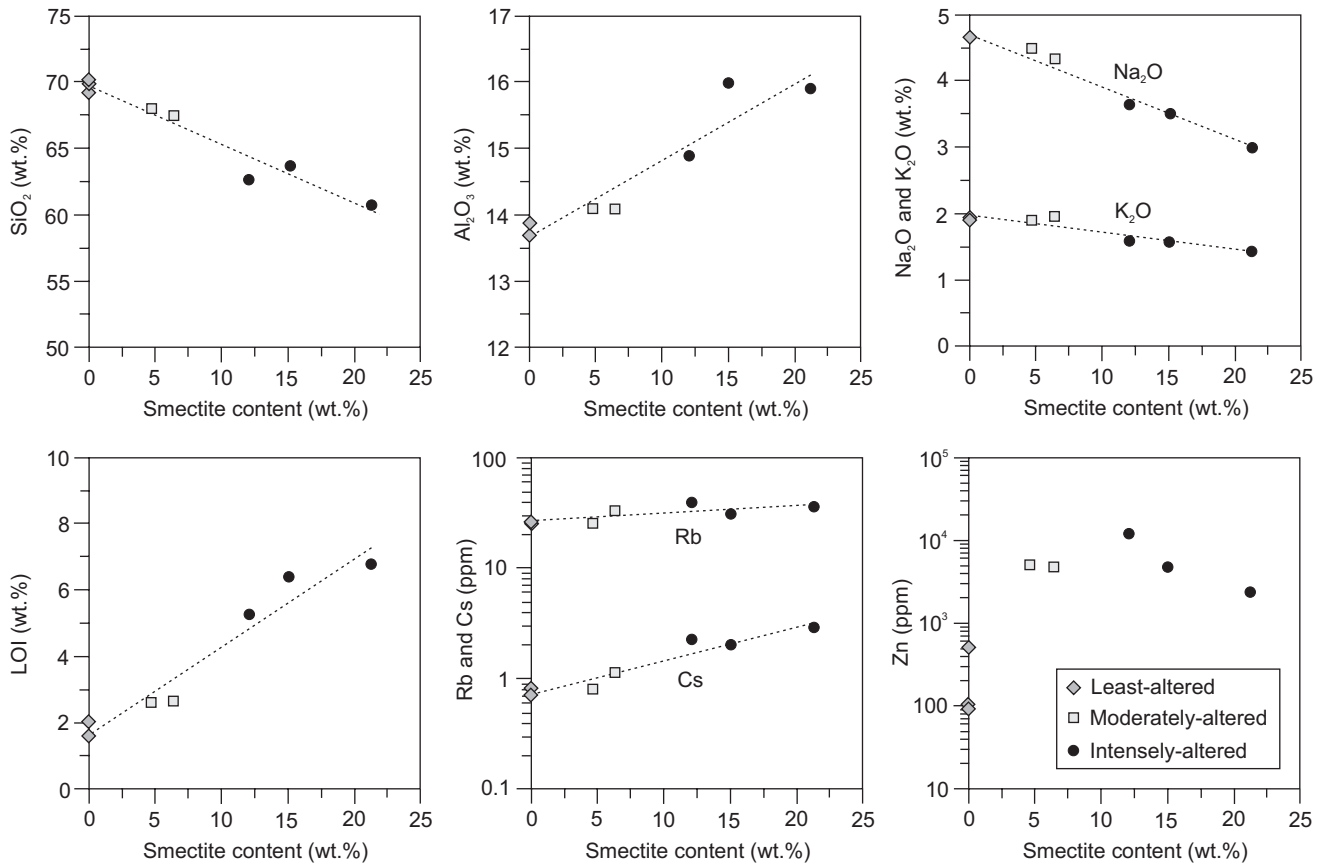


Figure 11 (Monecke et al.)

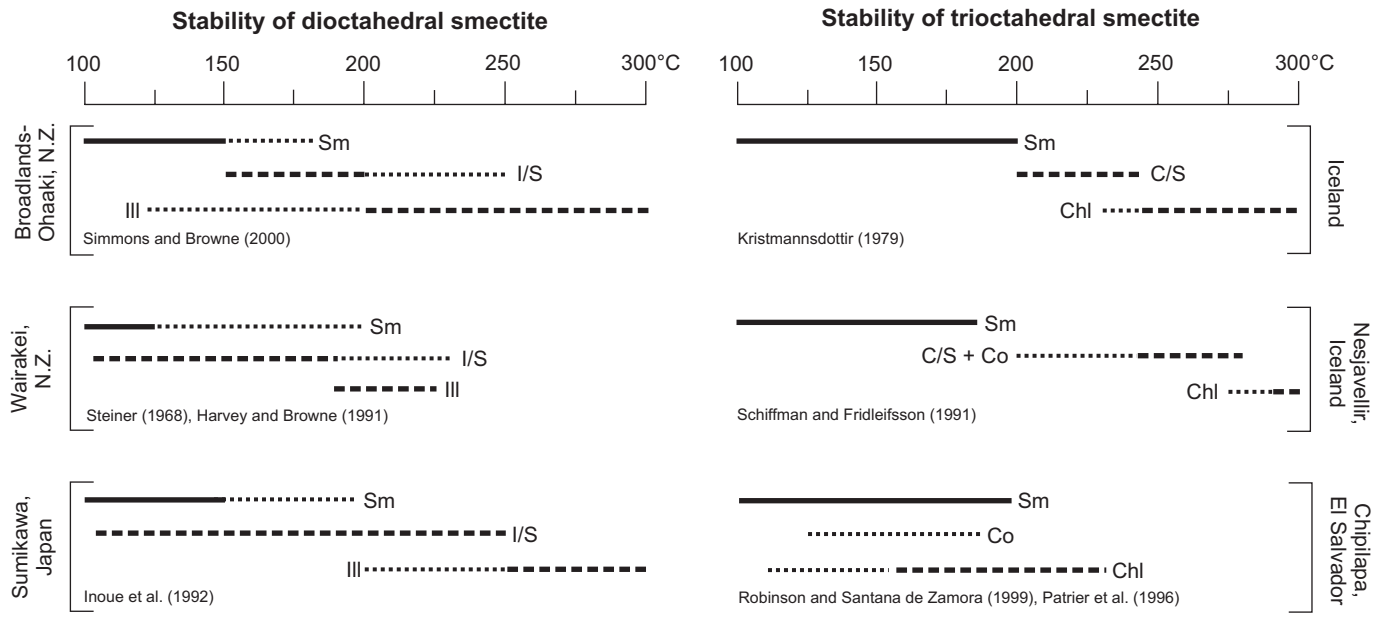


Figure 12 (Monecke et al.)

Jan Pašava · Anna Vymazalová · Sven Petersen
Peter Herzig

PGE distribution in massive sulfides from the PACMANUS hydrothermal field, eastern Manus basin, Papua New Guinea: implications for PGE enrichment in some ancient volcanogenic massive sulfide deposits

Received: 28 June 2004 / Accepted: 29 August 2004 / Published online: 29 October 2004
© Springer-Verlag 2004

Abstract The distribution of platinum group elements (PGE) in Cu- and Zn-rich samples from the Roman Ruins and Satanic Mills vent sites in the PACMANUS hydrothermal field (Papua New Guinea) was studied and compared to that from selected ancient volcanogenic massive sulfide (VMS) deposits. Samples from the Satanic Mills site are enriched in Pd and Rh when compared to samples from Roman Ruins and reach highest values in active and inactive Cu-rich black smoker chimneys and chalcopyrite-cemented dacite breccias (up to 356 ppb Pd and up to 145 ppb Rh). A significant positive correlation was established between Cu and Pd and Rh in samples from both vent sites. Comparisons of chondrite normalized patterns and values of Pd/Pt and Pd/Ir ratios in Cu-rich sulfides and probable source rocks (felsic volcanic rocks/MORB) along with the evidence for a magmatic component in the PACMANUS hydrothermal system indicate that leaching of back-arc volcanic rocks together with addition of magmatic volatiles to the convecting hydrothermal system was the most important factor for PGE enrichment at PACMANUS and likely at some PGE-enriched ancient VMS deposits.

Keywords Platinum group elements · Pd and Rh enrichment · Volcanogenic massive sulfides · Hydrothermal vents · Manus basin

Editorial handling: B. Lehmann

J. Pašava (✉) · A. Vymazalová
Czech Geological Survey, Klárov 131/3,
118 21 Praha 1, Prague, Czech Republic
E-mail: pasava@cgu.cz

S. Petersen · P. Herzig
Leibniz-Institut für Meereswissenschaften, IFM-GEOMAR,
Gebäude Ostufer, Wischhofstr. 1-3, Geb. 4, Raum 111,
24148 Kiel, Germany

Introduction

Layered igneous complexes are the principal sources of platinum group elements (PGE); however, PGE enrichments also occur in the sedimentary marine environment (Goldberg et al. 1963, 1988; Crocket et al. 1973; Hodge et al. 1985, 1986). This includes their concentration in manganese crusts (Clarke et al. 1985; McMurtry et al. 1989; Halbach et al. 1990; Hein et al. 1990a; Stuben et al. 1999), manganese nodules (Haynes et al. 1985; Manheim 1986; Hein et al. 1990b; Stuben et al. 1999), and in mid-ocean ridge volcanic exhalites (Crocket 1989, 1990; Pan and Xie 2001; Cave et al. 2003).

Hydrothermal systems on the seafloor represent modern analogues for ancient volcanic-hosted massive sulfide (VMS) deposits. In general, studies of submarine hydrothermal activity have been focussed on fields located on basaltic igneous crust at mid-ocean ridges. Such systems can be compared to some basalt-hosted massive sulfide deposits on land (Cyprus type); however, more than 50% of the known VMS deposits occur in felsic volcanic successions (Barrie and Hannington 1999).

In November 2000–January 2001 Ocean Drilling Program Leg 193 focused on sampling of altered dacites from the subsurface of the PACMANUS hydrothermal system in the eastern Manus basin, Papua New Guinea (Binns et al. 2002; Paulick and Herzig 2003). Poor core recovery in the sulfide-rich intervals prevented an assessment of the subseafloor sulfides and the recovery of variably altered volcanic rocks in the subsurface indicated that massive sulfide formation may be restricted to a thin veneer at the top of the extrusive rocks (Binns et al. 2002). In 2002, the British Geological Survey (BGS) lander-type Rockdrill was successfully deployed at the Roman Ruins site at PACMANUS from the German R/V Sonne to recover the missing sulfide-rich sections of the deposit and retrieved spectacular massive sulfides (sphalerite, chalcopyrite, pyrite and to a lesser

extent galena and sulfosalts), massive barite, nodular sulfide-anhydrite breccias, resedimented sulfides as well as clay-altered dacite from depths up to 5 m. Preliminary geochemical analyses revealed high Au and base metal concentrations reaching up to 58 g/t Au, and mineralogical investigations showed that gold enrichment is generally related to sphalerite-rich sections (Herzig et al. 2003; Petersen et al. 2003).

The main purpose of this research is to report on the preliminary results of the study of the distribution of PGE and especially the discovery of elevated Pd and Rh concentrations in both active and inactive black smoker sites at the PACMANUS hydrothermal field. These results are important for the explanation of extreme fractionation of PGE in some ancient volcanogenic massive sulfide deposits.

The PACMANUS hydrothermal field

The PACMANUS vent field is located in the eastern part of the Manus back-arc basin to the north of the subduction system at the New Britain trench (Fig. 1). It consists of five hydrothermally active sites, namely Rogers Ruins, Roman Ruins, Satanic Mills, Tsukushi and Snowcap, which occur at the top of the SW–NE trending Pual Ridge. This volcanic sequence is 20 km long, 1–1.5 km wide and rises 500–600 m above the surrounding ocean floor reaching a maximum height of about 1,640 meter below sea level (m.b.s.l.). The upper part of Pual Ridge is dominated by lavas of dacitic composition, whereas basaltic andesite crops out along the lower flanks of the

ridge (Binns and Scott 1993; Waters et al. 1996; Barriga et al. 2000). The surrounding basin is largely dominated by basaltic andesite and basalt.

Roman Ruins

This vent site (1,693–1,710 m.b.s.l. and 150 m across) contains numerous large columnar chimneys (up to 20 m in height) growing from a mound-like structure. Many chimneys are broken and some of them show later regrowth. Although many chimneys are inactive, there are active structures including black smokers and diffuser-style chimneys that emit clear fluid (Binns et al. 2002).

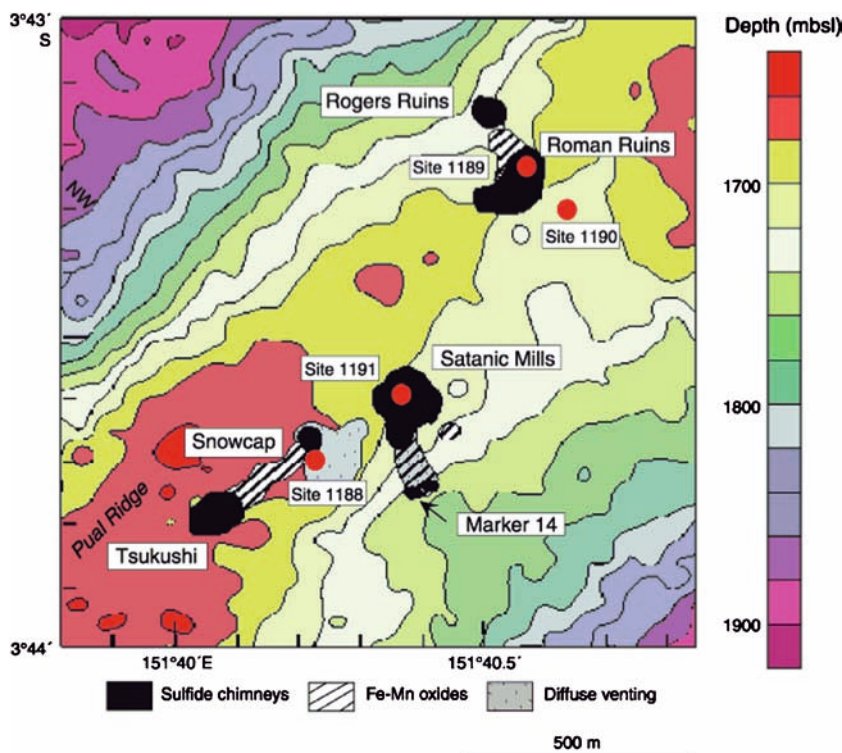
Satanic Mills

Satanic Mills is located at a depth of 1,708–1,720 m.b.s.l. and is almost 200 m across (Binns et al. 2002). It is characterized by more scattered chimneys and spires marked by intense venting of black and grey smoke in close proximity to structures that are emitting clear fluid.

Methods

A total of 21 sulfide samples (15 samples from Roman Ruins and 6 samples from Satanic Mills, for description see Tables 1, 2) were studied for their PGE content in the laboratories of the Czech Geological Survey in

Fig. 1 Active hydrothermal areas at PACMANUS vent field. ODP leg 193 sites (1188–1191). From http://www-odp.tamu.edu/publications/193_SR/193TOC.HTM



Prague. The drill core material from Roman Ruins was initially logged on board. Quarter core samples representing 10–50 cm of core length were crushed to a grain size below 2 mm on board with an impact mill for whole-rock geochemical investigations. Representative subsamples (50 to several 100 g) of sulfides from Satanic Mills that were taken by a TV-guided hydraulic and grab were processed in the same way. All the crushed samples were milled using an agate mill to reduce metal contamination. The samples for PGE analyses (20 g quart of the original sample) were pulverized and, after

preconcentration into Ni-button, PGE were determined by inductively coupled plasma mass spectrometry (ICP-MS) at the Faculty of Science, Charles University in Prague (Dr. V. Strnad—analyst). Certified reference material WMG-1 (mineralized gabbro) was used as the standard for PGE. Cu and Zn were determined commercially at Activation Laboratories Limited (Canada) using an assay with inductively coupled plasma optical emission spectrometry finish (ICP-OES). Gold was analysed by instrumental neutron activation analysis (INAA).

Table 1 Description of samples from Roman Ruins, Manus basin, PNG

Core number	Sample description
SO166-58GTV-5A	Chalcopyrite-dacite breccia with intensely altered dacite fragments cemented by massive chalcopyrite. This likely represents seafloor material below an active black smoker.
SO166-58GTV-8A3	Porous massive sphalerite with minor barite and some galena, sphalerite is cementing almost “fresh” dacite
SO166-54GTV-1	Massive chalcopyrite chimney with a central conduit rimmed by massive chalcopyrite, black smoker pieces
SO166-59GTV-s24	Interior of porous, large, inactive chimney, chalcopyrite with some black (high-T) sphalerite and rare pyrite, barite in cavities
SO166-59GTV-s63	Interior of porous, large, inactive chimney, chalcopyrite-rich conduit with minor black sphalerite
SO166-59GTV-2E	Outer part of the former chimney dominated by porous sphalerite-barite and some chalcopyrite in the interior of the porous sample

Table 2 Description of samples from Satanic Mills, Manus basin, PNG

Core number	Interval	Sample description
SO166-60RD	0–30	Porous fine grained pyrite with abundant porous sphalerite
SO166-60RD	30–60	Semi-massive clastic ore containing 1–3 cm rounded clasts of pyrite ± chalcopyrite in a matrix of anhydrite
SO166-60RD	60–90	Semi-massive clastic ore containing 1–3 cm rounded clasts of pyrite ± chalcopyrite in a matrix of anhydrite
SO166-63RD	0–50	Sandy pyrite ± chalcopyrite in a matrix of anhydrite and barite; the core most likely represents mass wasted material of chimney debris; the upper part is slightly more dense and contains more sphalerite
SO166-65RD	10–30	Porous chalcopyrite ± sphalerite with large 2–3 cm cavity (?) filled by porous chalcopyrite; dark sphalerite distributed throughout the sample, cavities are lined by late barite, also abundant barite in the matrix
SO166-65RD	30–40	Porous massive sphalerite with a red-brown color; fine-grained barite is abundant
SO166-66RD	10–30	Moderately to weakly porous, fine-grained massive chalcopyrite with minor pyrite
SO166-66RD	30–55	Massive sphalerite and barite; sulfides show ribbon texture; this core most likely represents chimney material
SO166-66RD	55–80	Massive sphalerite and barite; sulfides show ribbon texture; there is a chalcopyrite vein (1 cm) crosscutting the sphalerite below 75 cm; this core most likely represents chimney material
SO166-69RD	20–50	Pyrite and chalcopyrite clasts set in a matrix of honey-brown to dark-brown sphalerite + barite
SO166-69RD	50–85	Fine-grained sphalerite with some pyrite, chimney material
SO166-69RD	85–120	Dark to light brown porous sphalerite, often banded, with minor anhydrite filling voids
SO166-69RD	120–150	Dark to light brown porous sphalerite, often banded, with minor anhydrite filling voids
SO166-69RD	150–180	Dark brown massive sphalerite with barite with veins of anhydrite plus minor pyrite ± chalcopyrite
SO166-69RD	180–220	Brecciated material consisting of greenish, siliceous fragments set in a light-grey matrix of amorphous silica, barite, sphalerite and disseminated pyrite

Results

The results of PGE and other trace element determinations are summarized in Tables 3 and 4 and shown in Figs. 2a, b, 3a–f, and 4a, b.

It is apparent from the tables and figures that the geochemical composition of sulfide samples recovered by drilling from Roman Ruins as a whole differs significantly from those sampled at Satanic Mills. Sulfide samples from Roman Ruins studied here are generally characterized by higher Zn (average 19.8 wt.%) and lower Cu (average 5.8 wt.%), Pd and Rh values ($Pd_{avg} = 9.9$ ppb, $Rh_{avg} = 3.5$ ppb) when compared to the samples from Satanic Mills ($Zn_{avg} = 14.5$ wt.%, $Cu_{avg} = 19.3$ wt.%, $Pd_{avg} = 162.3$ ppb and $Rh_{avg} = 66.5$ ppb). The average concentrations of Pt, Ir and Ru are almost identical in sulfide samples from both vent sites (Roman Ruins: $Pt_{avg} = 5.5$ ppb, $Ir_{avg} = 0.8$ ppb and $Ru_{avg} = 1.8$ ppb; Satanic Mills: $Pt_{avg} = 3.7$ ppb, $Ir_{avg} = 0.7$ ppb and $Ru_{avg} = 1.9$ ppb). If we divide samples into Cu-rich (Cu

> Zn) and Zn-rich (Zn > Cu), we can document that Cu-rich samples at both vent sites are always characterized by higher Pd and Rh concentrations than the Zn-rich samples (Tables 3, 4). Zn-rich sulfide samples from Roman Ruins show average values of Pd=6.8 ppb, Pt=4.5 ppb, Rh=2.5 ppb, Ru=1.8 ppb, Ir=0.5 ppb and Au=14.5 ppm while Cu-rich samples from the same site are characterized by higher average PGE and Au values (Pd=18.4 ppb, Pt=8.2 ppb, Rh=6.2 ppb, Ru=2 ppb, Ir=1.8 ppb and Au=15.6 ppm). At Satanic Mills, Cu-rich samples from active and inactive black smoker-style chimneys have anomalously high Pd and Rh concentrations (maximum of 356 ppb Pd, 145 ppb Rh), while Zn-rich samples revealed rather low PGE values (Pd up to 24.4 ppb and Rh up to 9.9 ppb). Maximum Pd (356 ppb) and Rh (145 ppb) values were detected in a chalcopyrite-rich conduit of an inactive black smoker-style chimney at Satanic Mills (Table 4).

Significant positive correlation coefficients between Pd and Rh on one side and Cu on the other side were calculated for the whole set of samples ($n=21$) from

Table 3 Summary of geochemical data for samples from Roman Ruins, Manus basin, PNG

Core number	Depth	Ru (ppb)	Rh (ppb)	Pd (ppb)	Ir (ppb)	Pt (ppb)	Cu (%)	Au (ppm)	Zn (%)	Pd/Pt	Pd/Ir
60RD ^a	00–30	<1	4.6	10.8	0.5	2.4	4.6	12.4	18.1	4.5	21.6
60RD ^b	30–60	<5	3.2	11.7	0.3	4.3	8.3	1.5	1.5	2.7	39.0
60RD ^b	60–90	<1	1.5	3.5	6.2	11.6	6.2	1.2	0.8	0.3	0.6
63RD ^a	00–50	<5	4.6	14.7	0.2	5.8	8.8	8.0	12.4	2.5	73.5
65RD ^b	10–30	<5	6.9	21.0	0.3	13.7	12.9	57.2	12.2	1.5	70.0
65RD ^a	30–40	<5	2.3	5.6	0.2	5.5	1.1	9.2	44.7	1.0	28.0
66RD ^b	10–30	<5	13.2	37.3	0.4	3.3	28.3	2.4	0.9	11.3	93.3
66RD ^a	30–55	<1	1.5	3.6	0.5	5.5	1.2	28.8	33.1	0.7	7.2
66RD ^a	55–80	<5	0.5	4.5	0.4	3.0	0.5	27.3	33.5	1.5	11.3
69RD ^a	20–50	<5	5.7	17.2	0.1	<2.0	5.1	11.6	12.1	17.2	344.0
69RD ^a	50–85	<1	2.3	5.6	0.5	2.9	5.9	13.7	17.6	1.9	11.2
69RD ^a	85–120	<5	1.8	4.1	0.3	4.9	0.4	30.4	44.7	0.8	13.7
69RD ^a	120–150	<1	0.4	<1.0	0.5	1.9	0.3	11.9	32.3	0.3	1.0
69RD ^a	150–180	<5	1.7	6.4	0.8	8.4	3.8	2.4	4.2	0.8	8.0
69RD ^a	180–220	<5	1.7	2.3	1.0	7.7	0.2	4.0	30.0	0.3	2.3
∅	1.8	3.5	9.9	0.8	5.5	5.8	14.8	19.9	1.8	1.8	12.2
σ	0.0	3.1	8.9	1.4	3.3	6.8	14.3	14.5	4.5	4.5	81.7
∅ Cu-rich	2.0	6.2	18.4	1.8	8.2	13.9	15.6	3.8	4.0	4.0	50.7
∅ Zn-rich	1.8	2.5	6.8	0.5	4.5	2.9	14.5	25.7	2.9	2.9	47.4

Half values were used for statistical calculations of samples with values below detection limit

^aZn-rich

^bCu-rich

∅ average value, σ standard deviation

Table 4 Summary of geochemical data for samples from Satanic Mills, Manus basin, PNG

Core sample	Core number	Ru (ppb)	Rh (ppb)	Pd (ppb)	Ir (ppb)	Pt (ppb)	Cu (%)	Au (ppm)	Zn (%)	Pd/Pt
58–5A ^b	3.1	106.4	254.2	2.0	5.4	31.2	11.8	0.3	47.1	127.1
58–8A3 ^a	<1	1.2	2.0	0.5	8.1	0.7	12.3	53.3	0.2	4.0
54GTV-1 ^b	2.9	117.1	288.4	0.2	<2.0	26.4	10.2	2.5	288.4	1310.9
59GTV-s24 ^b	<2	10.7	26.5	<0.1	5.5	22.6	32.7	4.6	4.8	530.0
59GTV-s63 ^b	3.0	145.0	355.6	<0.1	<2.0	27.0	13.5	3.4	355.6	7112.0
59GTV-2E ^a	0.6	18.7	46.8	<0.1	<2.0	8.2	16.3	23.0	46.8	936.0
∅	1.85	66.5	162.3	0.7	3.7	19.3	16.1	14.5	123.8	1670.0
σ	1.0	53.4	130.5	0.7	1.6	10.2	7.1	17.5	132.1	2290.9
∅Cu-rich	2.5	94.8	231.2	0.6	3.2	26.8	17	2.7	72.3	2270.0
∅Zn-rich	0.6	10.0	24.4	0.3	4.6	4.5	14.3	38.1	5.3	470.0

Half values were used for statistical calculations of samples with values below detection limit

^aZn-rich

^bCu-rich

∅ average value, σ standard deviation

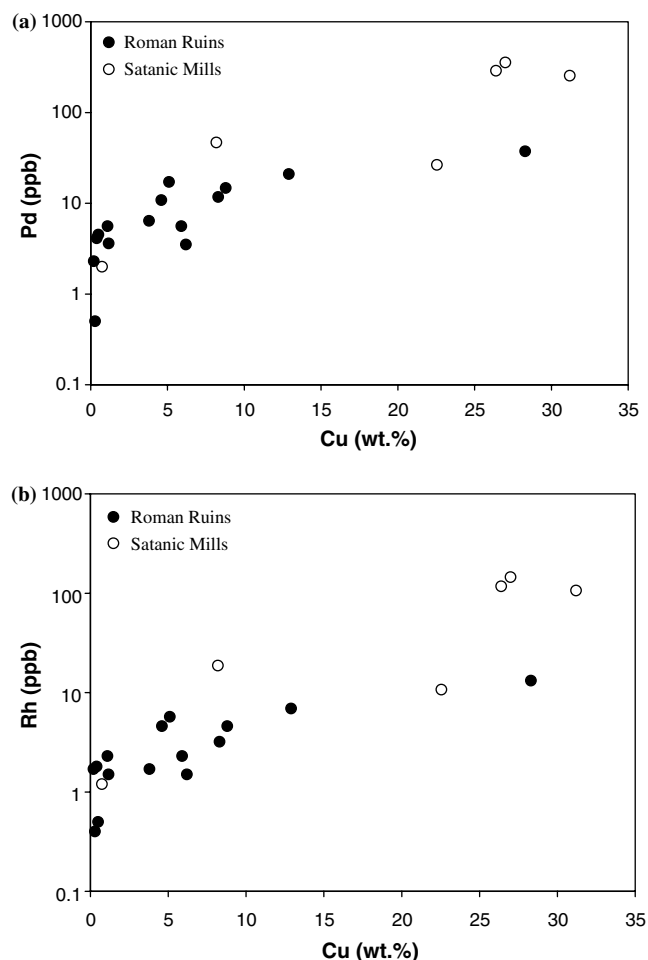


Fig. 2 Correlation of Pd (a) and Rh (b) with Cu in sulfide samples from Roman Ruins and Satanic Mills, Manus basin, PNG

both vent sites ($\text{Pd}/\text{Cu}_{\text{cc}}=0.76$, $\text{Rh}/\text{Cu}_{\text{cc}}=0.76$, Fig. 2a, b) and confirmed at each locality (Roman Ruins: $\text{Pd}/\text{Cu}_{\text{cc}}=0.94$, $\text{Rh}/\text{Cu}_{\text{cc}}=0.93$; Satanic Mills: $\text{Pd}/\text{Cu}_{\text{cc}}=0.78$ and $\text{Rh}/\text{Cu}_{\text{cc}}=0.79$) and also in both Zn- and Cu-rich sample types (Zn-rich samples: $\text{Pd}/\text{Cu}_{\text{cc}}=0.73$ and $\text{Rh}/\text{Cu}_{\text{cc}}=0.68$; Cu-rich samples: $\text{Pd}/\text{Cu}_{\text{cc}}=0.68$ and $\text{Rh}/\text{Cu}_{\text{cc}}=0.68$). No positive relationship was found between Au and Pd or Rh (mostly negative correlation coefficients). A general down hole decrease in Pd and Rh and a down hole increase in Pt and Ir concentrations is documented for the cores from Roman Ruins (Fig. 3a–d).

At Roman Ruins, Pd/Pt ratios range from 0.3 to 17.2 and Pd/Ir from 0.6 to 344 (Table 3). At Satanic Mills, Pd/Pt vary from 0.2 to 356 and Pd/Ir from 4 to 7,112 (Table 4).

Discussion

Crocket (1990) has determined Au, Pd and Ir in hydrothermal deposits from the Juan de Fuca and Mid-Atlantic ridges. He reported very low Pd values (3.2–

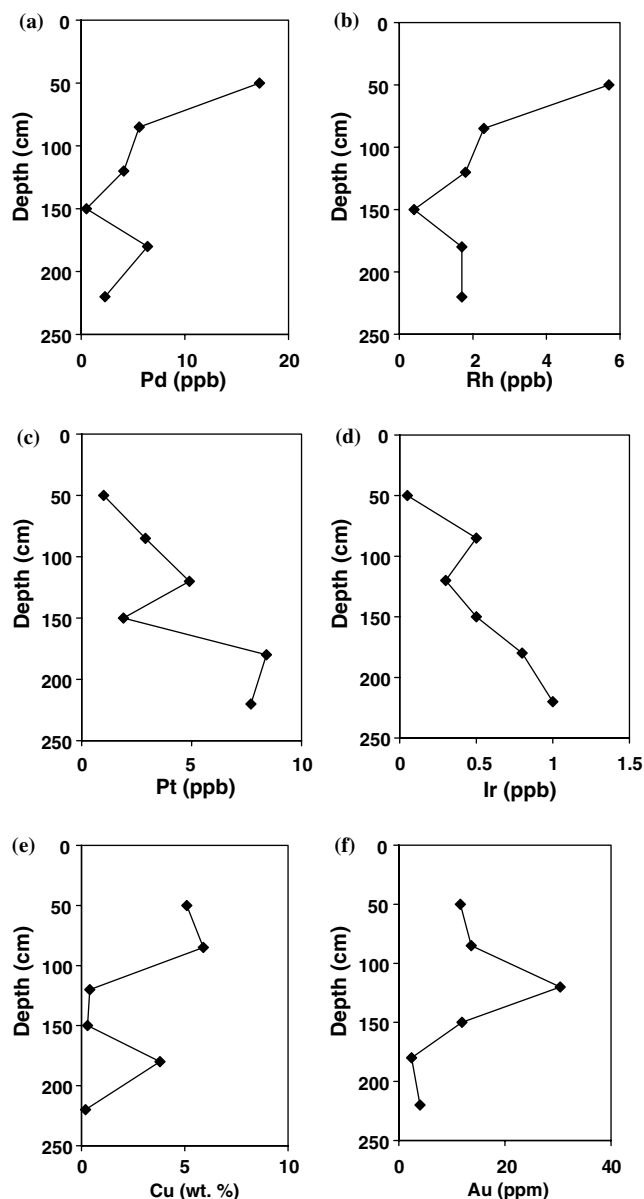


Fig. 3 Down core distribution of PGE, Au and Cu in the Core 69RD (core length 2.2 m; penetration 4.9 m) drilled at the Roman Ruins site. a Distribution of Pd, b distribution of Rh, c distribution of Pt, d distribution of Ir, e distribution of Cu and f distribution of Au

3.5 ppb) but rather high Au (from $6,100 \pm 566$ to $18,900$ ppb) and Ir values (7.6 ± 1.4 ppb) in two massive Cu–Fe sulfides from the central black smoker complex of the TAG hydrothermal area (26°N). These results are comparable with the situation at Roman Ruins where Cu-rich samples contain on average 18.4 ppb Pd (SD = 14.5). At Satanic Mills, however, massive chalcopyrite-rich samples are characterized by much higher Pd values (up to 356 ppb Pd). Crocket (1990) also reported results for a Zn-rich sulfide sample from the TAG area with 1,000 ppb Pd, 1.01 ± 0.57 ppb Ir and $2,690 \pm 10$ ppb Au. It should be noted that no elevated

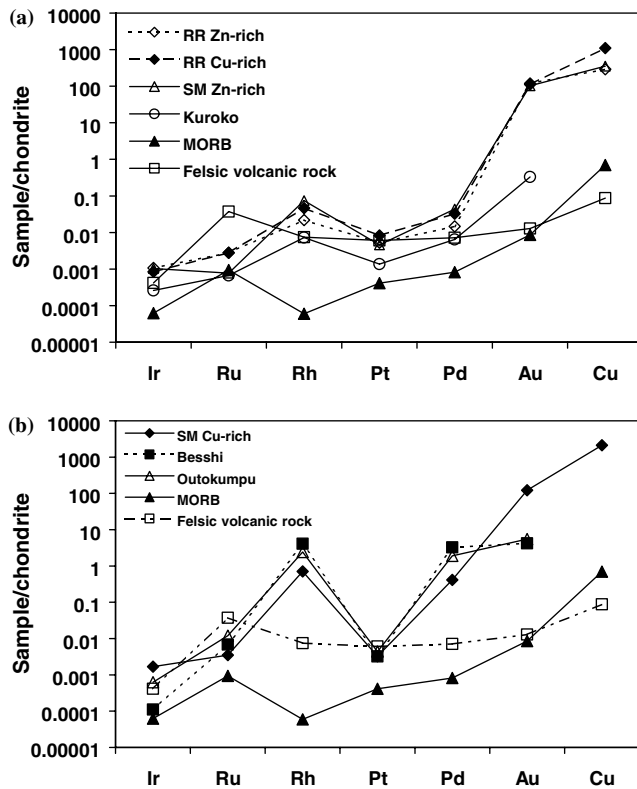


Fig. 4 PGE-Au-Cu chondrite normalized patterns. **a** Cu- and Zn-rich samples from Roman Ruins (*RR*) and Zn-rich samples from Satanic Mills (*SM*) compared to global MORB (Crocket 2002), felsic volcanic rock (data for Ir, Ru, Pt, Pd, Au and Cu from Borg et al. 1988 and data for Rh from Barnes et al. 1988) and Cu-rich sample from Kuroko deposit (from Pan and Xie 2001). **b** Cu-rich samples from Satanic Mills (*SM*) compared to global MORB (Crocket 2002), felsic volcanic rock (data for Ir, Ru, Pt, Pd, Au and Cu from Borg et al. 1988 and data for Rh from Barnes et al. 1988) and Cu-rich samples from the Besshi and Outokumpu VMS deposits (data from Pan and Xie 2001). Chondrite data are from Anders and Grevesse (1989)

PGE values have been found in any of our Zn-rich samples ($\text{Pd} = 0.5\text{--}46.8$ ppb, Tables 3 and 4).

Dacite, rhyodacite and basalt andesite lava flows and associated volcanoclastic rocks are the principal host rocks in the PACMANUS vent field (Pual Ridge). In terms of absolute PGE contents, Cu- and Zn-rich samples from Roman Ruins and Zn-rich samples from Satanic Mills are characterized by higher PGE and significantly higher Au concentrations than those from yellow and black ore of Kuroko deposits (Fig. 4a), reported by Pan and Xie (2001). The shape of PGE-chondrite normalized patterns for this group of samples shows many similarities including a slight Rh and Pd enrichment with a small negative Pt anomaly (Fig. 4a), possibly indicating a similar source of the metals. Chondrite normalized PGE patterns for Cu-rich samples from Satanic Mills and the patterns for the PGE-enriched Besshi and Outokumpu VMS deposits show more apparent Rh and Pd enrichments resulting in a more pronounced negative Pt anomaly compared to the first group of curves (Fig. 4b).

It is therefore not clear if the composition of PGE in source rocks was the most decisive control of PGE distribution in the PACMANUS hydrothermal system considering the fact that evidence of leaching from volcanogenic host rocks and a magmatic component related to Au enrichment into the system was presented by Moss et al. (2001). A magmatic contribution to the hydrothermal fluids at PACMANUS was previously suggested by various authors because of the presence of high F, SO_2 and elevated gas concentrations in the fluids, the presence of metal-rich melt inclusions in the host rock, and unusually low sulfur isotope ratios (Douville et al. 1999; Yang and Scott 1996; Gemmill et al. 1996). A mixing of seawater-derived and magmatic fluids was also suggested by Bach et al. (2003) for the PACMANUS hydrothermal system based on the study of rare-earth elements in anhydrite.

A very close relationship between Pd, Rh and Cu in the samples from the PACMANUS hydrothermal field is documented in Fig. 2a, b and suggests that Pd and Rh are closely associated with chalcopyrite. This observation is in agreement with the Pd and Rh enrichment in chalcopyrite from several ancient VMS deposits (Pan and Xie 2003) and data by Cabri et al. (2003), who reported high concentrations of Pd (up to 16,000 ppb) from chalcopyrite from Norilsk. The significant positive correlation between Cu and Pd and Rh and the similar behavior of these metals during magmatic fractionation (Fig. 4a, b) might indicate that these metals partitioned into the magmatic volatile phase.

Our detailed study of the core no. 69RD (Roman Ruins) revealed that Pd, Rh and Cu concentrations generally decrease down hole, similar to Au, while Pt and Ir values show a reverse trend (Fig. 3a–f). Local remobilization of Au and Pd during metamorphism and late hydrothermal alteration were, according to Pan and Xie (2001), responsible for the extreme Pd, Rh and Au enrichment in chalcopyrite-rich samples from several ancient VMS deposits. Moss et al. (2001) suggested a dual mechanism for the gold enrichment in the eastern part of the Manus basin including leaching of gold from Au-enriched seafloor rocks and additional input of Au through magmatic volatiles. A decrease in Au concentrations with depth in some cores from Roman Ruins together with low Au contents in the reworked nodular chalcopyrite-pyrite-anhydrite breccias at Roman Ruins indicate that the complex hydrothermal activity at the PACMANUS site may have resulted in zone refining of Au enriching the surface sulfides (Petersen et al. 2003). Similar mechanisms could be suggested for the PGE enrichment at the Satanic Mills and Roman Ruins vent sites.

In the eastern Manus basin, possible sources of PGEs in the hydrothermal fluids include felsic volcanic rocks, basaltic andesite to basalt and direct magmatic contributions. An average value of 4 ppb Pd, 6 ppb Pt and 0.2 ppb Ir ($\text{Pd}/\text{Pt}_{\text{avg}} = 0.7$, $\text{Pd}/\text{Ir}_{\text{avg}} = 20$) was calculated for rift-related felsic volcanic rocks (closest type of rocks with available PGE analyses) based on data by Borg

et al. (1988) and Barnes et al. (1988). In the absence of PGE data from the basaltic substrate from the eastern Manus basin, PGE data for global MORB has been used as one possible endmember. MORB contains on average 0.46 ppb Pd, 0.41 ppb Pt, 0.008 ppb Rh and 0.03 ppb Ir with ratios of $Pd/Pt_{avg}=1.1$ and $Pd/Ir_{avg}=15$ (Crocket 2002). Based on the comparison of Pd/Pt and Pd/Ir ratios, it is apparent that relative to the felsic or basaltic (MORB) source, Cu-rich hydrothermal sulfides at Satanic Mills are richer in Pd by some 100/65 times over Pt and by some 115/150 times over Ir, respectively. At Roman Ruins, Cu-rich hydrothermal sulfides show Pd/Pt-ratios that are six times higher than felsic source rocks and four times higher than MORB. Pd is enriched by a factor of 3 relative to a felsic or MORB source than Ir. It is difficult to estimate whether these fractionations reflect the situation in the original source rocks or occurred during the ascent of hydrothermal fluids and/or at the site of sulfide precipitation or even resulted from mixing with magmatic fluids. Based on our data, it seems likely that the overall lower PGE content at Roman Ruins and the distribution patterns resulted from conventional massive sulfide formation with negligible (if any) magmatic input, while at Satanic Mills, the higher PGE contents and the chondrite-normalized patterns may be the result of a pronounced magmatic volatile input into the convecting hydrothermal system.

The physico-chemical conditions of seafloor hydrothermal vent fluids have been well studied, and it is generally accepted that such fluids are reducing (near pyrite-pyrrhotite-magnetite buffer), slightly acidic ($pH=3-5$), with salinities within a factor of 0.2–2 times seawater, and temperatures immediately prior to exhalation in the range of 300–400°C; thus, bisulfide complexes rather than chloride/hydroxide complexes are most likely responsible for transporting Pt and Pd in such fluids (Wood 2002). Wood et al. (1992) and Pan and Wood (1994) reported that the relative Pt solubility in seafloor hydrothermal fluids is greater than or nearly equal to that of Pd over a wide range of temperatures, irrespective of the complexing agent. In our Cu-rich samples from both vent sites, Pt is depleted compared to Pd despite comparable concentrations in both the suggested source rocks at PACMANUS (felsic volcanic rocks and basalt). If Pt and Pd minerals are different in either the source rocks or at the depositional site, this could result in Pt:Pd concentration ratios different from those predicted on the basis of experimental solubility data (Wood 2002). One possible explanation might also be that seafloor hydrothermal fluids at PACMANUS became diluted after mixing with seawater and that this situation might have resulted in the precipitation of Pd and Rh together with chalcopyrite at higher temperatures ($>300^{\circ}C$), which is compatible with the down hole measurements at Roman Ruins obtained during Ocean Drilling Program Leg 193 (Hole 1189; Binns et al. 2002). It seems possible that Pt and Ir stayed in the solution until venting at the seafloor and were preferentially

taken up by ferromanganese minerals occurring in the vicinity of the hydrothermal vent sites. This would, for example, be in agreement with Koide et al. (1991), who reported anomalous Pt (average 274 ppb) and Ir (average 2.6 ppb) but almost negligible Pd (average 1 ppb) concentrations in ferromanganese minerals from a number of marine locations. This process, however, needs to be proved/disproved by further study of such samples (to our knowledge no PGE data are available from these Mn–Fe samples from the eastern part of the Manus Basin).

Pan and Xie (2001) studied the distribution of PGE and Au in selected ore samples from four VMS districts and showed that chalcopyrite-rich samples associated with mafic-ultramafic rocks from the Besshi deposit (Japan), the Geco deposit at Manitouwadge (Canada) and the Outokumpu deposit (Finland) locally have elevated contents of Pd (up to 1,800 ppb), Rh (up to 800 ppb) and Au (up to 14,000 ppb). These Pd and Rh values are well comparable with their concentrations in sulfide ore of the Langmuir deposit near Timmins, Ontario, Canada, an Archaean komatiite-related Ni–Cu deposit (Naldrett 1989). Conversely, no significant PGE enrichment was reported from sediments accumulating directly under the ultramafic-hosted Rainbow hydrothermal plume on the Mid-Atlantic Ridge (Cave et al. 2003). Our results from recent vent sites in the eastern Manus basin are consistent with the assumption of Wood (2002) that seafloor hydrothermal vent fluids are capable of transporting significant quantities of PGE and indicate that elevated PGE values (especially Pd and Rh) in Cu-ores of some ancient VMS deposits may be explained by magmatic contributions to a conventional convective hydrothermal system with perhaps subsequent hydrothermal alteration and metamorphic processes.

Conclusions

The study of the distribution of PGE in sulfide samples from Roman Ruins and Satanic Mills, two hydrothermal vent sites associated with felsic volcanic rocks in the eastern part of the Manus back-arc basin, Papua New Guinea, can be summarized as follows:

1. Zn-rich sulfide samples from Roman Ruins show low average PGE values while Cu-rich samples from the same site are characterized by higher average PGE and Au values. At Satanic Mills, Cu-rich samples from active and inactive chimneys have anomalously high Pd and Rh concentrations (maximum of 356 ppb Pd and 145 ppb Rh), while Zn-rich samples revealed rather low PGE values.
2. A significant positive correlation was established between Cu and Pd and Rh in Cu-rich samples at both vent sites. No other significant relationship was found between PGE, Au and base metals (Cu and Zn). At Roman Ruins, the content of Pd and Rh increases

with depth while Pt and Ir values show opposite trends. At Satanic Mills, a magmatic input into a convecting hydrothermal system may be indicated by the chondrite normalized patterns (strong Rh and Pd enrichment similar to some mafic-hosted VMS deposits) and the Pd and Rh enrichment over Pt and Ir when compared to the possible source rocks (felsic volcanic rock and basalts).

3. We suggest that Pd and Rh fractionated together with Cu, Fe and S at the site of mixing with seawater, forming chalcopyrite rich in Pd and Rh while Pt and Ir might be lost to the water column and preferentially trapped by associated ferromanganese minerals in the vicinity.

Acknowledgements This research was supported by Czech Geological Survey Grant 3240. This work is a contribution to the IGCP Project 502 "Global Comparison of Volcanic-hosted Massive Sulphide Districts". Cruise SO166 was funded by the German Federal Ministry for Education and Research through a grant to PMH (BMBF Grant 03G0166A). Additional support through the Leibniz Program of the German Research Foundation is also acknowledged. Special thanks to Alister Skinner and his professional Rockdrill team of the British Geological Survey for getting the sample off the seafloor. Critical comments from B. Lehmann on an early version of the MS were very useful. The current version of the manuscript benefited from a review by A. Koschinsky.

References

- Anders E, Grevesse N (1989) Abundances of the elements: meteoritic and solar. *Geochim Cosmochim Acta* 53:197–214
- Bach W, Roberts S, Vanko DA, Binns RA, Zeats CJ, Craddock PR, Humphris SE (2003) Controls of fluid chemistry and complexation on rare-earth element contents of anhydrite from the PACMANUS subseafloor hydrothermal system, Manus Basin, Papua New Guinea. *Miner Depos* 38:916–935
- Barnes SJ, Boyd R, Korneliussen A, Nillson LP, Often M, Pedersen RB, Robins B (1988) The use of mantle normalization and metal ratios in discriminating between the effects of partial melting, crystal fractionation and sulphide segregation on platinum-group elements, gold, nickel and copper: examples from Norway. In: Prichard HM, Potts PJ, Bowles JFW, Cribb SJ (eds) *Geo-Platinum*. Elsevier, Amsterdam, pp 113–143
- Barrie CT, Hannington MD (1999) Classification of volcanic-associated massive sulfide deposits based on host-rock composition. In: Barrie CT, Hannington MD (eds) *Volcanic-associated massive sulfide deposits: processes and examples in modern and ancient settings*. Reviews in Economic Geology, vol 8. Society of Economic Geologists, pp 1–11
- Barriga F, Binns R, Baldauf J, Miller DJ (2000) Anatomy of an active, felsic-hosted hydrothermal system, eastern Manus basin. Leg 193 Scientific Prospectus, Ocean Drilling Program, Texas A&M University, College Station, p 60
- Binns RA, Barriga FJAS, Miller DJ (2002) Leg 193 summary. In: Proceedings of the Ocean Drilling Program, Initial Reports, 193, College Station, pp 1–84
- Borg G, Tredoux M, Maiden KJ, Sellschop JPF, Wayward OFD (1988) PGE and Au distribution in rift-related volcanics, sediments and stratabound Cu/Ag ores of Middle Proterozoic age in central SWA/Namibia. In: Prichard HM, Potts PJ, Bowles JFW, Cribb SJ (eds) *Geo-Platinum*. Elsevier, Amsterdam, pp 303–317
- Cabri LJ, Sylvester PJ, Tubrett MN, Pereogedova A, Laflamme JHG (2003) Comparison of LAM-ICP-MS and micro-PIXE results for palladium and rhodium in selected samples of Noril'sk and Talnakh sulfides. *Can Mineral* 41:321–329
- Cave RR, Ravizza GE, German CR, Thomson J, Nesbitt RW (2003) Deposition of osmium and other platinum-group elements beneath the ultramafic-hosted Rainbow hydrothermal plume. *Earth Planet Sci Lett* 210:65–70
- Clarke AL, Humprey P, Johnson CJ, Pak DK (1985) Cobalt-rich manganese crust potential. OCS Study MMS 85–0006, Mineral Management Service, U.S. Department of Interior, pp 23
- Crocket JH (1989) PGE in mid-ocean volcanic exhalites; a major fractionation of PGE from gold. In: IAGOD 5th international platinum symposium, Abstracts, Bull Geol Soc Finland, 61, part 1, p 47
- Crocket JH (1990) Noble metals in seafloor hydrothermal mineralization from the Juan de Fuca and mid-Atlantic ridges: a fractionation of gold from platinum metals in hydrothermal fluids. *Can Mineral* 28:639–648
- Crocket JH (2002) Platinum-group element geochemistry of mafic and ultramafic rocks In: Cabri LJ (ed) *The geology, geochemistry, mineralogy and mineral beneficiation of platinum-group elements*. CIM Spec, vol 54, pp177–210
- Crocket JH, MacDougall JD, Harris RC (1973) Gold, palladium and iridium in marine sediments. *Geochim Cosmochim Acta* 37:2547–2556
- Douville E, Bienvenu P, Charlou JL, Donval JP, Fouquet Y, Appriou P, Gamo T (1999) Yttrium and rare earth elements in fluids from various deep-sea hydrothermal systems. *Geochim Cosmochim Acta* 63:627–643
- Gemmell JB, Binns RA, Parr JM (1996) Comparison of sulfur isotope values between modern back-arc and mid-ocean ridge seafloor hydrothermal systems. *EOS Tr Am Geophys Un* 77:W117
- Goldberg ED, Koide M, Schmitt RA, Schmitt RH (1963) Rare earth distribution in the marine environment. *J Geophys Res* 68:4209–4217
- Goldberg ED, Koide M, Yang JS, Bertine KK (1988) Comparative marine chemistries of the platinum group metals and their periodic table neighbors. In: Kramer JR, Allen HE (eds) *Metal speciation*. Lewis, London, pp 201–217
- Halbach P, Prause B, Koch K, Westholt M (1990) Platinum and palladium in Co-rich ferromanganese crust deposits. *Mar Min* 9:117–126
- Haynes BW, Law SL, Barron DC, Kramer GW, Maeda R, Magyar MJ (1985) Pacific manganese nodules: characterization and processing. U.S. Department of Interior, Bureau of Mines, Bulletin 679, p 44
- Hein JR, Schultz LM, Gein LM (1990a) Central Pacific cobalt-rich ferromanganese crusts: historical perspective and regional variability. In: Keating BH, Bolton BR (eds) *Geology and offshore mineral resources of the Central Pacific Basin*. Circ-Pac Council Energy Mineral Resource, Houston, Earth Sci Ser, vol 15, pp 261–283
- Hein JR, Schultz MS, Kang JK (1990b) Insular and submarine ferromanganese mineralization of the Tonga-Lau region. *Mar Mineral* 9:305–354
- Herzig PM, Petersen S, Kuhn T, Hannington MD, Gemmell JB, Skinner AC, Shipboard Scientific Party (2003) Shallow drilling of seafloor hydrothermal systems using R/V Sonne and the BGS Rockdrill: Conical Seamount (New Ireland Fore-Arc) and PACMANUS (Eastern Manus Basin), Papua New Guinea. *InterRidge News* 12:22–25
- Hodge VF, Stallard M, Koide M, Goldberg ED (1985) Platinum and palladium anomaly in the marine environment. *Earth Planet Sci Lett* 72:158–162
- Hodge VF, Stallard M, Koide M, Goldberg ED (1986) Determination of platinum and iridium in marine waters, sediments and organisms. *Anal Chem* 58:616–620
- Koide M, Goldberg ED, Niemeyer S, Gerlach D, Hodge V, Bertine KK, Padova A (1991) Osmium in marine sediments. *Geochim Cosmochim Acta* 55:1641–1648
- Mannheim FT (1986) Marine cobalt resources. *Science* 232:600–608
- McMurtry GM, Vonderhaar DL, Mahoney JJ, Gregson D, Tyne C (1989) Platinum-group metals in ferromanganese crusts from

- acific seamount. In: IAGOG 5th international platinum symposium, Abstracts, Bull Geol Soc Finland, vol 61, pp 47–48
- Moss R, Scott SD, Binns RA (2001) Gold content of Eastern Manus Basin volcanic rocks: implications for enrichment in associated hydrothermal precipitates. *Econ Geol* 96:91–107
- Naldrett AJ (1989) Platinum-group element deposits. In: Cabri LJ (ed) *Platinum-group elements: mineralogy, geology recovery*. CIM Spec, vol 23, pp197–231
- Pan P, Wood SA (1994) Solubility of Pt and Pd sulfides and Au metal in aqueous bisulfide solutions. II. Results at 200° to 350°C and saturated vapor pressure. *Miner Depos* 29:373–390
- Pan Y, Xie Q (2001) Extreme fractionation of platinum group elements in volcanogenic massive sulfide deposits. *Econ Geol* 96:645–651
- Paulick H, Herzig P (2003) Volcanic facies controls on mass transfer at the active, dacite-hosted PACMANUS hydrothermal system, Manus basin, Papua New Guinea (Ocean Drilling Program Leg 193). In: Eliopoulos D et al (eds) *Mineral exploration and sustainable development*. Millpress, Rotterdam, pp 167–170
- Petersen S, Herzig P, Hannington M, Gemmel B (2003) Gold-rich massive sulfides from the interior of the felsic-hosted PACMANUS massive sulfide deposit, Eastern Manus Basin (PNG). In: Eliopoulos D et al (eds) *Mineral exploration and sustainable development*. Millpress, Rotterdam, pp 171–174
- Stuben D, Glasby GP, Eckhardt JD, Berner Z, Mountain BW, Usui A (1999) Enrichments of platinum-group elements in hydrogenous, diagenetic and hydrothermal marine manganese and iron deposits. *Explor Min Geol* 8:233–250
- Waters JC, Binns RA, Naka J (1996) Morphology of submarine felsic volcanic rocks on Paul Ridge, eastern Manus basin, Papua New Guinea (abs) American Geophysical Union, Western Pacific Geophysics Meeting, Brisbane. Abstract Suppl EOS Tr Am Geophys Un 77:W120
- Wood SA (2002) The aqueous geochemistry of the platinum-group elements with applications to ore deposits. In: Cabri LJ (ed) *The geology, geochemistry, mineralogy and mineral beneficiation of platinum-group elements*. CIM Spec, vol 54, pp 211–249
- Wood SA, Mountain BW, Pan P (1992) The aqueous geochemistry of platinum, palladium and gold: recent experimental constraints and a re-evaluation of theoretical predictions. *Can Mineral* 30:955–982
- Yang K, Scott SD (1996) Possible contribution of a metal-rich magmatic fluid to a sea-floor hydrothermal system. *Nature* 383:420–423

International Research: **Back Arc Basins: Halbach *et al.*, cont...**

The conditions required for such an environment (propylitic) are produced by boiling fluids in the hydrothermal conduits, because the loss of CO₂, H₂S, and H₂O causes an increase of the pH in the residual fluid as well as a decreasing temperature.


The second type of alteration essentially consists of illite and SiO₂ phases (amorphous silica and quartz), some minor amounts of adularia, and pyrite impregnations. This mineralogy indicates a total breakdown of plagioclase and higher alteration temperatures. Thus, these alterites derive from sites more proximal to the epithermal ore-bearing veins. The fact that even more intensely mineralized ore samples existed in the Abangkomba area is documented by the gossan samples from the southern slope of the Kombaridge. These rocks represent completely oxidized sulphides and are highly ferruginous (30% Fe₂O₃). Since the samples were dredged from the surface of the Abangkomba, we expect less oxidized sulphidic min-

eralisations to exist in close vicinity to the place from which the gossan samples were taken.

Acknowledgements

The Bandamin research is part of the German-Indonesian geomarine cooperation and is funded by the German Federal Ministry of Education and Research (BMBF) and the Indonesian Ministry of Marine Affairs and Fisheries (DKP). We are thankful for this support. We also thank the staff and crew of the Indonesian RV BARUNA JAYA IV for their logistics and practical assistance during the cruise.

References

- Giggenbach, W.F. Magma degassing and mineral deposition in hydrothermal systems along convergent plate boundaries. *Econ. Geol.* 87:1927-1944, 1992.
- Halbach, P., B. Pracejus, E. Rahders, M. Karg, S. Sämann, B. Melchert, J. Post, J. Dühn, and M. Halbach. Recent Submarine Hydrothermalism in the Volcanically Active Western Banda-Island-Arc, East Flores Sea (Indonesia), BANDAMINI Cruise Report, FU-Berlin Dep. Rohstoff- u. Umweltgeologie, 2002.
- Hamilton, W. Tectonics of the Indonesian Region. U.S. Geological Survey professional paper, 1078, U.S. Geological Survey, Washington, 345 pp., 1979.
- McCaffrey, R. Active tectonics in the eastern Sunda and Banda arcs. *J. Geophys. Res.* 93:163-182, 1988.
- Silver, E.A., D. Reed, and R. McCaffrey. Back arc thrusting in the eastern Sunda arc, Indonesia: a consequence of arc-continent collision. *J. Geophys. Res.* 88:7429-7448, 1983.
- Van Bergen, M.J., P.Z. Vroon, J.C. Varekamp, and R.P.E. Poorter. The origin of the potassic rock suite from Batu Tara volcano (East Sunda Arc, Indonesia). *Lithos* 28:261-282, 1992.
- White, N.C. and J.W. Hedenquist. Epithermal Gold Deposits: Styles, characteristics and exploration. *SEG Newsletter* 23:8-13, 1995. 

Shallow drilling of seafloor hydrothermal systems using *R/V Sonne* and the BGS Rockdrill: Conical Seamount (New Ireland Fore-Arc) and Pacmanus (Eastern Manus Basin), Papua New Guinea

P. M. Herzig¹, S. Petersen¹, T. Kuhn¹, M. D. Hannington², J. B. Gemmell³, A. C. Skinner⁴
and SO-166 Shipboard Scientific and Technical Party

¹Leibniz Laboratory for Applied Marine Research, Freiberg University of Mining and Technology, Germany

²Geological Survey of Canada, Ottawa, Canada

³Center of Ore Deposit Research, University of Tasmania, Hobart, Tasmania, Australia

⁴British Geological Survey, Edinburgh, United Kingdom

Abstract

In September-October 2002, shallow seafloor drilling using the portable 5 m Rockdrill of the British Geological Survey and the German *R/V Sonne* revealed critical information on the sub-surface nature of two distinct hydrothermal systems in the New Ireland fore-arc and the Manus Basin of Papua New Guinea. Drilling of 39 holes at the summit plateau of Conical Seamount close to Lihir Island has indicated that previously

discovered epithermal-style gold mineralisation reaches to a depth of at least 4.5 m below seafloor with gold concentrations of up to 14.2 g/t Au. This discovery significantly extends the known surface extent of gold mineralisation (up to 230 g/t Au) at Conical Seamount. Almost 9 m of spectacularly textured massive sulphide core recovered from 10 holes drilled in only two days in the active Roman Ruins black smoker site of the Pacmanus area proves,

that massive sulphides extend to a depth of at least 5 m below seafloor. Spectacular concentrations of gold were found in several core sections including 0.5 m @ 28 g/t Au, 0.35 m @ 30 g/t Au, and 0.20 m @ 57 g/t Au, confirming the gold-rich nature of this particular back-arc deposit. Shallow seafloor drilling is a fast and cost efficient method that bridges the gap between surface sampling and deep (ODP) drilling and undoubtedly will become a standard

International Research: **Back Arc Basins: Herzig *et al.*, cont...**

practice in the future study of seafloor hydrothermal systems and massive sulphide deposits.

Introduction

Our current knowledge of seafloor hydrothermal systems and massive sulphide deposits is largely based on surface sampling by dredges, TV-guided grabs, submersibles and ROVs, and deep drilling by the Ocean Drilling Program (ODP). In the past decade, ODP has drilled a total of three different hydrothermal sites including Middle Valley at the Juan de Fuca Ridge (Zierenberg *et al.*, 1998), the active TAG hydrothermal mound at the Mid-Atlantic Ridge (Herzig *et al.*, 1998a, Humphris *et al.*, 1995), and the Pacmanus area in the eastern Manus Basin (Binns *et al.*, 2002). Due to the need to set casing for deep hard rock drilling, coring of the immediate subsurface is usually not possible during ODP operations, thus leaving a

significant gap between surface sampling and deep drilling. We have, for the first time, deployed the British Geological Survey (BGS) Rock-drill from the German *R/V Sonne* and successfully demonstrated that shallow seafloor drilling with a lander-type system is feasible from a non-drilling research vessel and significantly extends our understanding of the 3rd dimension of seafloor hydrothermal systems and massive sulphide deposits. Here, we present first results of a recent drilling and coring program at Conical Seamount (New Ireland fore-arc) and Pacmanus/Roman Ruins (Eastern Manus Basin).

Geological Setting of Drill Sites

Conical Seamount (Fig. 1) is one of several young volcanic cones discovered in the area south of Lihir Island in the New Ireland fore-arc in 1994 (Herzig *et al.*, 1994). It has a basal diameter of 2.5 km and rises

about 600 m above the surrounding seafloor (1.650 km water depth) with a well-developed summit plateau (150x200m) at 1.050 km water depth. First indications of gold-rich epithermal-style vein mineralisation at the summit plateau of Conical Seamount were discovered in 1994 (Herzig *et al.*, 1995) and confirmed 1998 (Herzig *et al.*, 1998b, 1999). Samples collected from the summit area include locally intense clay-silica alteration immediately adjacent to an eruptive fissure. Gold-rich polymetallic vein mineralisation occurs in an outer zone of this area while arsenic sulphides together with abundant amorphous silica are found at the margins. More than 1.200 kg of mineralized rock were recovered in 1998, consisting of stockworks and disseminated sulphides with gold concentrations locally reaching up to 230 g/t (avg. 26 g/t, n=40, Herzig *et al.*, 1999, Petersen *et al.*, 2002). The material recovered from Conical Seamount is similar to the ore currently being mined from the giant Ladolam epithermal gold deposit in the crater of Luise Volcano on Lihir Island, and both sites may be linked by the same magmatic system. For the marine environment, Conical Seamount represents a new type of mineralisation that is different from black smoker-type deposits and has been formed through contributions of magmatic fluids and metals (Petersen *et al.*, 2002). This has important implications for the understanding of epithermal-style ore mineralisation in submarine arcs as well as on the continents.

The *Pacmanus hydrothermal field* (Fig. 1) in the Eastern Manus back-arc basin is situated on the crest of Pual Ridge, an elongated feature composed of dacite with subordinate basaltic andesite and rhyodacite that stands 500-700 m above the surrounding basin floor (Binns *et al.*, 2002). Five principal areas of hydrothermal activity have been delineated at Pacmanus including Roman Ruins, which consists of

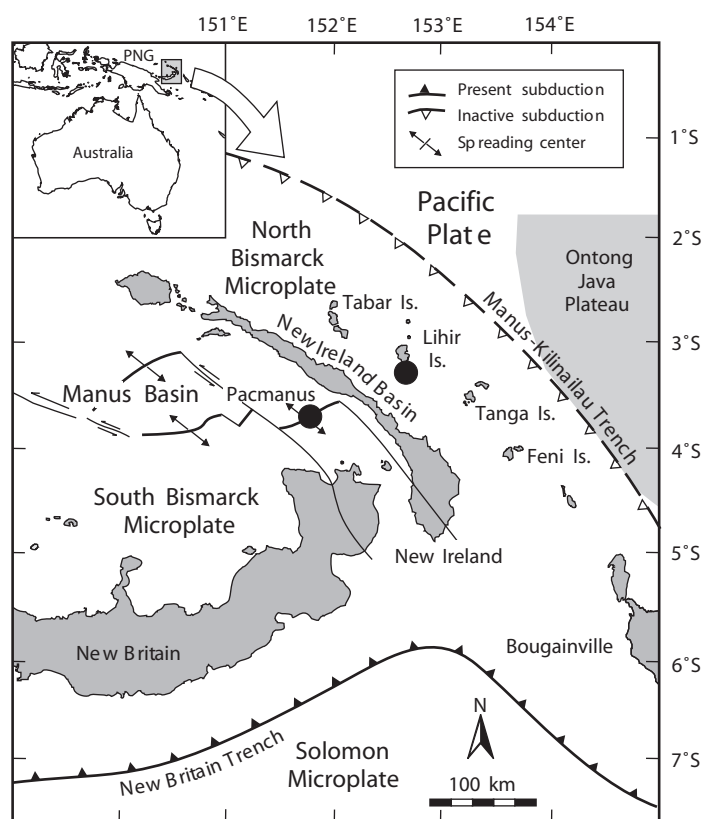


Figure 1. (Rock) drill sites (solid circles) at Conical Seamount (south of Lihir Island) and Pacmanus/Roman Ruins (Eastern Manus Basin). Cruise SO-166 of *R/V Sonne*.

International Research: Back Arc Basins: Herzig *et al.*, cont...

active and inactive black smoker chimneys with exit temperatures of up to 276°C (Binns *et al.*, 2002). The Pacmanus area was subject to ODP drilling during Leg 193; however, the massive sulphides were not cored due to casing requirements for deep drilling (Binns *et al.*, 2002).

Results

Out of 41 attempts, 39 holes were drilled in various areas of the summit plateau of Conical Seamount with only two core barrels returning without recovery (Table 1). The total penetration achieved was more than 91 m with individual penetration varying between 0.95 and 5.00 m (avg. 2.3 m). With an average recovery of 31%, almost 21 m of core were drilled with individual core length of up to 1.5 m (avg. 0.51 m).

Drilling at Conical Seamount has confirmed the sub-seafloor extent of surface gold mineralisation and associated epithermal-style alteration to a depth of at least 4.5 m below the seafloor and further supports analogies to the giant Ladolam epithermal gold deposit on Lihir Island. Drill-core samples of clay-silica alteration contain gold grades up to 14.2 g/t Au (30 g fire assay: Lihir Gold Ltd.) and appear to be part of a more extensive gold zone located below a carapace of relatively fresh ankaramite and trachybasalt. These samples contain a complex mineralogy including realgar, orpiment,

galena, sphalerite, some chalcopyrite and pyrite, together with amorphous silica, and possibly cinnabar. In addition to high concentrations of gold, shipboard XRF analyses indicate that the gold-rich samples contain high values of Pb (up to 2.6 wt.%), As (up to 9.250 ppm), and Sb (up to 954 ppm), and low contents of Cu (up to 0.3 wt.%) and Zn (up to 5.2 wt.%) which is a characteristic feature of a magmatic-hydrothermal style of mineralisation.

Drilling of 10 holes in only two days at Roman Ruins (Pacmanus site) achieved a total penetration of almost 36 m. The average penetration was 3.6 m (2.1-5.0 m) with a recovery of about 31 % (9-65 %), resulting in about 11 m of core of which almost 9 m are spectacularly textured massive sulphides. The longest sulphide cores taken measure 2.2 m (penetration 4.9 m), 1.9 m (penetration 5.0 m), and 1.4 m (penetration 2.8 m).

The sulphide-bearing cores are usually dominated by light brown to dark brown sphalerite with varying proportions of barite, pyrite and chalcopyrite. Galena and bluish sulphosalts are visible, but occur only as a minor to trace component in the sulphides. Anhydrite, amorphous silica and variably altered dacite fragments occur together with the sulphides. The textures, in most cases, resemble those of sulphides recovered from the surface of the Pacmanus field (Moss and Scott, 2001). Ribbon banded sphalerite, as observed in “beehive” smokers at various other seafloor hydrothermal sites, is common, as are relics of individual chalcopyrite-lined chimney orifices.

Drill site 60RD recovered a sphalerite±chalcopyrite and barite assemblage underlain by a nodular breccia of rounded chalcopyrite+pyrite clasts set in a matrix of anhydrite. This nodular texture

Table 1. Drilling statistics for sites Conical Seamount (New Ireland fore-arc) and Pacmanus/Roman Ruins (Eastern Manus Basin)

Parameter	Conical Smt	Roman Ruins
Number of holes	41	10
Technical failures	2	0
Holes without recovery	2	0
Total penetration	91.07 m	35.55 m
Individual penetration	0.95-5.00 m	2.06-5.00 m
Average penetration	2.34 m	3.56 m
Total core length	20.76 m	11.07 m*
Individual core length	0-1.50 m	0.35-2.20 m
Average core length	0.51 m	1.12 m
Average recovery	31%**	31%
Individual recovery	0-100%	9-65%

*8.87 m of massive sulphide

**based on 37 holes drilled with recovery



Figure 2. BGS Rockdrill during drilling operations with *R/V Sonne* in the New Ireland fore-arc and the Manus back-arc.

International Research: **Back Arc Basins:** Herzig *et al.*, cont...

Figure 3. Handling of core during Cruise SO-166 at Conical Seamount.

strongly resembles cores from the central part of the TAG hydrothermal field (Humphris *et al.*, 1995; Herzig *et al.*, 1998a). The presence of abundant anhydrite within this core is indicative of seawater penetrating into the massive sulphide mound and mixing with the hydrothermal fluid and/or conductively cooling in the subsurface. The nodular appearance of the chalcopyrite+pyrite fragments suggests that massive sulphides are reworked likely due to the formation and dissolution of anhydrite. This observation is supported by several cores that contain layers of fine-grained, clastic chalcopyrite+pyrite sand.

A 20 cm thick layer of massive, dense chalcopyrite separating layers of porous, massive sphalerite has been sampled in the upper part of one hole, while other holes contain a similar section where chalcopyrite is intergrown with black sphalerite. The complex intergrowths observed throughout the core sections imply a multi-staged hydrothermal evolution of the deposit.

Four of the holes drilled at Roman Ruins penetrated close to 5 m into the massive sulphide mound. Out of these, two holes (61RD and 69RD) ended in weakly to intensely altered dacite possibly indicating

that sulphide formation here is limited to a thin veneer above the underlying altered dacite. Core 69RD recovered 1.8 m (core length 2.2 m) of massive sulphide overlying strongly clay-silica altered and sulphide veined dacite that mark the onset of the stockwork zone.

Preliminary analyses of quarter core sections (varying in length from 10 to 50 cm) indicate high base and precious metal contents averaging close to 12 g/t Au, 170 g/t Ag, 21 wt.% Zn, 5 wt.% Cu, and 1 wt.% Pb. The most impressive grades come from hole 65RD which returned 0.4 m @ 35 g/t Au, 240 g/t Ag, 7.1 wt.% Cu, 26.9 wt.% Zn, and 0.6 wt.% Pb, including a section of 0.2 m with 57.2 g/t Au. Another exceptional result came from hole 66RD which returned 0.8 m @ 19.5 g/t Au, 190 g/t Ag, 7.7 wt.% Cu, 25.2 wt.% Zn, and 0.2 wt.% Pb. The longest core (69RD, penetration: 4.9 m) recovered 2.2 m @ 11.3 g/t Au, 160 g/t Ag, 2.4 wt.% Cu, 26.0 wt.% Zn, and 0.9 wt.% Pb.

Gold enrichment throughout the cores is related to sphalerite-rich sections. The highest grades occur in dark brown to black sphalerite that is associated with abundant chalcopyrite and was presumably deposited at higher temperatures. However, core sections that contain ribbon-banded, light brown sphaler-

ite are also enriched in gold. Low precious metal concentrations, despite high concentrations of Zn and Cu, have been observed in the lower parts of some cores, possibly indicating that zone refining is responsible for some of the precious metal enrichment observed at Pacmanus. This is consistent with the low gold contents in the reworked nodular chalcopyrite+pyrite+anhydrite breccias.

TV-guided grab sampling that accompanied the drilling program recovered massive sulphides as well as active and inactive chimneys from the Satanic Mills and Roman Ruins sites. Some samples from the mound surface at Roman Ruins show a knife-edge contact between least altered, black dacitic hyaloclastite set in a matrix of porous sphalerite and intensely clay-altered white dacite fragments cemented by chalcopyrite, pyrite and sphalerite. This suggests the presence of an alteration or high temperature front just below the seafloor. A strongly siliceous, black to dark brown layer occurs in several samples suggesting the presence of a siliceous cap in certain areas.

Conclusions

The successful drilling and coring operations with the BGS Rockdrill and *R/V Sonne* indicate that shallow seafloor drilling is filling the sampling gap between the seafloor and the deeper parts of hydrothermal systems. Drilling at Conical Seamount and Roman Ruins has provided information not previously available and attests to significant sub-surface mineralisation in both areas. Results obtained by drilling at the summit plateau of Conical Seamount now conclusively indicate that deeper drilling is required (and justified) to fully assess the gold resource of this deposit. At Roman Ruins, drilling with the BGS Rockdrill has not only proven the existence of massive sulphides in the sub-seafloor but also demonstrated their gold-rich nature. Shal-

International Research: Back Arc Basins: Herzig *et al.*, cont...

Figure 4. Drill core recovered with the BGS Rockdrill from the Pacmanus hydrothermal field.

low seafloor drilling will likely become a future standard practice in the evaluation of seafloor hydrothermal systems and portable drill rigs such as the Rockdrill may even advance to mission specific platform status within the new phase of ocean drilling (IODP).

Acknowledgements

Cruise SO-166 was funded by the German Federal Ministry for Education and Research through a grant to PMH. Additional funding through the Leibniz Program of the German Research Association is gratefully acknowledged. We thank Captain Martin Kull and his crew for their support during the entire drilling program, and Neil Campbell, Eileen Gillespie and David Smith for their professional handling of the Rockdrill.

References

Binns, R. A., F. Barriga, and D. J. Miller. Leg 193 summary. *Proceedings of*

the Ocean Drilling Program, Initial Reports 193, College Station, TX: 1-84, 2002.

Herzig, P.M., M. D. Hannington, B. McInnes, P. Stoffers, H. Villinger, R. Seifert, R. Binns, T. Liebe, and Scientific Party of the R/V Sonne cruise SO-94. Submarine volcanism and hydrothermal venting studied in Papua, New Guinea. *Trans. Am. Geophys. U., Eos* 75:513-516, 1994.

Herzig, P.M. and M. D. Hannington. Hydrothermal activity, vent fauna, and submarine gold mineralization at alkaline fore-arc seamounts near Lihir Island, Papua New Guinea. *Proceedings Pacific Rim Congress 1995*, Australasian Institute of Mining and Metallurgy, 279-284, 1995.

Herzig, P. M., S. E. Humphris, D. J. Miller, and R. A. Zierenberg, eds. *Proceedings of the Ocean Drilling Program, Scientific Results, Leg 158*. College Station, TX: 1-450, 1998a.

Herzig, P.M., M. D. Hannington, P.


Stoffers, and Shipboard Scientific Party. Petrology, gold mineralization and biological communities at shallow submarine volcanoes of the New Ireland Fore-Arc (Papua New Guinea). *InterRidge* 7:34-38, 1998b.

Herzig, P.M., S. Petersen, and M. D. Hannington. Epithermal-type gold mineralization at Conical seamount: a shallow submarine volcano south of Lihir Island, Papua New Guinea. In: Stanley *et al.* (eds), *Proceedings SGA-IAGOD Meeting London*, 1999.

Humphris, S. E., P. M. Herzig, D. J. Miller, J. C. Alt, K. Becker, D. Brown, G. Brüggemann, H. Chiba, Y. Fouquet, J. B. Gemmill, G. Guerin, M. D. Hannington, N. G. Holm, J. J. Honnorez, G. J. Itturino, R. Knott, R. Ludwig, K. Nakamura, S. Petersen, A.-L. Reysenbach, P. A. Rona, S. Smith, A. A. Sturz, M. K. Tivey, and X. Zhao. The internal structure of an active sea-floor massive sulphide deposit. *Nature* 377:713-716, 1995.

Moss, R. and S. D. Scott. Geochemistry and mineralogy of gold-rich hydrothermal precipitates from the Eastern Manus Basin, Papua New Guinea. *Canadian Mineralogist* 39:957-978, 2001.

Petersen, S., P. M. Herzig, M. D. Hannington, I. R. Jonasson, and A. Arribas. Submarine vein-type gold mineralization near Lihir island, New Ireland fore-arc, Papua New Guinea. *Econ. Geol.* 97:1795-1813, 2002.

Zierenberg, R.A., Y. Fouquet, D. J. Miller, J. M. Bahr, P. A. Baker, T. Bjerkgaard, C. A. Brunner, R. C. Duckworth, R. Gable, J. Gieskes, W. D. Goodfellow, H. M. Gröschel-Becker, G. Guerin, J. Ishibashi, G. Iturrino, R. H. James, K. S. Lackschewitz, L. L. Marquez, P. Nehlig, J. M. Peter, C. A. Rigsby, P. Schultheiss, W. C. Shanks III, B. R. T. Simoneit, M. Summit, D. A. H. Teagle, M. Urbat, and G. G. Zuffa. The deep structure of a sea-floor hydrothermal deposit. *Nature* 392:485-488, 1998. 

Kurzfassungen

GAC-MAC 2005, Halifax, Canada
(Annual Meeting of the Geological Association and the Mineralogical Association of Canada)

LOW-TEMPERATURE HYDROTHERMAL ALTERATION ASSOCIATED WITH
GOLD-RICH MINERALIZATION AT CONICAL SEAMOUNT, PAPUA NEW GUINEA

Thomas Monecke, Mark D. Hannington
Department of Earth Sciences, University of Ottawa, Canada

Sven Petersen, Peter M. Herzig
Leibniz-Institut für Meereswissenschaften, IFM-GEOMAR, Kiel, Germany

Reinhard Kleeberg
Institut für Mineralogie, TU Bergakademie Freiberg, Germany

In 2002, the German research vessel *Sonne* conducted drilling of the shallow-submarine, epithermal-like gold mineralization at Conical Seamount in the New Ireland fore arc of Papua New Guinea, employing a portable hard rock drilling device of the British Geological Survey. Drilling revealed that hydrothermal alteration of the trachybasalt lava is widespread at the summit plateau of the seamount. High-grade gold mineralization is confined to locally occurring veins of dark gray to black, porous amorphous silica with disseminated sulfides. Thin section microscopy as well as qualitative and quantitative XRD analysis have been conducted to determine the nature of hydrothermal alteration away from the mineralized veins. Statistical analysis of the derived quantitative phase abundances showed that three groups of samples can be distinguished. The first group of samples represents least-altered lava that consists of diopside, Ca-rich plagioclase, Na-rich sanidine, biotite, magnetite, and volcanic glass. Texturally unaltered clinopyroxene, plagioclase, and magnetite phenocrysts are abundant. The second group of samples was clearly affected by weak hydrothermal alteration. Pyrite and marcasite are abundant secondary phases. Because pyrite and marcasite frequently form pseudomorphs after primary magnetite, samples of this group contain lower amounts of magnetite when compared to the least-altered equivalents. The third group of samples is typified by the occurrence of substantial amounts of di- and trioctahedral smectite that largely replace volcanic glass. Minor vermiculite is present. Primary magnetite is largely replaced by pyrite and marcasite. These sulfides also form abundant veinlets or aggregates disseminated throughout the groundmass of the altered rocks. Clinopyroxene phenocrysts are partially replaced by fine grained secondary minerals including clay minerals. Based on the stability constraints of the observed alteration minerals, it has to be concluded that the widespread hydrothermal alteration at Conical Seamount was caused by lowtemperature hydrothermal fluids. In particular, the occurrence of smectite implies that the alteration preceded at temperatures below 150 to 200 °C. The hydrothermal fluids were nearneutral in composition because acid-type minerals have not been recognized in the drill core samples investigated. The abundant presence of sulfides and the lack of sulfates and secondary oxide minerals are indicative for a relatively reducing environment of alteration.

Siting of gold and characteristics of gold-bearing massive sulfides from the interior of the felsic-hosted PACMANUS massive sulfide deposit, Eastern Manus basin (PNG)

T. Ihle

Department of Economic Geology and Petrology, Freiberg University of Mining and Technology, Germany

S. Petersen, P.M. Herzig

Leibniz-Laboratory for Marine Sciences, IFM-GEOMAR, Kiel, Germany

M.D. Hannington

Department of Earth Sciences, University of Ottawa, Canada

Abstract. Precious- and base metal-rich massive sulfides from the interior of the active Roman Ruins site (PACMANUS) locally contain abundant native gold in two distinct mineralogical associations: (I) with chalcopyrite-sphalerite dominated mineral assemblages and (II) with sphalerite-barite-amorphous silica-rich mineral assemblages. The silver content is variable and is lower for Cu-Zn-hosted gold (avg. 3.6 wt. % Ag; range from 1.2 to 8.7 wt.% Ag) and higher for Zn-Ba-hosted gold (avg. 11.3 % Ag; range from 8.0 to 16.4 wt.% Ag). The latter is in marked contrast to previously published results for surface samples from PACMANUS that showed only high gold fineness values. The FeS-content of sphalerite associated with native gold is low in the Cu-Zn-rich core section (0.1 to 6.0 mole % FeS; avg. 0.6 mole % FeS), but higher in Zn-Ba-rich mineral assemblages (0.1 to 18.7 mole % FeS; avg. 6.5 mole % FeS) indicating a larger variability in the sulfur activity than previously documented. The combination of the siting of gold at Roman Ruins and the variability of the gold fineness and the Fe-content of associated sphalerite is distinct from most other seafloor hydrothermal systems and indicates that refining of primary gold is not responsible for the enrichment of gold in Zn-rich sulfide assemblages at Roman Ruins.

Keywords. Drilling, PACMANUS, gold-rich VMS, gold-fineness

1 Introduction

Primary gold enrichment in seafloor massive sulfides is common both in deposits in back-arc basins or volcanic arcs, where they are associated with bimodal or felsic volcanic rocks, and in ultramafic-hosted deposits along the Mid-Atlantic Ridge (Herzig et al. 1993; Moss and Scott 2001; Watanabe and Kajimura 1994; Murphy and Meyer 1998). In modern seafloor hydrothermal systems gold enrichment is commonly associated with Zn-rich mineral assemblages (Hannington et al. 1999). Native gold generally shows low Ag-contents and, in addition, the associated sphalerite is largely Fe-poor indicating a high activity of sulfur and oxygen during formation (Hannington et al. 1995). Investigations of surface samples from Satanic Mills at PACMANUS and Susu Knolls, both in the Eastern Manus Basin, documented a Cu-As-rich mineral assemblage hosting native gold (Moss and Scott 2001). Here, native gold grains are almost Ag-free and are largely hosted by tennantite and chalcopyrite in Zn-Cu-rich assemblages. In 2002, we successfully deployed the British Geological Survey (BGS) Rockdrill from the German R/V SONNE and drilled 10 holes (up to 5 m in length) at the Roman Ruins site at PACMANUS (Petersen et al. 2003). Here we report on the siting and mineral chemistry of gold from the precious-metal enriched drill core samples in order to document the similarities and differences to previously published results from the Eastern Manus Basin.

2 Geological Setting

The Manus Basin is a rapidly opening (~ 10 cm/yr) back-arc basin located north of the active New Britain subduction zone (Fig. 1). The regional tectonic complexity is a consequence of the northward subduction of the oceanic Solomon Microplate beneath the South Bismarck Microplate. True seafloor spreading occurs in the Central and Western Manus Basin whereas the Eastern Manus Basin is characterized by extensional rifting.

The Eastern Manus basin, host to several hydrothermal sites including PACMANUS, DESMOS, and SuSu knolls, represents a pull-apart structure in former island arc crust, and is situated between two sinistral fault zones (Binns et al. 2002). The PACMANUS hydrothermal field is situated near the bathymetric minimum of the elongated Y-shaped NE-SW trending Pual Ridge. The Ridge itself is terraced and consists of stacked 5-30 m thick lava flows representing a suite of eruptives formed by magmatic differentiation starting with basalt and ending with rhyodacite (Binns et al. 2002).

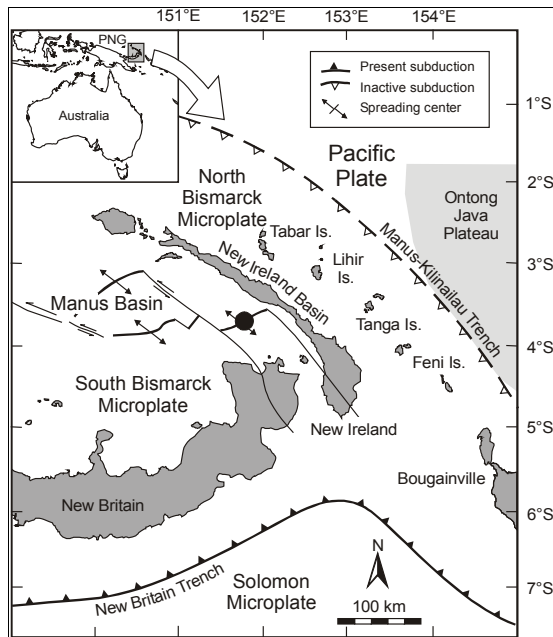


Figure 1: Location and plate tectonic setting of the PACMANUS hydrothermal field (solid circle).

3 Results

Two days of drilling at the active Roman Ruins vent site recovered 9 m of precious- and base-metal enriched massive sulfides with up to 57 g/t Au and

up to 585 ppm Ag. Average precious and base metal contents of individual drill core samples (¼ core sections, between 20 and 50 cm in length) are 10.8 ppm Au, 156 ppm Ag, 17.4 wt.% Zn, 4.2 wt. % Cu and 0.5 wt. % Pb (N=35). The gold is heterogeneously distributed in the cores and the highest grades are in sections that are mineralogically distinct. Section 65RD(010-030cm), which contains 57.2 g/t Au, 135 g/t Ag, 12.7 wt. % Cu, 12.2 wt. % Zn and 0.1 wt. % Pb consists of abundant chalcopyrite in close association with dark-brown sphalerite, whereas section 69RD(085-120cm) is dominated by porous, brown sphalerite plus barite and contains 30.4 g/t Au, 403 g/t Ag, 0.4 wt. % Cu, 44.7 wt. % Zn and 1 wt. % Pb.

Native gold in the Zn-Ba-rich section 69RD(085-120cm) occurs predominantly as micron-sized inclusions in chalcopyrite, sphalerite and to a lesser extent in amorphous silica (Table 1). Other, minor sulfides co-precipitated with sphalerite in this core, such as galena and pyrite, do not contain native gold. Gold grains in the Cu-Zn-rich section 65RD(010-030cm) are found as inclusions in chalcopyrite and pyrite, with few grains hosted by sphalerite and amorphous silica. Some grains are situated on grain boundaries between early co-precipitated chalcopyrite and sphalerite. Larger, isolated grains commonly occur at grain boundaries and in cavities of early chalcopyrite. Several gold grains in both mineral assemblages occur as late-stage cavity-fillings.

Table 1: Mode of occurrence of gold grains in drill core samples from Roman Ruins in comparison to published data from the Eastern Manus Basin (EMB = Satanic Mills and SuSu Knolls; Moss and Scott, 2001). ¹ – fractures in minerals.

	65RD	69RD	EMB
Inclusions in chalcopyrite	172	65	49
sphalerite	6	394	5
pyrite	27	1	-
amorphous silica	2	69	-
galena	-	1	-
tennantite	-	-	232
bornite	-	-	1
Grain boundaries	11	82	7
Cavity fill	12	35	4
Other	-	46	5 ¹
Total	230	693	303

The gold grains observed in both drill-core sections are mostly rounded and small (75% less than 4 µm; only few are between 6 and 10 µm), with smaller grains often occurring in clusters. The gold grains of the Zn-Ba mineral assemblage are distinctly

larger than those in the Cu-Zn-rich core section 65RD(010-030cm), however, none of the grains is larger than 10 μm in diameter (Fig. 2).

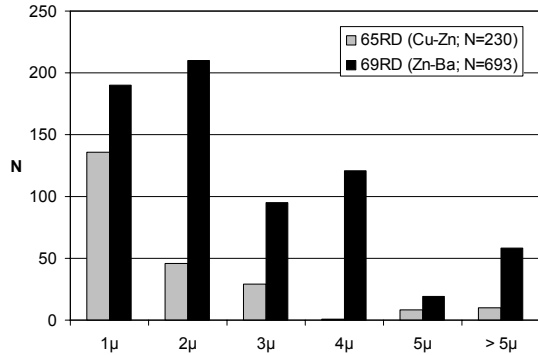


Figure 2: Grain size distribution of native gold in massive Cu-Zn- and Zn-Ba-rich assemblages from the interior of the Roman Ruins site at PACMANUS.

Gold grains contained in the Cu-Zn assemblage are generally Ag-poor (avg. 3.6 wt. % Ag, gold fineness ($1000 \cdot \text{Au}/(\text{Au}+\text{Ag})$) varies from 912 to 988, N=25) in contrast to the gold grains in Zn-Ba assemblages (avg. 11.3 % Ag, gold fineness varies from 836 to 920, N=51, Fig. 3).

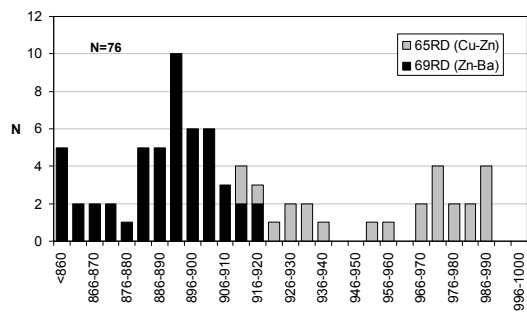


Figure 3: Gold-fineness ($1000 \cdot \text{Au}/(\text{Au}+\text{Ag})$) of native gold in massive Cu-Zn- and Zn-Ba-rich assemblages from the interior of the Roman Ruins site at PACMANUS (N=76).

Microprobe analyses of sphalerite from the Cu-Zn-rich core section 65RD(010-030cm) reveal a low Fe-content (avg. 0.6 mole % FeS, N=288; Fig. 4) indicating a high activity of sulfur during precipitation of this Cu-Zn-rich mineral assemblage. In contrast sphalerite from the Zn-Ba-rich section 69RD(085-120cm) is characterized by a more variable and higher Fe-content (avg. 6.6 mole % FeS, N=474) indicating a distinctly lower activity of sulfur for this mineral assemblage.

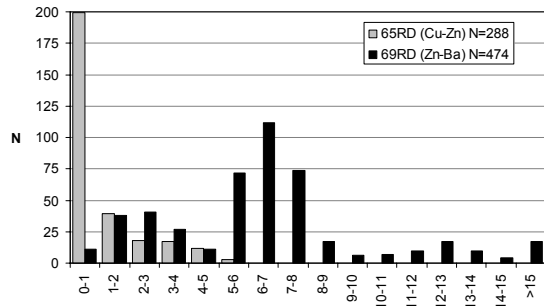


Figure 4: Mole % FeS in sphalerite from two Au-rich massive sulfide core sections from Roman Ruins, PACMANUS.

4 Discussion

The behavior of gold in seafloor hydrothermal systems has been discussed in detail in terms of solubility models based on aqueous chloride (AuCl_2^-) and reduced sulfur complexing (AuHS_2^- or AuHS^0 ; Hannington et al. 1986; Huston and Large 1989; Moss and Scott 2001). Gold may be transported as $\text{Au}(\text{HS})_2^-$ in fluids of weakly acid to near-neutral pH, low salinity, temperatures less than 350°C and moderately reducing conditions and high $\alpha\text{H}_2\text{S}$ (Seward and Barnes 1997). Benning and Seward (1996) and Gibert et al. (1998) have shown that the AuHS^0 -complex is the dominant complex for fluids with a lower pH and lower $\alpha\text{H}_2\text{S}$, while chloride complexing is only important for high-temperature fluids with a low pH, low sulfur concentrations and high salinities. The $\text{Au}(\text{OH})^0$ -complex may also play an important role in gold transport at temperatures between 300° and 500°C (Gammons and William-Jones 1997).

Our study revealed distinct differences between Satanic Mills and Roman Ruins with regard to the mineralogy of gold-bearing massive sulfide assemblage, and the host and fineness of native gold grains. Tennantite, the major host in samples studied by Moss and Scott (2001) is only a rare component in drill core samples from Roman Ruins and, when present, does not contain inclusions of native gold. Bornite another mineral commonly found at Satanic Mills is also rare or absent in samples from the interior of Roman Ruins. Also, the sulfur activity for the Zn-Ba-assemblage at Roman Ruins seems to be distinctly lower than documented for Satanic Mills by Moss and Scott (2001).

At Roman Ruins the association of native gold with two distinct mineral assemblages (Cu-Zn, Zn-

Ba), the variability in gold fineness and inferred sulfur activity suggest differences in transport and/or depositional controls between the two Au-rich mineral associations. Native gold in the Zn-Ba-rich mineral assemblage may be the result of remobilization, transport and re-precipitation of gold as suggested for other sites by Hannington et al. (1995), however, gold is commonly refined during this process separating Au from Ag and resulting in native gold containing distinctly less silver. This is not the case in our samples and indicates that refining of primary gold is not responsible for the enrichment of gold in Zn-rich sulfide assemblages at Roman Ruins. Gold may be precipitated by a large decrease in temperature in order to overcome the solubility maximum between 150° and 250°C or by oxidation of H₂S during mixing with seawater (Hannington et al. 1989). The presence of barite in the Zn-rich section 69RD(085-120cm) may be an indication for this mixing.

Precipitation of gold in the interior of Roman Ruins may therefore have proceeded from a chalcopyrite-rich stage with high-temperature fluids and relatively high α H₂S, as indicated by the low Fe-content of sphalerite and the high fineness of the native gold grains. Gold precipitation may then have continued to lower temperatures as a consequence of lowering α H₂S during continued precipitation of sulfides, probably with associated mixing with seawater. However, it is possible that the two different paragenetic relationships may be related to two different mineralizing events under different physico-chemical conditions.

Moss and Scott (2001) have shown that the AuHS⁰-complex is likely responsible for the transport of gold in fluids from PACMANUS. This is likely also true for the Zn-Ba mineral assemblage at Roman Ruins, since AuHS⁰ is stable at lower sulfur activities and the AuHS₂⁻-complex is only important at higher sulfur activities, not present at Roman Ruins.

Acknowledgements

This project is funded by the German Federal Ministry for Education and Research through a grant to PMH (grant: 03G0166A). Additional funding was provided by the Leibniz Program of the German Research Association. TI thanks the Society of Economic Geologists for a student research grant (2003).

References

- Benning LG & Seward TM (1996) Hydrosulphide complexing of Au(I) in hydrothermal solutions from 150 to 400°C and 500 to 1500 bars. *Geochim Cosmochim Acta* 60: pp. 1849-1871.
- Binns RA, Barriga F & Miller DJ (2002) Leg 193 summary. In: Binns RA, Barriga FJAS, Miller DJ (eds) *Proc ODP, Init Rep.* 193. College Station, TX: pp. 1-84.
- Gammons CH & Williams-Jones AE (1997) Chemical mobility of gold in the porphyry-epithermal environment. *Econ Geol* 92: pp. 45-59.
- Gibert F, Pascal M-L & Pichavant M (1998) Gold solubility and speciation in hydrothermal solutions: experimental study of the stability of hydrosulphide complex of gold (AuHS⁰) at 350 to 450°C and 500 bars. *Geochim Cosmochim Acta* 62: pp. 2931-2947.
- Hannington MD, Tivey MK, Larocque AC, Petersen S & Rona PA (1995) The occurrence of gold in sulfide deposits of the TAG hydrothermal field, Mid-Atlantic Ridge. *Can Mineral* 33: pp. 1285-1310.
- Hannington MD, Poulsen KH, Thompson JFH & Sillitoe RH (1999) Volcanogenic gold in the massive sulfide environment, in Barrie, C. T., and Hannington, M. D., eds., *Volcanic-associated Massive Sulfide Deposits: Processes and Examples in Modern and Ancient Settings.* *Rev Econ Geol* 8: pp. 325-356.
- Herzig PM, Hannington MD, Fouquet Y, von Stackelberg U & Petersen S (1993) Gold-rich polymetallic sulfides from the Lau back-arc and implications for the geochemistry of gold in sea-floor hydrothermal systems in the Southwest Pacific. *Econ Geol* 88: pp. 2182-2209.
- Huston DL & Large RR (1989) A chemical model for the concentration of gold in volcanogenic massive sulfide deposits. *Ore Geol Rev* 4: pp. 171-200.
- Moss R & Scott SD (2001) Geochemistry and mineralogy of gold-rich hydrothermal precipitates from the Eastern Manus Basin, Papua New Guinea. *Can Mineral* 39: pp. 957-978.
- Murphy PJ & Meyer G (1998) A gold-copper association in ultramafic-hosted hydrothermal sulfides from the Mid-Atlantic Ridge. *Econ Geol* 93: pp. 1076-1083.
- Petersen S, Herzig PM, Hannington MD & Gemmel JB (2003) Gold-rich massive sulfides from the interior of the felsic-hosted PACMANUS massive sulfide deposit, Eastern Manus Basin (PNG). In: Eliopoulos DG (ed) *Mineral Exploration and Sustainable Development, Proceedings of the 7th biennial SGA meeting Athens, Greece.* Millpress, Rotterdam: pp. 171-174.
- Seward TM & Barnes HL (1997) Metal transport by hydrothermal fluids, in Barnes, H. L. (ed) *Geochemistry of Hydrothermal Ore Deposits.* John Wiley & Sons Inc. New York: pp. 435-486.
- Watanabe K & Kajimura T (1994) The hydrothermal mineralization at Suiyo Seamount, in the central part of the Izu-Ogasawara Arc. *Res Geol* 44: pp. 133-140.

Mineralogische Untersuchungen an den hydrothermal alterierten Nebengesteinen der flachmarinen Goldvererzung des Conical Seamount, Papua Neuguinea

T. Monecke¹, S. Petersen², R. Kleeberg³, M. D. Hannington¹ und P. M. Herzig²

¹ Geologischer Dienst von Kanada, Ottawa

² Leibniz-Institut für Meereswissenschaften, IFM-GEOMAR, Kiel

³ Institut für Mineralogie, TU Bergakademie Freiberg

Einleitung

Der Bismarck-Archipel in Papua Neuguinea repräsentiert eines der wichtigsten Lagerstättendistrikte des zirkumpazifischen Raumes und weist mit der Lagesrtätte Ladolam auf der Insel Lihir die größte epithermale Goldvererzung der Welt auf [1]. Erste systematische Meeresbodenkartierungen im Umfeld der Insel Lihir wurden im Rahmen der Forschungsfahrt SO-94 vorgenommen und führten zur Entdeckung von mehreren untermeerischen Vulkanen in nur wenigen Kilometern Entfernung zur Insel. Vom Gipfelbereich eines dieser Vulkane, dem Conical Seamount, wurden hydrothermal alterierte und mineralisierte Laven geborgen [2].

Weitere Untersuchungen während der Fahrt SO-133 ergaben, daß hydrothermal alterierte Trachybasalte in weiten Teilen des Gipfelbereiches des Conical Seamount auftreten. Die alterierten Gesteine führen meist hohe Gehalte an Pyrit und Markasit, die entweder fein verteilt in dem Gestein auftreten oder stockwerkartige Gängchen bilden. Darüber hinaus kommen lokal sulfidführende, polymetallische Gänge vor, die durch extrem hohe Goldgehalte gekennzeichnet sind [3, 4]. Der Einsatz eines transportablen Bohrgerätes während der Forschungsfahrt SO-166 zeigte, daß sich die bis dahin lediglich von der Oberfläche bekannte Sulfidmineralisation auch zur Tiefe hin fortsetzt [5].

In dem vorliegenden Beitrag werden die mineralogischen Eigenschaften unterschiedlich stark hydrothermal alterierter Laven vom Conical Seamount beschrieben, die während der Forschungsfahrt SO-166 geborgen wurden. Ziel der mineralogischen Untersuchungen ist es, die physikochemischen Bedingungen der Nebengesteinsalteration zu rekonstruieren, die mit der Entstehung der Pyrit- und Markasitmineralisation einherging.

Geologischer Rahmen

Der Bismarck-Archipel befindet sich in einem tektonisch komplexen Umfeld. Im Oligozän und Miozän erfolgte entlang des Manus-Kilinau Grabens eine nach Südwesten gerichtete Subduktion der Pazifischen Platte. Im mittleren Miozän kam die konvergente Plattenbewegung zum Erliegen, da das Ontong Java Plateau nicht untergeschoben werden konnte [6]. Die Blockierung der Subduktion führte zu einer Plattenrotation und Entstehung einer neuen Subduktionszone entlang des Neu Britannien Grabens. Hier wird noch heute die Solomon See unter die Bismarck Mikroplatte geschoben (Abb. 1a).

Conical Seamount gehört einer Inselkette an, die sich über 260 km Länge parallel zur Küstenlinie von Neu Irland erstreckt (Abb. 1a). Der Vulkanismus entlang dieser

Inselkette erfolgte aufgrund extensioneller Bewegungen entlang großräumiger Störungen, die quer durch das Neu Irland Becken verlaufen [2]. Die ältesten vulkanischen Gesteine der Inselkette treten auf der Insel Simberi auf und werden mit 3,6 Ma datiert [7]. Die jüngsten bisher bekannten vulkanischen Aktivitäten erfolgten vor 2300 Jahren auf der Insel Feni [8].

Conical Seamount besitzt einen Basisdurchmesser von etwa 2,8 km und erhebt sich etwa 600 m über den umliegenden Meeresboden bis zu einer Wassertiefe von 1050 m (Abb. 1b). Der obere Teil des Vulkans wird von massiven Lavaflüssen aufgebaut, die kaskadenartig entlang der steilen Flanken des Seamount herabgeflossen sind und dabei kleine Stufen und Terrassen gebildet haben. Der Gipfelbereich des Seamount besitzt eine Ausdehnung von etwa 100 mal 200 m und wurde während der Forschungsfahrt SO-166 durch insgesamt 39 Bohrungen beprobt [5].

Mineralogische Untersuchungen

Zunächst wurde der Phasenbestand der Bohrkernproben (50 Gesamtgesteinsproben, die jeweils ein Bohrkernabschnitt von ca. 30 bis 60 cm Länge umfassen) mittels Röntgenpulverdiffraktometrie qualitativ und quantitativ bestimmt. Die quantitativen Untersuchungen erfolgten mit Hilfe der Rietveld-Methode [9, 10]. Basierend auf den Ergebnissen der quantitativen Phasenanalyse wurde eine Unterteilung der Proben in Gruppen mit ähnlichem Phasenbestand mittels hierarchischer Clusteranalyse vorgenommen. Diese statistische Analyse zeigte, daß drei Gruppen von Proben mit jeweils ähnlichem Phasenbestand unterschieden werden können.

Die erste Gruppe besteht aus Diopsid, Ca-reichen Plagioklas, Na-reichen Sanidin, Biotit, Magnetit und vulkanischem Glas. Die quantitativen Phasenanalysen zeigen, daß das vulkanische Glas zwischen 10 und 35 Gew.-% der Proben entspricht. Diopsid kommt in Konzentrationen von 30 bis 35 Gew.-% vor, während die Feldspatgehalte von 30 bis 45 Gew.-% schwanken. Die Gehalte an Biotit und Magnetit liegen meist unter 6 Gew.-%. Dünnschliffbeobachtungen legen nahe, daß der Phasenbestand der Proben nicht wesentlich durch die Prozesse der hydrothermalen Alteration modifiziert worden ist. Die häufig auftretenden Klinopyroxen- und Plagioklaseinsprenglinge erscheinen im optischen Mikroskop weitgehend unalteriert. Klinopyroxen bildet idiomorphe Kristalle, die Größen von bis zu 5 mm erreichen. Fast alle Klinopyroxeneinsprenglinge weisen oszillierende Zonierungen sowie eine deutliche Sektorzonierung auf. Die leistenförmigen Plagioklaseinsprenglinge sind bis zu 1 mm groß. Die Grundmasse der Trachybasalte besteht weitgehend aus vulkanischem Glas, in dem Pyroxen-, Biotit-, Plagioklas- und Sanidinmikrolithe auftreten. Magnetit kommt sowohl in Form kleiner Einsprenglinge als auch feinverteilt in der Grundmasse vor. Akzessorisch auftretender Apatit bildet kleine Kristalle, die meist von den Klinopyroxeneinsprenglingen beherbergt werden.

Trachybasaltproben der zweiten Gruppe bestehen zu 10 bis 35 Gew.-% aus vulkanischem Glas und beinhalten 25 bis 35 Gew.-% Diopsid, 30 bis 40 Gew.-% Feldspat und unter 6 % Biotit. Die Proben enthalten bis zu 10 Gew.-% Analcim und bis zu 4 Gew.-% K-reichen monoklinen Feldspat. Pyrit und Markasit erreichen bis zu 6 Gew.-% in den untersuchten Proben. Im Vergleich zu den nicht alterierten Gesteinen enthalten die Proben dieser Gruppe einen niedrigeren Anteil an Magnetit (unter 4 Gew.-%). Petrographische Untersuchungen zeigen, daß Pyrit und Markasit in den Trachybasalten dieser Gruppe häufig als Füllung von Gasblasen auftreten

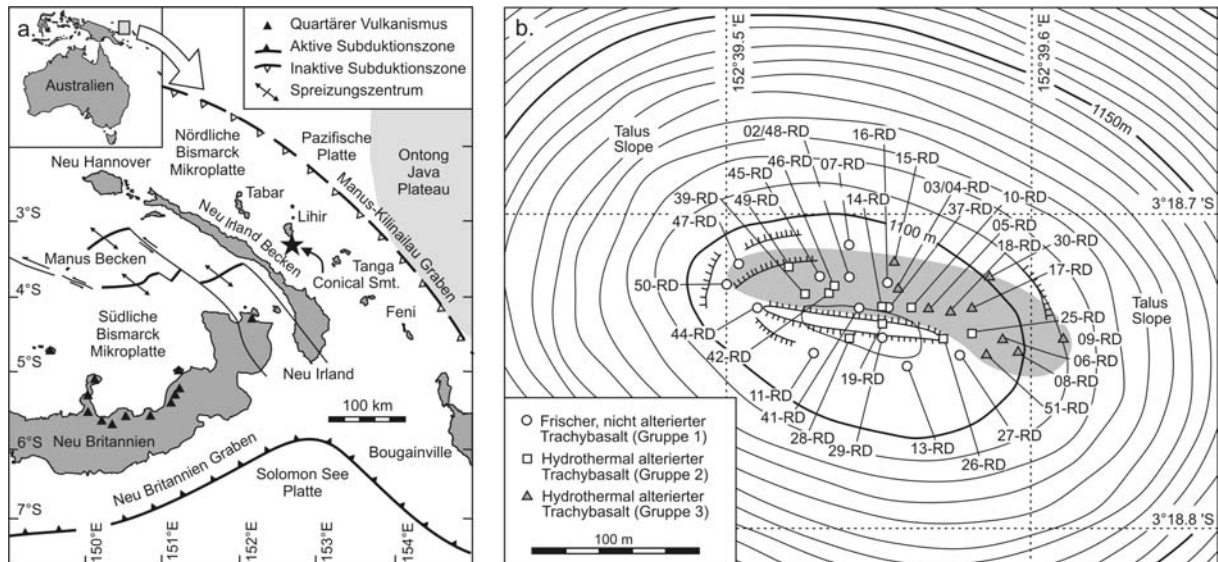


Abb. 1: a. Karte des Bismarck Archipelagos und Lage des Conical Seamount. b. Bathymetrische Karte des Gipfelbereiches des Conical Seamount mit Verteilung der unterschiedlich stark alterierten Gesteinsproben.

oder kleine Körner bilden, die fein in der Grundmasse verteilt sind. Primäre Magnetite sind teilweise oder vollständig von diesen Sulfiden verdrängt worden. Die gefügekundlichen Beobachtungen zeigen, daß die Proben dieser Gruppe leicht hydrothermal alteriert wurden. Von besonderem Interesse ist das Vorkommen von Analcim, ein sekundäres Mineral, daß sich häufig auch in modernen Geothermalsystemen an Land bildet.

Die dritte Probengruppe enthält neben vulkanischem Glas einen hohen Anteil an Tonmineralen. Der Diopsidgehalt schwankt zwischen 15 und 30 Gew.-%. Zusätzlich zu primärem Plagioklas und Sanidin (35 bis 50 Gew.-%) wurden in einigen Proben bis zu 5 Gew.-% eines K-reichen monoklinen Feldspates beobachtet. Es handelt sich hierbei vermutlich um ein Produkt der hydrothermalen Alteration. Der Biotitgehalt dieser Proben ist variabel. Magnetit konnte mit Hilfe der Röntgenbeugung nicht beobachtet werden. Die Gesamtgesteinsproben enthalten bis zu 10 Gew.-% Pyrit und Markasit. Röntgendiffraktometrische Untersuchungen an Tonmineralfraktionen zeigten, daß die alterierten Gesteine hohe Gehalte an Smektit aufweisen. Durch die Anpassung von modellierten Röntgendiffraktogrammen an die gemessenen Beugungsbilder der Tonmineralfraktionen konnte demonstriert werden, daß sowohl dioktaedrische als auch trioktaedrische Smekтите auftreten. Darüber hinaus wurde in den Tonmineralfraktionen Vermikulit angetroffen. Dünnschliffuntersuchungen haben gezeigt, daß in erster Linie das vulkanische Glas in der Grundmasse durch die Smekтите verdrängt wird. Smektit tritt in Säumen rund um alterierte Klinopyroxeneinsprenglinge auf oder bildet die Füllung von Rissen, die reliktsche Klinopyroxenkristalle durchziehen. Primärer Magnetit ist vollständig durch feine Verwachsungen von Sulfiden und vermutlich amorphen Phasen ersetzt. Die in den Proben enthaltenen Plagioklaseinsprenglinge erscheinen unter dem optischen Mikroskop weitgehend unalteriert. Rückstreuелектроненstrahlbilder zeigen jedoch, daß diese Phasen durch die hydrothermale Alteration chemisch verändert wurden. In vielen Fällen kam es durch die Überlagerung sekundärer chemischer Gradienten mit primären Zonierungen zur Bildung komplizierter Internstrukturen.

Interpretation der Ergebnisse

Die Bohrkampagne im Rahmen der Forschungsfahrt SO-166 zeigte, daß im Gipfelbereich des Conical Seamount sowohl frische, scheinbar nicht hydrothermal alterierte Trachybasalte als auch stark alterierte Äquivalente auftreten. Hydrothermal alterierte Proben kommen in erster Linie in dem nördlichen und östlichen Teil des Gipfelbereichs vor, während der südliche Bereich von frischen Trachybasalten dominiert wird (Abb. 1b). Meeresbodenbeobachtungen legen die Vermutung nahe, daß die Zone intensiver hydrothermalen Alteration von den im Süden auftretenden frischen Gesteine durch eine etwa 100 m lange vulkanische Struktur getrennt wird. Es handelt sich möglicherweise um die Aufstiegszone frischer Lava, die in den südlichen Teil des Gipfelbereiches abgefließen ist und die dort eventuell auftretenden hydrothermal alterierten Gesteine bedeckt hat. Eine solche Vermutung wird durch Beobachtungen an Bohrkernen gestützt, in denen intensiv hydrothermal alterierte Gesteine unterhalb frischer Trachybasalte auftreten [5].

Eine Rekonstruktion der physikochemischen Bedingungen, die während der Bildung der Pyrit- und Markasitmineralisation und der damit verbundenen Nebengesteinsalteration vorherrschte, kann anhand der relativen Stabilitäten der in den Proben auftretenden Minerale vorgenommen werden. Detaillierte Untersuchungen an aktiven Geothermalsystemen an Land haben gezeigt, daß di- und trioktaedrische Smektiten nur bei relativ niedrigen Temperaturen stabil sind. In einem Temperaturbereich von 150 bis 200°C kommt es zu einer Umwandlung dieser Phasen in Illit bzw. Chlorit [11, 12]. Aufgrund der Stabilitätsgrenze von Smektit muß daher davon ausgegangen werden, daß die in großen Teilen des Gipfelbereiches des Conical Seamount auftretende hydrothermale Alteration bei relativ niedrigen Temperaturen abgelaufen ist. Die Alteration scheint in einem leicht sauren bis alkalischen Milieu erfolgt zu sein, da Indikatorminerale für extrem saure Bedingungen wie Alunit, Kaolinit und Zunyit [13] in den Bohrproben nicht angetroffen wurden. Das gehäufte Auftreten von Sulfiden und das Fehlen sekundärer Sulfate und Oxide zeigt, daß die hydrothermale Alteration in einem relativ reduzierenden Umfeld stattgefunden hat.

Literatur

- [1] G.D. Carman *Econ Geol Spec Pub* **10**, 247-284 (2003).
- [2] P. Herzig et al. *EOS Trans Amer Geophys Union* **75**, 513-516 (1994).
- [3] P.M. Herzig et al. in *Mineral deposits: Processes to processing* (eds. C.J. Stanley et al.) 527-530 (Balkema, Rotterdam, 1999).
- [4] S. Petersen et al. *Econ Geol* **97**, 1795-1813 (2002).
- [5] P.M. Herzig et al. *InterRidge News* **12**, 22-26 (2003).
- [6] P.J. Coleman & L.W. Kroenke *GeoMar Lett* **1**, 129-134 (1981).
- [7] J.J. Rytuba et al. *US Geol Surv Bull* **2039**, 119-126 (1993).
- [8] P.S. Licence et al. in *Pacific Rim Congress 87* (ed. E. Brennan) 273-278 (Austral Inst Min Metall, Parkville, 1987).
- [9] T. Monecke et al. *Can Mineral* **39**, 1617-1633 (2001).
- [10] R. Kleeberg & J. Bergmann in *Powder diffraction. Proceedings of the II International School on Powder Diffraction* (eds. S.P.S. Gupta & P. Chatterjee) 63-76 (Allied Publ., New Delhi, 2002).
- [11] S.F. Simmons & P.R.L. Browne *Econ Geol* **95**, 971-999 (2000).
- [12] D. Robinson et al. *J metamorphic Geol* **20**, 167-174 (2002).
- [13] N.C. White & J.W. Hedenquist *SEG Newslett* **23**, 1-13 (1995).

Hydrothermale Prozesse und magmatische Einträge im PACMANUS Hydrothermalfeld, östliches Manus Becken (PNG)

S. Petersen¹, T. Kuhn¹, J. Scholten², M. D. Hannington³, T. Ihle⁴ und P. M. Herzig¹

¹ Leibniz-Institut für Meereswissenschaften, IFM-GEOMAR, Kiel
e-mail: spetersen@ifm-geomar.de

² Institut für Geowissenschaften, CAU Kiel

³ Geologischer Dienst von Kanada, Ottawa

⁴ Lehrstuhl für Lagerstättenlehre und Petrologie, TU Bergakademie Freiberg

Einführung

Im Rahmen der Forschungsfahrt SO-166 wurde das PACMANUS Hydrothermalfeld im Bereich des östlichen Manus Beckens durch Bohrungen (5 m) untersucht. Für die Flachbohrungen wurde der sogenannte "Rockdrill" des British Geological Survey eingesetzt, der bis zu 5 m lange Bohrkerne aus Wassertiefen bis zu 2000 m bergen kann.

Goldreiche submarine Hydrothermalvorkommen finden sich besonders entlang der Inselbögen und Back-Arc Becken des Südwest-Pazifik. Eines der ungewöhnlichsten Vorkommen ist das PACMANUS Hydrothermalfeld im östlichen Manus Becken (Abb. 1), das durch sehr hohe Edel- und Buntmetallgehalte gekennzeichnet ist (Binns und Scott, 1993). Aufgrund hoher Gas-, Fluor- und SO₂-Gehalte in den Fluiden, aufgrund des Auftretens metallreicher Glaseinschlüsse in den Nebengesteinen sowie aufgrund

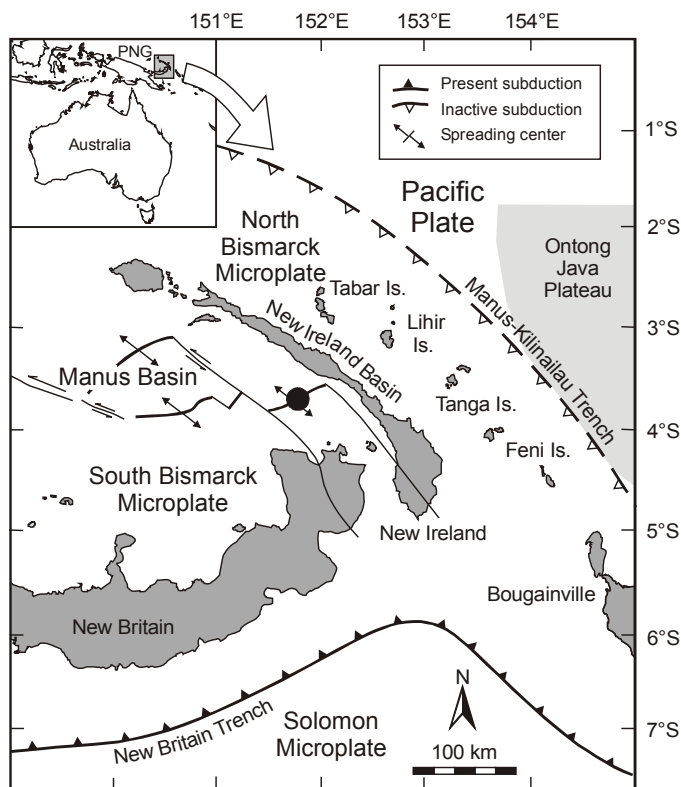


Abb. 1: Lagekarte des PACMANUS Hydrothermalfeldes im östlichen Manus Becken (PNG)

aufgrund niedriger Schwefelisotopenverhältnisse in den Sulfiden wurde eine Beteiligung magmatischer Lösungen an der Bildung dieses Vorkommens postuliert (Douville et al., 1999; Yang und Scott, 1996; Gemmell et al., 1996).

Im Rahmen der Forschungsfahrt SO-166 sollte geklärt werden, welche Prozesse zur Goldanreicherung in diesem Hydrothermalsystem führen, und ob sich ein magmatischer Eintrag in den Sulfiden selbst nachweisen lässt. Darüber hinaus sollte die dreidimensionale Struktur der Vererzung im oberflächennahen Bereich charakterisiert werden, da dieser im Rahmen des Ocean Drilling Program Leg 193 nicht gekernt werden konnten (Binns et al., 2002).

Ergebnisse

Die Proben aus dem Untergrund des PACMANUS Hydrothermalfeldes (Roman Ruins Gebiet) werden mineralogisch von Chalkopyrit und Sphalerit dominiert, unterscheiden sich aber deutlich von Oberflächenproben, wie sie mit Greifern und Tauchbooten gewonnen wurden. Fahlerze und Bornit treten mengenmäßig zurück, dafür zeigt das Auftreten von Anhydrit in mehreren Bohrkernen eine Zumischung von Meerwasser im oberflächennahen Bereich an (Herzig et al., 2003). Ein Teil der Bohrkernproben weist Texturen auf, die für die Resedimentation der Sulfide sprechen und ein Indiz für episodische hydrothermale Aktivität mit zwischenzeitlicher Erosion und Transport von Sulfidmaterial sind. Ähnliche Texturen sind bisher nur aus dem TAG Hydrothermalfeld im Nordatlantik beschrieben worden (Humphris et al., 1995). Eine langanhaltende hydrothermale Aktivität wird auch durch vorläufige Altersdatierungen an den Sulfiden bestätigt, die Alter zwischen <20 Jahre und ca. 2100 Jahren aufweisen.

Die geochemischen Analysen der erbohrten Massivsulfide zeigen insgesamt sehr hohe Gehalte an Kupfer, Zink, Blei, Gold und Silber, aber auch Arsen und Antimon sind deutlich angereichert (Tab. 1). So konnten Gehalte bis zu 57,2 ppm Au und 692 ppm Ag nachgewiesen werden. Die Buntmetallgehalte liegen bei durchschnittlich 4,2 Gew.-% Cu, 17,4 Gew.-% Zn und 0,5 Gew.-% Pb. Im Gegensatz zu publizierten Daten, die eine positive Korrelation von Gold mit Kupfer aufweisen, zeigen die Bohrkernproben eine positive Korrelation von Gold mit Zink. In einigen Kernen konnte eine Änderung in der Sulfidzusammensetzung mit der Tiefe beobachtet werden. So nehmen die Konzentrationen der Elemente Au, Ag, As, Cd, Ga, Pb, Sb und Zn mit der Tiefe ab. Diese Elementanreicherung im oberflächennahen Bereich ist vermutlich das Ergebnis episodischer hydrothermalen Aktivität, die zur Remobilisation dieser Elemente, zum Transport an die Oberfläche und dort zum Wiederabsatz führt. Dieser Prozess des "zone refining" wurde auch bei den Untersuchungen des TAG Hydrothermalfeldes nachgewiesen (Petersen et al., 2000) und scheint ein verbreiteter Prozess zu sein, der die Geochemie solcher Hydrothermalvorkommen noch während ihrer Bildung beeinflusst.

Die Beprobung von hochtemperierten Austrittsstellen im Bereich des PACMANUS Hydrothermalfeldes (Satanic Mills und Roman Ruins) durch den TV-Greifer erlaubt zusätzlich einen Vergleich zwischen diesen beiden Vorkommen. Dazu wurden neben den geochemischen Untersuchungen an Gesamtsulfiden auch Mikrosondenmessungen und die Schwefelisotopenwerte der Sulfide herangezogen. Die Sulfide von Satanic Mills sind durch niedrigere Schwefelisotopenverhältnisse gekennzeichnet ($-1,1$ bis $0,2$ ‰ $\delta^{34}\text{S}$, N=9), als diejenigen von Roman Ruins ($0,0$ bis $3,0$ ‰ $\delta^{34}\text{S}$, N=10) und scheinen einen erhöhten Eintrag an magmatischem Schwefel (Disproportionierung von SO_2) im Bereich von Satanic Mills anzudeuten. Dies steht im Einklang mit den erhöhten Gehalten an typisch "magmatogenen" Elementen wie As, Bi, Hg, In, Sb, Sn und Te in den Erzen von Satanic Mills im Vergleich zu den Proben von Roman Ruins (bis zu 6,2 Gew. % As, 145 ppm Bi, 78 ppm Hg, 341 ppm In, 9500 ppm Sb, 432 ppm Sn und 39 ppm Te in den Sulfiden von Satanic Mills).

Mikrosondenanalysen an gediegen Gold und Sphalerit zeigen, dass die physikochemischen Bedingungen während des Goldabsatzes sehr wechselhaft waren. Variationen der Silbergehalte in gediegen Gold ($[Au/(Au+Ag)*1000] = 784-989$) und der FeS-Gehalte in Zinkblende (0 bis 22,6 mol% FeS) weisen auf Unterschiede in der Schwefelaktivität der hydrothermalen Lösungen während des Goldabsatzes hin. Die Untersuchungen an den Bohrkernproben zeigen darüber hinaus deutliche Unterschiede zu publizierten Werten von Oberflächenproben (Moss und Scott, 2001). Dies kann als weiterer Hinweis darauf verstanden werden, dass Untersuchungen von Oberflächenproben nicht auf das Hydrothermalfeld als Ganzes übertragen werden können und Untersuchungen des Untergrundes notwendig sind.

Schlußfolgerung

Das Auftreten von Anhydrit im Innern des Sulfidhügels weist auf Meerwasserzirkulation im Untergrund hin. Sulfidtexturen belegen Erosions- und Transportprozesse, die ein höheres Alter des PACMANUS Hydrothermalfeldes andeuten. Episodische hydrothermale Aktivität und "zone refining" sind wichtige Prozesse in der Entwicklung dieses Massivsulfidvorkommens. Magmatische Einträge sind für das gesamte PACMANUS Hydrothermalsystem wahrscheinlich, lokal jedoch von unterschiedlicher Bedeutung, und besonders im Bereich des Satanic Mills Gebietes wirksam. Der Einsatz des British Geological Survey "Rockdrill" war der Erste seiner Art auf FS SONNE und hat in besonderer Weise gezeigt, dass der Einsatz beweglicher Bohrgeräte von der Sonne aus möglich ist.

Danksagung

Unser ausdrücklicher Dank gilt der Schiffsführung und der Mannschaft von FS SONNE sowie der britischen Bohrcrew, die in besonderer Weise zum Erfolg dieser Fahrt beigetragen haben. Dieses Projekt wurde mit Mitteln des BMBF (FK: 03G0166A) gefördert.

Literatur

- Binns, R. A., & Scott, S. D., 1993. Actively forming polymetallic sulfide deposits associated with felsic volcanic rocks in the eastern Manus back-arc basin, Papua New Guinea. *ECON GEOL* 88: 2222-2232.
- Binns, R. A., Barriga, F., & Miller, D. J., 2002. Leg 193 summary. *Proceedings of the Ocean Drilling Program, Initial Reports, 193*, College Station, TX: 1-84.
- Douville, E., Bienvenu, P., Charlou, J.-L., Donval, J. P., Fouquet, Y., Appriou, P., & Gamo, T., 1999. Yttrium and rare earth elements in fluids from various deep-sea hydrothermal systems. *GEOCHIM COSMOCHIM ACTA* 63: 627-643.
- Gemmell, J.B., Binns, R.A., & Parr, J.M., 1996. Comparison of sulfur isotope values between modern back-arc and mid-ocean ridge seafloor hydrothermal systems. *EOS TRANS, AM GEOPHYS UNION* 77: 117.
- Herzig, P.M., Petersen, S., Kuhn, T. Hannington, M.D., Gemmell, J.B., Skinner, A.C. & Shipboard Scientific Party (2003) Shallow drilling of seafloor hydrothermal systems using R/V SONNE and the BGS Rockdrill: Conical Seamount (New Ireland Fore-Arc) and Pacmanus (Eastern Manus Basin), Papua New Guinea, *InterRidge News*, 12(1): p. 22-25.
- Humphris, S. E., Herzig, P. M., Miller, D. J., Alt, J. C., Becker, K., Brown, D., Brüggemann, G., Chiba, H., Fouquet, Y., Gemmell, J. B., Guerin, G., Hannington, M. D., Holm, N. G., Honnorez, J. J., Itturino, G. J., Knott, R., Ludwig, R., Nakamura, K., Petersen, S., Reysenbach, A.-L., Rona, P. A., Smith,

S., Sturz, A. A., Tivey, M. K., & Zhao, X., 1995. The internal structure of an active sea-floor massive sulphide deposit. NATURE 377: 713-716.

Moss, R., & Scott, S. D., 2001. Geochemistry and mineralogy of gold-rich hydrothermal precipitates from the Eastern Manus Basin, Papua New Guinea. CAN MINERAL 39: 957-978.

Petersen, S., Herzig, P. M., & Hannington, M. D., 2000. Third dimension of a presently forming VMS deposit: TAG hydrothermal mound, Mid-Atlantic Ridge, 26°N. MIN DEP 35: 233-259.

Yang, K., & Scott, S. D., 1996. Possible contribution of a metal-rich magmatic fluid to a sea-floor hydrothermal system. NATURE 383: 420-423.

Tabelle 1: Geochemische Analysen von Sulfiden (Bohrkern- und Oberflächenproben; in Klammern die Anzahl der Proben) des PACMANUS Hydrothermalfeldes (PNG)

Kern	Cu	Zn	Pb	Fe	Ca	Ba	Au	Ag	As	Bi	Cd	Ga	Hg	In	Sb	Se	Sn	Te
	wt. %						ppm											
SO166-60RD																		
0-30 cm	4.6	18.1	0.56	21.9	0.1	6.6	12.35	112	2655	1.0	636	99	2	28	421	<3	3	<0.2
30-60 cm	8.3	1.5	0.08	26.1	7.6	1.3	1.46	5	1855	16.0	23	3	<1	7	24	24	3	2.5
60-90 cm	6.2	0.7	0.03	25.3	10.1	0.5	1.15	6	1950	11.0	11	3	<1	6	36	28	3	3.2
SO166-61RD																		
0-45 cm	1.3	22.4	0.78	4.7	0.1	19.5	8.26	188	1615	0.7	759	50	<1	7	600	<3	1	<0.2
45-90 cm	3.1	14.5	0.50	6.4	0.1	28.5	7.89	100	964	4.4	561	46	3	10	396	<3	3	<0.2
90-140 cm	0.2	32.1	2.31	2.3	0.1	20.0	6.10	542	2140	<0.2	762	11	14	0.1	943	<3	<0.5	<0.2
SO166-63RD																		
0-50 cm	8.8	12.4	0.54	22.3	4.9	3.0	8.05	106	2350	9.2	384	33	<1	15	362	9	2	0.2
SO166-65RD																		
0-10 cm	1.6	38.4	0.85	4.1	<0.1	15.0	16.45	264	2525	<0.2	1100	116	6	64	764	<3	3	<0.2
10-30 cm	12.9	12.2	0.13	12.9	<0.1	21.0	57.15	135	1505	<0.2	550	113	<1	109	472	<3	7	<0.2
30-40 cm	1.1	44.7	1.14	3.3	<0.1	9.1	9.20	410	4715	<0.2	1300	101	<1	28	1067	<3	1	<0.2
40-45 cm	9.8	0.1	0.02	<0.1	<0.1	<0.1	1.07	4	783	1.8	3	4	<1	9	8	6	6	<0.2
SO166-66RD																		
0-10 cm	0.6	33.1	0.26	6.5	<0.1	14.5	11.60	394	1825	<0.2	1040	39	<1	4	855	<3	1	<0.2
10-30 cm	28.3	0.9	0.02	26.6	<0.1	3.3	2.39	41	385	5.8	30	11	<1	44	28	<3	10	<0.2
30-55 cm	1.2	33.1	0.13	4.6	<0.1	18.0	28.8	192	766	<0.2	1120	148	<1	57	538	<3	21	<0.2
55-80 cm	0.5	33.5	0.30	3.8	<0.1	15.0	27.25	258	810	<0.2	1010	77	<1	22	613	<3	3	<0.2
SO166-67RD																		
0-20 cm	0.7	46.6	1.22	3.3	0.5	7.8	35.80	584	2380	<0.2	1570	119	14	4	1100	<3	3	<0.2
20-45 cm	2.7	10.5	1.04	12.7	9.3	5.9	8.96	140	1300	0.8	344	51	<1	17	233	<3	9	<0.2
45-70 cm,a	2.6	12.4	0.16	8.7	10.7	6.6	15.10	233	1100	0.7	457	62	<1	16	219	<3	4	<0.2
45-70 cm,b	0.5	35.2	0.86	2.3	5.5	11.0	15.70	468	1110	<0.2	1050	27	<1	0.1	707	<3	4	<0.2
70-80 cm	1.6	14.7	0.07	10.1	11.5	2.4	10.80	41	761	0.5	555	96	<1	22	137	<3	5	<0.2
80-110 cm	5.8	0.4	0.03	23.9	9.4	0.1	1.56	6	880	16.0	6	4	<1	6	16	27	3	1.9
110-125 cm	4.1	0.2	0.02	28.6	6.9	0.1	3.11	8	1340	15.0	5	7	<1	4	16	36	2	2.5
125-145 cm	3.8	0.2	0.03	22.5	11.6	<0.1	1.35	5	759	8.3	4	2	<1	4	13	19	6	0.6
145-160 cm	5.0	0.1	0.01	27.3	7.7	<0.1	1.75	6	1180	17.0	2	3	<1	3	10	58	2	1.3
160-180 cm	3.8	0.1	0.01	31.8	5.4	<0.1	2.00	5	1390	23.0	3	3	<1	3	11	59	2	2.2
180-190 cm	2.7	0.3	0.03	24.8	10.6	<0.1	2.20	6	1280	7.3	5	3	<1	4	17	14	1	0.3
SO166-68RD																		
0-34 cm	9.2	7.9	0.31	28.2	0.2	2.4	4.66	72	1915	16.0	243	36	<1	18	207	26	5	4.5
34-42 cm	0.2	0.2	0.01	32.1	7.0	0.1	1.41	2	660	19.0	6	1	<1	1	13	26	1	7.4
SO166-69RD																		
0-20 cm	0.1	40.2	1.92	5.1	0.1	13.0	0.94	32	4960	<0.2	866	38	4	0.2	924	<3	<0.5	<0.2
20-50 cm	5.1	12.1	0.11	25.9	<0.1	10.0	11.55	35	2270	3.9	400	66	1	22	273	7	4	<0.2
50-85 cm	5.9	17.6	1.15	18.3	<0.1	7.2	13.65	41	2725	1.9	619	93	2	40	548	4	23	<0.2
85-120 cm	0.4	44.7	0.99	3.8	<0.1	8.2	30.40	403	1225	<0.2	1520	135	4	7	812	<3	7	<0.2
120-150 cm	0.3	32.3	0.96	2.9	4.2	15.5	11.90	216	502	<0.2	1030	125	5	24	408	<3	24	<0.2
150-180 cm	3.8	4.2	0.04	10.7	16.4	3.5	2.44	17	488	1.9	110	10	<1	9	44	7	1	<0.2
180-220 cm	0.2	30.0	1.01	2.4	2.8	16.5	4.05	68	150	<0.2	581	6	3	0.3	120	<3	5	<0.2
Oberflächenproben																		
Roman Ruins																		
Sphalerit (7)	0.4	31.3	2.39	2.9	0.1	7.5	10.4	202	1720	<0.2	912	31	6	20	507	<3	5	<0.1
Si-reiche Kruste (1)	0.4	5.0	0.9	3.0	0.1	1.9	2.5	77	553	0.6	97	6	12	0.1	743	<3	3	<0.1
Py-reicher Dazit (2)	0.1	6.0	2.6	10.1	0.6	12.0	1.4	197	2095	<0.1	51	5	12	0.2	548	<3	4	<0.1
Satanic Mills																		
Cpy-conduits (4)	32.1	0.8	0.04	26.8	<0.1	0.3	9.06	36	2295	80.0	18	43	1	120	435	22	162	11
Cpy-Bn-Conduits (2)	39.9	2.8	0.16	17.3	<0.1	1.5	21.75	114	14295	73.5	74	324	1	163	1550	<3	49	4
Polymetallisch Cu (38)	17.1	10.3	0.40	13.2	0.1	16.7	18.03	185	8850	10.3	304	112	7	128	1263	5	4	0.2
Polymetallisch (41)	4.6	26.4	1.28	4.2	0.3	17.9	11.89	313	11300	0.6	890	130	25	51	1531	5	3	0.1
Sphalerit (15)	0.6	42.9	2.27	0.9	<0.1	10.7	8.10	342	8730	0.1	1448	146	39	23	718	9	4	0.1
Fahlerz (1)	29.0	9.5	0.26	9.2	<0.1	6.4	105.00	285	61900	5.8	334	178	1	341	9500	<3	9	0.1

Shallow drilling of seafloor hydrothermal systems: The missing link

P.M. Herzig, S. Petersen & T. Kuhn

Leibniz Laboratory of Applied Marine Research, Freiberg University of Mining and Technology, Germany

M.D. Hannington

Geological Survey of Canada, Ottawa, Canada

J.B. Gemmell

Center of Ore Deposit Research, University of Tasmania, Hobart, Tasmania, Australia

A.C. Skinner

British Geological Survey, Edinburgh, United Kingdom

Keywords: shallow seafloor drilling, sub-surface hydrothermal systems, submarine gold mineralization

ABSTRACT: In September-October 2002, shallow seafloor drilling using the portable 5 m Rockdrill of the British Geological Survey and the German R/V Sonne has revealed critical information on the sub-surface nature of two distinct hydrothermal systems in the New Ireland fore-arc and the Manus Basin of Papua New Guinea. Drilling of 39 holes at the summit plateau of Conical Seamount close to Lihir Island has indicated that previously discovered epithermal-style gold mineralization reaches to a depth of at least 4.5 m below seafloor with gold concentrations of up to 14.2 g/t Au over a core section of 30 cm. This discovery significantly extends the known surface extent of gold mineralization (up to 230 g/t Au) at Conical Seamount. Almost 9 m of spectacularly textured massive sulfide core recovered from 10 holes drilled in only two days in the active Roman Ruins black smoker site of the Pacmanus area proves, that massive sulfides extend to a depth of at least 5 m below seafloor. High concentrations of gold, locally up to 57 g/t Au over 20 cm of core length, confirm the gold-rich nature of this particular back-arc deposit. Shallow seafloor drilling is a fast and cost efficient method that bridges the gap between surface sampling and deep (ODP) drilling and undoubtedly will become a standard practice in the future study of seafloor hydrothermal systems and massive sulfide deposits.

1 INTRODUCTION

Our current knowledge of seafloor hydrothermal systems and massive sulfide deposits is largely based on surface sampling by dredges, TV-guided grabs, submersible, and ROVs, and deep drilling by the Ocean Drilling Program (ODP). In the past decade, ODP has drilled a total of three different hydrothermal sites including Middle Valley at the Juan de Fuca Ridge (Zierenberg et al., 1998), the active TAG hydrothermal mound at the Mid-Atlantic Ridge (Herzig et al., 1998, Humphris et al., 1995), and the Pacmanus area in eastern Manus Basin (Binns et al., 2002). Due to the need to set casing, coring of the immediate sub-surface is usually not possible during ODP operations, thus leaving a significant gap between surface and deep drilling information. We have, for the first time, deployed the British Geological Survey (BGS) Rockdrill from the German R/V Sonne and successfully demonstrated that shallow seafloor drilling with a lander-type system is feasible from a non-drilling research vessel and significantly extends our understanding of the 3rd dimension of seafloor hydrothermal systems and massive sulfide deposits. Here, we present first results of a recent drilling and coring program at Conical

Seamount (New Ireland fore-arc) and Pacmanus/Roman Ruins (Eastern Manus Basin).

2 GEOLOGICAL SETTING OF DRILL SITES

Conical Seamount is one of several young volcanic cones discovered in the area south of Lihir Island (New Ireland fore-arc, Papua New Guinea) in 1994 (Herzig et al., 1994). It has a basal diameter of 2.5 km and rises about 600 m above the surrounding seafloor at 1.650 m with a well-developed summit plateau (150 x 200 m) at 1.050 m water depth. First indications of gold-rich epithermal-style vein mineralization at the summit plateau of Conical Seamount were discovered in 1994 (Herzig et al., 1995) and confirmed 1998 (Herzig et al., 1998, 1999). Samples collected immediately adjacent to an eruptive fissure at the summit are locally intensely clay-silica altered. Gold-rich polymetallic vein mineralization occurs in an intermediate zone, while arsenic sulfides together with abundant amorphous silica occur at the margin. More than 1.200 kg of mineralized rock was recovered in 1998, consisting of stockwork and disseminated sulfides with gold concentrations locally reaching up to 230 g/t (avg. 26 g/t, n=40, Herzig et al., 1999, Petersen et al., 2002). The mate-

rial recovered from Conical Seamont is similar to the ore currently being mined from the giant Ladolam epithermal gold deposit in the crater of Luise Volcano on Lihir Island, and both sites may be linked by the same magmatic system. For the marine environment, Conical Seamont represents a new type of mineralization which is different from black smoker-type deposits and has been formed through contributions of magmatic fluids and metals (Petersen et al., 2002). This has important implications for the understanding of epithermal-style ore mineralization in submarine arcs as well as on the continents.

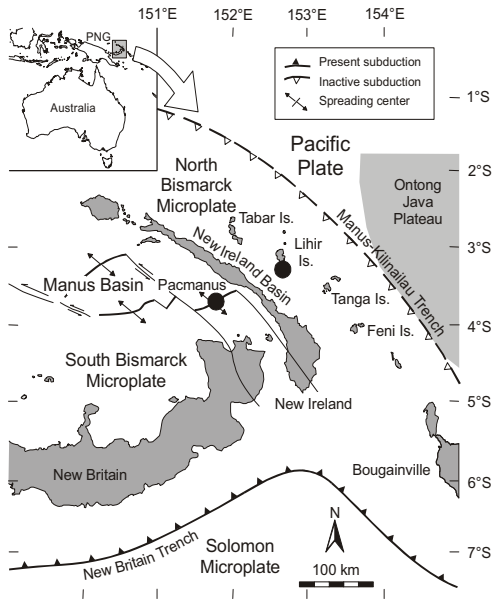


Figure 1. (Rock)drill sites (solid circles) Conical Seamont (south of Lihir Island) and Pacmanus/Roman Ruins (Eastern Manus Basin). Cruise SO-166 of R/V Sonne.

The *Pacmanus hydrothermal field* in the Eastern Manus Basin is situated on the crest of Pual Ridge, an elongated feature composed of dacite with subordinate basaltic andesite and rhyodacite that stands 500-700 m above the surrounding basin floor (Binns et al., 2002). Five principal areas of hydrothermal activity have been delineated at Pacmanus including Roman Ruins, which consists of active and inactive black smoker chimneys with exit temperatures up to 276°C (Binns et al., 2002). The Pacmanus area was subject to ODP drilling during Leg 193, however, the massive sulfides were not cored to casing requirements for deep drilling (Binns et al., 2002).

3 RESULTS

Out of 41 attempts, 39 holes were drilled in various areas of the summit plateau of Conical Seamont with only two core barrels returning without recovery (Table 1). The total penetration achieved was more than 91 m with individual penetration varying between 0.95 and 5.00 m (avg. 2.2 m). With an average recovery of 31 %, almost 21 m of core were recovered with individual core length of up to 1.5 m (avg. 0.51 m).

Table 1. Drilling statistics for sites Conical Sea-mount (New Ireland fore-arc) and Pacmanus/Roman Ruins (Manus Basin)

Parameter	Conical Smt.	Roman Ruins
Number of holes	41	10
Technical failures	2	0
Holes without recovery	2	0
Total penetration	91.07 m	35.55 m
Individual penetration	0.95-5.00 m	2.06-5.00 m
Average penetration	2.34 m	3.56 m
Total core length	20.76 m	11.07 m*
Individual core length	0-1.50 m	0.35-2.20 m
Average core length	0.51 m	1.11 m
Average recovery	31 %	31 %
Individual recovery	0-100 %	9-65 %

*8.87 m of massive sulfide

Drilling at Conical Seamont has confirmed the sub-seafloor extend of surface gold mineralization and associated epithermal-style alteration to a depth of at least 4.5 m below the seafloor and further proven analogies to the giant Ladolam epithermal gold deposit on Lihir Island. Drill core samples of clay-silica alteration contain gold grades up to 14.2 g/t Au over a section of 30 cm (30 g fire assay: Lihir Gold Ltd.) and appear to be part of a more extensive gold zone located below a carapace of relatively fresh ankaramite and trachybasalt. These samples contain a complex mineralogy including realgar, orpiment, galena, sphalerite, some chalcocopyrite and pyrite, together with amorphous silica, and possibly cinnabar. In addition to high concentrations of gold, shipboard XRF analyses indicate that the gold-rich samples contain high values of Pb (2.6 wt.%), As (8666 ppm), and Sb (1083 ppm), which is a characteristic feature of a magmatic-hydrothermal style of mineralization and alteration.

Drilling of 10 holes in only two days at Roman Ruins (Pacmanus site) has achieved a total penetration of almost 36 m with four of the holes penetrating close to 5 m into the massive sulfides. The average penetration was 3.6 m (2.1-5.0 m) with a recovery of about 31 % (9-65 %), resulting in about 11 m of core of which almost 9 m are spectacularly

textured massive sulfides. The longest sulfide cores taken measured 2.2 m (penetration 4.9 m), 1.9 m (penetration 5.0 m), and 1.4 m (penetration 2.8 m). The massive sulfides consist of sphalerite, chalcopyrite, pyrite, galena, tennantite, barite, anhydrite, and amorphous silica. Nodular chalcopyrite-anhydrite breccia occurring in part of the core is similar in nature to core samples recovered from the TAG hydrothermal field at the Mid-Atlantic Ridge during ODP Leg 158 in 1994 (Herzig et al., 1998, Humphris et al., 1995). Two out of 10 holes recovered least altered dacite. Drilling has shown that massive sulfide mineralization at Roman Ruins extends to a depth of at least 5 m.



Figure 2. BGS Rockdrill during drilling operations with R/V Sonne at Conical Seamount (New Ireland fore-arc, PNG).

Spectacular concentrations of gold were found in several core sections including 0.5 m @ 29 g/t Au, 0.35 m @ 30 g/t Au, and 0.20 m @ 58 g/t Au further proving the gold-rich nature of the Pacmanus hydrothermal field.

4 CONCLUSIONS

The successful drilling and coring operations with the BGS Rockdrill and R/V Sonne indicate that shallow seafloor drilling is filling the sampling gap between the seafloor and the deeper parts of a seafloor hydrothermal system. Drilling at Conical Seamount and Roman Ruins has provided information not previously available and attests to significant subsurface mineralization in both areas. Drilling results obtained by drilling at the summit plateau of Conical Seamount now conclusively indicate that deeper drilling is required (and justified) to fully assess the gold resource of this deposit. At Roman Ruins, drilling with the BGS Rockdrill has not only proven the existence of massive sulfides in the sub-seafloor but also demonstrated their gold-rich nature. Shallow seafloor drilling will likely become a future standard practice in the evaluation of seafloor hydrothermal systems and systems such as the Rockdrill may even

advance to mission specific platform status within the new phase of ocean drilling (IODP).

ACKNOWLEDGEMENTS

Cruise SO-166 was funded by the German Federal Ministry for Education and Research through a grant to PMH. Additional funding through the Leibniz Program of the German Research Association is greatly acknowledged.

REFERENCES

- Binns, R. A., Barriga, F., & Miller, D. J., 2002. Leg 193 summary, Proceedings of the Ocean Drilling Program, Initial Reports, 193, College Station, TX: 1-84.
- Herzig, P.M., Hannington, M.D., McInnes, B., Stoffers, P., Villinger, H., Seifert, R., Binns, R., Liebe, T., and Scientific Party R/V Sonne cruise SO-94, 1994. Submarine volcanism and hydrothermal venting studied in Papua, New Guinea. *Transactions American Geophysical Union, Eos*, 75, 513-516.
- Herzig, P.M. and Hannington, M.D., 1995. Hydrothermal activity, vent fauna, and submarine gold mineralization at alkaline fore-arc seamounts near Lihir Island, Papua New Guinea. Proceedings Pacific Rim Congress 1995, Australasian Institute of Mining and Metallurgy, 279-284.
- Herzig, P. M., Humphris, S. E., Miller, D. J., and Zierenberg, R. A., eds. 1998. Proceedings of the Ocean Drilling Program, Scientific Results, Leg 158, College Station, TX: 47-70.
- Herzig, P.M., Hannington, M.D., Stoffers, P., and Shipboard Scientific Party, 1998. Petrology, gold mineralization and biological communities at shallow submarine volcanoes of the New Ireland Fore-Arc (Papua New Guinea). *InterRidge*, 7, 34-38
- Herzig, P.M., Petersen, S., and Hannington, M.D., 1999. Epithermal-type gold mineralization at Conical seamount: a shallow submarine volcano south of Lihir Island, Papua New Guinea. In: Stanley et al. (eds), Proceedings SGA-IAGOD Meeting
- Humphris, S. E., Herzig, P. M., Miller, D. J., Alt, J. C., Becker, K., Brown, D., Brüggemann, G., Chiba, H., Fouquet, Y., Gemmill, J. B., Guerin, G., Hannington, M. D., Holm, N. G., Honnorez, J. J., Iturrino, G. J., Knott, R., Ludwig, R., Nakamura, K., Petersen, S., Reysenbach, A.-L., Rona, P. A., Smith, S., Sturz, A. A., Tivey, M. K., & Zhao, X., 1995. The internal structure of an active sea-floor massive sulphide deposit. *Nature*, 377, 713-716.
- Zierenberg, R.A., Fouquet, Y., Miller, D.J., Bahr, J.M., Baker, P.A., Bjerkgard, T., Brunner, C.A., Duckworth, R.C., Gable, R., Gieskes, J., Goodfellow, W.D., Gröschel-Becker, H.M., Guerin, G., Ishibashi, J., Iturrino, G., James, R.H., Lackschewitz, K.S., Marquez, L.L., Nehlig, P., Peter, J.M., Rigsby, C.A., Schultheiss, P., Shanks III, W.C., Simoneit, B.R.T., Summit, M., Teagle, D.A.H., Urbat, M., and Zuffa, G.G., 1998. The deep structure of a sea-floor hydrothermal deposit. *Nature*, 392, 485-488.

Shallow submarine gold mineralization at Conical Seamount, Papua New Guinea: Initial results of an alteration halo study

T. Monecke, S. Petersen, P.M. Herzig, R. Petzold, & R. Kleeberg
Institute of Mineralogy, Freiberg University of Mining and Technology, Germany

Keywords: shallow marine hydrothermal systems, gold deposits, alteration mineralogy

ABSTRACT: Trachybasalt of different alteration styles and intensities is the host to shallow submarine gold mineralization at Conical Seamount, Papua New Guinea. The gold-rich mineralization is confined to sulfide-bearing, black, amorphous silica-dominated veins hosted by silicic-altered trachybasalt as well as to disseminated sulfides or pyrite/marcasite veinlets contained in intensely argillic-altered host rocks. This association of gold is comparable to that of epithermal gold deposits occurring on land. The mineralogical composition of the hydrothermally altered trachybasalt suggests that the gold mineralization at Conical Seamount formed from near-neutral to weakly acidic and relatively reducing hydrothermal fluids.

1 INTRODUCTION

Between September 15 and October 4, 2002 cruise SO-166 of the German *RV Sonne* conducted drilling of a submarine gold mineralization at Conical Seamount in the New Ireland Basin of Papua New Guinea, employing a portable hard rock drilling device of the British Geological Survey (Herzig et al. this volume; Petersen et al. this volume). The shallow drilling confirmed the occurrence of widespread alteration and gold mineralization in the summit area of the seamount as inferred from previous investigations (Herzig et al. 1998, 1999; Petersen et al. 2002). Conical Seamount is located approximately 10 km south of the island of Lihir which is known for the giant Ladolam epithermal gold deposit (Moyle et al. 1990). The present paper reports preliminary results of an alteration halo study that is currently conducted on the drill core material. The aim of the mineralogical investigations is to provide new data constraining the character of the mineralizing fluids in this shallow marine hydrothermal system.

2 GEOLOGICAL SETTING

The Bismarck Archipelago, northeast of the main island of Papua New Guinea, consists of a series of islands (New Hanover, New Ireland, and Bougainville) that formed in an island arc position with respect to subduction of the Pacific plate along the Manus-Kilinau trench (Figure 1). The westward

subduction along this trench stopped in the Early Miocene due to the collision of the Ontong-Java plateau with the trench (Coleman & Kroenke 1981). The stalling of the subduction zone was accompanied by a subduction reversal resulting in the formation of the New Britain trench, at which the Solomon Sea microplate is currently subducted in a northward direction under the South Bismarck microplate (McInnes & Cameron 1994). Present day island arc volcanism occurs at the island of New Britain and back-arc basin extension takes place in the Manus Basin (Figure 1).

Conical Seamount belongs to the NW-SE trending Tabar-Lihir-Tanga-Feni volcanic chain that extends for approximately 260 km parallel to the coast line of New Ireland (Figure 1). The volcanism in the area belongs to a high-K calc-alkaline magma series and includes alkali-olivine basalts, trachybasalts, and foid-bearing mafic rocks (Kennedy et al. 1990). The melting appears to be related to the extension of the thickened crust of the New Ireland Basin where partial melts have risen through the old fore-arc crust along reactivated NE-SW trending faults (McInnes & Cameron 1994). The oldest volcanic rocks of the Tabar-Lihir-Tanga-Feni volcanic chain formed at Simberi Island at approximately 3.6 Ma (Rytuba et al. 1993).

Conical Seamount is the largest of a series of seamounts south of Lihir and has a basal diameter of approximately 2.8 km. The seamount is a simple volcanic cone that rises to more than 600 m above the surrounding seafloor to a water depth of 1050 m

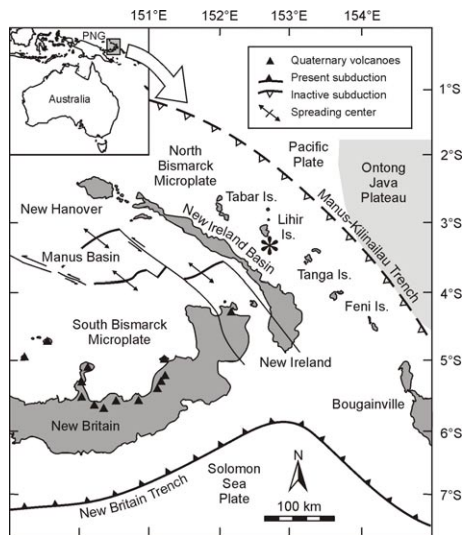


Figure 1. Map of the Bismarck Archipelago with the position of Conical Seamount (Herzig et al. 1998). The inset shows the location of the area northeast of the island of Papua New Guinea (PNG).

(Herzig et al. 1998, 1999). Conical Seamount has a small summit plateau with a relatively smooth topography permitting sampling with grab and drilling devices. Drilling of the mineralized zone and the surrounding trachybasalt during cruise SO-166 was successfully performed at a close spacing in the summit area to a maximum penetration of 5 m (Figure 2).

3 MATERIALS AND METHODS

The drill core material was initially logged on board to record variations in the relative abundance of alteration minerals with depth and to document alteration textures visible in hand specimens. Representative thin sections were prepared for petrographic inspections and 50 quarter core samples (25 to 60 cm core) were crushed to a grain size below 2 mm with an impact mill for whole-rock mineralogical and geochemical investigations. The crushed samples were repeatedly washed with distilled water to remove seawater salt. The washed material was then split with a riffle splitter and one split was taken for XRD analysis.

The preparation of XRD samples involved further crushing of the samples to a grain size below 0.4 mm. The finely crushed material was split and 1.80 g sample material and 0.20 g synthetic ZnO used as an internal standard for XRD analysis were mixed. Subsequent fine grinding to a grain size below 10 µm was performed under ethanol in a vibratory

McCrone micronizing mill for 5 min. After drying, the fine powder was homogenized in a vibrating mixer mill. The powder was then filled into a conventional top-loading holder. Step-scan XRD data were obtained on an URD-6 (Seifert-FPM) diffractometer that was equipped with a diffracted-beam graphite monochromator and a variable divergence slit. A Co tube was utilized and operated at 40 kV and 30 mA. Qualitative phase-analysis of the raw diffraction patterns was performed by a conventional search/match procedure. Subsequent quantitative phase analysis was conducted by the analytical procedure described by Monecke et al. (2001).

4 RESULTS

The results of the quantitative phase analysis were used for hierarchical cluster analysis by the Ward's method (squared Euclidean distance) to classify the samples numerically. The statistical analysis showed that four clusters can be distinguished due to significant compositional differences between individual groups of samples. These differences are interpreted to reflect variations in the style and intensity of the hydrothermal wall rock alteration because the petrographic evidence as well as seafloor observations suggest that the entire summit area of the Conical Seamount is covered by trachybasalt that probably showed little variation in its primary mineralogical composition.

The first group of samples primarily consists of diopside, Ca-rich plagioclase, Na-rich sanidine, biotite, magnetite, and volcanic glass. Quantitative phase analysis revealed that volcanic glass is an important component of this group of trachybasalts forming 10 to 35 wt.% of the samples. Diopside and feldspars occur in concentrations ranging from 30 to 35 wt.% and 30 to 45 wt.%, respectively. The biotite and magnetite contents of the samples are typically below 6 wt.%. Thin section inspection suggests that this group of samples was not significantly affected by hydrothermal alteration. Clinopyroxene and plagioclase phenocrysts are texturally unaltered. Clinopyroxene forms idiomorphic prismatic crystals that range in size up to 5 mm. Lath-shaped plagioclase phenocrysts have sizes of up to 1 mm. Some samples contain biotite tablets of similar size. The groundmass of the samples is made up of apparently unaltered volcanic glass with abundant clinopyroxene, biotite, plagioclase, and sanidine microcrysts as well as minor magnetite. Accessory apatite forms small prisms that are frequently located in the clinopyroxene phenocrysts. These least altered trachybasalts are moderately vesicular (10-15 vol.%).

Trachybasalt samples of the second group are composed of 10 to 35 wt.% volcanic glass in addition to 25 to 35 wt.% diopside, 30 to 40 wt.% feldspar and <6 wt.% biotite. Several trachybasalt samp-

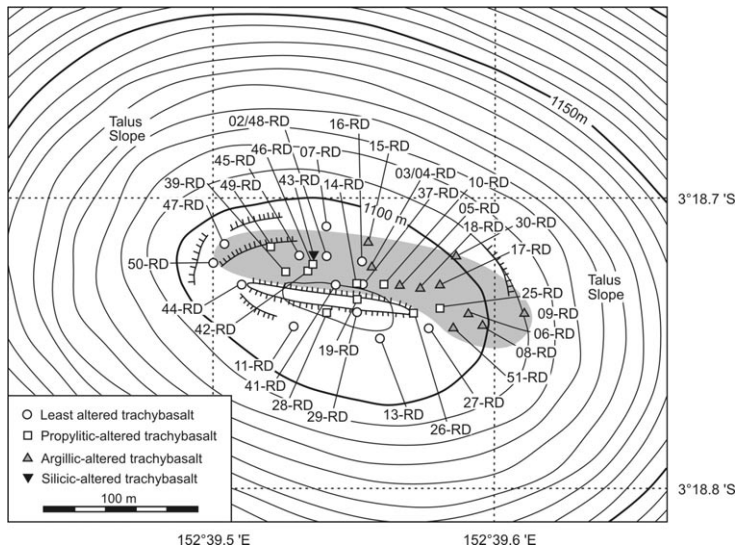


Figure 2. Bathymetric map of the summit area of Conical Seamount and locations of the BGS Rockdrill stations (modified after Petersen et al. 2002). The map also shows the distribution of samples of different alteration styles. The shaded area indicates the extent of surface and sub-surface gold mineralization as constrained by shallow drilling during research cruise SO-166.

les of this group contain analcime and K-rich monoclinic feldspar that occur in concentrations up to 10 wt.% and 4 wt.%, respectively. Pyrite and marcasite are relatively abundant phases and collectively form up to 6 wt.% of the rocks investigated. These samples contain lower amounts of magnetite (<4 wt.%) when compared to the least altered samples. Petrographic investigations revealed that pyrite and marcasite frequently occur as vesicle fillings or as small grains disseminated throughout the glassy groundmass. The sulfides also form pseudomorphs after primary magnetite or occur along fractures in clinopyroxene phenocrysts. The textural observations suggest that the samples of this group were only affected by weak hydrothermal alteration. The degree of textural preservation and the formation of secondary sulfides and zeolites are comparable to propylitic-altered volcanic rocks in some gold deposits on land.

The third group of samples is typified by the occurrence of substantial amounts of clay minerals in addition to variable amounts of volcanic glass. The concentration of diopside ranges from 15 to 30 wt.%. In addition to primary plagioclase and sanidine (35 to 50 wt.%), several samples of this suite contain K-rich monoclinic feldspar (up to 5 wt.%) as a product of the hydrothermal alteration. The biotite content is variable and magnetite is usually absent in trachybasalt of this group. The whole rock samples contain abundant pyrite and marcasite that collectively occur in concentrations up to 10 wt.%. Thin section inspection showed that the glassy

groundmass of the trachybasalt is largely replaced by clay minerals. The clinopyroxene phenocrysts are also partially replaced by fine grained secondary minerals including clay minerals and sulfides such as pyrite and marcasite. These sulfides also form pseudomorphs after primary magnetite or occur as small veinlets or aggregates disseminated throughout the groundmass of the altered volcanic rocks.

A single sample was found to contain up to 60 wt.% amorphous silica and clay minerals. K-rich monoclinic feldspar is an abundant phase occurring in concentrations up to 15 wt.%. In addition to pyrite and marcasite, galena and sphalerite were identified by XRD. Thin section inspection showed that pyroxene, plagioclase, and magnetite phenocrysts are completely destroyed and have been replaced by clay minerals, amorphous silica, and sulfides. Sulfides, clays, and euhedral adularia crystals are dispersed throughout the groundmass of the trachybasalt that is replaced by amorphous silica. In addition, the dark gray to black, porous amorphous silica fills the vesicles of the silicic-altered rocks. Arsenic sulfides such as realgar and orpiment are present in small amounts.

5 DISCUSSION

Drilling during research cruise SO-166 revealed that hydrothermal alteration at Conical Seamount is heterogeneous and that least altered trachybasalt is common in the upper five meters accessible to shal-

low drilling. The spatial distribution of the mineral associations is distinguished on the basis of the quantitative phase analysis (Figure 2). Hydrothermally altered samples were mainly recovered from the northern and eastern portions of the plateau whereas apparently unaltered trachybasalt was sampled from the southern part of the summit area. Camera surveys across several hundreds meters of the top of the Conical Seamount suggest that the zone of hydrothermal alteration and gold mineralization is separated from the area of least altered trachybasalt by an approximately 100 m long, east-west striking volcanic feature that may represent the feeder to an effusive eruption that covered the southern part of the summit area. This interpretation is in agreement with the occurrence of intensely altered material below least altered basalt in some drill cores. For instance, station 47-RD cored least altered trachybasalt in the upper 1.1 m whereas intensely altered material was recovered from the base of the 5 m deep drill hole (Herzig et al. 2003). Therefore, it seems possible that the entire top part of Conical Seamount is altered and mineralized at depth, but was partially covered by younger lava.

Previous investigations have shown that high gold grades in whole-rock samples are related to the occurrence of sulfide-bearing, black, amorphous silica-dominated veins (Herzig et al. 1999; Petersen et al. 2002). This association of gold as well as the textural, petrological, geochemical, and isotopic evidence indicates similarities between Conical Seamount and some epithermal systems on land. The results of the present study suggest that the deposition of gold in the sulfide-bearing siliceous veins was associated with a silicification of the host rocks whereas the pyrite and marcasite stockwork mineralization is typically hosted by argillic- and propylitic-altered trachybasalt. The occurrence of pyrite, marcasite, clay minerals, and K feldspar in hydrothermally altered trachybasalt recovered from the summit area of the Conical Seamount as well as the absence of detectable amounts of alunite, pyrophyllite, kaolinite, and zynite in drill core suggests that the alteration largely proceeded in a near-neutral to weakly acidic and relatively reduced low-sulfidation environment.

6 CONCLUSIONS

The gold occurrence of Conical Seamount represents a new type of hydrothermal mineralization at the modern seafloor. Shallow drilling employing a portable hard rock drilling device of the British Geological Survey revealed that the alteration mineralogy of trachybasalt recovered from the northern and eastern part of the summit area can be related to the upflow of near-neutral and reducing fluids to the seafloor. The alteration characteristics are similar to those of

some low-sulfidation epithermal precious metal deposits on land. The proximity of the Conical Seamount to the giant Ladolam deposit on Lihir Island implies that the submarine gold mineralization and the subaerial precious metal deposit may be linked to the same district-scale magmatic event.

ACKNOWLEDGEMENTS

Alteration logging was kindly supported by J.B. Gemmell and M.D. Hannington. We thank L. Franz for providing information on the petrography of the samples recovered during cruise SO-133. The research was supported by the German Federal Ministry of Education and Research through a grant to PMH (03G166A). Additional funding was provided by the Leibniz-Program of the German Research Foundation (DFG).

REFERENCES

- Coleman, P.J. & Kroenke, L.W. 1981. Subduction without volcanism in the Solomon Island arc. *Geo Mar Lett* 1: 129-134.
- Herzig, P.M., Petersen, S. & Hannington, M.D., 1999. Epithermal-type gold mineralization at Conical Seamount: A shallow submarine volcano south of Lihir Island, Papua New Guinea. *Mineral deposits: Processes to processing*. Balkema, Rotterdam. 527-530.
- Herzig, P.M., Hannington, M.D., Stoffers, P. & Shipboard Scientific Party 1998. Petrology, gold mineralization and biological communities at shallow submarine volcanoes of the New Ireland Fore-Arc (Papua-New Guinea): Preliminary results of R/V *Sonne* cruise SO-133. *InterRidge News* 7: 34-38.
- Herzig, P.M., Kuhn, T., Petersen, S. & Shipboard Scientific Party 2003. Cruise report SO-166 CONDRILL. *TU Bergakademie Freiberg*. 145 pp.
- Kennedy, A.K., Hart, S.R. & Frey, F.A. 1990. Composition and isotopic constraints on the petrogenesis of alkaline arc lavas: Lihir island, Papua New Guinea. *J Geophys Res* 95: 6929-6942.
- McInnes, B.I.A. & Cameron, E.M. 1994. Carbonated, alkaline metasomatic melts from a sub-arc environment: Mantle wedge samples from the Tabar-Lihir-Feni arc, Papua New Guinea. *Earth Planet Sci Lett* 122: 125-141.
- Monecke, T., Köhler, S., Kleeberg, R., Herzig, P.M. & Gemmell, J.B. 2001. Quantitative phase-analysis by the Rietveld method using X-ray powder-diffraction data: application to the study of alteration halos associated with volcanic-rock-hosted massive sulfide deposits. *Can Mineral* 39: 1617-1633.
- Moyle, A.J., Doyle, B.J., Hoogvliet, H. & Ware, A.R., 1990. Ladolam gold deposit, Lihir Island. *Geology of the Mineral Deposits of Australia and Papua New Guinea*. Austral Inst Mining Metallurgy, Melbourne. 1793-1805.
- Petersen, S., Herzig, P.M., Hannington, M.D., Jonasson, I.R. & Arribas, A., Jr., 2002. Submarine gold mineralization near Lihir Island, New Ireland fore-arc, Papua New Guinea. *Econ Geology* 97: 1795-1813.
- Rytuba, J.J., McKee, K.H. & Cox, D. 1993. Geochronology and geochemistry of the Ladolam gold deposit, Lihir island, and gold deposits and volcanoes of Tabar and Tatau, Papua New Guinea. *US Geol Surv Bull* 2039: 119-126.

Gold-rich massive sulfides from the interior of the felsic-hosted PACMANUS massive sulfide deposit, Eastern Manus Basin (PNG)

S. Petersen & P.M. Herzig

Leibniz-Laboratory for Applied Marine Research, Freiberg University of Mining and Technology, Germany

M.D. Hannington

Geological Survey of Canada, Ottawa, Canada

J.B. Gemmell

Center of Ore Deposit Research, University of Tasmania, Hobart, Tasmania, Australia

Keywords: drilling, Pacmanus, gold-rich VMS, zone refining

ABSTRACT: Gold- and base metal-rich massive sulfides were recovered from the interior of the PACMANUS hydrothermal field in the Eastern Manus Basin (Papua New Guinea) during a recent cruise of the German Research Vessel Sonne and the 5 m-Rockdrill of the British Geological Survey. Drilling retrieved spectacular massive sulfides±barite, nodular sulfide-anhydrite breccias, resedimented sulfides, as well as clay-altered dacite from depths up to 5 m. The core material consists largely of massive sphalerite, chalcopyrite, barite, and pyrite with subordinate galena and sulfosalts. High proportions of anhydrite and amorphous silica occur in some cores. Most cores display textures similar to those sampled from the surface of the PACMANUS site, however, breccias and resedimented, fine-grained clastic ores are also common. Preliminary analyses reveal high Au and base metal concentrations throughout the cores locally reaching up to 58 g/t Au over 20 cm of core length. The longest core recovered 2.2 m grading 11.3 g/t Au, 156 g/t Ag, 2.4 wt.% Cu, 26.5 wt.% Zn, and 0.9 wt.% Pb. Gold enrichment is clearly related to sphalerite-rich sections of the core. Variations in the base and precious metal content suggest that zone refining of selected elements and multiple episodes of hydrothermal activity have been important for the formation of the PACMANUS hydrothermal field.

1 INTRODUCTION

Gold-rich volcanic-hosted deposits have been found in various tectonic settings on the modern ocean floor. The majority of these Au-rich deposits is found in back-arc basins of the SW Pacific such as the Lau Basin (Herzig et al., 1993), the Manus Basin (Binns and Scott, 1993; Moss and Scott, 1993), the Woodlark Basin (Binns et al., 1993) or at arc volcanoes of the Izu-Ogasawara arc and the New Ireland fore-arc systems (Watanabe and Kajimura, 1994; Iizasa et al., 1999; Herzig et al., 1999; Petersen et al., 2002). Sampling of these modern seafloor deposits to date was largely restricted to the immediate surface and it seems unlikely that the reported base and precious metal grades for these sites are representative for the deposit as a whole. This has clearly been demonstrated by Ocean Drilling Program (ODP) drilling of the TAG hydrothermal mound on the Mid-Atlantic Ridge in 1994 (Humphris et al., 1995; Herzig et al., 1998a). Here, surface sampling prior to drilling has indicated rather high Au, Cu, and Zn values (summarized in *Petersen et al., 2000*). However, drilling indicated that the Au and Zn-enriched surface samples are only from a thin blanket overlying a dominantly barren pyritic massive sulfide body

at depth (Humphris et al., 1995; Herzig et al., 1998b; Petersen et al., 2000). Thus sub-surface drilling is required to fully assess the base and precious metal potential of individual deposits.

Here, we present the results of a recent drilling program with the German R/V Sonne and the portable, 5 m-Rockdrill of the British Geological Survey at the PACMANUS hydrothermal site in the Eastern Manus Basin (cf. Herzig et al., this volume).

2 GEOLOGICAL SETTING

The Manus Basin is a rapidly opening (~10 cm/yr) back-arc basin located between the fossil Manus-Kilinau Trench and the active New Britain subduction zone (Fig. 1). The regional tectonic complexity is a consequence of the northward subduction of the oceanic Solomon Microplate beneath the South Bismarck Microplate within a complex zone of oblique convergence between the major Indo-Australian and Pacific plates (Martinez and Taylor, 1996). True seafloor spreading occurs in the Central and Western Manus Basins, whereas the Eastern Manus Basin is characterized by extensional rifting.

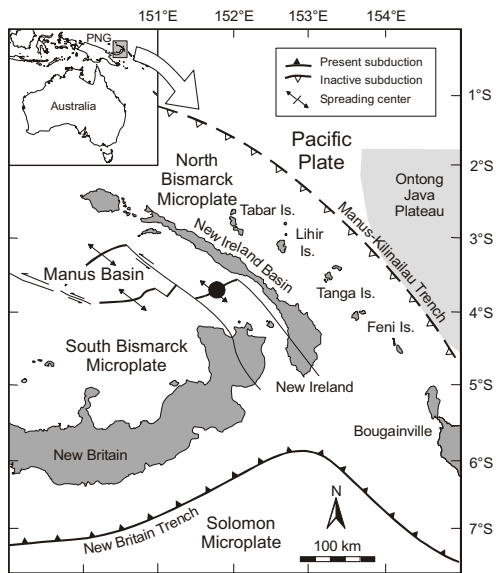


Figure 1. Location and plate tectonic setting of the PACMANUS hydrothermal field (solid circle).

The Eastern Manus Basin, which is host to several massive sulfide deposits including PACMANUS, DESMOS, and Suzu Knolls, is a pull-apart rift zone with east-west trending neovolcanic ridges composed of basaltic to rhyodacitic volcanics (Binns et al., 1993). The basin is bounded by two sinistral transforms, the Djual and Weitin Faults. PACMANUS is situated on the crest of Pual Ridge, an elongated ridge composed of dacite with subordinate basaltic andesite and rhyodacite that stands 500-700 m above the surrounding basin floor. The ridge itself is terraced and consists of stacked 5–30 m thick lava flows (Binns et al., 2002).

Five principal areas of hydrothermal activity (Roman Ruins, Satanic Mills, Tsukushi, Rogers Ruins, and Snowcap) have been delineated at the PACMANUS site. Except for Snowcap, they consist of active and inactive black smoker chimneys and spires on basal sulfide mounds. Hydrothermal fluids escape as acid (pH=2.5-3.5 at 25°C) black to gray smoke with exit temperatures up to 276°C or as clear fluids vigorously venting from nearby sulfide structures (Binns et al., 2002).

The Snowcap site is somewhat different and characterized by outcrops of dacite-rhyodacite lava and hyaloclastite, that are altered by a highly acid, oxidized fluid to an assemblage of cristobalite, less natroalunite, diaspore, and illite-montmorillonite and traces of pyrite, marcasite, chalcocopyrite, enargite, and (formerly molten) globules of native sulfur (Binns et al., 2002). This style of alteration might indicate that SO₂-bearing magmatic components were present in the fluid. A magmatic contribution

to the hydrothermal fluids at PACMANUS was also suggested by various authors because of the presence of high F, SO₂ and elevated gas concentrations in the fluids, and of metal-rich melt inclusions in the host rock (Douville et al., 1999; Yang and Scott, 1996).

3 RESULTS

Drilling at the Roman Ruins site recovered 9 m of spectacular massive sulfides. The sulfide-bearing cores are usually dominated by light brown to black sphalerite with varying proportions of barite, pyrite and chalcocopyrite. Galena and bluish sulfosalts are visible, but occur only as a minor to trace components in the sulfides. Anhydrite, amorphous silica and variably altered dacite fragments occur together with the sulfides. The textures, in most cases, resemble those of sulfides recovered from the surface of the PACMANUS field (Moss and Scott, 2001). Ribbon banded sphalerite as observed in “beehive” smokers at various other seafloor hydrothermal sites is common, as are relics of individual chalcocopyrite-lined chimney orifices.

Drillsite 60RD recovered a sphalerite±chalcocopyrite and barite assemblage underlain by a nodular breccia of rounded chalcocopyrite+pyrite clasts set in a matrix of anhydrite. This nodular texture strongly resembles cores from the central part of the TAG hydrothermal field (Humphris et al., 1995; Herzig et al., 1998a). The presence of abundant anhydrite within this core is indicative of seawater penetrating into the massive sulfide mound and mixing with the hydrothermal fluid and/or conductively cooling in the subsurface. The nodular appearance of the pyrite+chalcocopyrite fragments suggests that massive sulfides are reworked and transported. This is confirmed by several cores that contain layers of fine-grained, clastic chalcocopyrite+pyrite sand.

A 20 cm thick layer of massive dense chalcocopyrite separating layers of porous massive sphalerite has been sampled in the upper part of one hole, while other holes contain a similar section where chalcocopyrite is intergrown with black sphalerite. The complex intergrowths observed throughout the core sections imply a multi-staged hydrothermal evolution of the deposit.

Four of the holes drilled at Roman Ruins penetrated close to 5 m into the massive sulfide mound. Out of these, two holes (61RD and 69RD) ended in weakly to intensely altered dacite possibly indicating that sulfide formation here is limited to a thin veneer directly above and below the seafloor. Core 69RD recovered 1.8 m (core length 2.2 m) of massive sulfide overlying strongly clay-silica altered and sulfide veined dacite that mark the onset of the stockwork zone.

Preliminary analyses of quarter core sections (varying in length from 10 to 50 cm) using Instrumental Neutron Activation (Au, Ag) and assaying for Cu, Zn, and Pb indicate high base and precious metal contents for the cores averaging close to 13 g/t Au, 167 g/t Ag, 22 wt.% Zn, 5 wt.% Cu, and 1 wt.% Pb. The most impressive grades come from hole 65RD which returned 0.4 m @ 35.5 g/t Au, 232 g/t Ag, 7.1 wt.% Cu, 26.9 wt.% Zn, and 0.6 wt.% Pb including a section of 0.2 m with 57.7 g/t Au. Another exceptional result came from hole 66RD, which returned 0.8 m @ 20.2 g/t Au, 180 g/t Ag, 7.7 wt.% Cu, 25.8 wt.% Zn, and 0.2 wt.% Pb. The longest core (69RD; penetration: 4.9 m) recovered 2.2 m @ 11.3 g/t Au, 156 g/t Ag, 2.4 wt.% Cu, 26.5 wt.% Zn, and 0.9 wt.% Pb.

Gold enrichment throughout the cores is related to sphalerite-rich sections of the cores (Fig. 2). The highest grade occurs in dark brown to black sphalerite that is associated with abundant chalcopyrite and was presumably deposited at higher temperatures. However, core sections that contain ribbon-banded, light brown sphalerite are also enriched in gold. Low precious metal concentrations, despite high concentrations of Zn and Cu, have been observed in the lower parts of some cores possibly indicating that zone refining is responsible for some of the precious metal enrichment observed at PACMANUS. This is consistent with the low Au contents in the reworked nodular chalcopyrite + pyrite + anhydrite breccias.

TV-guided grab sampling that accompanied the drilling program recovered massive sulfides, as well as active and inactive chimneys from the Satanic Mills and Roman Ruins sites. Some samples from the mound surface at Roman Ruins show a knife-edge contact between least altered, black dacitic hyaloclastite set in a matrix of porous sphalerite and intensely clay-altered white dacite fragments cemented by chalcopyrite, pyrite and sphalerite. This suggests the presence of an alteration or high temperature front just below the seafloor. A strongly siliceous, black to dark brown layer occurs in several samples suggesting the presence of a siliceous cap in certain areas.

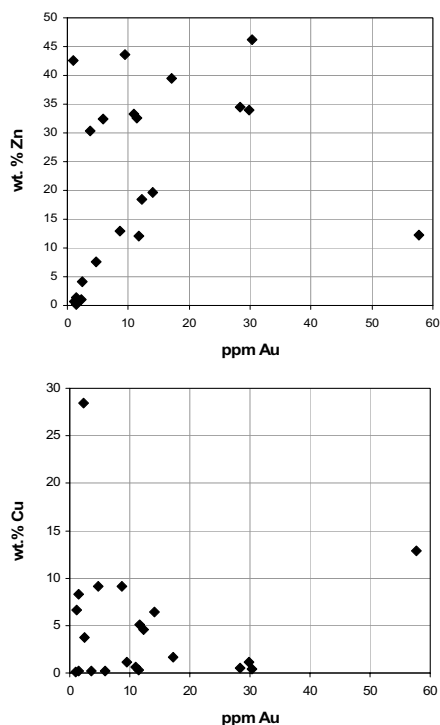


Figure 2. Covariation of Zn (top) and Cu (bottom) with Au in massive sulfides drilled from the PACMANUS hydrothermal field.

4 CONCLUSION

Drilling the upper parts of the PACMANUS hydrothermal field recovered spectacular massive sulfides and indicates high precious and base metal contents below the surface of the deposit. Gold enrichment is often related to Zn-rich parts of the core sections. The abundance of anhydrite and the occurrence of reworked sulfides implies that seawater penetration, reworking of primary sulfide material and possibly episodic hydrothermal activity are important processes at PACMANUS. A decrease in Au-concentration down hole suggests that the complex hydrothermal activity at the PACMANUS site resulted in zone refining of Au enriching the surface sulfides.

ACKNOWLEDGEMENTS

This project is funded by the German Federal Ministry for Education and Research through a grant to PMH (grant: 03G0166A). Additional funding was provided by the Leibniz Program of the German Research Association. JBG thanks the Australian Research Centers program and CODES.

REFERENCES

- Binns, R.A., Barriga, F., & Miller, D.J., 2002. Leg 193 summary, *Proceedings of the Ocean Drilling Program, Initial Reports, 193*, College Station, TX: 1-84.
- Binns, R.A., & Scott, S.D., 1993. Actively forming polymetallic sulfide deposits associated with felsic volcanic rocks in the eastern Manus back-arc basin, Papua New Guinea: *Economic Geology* 88: 2222-2232.
- Binns, R.A., Scott, S.D., Bogdanov, Y.A., Lisitsyn, A.P., Gordeev, V.V., Gurvich, E.G., Finlayson, E.J., Boyd, T., Dotter, L.E., Wheller, G.E., & Muravyev, K.G., 1993. Hydrothermal oxide and gold-rich sulfate deposits of Franklin Seamount, western Woodlark Basin, Papua New Guinea: *Economic Geology* 88: 2122-2153.
- Douville, E., Bienvenu, P., Charlou, J.-L., Donval, J.P., Fouquet, Y., Appriou, P., & Gamo, T., 1999. Yttrium and rare earth elements in fluids from various deep-sea hydrothermal systems: *Geochimica et Cosmochimica Acta* 63: 627-643.
- Herzig, P.M., Hannington, M.D., Fouquet, Y., von Stackelberg, U., & Petersen, S., 1993. Gold-rich polymetallic sulfides from the Lau back-arc and implications for the geochemistry of gold in sea-floor hydrothermal systems in the Southwest Pacific: *Economic Geology* 88: 2182-2209.
- Herzig, P.M., Humphris, S.E., Miller, D.J., and Zierenberg, R. A., (eds), 1998a. Proceedings of the Ocean Drilling Program, Scientific Results, College Station, TX.
- Herzig, P.M., Petersen, S., & Hannington, M.D., 1998b. Geochemistry and sulfur-isotopic composition of the TAG hydrothermal mound, Mid-Atlantic Ridge, 26°N, in Herzig, P. M., Humphris, S. E., Miller, D. J., and Zierenberg, R. A., eds., *Proc. ODP, Scientific Results, 158*, College Station, TX: 47-70.
- Herzig, P.M., Petersen, S., & Hannington, M.D., 1999. Epithermal-type gold mineralization at Conical Seamount: a shallow submarine volcano south of Lihir Island, Papua New Guinea, in Stanley, C.J., ed., *Mineral Deposits: Processes to Processing, Proceedings of the fifth biennial SGA meeting and the tenth Quadrennial IAGOD symposium London*, p. 527-530.
- Humphris, S.E., Herzig, P.M., Miller, D.J., Alt, J.C., Becker, K., Brown, D., Brüggmann, G., Chiba, H., Fouquet, Y., Gemmell, J.B., Guerin, G., Hannington, M.D., Holm, N. G., Honnorez, J.J., Iturino, G.J., Knott, R., Ludwig, R., Nakamura, K., Petersen, S., Reysenbach, A.-L., Rona, P. A., Smith, S., Sturz, A.A., Tivey, M.K., & Zhao, X., 1995. The internal structure of an active sea-floor massive sulphide deposit: *Nature* 377: 713-716.
- Iizasa, K., Fiske, R.S., Ishizuka, O., Yuasa, M., Hashimoto, J., Ishibashi, J., Naka, J., Horii, Y., Fujiwara, Y., Imai, A., & Koyama, S., 1999. A Kuroko-type polymetallic sulfide deposit in a submarine silicic caldera: *Science* 283: 975-977.
- Martinez, F., & Taylor, B., 1996. Backarc spreading, rifting, and microplate rotation, between transform faults in the Manus Basin, in Auzende, J.M., and Collot, J.Y., eds., *Sea-floor mapping in the West, Southwest and South Pacific: results and applications.*, 18. *Marine Geophysical Researches*: D. Reidel Publishing Company: 203-224.
- Moss, R., & Scott, S.D., 2001. Geochemistry and mineralogy of gold-rich hydrothermal precipitates from the Eastern Manus Basin, Papua New Guinea: *Canadian Mineralogist* 39: 957-978.
- Petersen, S., Herzig, P.M., & Hannington, M.D., 2000. Third dimension of a presently forming VMS deposit: TAG hydrothermal mound, Mid-Atlantic Ridge, 26°N: *Mineralium Deposita* 35: 233-259.
- Petersen, S., Herzig, P.M., Hannington, M.D., Jonasson, I.R., & Arribas, A., 2002. Submarine vein-type gold mineralization near Lihir island, New Ireland fore-arc, Papua New Guinea. *Economic Geology* 97: 1795-1813.
- Watanabe, K., & Kajimura, T., 1994. The hydrothermal mineralization at Suiyo Seamount, in the central part of the Izu-Ogasawara Arc: *Resource Geology* 44: 133-140.
- Yang, K., & Scott, S. D., 1996. Possible contribution of a metal-rich magmatic fluid to a sea-floor hydrothermal system: *Nature* 383: 420-423

Meeresbodenkartierung in der Umgebung von Lihir Island (Papua-Neuguinea) mit der Fächerecholotanlage auf FS SONNE während der Forschungsfahrten SO-94, SO-133 und SO-166: 3D-Modellierung der bathymetrischen Daten und tektonische Interpretation

Thomas Kuhn¹, Mark Hannington², Sven Petersen¹ und Peter Herzig¹

¹TU Bergakademie Freiberg, Lehrstuhl für Lagerstättenlehre und Petrologie und Leibniz-Labor für Angewandte Meeresforschung, Brennhausgasse 14, D-09596 Freiberg; e-mail: kuhnto@mineral.tu-freiberg.de

²Geological Survey of Canada 601 Booth Street; Ottawa, ON K1A 0E8; Canada

1 Einführung

Während der Forschungsfahrten SO-94, SO-133 und SO-166 wurden umfangreiche Meeresbodenkartierungen in der Umgebung von Lihir Island (Papua-Neuguinea) durchgeführt (Abb. 1). Dazu wurde die auf FS SONNE installierte Fächerecholotanlage verwendet (während SO-94 und 133 war dies das von Krupp Atlas stammende System HYDROSWEEP, während SO-166 das von Simrad stammende System EM 120). Die wiederholten Kartierungen im Arbeitsgebiet ermöglichten die Erfassung der Meeresbodentopographie in der Umgebung von Lihir Island auf einer Fläche von 70 km x 85 km.

Die Daten der drei Forschungsfahrten wurden zusammengefügt und die entsprechenden Übersichtskarten mit 90 m Gridweite mit dem Programmpaket GMT[®] erstellt, was die Analyse von großräumigen Meeresbodenstrukturen erlaubt. Für die 3D-Modellierung wurden die xyz-Daten als ASCII-Datei in das Programmpaket gOcad[®] importiert. Das Programm ermöglicht die Modellierung der Meeresbodenoberfläche mittels Triangulation zwischen den Datenpunkten.

2. Ergebnisse

Die Umgebung von Lihir Island ist Teil des Neuirlandbeckens, einem ehemaligen Forearc-Bereich, der zwischen der heute inaktiven Manus-Kilinau-Subduktionszone und der Insel Neuirland liegt (Abb. 1, Inset). Auf der Südwestseite von Neuirland befindet sich das Manus-Backarc-Becken, das durch aktive Spreizung charakterisiert ist. Es kann strukturell als Pull-Apart-Becken zwischen zwei sinistralen Transformstörungen beschrieben werden (Weitin und Djaul Störungszonen; vgl. Binns et al., 2002).

Die Meeresbodentopographie in der unmittelbaren Umgebung von Lihir Island wird durch submarine Rutschmassen und Sedimentfächer geprägt, die überwiegend aus dem terrigenen Abtragungsschutt der Insel bestehen. Der Sedimentfächer nordöstlich des Luisevulkans ist auf einen Sektorkollaps der Nordostflanke des

Vulkans zurückzuführen und zeigt die lokale Bedeutung tektonischer Ereignisse in diesem Gebiet auch für die Topographie (siehe Abb. 1). Terrigene Sedimentablagerungen füllen auch das Neuirlandbecken zwischen Neuirland und Lihir Island mit bis zu 7 km Mächtigkeit auf (Marlow et al., 1988).

Obwohl die Sedimente die strukturellen Merkmale des Neuirlandbeckens teilweise überdecken, können die jüngsten, aktiven tektonischen Elemente deutlich erkannt werden. Dies betrifft insbesondere die grabenförmigen Einsenkungen im zentralen Bereich des Beckens, die die älteren Sedimentablagerungen durchschneiden. Diese Strukturen verlaufen mit ihrem NW-SE orientiertem Streichen nahezu parallel zu den regionalen Transformstörungen im östlichen Manus Becken (Weitin und Djaul Transformstörung) sowie zur jetzt inaktiven Manus-Kilinailau-Subduktionszone (vgl. Gennerich, 2002). Die grabenförmigen Einsenkungen werden als rezente Dehnungsstrukturen interpretiert, die infolge von Blockrotationen zwischen den regionalen, linkslateralen Transformstörungen entstehen (Hannington et al., 2002). Als weitere Merkmale treten NNE-SSW sowie NE-SW orientierte Strukturen auf, die als konjugiertes Scherstörungspaar (Riedelscherflächen) interpretiert werden können und ihre Entsprechung in Störungszonen auf Neuirland finden (z.B. Rataman und Matakan Störungszonen; Hannington et al., 2002).

Die submarinen Vulkane Conical Seamount (epithermale Goldvererzung; Herzig et al., 1999; Petersen et al., 2002), Edison Seamount (niedrig-temperierte, diffuse hydrothermale Aktivität im Krater des Seamounts; Herzig et al., 1998) und TUBAF Seamount (submariner Vulkan mit Mantelxenolithen in Eruptivgesteinen; Franz et al., 2001) liegen alle im Streichen, teilweise sogar im Schnittpunkt der genannten Strukturelemente (Abb. 1). Die Xenolithe des TUBAF Seamount stellen einen Querschnitt durch die Forearc-Lithosphäre dar, die beim Aufstieg der Magmen mitgerissen wurden. Ihre Existenz belegt, dass die Störungen bis in große Tiefen reichen (ca. 30-70 km; Franz et al., 2001). Trotz sehr hoher Sedimentationsraten in unmittelbarer Umgebung von Lihir Island (ca. 50 mm/Jahr) ist der Gipfelbereich des TUBAF Seamounts kaum mit Sediment bedeckt, was auf ein geringes Alter der letzten Eruption hinweist. Damit sollten auch die Störungen, an deren Schnittpunkt der TUBAF Seamount auftritt, rezent aktiv sein.

3. Schlußfolgerungen

Auf der Grundlage der bathymetrischen Daten (2D- und 3D-Darstellung) können verschiedene Strukturelemente im Neuirlandbecken zwischen Neuirland und Lihir Island analysiert werden. Diese widerspiegeln die rezente Extension in diesem ehemaligen Forearc-Becken als Reaktion auf die tektonischen Bewegungen und das Backarc-Spreading im östlichen Manus Becken. Es wird vermutet, dass es sich bei den großen NW-SE orientierten Störungen um reaktivierte Strukturen (Tabar Fault?)

aus der Zeit der aktiven Subduktion entlang der Manus-Kilinailau-Subduktionszone handelt.

Literatur

- Binns, R.A., Barriga, F.J.A.S. and Miller, D.J., 2002. Proceedings of the Ocean Drilling Program, Initial Reports, 193, College Station, TX, 84 pp.
- Franz, L., Becker, K.-P., Kramer, W. and Herzig, P.M., 2001. Metasomatic mantle xenoliths from Bismarck microplate (Papua New Guinea) - petrologic and geochemical consequences and extent of slab induced metasomatism. *Journal of Petrology*, 43: 315-343.
- Gennerich, H., 2002. Der Tabar-Feni-Inselbogen und sein plattentektonisches Regime oder wie entsteht ein Inselbogen ohne eine aktive Subduktionszone. Shaker Verlag, Aachen, 196 pp.
- Hannington, M., Kuhn, T. and Petersen, S., 2002. Seafloor Mapping and Structural Geology. In: P.M. Herzig, T. Kuhn and S. Petersen (Editors), Detail Investigation of the Magmatic-Hydrothermal Gold Mineralization at Conical Seamount (New Ireland Basin, Papua New Guinea) and of Massive Sulfides at PACMANUS (Eastern Manus Basin, PNG) by Shallow Drilling - Cruise Report of RV SONNE cruise SO-166. Project No. 03G0166A, Freiberg University.
- Herzig, P.M., Hannington, M.D., Stoffers, P. and shipboard scientific party, 1998. Volcanism, Hydrothermal Processes and Biological Communities at Shallow Submarine Volcanoes of the New Ireland Fore-Arc (Papua New Guinea), Freiberg University of Mining and Technology.
- Herzig, P.M., Petersen, S. and Hannington, M.D., 1999. Epithermal-type gold mineralization at Conical Seamount: A shallow submarine volcano south of Lihir Island, Papua New Guinea. In: C.J. Stanley (Editor), *Mineral Deposits: Processes to Processing*. A.A. Balkema, London, pp. 527-530.
- Marlow, M.S., Exon, N.F., Ryan, H.F., and Dadisman, S.V., 1988. Offshore structure and stratigraphy of New Ireland Basin in northern Papua New Guinea, In: Halbouty, M. T. (Editor), *Geology and offshore resources of Pacific island arcs; New Ireland and Manus region, Papua New Guinea.*, 9. Circum-Pacific Council for Energy and Mineral Resources, Earth Science Series: Houston, TX, United States, Circum-Pacific Council for Energy and Mineral Resources, p. 137-155.
- Petersen, S. Herzig, P.M., Hannington, M.D., Jonasson, I.R., and Arribas, A. , 2002, Submarine Vein-Type Gold Mineralization near Lihir Island, New Ireland Forearc, Papua New Guinea. *Economic Geology*, 97(8), in press.

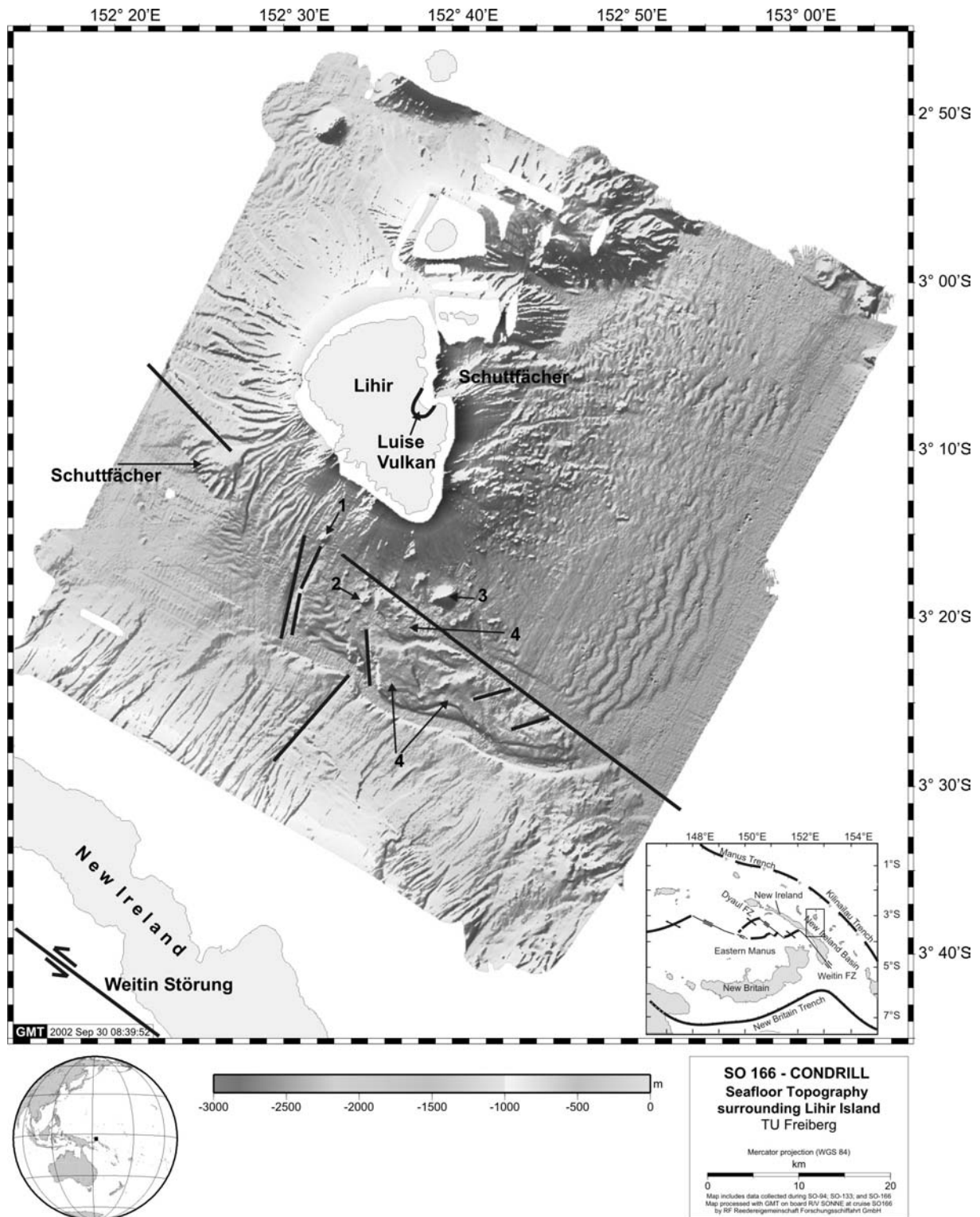


Abb. 1: Meeresbodentopographie in der Umgebung von Lihir Island. Die Karte wurde aus Daten der Forschungsfahrten SO-94, SO-133 und SO-166 erstellt. Exemplarisch wurden einige wichtige Strukturen markiert (schwarze Linien). Man beachte den parallelen Verlauf der NW-SE streichenden Struktur mit der Weitin Störung des östlichen Manus Beckens. 1: TUBAF Seamount, 2: Edison Seamount, 3: Conical Seamount, 4: zwischen den Störungen gehobene Krustenblöcke.

Auszüge aus Diplomarbeiten

Einführung

In der vorliegenden Arbeit wurde eine etwa 5cm dicke, etwa 50cm lange und etwa 40cm breite Scheibe von der Basis eines ca. 300 kg schweren inaktiven Schwarzen Rauchers analysiert. Ziel ist es geochemische und mineralogische Zonierungen innerhalb eines polymetallischen schwarzen Rauchers aus dem Satanic Mills Gebiet im PACMANUS Hydrothermalfeld, Papua Neuguinea, unter der besonderen Berücksichtigung des Auftretens und der Verteilung von Gold zu dokumentieren. Hauptaugenmerk lag auf der geochemischen Kartierung, die grafisch dargestellt werden soll. Zu diesem Zweck wurden 85 Kerne mit einem Durchmesser von 3,2 cm mit einem Hohlbohrer ausgesägt wurden (Abb. 1). Von jedem dieser Kerne wurde eine 1 cm dicke Scheibe abgesägt, aus welcher bei ausgewählten Kernen Dünnschliffe angefertigt wurden. Das verbliebene Reststück der Kerne wurde analysenfein gemahlen.

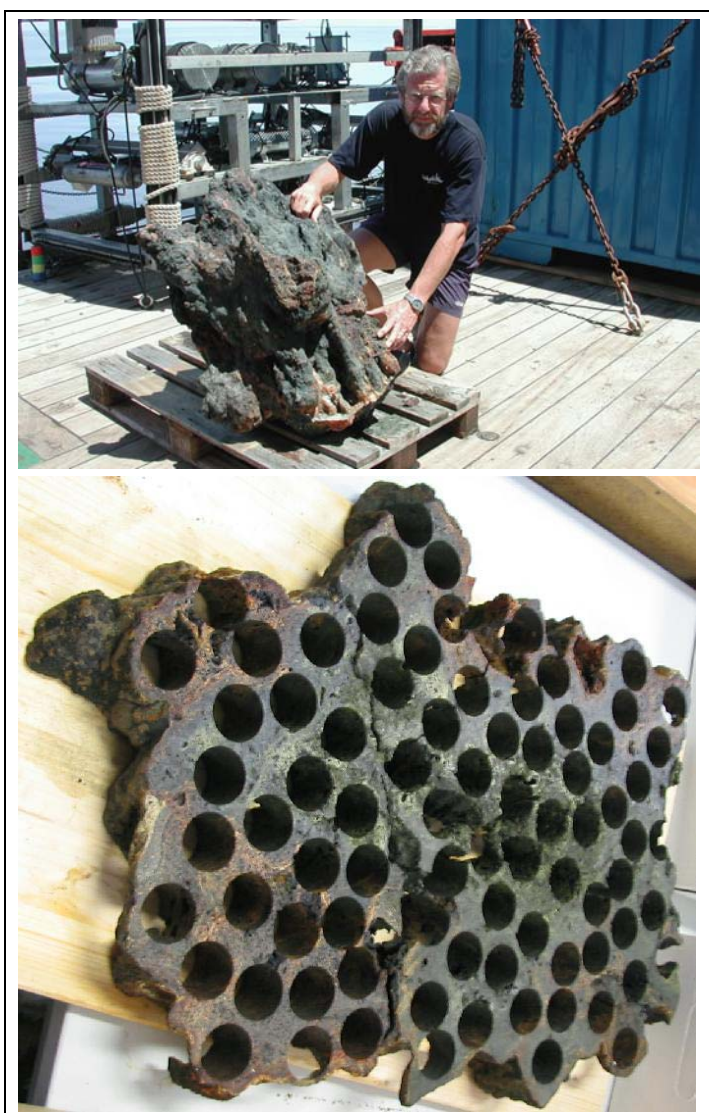


Abb. 1 Die Probe 59GTV nach der Probenahme sowie eine Übersicht über die Probenscheibe nach Entnahme der Kerne

Die Proben wurden mit Hilfe der Instrumentellen Neutronenaktivierung (INAA), ICP-OES sowie ICP-MS auf ihre Haupt- und Spurenmetallgehalte untersucht. Der Gesamtschwefel-Gehalt wurde mittels LECO ermittelt.

Mineralogie

Die Mineralogie der Scheibe wird vor allem von Sphalerit und Chalkopyrit dominiert, wobei Sphalerit vor allem an den Rändern und Chalkopyrit vor allem in der Mitte der Probe zu finden ist.

Insgesamt lassen sich vier verschiedene Bereiche differenzieren. Die rötlichen hellen Säume (Zone 1; durchgezogene Linien), welche die Probenscheibe durchziehen und die Grenzen ehemals separater Schlotstrukturen kennzeichnen, die porösen, kupferreichen und gelblichen Bereiche in der Mitte der Probe (Zone 3), die dunkelgrauen, beziehungsweise dunkelbraunen Bereiche an den Rändern (Zone 2) zwischen der kupferreichen Zone 3 und den rötlichen Bereichen der Zone 1, sowie die rötlichbraunen Bereiche der Zone 4 vor allem auf der linken Seite, welche offenbar Teile anderer (jüngerer?) Schlotstrukturen kennzeichnen, die miteinander verwachsen sind.

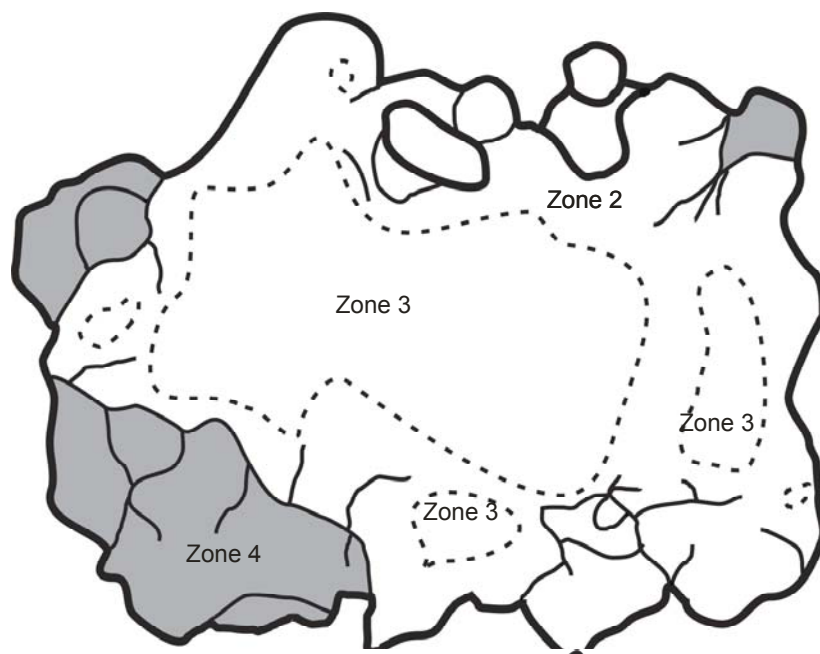


Abb. 2 Schematische Darstellung der Probenplatte. Durchgezogene Linien kennzeichnen die hellen Bereiche der Zone 1, wobei die dicken Linien die Aussenkanten der Probe darstellen. Die gestrichelten Linien umgrenzen die chalkopyritreiche Zone 3 von der sphaleritreichen Zone 2, während die grau eingefärbten Außenbereiche die Bereiche der Zone 4 kennzeichnen.

Die rötlichen Saumbereiche (Zone 1, durchgezogene dünne Linien in Abb. 2) bestehen überwiegend aus einer hellen, dispers verteilten, kolloomorphen Zinkblende mit einem hohen Anteil an amorpher Kieselsäure. In den Außenbereichen der Probe treten vereinzelt dünne Lagen von Fe-oxihydroxiden in Erscheinung.

Zone 2 ist vor allem durch Sphalerit und Baryt gekennzeichnet, welcher in zwei verschiedenen Generationen auftritt. Eine weitere wichtige Mineralphase dieses Bereiches sind die Fahlerze. Pyrit und Chalkopyrit treten nur untergeordnet auf. Pyrit tritt meist in Form kollomorpher Aggregate auf und wurden offenbar direkt nach dem büschelförmigen Baryt gebildet, welcher in diesem Bereich das älteste Mineral darstellt. Die Bildung des kollomorphen Sphalerits erfolgte in mehreren Schüben, die oftmals von Galenit, Jordanit oder Fahlerz gesäumt sind und damit späte Mineralphasen darstellen. Als letztes wurde amorphe Kieselsäure gebildet, die einen Saum um die Sulfide bildet. (Abb. 3).

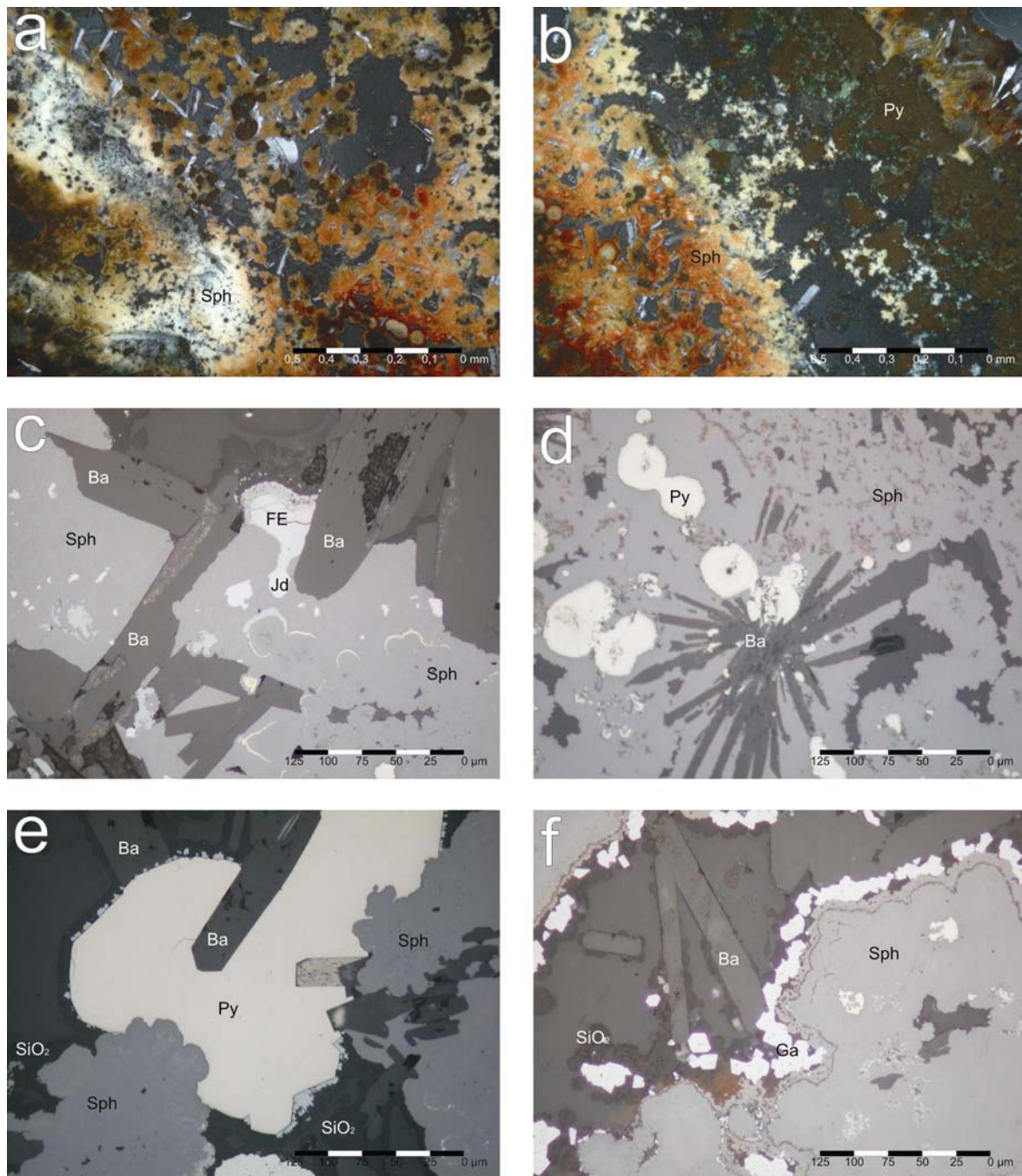


Abb. 3 Mikroskopische Aufnahmen aus den hellen, Kieselsäurereichen Saumbereichen der Zone 1 (a-b) und den dunklen zinkblendedominierten Bereichen der Zone 2 (c-f). a: kolloidaler Sphalerit (Sph) mit hohem Anteil an amorphem SiO₂ (SiO₂) unter gekreuzten Polarisatoren (Zone 1, 59-1-53). b: kolloidale Zinkblende mit hohem Anteil an amorphem SiO₂ sowie einem Pyritsaum (Py) am rechten oberen Bildrand bei gekreuzten Polarisatoren (Zone 1, 59-1-53). c: Später kolloidaler Sphalerit mit dünnen Chalkopyritbändern, Fahlerz (FE), Barytleisten (Ba) und Jordanit (Jd) (Zone 2, 59-1-44). d: Früher tropfenförmiger Pyrit, mit büscheligem, kogenetischem Baryt in kolloidalem Sphalerit (Zone 2, 50-1-54). e: Später kolloidaler Pyrit um Sphalerit und Baryt mit einem Saum aus amorphem SiO₂ (Zone 2, 59-1-58). f: Kolloidaler Sphalerit mit einem Saum aus Galenit mit spät gebildeten Barytleisten und einem Saum aus amorpher Kieselsäure (Zone 2, 59-1-54).

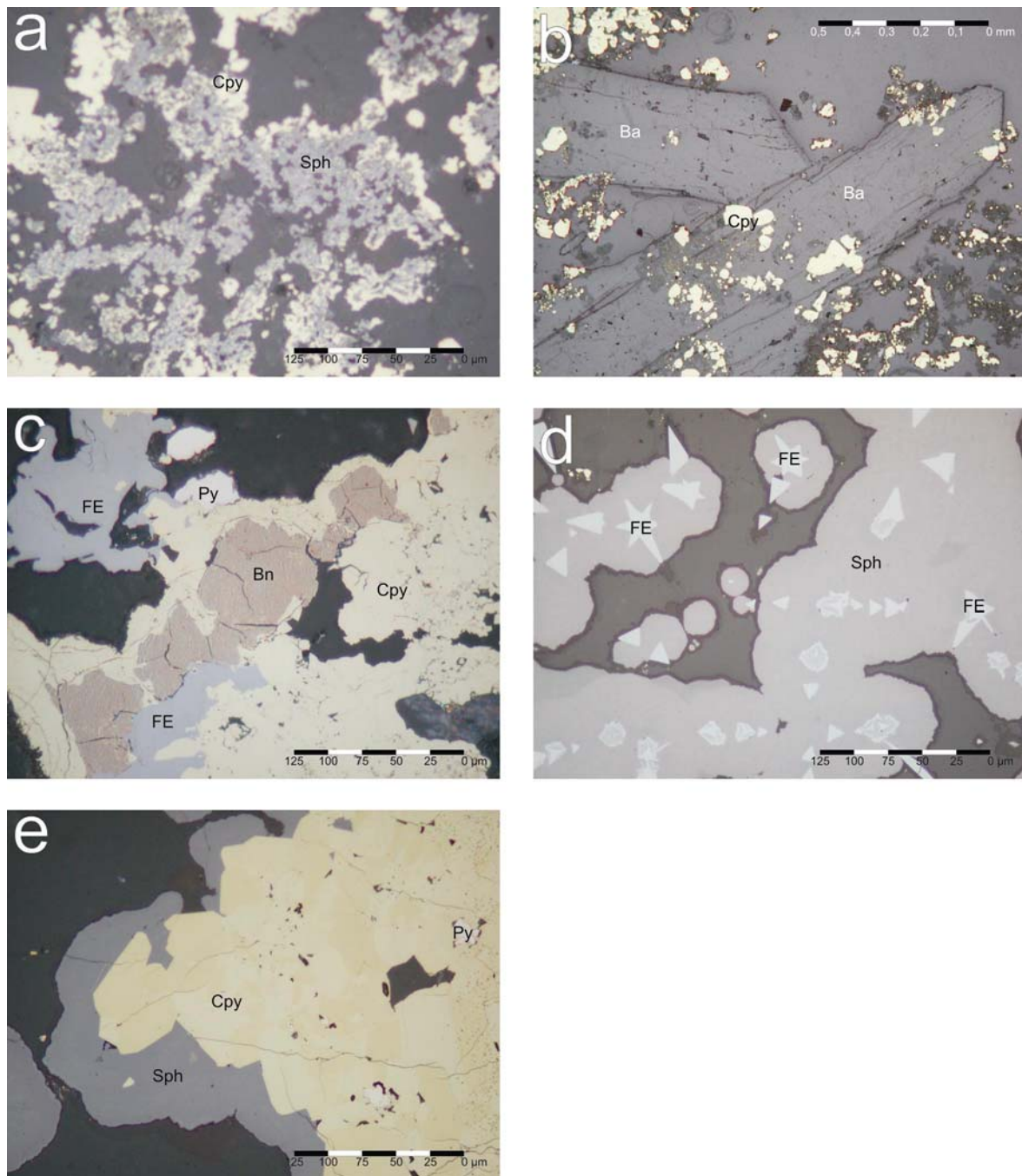


Abb. 4 Mikroskopische Aufnahmen der Cu-reichen Zone 3. a: Netzartiger Chalkopyrit um relictischen Sphalerit (Zone 3, 59-1-56). b: Große, spät gebildete Barytleisten mit Chalkopyrit (Zone 3, 59-1-55). c: Massiver Chalkopyrit mit Bornit, Fahlerzen und Pyrit (Zone 3, 59-1-46). d: Niedrig temperiert gebildeter Sphalerit mit Einschlüssen vonFahlerz und einem Saum aus amorphem SiO_2 aus dem Inneren eines Fluidkanals (Zone 3, 59-1-46). e: Typischer massiver Chalkopyrit mit tropfenförmigem relictischen Pyrit und einem Saum aus kolloidalem Sphalerit (Zone 3, 59-1-55,)

Die Farbe dieser Zone wird vor allem vom Eisengehalt des Sphalerit, aber auch von den relativen Anteilen an Baryt und Fahlerzen bestimmt. So erscheinen Bereiche mit überwiegend Sphalerit bräunlich und Bereiche mit überwiegend Baryt oder Fahlerz eher grau. Im Übergangsbereich zur Zone 3 steigt der Barytanteil in den Proben deutlich an.

Die Zone 3 besteht überwiegend aus Chalkopyrit mit wechselnden Anteilen an Baryt und untergeordnet Pyrit. Vereinzelt kommt es neben Chalkopyrit zur Kopräzipitation von Bornit (Abb. 4). Größere Fluidkanäle sind oft mit idiomorphen, dreieckigen Fahlerzkristallen, kollomorphem Sphalerit und amorpher Kieselsäure gefüllt (Abb. 4). Die aussenliegenden Bereiche der Zone 4 ähneln mineralogisch der Zone 2, sind aber durch ein fast völliges Fehlen von Cu-Sulfiden geprägt. Mineralogisch ist Sphalerit dominant, wobei aber auch Baryt häufig auftritt. Als Sulfide treten Fahlerz und Pyrit untergeordnet in Erscheinung. Diese Bereichen unterscheiden sich genetisch deutlich vom zentralen Hauptschlot. Es handelt sich dabei möglicherweise um jüngere Strukturen oder um Gleichaltrige, die mit dem Hauptschlot zusammengewachsen sind.

Verbreitung und Ausbildung von gediegen Gold in der Probe 59GTVA

Gediegen Gold konnte in der Probe, trotz der insgesamt recht hohen Gehalte, nur in fünf Dünnschliffen nachgewiesen werden. Dabei handelt es sich vor allem um die Dünnschliffe mit den höchsten Goldgehalten: 59-1-75 (58,5 ppm), 59-1-31 (50,7 ppm), 59-1-24 (32,7 ppm), 59-1-46 (26,8 ppm) sowie 59-1-33 (8,8 ppm); (Abb. 6). Die Probe 59-1-33 unterscheidet sich sowohl vom Goldgehalt als auch von der Ausbildung des Goldes deutlich von den anderen Proben. Im Dünnschliff 59-1-10, der mit 30,9 ppm ebenfalls sehr hohe Goldgehalte zeigte, konnte kein gediegen Gold nachgewiesen werden. Der Großteil der Goldkörner besitzt eine kugelige Gestalt und tritt in Form kleiner Nester bzw. in Form kurzer Schnüre auf. Die Korngröße variiert zwischen $<1\ \mu\text{m}$ und $8\ \mu\text{m}$, wobei mehr als 85% eine Korngröße von weniger als $4\ \mu\text{m}$ aufweisen (Abb. 5).

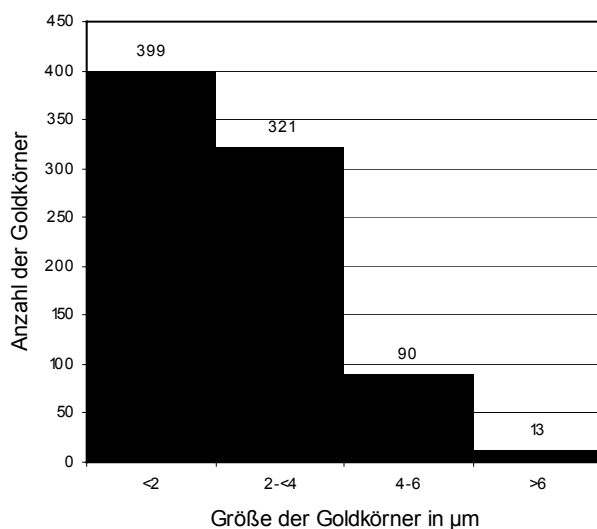


Abb. 5 Korngrößenverteilung der Goldkörner in den betrachteten Schliffen

Der überwiegende Teil der Goldkörner trat in Chalkopyrit (88,1%) auf. Des Weiteren befanden sich Goldkörner in Hohlräumen (2,3 %), in Sphalerit (2,1 %) und in Fahlerz (7,5 %). Nahezu 90% aller Goldkörner befanden sich im Inneren des Wirtsminerals.

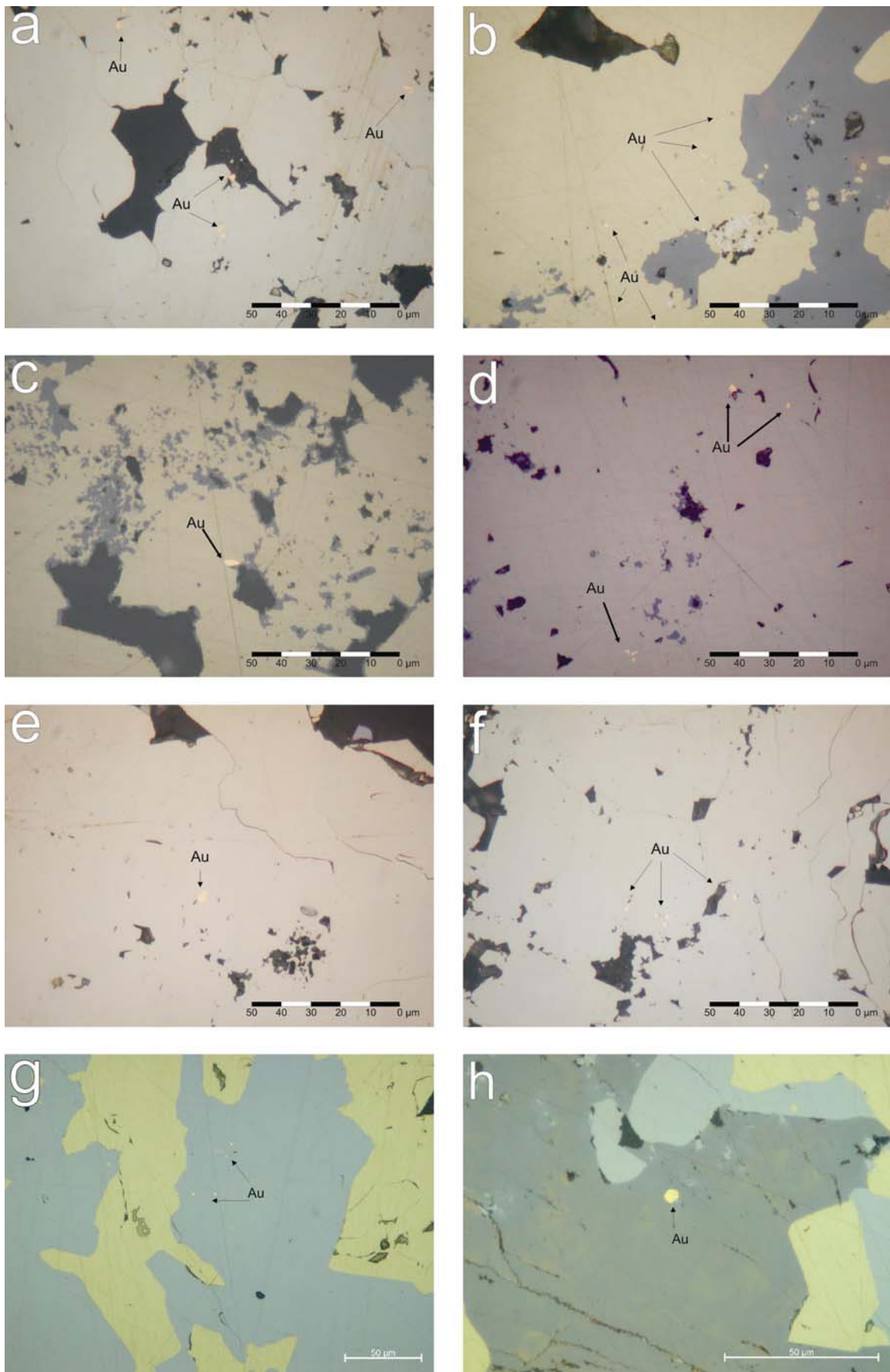


Abb. 6 a,e,f: gediegen Gold (Au) in Chalkopyrit (Cpy) aus Probe 59-1-75, b: gediegen Gold (Au) in Chalkopyrit (Cpy) aus Probe 59-1-24, c,d: gediegen Gold (Au) in Chalkopyrit (Cpy) aus Probe 59-1-31. g und h: gediegen Gold in Tennantit aus Probe 59-1-33.

In einigen Dünnschliffe wurde gediegen Gold in einer Menge gefunden, die eine Untersuchung der Goldverteilung innerhalb der Schliffe erlaubt (Abb. 7).

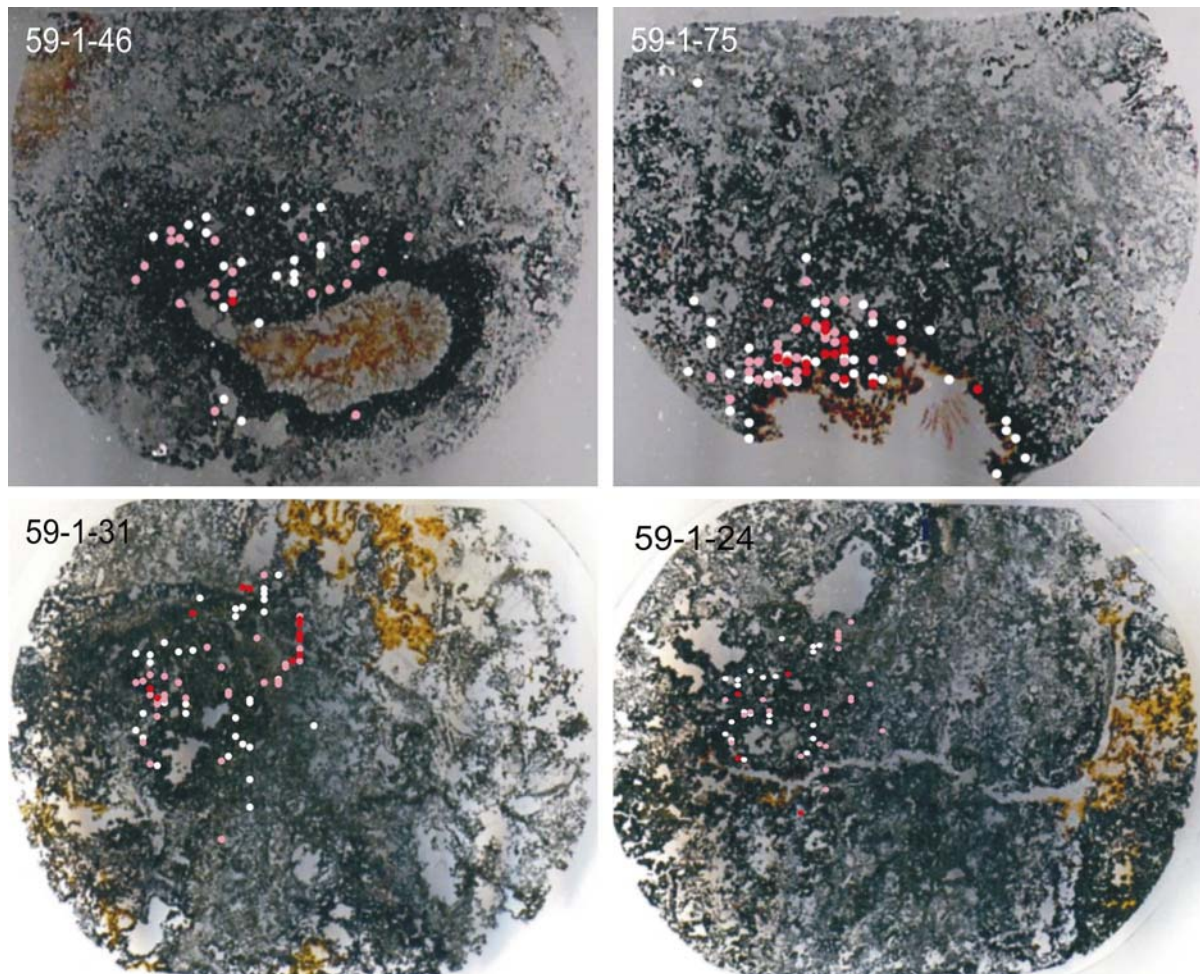


Abb. 7: Verteilung des Goldes innerhalb der Schliffe. Weiße Punkte sind einzelne Goldkörner, Rosa Punkte 2-5 Goldkörner und rote Punkte > 6 Goldkörner.

In den vier Schliffen zeigt sich, dass das Gold an ehemalige Fluidkanäle gebunden ist. Diese können mit einer deutlich ausgeprägten Chalkopyritwandung ausgekleidet sein, wie in den Schliffen 75 und 46, oder eher diffusere Strukturen wie in den Schliffen 31 und 24. Weiterhin fällt auf, dass sich die Goldkörner oft nicht im Zentrum der Chalkopyritwandungen befinden, sondern im Grenzbereich zu den umgebenden Mineralen.

Geochemische Analysen

Die Geochemie dieser Probe wird von den Haupterzmineralen bestimmt und variiert naturgemäß sehr stark. So treten insbesondere die Hauptelemente Cu, Fe, Zn und S in sehr unterschiedlichen Gehalten auf. Aussagekräftiger sind die Ergebnisse zu den Spurenelementen.

Im Vergleich zu typischen Massivsulfiden von Mittelozeanischen Rücken ist die Probe durch sehr hohe Edelmetallgehalte gekennzeichnet (bis 59 ppm Au und 670 ppm Ag), die Durchschnittsgehalte liegen jedoch in dem bisher bereits von Pacmanus bekannten Bereich (Moss et al., 2001). Stark erhöhte Gehalte weisen auch die Elemente As, Ba, Hg, In und Sb auf, während die Gehalte an Bi, Mo und Sn eher gering sind.

Die Gehalte an Co, Te und Se liegen meistens unterhalb der jeweiligen Nachweisgrenze (1 ppm Co; 0,1 ppm Te und 3 ppm Se).

Wichtiger als die absoluten Konzentrationen der jeweiligen Gehalte waren für diese Arbeit die geochemischen Korrelationen insbesondere der Spurenelemente. Aus diesem Grund wurden Korrelationskoeffizienten und eine Faktorenanalyse durchgeführt, um die jeweiligen Elementverteilungen innerhalb der Probe besser zu verstehen.

Geochemische Korrelationen

Bei 85 Proben zeigt bereits ein Korrelationskoeffizient von 0,283 eine statistisch signifikante Korrelation. Bis auf das Zinn zeigen alle Elemente mehr oder weniger stark ausgeprägte, statistisch signifikante Korrelationen mit mehreren anderen Elementen.

Bei den Hauptelementen Fe und Cu zeigt sich eine ausgeprägte positive Korrelation ($r = 0,965$), was darauf zurückzuführen ist, dass beide Elemente vornehmlich als Chalkopyrit auftreten. Sowohl Cu als auch Fe korrelieren stark negativ mit dem Zn ($r = -0,87$). Das liegt daran, dass Zn in der Probe vor allem als Sphalerit auftritt und Proben mit einem hohen Sphaleritgehalt meist arm an Chalkopyrit sind und umgekehrt (Abb. 8). Diese Hauptelemente sind also nicht unabhängig.

Eine ähnliche Rolle nimmt Baryt ein, welcher durch den Bariumgehalt der Proben repräsentiert wird. Die Bariumgehalte sind bei mittleren Zink- und Kupfergehalten am größten. Bei genauerer Betrachtung der Gesamtheit der Korrelationskoeffizienten zeigt sich, dass bestimmte Gruppen von Elementen gute Korrelationen zu einander aufweisen. Es lassen sich vier Gruppen von Elementen unterscheiden:

- Die Kupfer-Gold-Gruppe; mit Cu, Fe, Au, In, Bi und Mo
- die Blei-Zink-Gruppe; mit Pb, Zn, Ag, As, Tl, Ga, Cd und Hg
- die Barium-Gruppe; mit den Elementen Ba, Sr und Sb sowie
- eine Gruppe mit den Elementen Sn, Cr, S und Si, die nur geringe Korrelationskoeffizienten mit anderen Elementen aufweisen.

Auch innerhalb einer Gruppe zeigen sich deutliche Unterschiede in den Korrelationen. Während Fe und In eine ganz hervorragende Korrelation mit Cu zeigen, ist der Zusammenhang mit Au oder Bi zwar zu erkennen, aber wesentlich geringer ausgeprägt. Deutlich problematischer ist das Mo, das trotz statistisch signifikant positiven Korrelationskoeffizienten ($r = 0,385$) mit dem Cu eine kaum erkennbare positive Korrelation zeigt.

Tabelle 1: Geochemie von Bohrkernen der Probe 59GTVA.

Probennummer	Cu	Pb	Zn	SiO ₂	Fe	S _{total}	As	Ba	Au	Ag
Einheit	Gew.%	Gew.%	Gew.%	Gew.%	Gew.%	Gew.%	Gew.%	Gew.%	ppm	ppm
Methode	ICP-OES	ICP-OES	ICP-OES	ICP-OES	ICP-OES	LECO	INAA	INAA	INAA	INAA
59-1-01 SL	0,38	2,58	41,01	3,50	0,34	26,70	1,28	13,0	2,41	324
59-1-02 SL	0,75	1,69	37,75	5,20	1,15	24,40	0,71	15,0	7,34	336
59-1-03 SL	1,16	3,68	37,99	3,20	1	26,10	1,55	12,0	3,68	303
59-1-04 SL	0,46	1,16	44,12	1,60	0,34	28,20	0,41	10,0	13,50	400
59-1-05 SL	0,20	2,51	36,18	11,50	0,49	23,30	0,59	15,0	3,38	155
59-1-06 SL	3,18	2,09	30,53	10,30	3,67	24,60	1,28	12,0	6,54	180
59-1-07 SL	12,27	0,33	10,51	9,20	9,37	22,60	1,45	20,0	22,90	204
59-1-08 SL	0,35	2,32	42,72	3,00	0,31	27,90	0,75	10,0	4,13	231
59-1-09 SL	0,20	4,28	39,79	4,30	0,75	26,70	1,60	10,0	0,70	140
59-1-10 SL	0,69	0,48	39,44	0,70	0,27	26,60	0,34	17,0	30,90	410
59-1-11 SL	0,76	1,58	39,12	5,60	0,36	25,30	0,73	13,0	5,70	259
59-1-12 SL	18,84	0,32	17,20	3,30	11,26	27,60	2,31	12,0	31,00	406
59-1-13 SL	7,52	0,61	23,00	6,40	5,02	24,90	1,76	18,0	11,30	315
59-1-14 SL	1,68	1,55	29,46	4,40	1,01	21,80	1,04	22,0	10,40	292
59-1-15 SL	0,83	1,62	39,76	2,60	0,38	26,50	0,84	13,0	9,28	367
59-1-16 SL	0,72	2,06	42,44	1,60	0,43	27,70	0,82	10,0	5,97	455
59-1-17 SL	5,55	0,78	27,42	5,60	2,4	24,10	1,78	18,0	8,62	433
59-1-18 SL	9,18	0,51	17,94	6,60	4,21	21,30	2,04	23,0	13,70	376
59-1-19 SL	4,46	0,44	26,23	3,50	5,43	26,40	1,40	21,0	11,70	448
59-1-20 SL	18,17	0,34	14,35	3,90	15,25	28,80	0,40	12,0	24,40	390
59-1-21 SL	6,59	0,39	22,98	4,50	3,87	23,40	1,41	23,0	15,30	381
59-1-22 SL	10,08	0,21	16,53	2,10	7,41	24,00	1,12	24,0	18,80	387
59-1-23 SL	21,82	0,34	3,28	10,40	19,93	26,80	0,30	9,4	16,30	171
59-1-24 SL	22,55	0,11	4,63	6,40	18,68	27,30	0,31	13,0	32,70	177
59-1-25 SL	8,65	0,61	17,16	11,70	6,61	23,50	1,13	21,0	15,30	208
59-1-26 SL	3,20	3,06	32,49	5,30	2,18	25,80	2,17	12,0	3,10	267
59-1-27 SL	1,38	1,75	36,61	4,80	1,02	26,20	0,81	14,0	6,32	367
59-1-28 SL	0,59	0,90	39,70	3,90	2,22	26,40	0,41	12,0	6,50	400
59-1-29 SL	9,82	0,08	1,19	2,90	11,68	23,40	0,34	33,0	19,00	98
59-1-30 SL	16,06	0,56	9,50	7,80	15,32	26,90	0,36	16,0	12,00	188
59-1-31 SL	21,94	0,39	14,14	5,80	17,28	29,90	0,47	5,7	50,70	218
59-1-32 SL	10,23	0,65	14,65	5,70	8,25	23,80	0,89	23,0	15,90	157
59-1-33 SL	7,37	1,45	27,91	2,40	2,34	25,80	2,76	16,0	8,38	340
59-1-34 SL	5,87	0,72	20,98	5,60	3,02	23,30	1,72	28,0	21,70	302
59-1-35 SL	14,09	0,09	8,44	1,90	10,7	24,30	1,06	26,0	17,30	223
59-1-36 SL	23,34	0,29	8,71	4,20	20	30,60	0,26	9,0	16,60	140
59-1-37 SL	20,59	0,07	3,57	8,70	17,14	25,70	0,45	16,5	23,30	111
59-1-38 SL	14,92	0,19	8,36	3,20	11,05	23,80	1,00	25,0	16,20	171
59-1-39 SL	9,24	0,49	11,18	13,00	10,49	24,60	1,14	20,0	22,80	192
59-1-40 SL	10,92	0,26	12,22	1,60	8,6	23,40	0,65	24,0	28,10	322
59-1-41 SL	11,13	0,17	2,07	4,00	10,35	21,40	0,21	37,0	15,10	68
59-1-42 SL	24,37	0,95	6,00	8,20	20,98	29,90	0,48	4,5	10,20	185
59-1-43 SL	23,04	0,07	1,34	8,90	18,89	25,80	0,23	15,0	18,70	93
59-1-44 SL	4,13	2,39	26,11	7,70	6,04	24,90	1,08	18,0	10,80	250
59-1-45 SL	0,92	2,75	34,60	10,80	2,64	25,00	1,23	13,0	14,70	385
59-1-46 SL	14,79	0,59	15,78	5,20	11,61	27,00	1,18	15,0	26,80	247
59-1-47 SL	4,67	1,21	33,84	2,60	2,62	25,70	1,47	18,0	5,97	284

Tabelle 1: (Fortsetzung) Geochemie von Bohrkernen der Probe 59GTVA.

Probennummer	Bi	Cd	Cr	Ga	Hg	In	Mo	Sb	Sn	Sr	Tl
Einheit	ppm	ppm	ppm	ppm	ppm	ppm	ppm	ppm	ppm	ppm	ppm
Methode	ICP-MS	ICP-MS	ICP-OES	ICP-MS	INAA	ICP-MS	ICP-MS	INAA	ICP-MS	ICP-S	ICP-MS
59-1-01 SL	<0,2	1200	33	128	42	9,2	2,6	453	<0,5	1620	314
59-1-02 SL	<0,2	1140	112	120	22	32,0	10,0	882	<0,5	1520	104
59-1-03 SL	<0,2	1270	75	129	57	31,0	5,9	1890	0,6	1690	290
59-1-04 SL	<0,2	1740	105	209	46	30,0	2,5	1090	<0,5	1100	48
59-1-05 SL	<0,2	876	51	47	29	4,5	2,8	94,7	<0,5	1670	120
59-1-06 SL	<0,2	800	72	81	33	37,0	8,5	2340	<0,5	1590	127
59-1-07 SL	2,3	337	50	117	18	113,0	6,0	3470	<0,5	2000	28
59-1-08 SL	<0,2	1420	45	103	39	5,9	2,0	12,6	<0,5	1250	101
59-1-09 SL	<0,2	1090	59	46	40	1,6	6,8	229	0,7	1450	353
59-1-10 SL	<0,2	2450	26	400	43	157,0	1,7	2920	<0,5	1410	38
59-1-11 SL	<0,2	1340	48	119	40	14,0	2,2	63,5	<0,5	1430	88
59-1-12 SL	7,3	705	35	173	<3	176,0	5,1	3350	1,6	1200	13
59-1-13 SL	<0,2	837	64	143	21	72,0	3,5	3860	12,0	1670	61
59-1-14 SL	<0,2	1270	42	186	32	42,0	4,9	475	<0,5	2170	192
59-1-15 SL	<0,2	1870	39	205	50	23,0	1,8	88,4	3,7	1440	96
59-1-16 SL	<0,2	1800	52	201	41	15,0	1,5	587	<0,5	1100	98
59-1-17 SL	<0,2	1030	50	145	29	50,0	3,1	793	<0,5	1840	35
59-1-18 SL	<0,2	630	41	127	20	88,0	4,0	3090	11,0	2140	24
59-1-19 SL	<0,2	900	65	127	37	47,0	7,0	1950	<0,5	1660	56
59-1-20 SL	16,0	529	58	140	19	148,0	4,3	615	1,6	1130	101
59-1-21 SL	<0,2	831	35	155	31	63,0	3,6	1640	0,5	1950	47
59-1-22 SL	0,3	707	44	165	17	95,0	5,6	2710	0,6	2060	27
59-1-23 SL	10,0	51	94	104	4	157,0	9,0	432	2,4	874	44
59-1-24 SL	17,0	162	53	123	8	157,0	9,8	980	1,1	1240	26
59-1-25 SL	<0,2	531	61	110	18	72,0	6,4	1680	<0,5	2250	25
59-1-26 SL	<0,2	970	73	86	28	23,0	8,1	245	<0,5	1790	304
59-1-27 SL	<0,2	1380	56	171	40	24,0	4,5	707	<0,5	1540	62
59-1-28 SL	<0,2	1400	68	130	50	10,0	8,1	508	<0,5	1260	80
59-1-29 SL	0,8	38	37	89	<1	92,0	8,9	1110	0,6	3120	49
59-1-30 SL	19,0	251	37	101	8	111,0	11,0	410	5,8	1440	49
59-1-31 SL	35,0	412	53	126	23	175,0	14,0	1230	16,0	698	57
59-1-32 SL	1,4	399	37	92	10	82,0	3,8	676	0,7	2060	24
59-1-33 SL	<0,2	952	25	145	12	64,0	2,8	1310	4,9	1650	57
59-1-34 SL	<0,2	743	23	126	18	56,0	4,1	896	1,3	2220	36
59-1-35 SL	0,7	348	25	140	9	108,0	5,3	2110	2,1	2280	9
59-1-36 SL	33,0	219	46	100	<1	175,0	12,0	383	14,0	799	26
59-1-37 SL	17,0	132	43	91	<1	159,0	12,0	1120	4,4	1630	15
59-1-38 SL	2,7	335	27	110	<1	112,0	5,8	1420	1,3	2060	10
59-1-39 SL	1,3	365	72	105	11	89,0	6,9	2680	1,7	2150	125
59-1-40 SL	3,0	450	18	125	<1	105,0	5,1	2550	1,4	2600	23
59-1-41 SL	1,6	44	25	73	<1	78,0	7,8	401	1,0	2780	17
59-1-42 SL	37,0	80	96	81	6	169,0	12,0	203	3,9	442	117
59-1-43 SL	17,0	41	40	80	<1	169,0	12,0	775	3,6	1260	12
59-1-44 SL	0,8	656	58	90	16	45,0	15,0	1480	1,0	2180	165
59-1-45 SL	<0,2	1090	55	137	30	25,0	11,0	1510	4,9	1740	237
59-1-46 SL	8,5	595	39	128	9	135,0	4,6	2400	4,4	1380	64
59-1-47 SL	<0,2	1040	28	134	30	37,0	3,4	515	<0,5	1520	46

Tabelle 1: (Fortsetzung) Geochemie von Bohrkernen der Probe 59GTVA.

Probennummer	Cu	Pb	Zn	SiO ₂	Fe	S _{total}	As	Ba	Au	Ag
Einheit	Gew. %	Gew. %	Gew. %	Gew. %	Gew. %	Gew. %	Gew. %	Gew. %	ppm	ppm
Methode	ICP-OES	ICP-OES	ICP-OES	ICP-OES	ICP-OES	LECO	INAA	INAA	INAA	INAA
59-1-48 SL	12,52	0,11	7,38	1,50	9,93	22,50	0,78	29,0	15,30	139
59-1-49 SL	20,20	1,03	11,92	11,30	18,54	28,50	0,66	1,8	8,22	182
59-1-50 SL	24,71	0,23	3,04	13,10	20,98	27,10	0,19	4,8	10,70	87
59-1-51 SL	16,50	0,14	7,89	4,50	12,73	25,30	1,26	21,0	9,14	181
59-1-52 SL	0,59	3,91	44,29	9,30	0,52	23,80	1,78	7,5	7,22	400
59-1-53 SL	4,14	1,69	33,70	11,50	3,95	24,20	1,44	14,0	8,65	355
59-1-54 SL	1,01	2,14	41,14	9,40	3,2	24,30	0,70	10,0	4,48	313
59-1-55 SL	21,61	0,56	3,49	9,60	19,23	26,80	0,33	9,4	11,20	160
59-1-56 SL	19,59	0,88	12,55	10,10	17,21	28,00	0,58	5,6	8,04	132
59-1-57 SL	16,87	0,28	12,73	2,50	12,38	26,50	1,34	18,0	9,14	153
59-1-58 SL	2,81	1,44	27,74	6,70	5,23	23,90	0,95	20,0	12,40	291
59-1-59 SL	3,99	1,00	29,72	6,30	4,42	24,40	0,86	17,0	20,70	440
59-1-60 SL	0,30	1,37	21,77	31,20	7,62	22,20	0,62	7,2	2,27	128
59-1-61 SL	2,69	0,61	29,66	7,80	3,5	23,80	0,84	20,0	8,04	381
59-1-62 SL	7,51	0,22	15,63	2,20	6,38	22,40	0,71	31,0	19,70	262
59-1-63 SL	26,98	0,22	3,42	5,10	22,1	29,50	0,22	7,8	13,50	180
59-1-64 SL	17,71	0,10	6,88	3,20	14,34	25,70	0,95	22,0	10,60	119
59-1-65 SL	4,26	1,14	26,85	4,40	5,2	24,10	0,90	21,0	10,90	298
59-1-66 SL	7,26	0,89	19,30	6,90	7,62	24,00	1,02	22,0	21,30	324
59-1-67 SL	1,31	2,25	44,01	5,30	0,46	26,00	0,11	13,0	5,50	347
59-1-68 SL	10,50	0,34	18,19	4,80	5,11	23,40	2,26	23,0	17,00	317
59-1-69 SL	12,16	0,41	11,81	3,90	9,51	24,20	0,79	23,0	15,10	139
59-1-70 SL	10,61	0,18	7,65	4,40	9,23	21,90	0,31	29,0	14,70	92
59-1-71 SL	6,39	0,28	20,27	2,20	6,14	23,80	0,43	24,0	14,00	294
59-1-72 SL	6,32	0,55	17,88	2,70	4,42	22,40	1,22	27,0	12,70	291
59-1-73 SL	3,79	0,97	28,65	3,00	2,94	24,30	0,93	21,0	19,90	668
59-1-74 SL	2,28	2,54	37,21	3,80	1,5	26,00	1,46	15,0	4,05	304
59-1-75 SL	15,82	0,46	11,87	4,00	13,43	26,60	0,80	16,0	58,50	225
59-1-76 SL	12,69	0,34	8,92	4,40	9,79	23,60	1,25	25,0	15,10	121
59-1-77 SL	13,06	0,10	7,09	5,50	11,33	23,30	0,50	25,0	16,00	111
59-1-78 SL	5,09	0,61	32,08	2,60	4,3	26,30	0,87	16,0	14,10	466
59-1-79 SL	0,67	1,20	40,49	8,30	2,41	25,40	0,78	13,0	7,77	468
59-1-80 SL	3,83	1,18	17,09	10,10	4,84	21,30	1,04	23,0	12,90	215
59-1-81 SL	12,99	0,23	9,64	5,30	9,86	23,80	1,30	21,0	9,93	214
59-1-82 SL	1,73	1,50	37,27	6,40	1,39	24,90	0,90	15,0	13,00	607
59-1-83 SL	0,39	2,92	41,72	6,70	1,65	26,00	1,32	9,4	5,36	383
59-1-84 SL	5,56	1,09	19,97	12,00	5,16	21,70	1,08	18,0	8,79	257
59-1-85 SL	1,18	3,00	39,01	5,10	4,04	28,40	0,74	10,0	6,39	344
Mittelwert	8,79	1,06	22,13	6,03	7,49	25,18	0,96	16,97	13,86	272
Median	6,59	0,61	19,97	5,20	5,23	24,90	0,89	16,00	12,40	267
Min	0,20	0,07	1,19	0,70	0,27	21,30	0,11	1,80	0,70	68
Max	26,98	4,28	44,29	31,20	22,10	30,60	2,76	37,00	58,50	668
Stabw	7,66	0,99	13,35	4,13	6,26	2,12	0,54	7	9,45	122

Tabelle 1: (Fortsetzung) Geochemie von Bohrkernen der Probe 59GTVA.

Probennummer	Bi	Cd	Cr	Ga	Hg	In	Mo	Sb	Sn	Sr	Tl
Einheit	ppm	ppm	ppm	ppm	ppm	ppm	ppm	ppm	ppm	ppm	ppm
Methode	ICP-MS	ICP-MS	ICP-OES	ICP-MS	INAA	ICP-MS	ICP-MS	INAA	ICP-MS	ICP-OES	ICP-MS
59-1-48 SL	0,4	305	18	122	<1	105,0	5,0	1810	7,7	2540	8
59-1-49 SL	23,0	168	80	84	5	134,0	9,5	237	2,8	249	142
59-1-50 SL	33,0	69	87	74	<1	154,0	11,0	188	1,9	582	22
59-1-51 SL	6,0	328	18	112	<1	116,0	7,6	1220	1,7	1840	8
59-1-52 SL	<0,2	1180	31	100	36	12,0	4,4	684	<0,5	1250	418
59-1-53 SL	<0,2	1090	38	149	43	44,0	6,7	1940	<0,5	1690	124
59-1-54 SL	<0,2	1330	51	123	34	9,6	11,0	841	11,0	1340	127
59-1-55 SL	12,0	58	49	89	<1	146,0	7,6	183	1,6	1020	43
59-1-56 SL	20,0	127	60	77	7	120,0	6,4	191	0,8	580	137
59-1-57 SL	7,7	430	23	105	13	112,0	6,4	1070	1,8	1560	7
59-1-58 SL	<0,2	805	46	109	39	37,0	14,0	1440	1,4	2860	170
59-1-59 SL	0,3	1050	31	165	11	65,0	9,2	2780	1,1	2500	110
59-1-60 SL	<0,2	498	96	45	17	3,5	7,4	65,1	0,9	691	175
59-1-61 SL	<0,2	1040	40	133	28	31,0	5,7	1980	2,5	2190	52
59-1-62 SL	<0,2	626	31	153	17	73,0	6,4	2030	1,5	2720	25
59-1-63 SL	16,0	83	49	102	<1	177,0	6,9	399	3,3	855	25
59-1-64 SL	5,7	292	31	102	6	126,0	5,8	993	2,3	1820	6
59-1-65 SL	0,4	831	42	124	19	41,0	9,5	1510	1,2	2450	71
59-1-66 SL	3,1	666	55	125	18	81,0	8,9	2070	1,4	2610	116
59-1-67 SL	<0,2	1250	29	124	43	11,0	2,1	17	1,9	1560	125
59-1-68 SL	1,4	665	23	149	13	98,0	3,3	2970	10,0	2280	23
59-1-69 SL	1,0	298	32	95	11	108,0	5,8	1950	1,5	1960	19
59-1-70 SL	0,9	237	31	84	10	84,0	7,7	527	1,7	2610	37
59-1-71 SL	<0,2	770	36	147	<1	62,0	8,3	1040	10,0	2310	37
59-1-72 SL	<0,2	619	28	129	<1	62,0	5,7	2280	0,7	3040	22
59-1-73 SL	0,4	1220	32	211	27	73,0	5,9	3760	1,7	2680	58
59-1-74 SL	<0,2	1010	38	104	26	22,0	6,5	512	1,8	1760	131
59-1-75 SL	14,0	328	46	128	9	129,0	7,1	1230	3,8	1730	112
59-1-76 SL	2,6	204	32	104	6	121,0	7,2	2500	2,1	2190	22
59-1-77 SL	1,00	241	28	100	14	117	3,0	1150	3,0	2030	13
59-1-78 SL	0,5	1280	38	219	27	61,0	5,4	1100	2,4	1490	27
59-1-79 SL	<0,2	1130	47	100	32	7,4	7,0	1030	1,3	1730	114
59-1-80 SL	1,8	500	43	87	15	50,0	7,7	1810	0,9	3190	295
59-1-81 SL	0,5	379	32	120	12	122,0	3,7	3140	1,9	1930	12
59-1-82 SL	<0,2	1470	40	203	78	33,0	3,7	2890	2,4	1620	70
59-1-83 SL	<0,2	1160	46	86	50	4,2	8,8	562	18,0	1680	420
59-1-84 SL	<0,2	596	46	118	17	49,0	5,1	1060	1,0	1960	154
59-1-85 SL	<0,2	1170	57	121	47	13,0	7,0	1000	30,0	1360	141
Mittelwert	4,4	741	47	125	20,6	76,4	6,6	1323	2,8	1747	90
Median	0,3	666	43	121	18,0	72,0	6,4	1090	1,5	1690	57
Min	<0,2	38	18	45	<3,0	1,6	1,5	13	<0,5	249	6
Max	37,0	2450	112	400	78,0	177,0	15,0	3860	30,0	3190	420
Stabw	8,8	501	20	47	17,1	52,6	3,1	994	4,8	624	93

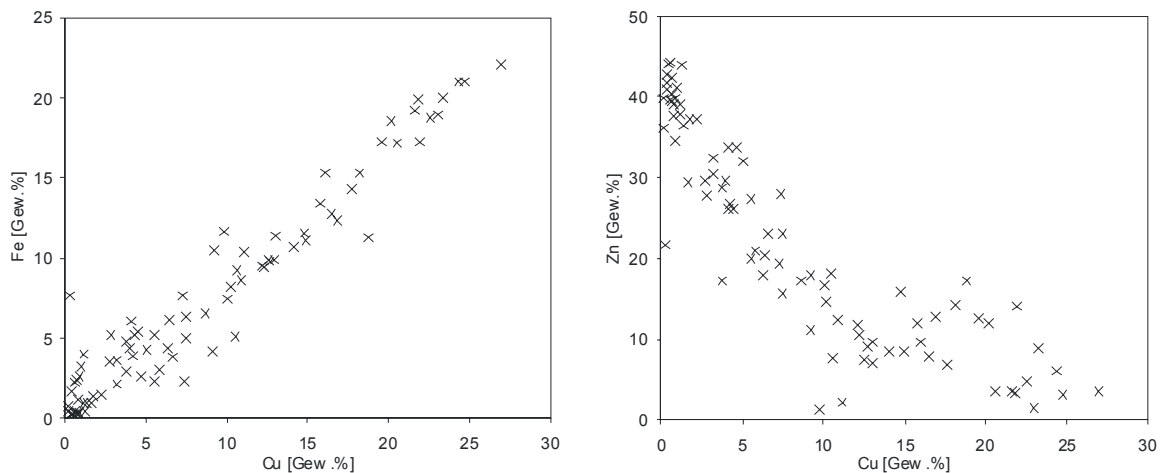


Abb. 8: Korrelation von Fe gegen Cu und von Zn gegen Cu. Erkennbar ist die stark positive Korrelation von Cu und Fe ($r = 0,965$) und die stark negative Korrelation von Cu und Zn ($r = -0,87$).

Ein sehr ähnliches Bild bieten die Elemente der Blei-Zink-Gruppe. Auch hier gibt es Elemente mit einer deutlich ausgeprägten positiven Korrelation zu Zn, wie es beispielsweise bei Cd ($r = 0,923$) und Hg ($r = 0,865$) der Fall ist, während Ag ($r = 0,664$), Pb ($r = 0,776$) und Tl ($r = 0,541$) eine deutlich geringere positive Korrelation zeigen. Die positive Korrelation bei Ga ($r = 0,353$) und As ($r = 0,254$) ist dagegen kaum noch zu erkennen.

In der Barium-Gruppe zeigt sich eine sehr gute Korrelation von Ba mit Sr ($r = 0,879$), während die Korrelation von Ba mit Sb ($r = 0,411$) weniger ausgeprägt ist. Antimon zeigt aber eine statistisch signifikante positive Korrelation mit As ($r = 0,407$).

Bei den Elementen Cr, Zn, S und SiO_2 sind die Korrelationen uneindeutig. Stellt man den Gesamtschwefel gegen Zn ($r = 0,072$) und Cu ($r = 0,360$) dar, so zeigt sich, dass S in der gesamten Probe mit konstanten Gehalten auftritt, gänzlich unabhängig von den wechselnden Zn- und Cu-Gehalten. Dieses Verhalten ist unter der Annahme erklärbar, dass es sich beim Schwefel vor allem um Sulfidschwefel handelt.

Bei Sn sind Korrelationen schwierig, weil es generell nur mit sehr geringen Gehalten in der Probe auftritt. Auch beim Cr ist eine eindeutige Zuordnung zu anderen Elementen schwer möglich. Es korreliert leicht negativ mit Ba und leicht positiv mit SiO_2 . Das SiO_2 zeigt bis auf Cr keine deutliche Korrelation mit anderen Elementen.

Betrachtet man die Korrelationen des Au, so zeigt sich eine positive Korrelation mit den anderen Elementen der Kupfer-Gold-Gruppe ($r_{\text{Cu/Au}} = 0,459$). Gleichzeitig zeigt Au auch eine schwach ausgeprägte positive Korrelation mit Elementen der Bariumgruppe wie Ba ($r_{\text{Ba/Au}} = 0,187$) und Sb ($r_{\text{Sb/Au}} = 0,369$). Auch wenn hier der Korrelationskoeffizient darauf hinweist, dass kein statistisch signifikanter Zusammenhang zwischen Ba und Au besteht, zeigt die grafische Darstellung eine deutliche lineare Abhängigkeit. Zu den Elementen der Blei-Zink-Gruppe hingegen hat Au eine stark negative Korrelation ($r_{\text{Zn/Au}} = -0,451$; Abb. 9). Eine Ausnahme bildet hier das Ag, zu dem keine erkennbare Korrelation auftritt.

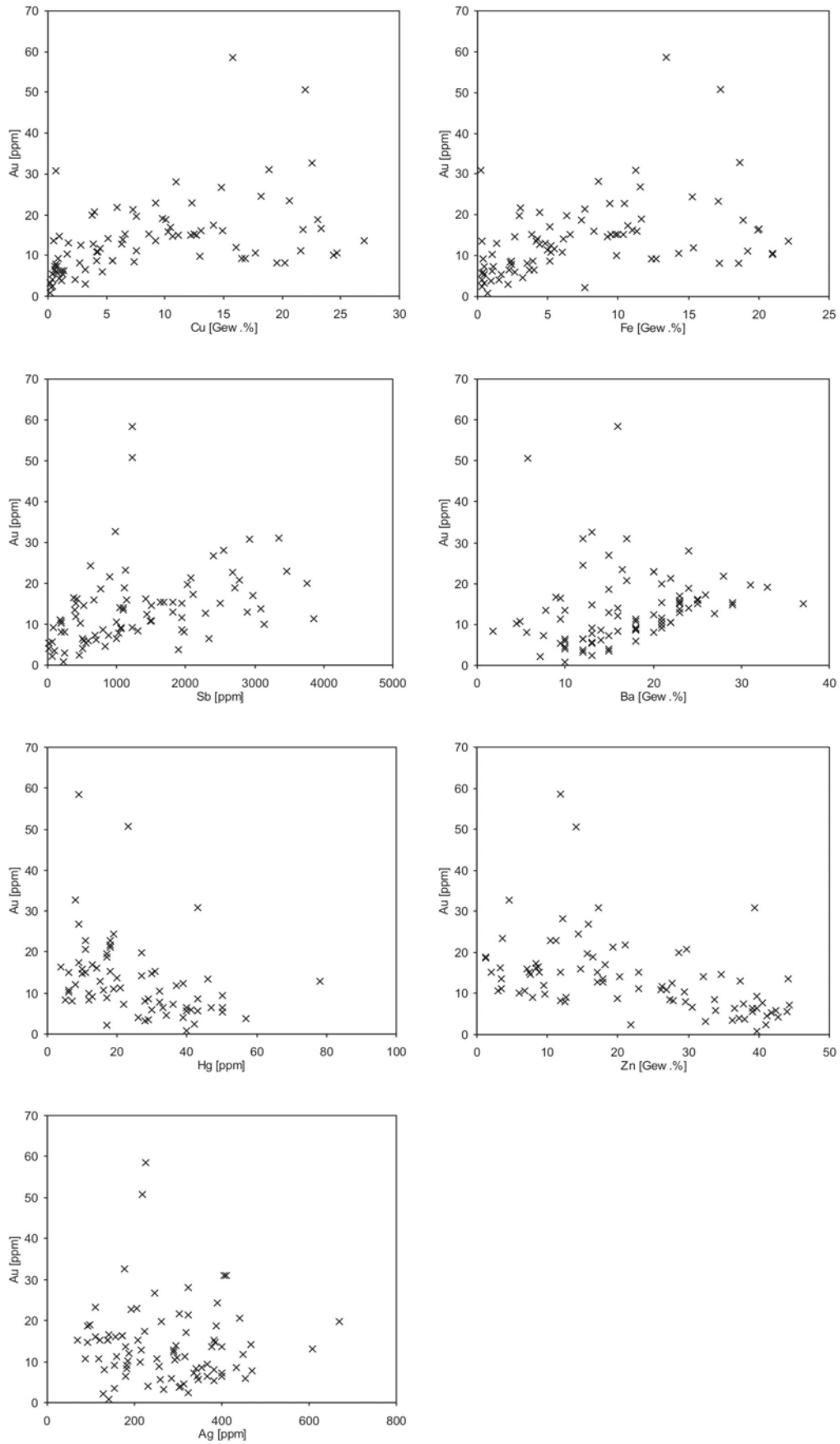


Abb. 9 Korrelation von Au mit ausgewählten anderen Elementen; Fe ($r = 0,414$), mit Cu ($r = 0,459$), mit Sb ($r = 0,369$), mit Ba ($r = 0,187$), mit Hg ($r = -0,363$) mit Zn ($r = -0,451$) und mit Ag ($r = -0,045$).

Faktorenanalyse

Während die Korrelationskoeffizienten direkte Zusammenhänge zeigen, können mit Hilfe der Faktorenanalyse komplexe Zusammenhänge gefunden werden, denen die Ausgangsvariablen zugrunde liegen. Die Faktorenanalyse ist eine Datenreduktionsmethode, durch welche der hohe Grad an Komplexität, der durch die Vielzahl von abgebildeten Variablen entsteht, handhabbar und oft auch interpretierbar gemacht werden soll. Dazu werden die Variablen auf möglichst wenige Faktoren, die hinter ihnen stehen, reduziert (Brosius, 1998).

Die Datenreduktion mit Hilfe der Hauptkomponentenanalyse lieferte 5 Faktoren mit Eigenwerten >1 (Tabellen 2 und 3). Die Faktorenanalyse wurde mit 19 der 21 Elementen durchgeführt, dabei wurden Elemente mit extrem niedrigen Korrelationen wie Schwefel und Zinn ignoriert, um aussagekräftigere Modellierungen zu ermöglichen (Brosius, 1998). Wie Tabelle 2 zeigt, erklärt bereits der erste Faktor 40,3 % der Gesamtvarianz. Die ersten drei Faktoren können gemeinsam 72,9% der Gesamtvarianz erklären. Für die Darstellung wurde keine Rotation durchgeführt.

Stellt man die ersten beiden Faktoren gegeneinander dar, findet sich die Einteilung der Elemente in die vier Gruppen hier wieder (Abb. 10). Es zeigt sich, dass bestimmte Elemente so eng miteinander verknüpft sind (beispielsweise Cu, Fe und In oder Zn, Cd und Hg), dass sie wahrscheinlich gemeinsame Minerale bilden. Andere Elemente hingegen sind weniger stark mit den Hauptelementen verknüpft. Gold beispielsweise scheint ebenso sehr zu Cu zu tendieren wie zu Ba. Auch Bi und Mo setzen sich leicht vom Cu ab. In ähnlicher Weise entfernen sich As und Ga sowie Pb und Tl vom Zn. Das weist möglicherweise darauf hin, dass diese Elemente eigene Minerale bilden, die aber mit den Zinkmineralen assoziiert sind.

Tabelle 2: Ergebnisse der Faktorenanalyse; erklärte Gesamtvarianz der ersten 10 Komponenten.

Komponente	Anfängliche Eigenwerte			Summe von quadrierten Faktorladungen für Extraktion		
	Gesamt	% der Varianz	kumulativ %	Gesamt	% der Varianz	kumulativ %
1	7,665	40,342	40,342	7,665	40,34	40,34
2	4,000	21,053	61,395	4,000	21,05	61,40
3	2,185	11,498	72,893	2,185	11,50	72,89
4	1,190	6,262	79,155	1,190	6,26	79,16
5	1,006	5,293	84,448	1,006	5,29	84,45
6	,873	4,593	89,041			
7	,497	2,617	91,659			
8	,396	2,085	93,743			
9	,281	1,480	95,223			
10	,248	1,307	96,530			

Extraktionsmethode: Hauptkomponentenanalyse.

Die Darstellung von Faktor 1 gegen Faktor 3 (Abb. 11) zeigt ein ähnliches Bild. Die Elemente der Kupfer-Gold-Gruppe sind dabei stärker konsolidiert, obwohl das Mo noch weiter entfernt liegt. In ähnlicher Weise erscheinen die Elemente der Blei-Zink-Gruppe stärker konsolidiert, wobei das Ga stärker isoliert ist. Bei den Elementen der Bariumgruppe, ist das Sb deutlich von den anderen beiden Elementen abgerückt.

	Komponente				
	1	2	3	4	5
Cu	-,949	-,051	,178	,020	-,208
Pb	,732	-,513	-,168	,091	-,115
Zn	,946	-,196	,167	-,041	,033
Fe	-,960	-,186	,110	,016	-,041
As	,385	,266	-,197	,541	-,604
Ba	-,082	,831	-,460	-,126	,173
Au	-,493	,385	,393	,280	,229
Ag	,673	,239	,471	,228	,096
Bi	-,741	-,433	,358	,026	-,045
Cd	,897	,028	,384	-,096	,077
Ga	,366	,487	,708	-,020	,120
In	-,890	,147	,338	,105	-,125
Mo	-,475	-,376	-,175	,281	,496
Sb	,025	,676	,119	,621	,053
Sr	,146	,729	-,546	,060	,290
Tl	,529	-,526	-,254	,271	-,041
Cr	,006	-,699	,143	,235	,270
SiO2	-,131	-,574	-,281	,356	,174
Hg	,852	-,188	,243	-,012	,103

Tabelle 3:
Hauptkomponentenmatrix der Faktorenanalyse. Fünf Komponenten extrahiert.

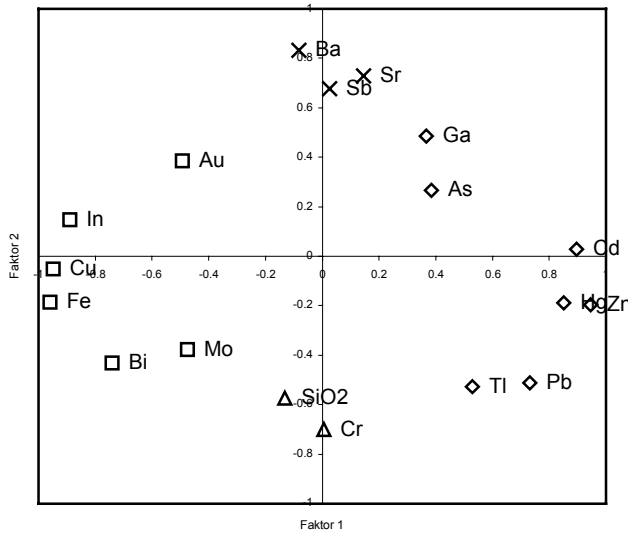


Abb. 10: Grafische Darstellung der Ergebnisse der Faktorenanalyse. Plot von Faktor 1 gegen Faktor 2. Die Symbole der Elemente entsprechen den vier Gruppen, in die sie nach ihren Korrelationskoeffizienten eingeteilt wurden: □:Kupfer-Gold-Gruppe, ◇: Blei-Zink-Gruppe, X: Barium-Gruppe, △: Restgruppe

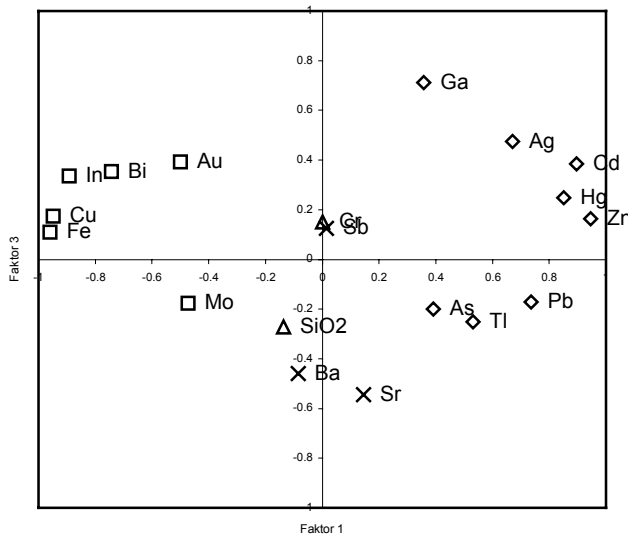


Abb. 11: Grafische Darstellung der Ergebnisse der Faktorenanalyse. Plot von Faktor 1 gegen Faktor 3. Die Symbole der Elemente entsprechen den vier Gruppen, in die sie nach ihren Korrelationskoeffizienten eingeteilt wurden: □:Kupfer-Gold-Gruppe, ◇: Blei-Zink-Gruppe, X: Barium-Gruppe, △: Restgruppe

Geochemische Karten

Erfasst man die Probenscheibe mit Hilfe eines Rasters, können den Probenpunkten Koordinaten zugeordnet werden und mit Hilfe eines Interpolationsverfahrens geochemische Karten erzeugt werden. In der vorliegenden Arbeit wurde das Point Kriging als Interpolationsverfahren verwendet, bei der unter Einbeziehung möglicher Trends die wahrscheinlichsten Werte für ein bestimmtes Punktgitter berechnet werden.

Die kartographische Darstellung der Hauptelemente Cu, Ba und Zn zeigt, dass die mineralogische Einteilung der Probenscheibe weitgehend zutreffend ist, obwohl sich zwischen der Zn-reichen Randzone und dem Cu-reichen Kern eine Ba-reiche Zwischenzone befindet, die bei den mikroskopischen Untersuchungen so nicht auffiel (Abb. 12). Es zeigt sich weiterhin, dass sich das Zn vor allem auf die Schlotbereiche im unteren und linken Teil der Probenscheibe und in den Außenbereichen der Probe beschränkt ist.

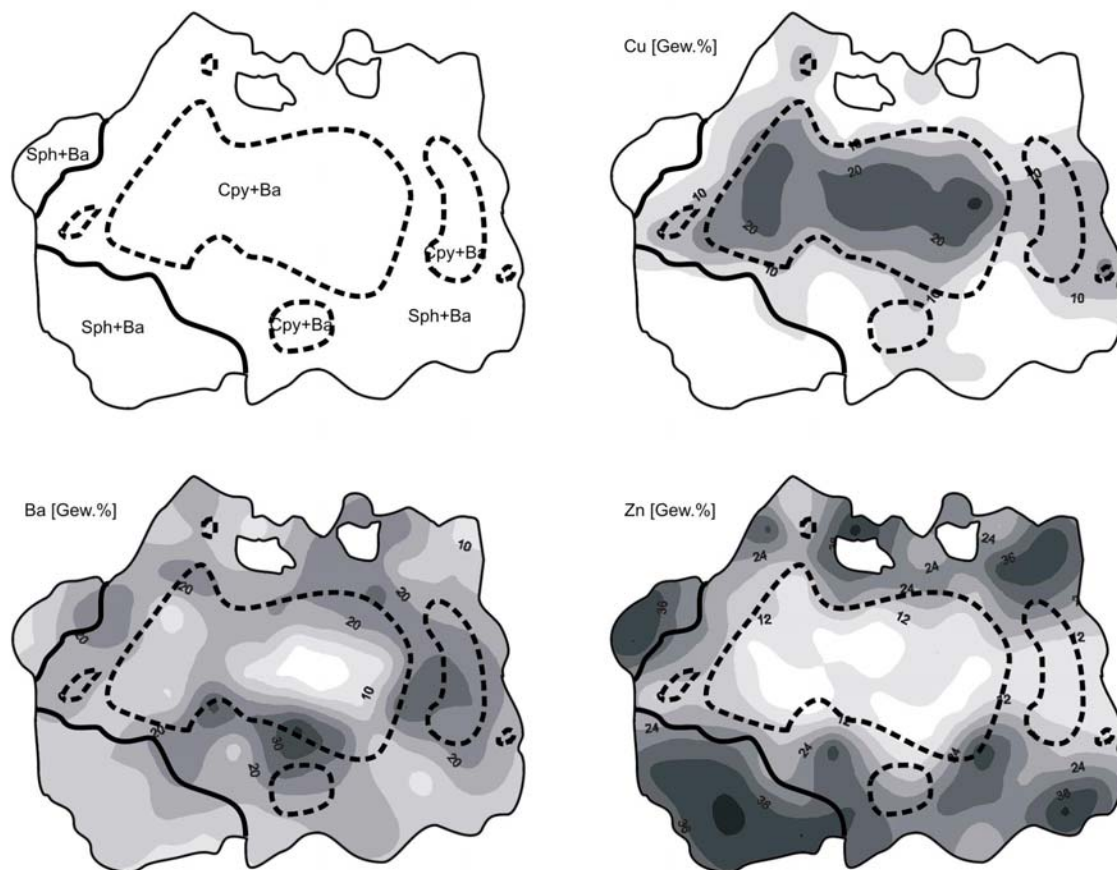


Abb. 12: Geochemische Karten der Elemente Cu, Ba und Zn

Auffällig ist, dass die geochemische Karte des Cu für den unter dem Hauptbereich liegenden chalkopyritreichen Bereich keine erhöhten Cu-Gehalte zeigt. Dies ist vor allem ein geometrischer Effekt, der daraus resultiert, dass in den geochemischen Karten Probenpunkte von 30mm Durchmesser zu mathematischen Gitterpunkten reduziert

wurden. Dies kann insbesondere bei punktuell erhöhten Gehalten zu leichten Verschiebungen führen.

Die geochemischen Karten der Hauptelemente sind nicht spektakulär, da sie die bereits bekannten mineralogischen Aussagen im Ganzen nur bestätigen. Von besonderem Interesse ist jedoch die Verteilung der Spurenelemente. Insbesondere die Verteilung von Bi, In, Te, Sn, u.a. ist im Detail bisher nicht untersucht worden. Die Unterteilung der Elemente in Gruppen wird beibehalten und ist insoweit sinnvoll, als das jede Gruppe stellvertretend für ein Hauptmineral in der Probenscheibe steht.

Die Darstellung der Elemente der Kupfer-Gold-Gruppe (Abb. 13) zeigt zunächst die deutliche Ähnlichkeit in den Verteilungen von Fe und Cu, was auf das gemeinsame Auftreten als Chalkopyrit zurückzuführen ist. Weiterhin fällt auf, dass sich In und Bi sehr stark wie das Cu verhalten. Dies wurde durch die im vorherigen Kapitel berechneten Korrelationskoeffizienten schon angedeutet. Es kann daher gefolgert werden, dass sowohl In als auch Bi zumindest teilweise in den Chalkopyrit eingebaut werden. Beim In ist bemerkenswert, dass es in der goldreichen Probe 59-1-10 aus dem unteren Bereich der Probenscheibe ein Maximum aufweist, obwohl die Kupfergehalte dort nur gering sind. Es ist bekannt, dass In in hochtemperierten, kupferreichen Proben in Sphalerit eingebaut werden kann (Schwarz-Schampera, 2000).

Das Mo hingegen zeigt deutliche Unterschiede in seiner Verteilung. Trotz seiner hohen Korrelationskoeffizienten zu Elementen der Kupfer-Gruppe, vor allem zum Fe ($r = 0,490$), liegen die Verteilungsmaxima an deutlich anderen Stellen. Während andere Proben aus dem PACMANUS Hydrothermalfeld einen durchschnittlichen Mo-Gehalt von 97 ppm aufweisen (Hannington et al., 2004), sind die Gehalte in der hier untersuchten Probe mit durchschnittlich 6 ppm sehr gering. Die Verteilungskarte von Mo ist daher aufgrund der geringen Mo-Gehalte (1,5 ppm bis 15ppm) mineralogisch nicht aussagekräftig.

Ebenso ungewöhnlich ist die Verteilung des Au. Die Verteilungsmaxima liegen zwar in kupferreichen Zonen, das Gold ist also ohne Zweifel vor allem an Chalkopyrit oder koexistierende Minerale gebunden, die höchsten Gehalte finden sich aber in den randlich gelegenen, kleinen Chimneystrukturen. Interessant ist hier vor allem die Probe 59-1-75 vom rechten Rand der Probenscheibe, bei der es sich im Wesentlichen um eine angeschnittene, chalkopyritreiche Fluidbahn in einer sphaleritreichen Matrix handelt. Die hohen Goldgehalte liegen hier fast ausschließlich in der dünnen Wand des Fluidkanals. Ähnlich verhält es sich bei der Probe 59-1-46, die in der Karte als Gold-Maximum in einer kupferreichen Zone nahe dem oberen Rand in Erscheinung tritt.

Betrachtet man die geochemischen Karten der Elemente der Blei-Zink-Gruppe (Abb. 14), so fällt zunächst auf, dass sich diese Elemente vor allem auf die Probenränder konzentrieren. Insbesondere die geochemische Karte des Zn zeigt, dass Sphalerit fast in der gesamten Probe auftritt, sich aber in den äußersten Randbereichen konzentriert.

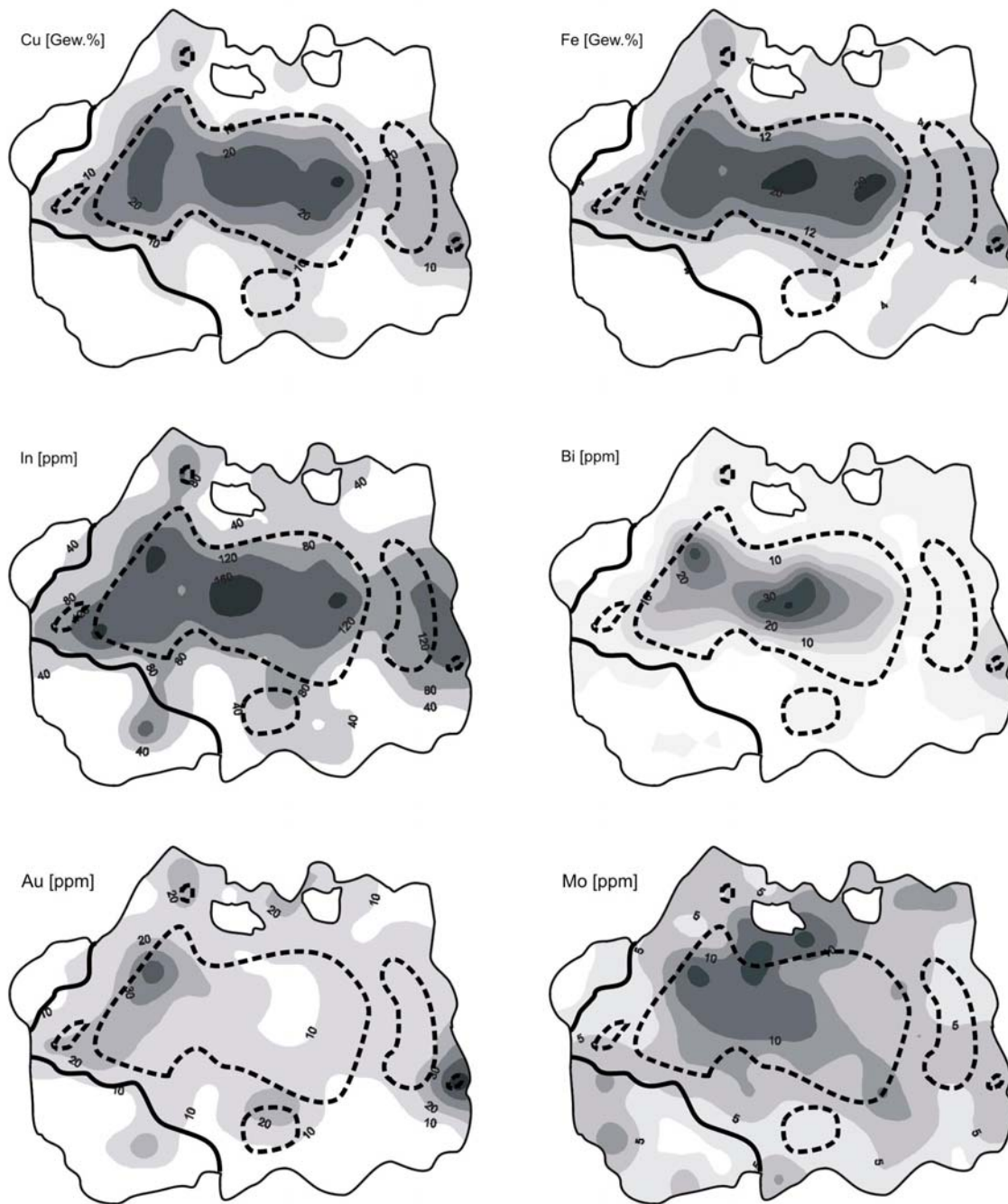


Abb. 13: Geochemische Karten von Cu, Fe, In, Bi, Au und Mo.

Es zeigt sich außerdem, dass die Verteilungsmuster von Cd, Hg, Tl und Pb denen des Zn sehr ähnlich sind. Die Verteilungen der Elemente Ga, Ag und As hingegen zeigen leichte Abweichungen zur Verteilung des Zn. Ähnlich den anderen Elementen gruppieren auch sie sich um die kupferreichen Zonen, ihre Verteilungsmaxima liegen jedoch teilweise deutlich anders als das des Zn. Generell liegen die höchsten Gehalte an diesen Elementen entweder in den separaten jüngeren Zonen im unteren, linken Bereich der Probe oder in den beiden separaten Schlotstrukturen im oberen Bereich der Probe (Probe 59-1-67 und 59-1-73). Das Fehlen von Kupfersulfiden in diesen beiden Schloten weist darauf hin, dass die hier auftretenden hydrothermalen Fluide eine geringe Austrittstemperatur hatten. Dies kann dadurch begründet werden, dass diese Strukturen

entweder in der Spätphase der hydrothermalen Aktivität entstanden oder die Fluide bereits weiter unten in der Schlotstruktur abgekühlt worden sind.

Blei und Zn treten in der Probe vorwiegend als Galenit und Sphalerit auf. Die Elemente Cd, Pb, Ga, As und Hg können das Zink des Sphalerits diadoch ersetzen (Rösler, 1990). Daher können die ähnlichen Verteilungsbilder dieser Elemente durch den Einbau in den Sphalerit erklärt werden, wobei Hg auch als Cinnabarit (HgS) in Erscheinung treten könnte, der in der Proben allerdings nicht nachgewiesen wurde. Die deutlich unterschiedlichen Verteilungsmuster von Fe und Zn weisen darauf hin, dass der Sphalerit relativ arm an Eisen ist. Dies konnte durch mikroskopische Untersuchungen bestätigt werdend da Zinkblende in diesem Bereichen als Honigblende auftritt.

Da As, Ag und Ga deutlich andere Verteilungsmuster aufweisen, müssen hier andere Minerale für den Elementeinbau verantwortlich sein. Ein Mineral, das häufig neben Sphalerit auftritt, ist Fahlerz. Insbesondere Tennantit ($\text{Cu}_3\text{AsS}_{3,25}$), enthält As, kann aber auch Ag, Ga, Sn und Hg enthalten. Weitere mögliche Minerale sind Arsen-Blei-Sulfosalze, wie beispielsweise Jordanit ($\text{Pb}_4\text{As}_2\text{S}_7$) oder typische Arsensulfide wie Realgar (AsS) und Auripigment (As_2S_3). Ein typischer Silberträger ist der relativ häufige Galenit. Da die Pb/Ag Verteilungsmuster insbesondere im linken unteren Bereich der Probenscheibe deutlich voneinander abweichen, kommt Galenit zumindest nicht als einziges Silbermineral in Frage.

Barium tritt in der Probenscheibe in Form von Baryt als sehr häufiges Mineral auf. Im Baryt ($\text{Ba}[\text{SO}_4]$) können große Teile des Ba durch Sr ersetzt werden. Auf diese Weise kann die praktisch identische Verteilung von Sr und Ba in der Probenscheibe erklärt werden (Abb. 15).

Das Sb zeigt trotz hoher Korrelationskoeffizienten ($r_{\text{Sb}/\text{Ba}} = 0,411$) eine deutlich andere Verteilung, die aber der Verteilung des Ag ähnelt. Möglicherweise tritt Sb in der Probe als Antimonit (Sb_2S_3) oder Pyrargyrit (Ag_3SbS_3) auf. Wahrscheinlich tritt Antimon aber als weiteres Fahlerz, nämlich als Tetraedrit, in Erscheinung ($\text{Cu}_3\text{SbS}_{3,25}$). Eine genauere Aussage ist ohne Mokrosondenanalytik nicht möglich.

Darüber hinaus gibt es noch einige Elemente, deren Zuordnung schwierig ist (Abb. 15). Schwefel ist über die gesamte Probenscheibe mit Gehalten zwischen 21 Gew.% und 29 Gew.% verteilt. Die geochemische Karte zeigt, dass der Schwefelgehalt in den sulfiddominierten (Sphalerit und Chalkopyrit) Bereichen leicht höher ist als in den sulfatdominierten (Baryt) Zonen. Die ist darauf zurückzuführen, dass S in Sulfiden einen höheren Anteil als in Sulfaten ausmacht. Kieselsäure (SiO_2) tritt ohne ein klar erkennbares Muster mit wechselnden Häufigkeiten in der gesamten Probe auf. Einzig die mit 31 Gew.% stark erhöhten Gehalte in Probe 59-1-60 (vom rechten unteren Rand der Probenscheibe) sind bemerkenswert. Da amorphe Kieselsäure nur bei geringen Temperaturen gebildet wird, handelt es sich bei Probe 59-1-60 möglicherweise um ein lokales Temperaturminimum. Die Anordnung ehemaliger Schlotbegrenzungen auf der Probe zeigt, das es sich dabei beispielsweise um einen Hohlraum gehandelt haben könnte, der durch zusammenwachsende separate Schlotstrukturen entstanden ist und im weiteren Verlauf dieses Prozesses vollständig verfüllt wurde.

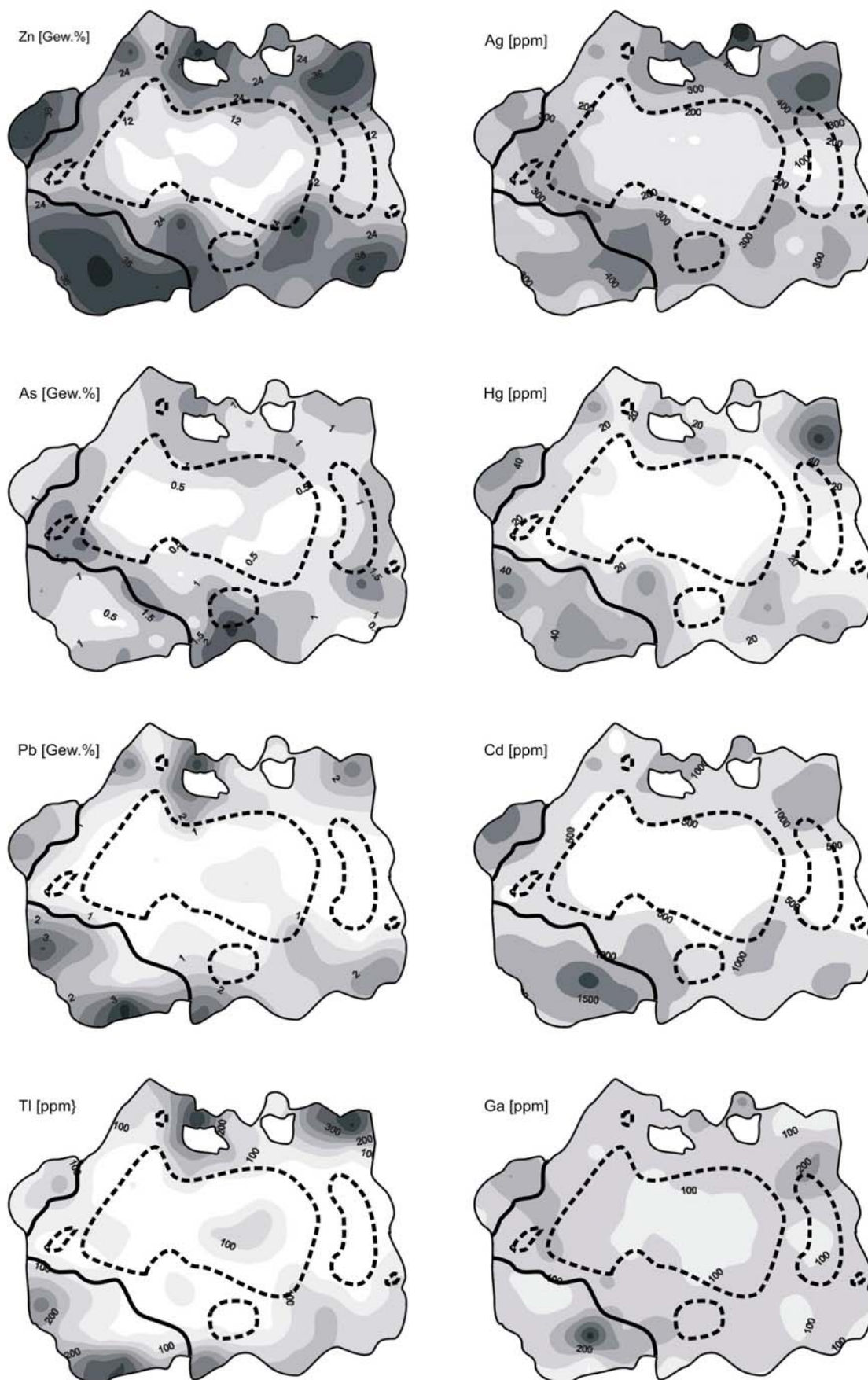


Abb. 14: Geochemische Karten von Zn, Ag, As, Hg, Pb, Cd, Tl und Ga.

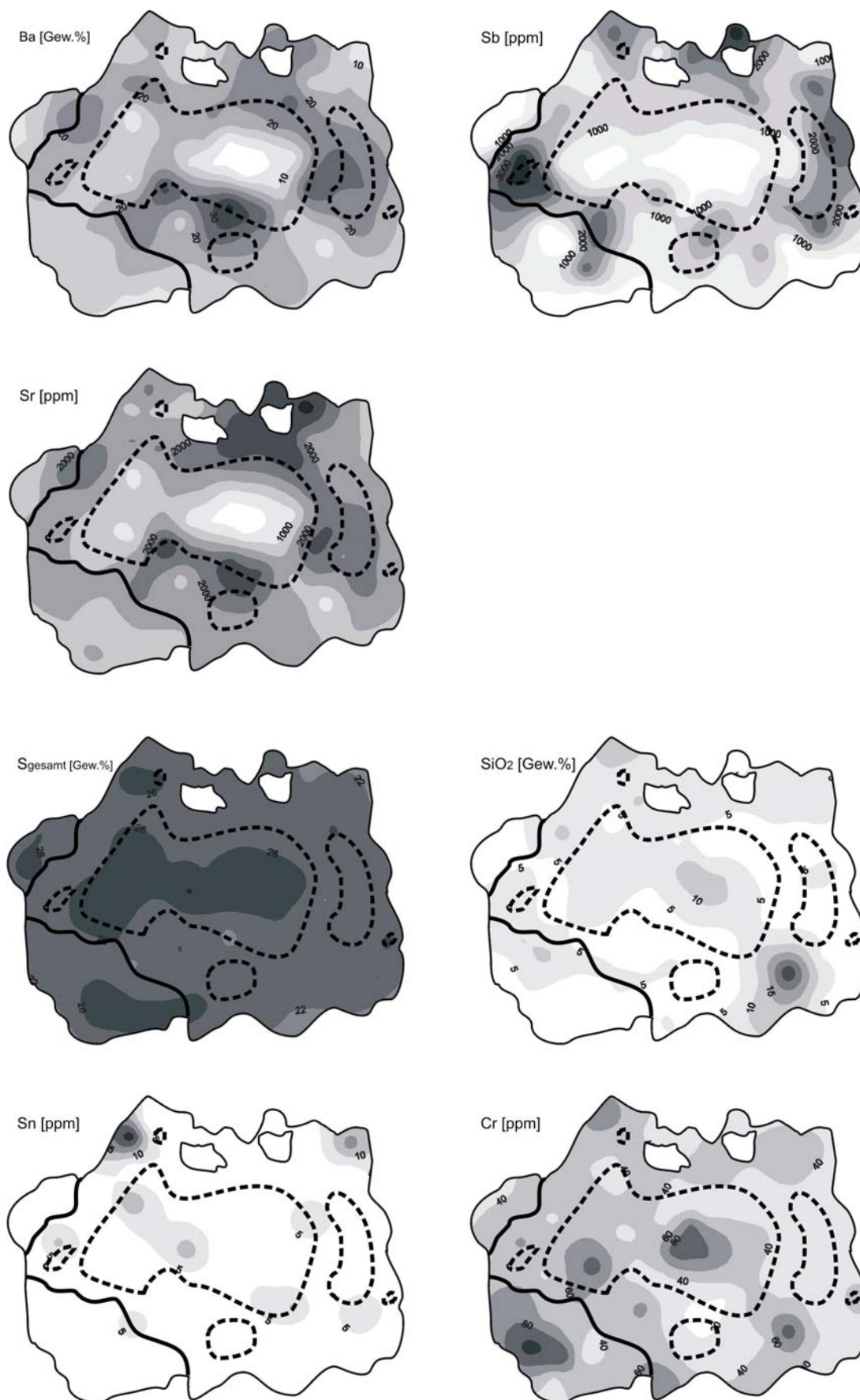


Abb. 15: Geochemische Karten von Ba, Sr und Sb., S_{ges}, SiO₂, Sn und Cr.

Zinn tritt nur mit sehr geringen Gehalten punktuell auf und zeigt ebenfalls keinerlei geochemische Präferenz. Ähnlich wie beim Molybdän sind hier die Gehalte zu gering (<1 ppm – 30 ppm) um eine zuverlässige Aussage zu treffen.

Die Bewertung der Chromverteilung ist schwierig, da Cr in der gesamten Probe mit geringen Gehalten auftritt, aber keine eigenen Chromminerale gefunden wurden und Cr auch sonst nur selten in andere Minerale eingebaut wird. Da Cr eine positive Korrelation mit SiO₂ aufweist ($r = 0,466$) und amorphe Kieselsäure sich erst bei niedrigen Temperaturen bildet, kann möglicherweise gefolgert werden, dass Cr in Minerale eingebaut wird, die erst bei niedrigen Temperaturen gebildet werden.

Genese der Zonierung

Die Probenscheibe 59GTVA besitzt die für schwarze Raucher klassische Zonierung aus Hochtemperaturkern mit Chalkopyrit, während der Rand von Mineralen mit niedrigeren Bildungstemperaturen wie dem Sphalerit oder dem Baryt gebildet wird. Es lassen sich in der Probe verschiedene einzelne Schlotstrukturen differenzieren. Am deutlichsten kommt dies am oberen Rand der Probenscheibe zum Vorschein, wo zwei kleinere Schlotstrukturen nur durch dünne Stege mit dem Rest der Probe verbunden waren (Probe 59-1-59 und Probe 59-1-73). Augenscheinlich kennzeichnen die kieselensäurereichen, rötlichen Sphaleritstrukturen die Randbereiche weiterer ehemals einzelner Schlote. Die Probenscheibe besteht also aus einer Vielzahl ehemals autonomer Schlote, von denen einige auch eigene chalkopyritreiche Zentralbereiche aufweisen. Am unteren und am linken Rand der Probe befinden sich zinkreiche Zonen, bei denen es sich vermutlich um jüngere Schlotstrukturen handelt, die bei geringen Temperaturen entstanden sind. Die Fluide, die diese Strukturen aufgebaut haben, waren entweder nie heiß genug für den Transport von Kupfer oder wurden bereits in tieferen Bereichen des Schlotes abgekühlt.

Die Zonierungen entstehen durch Sulfidpräzipitation in Hohlräume oder durch Ersetzen existierender Minerale in Abhängigkeit ihrer Löslichkeiten. Die Bildung von Chalkopyrit und Sphalerit ist vor allem abhängig von Temperatur und pH-Wert, wobei Chalkopyrit typischerweise bei hohen Temperaturen (>300°C) und Verwachsungen aus Sphalerit und Baryt bei deutlich niedrigeren Temperaturen (175 °C - 250 °C) gebildet werden (Hannington et al., 1995). Da die Temperaturen vor allem durch konduktive Abkühlung und Mischung mit dem Meerwasser gesenkt werden, existiert ein steiler Temperaturgradient vom Inneren zum Rand des Schwarzen Rauchers, der schließlich zur Ausbildung der vorliegenden Zonierung führt. Auch die Elementverteilung kann teilweise auf diese Weise erklärt werden. Untersuchungen lassen vermuten, dass Elemente wie Co, Se und Mo vor allem in hochtemperierten Fluiden angereichert sind, während die Elemente Zn, Ag, Cd, Pb und Sb eher in niedrig temperierten Fluiden auftreten (Trefry et al., 1994). Die Existenz des Temperaturgradienten liefert auch eine Erklärung für die relativ schmalen Chalkopyritauskleidungen der beiden deutlich zu erkennenden Fluidbahnen im oberen Bereich der Probenscheibe (59-1-46) und im rechten unteren Bereich (59-1-75), da hier durch die relativen dünnen Schlotwände eine Abkühlung wesentlich schneller und auf kleinerem Raum erfolgte.

Das Fehlen von Anhydrit in der Probe bestätigt den visuellen Eindruck bei der Probenahme, dass der schwarze Raucher inaktiv war und sich Anhydrit, wenn er denn vorhanden war, aufgrund seiner retrograden Löslichkeit bereits wieder aufgelöst hat. Die mineralogischen Untersuchungen haben in den zentralen Bereichen reliktschen Sphalerit und frühen, „büschelige“ Baryt gezeigt. Sie sind vermutlich aus der niedrig temperierten Anfangszeit der hydrothermalen Aktivität verblieben und wurden mit steigenden Temperaturen teilweise ersetzt. In einigen Schloten wurden kolloidaler Pyrit gefunden, der offenbar noch vor oder gleichzeitig mit dem büscheligen Baryt gebildet wurde. Mit weiterer Erhöhung der Fluidtemperatur im Inneren des schwarzen Rauchers wurden schließlich erst Fahlerz und dann Chalkopyrit gebildet. Es lassen sich zwei Generationen von Fahlerz unterscheiden. Zum einen eine hochtemperierte Generation, welche gemeinsam mit Chalkopyrit in Form idiomorpher Kristalle auftritt, zum anderen eine niedrig temperierte Generation, die vor allem an kolloidalem Sphalerit gebunden ist.

Bei der Bildung von Chalkopyrit und Fahlerz wurden vermutlich auch die ehemaligen Schlotgrenzen überprägt, so dass nur ein großer zentraler Chalkopyritkern zurückblieb. Beim Nachlassen der Fluidaktivität kam es dann zu einer Erniedrigung der Temperatur, die dann zur Ausbildung der großen Barytleisten in den Hohlräumen und danach zur Bildung des kolloidalen Sphalerit führte. Da die großen Barytkristalle lange Wachstumszeiträume benötigen, kann vermutet werden, dass sie aus der Schlussphase der hydrothermalen Aktivität stammen. Ein weiteres Indiz dafür sind die dünnen Lagen aus kolloidalem Sphalerit auf Chalkopyrit des zentralen Bereichs. Der Sphalerit im Randbereich zeigt oft eine deutliche Zonierung mit gelegentlichen Bändern aus Fahlerz und Chalkopyrit. Dies ist ein Indiz dafür, dass die Entwicklung der Probe in mehreren Phasen mit wechselnden Fluidtemperaturen und Schwefelaktivitäten verlief.

Auftreten und Verteilung von Gold

Von den möglichen Komplexen für den Transport von Gold in sauren, reduzierenden hydrothermalen Fluiden ist in dieser Probe der $\text{Au}(\text{HS})^\circ$ -Komplex der wahrscheinlich bedeutendste (Moss et al., 2001). Typisches Indiz für eine hohe H_2S -Aktivität ist relative Eisenarmut der Zinkblende, die sich sowohl optisch als auch geochemisch nachweisen lässt. Ein weiteres Indiz wäre ein geringer Silbergehalt in den Goldkörnern. Ohne Mikrosondendaten kann aber diesbezüglich keine Aussage getroffen werden. Der pH-Wert und die Temperatur können nur geschätzt werden, es bietet sich aber an, die Literaturdaten von Moss et al., 2001 zu nutzen, die von einer Temperatur um $250\text{ }^\circ\text{C}$ und einem pH-Wert von 3 ausgehen (Abb. 16). Wie die Grafik zeigt, fallen die hydrothermalen Fluide des Satanic Mills Hydrothermalfeldes genau in das Stabilitätsfeld des $\text{Au}(\text{HS})^\circ$ -Komplexes. Eine Durchmischung mit Meerwasser ist der effektivste Prozess, um eine Präzipitation von Gold zu bewirken (Hannington et al., 1989).

Mit einem Goldgehalt von durchschnittlich 13,86 ppm enthält die vorliegende Probe verhältnismäßig viel Gold. In dieser Arbeit soll nicht nur die Menge, sondern auch das Auftreten von Gold dokumentiert werden. Die geochemische Karte des Goldes (Abb. 17) zeigt, dass sich das Gold nicht, wie es die Korrelationskoeffizienten vermuten lassen, direkt in den kupferreichen Zonen befindet, sondern sich auf deren Ränder konzentriert.

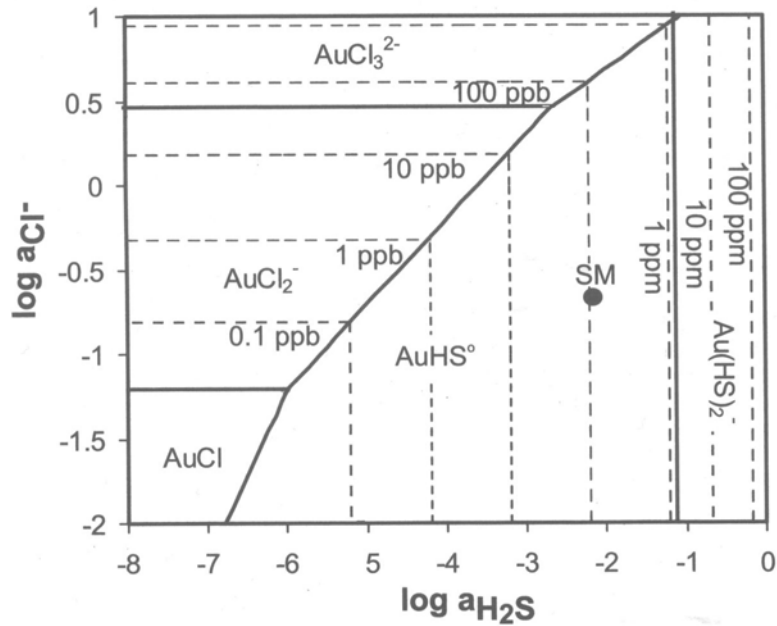


Abb. 16: Stabilitätsfelddiagramm einzelner Gold-Komplexe mit der Position der hydrothermalen Fluide des Satanic Mills Hydrothermalfeldes.

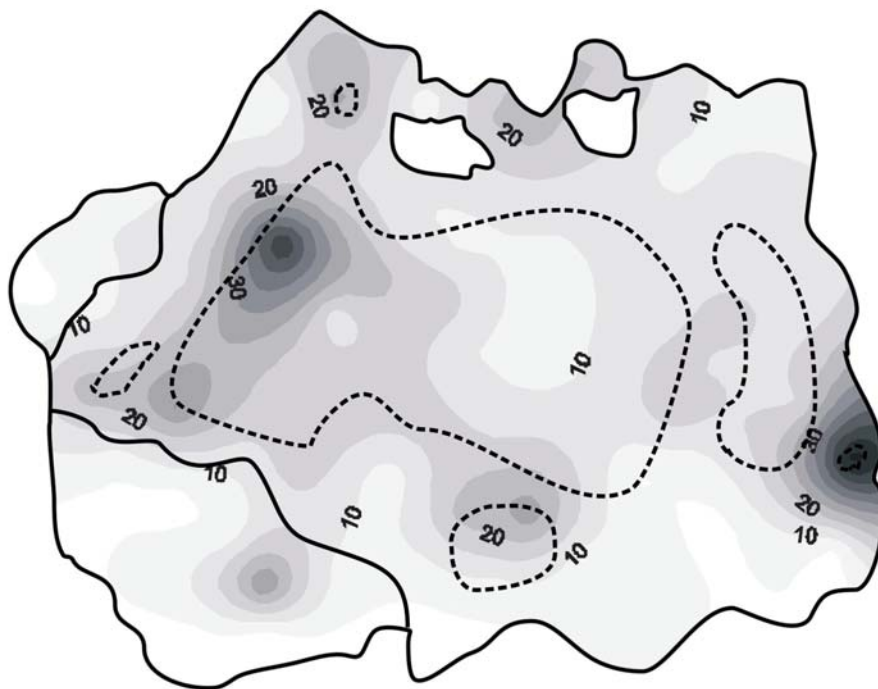


Abb. 17: Verteilung von Gold innerhalb der Probe 59GTVA.

Es ist weiterhin auffällig, dass es lokale Goldmaxima gibt. Von besonderer Bedeutung sind dabei die Proben 59-1-46 (26,8 ppm), 59-1-31 (50,7 ppm), 59-1-24 (32,7 ppm), 59-1-75 (58,5 ppm) und 59-1-10 (30,9 ppm). Bei den Proben 46 und 75 handelt es sich um die zentralen Fluidkanäle ehemals separater Schlotstrukturen. In den porösen Wänden dieser kleinen Kanäle kommt es schnell zu einem Zutritt von Meerwasser und den damit

verbundenen Änderungen der geochemischen Bedingungen. Da diese Wände dünn sind, ist der thermische Gradient steil und die Durchmischungszone mit dem Meerwasser sehr schmal, was zu einer schlagartigen Bildung des Chalkopyrits auf einem sehr begrenzten Raum führt. Durch das damit verbundene Absinken der H_2S -Fugazität kommt es gleichzeitig zu einer Präzipitation des Goldes. Auch bei den Proben 31 und 24 gruppieren sich die Goldkörner um massivere Chalkopyritstrukturen, die Ursache für die Präzipitation kann also auch hier ein schlagartiger Verlust des H_2S durch Sulfidbildung sein. Im Gegensatz zu den Proben 75 und 46 handelt es sich hier allerdings nicht um ehemals separate Schlotstrukturen, der thermische Gradient müsste demnach deutlich flacher sein. Andererseits liegen beide Proben am Rand des zentralen Chalkopyritkerns der Probenscheibe, wodurch eine Abkühlung bzw. Durchmischung durch seitlich zutretendes Meerwasser möglich ist.

Ein anderer möglicher Aspekt ist ein Wechsel der Goldgehalte in den Fluiden. Es ist also durchaus vorstellbar, dass die Goldanreicherung im hydrothermalen Fluid im Laufe der Entwicklung abgesunken ist. In diesem Fall könnte man die Proben mit den starken Goldanreicherungen als Relikte einer frühen Phase der Entwicklung des Hydrothermalfeldes ansehen, um die herum sich später der Rest des schwarzen Rauchers gebildet hat. Ein solcher Ansatz ist für die Erklärung der lokalen Goldmaxima aber nicht notwendig, da sie auch über die Breite der Durchmischungszone mit dem Meerwasser erklärt werden können.

Eine Besonderheit stellt die Probe 59-1-10 dar. Sie ist fast völlig frei von Chalkopyrit und stammt offensichtlich aus einem Bereich der Probe, der bei niedrigeren Temperaturen gebildet worden ist. Bei den mikroskopischen Untersuchungen wurde kein freies Gold gefunden. Aussagen über das Wirtsmineral sind daher schwierig zu treffen, wahrscheinlich handelt es sich aber um submikroskopische Körnchen im Sphalerit, wie sie auch von Moss et al. (2001) aus dem PACMANUS Hydrothermalfeld angenommen wurden. Trotz der geringeren Temperaturen kann auch hier problemlos der $\text{Au}(\text{HS})^\circ$ -Komplex für den Goldtransport verantwortlich gemacht werden, da er bis zu einer Temperatur von 120°C der stabilste Goldkomplex in den Fluiden des PACMANUS Hydrothermalfeldes ist (Moss et al., 2001).

Vernachlässigt man die lokalen Goldmaxima in der Probe, so fällt auf, dass die geringen Goldgehalte im Inneren des zentralen chalkopyritreichen Kerns zum Rand des Kerns langsam ansteigen, um dann zum Rand hin wieder abzusinken. Die Goldpräzipitation findet also vor allem in der Übergangszone Chalkopyrit/Baryt statt. Die Barytzone kann als der Bereich angesehen werden, in dem das sulfatreiche Meerwasser auf das hydrothermale Fluid trifft. Es kommt an dieser Stelle zu umfangreichen Veränderungen des geochemischen Milieus, was die Goldpräzipitation erklärt. Die Dicke der Außenwand, die Größe des schwarzen Rauchers sowie die hohe Porosität bewirken, dass die Durchmischungszone von Meerwasser und hydrothermalen Fluid relativ breit ist. Es kommt daher nicht zu einer schlagartigen Goldbildung mit sehr hohen lokalen Gehalten, sondern zu einer größeren Verteilung des Goldes innerhalb der Durchmischungszone. Das Fehlen einer scharfen Ausfällungsfront ist auch ein Indiz dafür, dass boiling bei der Goldpräzipitation keine oder nur eine untergeordnete Rolle gespielt hat.

Zusammenfassung

In der vorliegenden Untersuchung sollten die geochemischen Zonierungen innerhalb eines schwarzen Rauchers mineralogisch und geochemisch dokumentiert werden. Die untersuchte Probenscheibe weist eine stark temperaturbestimmte Zonierung auf. An einen Kern mit Hochtemperaturmineralen wie Chalkopyrit schließt sich eine niedriger temperierte Zone mit Baryt an, auf die wiederum eine noch niedriger temperierte Zone mit kolloidaler eisenarmer Zinkblende folgt. An den zentralen Schlot sind seitlich weitere Zn-reiche Schlote angewachsen.

Die Analyse der geochemischen Daten mit Hilfe der Korrelationskoeffizienten und der Faktorenanalyse hat gezeigt, dass es möglich ist, die gemessenen Elemente grob in vier Gruppen einzuteilen und diese Gruppen jeweils einzelnen Zonen zuzuweisen. Die Elemente Cu, Fe, In, Bi und Au sind vor allem mit dem hochtemperiert gebildeten Kern assoziiert, die Elemente Ba und Sr finden sich im Baryt, während andere Elemente wie Pb, Zn, Hg, Cd, Tl, Ga, Ag, As und Sb vor allem auf den Rand der Probenscheibe konzentrieren und dort in Mineralen wie Sphalerit (vor allem Zn, Cd, Hg), Fahlerz (mit As, Sb, Ga, Tl, Hg), Arsensulfiden (mit As, Pb) und Galenit (mit Pb, Ag) auftreten. Insbesondere bei den extrem niedrig temperierten Bildungen kommt es dabei oft vor, dass sich Mineralgemische bilden, die sich kaum mehr in einzelne Minerale aufgliedern lassen. Andere Elemente wie S, SiO₂ sowie die Spurenelemente Cr, Mo und Sn ließen sich nur schwer in eine der Gruppen einordnen.

Der Goldtransport in der Probe wurde vermutlich hauptsächlich durch den Au(HS)⁰-Komplex realisiert. Dafür sprechen Indizien wie eine hohe H₂S-Aktivität, welche durch die Eisenarmut des Sphalerit belegt wird, die hohen Bildungstemperaturen von wahrscheinlich mehr als 250 °C und der niedrige pH-Wert der Lösungen (pH ~ 3; Douville et al., 1999). Die Goldpräzipitation wird vermutlich vor allem durch eine Mischung des hydrothermalen Fluids mit dem Meerwasser bewirkt. Innerhalb der Probe tritt das Gold vor allem in zwei Ausprägungen auf. Zum einen gibt es eine Reihe von lokalen Maxima, zum anderen gibt es einen generellen Anstieg der Goldgehalte in der Übergangszone vom chalkopyritreichen Kern zur barytreichen Zone. In beiden Fällen wird die Goldpräzipitation durch eine Erniedrigung der H₂S-Aktivität und einer Abkühlung des hydrothermalen Fluids durch die Durchmischung mit dem Meerwasser erreicht. Im Grenzbereich des chalkopyritreichen Kerns findet dieser Prozess in einer relativ breiten Durchmischungszone statt. Im Gegensatz dazu sind die lokalen Goldmaxima immer mit massiven Chalkopyritwänden direkt an den Fluidkanälen assoziiert. Offenbar ist hier die Durchmischungszone wesentlich schmaler, so dass sich die Goldpräzipitation und die Bildung von Chalkopyrit auf einem wesentlich kleineren Raum vollziehen.

Titel der Diplomarbeit: Einfluss multipler Episoden hydrothermaler Aktivität auf die Remobilisierung und Anreicherung von Gold, Silber, Kupfer und Zink in massiven Sulfiden im PACMANUS Hydrothermalfeld (Manusbecken, Papua Neu Guinea)

Methodik

Für die Diplomarbeit wurden die Bohrkern 60RD, 65RD sowie 69RD der Forschungsfahrt SO-166 verwendet. Aus diesen Kernen wurden insgesamt 14 Proben für geochemische Untersuchungen mittels INAA (Instrumental Neutron Activation Analyses), ICP-OES (Inductively coupled plasma optical emission spectrometry) sowie ICP-MS (Inductively coupled plasma mass spectrometry) entnommen. Weiterhin wurden von 20 repräsentativen Stücken Dünnschliffe für mikroskopische Untersuchungen angefertigt und für die quantitative Mineralanalytik (gediegen Gold und Sphalerit) mittels Mikrosonde verwendet. Ein weiterer Schwerpunkt war die Anwendung der Untersuchung radiogener Isotope (U/Th) an 11 ausgewählten Proben um die Natur des hydrothermalen Systems, insbesondere die zeitliche Einordnung desselben, zu verstehen. Diese Untersuchung erfolgte unter Aufsicht von DR. J. SCHOLTEN von der Universität Kiel. Basis für die Erklärung der Anreicherung von Au, Ag, Cu und Zn in den drei untersuchten Bohrkernen bildete neben der oben aufgeführten Analytik der Vergleich mit Untersuchungen der Oberflächenproben (Moss et al., 2001) als auch Resultate der ODP Bohrung 193 (Yeats et al., 2001; Moss und Scott, 2001; Moss et al., 2001; Binns et al., 2002; Lowell und Yao, 2002; Yang und Scott, 2002; Bach et al., 2003; Paulick et al., 2003; Roberts et al., 2003; Lackschewitz et al., 2004; Vanko et al., 2004). In den angeführten Arbeiten wurden bereits die Nebengesteine der hydrothermalen Vererzung charakterisiert, so dass diese Erkenntnisse ebenfalls in die Arbeit eingebunden werden konnten. Hauptaugenmerk waren neben der detaillierten Beschreibung der Bohrkern die Beschreibung und Charakterisierung der Prozesse, welche für den Transport sowie die Anreicherung der Goldkörner an den untersuchten Proben ursächlich waren.

Resultate und Interpretation

Die mineralogischen und petrologischen Untersuchungen zeigten, dass die untersuchten hydrothermalen Präzipitate vier unterschiedlichen Mineralparagenesen zuzuordnen:

- nodulare Pyrit-Chalkopyrit-Anhydrit-Brekkzien
- massive, lokal goldreiche Chalkopyrit-Sphalerit-Aggregate
- massive, lokal goldreiche Sphalerit-Baryt(±amorphe Kieselsäure)-Aggregate
- Baryt-amorphe Kieselsäure dominierte Proben.

Vergleichbare Brekkzien fehlen in den von Moss und Scott (2001) beschriebenen Oberflächenproben.

Mineralogie

Die massiven Chalkopyrit-Sphalerit Aggregate repräsentieren die typische Mineralogie eines zonierten Chimneys mit Chalkopyrit-reichem Interieur sowie Sphalerit-reichem Exterieur. Covellin ist immer mit Chalkopyrit und frühem Fe-reichem Sphalerit assoziiert. Frühe Mineralisationsereignisse sind in den untersuchten Dünnschliffen charakterisiert durch dunkelbraunen Fe-reichen

Sphalerit, Chalkopyrit und vereinzelt Pyrrhotin. Der beobachtete Sphalerit ist überwiegend zoniert mit einem Fe-reichem Kern und Fe-armen Rändern. Die jüngsten Phasen hydrothermaler Aktivität sind gekennzeichnet durch das Auftreten von Auripigment und Realgar. Die dritte Mineralparagenese ist durch das Auftreten von porösen Sphaleritaggregaten sowie Rosetten aus prismatischem Baryt gekennzeichnet. Spurenminerale sind hier Fahlerz, Covellin sowie As-Sulfide. Zwei der untersuchten Proben sind zudem an Au angereichert. Eine goldreiche Probe besteht überwiegend aus Sphalerit sowie amorpher Kieselsäure (69RD(101-105)). Die Baryt-amorphe Kieselsäure Paragenese wurde lediglich in einem Schliff festgestellt (60RD(000-004)). Vergleichbare Oberflächenproben wurden nicht beschrieben.

Auftreten von gediegen Gold

Die Au-Anreicherung ist insgesamt gesehen sehr heterogen verteilt und konzentriert sich auf zwei Teilkern: 65RD(030-040) und 69RD(085-120). Um die Au-Anreicherung näher zu spezifizieren wurden in 4 Au-reichen Dünnschliffen (69RD(019-026), 65RD(026-030), 69RD(101-105) und 69RD(108-112) die Verteilung der Goldkörner bestimmt. Sie gehören zu zwei Mineralparagenesen: Chalkopyrit-Sphalerit (65RD) sowie Sphalerit±Baryt±amorphe Kieselsäure (69RD). Die Verteilung der Goldkörner ist in Tabelle 1 wiedergegeben.

Tab. 1: Verteilung der Goldkörner innerhalb der Bohrkern 65RD, 69RD sowie in Sulfiden des Manusbeckens

	65RD	69RD	Oberflächenproben ¹
Einschlüsse in Chalkopyrit	172	65	49
Sphalerit	6	394	5
Pyrit	27	1	-
Amorphe Kieselsäure	2	69	-
Galenit	-	1	-
Tennantit	-	-	232
Bornit	-	-	1
Korngrenze zw. Sphalerit/Chalkopyrit	11	74	7 ²
Galenit/Chalkopyrit	-	1	-
Amorphe Kieselsäure/Sphalerit	-	4	-
Tennantit /Sphalerit/Chalkopyrit	-	2	-
Chalkopyrit/Pyrit/Sphalerit	-	1	-
Hohlraumfüllung	12	35	4
Risse in Mineralen	-	46	5
Summe	230	693	303

¹ – Oberflächenproben (PACMANUS und Susu Knolls; MOSS UND SCOTT, 2001), ² – alle Korngrenzen

Goldkörner in Kern 69RD kommen überwiegend als mikrometergroße Einschlüsse in Sphalerit, Chalkopyrit und amorpher Kieselsäure vor. Goldkörner in amorpher Kieselsäure oder in der Nähe von Galenit repräsentieren vermutlich die letzten Phasen der Goldremobilisation und sind möglicherweise Hinweise für mehrphasige Mineralisationsereignisse. Verschiedene Körner kommen als auch späte Hohlraumfüllungen vor. Die in den Bohrkernen beobachteten Goldkörner sind überwiegend rund und schmal. Goldkörner > 5µ zeigen meist unregelmäßige oft kantige Formen. Kleine Körner (< 3µ) treten oft gehäuft in Gruppen mit mehr als 5 Körnern auf. Die Mehrzahl der Körner ist < 4µ und damit etwas größer als diejenigen von Oberflächenproben, wo die Mehrzahl der Körner < 2µ ist (siehe Abbildung 1).

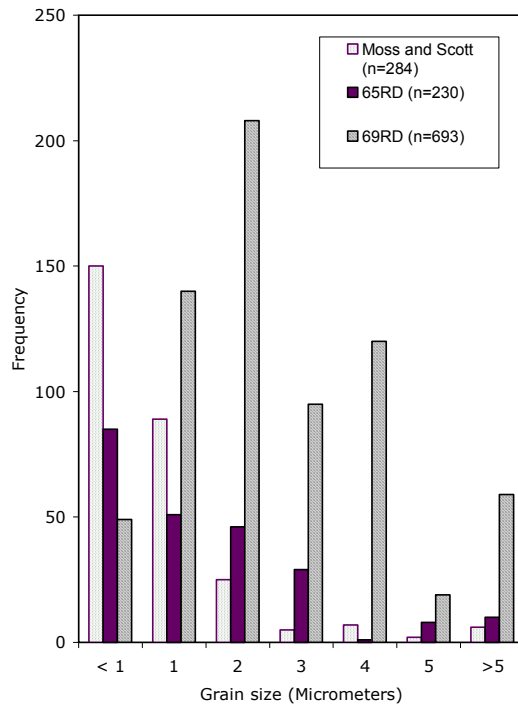


Abb. 1: Korngrößenverteilung der Goldkörner aus den Bohrkernen 65RD und 69RD (Korngröße bis 10 μ m) im Vergleich zu Ergebnissen von Oberflächenproben des PACMANUS und des Susu Hydrothermalfeld (Moss und Scott, 2001).

Kleine Goldkörner (< 3 μ) treten bevorzugt in den mehr von Chalkopyrit dominierten Proben auf (65RD, und Oberflächenproben), während die Goldkörner im Kern 69RD deutlich größer sind. Das Gold in den Oberflächenproben ist überwiegend an Verwachsungen von Chalkopyrit, Covellin, Tennantit und Bornit gebunden und tritt dabei überwiegend als Einschluss in Tennantit sowie Chalkopyrit auf. Sphalerit ist eher selten. Solche Cu-As-reichen Paragenesen wurden in den untersuchten Bohrkernen nicht beobachtet, was insbesondere auf das Fehlen von Tennantit in den Bohrkernproben zurückzuführen ist. Goldreiche Chalkopyrit-Sphalerit Paragenesen sind insgesamt relativ selten in rezenten submarinen Sulfidlagerstätten anzufinden (Hannington et al., 2005). Eine Cu-Au-Assoziation ist in Cu-reichen Sulfiden des an ultramafische Gesteine gebundenen Logatchev Hydrothermalfeldes am Mittelatlantischen Rücken gefunden worden (Krasnov et al., 1995, Murphy und Meyer, 1998) ist aber vermutlich an spezielle sekundäre Prozesse gebunden sie eine Anreicherung von Au und Cu in den Oberflächenproben bewirkt haben.

Geochemie

Die geochemischen Analyse von 14 Bohrkernproben reflektiert die schon dargestellte mineralogische Zusammensetzung der untersuchten Proben. Hohe Fe-Gehalte in einigen Proben (2.4-40.3 Gew. %) sowie hohe S-Gehalte (23.6-38.7 Gew. %) zeigen das deutliche Auftreten von Pyrit und Chalkopyrit in den untersuchten Proben an. Die ebenfalls teilweise hohen Gehalte an Zn (0.12- 44.66 Gew. %) und Cu (0.19-12.89 Gew. %) dokumentieren die Dominanz von Sphalerit und Chalkopyrit in einigen Proben. Lokal erhöhte Gehalte an Ba, Ca sowie SiO₂ reflektieren lokal das Vorkommen von Baryt, Anhydrit und amorpher Kieselsäure wider. Die Abwesenheit von Anhydrit im Kern 65RD ist vermutlich auf die retrograde Löslichkeit von Anhydrit bei Temperaturen unter 150°C (Blount und Dickson, 1969) und zeigt das der beprobte Bereich hydrothermal nicht aktiv war. Der Pb-Gehalt einiger Proben ist mit bis zu 1,9 Gew. % deutlich erhöht.

Die Gehalte an ausgewählten Spurenelementen sind lokal erhöht und variieren mitunter sehr deutlich (u.a. As, Sb, Au und Ag). Die durchschnittlichen Gehalte betragen in absteigender Folge: 0,2 Gew. % As, 673 ppm Cd, 459 ppm Sb, 149 ppm Ag, 70 ppm Ga, 27 ppm Co sowie 26 ppm In. Im Gegensatz dazu sind die durchschnittlichen Gehalte an Mo (39 ppm), Se (6,3 ppm), U (3,4 ppm), Bi (2,8 ppm) sowie Hg (2,1 ppm) vergleichsweise niedrig. Die Anreicherung an As, Sb, Ba und Pb ist typisch für Massivsulfidvorkommen in vulkanische Bögen die mit felsischen Vulkaniten assoziiert sind (Herzig und Hannington, 2000).

Die Goldgehalte der untersuchten Proben variieren von 0,94 bis 57 ppm Au mit einem Durchschnittsgehalt von 12,4 ppm (N=14). Es besteht keine Korrelation zwischen dem Au-Gehalt und den Konzentrationen von Zn, Cu, Pb und SiO₂. Eine positive Korrelation konnte allerdings zwischen Au und den Gehalten an Cd, Ga, In sowie Sb nachgewiesen werden. Eine negative Korrelation existiert zwischen Ag und CaO, welche mit der inversen Beziehung zwischen Ag und Anhydrit in hydrothermalen Präzipitaten erklärt wird (Moss und Scott, 1996). Silber zeigt eine positive Korrelation mit Cu, S und Ba. Die Korrelation zwischen Au, Ag und Sb impliziert möglicherweise eine gleichzeitige Präzipitation von Mineralen, die diese Elemente enthalten. Im Vergleich zwischen den vorliegenden Daten und den Oberflächenproben (Moss and Scott, 2001) zeigt vergleichbare Zn-Konzentrationen an. Die Cu-Gehalte in den Oberflächenproben sind jedoch doppelt so hoch wie in den hier untersuchten Bohrkernen. Ebenfalls erhöht sind in den Oberflächenproben die Gehalte an Pb, Ag, As und Sb.

Tab. 2: Durchschnittliche Gehalte an ausgewählten Elementen von Bohrkernproben aus dem Roman Ruins Hydrothermalfeld (diese Arbeit) im Vergleich zu anderen submarinen Massivsulfidvorkommen in verschiedenen geotektonischen Milieus.

Tektonisches Milieu	Name der Lagerstätte	N	Cu Gew. %	Zn Gew. %	Pb Gew. %	Fe Gew. %	Ba Gew. %	Au ppm	Ag ppm	As ppm	Sb ppm
Sedimentfreier Mittelozeanischer Rücken	¹	1454	3.9	9.0	0.2	24.7	3.0	1.0	125	430	60
	Mt. Jourdanne ²	7	2.0	18.4	1.2	15.6	nd	5.2	750	5760	450
Sediment-führende Mittelozeanische Rücken	Escanaba Trog	35	2.2	7.1	1.7	30.5	3.6	1.5	205	6290	1000
	Guaymas Becken ⁴	22	0.4	2.2	0.4	17.4	10.4	0.2	82	100	110
	Middle Valley ⁵	92	0.4	1.5	<0.1	30.2	1.8	0.2	7	63	11
Inselbogen-systeme	Suiyo Seamount ⁶	13	12.8	17.5	0.7	15.0	0.1	27.7	160	1170	585
Intrakontinentaler Back-Arc	Okinawa Trog	40	3.3	20.2	11.8	6.2	7.2	3.1	2304	17500	6710
Intraozeanischer Back-Arc	Lau Basin ⁸	87	5.5	27.6	0.3	7.4	10.8	3.2	120	1900	76
	Roman Ruins Bohrkern (diese Arbeit)	14	4.3	22.2	0.5	13.7	9.1	12.4	149	2022	459

Abkürzungen: nd=keine Daten : ¹ Herzig und Hannington (1995); ² Muench et al. (1999, 2001); ³ Koski et al. (1988) und Koski et al. (1994); ⁴ Koski et al. (1985) und Peter und Scott (1988); ⁵ Ames et al. (1993) und Krasnov et al. (1993); ⁶ Watanabe und Kajimura (1993, 1994); ⁷ Halbach et al. (1989) mit zusätzlichen Daten von Aoki und Nakamura (1989) und Nakamura et al. (1990); ⁸ Fouquet et al. (1993), Herzig et al. (1993) und Petersen et al. (2004); ⁹ Moss und Scott (2001).

Bei einem Vergleich der geochemischen Daten der Bohrkernproben mit der Durchschnittszusammensetzung andere submariner Massivsulfidvorkommen sind Ähnlichkeiten in den Konzentrationen von Cu und Zn mit denen von Vorkommen im Izu-Ogasawara Inselbogen, Mt. Jourdanne (Indischer Ozean) sowie von Proben aus dem Lau Becken vorhanden (Tab. 2). Die Gehalte an Au, Ag, Sb und As in Bohrkernen von Roman Ruins sind denen von Proben des Suiyo Seamount (submariner Vulkan in einem Inselbogenmilieu) und aus dem Lau Becken vergleichbar.

Mineralchemie

Die Unterschiede in der Mineralogie zwischen den beiden goldreichen Probenotypen spiegelt sich auch in den unterschiedlichen Ag-Gehalten der Goldkörner aus beiden Paragenesen wider. Insgesamt wurden 76 Goldkörner hinsichtlich ihres Silbergehaltes untersucht. Die Goldkörner der Sphalerit-Barit-Kieselsäure-Assoziation sind generell an Ag angereichert (bis zu 16,4 Gew. % Ag; \bar{x} 11,1 Gew. % Ag, N=51). Im Gegensatz dazu sind die untersuchten Goldkörner der Chalkopyrit-Sphalerit-Assoziation mit einem maximalen Gehalt von 8,7 Gew. % Ag (\bar{x} 3,6 Gew. % Ag, N=25) generell silberarm. Die Häufigkeitsverteilung der Goldreinheit zeigt eine deutlich bimodale Verteilung.

Insgesamt lässt sich festhalten, dass vergleichbar hohe Silbergehalte in gediegen Gold bisher von keiner anderen submarinen Massivsulfidlagerstätten beschrieben worden sind.

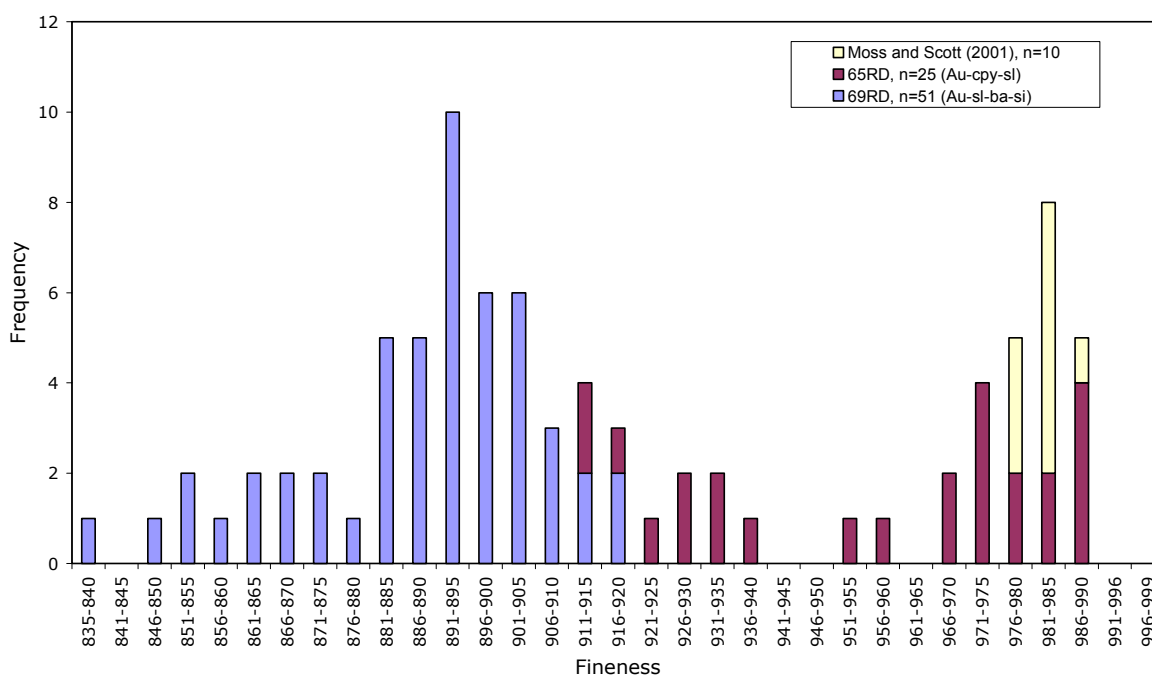


Abb. 2: Häufigkeitsverteilung der Goldfeinheit der untersuchten Goldkörner aus den Bohrkernen 65RD, 69RD sowie aus Oberflächenproben (MOSS UND SCOTT, 2001); Au-Cpy-Sl: Gold-Chalkopyrit-Sphalerit-reiche Proben, Au-Sl-Ba-Si: Gold-Sphalerit(±Barit±Kieselsäure)-reiche Proben

Weiterhin wurden mittels Mikrosonde in 12 repräsentativen Dünnschliffen Sphalerite hinsichtlich ihrer Zusammensetzung untersucht. Der FeS-Gehalt im mit Pyrit koexistierenden Sphalerit ist in erster Näherung umgekehrt proportional zur Schwefelaktivität (Barton und Toulmin, 1964; Scott und Barnes, 1971). Die Untersuchungsergebnisse zeigten, dass die Spurenelementgehalte, insbesondere die Gehalte an Pb, Cd und Sb, in Sphalerit angehoben sind. Die Gehalte an Hg, Te, Ga, Mn sowie Se sind generell sehr niedrig und oftmals unterhalb der jeweiligen Nachweisgrenze.

Ingesamt variiert der FeS-Gehalt von $< 0,01$ bis 27,9 mol FeS (N=1560). Die Gehalte an Cu und Fe sind lokal mit max. 16,04 Gew. % Fe und 8,51 Gew. % Cu deutlich erhöht. Dies deutet auf Einschlüsse innerhalb der untersuchten Sphalerite hin. In Abb. 4 ist daher die Verteilung der auf Cu korrigierten Analysen der FeS-Gehalte der goldreichen Proben dargestellt.

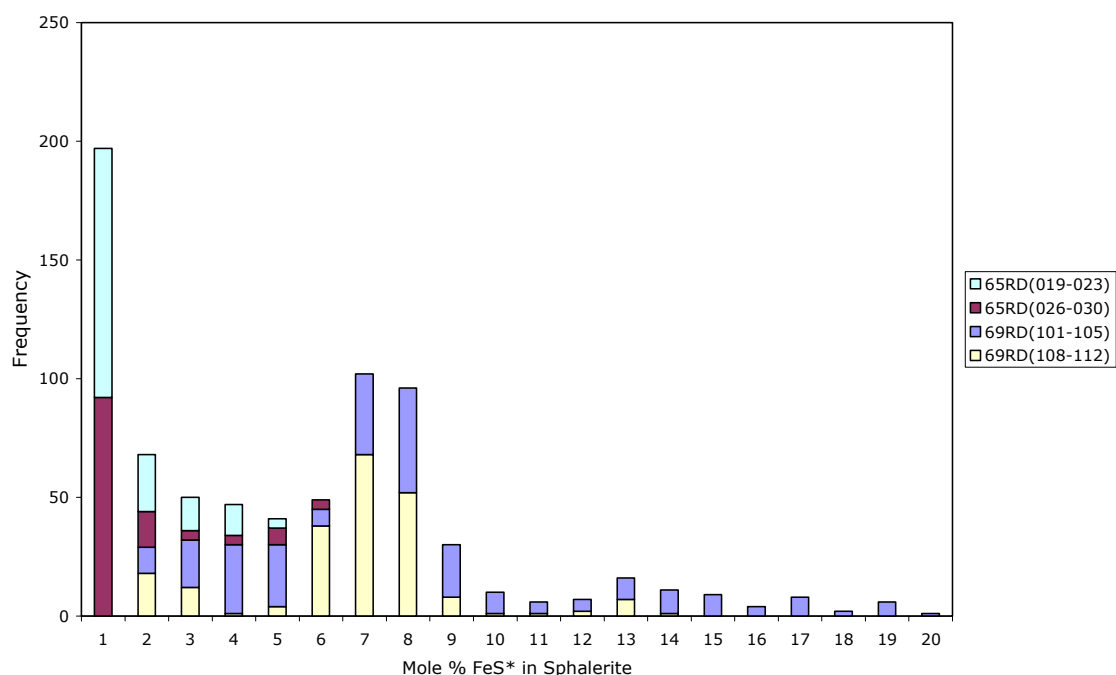


Abb 4: Gehalte von FeS in Sphalerit goldreicher Dünnschliffe.

Die Verteilung der FeS*-Gehalte in den Sphaleriten aller drei untersuchten Bohrkerne zeigt deutlich unterschiedliche Verteilungsmuster (Abb. 5). Die Kerne 60RD sowie 69RD zeigen eine bimodale Verteilung mit Fe-armen Sphaleriten, meist im Topbereich der untersuchten Kerne, sowie früh präzipitierte, deutlich Fe-reiche Sphalerite im ganzen Kern verteilt. Die Sphalerite im Kern 65RD sind durchweg Fe-reicher und mehr heterogen verteilt. Die Verteilung innerhalb der Bohrkerne zeigt ein Anwachsen der FeS-Gehalte zur Mitte des Kerns hin (goldreiche Proben 69RD(101-105) und 69RD(108-112)). Mikroskopische Untersuchungen an ausgewählten Dünnschliffen zeigen generell die unterschiedlichen Phasen der Sphaleritpräzipitation. Diese unterschiedlichen Stadien können anhand der mehr dunkelbraunen bis braunen frühen Fe-reichen Sphalerite im Gegensatz zu den mehr honigfarbenen, meist dendritisch auftretenden Fe-armen Sphalerite unterschieden werden. Die Wachstumszonen zeigen Wechsel in der Bildungstemperatur an, aber auch eine multiphase hydrothermale Aktivität, die durch unterschiedliche Phasen der

Mineralisation im Wechsel mit hydrothormaler Wiederaufarbeitung geprägt sind. Ursachen für die unterschiedlichen Fe-Gehalte liegen auch in der Auflösung früh gebildeter Sphalerite während der Interaktion mit späten hydrothermalen Lösungen oder durch die Präzipitation von Pyrit verbunden mit sauren Bedingungen, welche zur Auflösung primärer Fe-reicher Sphalerite führt. Diese werden dann oberflächennah als Fe-arme Sphalerite wieder ausgefällt (Tivey et al., 1995; Petersen 2000). Die Erniedrigung des pH-Wertes durch die Präzipitation von Sulfiden ist möglicherweise ebenso kausal für die lokal bevorzugte Bildung von Markasit im Gegensatz zu Pyrit verantwortlich (Murowchick und Barnes, 1986).

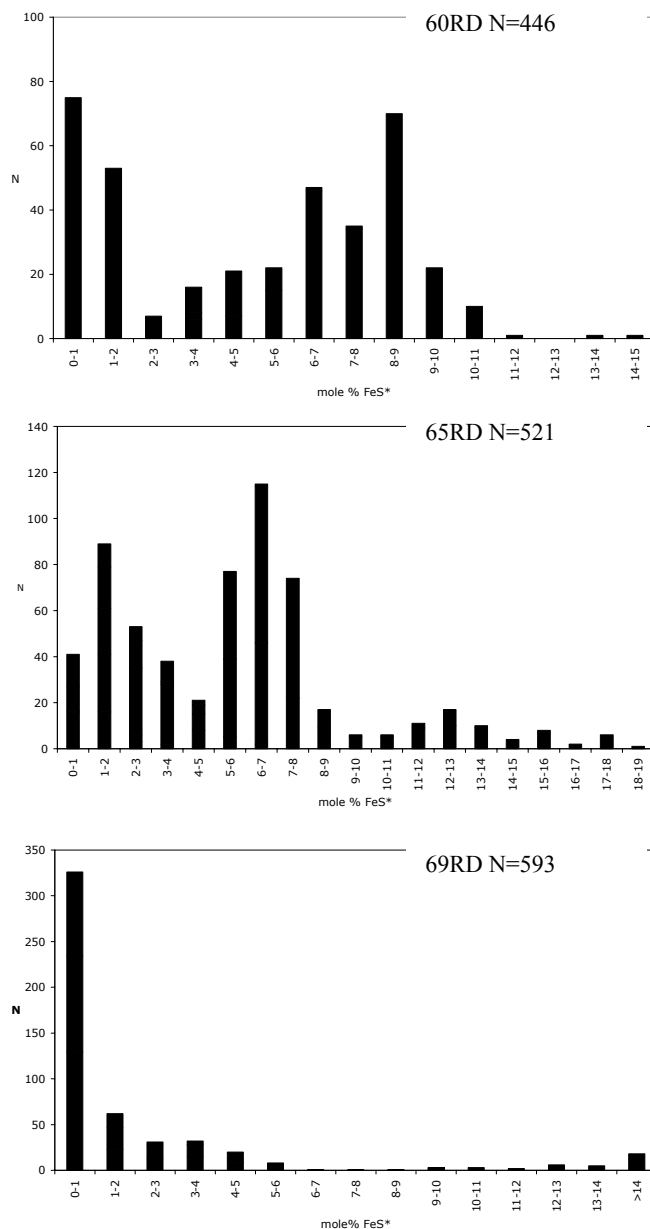


Abb. 5: Histogramme des FeS-Gehaltes in Sphalerit dreier Bohrkern vom Roman Ruins Hydrothermalfeld (60RD, 65RD und 69RD).

Altersdatierungen

Die an ausgewählten Sulfiden durchgeführte Bestimmung des $^{230}\text{Th}/^{234}\text{U}$ -Ungleichgewichtes erlaubt die Altersbestimmung hydrothermalen Ablagerungen. Dieses Ungleichgewicht erlaubt eine Datierung im Bereich von < 1.000 bis 300.000 Jahre (LALOU UND BRICHET, 1987).

Die Methode basiert auf der Annahme, dass während der authigenen Präzipitation Uran inkorporiert wird und alles ^{230}Th in diesen Präzipitaten ausschließlich aus dem Zerfall von ^{234}U resultiert und kein terrigenes ^{230}Th in das System eingebunden ist (SCHOLTEN ET AL., 2000). Indirekter Beweis hierfür ist die Abwesenheit von ^{232}Th , welches nur terrigen vorkommt. Die an den Sulfidfragmenten bestimmten Alter sind in Tab. 3 aufgeführt. Das Verhältnis $^{234}\text{U}/^{238}\text{U}$ in den Sulfiden entspricht weitestgehend dem Verhältnis im Meerwasser ($^{234}\text{U}/^{238}\text{U}=1.149$). Die geringen Urangehalte sind möglicherweise auch ein Resultat der Rekristallisation der Sulfide als Resultat der Zirkulation hydrothermalen Lösungen und Meerwasser durch die Massivsulfide nach ihrer Bildung. Dieser Effekt wurde schon von KRASNOV ET AL. (1995) für die submarine Bent Hill Ablagerung beschrieben.

Tab. 3: Vorläufige Altersbestimmung für Sulfidfragmente vom Roman Ruins Hydrothermalfeld (Dr. J. SCHOLTEN, UNIVERSITÄT KIEL, pers. Mitteilung)

Probe	^{232}Th		^{230}Th		U238		U234	
	dpm/g	+/-	dpm/g	+/-	dpm/g	+/-	dpm/g	+/-
SO166-60RD(030)	1.13E-08	2.47E-10	1.32E-02	7.94E-04	2.632	0.014	3.024	0.033
SO166-60RD(049)	1.21E-08	1.73E-10	1.34E-02	3.91E-04	3.893	0.044	4.474	0.077
SO166-60RD(085)	5.19E-08	2.49E-09	5.78E-02	6.79E-03	0.186	0.002	0.197	0.003
SO166-63RD(030)	4.33E-09	3.40E-10	7.63E-02	5.90E-03	3.501	0.032	4.070	0.059
SO166-65RD(043)	9.10E-09	1.82E-10	1.09E-02	7.83E-04	1.080	0.016	1.225	0.029
SO166-66RD(060)	3.13E-09	4.79E-11	3.81E-03	6.32E-04	0.063	0.001	0.059	0.002
SO166-68RD(034)	1.20E-08	1.80E-09	5.12E-04	1.36E-05	12.551	0.147	14.554	0.253
SO166-68RD(042)	8.11E-09	1.73E-09	5.52E-02	6.32E-03	7.460	0.040	8.751	0.080
SO166-69RD(186)	1.00E-07	8.64E-09	1.20E-01	5.58E-03	5.382	0.050	6.287	0.084

Probe	$^{234}\text{U}/^{238}\text{U}$		Th230/234		Th230/238		Alter	
		+/-		+/-		+/-	y	+/-
SO166-60RD(030)	1.149	0.011	0.004	0.002	0.005	0.002	470	170
SO166-60RD(049)	1.149	0.015	0.003	0.001	0.003	0.001	320	90
SO166-60RD(085)	1.058	0.015	0.294	0.152	0.311	0.156		
SO166-63RD(030)	1.163	0.013	0.019	0.008	0.022	0.009	2050	860
SO166-65RD(043)	1.135	0.021	0.009	0.004	0.010	0.004		
SO166-66RD(060)	0.932	0.027	0.065	0.041	0.061	0.036		
SO166-68RD(034)	1.160	0.015	0.000	0.000	0.000	0.000	<20	
SO166-68RD(042)	1.173	0.009	0.006	0.003	0.007	0.004	690	340
SO166-69RD(186)	1.168	0.011	0.019	0.007	0.022	0.007	2100	700

Die untersuchten hydrothermalen Präzipitate umfassen einen Bildungszeitraum von ca. 2000 Jahren. Die ältesten Proben sind die resedimentierte Probe 63RD(030) sowie eine Probe aus dem unteren Bereich des Bohrkerns 69RD. Zu beachten ist die hohe Standardabweichung der Ergebnisse, die aufgrund der äußerst niedrigen

Konzentrationen an U und Th entstanden sind. Die untersuchten Fragmente sind vermutlich teilweise ein Resultat intensiver hydrothermalen Wiederaufarbeitung, die eine Altersdatierung im Moment nicht möglich macht. SCHOLTEN ET AL. (2000) merken ebenfalls an, dass ein geschlossenes System für U und Th lediglich für Sulfidablagerungen unmittelbar unter der Meeresoberfläche existiert. Eine Wiederholung der Messungen mit deutlich mehr Probenmaterial sowie die Messung weiterer Proben ist daher notwendig, um die bisherigen Ergebnisse zu verifizieren.

Interpretation

Basierend auf den Untersuchungen an Oberflächenproben gingen MOSS und SCOTT (2001) davon aus, dass gediegenes Gold in den Sulfiden des PACMANUS Hydrothermalfeldes generell silberarm ist und mit einer Cu-As-reichen Mineralparagenese, Tennantit und Chalkopyrit, verbunden ist. Die bisher aufgezeigten Ergebnisse der Bohrkernproben zeigen, dass die Goldverteilung im PACMANUS Feld wesentlich komplizierter ist, als bisher angenommen wurde. Die von MOSS UND SCOTT (2001) angenommenen Transportmechanismen können diese Untersuchungsergebnisse nur teilweise erklären und bedürfen einer weiteren detaillierteren Untersuchung.

In den Cu-Zn-reichen Mineralassoziationen kommt Gold überwiegend als Einschluss in Chalkopyrit vor. Im Gegensatz zur Zn-Ba-Si-reichen Mineralparagenese, bei der Gold als Einschluss sowohl im Sphalerit als auch in amorpher Kieselsäure, Galenit und Chalkopyrit auftritt. Die Goldkörner im Sphalerit kommen dabei meist zusammen mit Chalkopyrit vor. Dies deutet eine relativ hohe Bildungstemperatur des Sphalerit an. Die Cu-Zn-reiche Mineralassoziation ist durch niedrige FeS-Gehalte des Sphalerit und einem niedrigen Silbergehalt der Goldkörner (\varnothing 3.58 Gew. % Ag) gekennzeichnet, was auf eine relativ hohe Schwefelaktivität während der Goldabscheidung hinweist. Dagegen ist der FeS-Gehalt in der Zn-Ba-Si-reichen Mineralassoziation deutlich höher und auch die Goldkörner weisen erhöhte Silbergehalte auf (\varnothing 11.23 Gew. % Ag). Dies könnte auf eine niedrigere Schwefelaktivität während der Präzipitation von gediegenem Gold in dieser Paragenese hinweisen.

Diese Unterschiede reflektieren wahrscheinlich Differenzen in der Fluidchemie (z.B. Schwefelaktivität) oder in der Temperatur der beteiligten Lösungen, die zu unterschiedlichen Transport- und Ablagerungsverhalten in Abhängigkeit der Löslichkeitsprodukte und Stabilitätsfelder der beteiligten Elemente (Ag, Au, Cu und Zn) führt. Silber wird dabei meist als AgCl_2^- -Komplex transportiert und ist in Hinsicht auf eigenständige Silberminerale (u.a. Ag_2S) untersättigt.

Eine mögliche Interpretation der Verteilung von Gold im PACMANUS Hydrothermalfeld stellt die Remobilisation von Gold aus einer früheren, hochtemperiert gebildeten Mineralisationsphase dar (Gold als Einschluss in frühem Chalkopyrit), die von einer Rekonzentration des Goldes in den kühleren Außenbereichen des Mounds (Zn-Ba-Si-Assoziation) als Resultat einer lang anhaltenden oder wiederkehrenden Zirkulation hydrothermalen Lösungen gefolgt wird. Dieser Prozess führt jedoch im Allgemeinen, aufgrund der unterschiedlichen Löslichkeiten von Au und Ag, zu einer Trennung von Ag und Au und einer Erhöhung der Goldreinheit in den sekundären Goldkörnern (Hannington et al., 1991). Die hier gemessenen stark erhöhten Silbergehalte in den Goldkörnern der Zn-reichen Paragenese sprechen deutlich gegen diesen Prozess als Anreicherungs- und Transportprozess für das Gold im Bereich von Roman Ruins. Phasenseparation würde diesen Komplex aufgrund der Freisetzung von H_2S in die

Dampfphase destabilisieren. Während die gemessenen Austrittstemperaturen in PACMANUS unterhalb des Kochkurve für Wasser liegen, lassen Untersuchungen an Fluideinschlüssen in ODP-Bohrkernen aus dem Untergrund den Schluss zu, dass unterhalb des Meeresbodens erheblich höhere Temperaturen vorliegen (Vanko et al., 2001). Phasenseparation kann daher nicht generell als Prozess im Untergrund ausgeschlossen werden.

Die hier beschriebenen Unterschiede zwischen Satanic Mills und Roman Ruins deuten eventuell auf Unterschiede in den Fluidwegsamkeiten im Untergrund hin. Die Wärmequelle des Pacmanus Hydrothermalfeldes könnte z.B. im Bereich von Snowcap liegen, welches durch das Auftreten von extrem sauren Fluiden gekennzeichnet ist. Vermutlich wird ein Teil der aufsteigenden Lösungen im Untergrund abgelenkt und speist die mehrere hundert Meter auseinander liegenden Raucher von Satanic Mills und Roman Ruins. Dabei könnte die Nähe des Satanic Mills Feldes zu Snowcap und der postulierten Wärmequelle einen erhöhten Eintrag magmatischer Komponenten erklären, wohingegen Roman Ruins zu weit entfernt ist und durch konventionelle Fluide geprägt wird. Permeable Schichten (z.B. resedimentierte Hyaloklastite; PAULICK ET AL., 2003) könnten dabei die bevorzugten Wegsamkeiten für die hydrothermalen Lösungen in diesem Hydrothermalfeld sein (siehe Abb. yx). Diese permeablen Schichten werden von lokal von nichtpermeablen Schichten überdeckt (frischer und schwach alterierter Dazit; PAULICK ET AL., 2003). Der frische Dazit im Bereich von Snowcap ist möglicherweise für die dort derzeit vermindert auftretende hydrothermale Aktivität verantwortlich.

Die vorläufigen Altersbestimmungen zeigen, dass Teile des Systems seit ca. 2000 Jahren aktiv sind und während dieser Zeit können sowohl Au und Ag als auch Cu und Zn durch unterschiedliche Prozesse angereichert worden sein. Detaillierte Untersuchungen und eine größere Anzahl an Proben sind notwendig, um die Altersstellung der Sulfide zueinander besser zu verstehen.

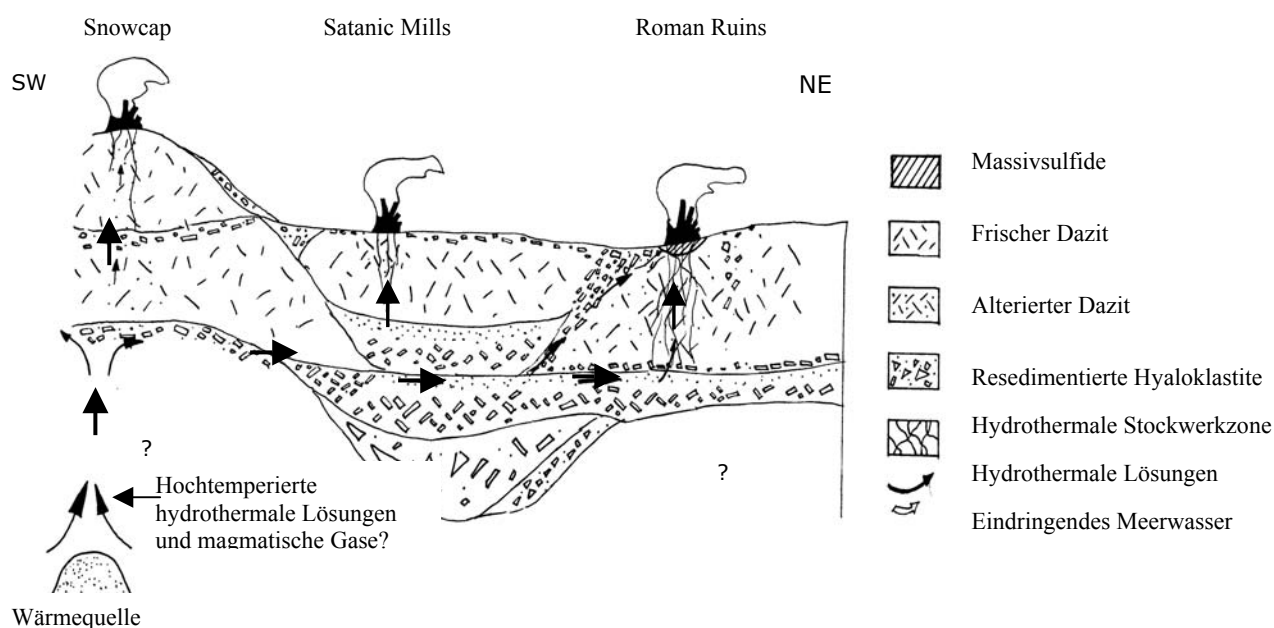


Abb. 6: Vereinfachte Darstellung des Roman Ruins Hydrothermalfeldes mit den unmittelbar benachbarten Hydrothermalfeldern Snowcap und Satanic Mills. Die von den hydrothermalen Lösungen bevorzugten Wegsamkeiten befinden sich inmitten der resedimentierten Hyaloklastite. Nebengesteine sind meist alterierte Dazite. Die Wärmequelle wird aufgrund geophysikalischer Daten unterhalb von Snowcap vermutet. Modifiziert nach PAULICK ET AL. (2003) und LACKSCHEWITZ ET AL. (2004). Darstellung ist ohne Maßstab.

Publikationen, die nach Abschluß des Vorgängerprojektes EDISON II (BMBF 03G0133) erschienen sind

Petersen, S., Herzig, P.M., Hannington, M.D., Jonasson, I.R., and Arribas, A.J. (2002)
Submarine vein-type gold mineralization near Lihir island, New Ireland fore-arc, Papua
New Guinea: *Economic Geology*, v. 97, p. 1795-1813.

Gemmell, J.B., Sharpe, R., Jonasson, I.R., and Herzig, P.M. (2004) Sulfur isotope evidence
for magmatic contributions to submarine and subaerial gold mineralization: Conical
Seamount and the Ladolam gold deposit, Papua New Guinea: *Economic Geology*, v. 99,
p. 1711-1725.

Müller, D., Franz, L., Petersen, S., Herzig, P.M., and Hannington, M.D. (2003) Comparison
between magmatic activity and gold mineralization at Conical Seamount and Lihir Island,
Papua New Guinea: *Mineralogy and Petrology*, v. 79, p. 259-283.

Submarine Gold Mineralization Near Lihir Island, New Ireland Fore-Arc, Papua New Guinea

SVEN PETERSEN, PETER M. HERZIG,

*Department of Economic Geology and Leibniz Laboratory for Applied Marine Research,
Freiberg University of Mining and Technology, Brennhausgasse 14, D-09599 Freiberg, Germany*

MARK D. HANNINGTON,[†] IAN R. JONASSON,

Geological Survey of Canada, 601 Booth Street, Ottawa, Canada, K1A 0E8

AND ANTONIO ARRIBAS, JR.

Placer Dome Exploration, Inc., 240 S. Rock Blvd. #117, Reno, Nevada 89502

Abstract

Gold-rich, siliceous veins with disseminated polymetallic sulfides and pyritic stockwork mineralization have been recovered from the top of Conical seamount, a shallow (1,050-m water depth) submarine volcano located about 10 km south of Lihir island, Papua New Guinea. Grab samples from the summit of Conical seamount contain the highest concentration of gold yet reported from the modern sea floor (max 230 ppm Au; avg 26 ppm, $n = 40$). The gold occurs in sulfide-rich veins of black amorphous silica hosted by intensely altered, high K calc-alkaline basalts. Sulfides in the veins consist of sphalerite, galena, pyrite, chalcopyrite, marcasite, and a variety of Cu-Pb-As-Sb sulfosalts. The gold occurs as native gold and electrum in the amorphous silica and as inclusions in the sulfides. The highest gold concentrations are associated with high Ag, As, Sb, and Hg. Zoned alteration adjacent to the veins consists of illite, smectite, amorphous silica, K feldspar, secondary plagioclase, minor chlorite, and trace carbonate. The association of gold with illite, smectite, amorphous silica, and K feldspar indicates deposition from near neutral pH hydrothermal fluids. However, the auriferous polymetallic sulfide veins and the associated alteration are overprinted on stockwork pyrite mineralization that is associated with earlier acid alteration containing alunite, aluminum phosphate sulfates, kaolinite, and other clay minerals. The platy habit of the alunite in this assemblage, the presence of aluminum phosphate sulfate minerals, and the sulfur isotope ratios of the crystalline pyrite (-8.6 to -0.2% $\delta^{34}\text{S}$, $n = 28$) and alunite (7.5 and 6.4% $\delta^{34}\text{S}$) are consistent with a contribution of magmatic volatiles in the earliest stages of the hydrothermal system. Framboidal pyrite within and at the margins of the mineralized zone has $\delta^{34}\text{S}$ values suggesting involvement of biogenic activity (-11.6 to -13.9% $\delta^{34}\text{S}$).

The gold-rich veins at Conical seamount are distinct from sea-floor massive sulfide deposits and represent a new style of mineralization on the modern sea floor. The mineralogy, alteration, geochemistry, and texture of the veins resemble those of some subaerial epithermal gold deposits and indicate that features long considered to define a subaerial setting can also form in a submarine environment. The proximity of Conical seamount to the giant Ladolam epithermal gold deposit on nearby Lihir island also raises the possibility that both subaerial and submarine gold mineralization in the region may be related to the same district-scale magmatic events.

Introduction

IN 1998, THE German research vessel *Sonne* (cruise SO133) conducted detailed mapping and sampling in a seismically and volcanically active zone with high heat flow in the New Ireland Basin, Papua New Guinea (Fig. 1). The region is best known for the giant Ladolam epithermal gold deposit (ca 40 million oz contained Au) located in the Luise volcano on the island of Lihir (Moyle et al., 1990). During reconnaissance surveys carried out in 1994 (cruise SO94), a number of previously unknown submarine volcanoes were located between Lihir island and the New Ireland arc (Herzig et al., 1994; Herzig and Hannington, 1995a; Herzig et al., 1999). One of the largest volcanic cones, Conical seamount, is located about 10 km south of Lihir island at a water depth of 1,050 m. A follow-up sampling program during SO133 recovered more than 1,200 kg of altered and mineralized volcanic rocks from the summit of the volcano.

The mineralization at Conical seamount consists of veins of amorphous silica and polymetallic sulfides with unusually high concentrations of Au, Ag, As, Sb, Pb, and Hg—a previously unknown style of sea-floor mineralization. The mineralized samples recovered from the volcano have a number of important similarities with precious- and base-metal epithermal mineralization formed in subaerial environments. This paper documents the main features of hydrothermal mineralization at Conical seamount and discusses the origin and evolution of the mineralization in comparison to gold-rich, auriferous sea-floor massive sulfide deposits and subaerial epithermal systems.

Geological Setting

The New Ireland Basin of Papua New Guinea occupies a fore-arc position, with respect to the formerly active Manus-Kilinau arc-trench system, and contains a series of Pliocene to Recent alkaline volcanoes, referred to as the Tabar-Lihir-Tanga-Feni island chain, built on rifted Miocene sedimentary

[†] Corresponding author, e-mail: petersen@mineral.tu-freiberg.de

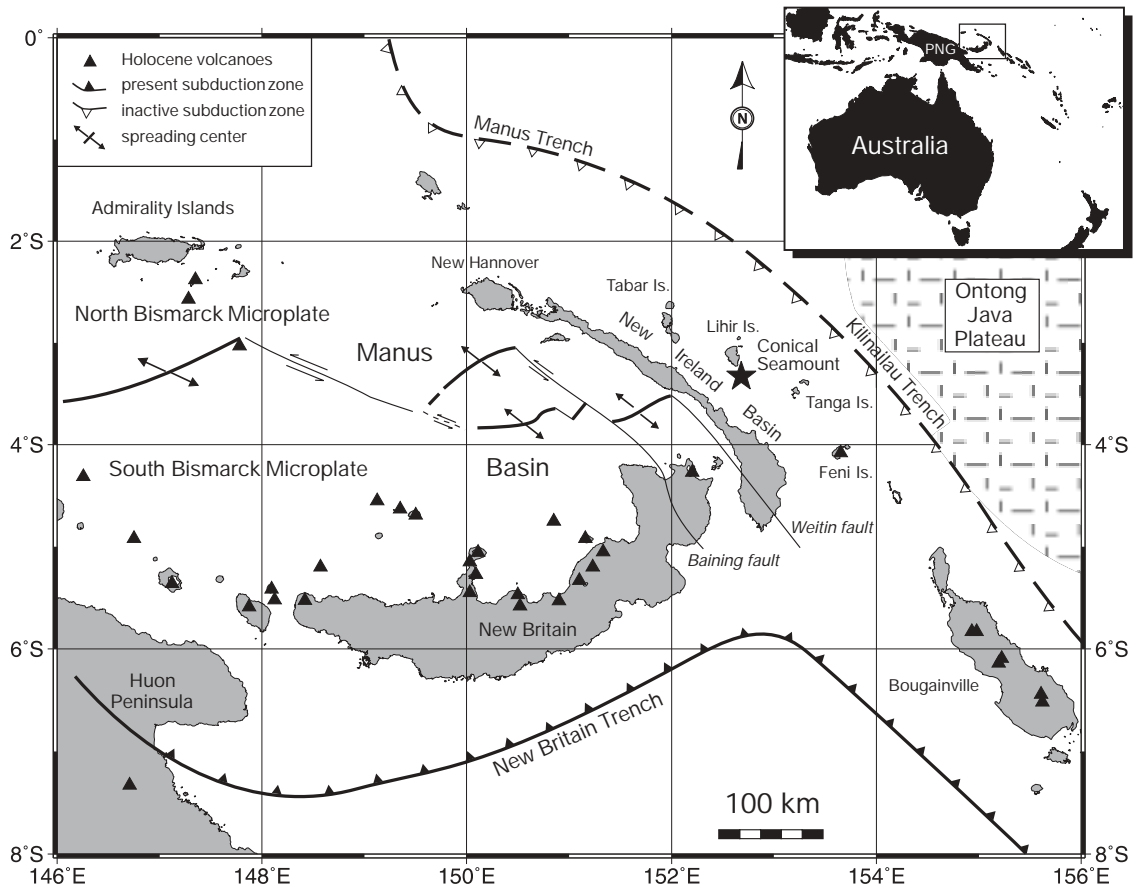


FIG. 1. Simplified regional geological map showing major tectonic elements in the New Ireland and Bismarck Sea region, and the location of Conical seamount close to Lihir island, Papua New Guinea.

basement (Johnson, 1979; Wallace et al., 1983). Together with New Ireland, the Tabar-Feni chain forms part of the Bismarck archipelago (Fig. 1). In the Early Miocene, this region was dominated by westward subduction of the Pacific plate beneath New Ireland. Between 24 and 11 m.y. ago, southwest subduction along the Manus-Kilinailau Trench was blocked by the collision of the Ontong Java plateau with the trench (Kroenke, 1972; Moberley, 1972; Coleman and Kroenke, 1981). The resulting plate rotation and stress relocation caused a subduction reversal, from the southwest to the northeast, and the formation of the presently active north-northeast-facing New Britain Trench (Fig. 1). Volcanic activity in the Tabar-Feni island chain, which began about 3.5 m.y. ago, appears to be related to extension along northeast-trending structures that cut across the New Ireland basin (Stewart and Sandy, 1988; McInnes and Cameron, 1994). Since Pliocene-Pleistocene time, partial melts associated with extension in the thickened crust of the New Ireland basin have risen through the old fore-arc crust along reactivated faults to form the volcanic islands of the Tabar-Feni chain.

The most recent, dated volcanic eruptions in the island chain occurred 2,300 yr ago on Feni island, in the extreme southeast (Licence et al., 1987). The few radiometric dates of older rocks indicate that the most recent volcanic eruptions on Lihir island occurred at about 1.1 Ma (Johnson et al.,

1976). However, records of recent seismic activity in the New Ireland region show a number of shallow earthquake epicenters near Lihir island, to the south and southwest. The earthquake epicenters occupy a diffuse, northeast-southwest corridor between Lihir and New Ireland (Fig. 2), with some of the epicenters coinciding with the location of the recently discovered volcanoes south of Lihir (Herzig et al., 1994; Fig. 3).

The volcanic rocks of the Tabar-Feni chain belong to the high K, SiO₂-undersaturated magma series and include basanite, alkali-olivine basalt, olivine nephelinite, tephrite, ankaramite, trachybasalt, trachyandesite, tephritic phonolite, and phonolitic trachyte (Johnson, 1979; Wallace et al., 1983; Johnson et al., 1988; Kennedy et al., 1990a, b; McInnes, 1992; McInnes and Cameron, 1994; Patterson et al., 1997). These rocks are unique among the islands of the Bismarck archipelago and are consistent with a model that involves local extension in an area of regional convergence and compression (McInnes and Cameron, 1994). The petrological, geochemical, and isotopic characteristics of the volcanic rocks of Lihir island are somewhat different from those of the rest of the Tabar-Feni chain, suggesting a less enriched mantle source beneath Lihir (Kennedy et al., 1990b; Patterson et al., 1997). Recent petrological studies of the volcanic seamounts south of Lihir island indicate that the depleted arc mantle in this region has been enriched in volatiles and alkalis from the

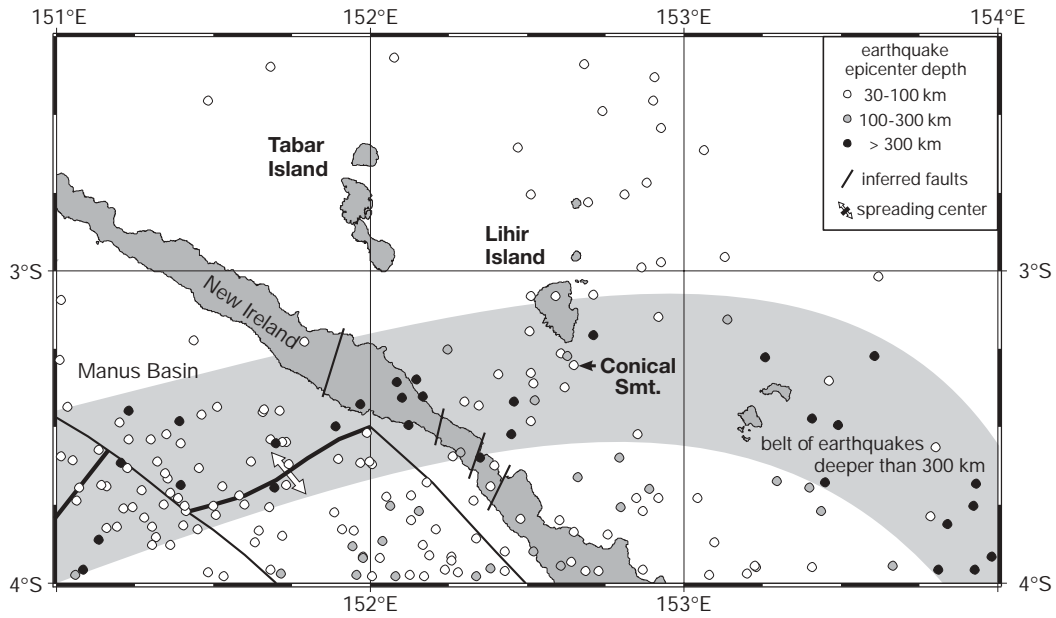


FIG. 2. Location of shallow earthquake epicenters, from 1970 to 2001, in the vicinity of Lihir island. Note the cluster of shallow and mid-depth earthquakes between Lihir island and New Ireland, but not at Tabar. Source: Port Moresby Geophysical Observatory, Earthquake Map of the Papua New Guinea region for 1964 to 1994.

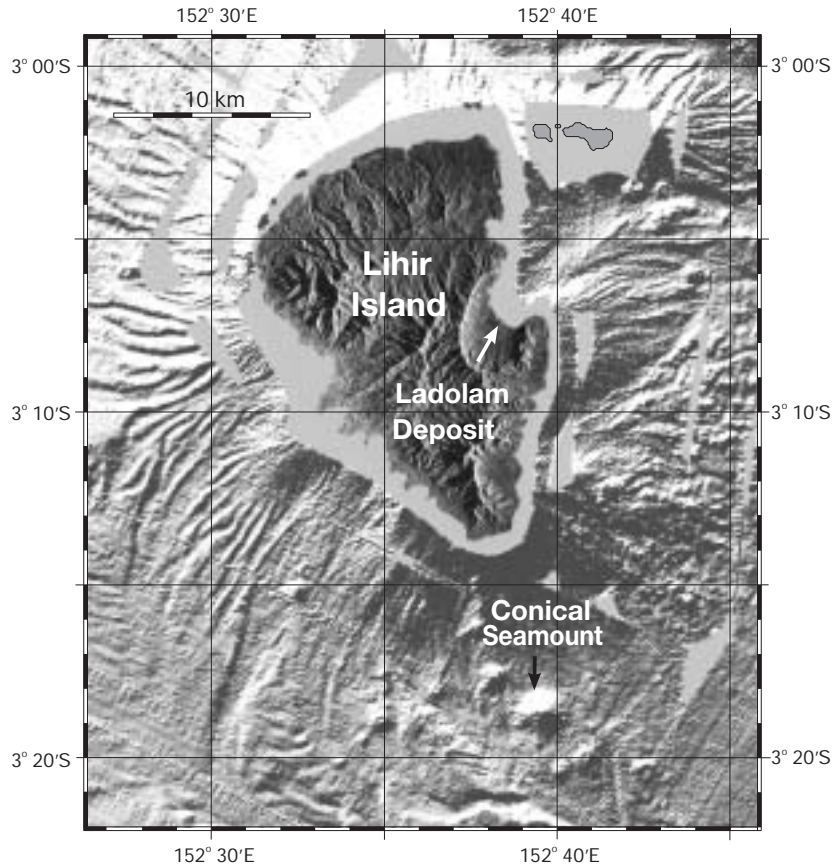


FIG. 3. Shaded, bathymetric relief of the area surrounding Lihir island, showing the location of Conical seamount and other small seamounts south of Lihir that were discovered during *Sonne* cruise SO94 in 1994. The giant Ladolam epithermal gold deposit is located approximately 21 km north of Conical seamount (SAR simulated aperture radar image of Lihir island was provided by Lihir Mining Co., Ltd.).

subducted slab (McInnes et al., 1999, 2001; Franz et al., 2002). Metasomatism and oxidation of the mantle underlying Lihir island are also thought to have been responsible for enrichment of Au, Cu, Pt, and Pd in the source region of the alkaline magmas (McInnes et al., 1999).

Conical Seamount Geology

Conical seamount is the largest of at least six submarine volcanoes located south of Lihir (Fig. 3). It has a basal diameter of approximately 2.8 km and rises more than 600 m above the surrounding sea floor to a minimum water depth of 1,050 m (Fig. 4). The volcano forms a simple cone and has a small summit plateau measuring about 100×200 m. Mapping of the summit area, using a TV-controlled grab, revealed a 100-m long, east-west-striking cleft or depression, which is interpreted to be an eruptive fissure (Fig. 5). The upper part of the volcano is constructed of massive flows, pillow lavas, and talus breccia consisting of moderately vesicular flow fragments and scoria. Individual flows, including tubes and lobes up to several meters across, have cascaded down the steep flanks of the volcano, or, rarely, appear to have drained back into the fissure. The flow fronts are commonly broken, producing small steps and terraces on the upper slopes of the volcano.

Least altered volcanic rocks recovered from Conical seamount comprise relatively fresh, vesicular, high K calc-alkaline to shoshonitic, pyroxene-phyric trachybasalt (ankaramite) with abundant phenocrysts of diopside, magnetite, rare olivine, and phlogopite (Herzig et al., 1994, 1999). Plagioclase and magnetite are common in the matrix and occur as small phenocrysts. The lavas are geochemically similar to the sub-aerial portions of the Tabar-Feni island chain; however, they do not show the same compositional range as those collected from the islands (Herzig et al., 1994; Stracke, 1996; Farr et al., 1999). Enrichments in large ion lithophile elements,

coupled with relatively low abundances of high field strength elements and moderate, light rare earth element enrichments, indicate their arclike affinity (Table 1).

Mineralization and Alteration

Mineralization and alteration are exposed on the sea floor at the summit of Conical seamount near the eruptive fissure (Fig. 5). Talus slopes leading away from the fissure and debris within the fissure are heavily stained by Fe oxides. Lava flows adjacent to the fissure are intensely altered and mineralized on exposed surfaces where large blocks of lava (up to 1 m) have spalled off. Intense Fe staining is also observed between flows and where talus and sediment have accumulated at the toes of the flows. Sediment that has ponded on the summit plateau near the eruptive fissure is also Fe stained or mottled in appearance. Grabs of this material recovered altered and mineralized basalt breccia and clay-rich, pyritic mud from immediately beneath the sediment cover. Much of this material may be weathered debris from the mineralized lavas. Other samples recovered from the summit area included intensely altered basalt blocks with distinctive, vein-style mineralization (e.g., Fig. 6a, b).

Vein paragenesis

Three stages of hydrothermal mineralization are recognized among the altered samples. Stage 1 mineralization consists of stockwork-type veinlets and disseminations of pyrite \pm marcasite with illite/smectite-amorphous silica \pm chlorite \pm kaolinite alteration. The pyrite veins are locally semimassive, with pyrite contents in places exceeding 20 vol percent in the bulk rock. Stage 1 pyrite veins are associated with intense silicification of the basalt breccias, which has destroyed the primary magmatic textures of the rocks. Alunite-bearing, clay-rich assemblages are also found with the pyrite veins. This alteration consists of pyrite with cristobalite, platy natro-alu-

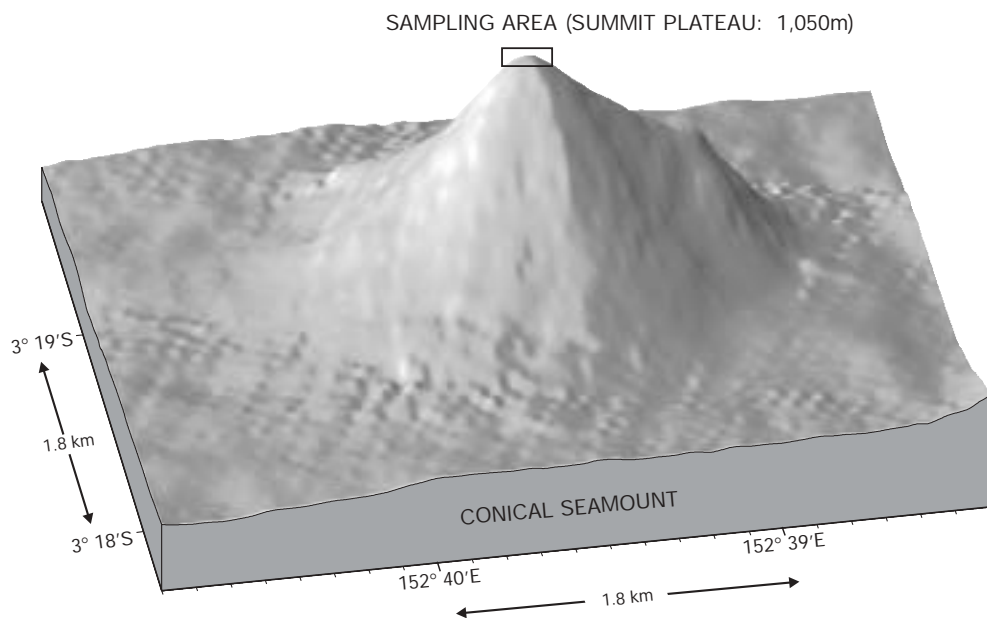


FIG. 4. Three-dimensional view of Conical seamount, showing the distinctive cone shape of the volcano and the area of the small summit plateau that was sampled. The actual slope angle is 15° .

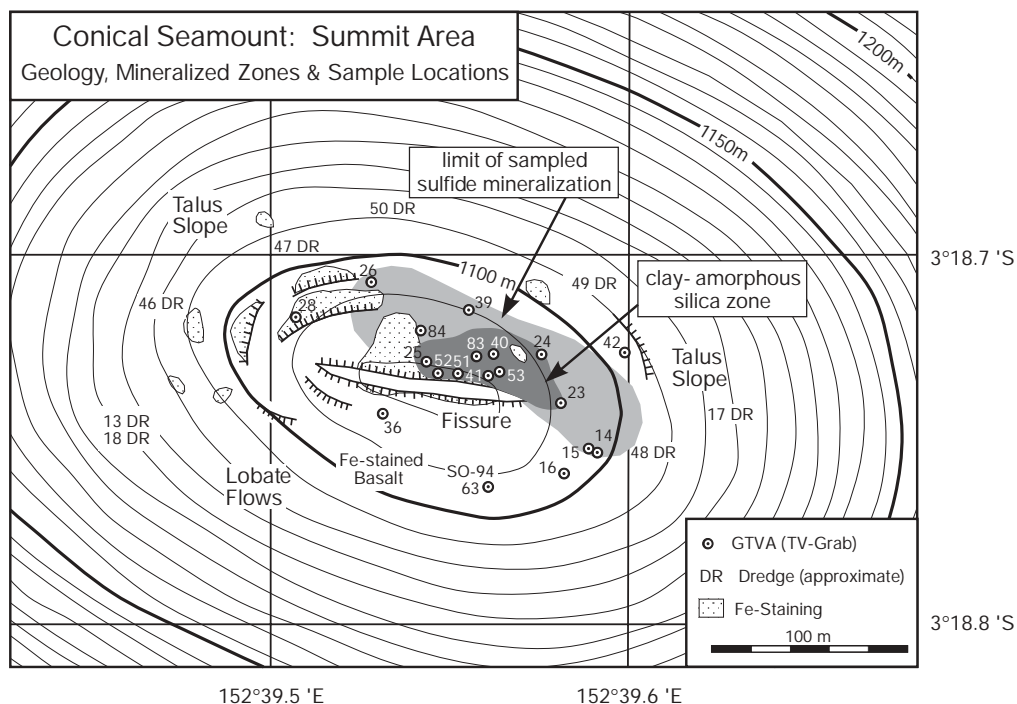


FIG. 5. Sketch map of the summit plateau of Conical seamount, showing sample locations and the distribution of the different mineralized zones. Numbers indicate the locations of TV-controlled grab samples and approximate locations of dredges (DR). Contour interval is 5 m.

nite, and rare, Ca-Sr-bearing aluminum phosphate sulfates (aluminum phosphate sulfate minerals in the woodhouseite-svanbergite solid solution series; Fig. 7a-c).

Stage 2 mineralization consists of black, amorphous silica-filled veins with disseminated polymetallic sulfides (mainly sphalerite, chalcopyrite, galena, pyrite, and Cu-Pb-As-Sb sulfosalts) and native gold and electrum. The amorphous silica veins are up to several centimeters in thickness and cut strongly altered basalt breccias with locally abundant, disseminated sulfides in the wall rock (Fig. 6b). These veins are the main carrier of gold and consist of multiple generations of amorphous silica filling open spaces in the basalt breccias and cementing fine-grained sulfides (Fig. 6c, d) and altered wall-rock clasts. The amorphous silica in the veins is locally anisotropic, suggesting that it has partially crystallized to a more ordered (chalcedony) structure. Alteration adjacent to the veins and in clasts of altered wall rock consists of amorphous silica, illite, smectite, K feldspar, secondary plagioclase (Na-K feldspar after primary Ca plagioclase), minor chlorite, and traces of kaolinite and barite (Fig. 7d-f). The presence of K feldspar is the most characteristic feature of this alteration (Fig. 7e). The rhombic habit of some of the K feldspar suggests that it is adularia. Rare prismatic and needle-shaped apatite is also locally found associated with the K feldspar (Fig. 7f).

Stage 3 mineralization consists of arsenic sulfides (realgar and orpiment), lesser antimony-sulfides (stibnite), and minor pyrite, filling fractures, vugs and open spaces, and as overgrowths on stage 2 polymetallic sulfides. Fractures lined with arsenic- and antimony-sulfides locally crosscut gold-bearing stage 2 veins, clearly indicating that the As-Sb mineralization

postdates the main gold stage. Stage 3 mineralization is not associated with an obvious alteration assemblage, and locally occurs in weakly altered samples well outside the main mineralized zone. It is associated with abundant, late-stage amorphous silica, which fills open cavities and fractures along with the arsenic- and antimony-sulfides.

Because stage 1 and stage 2 veins were found mainly in different samples and in different parts of the summit area (Fig. 5), the relationship between the first two vein stages is not always clear. In general, it appears that the stockwork-type and disseminated Fe sulfide mineralization occurred mainly during an earlier stage, prior to the introduction of polymetallic sulfides. This is indicated by the presence of clasts of intensely altered basalt with locally abundant, disseminated pyrite, pyrite veinlets, and semimassive pyrite in the stage 2 veins. The interpreted paragenesis of the veins is shown in Figure 8.

Alteration associated with stage 2, gold-bearing veins

Alteration associated with stage 2, gold- and polymetallic sulfide-bearing veins is mainly restricted to vein selvages (up to 5 cm) and brecciated basalt fragments included in the veins. Alteration rims on the stage 2 veins are typically bleached (Fig. 6b), but primary textures are commonly preserved. Clinopyroxene in the wall rock is completely replaced by pyrite, and calcic plagioclase is converted to montmorillonite, sodic illite, secondary plagioclase (Na-K feldspar), and K feldspar. The microlite matrix, composed mainly of minute plagioclase needles and skeletal clinopyroxene, is similarly altered, but mainly to illite. Magnetite is converted to mixtures of leucosene

TABLE 1. Geochemistry of Altered and Least Altered Basalts from Conical Seamount

	Least altered			Silicified		Weakly chloritized		Clay-altered			
	07-2G	12-3A	50-1C	25-5A-1	25-6A-2B	25-8C	83-2E	83-2B-1A	14-2G	15-2F	40-2B-1
Wt %											
SiO ₂	48.41	48.12	47.75	52.30	52.10	50.40	48.00	46.10	44.10	39.80	26.70
TiO ₂	0.76	0.75	0.73	0.96	0.92	0.80	0.82	0.95	0.90	0.62	1.03
Al ₂ O ₃	15.21	15.12	15.07	17.00	16.80	15.90	16.70	18.90	18.90	8.50	20.20
Fe ₂ O ₃	10.74	10.47	10.42	6.78	7.31	9.14	11.20	11.40	12.00	17.40	14.00
MnO	0.21	0.20	0.18	0.10	0.10	0.16	0.15	0.05	0.09	0.08	0.34
MgO	6.71	6.56	6.34	4.27	4.08	5.21	3.72	1.60	3.03	2.88	17.30
CaO	12.53	11.86	11.63	9.43	9.48	11.00	7.02	3.91	8.28	6.49	0.86
Na ₂ O	2.80	2.78	2.82	2.11	1.87	2.33	1.67	1.69	2.35	1.48	1.11
K ₂ O	2.85	2.77	3.03	3.95	4.62	2.88	4.60	6.09	2.05	0.79	0.11
P ₂ O ₅	0.40	0.39	0.38	0.27	0.22	0.37	0.44	0.50	0.42	0.16	0.54
L.O.I.	0.60	1.17	0.50	2.40	3.30	2.60	5.30	8.40	8.30	21.60	14.20
Total	101.21	100.18	98.85	99.57	100.80	100.79	99.62	99.59	100.42	99.80	96.39
CO _{2total}	<0.10	<0.10	0.10	0.10	0.20	0.10	0.10	0.10	0.30	0.30	0.10
S	<0.01	<0.01	<0.01	1.62	2.75	0.40	5.03	8.82	6.78	13.20	7.21
Ppm											
Au	<0.005	<0.005	<0.005	0.42	0.75	0.98	1.64	1.60	<0.005	0.06	0.06
Ag	<0.1	0.1	0.2	33	14	11	16	6	2	3	1
Ba	220	244	211	303	307	243	299	266	260	160	<20
Br	8	10	5	9	<1	7	5	21	6	8	20
Co	35	37	36	35	40	34	38	48	38	30	48
Cr	136	136	145	113	110	103	107	115	69	60	134
Cu	99	122	105	792	304	242	241	238	180	140	1190
Ga	16	17	16	25	22	18	18	20	19	17	25
Hf	1.5	1.7	1.4	2.0	1.9	1.5	1.6	1.8	1.7	1.4	2
Mo	0.9	0.7	0.9	2.7	3.1	1.7	4.4	2.4	3.6	94	5.9
Nb	1.3	1.5	1.3	1.8	1.7	1.4	1.5	1.7	1.6	1.3	2
Ni	32	33	33	24	29	29	29	39	31	27	38
Pb	5	7	7	5,770	2,920	960	1,670	1,320	7	100	880
Rb	63	49	60	54	60	46	52	72	51	14	1.1
Sc	41	40	41	50	41	39	39	35	34	30	52
Sn	1.1	0.8	0.8	1.3	2.1	0.8	1.6	1.2	1.4	1.0	0.9
Sr	912	974	943	1,210	1,280	1,090	1,180	1,210	1,300	780	32
Ta	0.09	0.10	0.09	0.11	0.10	0.09	0.09	0.1	<0.2	<0.2	0.12
Th	0.89	0.85	0.85	1.30	1.10	0.86	0.94	1.1	1.00	0.81	1.2
Tl	0.3	0.3	0.4	5.0	20	13	3.9	3.7	0.4	0.5	0.61
U	0.62	0.56	0.61	4.0	2.3	1.3	1.7	3.3	1.5	7.4	4.8
V	307	314	314	275	289	325	333	377	340	180	428
W	<1	<1	<4	<1	<4	<1	<1	<4	<4	<4	<4
Zn	69	72	77	673	310	1,300	419	545	68	110	1,740
Y	19	19	19	10	11	18	16	17	15	8	23
Zr	55	61	57	70	66	55	58	69	61	50	74
La	9.5	9.7	9.6	5.4	5.6	9.2	9.7	11.0	13.0	3.6	13.0
Ce	22.0	22.0	20.0	11.0	13.0	21.0	22.0	24.0	27.0	7.9	29.0
Pr	3.3	3.3	3.0	1.6	1.8	2.9	3.0	3.4	4.1	1.3	4.1
Nd	16.0	16.0	15.0	7.6	8.8	14.0	14.0	17.0	17.0	6.4	19.0
Sm	4.0	3.8	3.9	2.3	2.4	3.6	3.6	4.5	3.9	1.7	4.9
Eu	1.4	1.3	1.3	0.9	1.0	1.3	1.1	1.4	1.2	0.6	1.4
Gd	4.3	3.9	4.1	2.5	2.6	3.8	3.5	4.6	3.7	1.7	5.0
Tb	0.60	0.58	0.62	0.35	0.39	0.56	0.52	0.69	0.51	0.25	0.72
Dy	3.5	3.2	3.3	2.1	2.2	3.0	2.9	3.7	2.7	1.5	4.1
Ho	0.65	0.61	0.65	0.39	0.41	0.62	0.57	0.72	0.50	0.29	0.81
Er	1.7	1.6	1.7	1.0	1.1	1.5	1.5	1.8	1.3	0.72	2.1
Tm	0.26	0.24	0.26	0.16	0.16	0.23	0.23	0.28	0.21	0.10	0.33
Yb	1.7	1.6	1.6	1.1	1.1	1.6	1.5	1.8	1.3	0.73	2.1
Lu	0.27	0.26	0.26	0.17	0.18	0.24	0.23	0.28	0.22	0.10	0.32

Methods: major elements (wt %) by a combination of ICP and XRF; sulfur and total carbon as carbonate by combustion and infrared detection; Au, Br, and W by INAA; Ag, Ba, Co, Cr, Cu, Ga, Hf, Mo, Nb, Ni, Pb, Rb, Sc, Sn, Sr, Ta, Th, Tl, U, V, Zn, Y, Zr by ICP-ES; REE by ICP-MS

Notes: chemical analyses were carried out at the Geological Survey of Canada, Freiberg University of Mining and Technology, and, commercially, at Actlabs Ltd. (Canada)

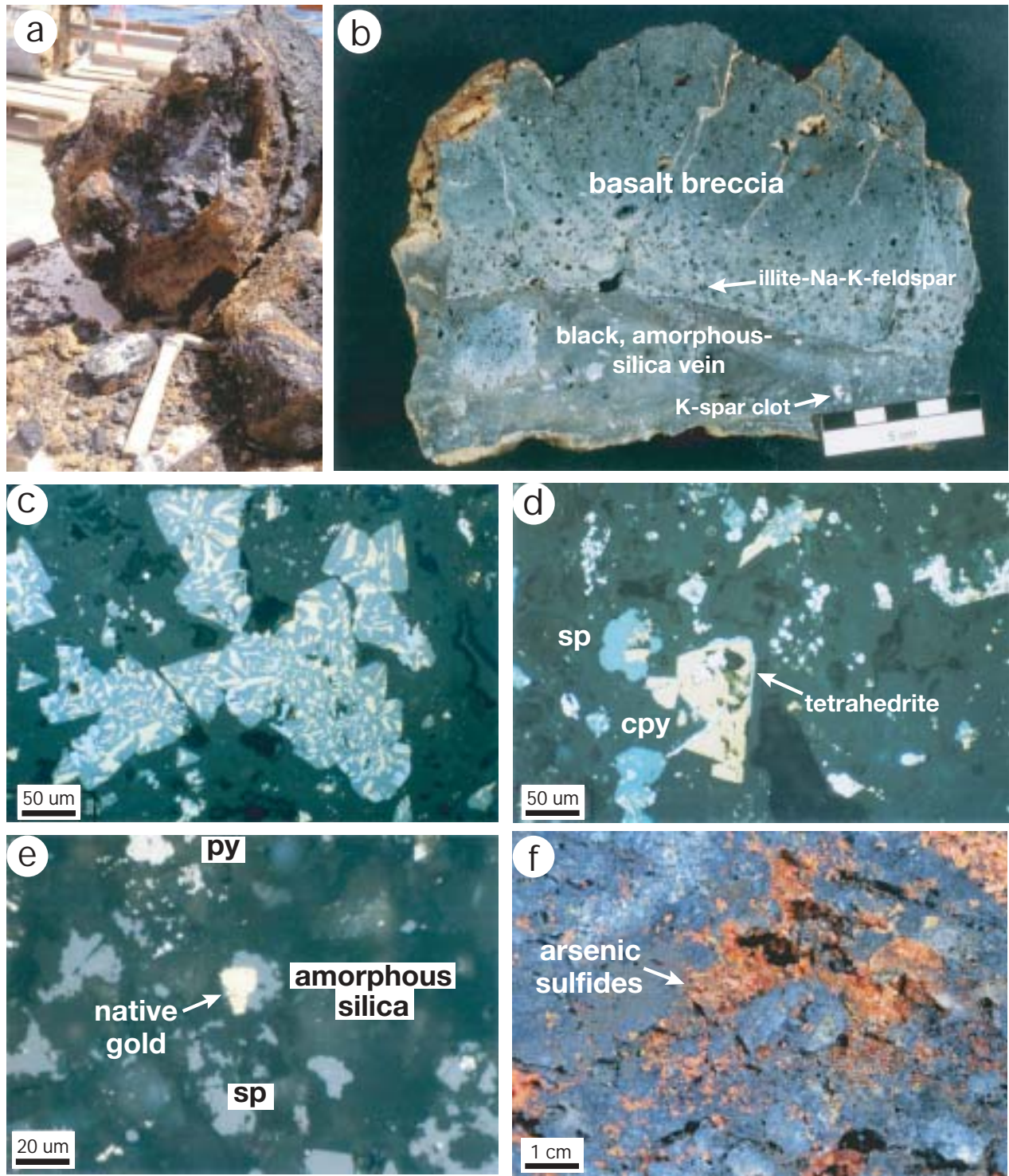


FIG. 6. a. Discovery sample (63GTV) recovered in 1994. The sample is a large block of weathered basalt, showing a gossanous exterior and an amorphous silica-filled cavity at the center of the block. Samples from the amorphous silica-rich part of the block contained up to 17 ppm Au. b. Altered basalt cut by a black, amorphous silica-filled vein (bottom) hosting the disseminated, polymetallic sulfides and gold. Distinctive white to gray bleaching of the basalt is evident in the alteration rim adjacent to the vein. The white patches in the alteration rim consist mainly of illite and secondary plagioclase (Na-K feldspar). White clots (up to 1 cm) in the vein itself consist mainly of K feldspar (possibly adularia). c. Polymetallic sulfides (sphalerite + chalcopyrite + galena) associated with minor, fine-grained pyrite in a matrix of porous amorphous silica. The textures of the sulfides clearly indicate coprecipitation in a single stage. d. Fine-grained chalcopyrite, sphalerite, galena, and pyrite in a matrix of amorphous silica. The central chalcopyrite grain is rimmed by tetrahedrite. e. Native gold (center) intergrown with corroded sphalerite (sp) and minor pyrite (py) in a matrix of amorphous silica (si) from the vein shown in (b). f. Example of late, stage 3 orpiment and realgar, filling open cavities in the altered basalt.

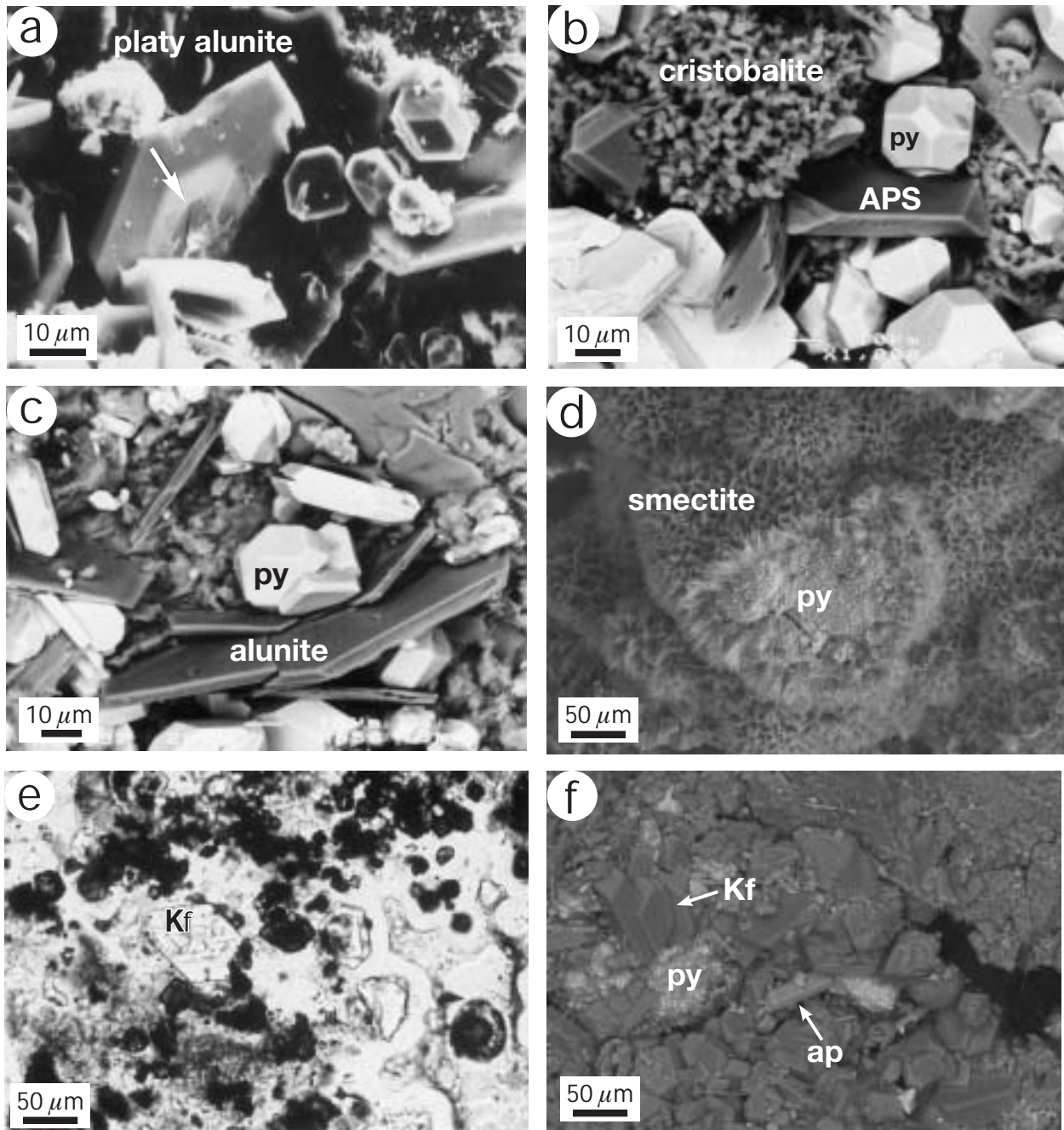


FIG. 7. Alteration mineralogy of Conical seamount samples. a. Platy alunite with K-enriched core (arrow, slightly lighter in color). Secondary electron image. b. Fine-grained masses of cristobalite with abundant pyrite (py) and intergrown alunite-aluminum phosphate sulfates (woodhouseite-svanbergite; dark gray). SEM-backscattered electron image. APS = aluminum phosphate sulfate. c. Rare, large (up to 50 μm), platy alunite crystals and pyrite (py). SEM-backscattered electron image. d. Smectite layer coating globular pyrite (py). SEM-backscattered electron image. e. K feldspar (Kf, possibly adularia) intergrown with fine-grained sphalerite (dark), both embedded in amorphous silica from a gold-rich, sulfide-bearing, stage 2 vein. Transmitted light. f. Abundant K feldspar (Kf) associated with long, prismatic and needle-shaped apatite (ap) and minor pyrite (py), in a cavity of a stage 2 gold-bearing vein. Rounded aggregates of amorphous silica are also present. SEM-backscattered electron image.

(rutile and anatase), boehmite, corundum, hematite, and amorphous silica. Some pyritization of magnetite is also observed close to the sulfide veins. At distances of 1 to 2 cm from the veins, the alteration is dull gray and contains more secondary plagioclase and K feldspar. Magnetite is partly altered

to leucoxene (rims on crystals) and pyrite. Clinopyroxene and plagioclase are partly replaced by secondary plagioclase and smectite. Matrix microlites are altered locally to illite and K feldspar, intimately mixed with amorphous silica. Pyrite is commonly disseminated throughout these alteration zones.

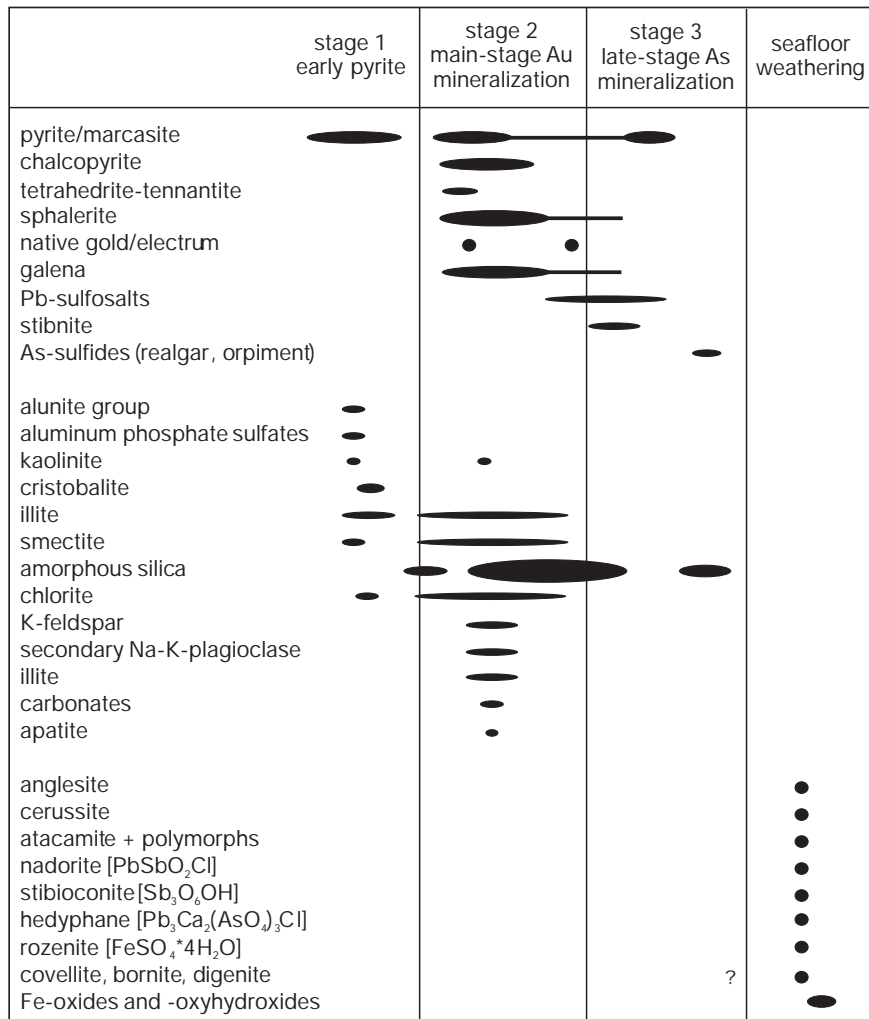


FIG. 8. Interpreted paragenetic sequence of ore and gangue minerals in the three main vein stages recognized at Conical seamount.

The intensity of alteration of the basaltic/microlite matrix and the extent of replacement of phenocrysts of clinopyroxene and magnetite in the wall rock adjacent to the sulfide veins diminishes away from the veins and inward from clast margins. The least-altered zones contain unaltered magnetite, clinopyroxene, and partly altered plagioclase in a glassy matrix. Holocrystalline interiors of the basalt clasts are bleached by amorphous silica addition but are not strongly altered. Vesicles may be partly filled by siderite, ankerite, quartz, and, rarely, by zeolites such as mordenite and analcime.

Overall, the altered zones adjacent to the sulfide-bearing veins appear to have lost considerable Ca, Mg, and lesser Na, and have acquired K and SiO₂ (Table 1). This alteration can be readily distinguished from weathering rinds on the basalt blocks, where plagioclase and microlite matrix materials are mainly altered to smectite and other montmorillonite group clays, and clinopyroxene phenocrysts are typically well preserved. Sea-floor weathering effects are also characterized by the alteration of magnetite to a mixture of hematite, leucosene, goethite, and amorphous silica. No sulfides are present in the gossans.

Deposit-scale zoning

Detailed sampling and camera surveys across the summit area of the volcano show a strong zonation of mineralization styles and attendant alteration away from the central cleft or fissure (Fig. 5). A clay-rich, amorphous silica zone, associated with stage 1 pyrite mineralization, occurs immediately adjacent to the eruptive fissure. This is the dominant alteration exposed at the sea floor. Much of the clay alteration in this zone may be related to sea-floor weathering of the intense, pyritic sulfide mineralization closest to the eruptive fissure. However, locally abundant, disseminated pyrite, pyrite-lined fractures, and a few pyrite veinlets also occur in samples of volcanic rocks from well outside the mineralized zone. The gold-rich, stage 2 veins occur in an intermediate zone of moderately altered basalt breccias, outside the clay-silica zone. Stage 3 arsenic sulfides, together with abundant, late-stage amorphous silica, occur as fine fracture fillings and lining vesicles in moderately to weakly altered basalt in the outermost zone. However, similar arsenic mineralization also overprints the polymetallic sulfides and associated alteration of stage 2, closer to the center of the mineralization.

Widespread but discontinuous patches of Fe-stained sediment are found over a strike length of at least 250 m, and up to 100 m from the main mineralized zone. This suggests that low-temperature, diffuse hydrothermal venting was formerly active over large parts of the summit area. However, the abundance of Fe oxides and the absence of any fauna imply that the hydrothermal system has been long extinct. Gossan-like, Fe oxide crusts sampled in the outermost zone appear to be the weathering products of altered and mineralized (pyrite-bearing) basalt. There is no evidence of massive sulfides at the sea floor, and no indication from observations on the flank of the volcano that preexisting massive sulfides have been eroded away. However, dredging from 1,250-m water depth to 1,100 m did recover altered lavas with weak, disseminated pyrite mineralization and thick Fe oxide crusts well down the flanks of the volcano.

Mineralogy and Geochemistry

The mineralogy of the stage 1 veins consists of granular pyrite and lesser colloform marcasite, as well as fine-grained disseminated and framboidal pyrite in moderately to strongly altered basalt. Gold-rich, stage 2 veins are mineralogically complex and include locally abundant sphalerite, galena, pyrite, chalcopyrite, minor marcasite, and minor Cu-Pb-As-Sb sulfosalts, including tetrahedrite, tennantite, jordanite, and, in one case, an unidentified Cd-Zn-Pb sulfide, as well as native gold and electrum (Fig. 8). Microprobe analyses of sphalerite show moderate to low Fe contents, averaging 5.2 mole percent FeS ($n = 208$; Table 2), with 90 percent of the analyses below 8 mole percent FeS. Fine-grained galena (Fig. 6c), minor bladed stibnite, colloform sulfosalts with a highly variable mineral chemistry (i.e., Fe, Pb, As, Sb, Hg, and Ag; Table 2), and an unknown Fe-As-Sb sulfide ($As_{0.80}Sb_{0.15}Fe_{1.08}S_3$; Table 2) are intergrown with sphalerite, chalcopyrite, and amorphous silica in the matrix of the veins. Minor bornite, covellite, and digenite, which are locally present with the sulfides, are interpreted to be secondary. The stage 3, arsenic-rich sulfides are mainly realgar and several polymorphs, such as alacranite (As_4S_4 ; Burns and Percival, 2001). Crystals of realgar that line the late fractures and open spaces are commonly overgrown by distinctive colloform orpiment.

Sea-floor oxidation has produced abundant Fe oxyhydroxides and a number of less abundant, but common, secondary minerals, including jarosite, polymorphs of atacamite ($Cu_2Cl(OH)_3$), the oxychloride nadorite ($PbSbO_2Cl$), stibioconite (Sb_3O_6OH), hedyphane ($Pb_3Ca_2(AsO_4)_3Cl$), and rozenite ($FeSO_4 \cdot 4H_2O$), as well as bornite, digenite, covellite, anglesite, and cerussite.

The gold-bearing, stage 2 veins contain between 75 and 85 wt percent combined silica and sulfides, together with 15 to 25 wt percent altered wall rock and clay minerals (Table 3). Average base-metal concentrations for all mineralized samples are 1.7 wt percent Zn, 0.3 wt percent Cu, and 1.1 wt percent Pb ($n = 40$). The black, amorphous silica-filled veins contain, on average, 4.1 wt percent Zn, 2.3 wt percent Pb, and close to 1.0 wt percent Cu ($n = 10$), with maximum values reaching 7.7 wt percent Zn, 3.3 wt percent Pb, and 1.9 wt percent Cu. The highest concentrations of gold (avg 25 ppm, $n = 40$; Table 3) and silver (avg 216 ppm, $n = 40$) occur in the sulfide-rich, stage 2 veins. Within this suite of samples, the highest gold values (up to 230 ppm Au)

occur in black, amorphous silica with abundant, disseminated polymetallic sulfides (avg 68 ppm Au, $n = 10$).

Pyrite-dominated, stage 1 stockwork mineralization, pyrite/marcasite crusts, and disseminated pyrite mineralization are generally gold poor, compared to the stage 2 veins, and contain much lower base metals. Combined Zn + Pb + Cu for these samples is generally less than 0.1 wt percent (Table 3), and the average precious-metal concentration is only 0.4 ppm Au and 3 ppm Ag ($n = 11$). Stage 3 As-Sb mineralization is not associated with significant gold.

Gold concentrations correlate most strongly with copper ($r = 0.81$), zinc ($r = 0.71$), silver ($r = 0.82$), and antimony ($r = 0.79$; Fig. 9). The highest precious-metal contents are typically associated with high concentrations of As, Cd, Hg, Sb, and Tl (up to 2.5 wt % As, avg 3,200 ppm; up to 840 ppm Cd, avg 226 ppm; up to 174 ppm Hg, avg 39 ppm; up to 3,200 ppm Sb, avg 612 ppm; up to 510 ppm Tl, avg 68 ppm). No discrete, Hg-bearing minerals have been observed, but mercury is notably enriched in some samples, most likely in sphalerite and vein pyrite and marcasite. The concentrations of Bi, Se, and Te are below their analytical detection limits (<0.5 , <5 , and <0.2 ppm, respectively) in all samples. Although gold-rich samples are typically enriched in arsenic (mainly in pyrite and marcasite), correlation coefficients for gold and arsenic are low, owing to the low gold content of the arsenic-rich, stage 3 mineralization. Similarly, there is little or no correlation between gold and iron ($r = -0.19$), reflecting the low gold content of the stage 1 pyrite mineralization. The trace-element associations in the mineralized samples are summarized in Figure 10 by means of a factor analysis using 14 elements.

Occurrence of Gold and Silver

Gold occurs mainly as discrete grains of native gold and electrum (10–31 wt % Ag, avg = 22 wt %, $n = 87$) in the stage 2, sulfide-bearing amorphous silica veins. Ore microscopy reveals a heterogeneous distribution of gold grains, and two types of gold can be distinguished, based on their morphology and chemistry. The first type is intergrown with disseminated sphalerite, galena, and rare chalcopyrite or pyrite (Fig. 6d). This gold forms small (<5 – $20 \mu\text{m}$), irregular to subhedral grains and is characterized by moderate to high silver contents with a gold fineness between 707 and 843 (avg 787, $n = 57$). The second type of gold occurs as free grains in the amorphous silica, locally lining open cavities. This gold is relatively silver rich, with a fineness between 690 and 787 (avg 721, $n = 20$). The grains are irregular in shape, commonly dendritic, and up to $30 \mu\text{m}$ in size. A few gold grains show an increasing silver content from core to rim.

Gold was also observed as small inclusions in millimeter-sized grains of sphalerite and galena, disseminated in altered basalt. The host sulfides are thought to represent stage 2 mineralization in the wall rock adjacent to the veins. The fineness of this gold is highly variable, ranging from 705 to 893 (avg 820, $n = 10$), but no relationship between the gold fineness and the host mineral was observed. No visible gold was found associated with the early, stage 1 pyrite or the late, stage 3 As-Sb mineralization.

Silver occurs mainly in tetrahedrite, which contains up to 18 wt percent Ag, and in electrum. Galena and sphalerite show only traces of silver, but disseminated and cavity-lining

TABLE 2. Summary of Microprobe Analyses (in wt %) of Selected Minerals from Conical Seamount

Native gold and electrum (n = 83)													
	Ag	As	Au	Cu	Fe	Zn	Pb	Hg	Bi	Te	S		Total
Avg	21.67	<0.02	75.05	0.24	0.22	0.77	0.44	<0.02	0.15	0.04	0.32		98.68
Minimum	10.43	<0.02	62.45	<0.02	<0.02	<0.02	<0.02	<0.02	<0.02	<0.02	<0.02		77.52
Maximum	30.83	0.05	87.42	1.98	1.10	7.21	6.19	<0.02	0.43	0.11	2.10		104.77
Pyrite (n = 259)													
	Ag	As	Au	Cu	Fe	Zn	Co	Mn	Mo	Sb	Se	S	Total
Avg	0.03	0.97	<0.03	0.17	44.01	0.06	<0.02	0.05	nd	0.05	<0.02	52.99	98.34
Minimum	<0.02	<0.05	<0.03	<0.02	37.96	<0.02	<0.02	<0.02	nd	<0.02	<0.02	48.21	97.03
Maximum	1.64	5.43	0.07	4.84	46.43	3.51	0.04	0.32	nd	1.90	0.03	54.53	101.85
Sphalerite (n = 208)													
	Ag	As	Au	Cu	Fe	Zn	Pb	Mn	Cd	Sb	Se	S	Total
Avg	<0.02	0.05	<0.03	0.20	3.16	61.42	0.05	0.35	0.59	0.03	<0.02	33.31	99.14
Minimum	<0.02	<0.05	<0.03	<0.02	0.12	44.09	<0.02	<0.02	0.04	<0.02	<0.02	31.27	92.74
Maximum	0.83	0.87	0.34	6.51	13.39	64.72	1.47	1.36	1.40	1.03	0.07	34.26	101.74
Chalcopyrite (n = 7)													
	Ag	As	Au	Cu	Fe	Zn	Pb	Mn	Cd	Sb	Se	S	Total
Avg	0.13	<0.05	nd	33.91	30.31	0.67	<0.02	<0.02	0.04	<0.02	0.14	34.09	99.91
Minimum	<0.02	<0.05	nd	33.30	29.50	0.10	<0.02	<0.02	<0.02	<0.02	<0.02	33.20	98.80
Maximum	0.30	0.1	nd	34.4	30.90	1.60	<0.02	<0.02	0.20	<0.02	0.40	34.70	101.50
Galena (n = 7)													
	Ag	As	Au	Cu	Fe	Zn	Pb	Hg	Bi	Sb	Se	S	Total
Avg	0.53	0.03	nd	0.07	0.09	0.44	85.67	<0.02	0.39	0.41	<0.02	14.36	102.84
Minimum	0.10	<0.02	nd	<0.02	<0.02	<0.02	84.20	<0.02	<0.02	0.10	<0.02	14.00	100.60
Maximum	1.00	0.10	nd	0.1	0.20	1.40	87.20	<0.02	0.80	0.80	<0.02	15.20	105.60
Ag-bearing tetrahedrite (n = 14)													
	Ag	As	Au	Cu	Fe	Zn	Pb	Mn	Cd	Sb	Se	S	Total
Avg	15.78	5.71	<0.03	26.67	6.06	1.59	nd	<0.02	nd	20.15	<0.02	24.66	100.61
Minimum	11.52	4.66	<0.03	25.23	5.05	0.78	nd	<0.02	nd	13.40	<0.02	23.50	98.30
Maximum	18.17	9.76	<0.03	29.91	6.81	2.59	nd	<0.02	nd	22.11	0.04	26.25	102.03
Unknown Fe-As-Sb sulfide (n = 14)													
	Ag	As	Au	Cu	Fe	Zn	Pb	Mn	Cd	Sb	Se	S	Total
Avg	<0.02	25.28	0.04	0.05	25.41	0.62	0.08	<0.02	<0.02	7.53	0.09	40.64	99.78
Minimum	<0.02	23.07	<0.03	<0.02	24.64	0.13	<0.02	<0.02	<0.02	6.32	0.04	39.97	98.77
Maximum	0.03	27.43	0.11	0.21	26.06	1.31	0.65	0.03	0.03	8.67	0.13	41.02	100.81
Unknown colloform sulfosalts													
	Ag	As	Au	Cu	Fe	Zn	Pb	Hg	Sb	Se	O	S	Total
1	1.01	13.17	0.05	0.73	30.12	0.05	1.24	0.19	5.79	0.08	na	41.56	93.99
2	1.36	12.51	0.37	0.82	27.59	0.08	4.63	0.15	7.67	0.05	na	39.86	95.10
3	1.42	11.62	0.24	0.92	24.91	0.06	8.63	0.11	9.22	0.03	0.67	37.31	95.15
4	0.12	0.59	0.15	0.56	32.99	0.06	13.97	0.41	0.93	<0.02	3.30	44.11	97.21
5	0.21	0.67	0.04	0.20	33.80	0.06	13.29	0.35	0.91	<0.02	2.81	45.17	97.52
6	0.12	0.66	0.17	0.43	34.47	0.09	12.98	0.41	0.91	<0.02	3.08	45.37	98.69
7	0.01	2.68	0.06	0.76	22.21	2.04	23.74	0.38	3.70	0.05	1.81	37.04	94.52
8	0.38	1.39	0.16	0.03	36.36	<0.02	0.33	0.44	4.84	<0.02	2.21	50.21	96.39
9	0.49	1.58	0.18	0.03	36.69	<0.02	0.15	0.43	4.67	<0.02	2.08	50.30	96.63

Note: Low totals are the result of analyzing small aggregates or individual grains; high totals are a result of the stimulation of the sulfide host minerals
Abbreviations: na = not analyzed, nd = not detectable

pyrite and marcasite contain up to 1.9 wt percent Ag, together with high As, Cu, Sb, and Hg. Elevated concentrations of silver, up to 0.5 wt percent Ag, were also found in some late-stage orpiment and realgar and late covellite.

Sulfur Isotopes

The sulfur isotope ratios of sulfides and sulfates (alunite and aluminum phosphate sulfate minerals) recovered during

cruise SO94 were analyzed at the Geological Survey of Japan, Tsukuba, following the KIBA procedure (Sasaki et al., 1979). Sulfides obtained during cruise SO133 were analyzed at Freiberg University of Mining and Technology, using a Finnigan Delta E mass spectrometer and the procedure of Ueda and Krouse (1986). Sulfide mineral separates were prepared at Freiberg University by hand picking under a binocular microscope. All samples were checked for impurities by XRD.

TABLE 3. Representative Geochemical Analyses of Different Vein Types at Conical Seamont

Wt %	All stage 2 mineralized samples				Au-rich, stage 2 veins					Au-poor, stage 1 pyrite veins					
	17-3B	17-4A	53-3A	Range (n = 40)	Avg	25-5C3	25-6A2A	25-8C5	Range (n = 10)	Avg	14-An9	39-1	40-1	Range (n = 11)	Avg
Fe	11.82	9.93	9.09	2.9-20.8	8.3	4.90	4.77	5.40	4.5-12.2	6.0	38.82	39.03	24.48	13.2-39.0	25.5
Cu	0.13	0.02	0.08	0.01-1.9	0.3	0.85	1.11	1.87	0.3-1.9	1.0	0.01	0.01	0.20	0.01-0.2	<0.1
Pb	1.30	0.11	4.00	0.04-4.0	1.1	3.21	3.09	1.68	0.6-3.3	2.3	<0.01	0.03	0.09	<0.01-0.1	<0.1
Zn	6.50	3.00	2.70	0.02-7.7	1.7	5.31	6.07	7.74	0.7-7.7	4.1	0.03	0.01	0.14	0.01-0.1	<0.1
S	15.80	11.50	6.84	0.2-16.1	5.8	7.83	8.49	7.08	2.2-16.1	7.7	44.40	43.20	22.70	15.1-44.4	26.9
SiO ₂	45.60	44.90	52.40	33.6-79.8	56.0	65.90	69.50	na	52.0-69.5	62.2	6.50	5.30	23.00	5.3-42.8	22.5
Al ₂ O ₃	7.80	13.60	9.40	3.1-18.3	10.5	4.50	3.10	4.57	3.1-12.6	6.1	4.10	6.40	8.90	4.1-14.3	8.2
MgO	0.76	1.58	2.03	0.3-7.4	2.2	0.67	0.28	0.35	0.3-3.8	1.0	0.09	0.18	5.51	0.1-5.6	2.0
CaO	2.04	4.34	1.69	0.2-12.5	4.0	0.22	0.43	0.36	0.2-7.2	1.7	0.51	0.24	5.15	0.2-7.6	2.7
MnO	0.06	0.05	0.02	0.01-0.9	0.1	0.11	0.13	0.11	<0.1-0.2	0.1	0.05	0.04	0.15	0.04-0.2	0.1
N ₂ O	1.04	1.41	0.99	0.3-2.4	1.5	0.45	0.32	na	0.3-1.6	0.7	0.44	0.29	1.33	0.3-2.2	0.9
K ₂ O	0.58	0.64	2.05	0.3-6.7	1.7	1.17	1.04	1.90	1.0-3.7	1.8	0.34	0.11	0.43	0.1-1.4	0.5
TiO ₂	0.36	0.62	0.49	0.1-1.0	0.5	0.24	0.11	0.22	0.1-0.7	0.3	0.16	0.34	0.64	0.2-1.0	0.5
Ppm															
Au	25	0.6	17	0.2-230	25	12	99	230	12.1-230	68	0.04	0.28	0.69	0.04-1.3	0.4
Ag	760	20	60	2.6-1,200	216	165	791	1160	165-1,200	588	2.5	1.8	15	1.5-15	4.6
Ppm															
As	1,500	820	3,300	250-25,000	3,200	7,350	5,170	2,950	1,200-11,500	5,660	680	9,500	980	520-13,100	4,115
Bi	<0.5	<0.5	<0.5	<0.5	<0.5	<0.5	<0.5	<0.5	<0.5	<0.5	<0.5	<0.5	<0.5	<0.5	<0.5
Cd	520	450	310	0.7-840	226	570	840	754	54-840	439	0.3	1.2	8.2	0.1-8.2	2
Co	24	30	37	6-120	29	11	7	9	6-31	13	18	21	34	17-72	32
Ga	12	19	22	5-35	19	25	35	na	24-35	29	5.4	5.4	12	5.4-16	9.8
Hg	80	8	40	<1-174	39	83	55	49	32-174	78	10	55	3	3-130	53
In	<0.05	<0.05	<0.05	<0.05-0.6	0.1	<0.05	<0.05	na	<0.05	<0.05	<0.05	<0.05	0.64	<0.05-0.6	0.2
Mo	94	41	6	<1-300	46	<1	32	159	<1-159	41	40	<5	52	<5-417	83
Ni	46	44	24	12-130	30	15	12	14	12-26	16	18	24	34	16-49	29
Sb	660	120	92	21-3,200	612	623	2030	2600	522-3,200	1,770	4.3	23	17	4.3-210	40
Se	<5	<5	<5	<5-24	<5	<5	<5	24	<5-24	8	<5	18	13	<3-18	7
Sn	1.5	8.1	2.7	<0.5-11	2.5	<0.5	0.9	na	<0.5-3.6	1.6	1	1.7	2.4	0.7-6.2	2.3
Te	0.2	<0.2	0.8	<0.2-1.2	<0.2	<0.2	<0.2	na	<0.2	<0.2	<0.2	<0.2	<0.2-0.5	<0.2	
Tl	100	16	49	5.0-510	68	130	22	na	18-130	51	5.6	55	26	5.6-55	20

Methods: major elements (wt %) by a combination of ICP and XRF; sulfur by combustion and infrared detection; Au, As, Co, Hg, Mo, Sb, and Se by INAA; Fe, Cu, Pb, Zn, Ag, Cd, Ga, Ni, Sn, Te, and Tl by ICP-ES; Bi and In by ICP-MS; chemical analyses were carried out at the Geological Survey of Canada, Freiberg University of Mining and Technology, and, commercially, at Actlabs Ltd. (Canada)

Abbreviations: na = not analyzed

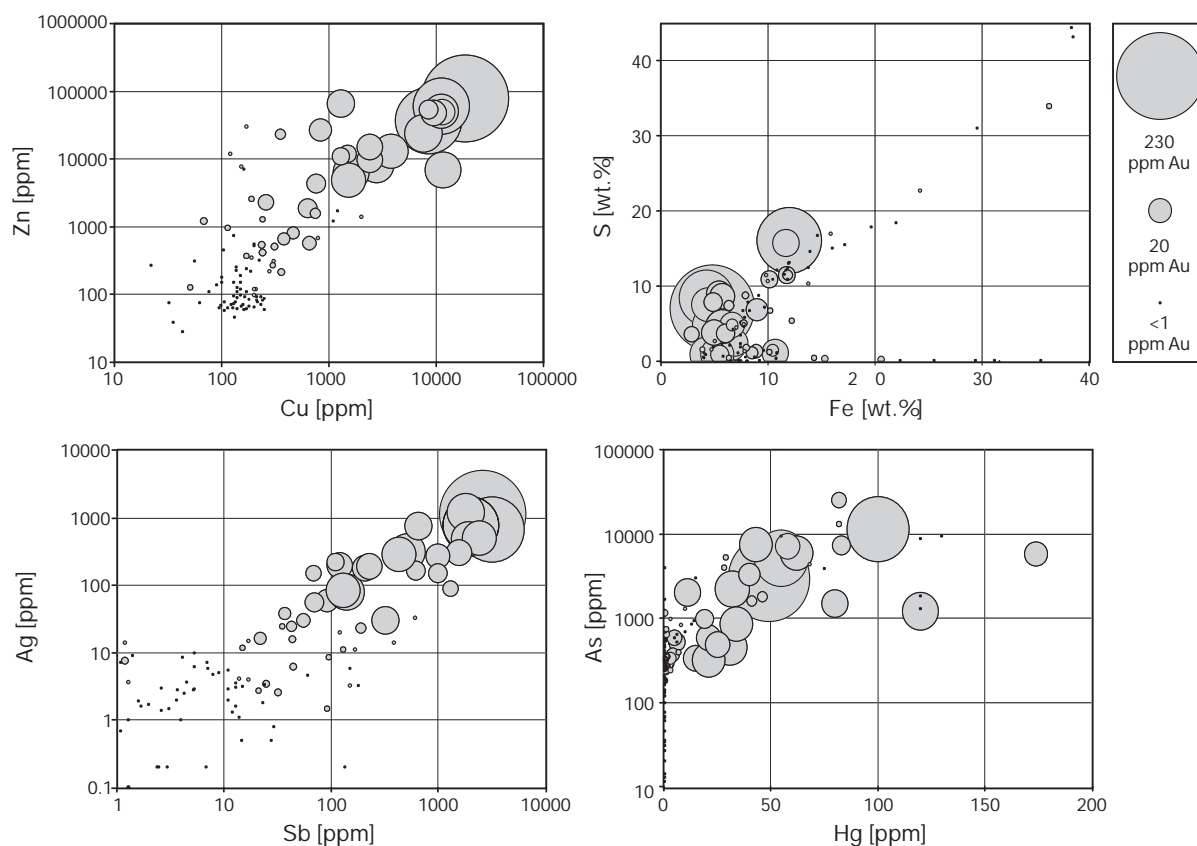


FIG. 9. Correlation plots showing the relationship between high gold concentrations (bubble size) and selected elements. The symbol size is proportional to the gold content of each sample ($n = 94$). The largest symbol corresponds to a gold concentration of 230 ppm; the smallest corresponds to gold concentrations below 1 ppm. Correlation coefficients for the gold-element pairs are 0.81 (Cu-Au), 0.71 (Zn-Au), 0.82 (Ag-Au), 0.79 (Sb-Au), 0.31 (Hg-Au), -0.19 (Fe-Au), and -0.01 (S-Au).

At Freiberg, sulfur was extracted from the sulfides by digestion in CrCl_2 -HCl and precipitation as AgS_2 , prior to isotope analysis. Sulfur was extracted from sulfide-bearing alunite by dissolution in NaOH solution and precipitation of barite. All results are reported relative to the Canyon Diablo Troilite (CDT). The reproducibility of the results in all cases is better than 0.2 per mil.

The sulfur isotope ratios of the entire suite of sulfide samples range from -13.9 to 2.0 per mil ($n = 28$), with characteristic sulfur isotope values for different stages of the mineralization (Table 4). Stage 1 pyrite-marcasite veinlets and disseminated pyrite mineralization, not associated with gold, have $\delta^{34}\text{S}$ values ranging from -8.6 to -0.2 per mil ($n = 16$), whereas bulk sulfides from the gold-rich, stage 2 polymetallic veins have a narrow range of $\delta^{34}\text{S}$ values from -0.8 to 1.5 per mil ($n = 7$). Two samples of the late, stage 3 arsenic mineralization have $\delta^{34}\text{S}$ values of 1.7 and 2.0 per mil. Framboidal pyrite and marcasite in samples collected within and at the periphery of the mineralized system have the lowest $\delta^{34}\text{S}$ values, from -11.6 to -13.9 per mil ($n = 3$), possibly indicating the influence of bacteriogenic sulfate reduction. A more detailed study of these variations, using conventional and laser ablation analyses, is presented by J.B. Gemmeil et al. (unpub. data).

The main-stage, polymetallic sulfides, having $\delta^{34}\text{S}$ values from -0.8 to 1.5 per mil, are thought to have formed from a

combination of sulfur leached from the underlying volcanic rocks and reduced seawater sulfate, similar to that found in a majority of sea-floor hydrothermal systems (e.g., Shanks et al., 1995). However, the negative sulfur isotope ratios of the stage 1 pyrite more closely resemble the $\delta^{34}\text{S}$ values of sulfides in a number of sea-floor hydrothermal systems (Fig. 11) where a contribution of magmatic volatiles to the hydrothermal fluids has been shown (e.g., Hine Hina field in the Lau basin, the Desmos Site in the Manus Basin, and Brothers seamount in the Southern Kermadec arc; Gamo et al., 1997, Herzig et al., 1998, Gemmeil et al., 1999, de Ronde et al., 2000).

Two analyses of alunite (\pm aluminum phosphate sulfate minerals), coexisting with early pyrite (Fig. 7a, b, c), indicate $\delta^{34}\text{S}$ values for sulfate of 7.5 and 6.4 per mil. Pyrite in the same samples has $\delta^{34}\text{S}$ values of -2.9 and -2.3 per mil. The sulfate values are 8.7 to 10.4 per mil higher than that of coexisting pyrite, consistent with the expected sense of isotopic fractionation between sulfate and sulfide in the hydrothermal fluids. However, the $\Delta^{34}\text{S}_{\text{al-py}}$ values for the alunite (\pm aluminum phosphate sulfate)-sulfide pairs are much smaller than expected for equilibrium between these minerals (e.g., $\Delta^{34}\text{S}_{\text{al-py}} = 16$ – 28 ‰ for a temperature range of 200° – 350°C ; Rye et al., 1992; Arribas et al., 1995). $\Delta^{34}\text{S}_{\text{al-py}}$ values of 8.7 to 10.4 per mil would require a temperature of at least 400°C

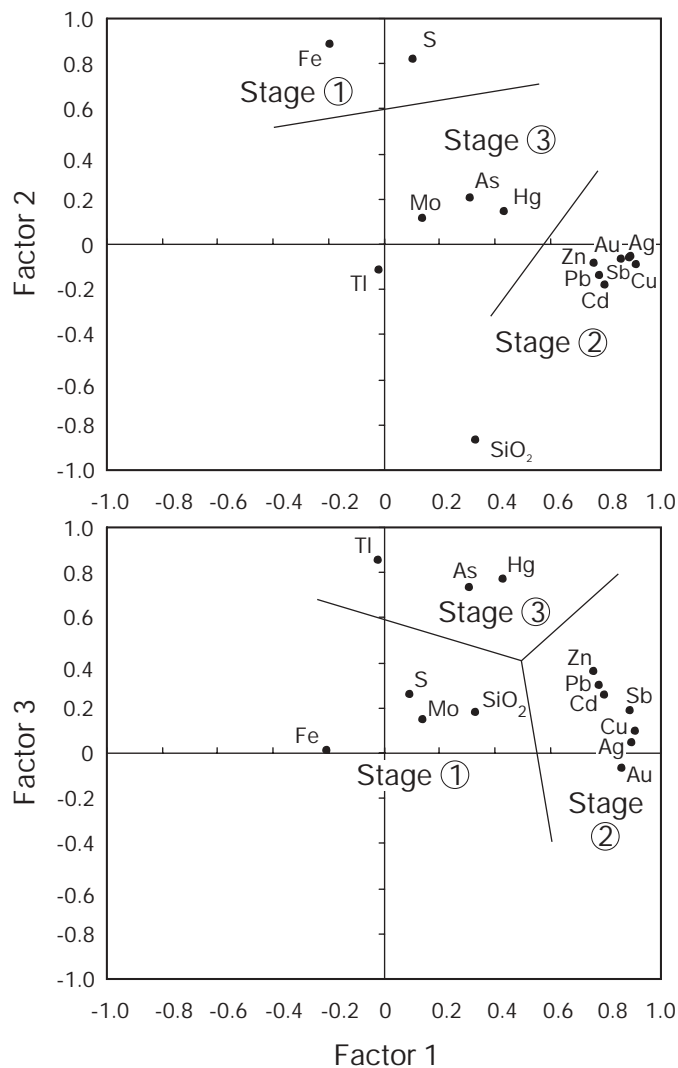


FIG. 10. Principal components analyses (14 elements, orthogonal rotation) of the geochemical data for mineralized samples from Conical seamount, showing the distinction between the different vein types: early pyrite mineralization (stage 1), gold-rich, sulfide-bearing veins (stage 2), and late arsenic mineralization (stage 3).

and H_2S/SO_4 ratios in the hydrothermal fluid of less than 1 (Rye et al., 1992). As discussed below, these conditions are unlikely to apply to Conical seamount. In particular, a low H_2S/SO_4 ratio of <1 is improbable, since Fe sulfides are always present and more abundant than alunite or other sulfates. Although pulses of magmatic vapor, which could result in occasional high SO_4 values, are possible and likely, at least some of the aqueous sulfate appears to have exchanged with H_2S in the hydrothermal fluid. Therefore, isotopic equilibrium was not achieved, and the difference in $\delta^{34}S$ values cannot be used to estimate formation temperature or H_2S/SO_4 ratio.

Conditions of Mineralization

Gold deposition at Conical seamount occurred during a stage of vein mineralization characterized by amorphous silica and disseminated polymetallic sulfides, and accompanied by alteration that is indicative of near-neutral to weakly acidic

TABLE 4. Sulfur Isotope Ratios of Sulfides and Sulfates from Conical Seamount

Sample no.	$\delta^{34}S$ (‰)
Stage 1 pyrite	
SO94/33GTVA-4	-3.0
SO94/63GTVA-1/A	-8.6
SO94/63GTVA-1/E	-5.1
SO94/63GTVA-1/K	-7.6
SO133/Eastern S.1A	-5.2
SO133/Eastern S.1B	C5.2
SO133/39GTVA(1-5mm)	-0.8
SO133/39GTVA-2c	-0.2
SO133/40GTVA	-2.6
SO133/40GTVA(<0.5mm)	-3.5
SO133/40GTVA-2B1	-1.2
SO133/41GTVA(1-5mm)	-1.9
SO133/83GTVA(1-5mm)	-1.3
SO133/83GTVA(py sphere)	-7.3
Stage 1 pyrite and alunite (\pm APS) ¹	
SO94/33GTVA-2A2 sulfate	+7.5
SO94/33GTVA-2A2 pyrite	-2.9
SO94/33GTVA-5 sulfate	+6.4
SO94/33GTVA-5 pyrite	-2.3
Stage 2 mixed sulfides	
SO133/25GTVA-5C3	+1.4
SO133/25GTVA-8C1	+1.5
SO133/25GTVA-8C5	+1.0
SO133/25GTVA-8C6	+0.5
Stage 2 sphalerite	
SO133/23GTVA-1A	-0.8
SO133/53GTVA-3A	-0.5
SO133/83GTVA	+0.8
Stage 3 As sulfides	
SO133/26GTVA alacranite	+1.7
SO133/26GTVA realgar	+2.0
Framboidal pyrite-marcasite ²	
SO133/28GTVA-2	-11.6
SO133/53GTVA-1A1	-13.9
SO133/53GTVA-1A2	-13.0

¹ Data for stage 1 pyrite and alunite (\pm APS) are from coexisting phases

² Framboidal pyrite and marcasite from samples of weakly altered basalt

hydrothermal fluids (amorphous silica, K feldspar, illite, smectite, secondary plagioclase, and minor chlorite and kaolinite). The predominance of pyrite, the absence of pyrrhotite in the veins, and the moderate to low Fe content of sphalerite as well as the occurrence of tetrahedrite-tennantite and chalcocopyrite are indicative of an intermediate sulfidation state for the main, stage 2 sulfide assemblage.

Fluid inclusion measurements were not possible because of a lack of workable inclusions in either the fine-grained sulfides or the gangue minerals from the auriferous veins. However, the maximum temperature of the gold-rich, stage 2 mineralization was most likely limited by the boiling temperature of seawater at the depth of the summit of Conical seamount ($<310^\circ\text{C}$). Indeed, boiling may be indicated by large variations in sulfur isotope ratios in laser ablation analyses of individual sulfide grains (J.B. Gemmel et al., unpub. data). The

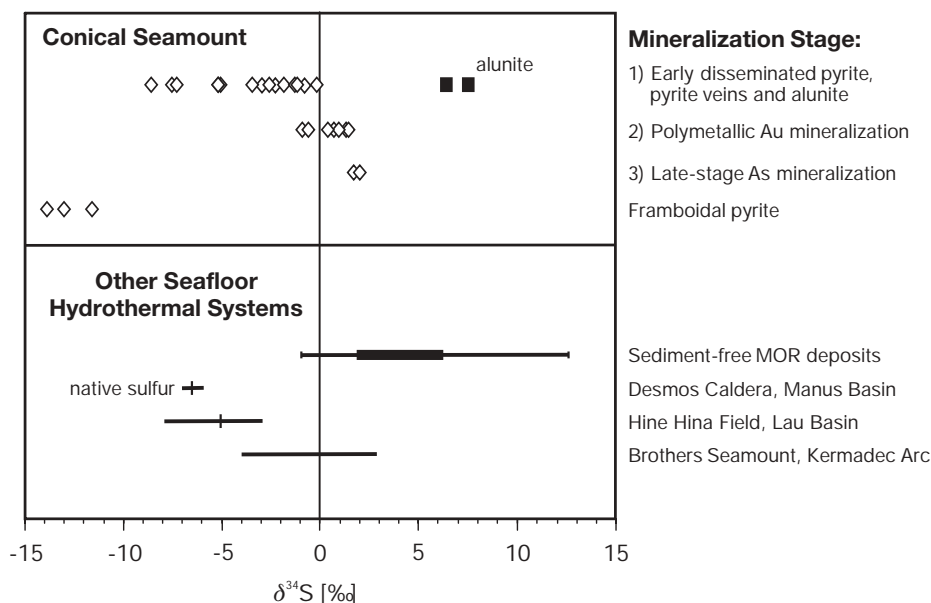


FIG. 11. Sulfur isotope ratios of sulfides and alunite from Conical seamount, in comparison to other sea-floor hydrothermal systems. Data for sea-floor hydrothermal systems are from Herzig et al. (1998), Gemmell et al. (1999), de Ronde et al. (2000), Petersen et al. (2000), and references therein.

deposition of abundant, amorphous silica and chalcedony, rather than quartz, in the stage 2 veins is an indication that quenching of the gold-bearing fluids was sufficient to exceed amorphous silica solubility (Fournier, 1985). However, amorphous silica is also abundant in the late As-Sb mineralization (stage 3), which we interpret to have formed mainly at low temperatures (ca 85°–100°C), similar to that of amorphous silica deposition in other sea-floor hydrothermal systems (e.g., Herzig et al., 1988). Preliminary oxygen isotope analyses of the late-stage amorphous silica indicate temperatures of mainly <100°C (Table 5).

Discussion and Conclusions

The high gold concentrations, relatively low base-metal contents, and distinctive, vein-style mineralization at Conical seamount are unique among explored, modern sea-floor

hydrothermal systems (Fig. 12; Table 6). The gold-bearing veins at Conical seamount are the most gold-rich samples yet recovered from the modern sea floor, exceeding the maximum concentrations reported for sea-floor massive sulfides by at least a factor of four (cf. Herzig and Hannington, 2000). High concentrations of precious metals, as well as As, Sb, Pb, and Hg, have been reported from several sea-floor hydrothermal systems, most notably in the Okinawa trough, the Manus Basin, at Palinuro seamount (Tyrrhenian Sea), and at Suiyo seamount and Mjojjin knoll on the volcanic front of the Izu-Ogasawara arc (cf. Hannington et al., 1999). However, in these systems, the enrichment of precious metals is largely restricted to massive sulfides deposited on the sea floor. Gold-rich, vein-style mineralization of the type found at Conical seamount has not been previously documented.

Rare occurrences of free gold have been found in a number of modern black smoker systems, e.g., Snakepit, Mir Mound, Lau basin, and Eastern Manus Basin (Fouquet et al. 1993; Herzig et al., 1993; Hannington et al., 1995; Moss and Scott, 2001). However, the abundance of free gold in the veins at Conical seamount is unusual for sea-floor mineralization. The range of gold fineness values measured in samples from Conical seamount (690–893) is also distinct from that of gold in black smokers. The few published analyses of gold in high-temperature black smokers indicate uniformly high fineness (e.g., ≥ 950), whereas the Ag-rich gold at Conical seamount more closely resembles that of lower-temperature, subaerial epithermal vein systems (e.g., Spycher and Reed, 1989; Morrison et al., 1991).

The vein system at Conical seamount has a number of other mineralogical, chemical, and textural characteristics in common with some subaerial epithermal systems (e.g., Hedenquist et al., 1996). These include: (1) the distinctive vein-filling textures, (2) the high gold-to-base metal ratios (Fig. 12),

TABLE 5. Oxygen Isotope Ratios of Amorphous Silica from Conical Seamount

Sample no.	$\delta^{18}\text{O}$ (‰)	T_1 (°C) ¹ Fluid 0‰	T_2 (°C) Fluid 10‰
SO94/63-1D1	38.1	14.8	56.2
SO94/63-1D2	37.5	16.9	59.3
SO94/63-1D3	37.3	17.6	60.3
SO94/63-1Ka	34.5	27.8	76.1
SO94/63-1Kb	36.4	20.7	65.2
SO133/15GTVA	38.0	15.1	56.7
SO133/17DR	33.6	31.4	81.7
SO133/26GTVA-1A	26.5	64.6	137.7

¹ Formation temperatures have been calculated using the expression for the fractionation factor from Kita et al. (1985), and assuming end member $\delta^{18}\text{O}_{\text{H}_2\text{O}}$ values of 0 and 10‰

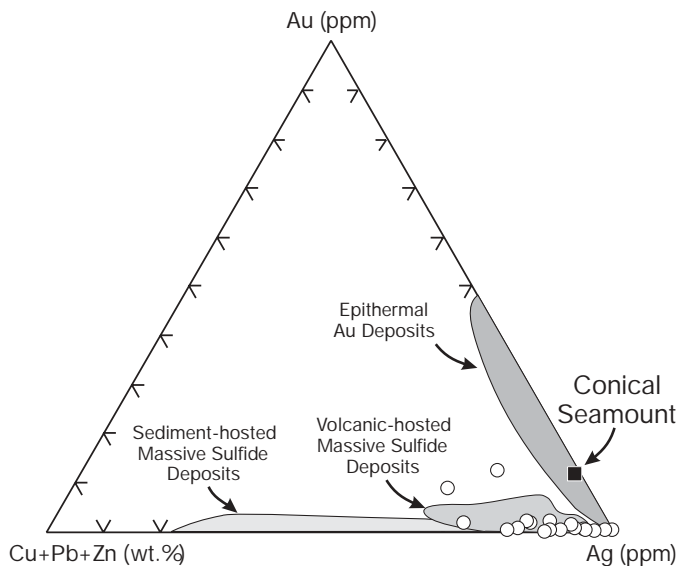


FIG. 12. Comparison of average Au, Ag, and base-metal (Cu + Pb + Zn) content of samples from Conical seamount (square) and other auriferous sea-floor sulfide deposits (circles; data from Hannington et al., 1999; Suiyo seamount, Manus Basin, and Lau basin). Compositional fields for typical epithermal gold deposits, volcanogenic massive sulfide deposits, and sedimentary-exhalative massive sulfide deposits are also shown (modified from Poulsen and Hannington, 1995).

(3) an enrichment in the epithermal suite of elements (e.g., Ag, As, Sb, Hg), (4) the association of illite-smectite \pm K feldspar alteration and amorphous silica with the main stage of gold mineralization, (5) the presence of alunite-bearing mineralization at an early stage in the evolution of the hydrothermal system, and (6) a late stage of low-temperature, As-Sb mineralization.

Several lines of evidence, mostly empirical in nature, also suggest that magmatic aqueous fluids may have played a role in the evolution of the hydrothermal system at Conical seamount. Intergrowths of alunite and aluminum phosphate sulfate minerals, such as those documented at Conical seamount, are commonly observed in epithermal deposits within areas of hypogene advanced argillic alteration (e.g., Stoffregen and Alpers, 1987; Aoki, 1991), in high-sulfidation epithermal deposits (e.g., Hedenquist et al., 1994, 1998), and in the upper parts of some porphyry deposits (e.g., Watanabe and Hedenquist, 2001). These assemblages are interpreted to have formed from acidic fluids generated by adsorption of magmatic vapor by meteoric water, as documented from oxygen and hydrogen isotope data (e.g., Rye et al., 1992; Arribas, 1995). The acidity required to form the alunite results from the presence of magmatic HCl, and the disproportionation of magmatic SO_2 and dissociation of the resulting H_2SO_4 (Meyer and Hemley, 1967; Rye et al., 1992; Giggenbach, 1997). This hypogene style of advanced argillic alteration is typically associated with alunite crystals having a characteristic platy habit, similar to that observed in samples from Conical

TABLE 6. Bulk Geochemistry of Conical Seamount Mineralization and Other Modern Sea-Floor Sulfide Deposits

	n	Au (ppm)	Ag (ppm)	As (ppm)	Hg (ppm)	Sb (ppm)	Cu (wt %)	Fe (wt %)	Zn (wt %)	Pb (wt %)	Ba (wt %)	Au/Ag	$\frac{\text{Cu}}{\text{Cu} + \text{Zn}}$	Reference	
Conical seamount															
All stage 2 mineralized samples	40	25.0	216	3,200	39	612	0.3	8.3	1.7	1.0	<0.1	0.12	0.15	1	
Au-rich, stage 2 veins	10	67.6	588	5,660	78	1,770	1.0	6.0	4.1	2.3	<0.1	0.11	0.20	1	
Au-poor, stage 1 pyrite veins	11	0.4	5	4,115	53	40	<0.1	25.5	<0.1	<0.1	<0.1	0.08		1	
Sediment-free, mid-ocean ridge deposits															
Sediment-free, mid-ocean ridge deposits	890	1.2	113	235	9	46	4.3	23.6	11.7	0.2	1.7	0.01	0.27	2	
Sedimented mid-ocean ridge deposits															
Sedimented mid-ocean ridge deposits	57	0.8	140	3,000	23	600	1.3	24.0	4.7	1.1	7.0	0.01	0.22	2	
Intracontinental back-arc deposits															
Okinawa trough	40	3.1	2,304	17,500	192	6,710	3.3	6.2	20.2	11.8	7.2	<0.01	0.14	3	
Intraoceanic back-arc deposits															
Manus Basin	26	15.0	230	11,000	17	1,130	10.9	14.9	26.9	1.7	7.3	0.07	0.29	4	
Submarine arc volcano deposits															
Palinuro seamount (Thyrrhenian Sea)	15	3.4	270	3,400	1,400	750	0.5	15.1	17.9	8.6	16.3	0.01	0.03	5	
Suiyo seamount (Izu-Bonin Arc)	13	27.7	162	1,168		585	12.8	15.0	17.5	0.7	<0.1	0.17	0.42	6	
Myojin Knoll (Izu-Bonin Arc)	37	20.0	1,213	5,044		3,564	5.5	10.5	21.9	2.3	6.7	0.02	0.20	7	

References: 1 = this study, 2 = Herzig and Hannington, 1995b, 3 = Halbach et al., 1989, with additional data from Aoki and Nakamura, 1989, and Nakamura et al., 1990, 4 = Binns and Scott, 1993, Scott and Binns, 1995, 5 = Puchelt and Laschek, 1986, 6 = Watanabe and Kajimura, 1993, 1994, 7 = Iizasa et al., 1999

seamount (Fig. 7a-c). In contrast, alunite crystals formed in the steam-heated or supergene environments are typically rhombohedral, commonly with a pseudocubic habit (Arribas, 1995).

Mineralogical, chemical, and isotope evidence at Conical seamount indicate a change in the nature of the hydrothermal fluid during the evolution of the system. Acidic alteration of hypogene origin is present during an earlier stage of mineralization, which is dominated by pyrite and marcasite and stockwork-like veining. However, no minerals diagnostic of acid conditions were observed in samples of the main gold and polymetallic sulfide stage, or from late As-Sb mineralization. This evolution from alunite-bearing to nonalunite-bearing assemblages likely reflects an increase in H_2S/SO_4 with time, and is consistent with the observed shift in $\delta^{34}S_{H_2S}$ from lighter to heavier values (e.g., from $\delta^{34}S_{H_2S} = -8.6$ to -0.2% for the early stage, to $\delta^{34}S_{H_2S} = -0.8$ to 1.5% for the main gold stage), assuming that the bulk $\delta^{34}S$ values remained relatively constant. A contribution of magmatic volatiles in the early stages of the hydrothermal system is consistent with the observed ranges of $\delta^{34}S$ values in coexisting alunite and pyrite from the stage 1 veins, although the available evidence indicates that full equilibration between aqueous sulfide and sulfate in the hydrothermal fluid was not achieved.

The distinctive, vein-type mineralization at Conical seamount has some similarities to the epithermal-style mineralization in the giant Ladolam gold deposit on Lihir, including the occurrence of gold mainly in sulfide breccias and stringers, the dominant adularia + pyrite alteration, and the presence of subordinate arsenopyrite, tetrahedrite, tennantite, chalcopyrite, galena, and sphalerite in the ore (Moyle et al., 1990; Carman, 1993, 1994). At Ladolam, the gold mineralization is thought to be genetically linked to the release of magmatic-hydrothermal fluids from a subvolcanic porphyry system during unroofing of the Luise volcano (Sillitoe, 1994). The proximity of Conical seamount to Lihir, and the similar alkaline volcanic rocks at both sites, raise the possibility that the Ladolam and Conical seamount gold systems were related to the same regional-scale magmatic event(s). This is supported by the similar radiometric ages for the polymetallic mineralization at Conical seamount ($93,000 \pm 7,000$ yr, based on U/Th dating of pyrite; J. Scholten, pers. commun., 2001), and for the gold mineralization at Lihir (ca 150,000 yr; Davies and Ballantyne, 1987).

The present mapping and sampling at Conical seamount suggest that the entire upper part of the volcano may be mineralized. However, the difficulty of sampling the steep flanks of the volcano prevents a proper assessment of the extent and character of mineralization at depth. Understanding the full nature of the mineralization at Conical seamount requires samples from deeper portions of the system (i.e., drilling). Until such time as these are available, all that we can conclude is that Conical seamount represents a new style of sea-floor mineralization with characteristics, and possibly an origin, intermediate between subaerial epithermal and conventional, submarine massive sulfide deposits. The similarity of mineralogy, alteration, geochemistry, and vein textures to those of some subaerial epithermal gold deposits indicates that some features, long thought to define a subaerial setting, can also form in a submarine environment at depths of at

least 1 km and, thus, are not unique or diagnostic of subaerial systems.

Acknowledgments

Principal funding for this research was provided by the German Federal Ministry for Education and Research (BMBF Grants 03G0094A and 03G0133A to PMH). Additional support was provided by the Leibniz-Program of the German Research Foundation, Natural Resources Canada (GSC contribution no. 2002114), the German-Canadian Program on Scientific and Technical Cooperation (032/98 GEO), and the European EU-HCM program. We thank masters, officers, and crew of the R/V Sonne for their expert technical assistance during our research cruises in the New Ireland basin, and R. Liebscher and M. Drischel for analytical help. Special thanks to K.-P. Becker and Katherine Venance for assistance with microprobe work and XRF analyses, Peter Belanger, Geological Survey of Canada, for ICP analyses, and A. Sasaki for assistance with S isotope analyses at the Geological Survey of Japan. The manuscript was much improved through critical reviews by Cornel de Ronde, Pat Browne, and Jeff Hedenquist.

September 20, 2000; August 12, 2002

REFERENCES

- Aoki, M., 1991, Mineralogical features and genesis of alunite solid solution in high temperature magmatic-hydrothermal systems: Geological Survey Japan Report, v. 277, p. 35–37.
- Aoki, M., and Nakamura, K., 1989, The occurrence of chimneys in Izena Hole No. 2 orebody and texture and mineral compositions of the sulfide chimneys: Deep Sea Research, JAMSTEC Symposium, Proceedings, v. 5, p. 197–210 (in Japanese with English abstract).
- Arribas, A. Jr., 1995, Characteristics of high sulfidation deposits, and their relation to magmatic fluid, in Thompson, J.F.H., ed., Magmas, fluids, and ore deposits: Mineralogical Society of Canada, Short Course, vol. 23, p. 419–454.
- Arribas, A., Cunningham, C.G., Rytuba, J.J., Rye, R.O., Kelly, W.C., Podwysocki, M.H., McKee, E.H., and Tosdal, R.M., 1995, Geology, geochronology, fluid inclusions, and isotope geochemistry of the Rodalquilar gold alunite deposit, Spain: ECONOMIC GEOLOGY, v. 90, p. 795–822.
- Binns, R.A., and Scott, S.D., 1993, Actively forming polymetallic sulfide deposits associated with felsic volcanic rocks in the eastern Manus back-arc basin, Papua New Guinea: ECONOMIC GEOLOGY, v. 88, p. 2226–2236.
- Burns, P.C., and Percival, J.B., 2001, Alacranite, As_4S_4 : A new occurrence, new formula, and determination of the crystal structure: Canadian Mineralogist, v. 39, p. 809–818.
- Carman, G.D., 1993, Transitional magmatic to epithermal mineralization at the Lihir island gold deposit, PNG [abs.]: Implications for the evolution of ore-forming fluids from fertile magmas: Geological Society Australia, Abstracts with Program, v. 34, p. 12–13.
- 1994, Genesis of the Ladolam gold deposit, Lihir island, Papua New Guinea: Unpublished PhD thesis, Melbourne, Australia, Monash University, 263 p.
- Coleman, P.J., and Kroenke, L.W., 1981, Subduction without volcanism in the Solomon Islands arc: Geo-Marine Letters, v. 1, p. 129–134.
- Davies, R.M., and Ballantyne, G.H., 1987, Geology of the Ladolam gold deposit, Lihir island, Papua New Guinea: Australasian Institute of Mining and Metallurgy, Pacific Rim Congress, Parkville, 1987, Proceedings, p. 943–949.
- de Ronde, C., Hannington, M.D., Stoffers, P., Wright, I., Gennerich, H.-H., Browne, P., and Herzig, P.M., 2000, Massive sulfide mineralisation associated with a frontal arc volcano: Brothers hydrothermal system, Southern Kermadec arc, New Zealand, in Gemmel, J.B., and Pongratz, J., eds., Volcanic environments and massive sulfide deposits: Hobart, University of Tasmania, Centre for Ore Deposits Research, Special Publication 3, p. 37–38.
- Farr, L.C., Perfit, M.R., Heatherington, A., Jonasson, I., Hannington, M., and Herzig, P., 1999, Petrology and geochemistry of alkaline lavas and associated hydrothermal deposits from seamounts in the Tabar-to-Feni island Arc, Papua New Guinea (PNG): EOS, American Geophysical Union Transactions, v. 80, p. F1092.

- Fouquet, Y., Wafik, A., Cambon, P., Mevel, C., Meyer, G., and Gente, P., 1993, Tectonic setting and mineralogical and geochemical zonation in the Snake Pit sulfide deposit (Mid-Atlantic Ridge at 23°N): *ECONOMIC GEOLOGY*, v. 88, p. 2018–2036.
- Fournier, R.O., 1985, The behavior of silica in hydrothermal solutions, in Berger, B.R., and Bethke, P.M., eds., *Geology and geochemistry of epithermal systems: Reviews in Economic Geology*, v. 2, p. 45–62.
- Franz, L., Becker, K.-P., Kramer, W., and Herzig, P.M., 2002, Metasomatic mantle xenoliths from the Bismarck microplate (Papua New Guinea)—Thermal evolution, geochemistry, and extent of slab induced metasomatism: *Journal of Petrology*, v. 43, p. 315–343.
- Gamo, T., Okamura, K., Charlou, J.-L., Urabe, T., Auzende, J.-M., Ishibashi, J., Shitashima, K., Chiba, H., and ManusFlux Shipboard Scientific Party, 1997, Acidic and sulfate-rich hydrothermal fluids from the Manus back-arc basin, Papua New Guinea: *Geology*, v. 25, p. 139–142.
- Gemmell, J.B., Binns, R.A., and Parr, J.M., 1999, Submarine, high sulfidation alteration within DESMOS caldera, Manus Basin, PNG, in Stanley, C.J., et al., eds., *Mineral deposits: Processes to processing: Fifth Biennial SGA Meeting and the Tenth Quadrennial IAGOD Symposium*, London, Proceedings, p. 503–506.
- Giggenbach, W.F., 1997, The origin and evolution of fluids in magmatic-hydrothermal systems, in Barnes, H.L., ed., *Geochemistry of hydrothermal ore deposits*, 3rd ed.: New York, John Wiley and Sons, p. 737–796.
- Halbach, P., Nakamura, K., Wahsner, M., Lange, J., Sakai, H., Kaselitz, L., Hansen, R.-D., Yamano, M., Post, J., Prause, B., Seifert, R., Michaelis, W., Teichmann, F., Kinoshita, M., Marten, A., Ishibashi, J., Czerwinski, S., and Blum, N., 1989, Probable modern analogue of Kuroko-type massive sulphide deposits in the Okinawa trough back-arc basin: *Nature*, v. 338, p. 496–499.
- Hannington, M.D., Tivey, M.K., Larocque, A.C., Petersen, S., and Rona, P.A., 1995, The occurrence of gold in sulfide deposits of the TAG hydrothermal field, Mid-Atlantic Ridge: *Canadian Mineralogist*, v. 33, p. 1285–1310.
- Hannington, M.D., Poulsen, K.H., Thompson, J.F.H., and Sillitoe, R.H., 1999, Volcanogenic gold in the massive sulfide environment: *Reviews in Economic Geology*, v. 8, p. 325–356.
- Hedenquist, J.W., Matsuhisa, Y., Izawa, E., White, N.C., Giggenbach, W.F., and Aoki, M., 1994, Geology, geochemistry, and origin of high sulfidation Cu-Au mineralization in the Nansatsu district, Japan: *ECONOMIC GEOLOGY*, v. 89, p. 1–30.
- Hedenquist, J.W., Izawa, E., Arribas, A., White, N.C., 1996, Epithermal gold deposits: Styles, characteristics, and exploration: *Resource Geology Special Publication*, v. 1, 17 p.
- Hedenquist, J.W., Arribas, A., Jr., and Reynolds, T.J., 1998, Evolution of an intrusion-centered hydrothermal system: Far-Southeast Lepanto porphyry and epithermal Cu-Au deposits, Philippines: *ECONOMIC GEOLOGY*, v. 93, p. 373–404.
- Herzig, P.M., and Hannington, M.D., 1995a, Hydrothermal activity, vent fauna, and submarine gold mineralization at alkaline fore-arc seamounts near Lihir island, Papua New Guinea: *Australasian Institute of Mining and Metallurgy, PACRIM*, Melbourne, Australia, 1995, Proceedings, p. 279–284.
- 1995b, Polymetallic massive sulfides at the modern sea floor: A review: *Ore Geology Reviews*, v. 10, p. 95–115.
- 2000, Polymetallic massive sulfides and gold mineralization at mid-ocean ridges and in subduction-related environments, in Cronan, D.S., ed., *Marine mineral deposits: Boca Raton, Florida, CRC Press*, p. 347–368.
- Herzig, P.M., Becker, K.P., Stoffers, P., Bäcker, H., and Blum, N., 1988, Hydrothermal silica chimney fields in the Galapagos Spreading Center at 86°W: *Earth and Planetary Science Letters*, v. 89, p. 261–272.
- Herzig, P.M., Hannington, M.D., Fouquet, Y., von Stackelberg, U., and Petersen, S., 1993, Gold-rich polymetallic sulfides from the Lau back-arc and implications for the geochemistry of gold in sea-floor hydrothermal systems in the Southwest Pacific: *ECONOMIC GEOLOGY*, v. 88, p. 2182–2209.
- Herzig, P.M., Hannington, M.D., McInnes, B., Stoffers, P., Villinger, H., Seifert, R., Binns, R., Liebe, T., and Scientific Party, 1994, Submarine alkaline volcanism and active hydrothermal venting in the New Ireland fore-arc basin, Papua New Guinea: *EOS, American Geophysical Union Transactions*, v. 75, p. 513–516.
- Herzig, P.M., Hannington, M.D., and Arribas, A., 1998, Sulfur isotopic composition of hydrothermal precipitates from the Lau back-arc: Implications for magmatic contributions to seafloor hydrothermal systems: *Mineralium Deposita*, v. 33, p. 226–237.
- Herzig, P.M., Petersen, S., and Hannington, M.D., 1999, Epithermal-type gold mineralization at Conical seamount: A shallow submarine volcano south of Lihir island, Papua New Guinea, in Stanley, C.J., et al., eds., *Mineral deposits: Processes to processing: Fifth Biennial SGA meeting and the Tenth Quadrennial IAGOD Symposium*, London, Proceedings, p. 527–530.
- Iizasa, K., Fiske, R.S., Ishizuka, O., Yuasa, M., Hashimoto, J., Ishibashi, J., Naka, J., Horii, Y., Fujiwara, Y., Imai, A., and Koyama, S., 1999, A kuorko-type polymetallic sulfide deposit in a submarine silicic caldera: *Science*, v. 283, p. 975–977.
- Johnson, R.W., 1979, Geotectonics and volcanism in Papua New Guinea: A review of the late Cenozoic: Bureau of Mineral Resources, *Journal of Australian Geology and Geophysics*, v. 4, p. 181–207.
- Johnson, R.W., Wallace, D.A., and Ellis, D.J., 1976, Feldspathoid-bearing potassic rocks and associated types from volcanic islands off the coast of New Ireland, Papua New Guinea: A preliminary account of geology and petrology, in Johnson, R.W., ed., *Volcanism in Australasia*: Amsterdam, Elsevier, p. 297–316.
- Johnson, R.W., Perfit, M.R., Chappell, B.W., Jaques, A.L., Shuster, R.D., and Ridley, W.I., 1988, Volcanism in the New Ireland basin and Manus Island region: Notes on the geochemistry and petrology of some dredged volcanic rocks from a rifted-arc region, in Marlow, M.S., Dadisman, S.V., and Exon, N.F., eds., *Geology and offshore resources of Pacific Island Arcs—New Ireland and Manus Region, Papua New Guinea: Circum-Pacific Council for Energy and Mineral Resources, Earth Science Series*, v. 9, p. 113–130.
- Kennedy, A.K., Grove, T.L., and Johnson, R.W., 1990a, Experimental and major element constraints on the evolution of lavas from Lihir island, Papua New Guinea: *Contributions to Mineralogy Petrology*, v. 104, p. 722–734.
- Kennedy, A.K., Hart, S.R., and Frey, F.A., 1990b, Composition and isotopic constraints on the petrogenesis of alkaline arc lavas: Lihir island, Papua New Guinea: *Journal of Geophysical Research*, v. 95, p. 6929–6942.
- Kita, I., Taguchi, S., and Matsubaya, O., 1985, Oxygen isotope fractionation between amorphous silica and water at 34–93°C: *Nature*, v. 314, p. 83–84.
- Kroenke, L.W., 1972, Geology of the Ontong Java Plateau: Reports of the Hawaii Institute of Geophysics, v. 72–75, 119 p.
- Licence, P.S., Terril, J.E., and Fergusson, L.J., 1987, Epithermal gold mineralization, Ambittle Island, Papua New Guinea: *Australian Institute of Mining and Metallurgy, Pacific Rim Conference, Melbourne, 1987, Proceedings*, p. 273–278.
- McInnes, B.I.A., 1992, A glimpse of ephemeral subduction zone processes from Simberi Island, Papua New Guinea: Unpublished Ph.D. thesis, Ottawa, Canada, University of Ottawa, 235 p.
- McInnes, B.I.A., and Cameron, E.M., 1994, Carbonated, alkaline metasomatic melts from a sub-arc environment: Mantle wedge samples from the Tabar-Lihir-Tanga-Feni arc, Papua New Guinea: *Earth and Planetary Science Letters*, v. 122, p. 125–141.
- McInnes, B.I.A., McBride, J.S., Evans, N.J., Lambert, D.D., and Andrew, A.S., 1999, Osmium isotope constraints on ore metal recycling in subduction zones: *Science*, v. 286, p. 512–516.
- McInnes, B.I.A., Gregoire, M., Binns, R.A., Herzig, P.M., and Hannington, M.D., 2001, Hydrous metasomatism of oceanic sub-arc mantle, Lihir, Papua New Guinea: *Petrology and geochemistry of fluid-metasomatised mantle wedge xenoliths: Earth and Planetary Science Letters*, v. 188, p. 169–183.
- Meyer, C., and Hemley, J.J., 1967, Wallrock alteration, in Barnes, H.L., ed., *Geochemistry of hydrothermal ore deposits*: New York, Holt, Rinehart, and Wilson, p. 166–215.
- Moberley, R. Jr., 1972, Origin of lithosphere behind island arcs, with reference to the western Pacific: *Geological Society of America Memoirs*, v. 132, p. 35–55.
- Morrison, G.W., Rose, W.J., and Jaireth, S., 1991, Geological and geochemical controls on the silver content (fineness) of gold-silver deposits: *Ore Geology Reviews*, v. 6, p. 333–364.
- Moss, R., and Scott, S.D., 2001, Geochemistry and mineralogy of gold-rich hydrothermal precipitates from the Eastern Manus Basin, Papua New Guinea: *Canadian Mineralogist*, v. 39, p. 957–978.
- Moyle, A.J., Doyle, B.J., Hoogvliet, H., and Ware, A.R., 1990, Ladolam gold deposit, Lihir island, in Hughes, F.E., ed., *Geology of the mineral deposits of Australia and Papua New Guinea*, v. 2: Parkville, Australasian Institute of Mining and Metallurgy, p. 1793–1805.
- Nakamura, K., Marumo, K., and Aoki, M., 1990, Discovery of a black smoker vent and a pockmark emitting CO₂-rich fluid on the seafloor, Izena cauldron in the Okinawa trough: Deep Sea Research, *JAMSTEC Symposium, Proceedings*, v. 6, p. 33–50 (in Japanese with English abstract).
- Patterson, D.B., Farley, K.A., and McInnes, B.I.A., 1997, Helium isotopic composition of the Tabar-Lihir-Tanga-Feni island arc, Papua New Guinea: *Geochimica et Cosmochimica Acta*, v. 61, p. 2485–2496.

- Petersen, S., Herzig, P.M., Hamington, M.D., 2000, Third dimension of a presently forming VMS deposit: TAG hydrothermal mound, Mid-Atlantic Ridge, 26°N: *Mineralium Deposita*, v. 35, p. 233–259.
- Poulsen, K.H., and Hamington, M.D., 1995, Volcanic-associated massive sulfide gold, in Eckstrand, R.O., Sinclair, W.D., and Thorpe, R.I., eds., *Geology of Canadian mineral deposit types: Geological Society of America, Geology of Canada, DNAG (Decade of North American Geology) vol. 8*, p. 183–196.
- Puchelt, H., and Laschek, D., 1986, Forschungsfahrt Sonne 41 HYMAS I: Sonne Cruise Report, Karlsruhe University, p. 331.
- Rye, R.O., Bethke, P.M., and Wassermann, M.D., 1992, The stable isotope geochemistry of acid sulfate alteration: *ECONOMIC GEOLOGY*, v. 87, p. 225–262.
- Sasaki, A., Arikawa, Y., and Folinsbee, R.E., 1979, KIBA reagent method of sulfur extraction applied to isotope work: *Bulletin of the Geological Survey of Japan*, v. 30, p. 241–245.
- Scott, S.D., and Binns, R.A., 1995, Hydrothermal processes and contrasting styles of mineralization in the western Woodlark and eastern Manus Basins of the western Pacific, in Parson, L.M., Walker, C.L., and Dixon, D.R., eds., *Hydrothermal vents and processes: Geological Society of London, Special Publication no. 87*, p. 191–206.
- Shanks, W.C. III, Böhlke, J.K., and Seal, R.R. II, 1995, Stable isotopes in mid-ocean ridge hydrothermal systems: Interactions between fluids, minerals, and organisms, in S.E. Humphris, R.A. Zierenberg, L.S. Mullineaux, and R.E. Thompson, eds., *Seafloor hydrothermal systems: Physical chemical, biological, and geological interactions: American Geophysical Union, Monograph 91*, p. 194–221.
- Sillitoe, R.H., 1994, Erosion and collapse of volcanoes: Causes of telescoping in intrusion-centered ore deposits: *Geology*, v. 22, p. 945–948.
- Spycher, N.F., and Reed, M.H., 1989, Evolution of a Broadlands-type epithermal ore fluid along alternative P-T paths: Implications for the transport and deposition of base, precious, and volatile metals: *ECONOMIC GEOLOGY*, v. 84, p. 328–359.
- Stewart, W.D., and Sandy, M.J., 1988, Geology of New Ireland and Djaul Islands, Northeastern Papua New Guinea, in Marlow, M.S., et al., eds., *Geology and off-shore resources of Pacific Island Arcs-New Ireland and Manus region, PNG: Earth Science Series*, v. 9, p. 13–30.
- Stracke, A., 1996, *Geochemie von Seamount-Basalten und Inselbogen-Vulkaniten der Tabar-Lihir-Tanga-Feni-Inselkette, Papua New Guinea: Unpublished MSc thesis, Germany, University of Tübingen*, 79 p.
- Stoffregen, R.E., and Alpers, C.N., 1987, Woodhouseite and svanbergite in hydrothermal ore deposits: Products of apatite destruction during advanced argillic alteration: *Canadian Mineralogist*, v. 25, p. 201–211.
- Ueda, A., and Krouse, H.R., 1986, Direct conversion of sulphide and sulphate minerals to SO₂ for isotope analyses: *Geochemical Journal*, v. 20, p. 209–212.
- Wallace, D.A., Johnson, R.W., Chapell, B.W., Arculus, R.J., Perfit, M.R., and Crick, I.H., 1983, *Cainozoic volcanism of the Tabar, Lihir, Tanga, and Feni islands, Papua New Guinea: Geology, whole-rock analyses, and rock forming mineral composition: Bureau Mineral Resources, Geology, and Geophysics Australia Report 243 (microfiche)*.
- Watanabe, Y., and Hedenquist, J.W., 2001, Mineralogic and stable isotopic zonation at the surface over the El Salvador porphyry copper deposit, Chile: *ECONOMIC GEOLOGY*, v. 96, p. 1775–1798.
- Watanabe, K., and Kajimura, T., 1993, Topography, geology, and hydrothermal deposits at Suiyo seamount: Deep Sea Research, JAMSTEC Symposium, Proceedings, v. 9, p. 77–89 (in Japanese with English abstract).
- 1994, The hydrothermal mineralization at Suiyo seamount, Izu-Ogasawara arc: *Resource Geology*, v. 44, p. 133–140 (in Japanese).

Sulfur Isotope Evidence for Magmatic Contributions to Submarine and Subaerial Gold Mineralization: Conical Seamount and the Ladolam Gold Deposit, Papua New Guinea

J. BRUCE GEMMELL,[†] ROBINA SHARPE,

Centre for Ore Deposit Research (CODES SRC), University of Tasmania, Private Bag 79, Hobart, Tasmania, Australia 7001

IAN R. JONASSON,

Geological Survey of Canada, 601 Booth Street, Ottawa, Ontario, Canada K1A 0E8

AND PETER M. HERZIG

Institute for Mineralogy, Freiberg University of Mining and Technology, Brennhausgasse 14, D-09599, Freiberg, Germany

Abstract

Conical seamount is a submarine alkali basalt volcano situated 10 km south of Lihir Island in the Tabar-Feni island chain, Papua New Guinea. Polymetallic (Zn-Pb-Ag-Au-As-Sb) veins, pyritic stockwork, and hydrothermally altered rocks discovered on the summit of Conical seamount represent a unique example of submarine gold mineralization with mineralogical, chemical, and textural characteristics common to some subaerial epithermal systems. The giant Ladolam epithermal gold deposit (42 Moz Au) is situated in the crater of an alkali stratovolcano on Lihir Island. Portions of the epithermal mineralization and alteration assemblages at Ladolam are similar to those observed on Conical seamount.

Conical seamount has the lightest, hydrothermal (i.e., nondiagenetic) sulfide $\delta^{34}\text{S}$ values (-17.5 to $+6.1\text{‰}$) measured to date from modern sea-floor hydrothermal systems. A previous model for the Conical seamount hydrothermal system suggested a contribution of magmatic volatiles in the earliest stages of mineralization (stage 1), followed by a combination of sulfur leached from the underlying volcanic rocks and reduced seawater sulfate during the main base and precious metal precipitating event (stage 2). New sulfur isotope data allow a reinterpretation of this model that suggests a greater input of magmatic volatiles, plus boiling, throughout both stage 1 and 2 mineralization.

Sulfides from the Ladolam gold deposit have a range of sulfur isotope values (-12.9 to $+3.6\text{‰}$) similar to that of Conical seamount. These sulfur isotope data have previously been interpreted as the result of magmatic volatiles escaping from a crystallizing magma and mixing with dilute meteoric ground water. Anhydrite associated with the gold mineralization has two populations of $\delta^{34}\text{S}$ values ($8\text{--}14$ and $20\text{--}22\text{‰}$), which indicate the interaction of magmatic volatiles with seawater that has previously been discounted. The range of sulfide and sulfate $\delta^{34}\text{S}$ values at Ladolam is reinterpreted to be due to a complex interaction of magmatic hydrothermal fluids, meteoric ground water, and seawater. Native sulfur in thermal areas in Luise caldera and pyrite in offshore hydrothermal vents in Luise harbor have similar $\delta^{34}\text{S}$ values to the Ladolam epithermal mineralization, indicating that fluids similar to the young Ladolam ore-forming event are still reaching the floor of Luise caldera.

Sulfur isotope data from Conical seamount and the Ladolam deposit suggest that magmatic volatiles have contributed a significant amount of sulfur to both these gold-rich hydrothermal systems.

Introduction

MAGMATIC contributions to the genesis of both active and extinct volcanic-hosted massive sulfide (VHMS) and epithermal deposits have been the subject of considerable debate (e.g., Hedenquist and Lowenstern, 1994). Sillitoe et al. (1996), Hannington (1997), and Hannington et al. (1999) recognized that the same characteristic geological and geochemical features that separate epithermal deposits into high- and low-sulfidation styles occur within the family of polymetallic (Cu-Pb-Zn-Ag-Au) sea-floor, volcanic-hosted massive sulfide deposits situated in submarine, arc tectonic environments. Resolving the role and significance of magmatic fluid is critical to the understanding the sources of sulfur and metals in the formation of mineral deposits in submarine settings (de Ronde, 1995; Herzig and Hannington, 1995a; Sillitoe et al., 1996; Yang and

Scott, 1996; Herzig et al., 1998a; Gemmell et al., 1999; Hannington et al., 1999). This paper contributes data relevant to constraining the source(s) of sulfur in two gold-rich hydrothermal systems in the southwestern Pacific Ocean: the submarine Conical seamount system and the subaerial Ladolam gold deposit on Lihir Island, Papua New Guinea.

Petersen et al. (2002) published initial sulfur isotope data for Conical seamount, and two sulfur isotope studies on the Ladolam deposit have been published by Müller (2002a) and Carman (2003). We report new laser-ablation and conventional sulfur isotope data for Conical seamount, as well as new conventional sulfur isotope data for the Ladolam deposit, active hot spring deposits on Lihir Island, and pyritic hydrothermal vents in Luise harbor, offshore from Lihir Island. These data are used to refine interpretations of the sources of sulfur for both Conical seamount and the Ladolam hydrothermal systems.

[†] Corresponding author: e-mail, Bruce.Gemmell@utas.edu.au

Regional Setting

The Pliocene-Pleistocene Tabar-Feni island chain, which includes Lihir Island and Conical seamount, occurs in a complex tectonic zone at the eastern edge of the Bismarck Sea. These islands are located in the former Oligocene fore-arc region of New Ireland on a large uplifted block raised by regional southward compression along the Manus-Kilinau trench (Fig. 1A), and the present volcanism throughout the island chain is most likely related to subduction from the south along the New Britain-Solomon trench (Exon et al., 1986; Stewart and Sandy, 1988; McInnes et al., 1999, 2001). The mafic to intermediate volcanic rocks occurring on the Tabar-Feni islands formed from a high K, alkaline, SiO₂-undersaturated magma (Kennedy et al., 1990; McInnes, 1992; McInnes et al., 1999). These highly oxidized, sulfur-rich alkaline melts are interpreted to be generated by partial remelting of metasomatically enriched Oligocene mantle wedge regions (McInnes and Cameron, 1994; McInnes et al., 1999, 2001) and are considered to have risen through the old fore-arc crust along reactivated transfer faults (Herzig et al., 1998b).

Conical Seamount

Conical seamount is a submarine volcano located 10 km south of Lihir Island in the Tabar-Feni island chain, eastern Papua New Guinea (Fig. 1B; Herzig et al., 1994; Herzig and Hannington, 1995b). Conical seamount consists of vesicular, coherent, and brecciated pyroxene-phyric, alkali-olivine basalt and trachybasalt and is considered the first example of sea-floor hydrothermal activity associated with alkaline volcanism in an arc tectonic setting (Herzig et al., 1994; Herzig and Hannington, 1995b; Petersen et al., 2002).

A comprehensive sampling program, via TV-controlled grab and dredging, recovered more than 1,200 kg of mineralized

material (Herzig et al., 1998c). Polymetallic (Zn-Pb-Ag-Au-As-Sb) veins, pyritic stockwork, and hydrothermally altered rocks discovered on the summit of Conical seamount provide an example of submarine gold-rich mineralization. There are a number of mineralogical, chemical, and textural characteristics in common with some subaerial epithermal systems (Herzig et al., 1998b, c; Petersen et al., 2002). Gold concentrations in samples from Conical seamount reach 230 ppm Au, with an average of 25 ppm ($n = 40$) and are the highest yet discovered on the present-day sea floor (Herzig et al., 1999; Petersen et al., 2002). Three stages of mineralization are observed at Conical seamount (Table 1), and these stages occur in three distinct zones: inner, intermediate, and outer (Fig. 2). All three mineralization stages occur in the inner zone, whereas the intermediate and outer zones both contain only stages 1 and 3. The main, gold-bearing stage 2 mineralization is confined to a relatively small area near the summit fissure. Examples of the Conical seamount mineralization stages analyzed in this study are shown in Figure 3.

Ladolam Deposit, Lihir Island

Lihir Island consists of several Pliocene to Pleistocene strato-volcanoes (Fig. 4A) composed mainly of alkali basalts, trachybasalts, and trachyandesites (Wallace et al., 1983; Kennedy et al., 1990; Moyle et al., 1990; Müller et al., 2001, 2002a, b). The youngest of these structures, the Luise volcano (0.35–0.9 Ma; Davies and Ballantyne, 1987), hosts the Ladolam Au deposit. Economic concentrations of gold occur in four main areas within the caldera (Lienetz, Minifie, Kapit, and Coastal zones). The total Au resource is 471 million tons (Mt) at 2.75 g/t Au for a total of 42 Moz Au (S. Hunt, pers. commun., 2001). Carman (1994, 2003) divided the mineralization at Ladolam into three stages: porphyry, transitional,

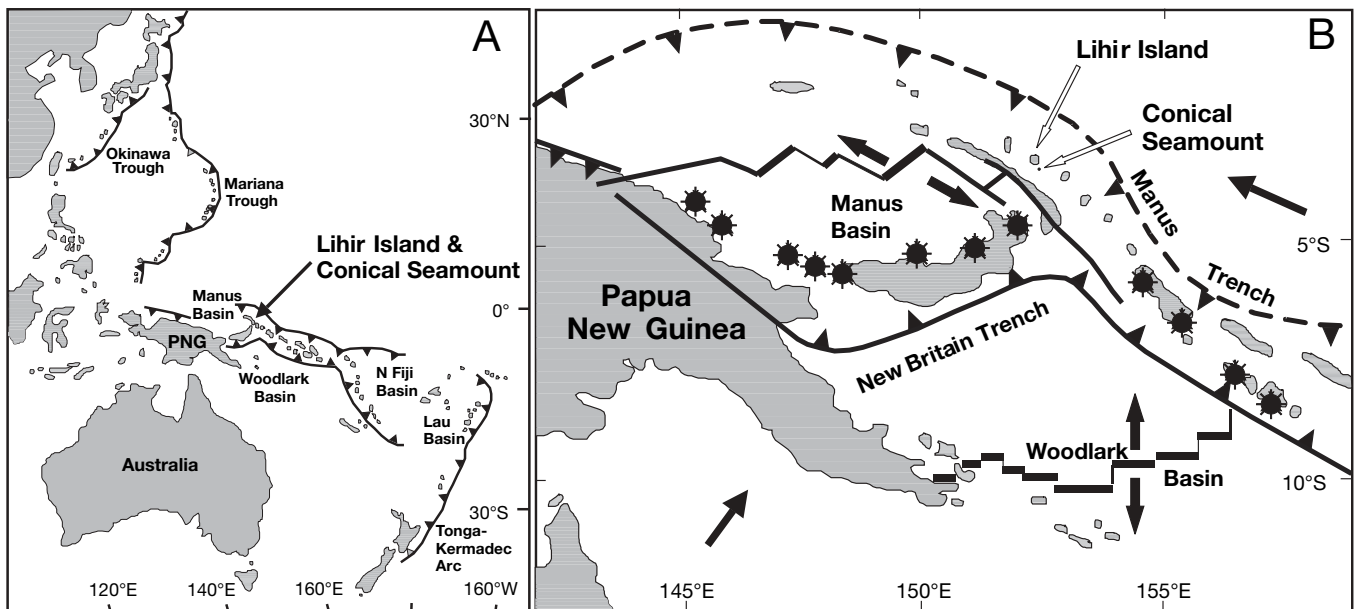


FIG. 1. A. Location of Lihir Island and Conical seamount in the southwest Pacific Ocean. Subduction trenches and important submarine hydrothermal sites of the western and southwestern Pacific Ocean are shown. B. Location of Lihir Island and Conical seamount in relationship to the tectonic features of eastern Papua New Guinea. Black star symbols are active volcanoes. Modified from Shipboard Scientific Party (2002).

TABLE 1. Characteristics of Mineralization at Conical Seamount and the Ladolam Deposit

	Stage	Style	Mineralogy	Alteration	Relationship to gold mineralization
Conical seamount ¹					
	1	Stockwork veins, veinlets, and disseminations	Pyrite ± marcasite	Illite/smectite, amorphous silica, ± chlorite, kaolinite, alunite, and rare aluminum phosphate sulfate minerals	Preminalization
	2	Veins and disseminations	Sphalerite, chalcopyrite, galena, pyrite, Cu-Pb-As-Sb sulfosalts, native gold, electrum	Amorphous silica-chalcedony, illite, smectite, adularia, secondary Na-K plagioclase, chlorite, kaolinite, barite, and rare apatite	Synmineralization
	3	Filling fractures, vesicles, and overgrowths	Realgar, alacranite, orpiment, stibnite, pyrite, amorphous silica	No obvious alteration	Postmineralization
Ladolam deposit ²					
	I	Porphyry veinlets and disseminations	Chalcopyrite, molybdenite, pyrite	Biotite, orthoclase, albite, anhydrite, rutile, muscovite, magnetite, pyrite, ± tremolite, apatite, tourmaline, chlorite, calcite	Preminalization, related to porphyry-style mineralization
	II	Transitional epithermal veins and breccia matrix	Shallow: pyrite, ± marcasite, arsenopyrite Deep: pyrite ± sphalerite, galena, pyrrhotite, chalcopyrite, molybdenite	Shallow: adularia Deep: adularia, anhydrite, pyrite, vermiculite ± barite, calcite	Synmineralization
	III	Late epithermal veins	Pyrite, marcasite	Argillic/advanced argillic-kaolinite ± alunite, smectite Silicic quartz, mixed layer clay ± adularia, anhydrite, calcite	Postmineralization, postdates refractory ores, possible redistribution of gold

¹ Petersen et al. (2002)² Carman (1994, 2003)

and epithermal (Table 1). The Ladolam hydrothermal system is still active, with thermal areas within Luise caldera (Fig. 4B) consisting of mud pools, boiling springs of chloride and

acid sulfate fluids, and low-temperature fumaroles (Wallace et al., 1983; Moyle et al., 1990). At the shoreline, and extending up to 100 m offshore, active hydrothermal venting (Fig. 4B) has formed crusts of colloform-banded pyrite in volcaniclastic sand (Pichler et al., 1999).

Sulfur Isotope Geochemistry

Methods

Although a minor amount of the sulfide from Conical seamount is coarse enough for separation by conventional methods, the very fine grained nature of the majority of the sulfides requires use of the laser-ablation technique to obtain $\delta^{34}\text{S}$ data. The laser-ablation technique also allows for detailed analysis of in situ mineral intergrowths and traverses across multigenerational veins. These types of detailed sulfur isotope analyses have not been reported previously for samples from Conical seamount. New $\delta^{34}\text{S}$ data for the Ladolam deposit, Luise caldera thermal areas, and Luise harbor offshore hydrothermal vents were obtained using conventional methods. Details of the analytical procedures are listed in Table 2.

Conical seamount

One hundred and two (43 conventional and 59 laser-ablation) sulfur isotope analyses of pyrite, sphalerite, and galena from stages 1 and 2 indicate $\delta^{34}\text{S}$ values ranging from -17.5 to

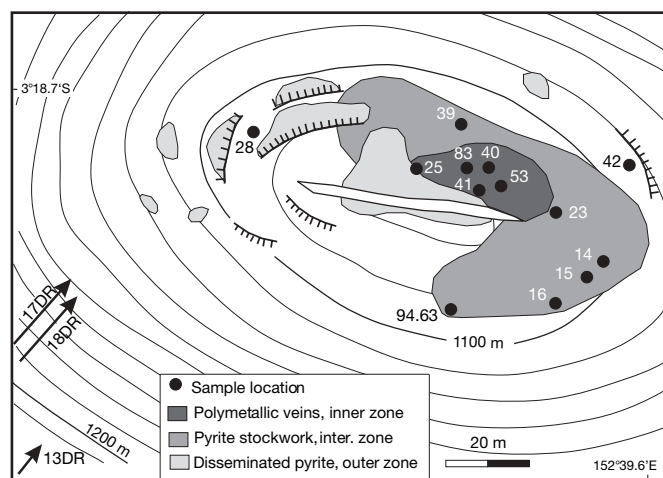


FIG. 2. Bathymetric map of the summit plateau region of Conical seamount, illustrating the different zones of mineralization and alteration. Hachured lines are scarps and open gash is an eruptive fissure (ridge) across top of the seamount. Sulfur isotope sample locations, from TV grab sampling, shown as black circles. Lines with arrows indicate dredge sample tracks and dredge direction. Modified from Petersen et al. (2002).

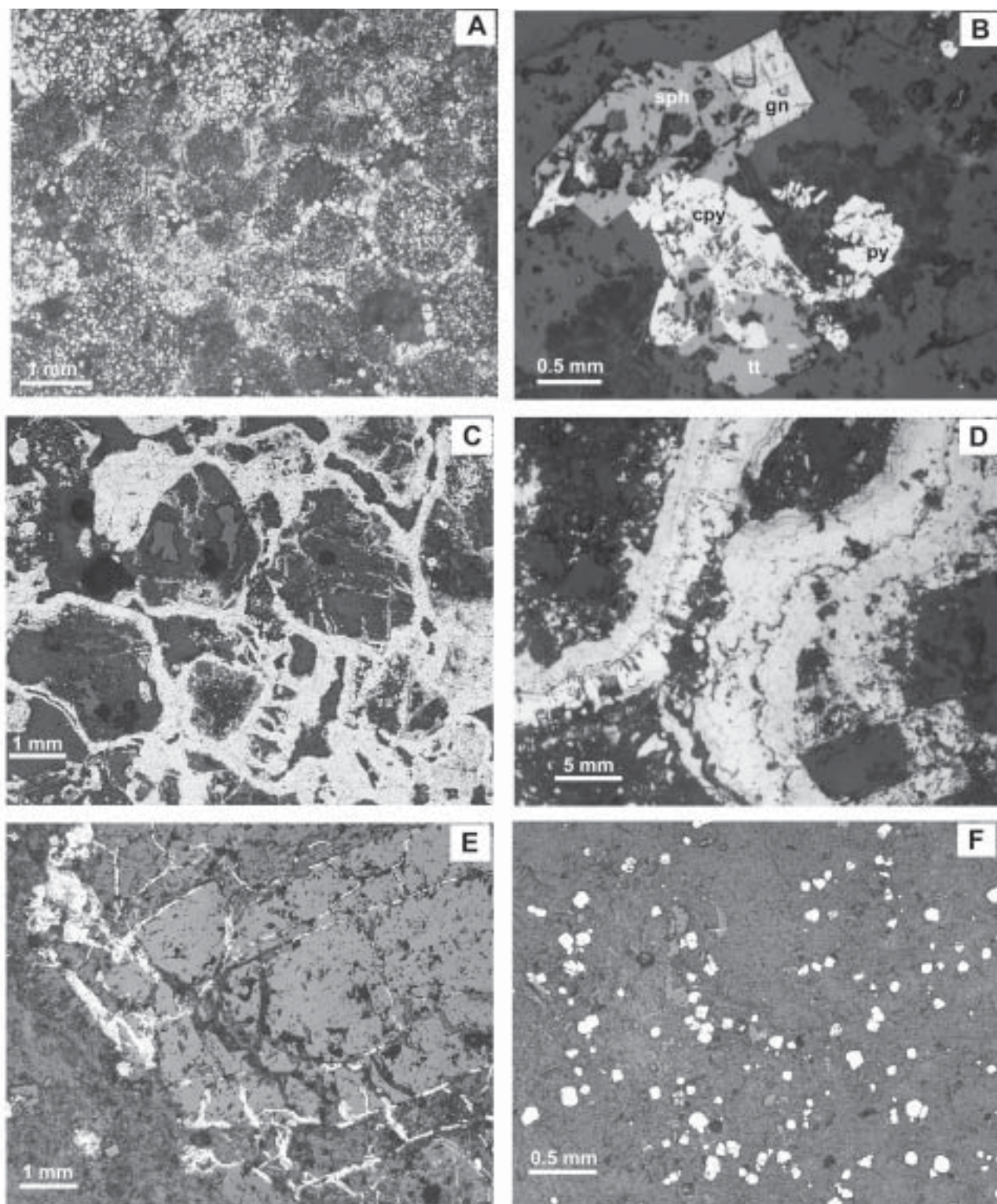


FIG. 3. Examples of Conical seamount mineralization stages analyzed in this study. A. Stage 1 pyrite-marcasite replacing magnetite, veinlets through altered clinopyroxene and magnetite, and scattered grains in basalt breccia (sample 25GTVA-4; inner zone). B. Stage 2 galena (gn), sphalerite (sph), chalcopyrite (cp), tetrahedrite-tennantite (tt) and pyrite (py) in silicified basalt (sample 25GTVA-5C; inner zone). C. Stage 1 pyrite-marcasite grains disseminated in basalt groundmass, lining vesicles, rimming and replacing pyroxene phenocrysts, and as colloform and crustiform veins in basalt breccia (sample 39GTVA-1D; intermediate zone). D. Stage 1 banded pyrite veins in silica-pyrite-altered basalt breccia (sample 39GTVA-2C; intermediate zone). E. Stage 1 pyrite filling fractures, rimming magnetite phenocrysts and occurring as disseminated grains in the groundmass of weakly altered basalt (sample 14GTVA-4A; outer zone). F. Stage 1 disseminated pyrite in weakly clay-altered basalt (sample 14GTVA-3; outer zone).

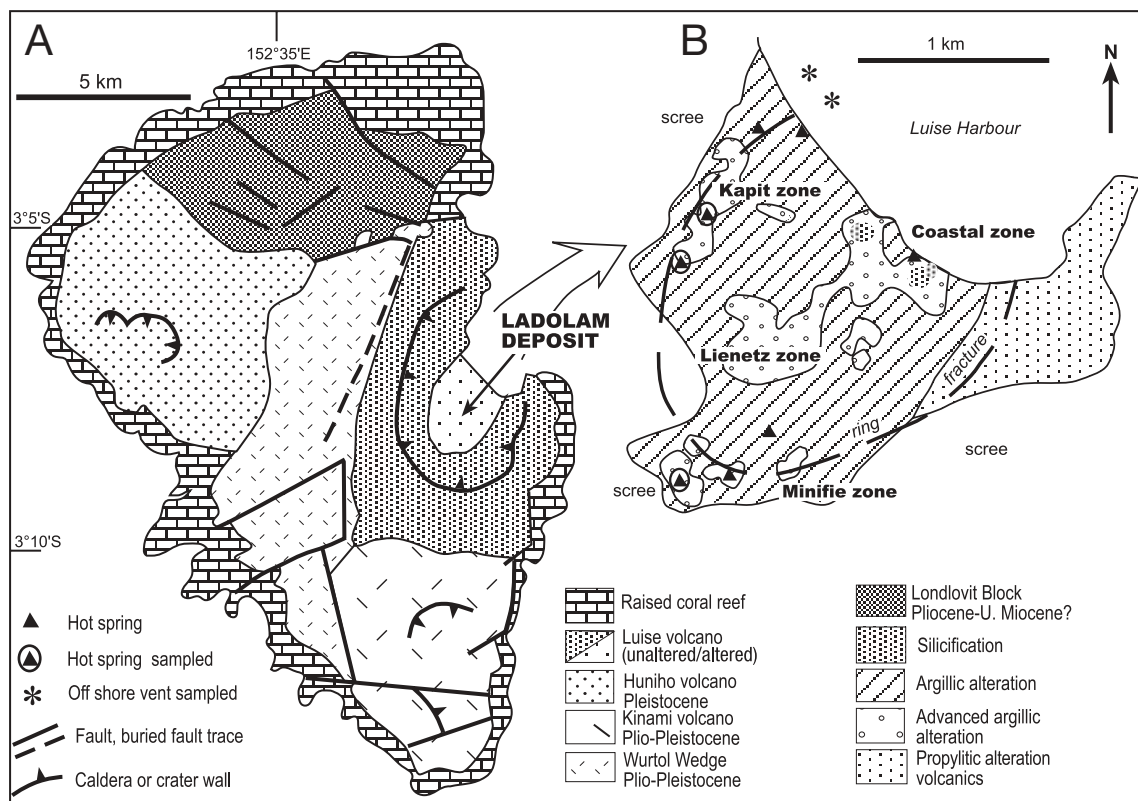


FIG. 4. A. Geology of Lihir Island. B. Location of alteration and mineralized zones of the Ladolam deposit and locations of fumaroles within the crater and offshore hydrothermal vents in the harbor. Modified from Moyle et al. (1990), Richards (1995) after Wallace et al. (1983), and Corbett and Leach (1998).

+6.1 per mil, with a mean of -1.9 per mil (Tables 2–3, Fig. 5A). Stage 1 pyrite varies from -17.5 to $+6.1$ per mil, with a mean of -1.6 per mil. The $\delta^{34}\text{S}$ values of stage 2 base metal sulfide vary over a smaller range of -9.5 to $+3.9$ per mil, with a mean of -2.1 per mil. Petersen et al. (2002) reported 28 sulfide and three sulfate $\delta^{34}\text{S}$ values from Conical seamount, indicating similar ranges (Table 3).

A comparison of sulfur isotope values between paragenetic stages through the inner, intermediate, and outer mineralized zones is given in Table 3 and Figure 5B. Sulfur isotope values for all sulfides from stages 1 and 2 in the inner zone vary from -13.9 to $+6.0$ per mil, with a mean of -1.2 per mil (Fig. 5C). Stage 2 sphalerite (-3.0 to $+1.1\text{‰}$; mean = -1.1‰) and galena (-9.5 to $+3.9\text{‰}$; mean = -4.4‰) lie within the range of stage 1 pyrite (-13.9 to $+6.0\text{‰}$; mean = -2.3‰). The inner zone appears to have two populations of $\delta^{34}\text{S}$ values (Fig. 5C); the majority of values range from -4 to $+6$ per mil, with a second population between -7 to -14 per mil. The group of lower $\delta^{34}\text{S}$ values data consists of pyrite and galena in altered basalt breccias, and the group of higher $\delta^{34}\text{S}$ values consists of pyrite, sphalerite, and galena in both altered basalt breccias and pyrite veins. Sulfur isotope values for stage 1 pyrite in the intermediate zone vary from -7.3 to $+3.3$ per mil, with a mean of -0.1 per mil (Fig. 5C). Sulfur isotope values for all stage 1 pyrite in the outer zone vary from -17.5 to $+6.1$ per mil, with a mean of -4.7 per mil (Fig. 5C).

Although the Conical seamount sulfides have a wide range of $\delta^{34}\text{S}$ values, these values vary systematically both in time and space. There is a paragenetic trend from the lowest $\delta^{34}\text{S}$ values in stage 1 pyrite, followed by stage 2 sphalerite and galena, with the late-stage arsenic minerals having the highest $\delta^{34}\text{S}$ values, as noted by Petersen et al. (2002). In conjunction with this shift to higher $\delta^{34}\text{S}$ values with successive paragenetic stages, there is a variation from higher $\delta^{34}\text{S}$ values in the inner and intermediate zones to progressively lower $\delta^{34}\text{S}$ values in the outer zone (Fig. 5C). The fractionation between sulfide pairs (Table 2) leads to unrealistic temperatures for sulfur isotope geothermometers and indicates that the sulfides did not precipitate in isotopic equilibrium.

Ladolam deposit, Lihir Island

New sulfide and sulfate $\delta^{34}\text{S}$ data for epithermal mineralization, anhydrite veins, sulfur deposited from fumaroles, and pyrite associated with offshore hydrothermal vents are given in Table 4. These data are compared to published $\delta^{34}\text{S}$ data by Müller et al. (2002a) and Carman (2003) in Figure 6A and Table 5.

Figure 6B compares sulfide and sulfate $\delta^{34}\text{S}$ values for the Ladolam deposit with the new data. The $\delta^{34}\text{S}$ analyses of epithermal mineralization determined in this study lie within the range of $\delta^{34}\text{S}$ values for epithermal mineralization as reported by Müller et al. (2002a) and Carman (2003). The

TABLE 2. Conical Seamount Sulfur Isotope Data

Sample no.	Description	Paragenetic stage	Mineral	$\delta^{34}\text{S}$ (‰)	Method ¹
Inner zone					
25 GTVA 4	Mineralized amorphous silica-altered basalt breccia-sulfide separate	2	Galena	-9.5	Conv.
25 GTVA 4	Mineralized amorphous silica-altered basalt breccia-sulfide separate	2	Sphalerite	-0.8	Conv.
25 GTVA-4	Euhedral pyrite in matrix of amorphous silica-altered basalt breccia	1	Pyrite	1.2	Laser
25 GTVA-4	Subhedral pyrite in matrix of amorphous silica-altered basalt breccia	1	Pyrite	1.2	Laser
25 GTVA-4	Euhedral pyrite in matrix of amorphous silica-altered basalt breccia	1	Pyrite	2.6	Laser
25 GTVA 5C	Mineralized amorphous silica-altered basalt breccia-sulfide separate	2	Sphalerite	-3.0	Conv.
25 GTVA-5C	Pyrite in Fe oxide-realgar-amorphous silica basalt breccia matrix	1	Pyrite	1.2	Laser
25 GTVA-5C	Pyrite in Fe oxide-realgar-amorphous silica basalt breccia matrix	1	Pyrite	2.0	Laser
25 GTVA-5C	Anhedral pyrite in matrix of amorphous silica-altered basalt breccia	1	Pyrite	1.8	Laser
25 GTVA-6A(i)	Sulfide vein in amorphous silica-altered basalt breccia	2	Sphalerite	-1.2	Conv.
25 GTVA-6A(ii)	Sulfide vein in amorphous silica-altered basalt breccia	2	Pyrite	-2.4	Conv.
25 GTVA-6B	Mineralized amorphous silica-altered basalt breccia	2	Pyrite	0.9	Conv.
25 GTVA 6B1	Mineralized amorphous silica-altered basalt breccia	2	Sphalerite	1.1	Conv.
25 GTVA-8	Pyrite replacing clast in amorphous silica-altered basalt breccia	1	Pyrite	2.1	Laser
25 GTVA-8A	Anhedral pyrite in matrix of amorphous silica-altered basalt breccia	1	Pyrite	1.9	Laser
25 GTVA-8A	Anhedral pyrite in matrix of amorphous silica-altered basalt breccia	1	Pyrite	1.8	Laser
25 GTVA 8C	Semimassive sulfide in amorphous silica altered basalt breccia	2	Galena	-0.8	Conv.
25 GTVA 8C2	Semimassive sulfide in amorphous silica altered basalt breccia	2	Sphalerite	0.8	Conv.
40-GTVA-1	Altered basalt-sulfide concentrate	1	Pyrite	-2.6	Conv.
40 GTVA-1B	Disseminated pyrite in altered basalt	1	Pyrite	-7.5	Conv.
40 GTVA-2	Clay-pyrite altered basalt-sulfide separate	1	Pyrite	-0.4	Conv.
40 GTVA-2	Clay-pyrite altered basalt-sulfide separate	1	Pyrite	-0.4	Conv.
40 GTVA-2	Euhedral pyrite in matrix of clay-amorphous silica altered basalt	1	Pyrite	4.0	Laser
40 GTVA-2	Euhedral pyrite in matrix of clay-amorphous silica altered basalt	1	Pyrite	3.1	Laser
40 GTVA-2.2	Pyrite vein in clay-amorphous silica altered basalt	1	Pyrite	6.0	Laser
40 GTVA-2.2	Pyrite vein in clay-amorphous silica altered basalt	1	Pyrite	4.6	Laser
41 GTVA-1A	Euhedral pyrite in altered feldspar	1	Pyrite	2.6	Laser
41 GTVA-1A	Subehedral pyrite in clay-amorphous silica-altered basalt	1	Pyrite	4.8	Laser
53 GTVA 1B	Sulfide-amorphous silica alteration of basalt-sulfide separate	1	Pyrite	-13.7	Conv.
53 GTVA-1A	Sulfide-amorphous silica alteration of basalt-sulfide separate	1	Pyrite	-11.5	Conv.
53 GTVA-1A	Subhedral pyrite in sulfide-amorphous silica alteration of basalt	1	Pyrite	-13.4	Laser
53 GTVA-1A	Spongy pyrite in sulfide-amorphous silica alteration of basalt	1	Pyrite	-9.4	Laser
53 GTVA-1A	Finely banded pyrite rim of cavity in basalt	1	Pyrite	-11.6	Laser
53-GTVA-1A	Sulfide-amorphous silica alteration of basalt-sulfide separate	1	Pyrite	-13.9	Conv.
53-GTVA-1A2	Sulfide-amorphous silica alteration of basalt-sulfide separate	1	Pyrite	-13.0	Conv.
53 GTVA 2A	Amorphous silica-chlorite alteration of basalt-sulfide separate	2	Galena	-2.5	Conv.
53 GTVA 2A	Amorphous silica-chlorite alteration of basalt-sulfide separate	2	Sphalerite	-3.0	Conv.
53 GTVA-2A	Pyrite in amorphous silica-chlorite alteration of basalt breccia	1	Pyrite	1.5	Laser
53 GTVA-2A	Spongy pyrite in amorphous silica-chlorite alteration of basalt breccia	1	Pyrite	3.6	Laser
53 GTVA-2A	Spongy pyrite in amorphous silica-chlorite alteration of basalt breccia	1	Pyrite	4.3	Laser
53 GTVA-2A	Galena in amorphous silica-chlorite alteration of basalt breccia	2	Galena	3.9	Laser
53 GTVA 2B	Amorphous silica-chlorite alteration of basalt-sulfide separate	1	Pyrite	-9.6	Conv.
53 GTVA 3A	Sulfide-sulfosalt veins in amorphous silica matrix-sulfide separate	2	Galena	-2.5	Conv.
53 GTVA 3A	Sulfide-sulfosalt veins in amorphous silica matrix-sulfide separate	2	Sphalerite	-1.7	Conv.
83 GTVA 2A1	Disseminated pyrite in amorphous silica-altered basalt-sulfide separate	1	Pyrite	-1.7	Conv.
83 GTVA-2B2	Subehedral pyrite in amorphous silica-altered basalt	1	Pyrite	5.7	Laser
83 GTVA-2C1	Pyrite veinlets in amorphous silica-altered basalt-sulfide separate	1	Pyrite	2.9	Laser
83 GTVA-2C1	Subhedral disseminated pyrite in amorphous silica-altered basalt	1	Pyrite	0.0	Laser
83 GTVA-2C1	Eu- and/or subhedral pyrite lining vesicle in amorphous silica-altered basalt	1	Pyrite	0.6	Laser
83 GTVA 2C1	Pyrite veinlet in amorphous silica-altered basalt-sulfide separate	1	Pyrite	-2.7	Conv.
Intermediate zone					
23 GTVA 1	Pyrite in amorphous silica-altered basalt breccia-sulfide separate	1	Pyrite	-7.3	Conv.
23 GTVA-1	Pyritic mud	1	Pyrite	-5.6	Conv.
23 GTVA-5	Rim of pyrite band, amorphous silica-altered basalt breccia	1	Pyrite	-0.5	Laser
23 GTVA-5	Center of pyrite band, amorphous silica-altered basalt breccia	1	Pyrite	-1.6	Laser
23 GTVA-5	Disseminated pyrite in amorphous silica-altered basalt breccia	1	Pyrite	-3.9	Laser
23 GTVA-5	Spongy pyrite in matrix of amorphous silica-altered basalt breccia	1	Pyrite	-4.4	Laser
23 GTVA-5	Anhedral pyrite in matrix of amorphous silica-altered basalt breccia	1	Pyrite	-4.4	Laser
39 GTVA 1X	Massive colloform sulfide-sulfide separate	1	Pyrite	-3.9	Conv.
39 GTVA-1A	Pyrite-sulfide rock with native S on surface	1	Pyrite	-0.1	Conv.
39 GTVA-1C	Pyrite-sulfide rock with native S on surface	1	Pyrite	0.9	Conv.
39 GTVA-1D	Colloform banded pyrite	1	Pyrite	2.6	Laser
39 GTVA-1D	Anhedral pyrite in semimassive pyrite	1	Pyrite	1.6	Laser
39 GTVA-1D	Massive aggregate pyrite in semimassive pyrite	1	Pyrite	2.4	Laser
39 GTVA-1D	Spongy, anhedral pyrite in semimassive pyrite	1	Pyrite	1.3	Laser

TABLE 2. (Cont.)

Sample no.	Description	Paragenetic stage	Mineral	$\delta^{34}\text{S}$ (‰)	Method ¹
39 GTVA-1E	Pyrite rim around amorphous silica-altered basalt breccia clast	1	Pyrite	2.3	Laser
39 GTVA-1E	Pyrite matrix of altered basalt breccia	1	Pyrite	1.8	Laser
39 GTVA-1E	Radial zoned pyrite replacement of basalt clast	1	Pyrite	0.9	Laser
39 GTVA-1E	Euhedral pyrite lining cavity in altered basalt breccia	1	Pyrite	1.2	Laser
39 GTVA-2A	Spongy pyrite in center of crustiform pyrite vein	1	Pyrite	1.1	Laser
39 GTVA-2A	Massive pyrite in middle of pyrite vein	1	Pyrite	3.3	Laser
39 GTVA-2A	Spongy pyrite from margin of pyrite vein	1	Pyrite	1.7	Laser
39 GTVA-2A	Pyrite veins in weakly altered basalt-sulfide separate	1	Pyrite	-2.1	Conv.
39 GTVA-2C	Pyrite at wall rock-vein margin	1	Pyrite	1.9	Laser
39 GTVA-2C	Band of spongy pyrite toward middle of vein	1	Pyrite	0.8	Laser
39 GTVA-2C	Radial and/or spherical spongy pyrite from middle of vein	1	Pyrite	-1.5	Laser
39 GTVA-2C	Band of pyrite in middle of vein	1	Pyrite	0.7	Laser
39 GTVA-2C	Band of radial pyrite near outer vein margin	1	Pyrite	0.3	Laser
39 GTVA-2C	Subhedral pyrite grains at outer vein rim	1	Pyrite	-1.1	Laser
39 GTVA-2C	Subhedral pyrite in weakly altered basalt	1	Pyrite	1.9	Laser
39 GTVA-2C	Pyrite vein in weakly altered basalt-sulfide separate	1	Pyrite	0.4	Conv.
39 GTVA-2D	Pyrite vein in weakly altered basalt-sulfide separate	1	Pyrite	-1.1	Conv.
39 GTVA-2E	Pyrite vein in weakly altered basalt-sulfide separate	1	Pyrite	-0.4	Conv.
39 GTVA-2H	Pyrite vein in weakly altered basalt-sulfide separate	1	Pyrite	-0.3	Conv.
39 GTVA-3C	Pyrite alteration on outer surface of basalt-sulfide separate	1	Pyrite	0.5	Conv.
39-GTVA-2C	Pyrite veins in weakly altered basalt-sulfide separate	1	Pyrite	-0.2	Conv.
			Pyrite		
			Pyrite		
Outer zone					
13 DR-8C	Anhedral pyrite in weakly clay-altered basalt	1	Pyrite	4.6	Laser
14 GTVA 2X1	Pyrite in vesicles in basalt-sulfide separate	1	Pyrite	-3.8	Conv.
14 GTVA 2Y1	Pyrite in vesicles in basalt-sulfide separate	1	Pyrite	-5.0	Conv.
14 GTVA-3	Anhedral pyrite in weakly clay-altered basalt	1	Pyrite	-6.2	Conv.
14 GTVA-3	Euhedral pyrite in weakly clay-altered basalt	1	Pyrite	-1.5	Laser
14 GTVA-3	Massive pyrite at centre of pyrite vein	1	Pyrite	-3.1	Laser
14 GTVA-3	Spongy pyrite at margin of pyrite vein	1	Pyrite	-6.9	Laser
14 GTVA-3	Spongy pyrite at margin of pyrite vein	1	Pyrite	-2.4	Laser
14 GTVA-3	Massive well-formed pyrite in middle of vein	1	Pyrite	-4.6	Laser
14 GTVA-3	Spongy pyrite grain at rim of pyrite vein	1	Pyrite	-8.8	Laser
14 GTVA-4A	Pyrite rim to weakly altered clast in basalt breccia	1	Pyrite	-15.6	Laser
15 GTVA 2D	Pyrite in weak clay-amorphous silica altered basalt-sulfide separate	1	Pyrite	-17.5	Conv.
28-GTVA-2	Pyrite in weak amorphous silica altered basalt-sulfide separate	1	Pyrite	-11.6	Conv.
42 GTVA-2-2	Subhedral pyrite in oxidized margin of unaltered basalt	1	Pyrite	5.3	Laser
42 GTVA-2-2	Spongy pyrite within oxidized basalt	1	Pyrite	6.1	Laser
Conical 1	Pyrite concentrate, location unknown	1	Pyrite	-5.2	Conv.
Conical 2	Pyrite concentrate, location unknown	1	Pyrite	-5.2	Conv.

Abbreviations: Conv. = conventional sulfur isotope analysis, Dr = dredge sample, GTVA = TV grab sample

Paragenetic stage: 1 = early disseminated, vein, and semimassive pyrite, 2 = pyrite and polymetallic sulfides, and sulfosalts with gold mineralization

¹For conventional sulfur isotope analyses, sulfides were handpicked or drilled out with the aid of a small-diameter dental drill; petrographic examination aided selection of sample sites that were monomineralic; the drill was cleaned between each sample extraction to ensure no cross-sample contamination; conventional sulfide separates were combusted with excess Cu_2O to produce SO_2 , according to the methodology of Robinson and Kusakabe (1975); micro-analytical determinations of sulfur isotopes used the Nd:YAG laser-ablation instrument at the Central Science Laboratory, University of Tasmania; operational procedures are reported in Huston et al. (1995); sulfur isotope ratios for both the conventional and laser-ablation methods were measured using a VG Isogas Sira II mass spectrometer located at the University of Tasmania; results are reported in standard notation relative to the Canon Diablo Troilite standard (CDT); sulfide standards (Rosebery 12.4‰ and Broken Hill 3.4‰) and a reference SO_2 gas were analyzed each day with the conventional or laser analyses to verify analytical procedures and quality of results; sample reproducibility is typically ± 0.5 per mil; precision (1σ) of laser-ablation sulfur isotope analyses is 0.3 to 0.5 per mil compared to a precision of 0.1 to 0.3 per mil for conventional analyses at the University of Tasmania stable isotope facility (Huston et al., 1995)

fumarolic native sulfur and pyrite in offshore vents have the same $\delta^{34}\text{S}$ values as the Ladolam mineralization. New analyses of anhydrite show a greater range of $\delta^{34}\text{S}$ values (8.4–21.4‰) than previously reported (8.6–13‰, Table 5), indicating that anhydrite has two distinct populations of $\delta^{34}\text{S}$ values, one between 8 and 14 per mil and one between 20 and 22 per mil, although the possibility that there is a continuous range of $\delta^{34}\text{S}$ values cannot be ruled out, given the small number of samples analyzed.

Comparison between Conical seamount and the Ladolam deposit

Conical seamount and the Ladolam deposit have a similar range of sulfide $\delta^{34}\text{S}$ values (Fig. 7). Sulfides in the porphyry and transitional mineralization at Ladolam have $\delta^{34}\text{S}$ values consistent with those of stage 1 and 2 mineralization in the inner and intermediate zones at Conical seamount (Fig. 7). The epithermal mineralization at Ladolam has lower $\delta^{34}\text{S}$

TABLE 3. Summary of Conical Seamount Sulfur Isotope Data

		Mineral and analytical method	<i>n</i>	Mean (‰)	Minimum (‰)	Maximum (‰)
This study	Overall	All sulfides	102	-1.9	-17.5	6.1
		Conventional	43	-5.2	-17.5	1.1
		Laser	59	0.2	-15.6	6.1
	Stage 1	Pyrite	88	-1.6	-17.5	6.1
		Pyrite - conventional	30	-5.0	-17.5	0.9
		Pyrite - laser	58	0.1	-15.6	6.1
	Stage 2	Pyrite - conventional	2	0.8	-2.4	0.9
		Galena	4	-2.2	-9.5	3.9
		Galena - conventional	3	-4.3	-9.5	-0.8
		Galena - laser	1	3.9		
		Sphalerite - conventional	7	-1.1	-3.0	1.1
Petersen et al. (2002) ¹	Stage 1	Pyrite	15	-3.6	-8.6	-0.2
		Alunite	2	6.9	6.4	7.5
	Stage 2	Sphalerite-galena	7	0.6	-0.8	1.5
	Stage 3	Arsenic minerals	2	1.9	1.7	2.0
	Framboidal	Pyrite	3	-12.8	-13.9	-11.6

Abbreviations: *n* = number of analyses, arsenic minerals = realgar and alacranite

¹ All Petersen et al. (2002) samples analyzed by conventional method

TABLE 4. Ladolam Deposit, Luise Caldera, and Luise Harbor Sulfur Isotope Data

Sample	Location	Description	Mineral	$\delta^{34}\text{S}$ (‰)	Source ¹
Lihir 1	Lienetz	Stage III epithermal ore	Pyrite	-8.1	1
Lihir 1	Lienetz	Stage III epithermal ore	Pyrite	-10.0	1
Lihir 2	Lienetz	Stage III epithermal ore	Pyrite	-9.2	1
Lihir 4	Minifie	Stage III epithermal ore	Pyrite	-10.4	1
Lihir 4	Minifie	Stage III epithermal ore	Pyrite	-5.2	1
Lihir 5	Minifie	Stage III epithermal ore	Pyrite	-4.2	1
Lihir 6	Minifie	Stage III epithermal ore	Pyrite	-1.6	1
Lihir 6	Minifie	Stage III epithermal ore	Pyrite	-1.6	1
DDHL42-419	Lienetz	Anhydrite zone	Anhydrite	20.7	2
DDHL42-428	Lienetz	Anhydrite zone	Anhydrite	10.4	2
DDHL42-458	Lienetz	Anhydrite zone	Anhydrite	8.4	2
DDHL42-464	Lienetz	Anhydrite zone	Anhydrite-carbonate	12.5	2
DDHL44-321	Lienetz	Anhydrite zone	Anhydrite-carbonate	11.4	2
DDHL51-305	Lienetz	Anhydrite zone	Anhydrite	10.6	2
DDHL58-394	Lienetz	Anhydrite zone	Anhydrite	9.5	2
DDHL97-225	Minifie	Anhydrite zone	Anhydrite	10.5	2
DDHL122-210	Minifie	Anhydrite zone	Anhydrite	21.4	2
DDHL129-208	Minifie	Anhydrite zone	Anhydrite-carbonate	11.9	2
Minifie	Minifie	Fumarole	Native sulfur	-7.3	2
UK-1	Upper Kapit	Fumarole	Native sulfur	-7.2	2
UK-3(ii)	Upper Kapit	Fumarole	Native sulfur + clay	-5.0	2
LH-1	Luise harbor	Offshore vents	Pyrite-marcasite	-7.6	2
LH-3A	Luise harbor	Offshore vents	Pyrite-marcasite	-6.7	2
LH-3B	Luise harbor	Offshore vents	Pyrite-marcasite	-7.5	2
LH-7	Luise harbor	Offshore vents	Pyrite-marcasite	-7.9	2

All analyses by conventional sulfur isotope method

¹ Source: 1 = this study, 2 = M. Hannington, unpublished data

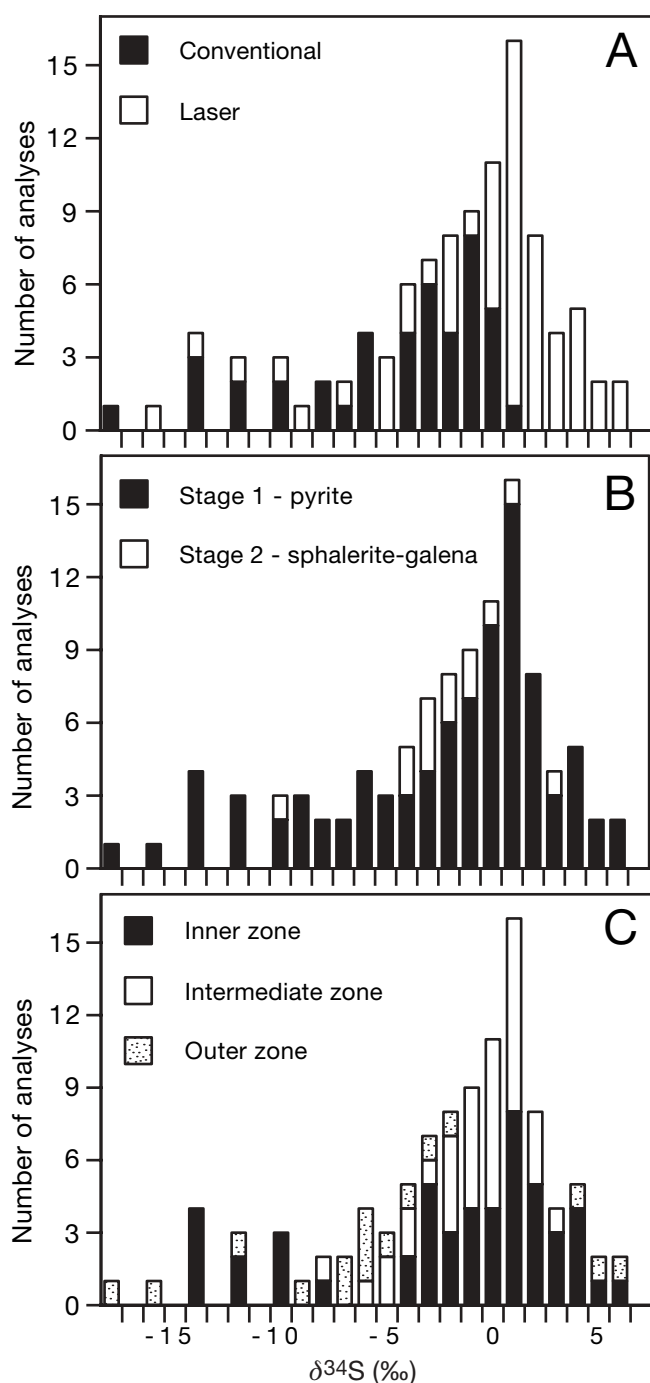


FIG. 5. Histograms of sulfide $\delta^{34}\text{S}$ analyses generated in this study for Conical seamount. A. Comparison of conventional vs. laser-ablation sulfide $\delta^{34}\text{S}$ values. B. Distribution of $\delta^{34}\text{S}$ values based on paragenetic stages. C. Distribution of $\delta^{34}\text{S}$ values based on mineralized zones. Data from Table 2.

values than the porphyry and transitional mineralization but similar values to the stage 1 mineralization in the outer zone at Conical seamount.

Comparison with other sea-floor hydrothermal systems

Sulfur isotope data for sulfide minerals and native sulfur from modern sea-floor hydrothermal sites have a wide range of values (Fig. 8). The $\delta^{34}\text{S}$ values for sulfides for unsedimented

midocean ridges range from approximately -1 to $+11$ per mil, whereas the range for sedimented midocean ridges is -4 to $+17$ per mil. For midocean ridge hydrothermal systems, Shanks et al. (1995) concluded that the $\delta^{34}\text{S}$ values of vent fluid H_2S indicate that midocean ridge basalt (MORB) sulfur is the principal sulfur source, with a small contribution from inorganically reduced seawater sulfate. For hydrothermal systems in the sedimented-ridge environment the sources of sulfur include MORB, inorganic reduction of seawater sulfate, and a minor component of organically reduced seawater sulfate (Goodfellow and Franklin, 1993; Shanks et al., 1995; Goodfellow et al., 1999).

Sulfides from sea-floor hydrothermal systems forming in arc environments of the western Pacific (Fig. 1A) have $\delta^{34}\text{S}$ values that range from -8 to $+16$ per mil (Fig. 8). A comparison of the data in Figure 8 shows that the sulfur in sulfide minerals at Conical seamount is the lightest yet recorded for hydrothermal systems on the sea floor.

De Ronde (1995) concluded that active sea-floor systems located within back- or island arc environments may provide a link between the processes common to midocean ridge hydrothermal systems and those in subaerial settings, in terms of magmatic contributions to the hydrothermal fluid. Herzig et al. (1998c) suggested that the light sulfur in sulfides ($\delta^{34}\text{S} = -7.3$ to -2.8‰ , $n = 12$) and native sulfur ($\delta^{34}\text{S} = -4.8$ to -2.4‰ , $n = 3$) from the Hine Hina site in the Lau basin implied an ^{34}S -depleted source of probable magmatic origin. Samples from the DESMOS caldera, in the eastern Manus basin, have $\delta^{34}\text{S}$ values of -7 to -6 per mil ($n = 6$) for native sulfur forming in association with an advance argillic alteration. These $\delta^{34}\text{S}$ values are interpreted to be of magmatic derivation (Gamo et al., 1997; Gemmeil et al., 1999). Samples from the PACMANUS site, also in the eastern Manus basin, have $\delta^{34}\text{S}$ values of -3 to $+8$ per mil ($n = 85$) for sulfides and 2 per mil for native sulfur that are interpreted to indicate a magmatic component in the hydrothermal fluid (Gemmeil et al. 1996; J. B. Gemmeil, unpub. data). Samples from another hydrothermal site in the eastern Manus basin, SuSu Knoll, have $\delta^{34}\text{S}$ values of sulfides -3 to 0 per mil ($n = 13$) for sulfides and -7 to $+2$ per mil ($n = 13$) for native sulfur that are interpreted to be magmatic (J. B. Gemmeil, unpub. data). Samples from the Brothers volcano in the southern Kermadec arc have $\delta^{34}\text{S}$ values of -4 to $+3$ per mil for sulfides and -8 to -6 per mil for native sulfur, which de Ronde et al. (2000) suggested may indicate a magmatic sulfur component.

Comparison to epithermal deposits

Sulfides from low-sulfidation epithermal deposits (Fig. 9) have $\delta^{34}\text{S}$ values between -6 and $+5$ per mil, with the majority close to 0 per mil (Ohmoto and Rye, 1979, Field and Fifarek, 1985). Cooke and Simmons (2000) concluded that the waters that precipitate low-sulfidation epithermal mineralization have a magmatic volatile source for sulfur. Alkalic epithermal deposits have sulfide $\delta^{34}\text{S}$ values that vary from -7.9 to $+5.5$ per mil in the early magmatic-hydrothermal system, to -15 to $+8$ per mil (typically $<0\text{‰}$) in the epithermal system (Richards, 1995). Stable isotope compositions indicate a high proportion of magmatic fluids in most alkalic epithermal systems (Jensen and Barton, 2000). Sulfides from high-sulfidation epithermal deposits have $\delta^{34}\text{S}$ values that vary from -10 to $+8$ per mil

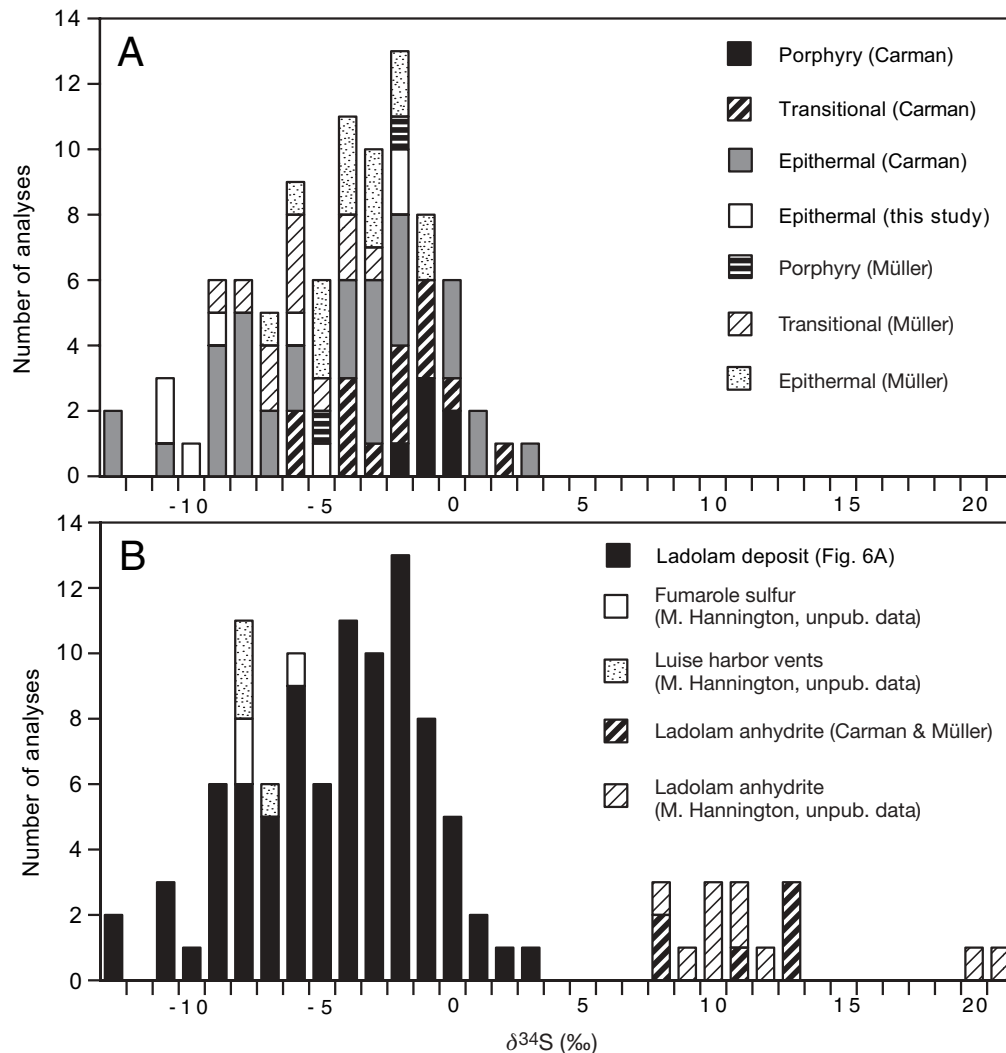


FIG. 6. Histograms of sulfide and sulfate $\delta^{34}\text{S}$ analyses for the Ladolam deposit. A. All sulfide $\delta^{34}\text{S}$ values for the different mineralization styles at the Ladolam deposit. B. $\delta^{34}\text{S}$ values for sulfides and anhydrite from the Ladolam deposit as well as native sulfur from thermal areas in Luise caldera and pyrite from offshore hydrothermal vents in Luise harbor. Data from Table 4, Müller et al. (2002a), and Carman (2003).

(Arribas, 1995), with the source of sulfur generally interpreted to be magmatic (Cooke and Simmons, 2000). Although sulfur isotope data for sulfides from Conical seamount and the Ladolam deposit overlap the data from all the different types of epithermal deposit, they are most similar to the epithermal portion of the alkalic-type epithermal deposits, inasmuch as they extend to unusually low $\delta^{34}\text{S}$ values.

Discussion

Comparison of analytical methods

A summary of the sulfur isotope data for Conical seamount (Table 3) illustrates that the conventional analyses tend to have a slightly narrower range (-17.5 to $+1.1\text{‰}$; mean = -5.2‰) compared to the laser-ablation analyses (-15.6 to $+6.1\text{‰}$; mean = 0.2‰). Although there appears to be a bias toward positive values obtained by the laser-ablation method compared to the conventional method (Table 3, Fig. 5A),

close examination of the data suggests that this is not a consistent relationship throughout the sample suite. For example, pyrite from clay-pyrite alteration of basalt (sample 39GTVA-2C, Table 2) was analyzed both by laser-ablation and conventional methods with very similar results. The laser-ablation $\delta^{34}\text{S}$ values were -1.5 to $+1.9$ per mil ($n = 7$, mean = 0.4‰), whereas a pyrite separate analyzed by the conventional method has a $\delta^{34}\text{S}$ value of 0.4 per mil. Pyrite from pervasive amorphous silica-pyrite alteration of basalt (sample 53GTVA-1A, Table 2) has laser-ablation $\delta^{34}\text{S}$ values of -9.4 , -11.6 , and -13.4 per mil (mean = -12.8‰), and similar values of -11.5 , -13.0 , and -13.9 per mil (mean = -11.5‰) were obtained by the conventional method. Stringent analytical procedures (daily calibration using international sulfur isotope standards) adhered to in this study indicate that differences between the laser and conventional $\delta^{34}\text{S}$ analyses are due to sulfur isotope heterogeneity in the sulfides at Conical seamount, not a bias in the analytical method.

TABLE 5. Summary of Ladolam Deposit, Luise Caldera, and Luise Harbor Sulfur Isotope Data

	Mineral	<i>n</i>	Mean (‰)	Minimum (‰)	Maximum (‰)
This study ¹	Ladolam deposit	Stage III epithermal-pyrite	-6.3	-10.4	-1.6
		Anhydrite	12.7	8.4	21.4
	Kapit fumaroles	Native sulfur	3	-6.5	-7.5
	Luise harbor vents	Pyrite-marcasite	4	-7.4	-7.9
Carman (2003) ²	Ladolam deposit	Stage I porphyry-pyrite	6	-0.4	0.2
		Stage II transitional-pyrite, pyrrhotite	14	-2.0	-5.3
		Stage III epithermal-pyrite, marcasite, pyrrhotite, chalcopyrite	58	-4.3	-12.9
		Anhydrite	3	13	13
Müller et al. (2002a) ³	Ladolam deposit	Stage I porphyry-pyrite	2	-3.2	-4.8
		Stage II transitional-pyrite	11	-5.3	-8.8
		Stage III epithermal-pyrite	15	-2.9	-6.0
		Anhydrite	3	9.4	8.6

Abbreviations: *n* = number of analyses

¹Ladolam deposit pyrite data from this study, analyzed by conventional method; Ladolam anhydrite, Kapit fumarole, and Luise harbour vent data from M. Hannington (unpub. data), analyzed by conventional method

²Carman (2003) samples analyzed by laser ablation and SHRIMP methods

³All Müller et al. (2002a) samples analyzed by conventional method

Conical seamount

Previous studies have suggested that sources of sulfur in sea-floor hydrothermal systems are direct magmatic emanations, inorganic reduction of seawater sulfate, leached magmatic sulfide, leached sulfate minerals followed by partial

reduction, and a minor component of organically reduced seawater sulfate (Sangster, 1968; Ohmoto and Rye, 1979; Shanks et al., 1981; Ohmoto, 1986; Taylor, 1987; Solomon et al., 1988; Goodfellow and Franklin, 1993; Shanks et al., 1995; Goodfellow et al., 1999). Petersen et al. (2002) proposed a model for the evolution of the Conical seamount hydrothermal system where the very low $\delta^{34}\text{S}$ values for early framboidal pyrite and marcasite possibly indicates the influence of bacteriogenic sulfate reduction. They concluded that the platy habit of the alunite, the presence of aluminum phosphate sulfate minerals, and $\delta^{34}\text{S}$ values of coexisting pyrite and alunite are consistent with a contribution of magmatic volatiles in the earliest stages (i.e., stage 1) of the hydrothermal system. Petersen et al. (2002) proposed that the stage 2 polymetallic sulfides formed from a combination of sulfur leached from the underlying volcanic rocks and reduced seawater sulfate, similar to that found in the majority of sea-floor hydrothermal systems. We examine alternative explanations below, especially for stage 2 mineralization.

In order to explain the variation of $\delta^{34}\text{S}$ values at Conical seamount the potential sources of sulfur and the depositional processes at the time of mineralization need to be evaluated. The temperatures of formation were $<310^\circ\text{C}$ for stage 2 and $<100^\circ\text{C}$ for stage 3 at Conical seamount, whereas no temperature estimate was given for stage 1 (Petersen et al., 2002). We interpret that the sulfide, sulfosalt, alteration mineralogy, and temperature-solubility relationships for base and precious metals of stages 1 and 2 mineralization indicate a temperature range of between 300° to 200°C . Sulfides precipitating from inorganically reduced seawater sulfate (sulfate in the present ocean is $21.0 \pm 0.2\text{‰}$; Rees et al., 1978) at temperatures between 300° and 200° would have $\delta^{34}\text{S}$ values

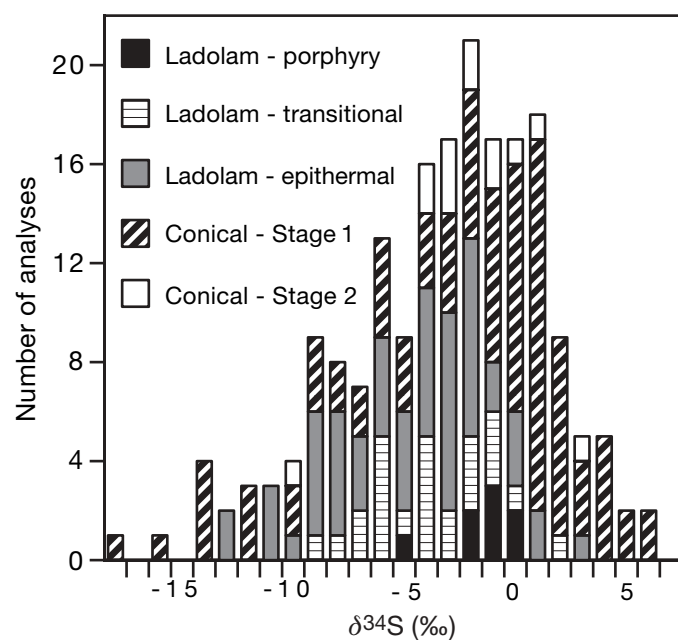


FIG. 7. Histogram comparing sulfide $\delta^{34}\text{S}$ values for the different mineralization styles at Ladolam and the mineralized stages at Conical seamount. Data from Tables 2 and 4, Müller et al. (2002a), and Carman (2003).

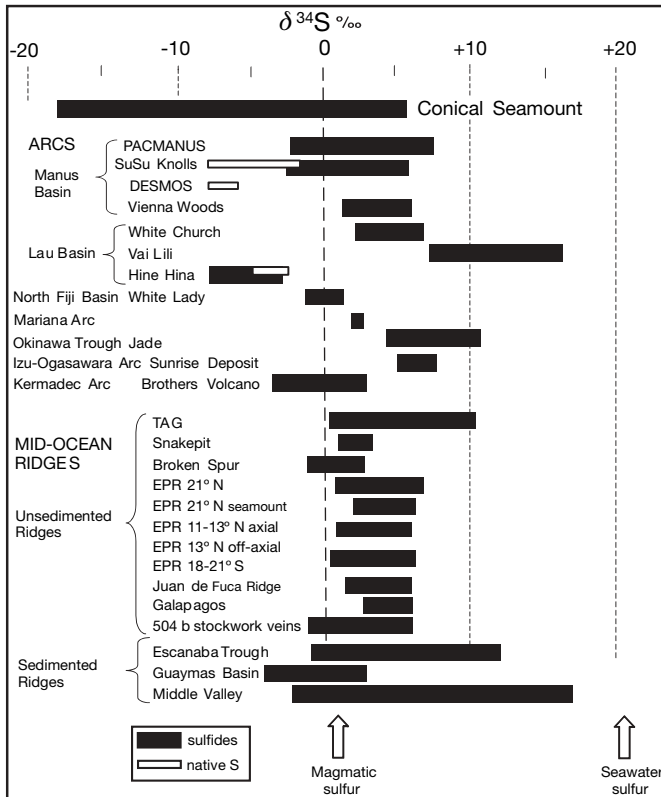


FIG. 8. Comparison of $\delta^{34}\text{S}$ values for hydrothermal sites on midocean ridges and arc environments on the modern sea floor. Modified from Gemmell and Sharpe (1998) with additional data from Gemmell et al. (1999), Goodfellow et al. (1999), Iizasa et al. (1999), and de Ronde et al. (2000).

from -4 to $+21$ per mil, depending on the amount of reduction and extent of equilibrium (Ohmoto and Rye, 1979). The majority of $\delta^{34}\text{S}$ values for stage 1 and 2 sulfide minerals at Conical seamount (-17 to $+6\text{‰}$) are significantly lower than

the predicted values, indicating that reduced seawater sulfate was not the primary source of sulfur.

Petersen et al. (2002) suggested that leaching of volcanic rock sulfur was a major source of sulfur in stage 2 mineralization. The average $\delta^{34}\text{S}$ value for total sulfur (sulfide and sulfate) in midocean ridge basalt is near 0 per mil and andesites in island-arc environments have $\delta^{34}\text{S}_{\text{total}}$ values between 5 and 7 per mil (Ueda and Sakai, 1984; Woodhead et al., 1987). Although $\delta^{34}\text{S}_{\text{total}}$ values are not available for the Conical seamount alkali basalts, the isotopic signature of the Conical seamount sulfides in stages 1 and 2 requires a source of light sulfur that cannot be explained by simple nonequilibrium mixing between SO_4 and H_2S leached from the volcanic host rocks.

Therefore, based on these factors, other sulfur sources and/or processes, such as organic reduction of seawater sulfate, evolution of light sulfur directly from magmatic volatiles, and/or boiling are required to explain the light sulfur at Conical seamount. Organically reduced seawater sulfate in marine sediments has been considered an important source of isotopically light sulfur in some sea-floor hydrothermal systems (Shanks et al., 1995). The maximum temperature estimated for the production of organically reduced seawater sulfate is $<120^\circ\text{C}$ (Canfield, 2001). Petersen et al. (2002) suggested that bacteriogenic sulfate reduction might be involved in the formation of the framboidal pyrite, due to their low $\delta^{34}\text{S}$ values (Table 3). Hydrothermal sulfides in veins, veinlets, and disseminations with alteration in stages 1 and 2 throughout all the mineralized zones, also have very low $\delta^{34}\text{S}$ values, some lower than the framboidal pyrite (Table 2). Therefore, at temperatures between 300° and 200°C organically reduced seawater sulfate was not a significant source of sulfur in sulfide minerals from stages 1 and 2 mineralization at Conical seamount.

Our new data suggest that there was a more significant role for magmatic sulfur and boiling throughout the paragenesis than was previously recognized and that the negative sulfur isotope values in framboidal pyrite reported by Petersen et al.

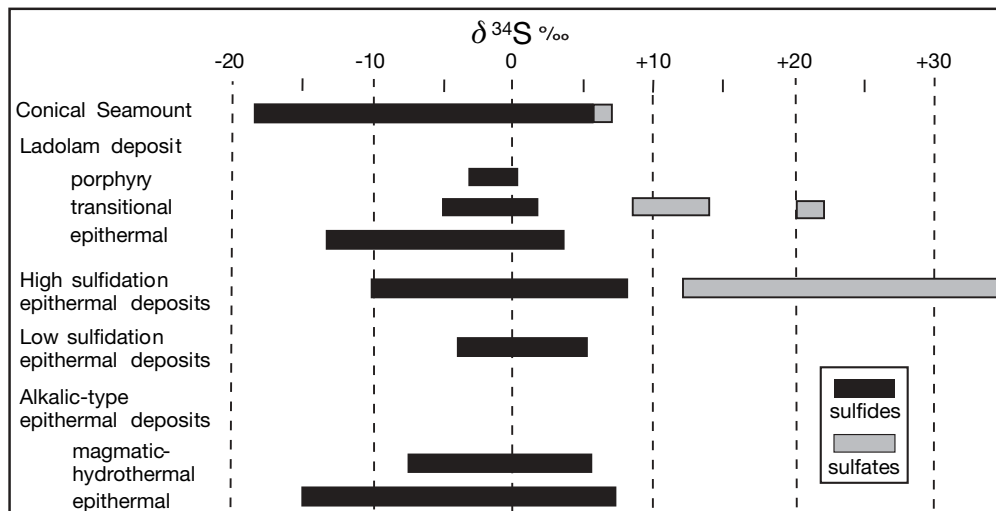


FIG. 9. Comparison of $\delta^{34}\text{S}$ values from Conical seamount and the Ladolam deposit with high-sulfidation epithermal deposits (Arribas, 1995), low-sulfidation epithermal deposits (Field and Fifarek, 1985), and the alkalic subtype of low-sulfidation epithermal deposits (Richards, 1995).

(2002) probably reflect the same strong magmatic sulfur contribution that is evident in the main stage 1 mineralization. At magmatic temperatures the dominant sulfur species is SO_2 (Sakai et al., 1984; Wallace and Carmichael, 1992), whereas as the magmatic volatiles cool below 400°C , magmatic SO_2 will disproportionate to H_2S and H_2SO_4 . This process will enrich ^{32}S in the sulfide and ^{34}S in the sulfate (Ohmoto and Rye, 1979; Ohmoto and Lasaga, 1982). Sulfides precipitated from this sulfur will have $\delta^{34}\text{S}$ values <0 per mil, and coexisting sulfate minerals will have $\delta^{34}\text{S}$ values >0 per mil, although substantially lower than seawater sulfate (Herzig et al., 1998a). The $\delta^{34}\text{S}$ values for alunite (6–8‰) formed with pyrite in stage 1 at Conical seamount are markedly lower than present seawater, indicating that the sulfur in alunite was derived from magmatic volatiles.

McKibben and Eldridge (1990) determined that boiling of a hydrothermal fluid, accompanied by separation of a volatile phase, caused radical variation in the isotopic composition of sulfides. They concluded that boiling involves the loss of aqueous H_2 and H_2S into the vapor phase that causes an increase in the oxidation state of the residual liquid, leading to significant fractionation of sulfur isotopes. This fractionation can cause rapid shifts from positive to negative $\delta^{34}\text{S}$ values of sulfides that are highly variable at the grain scale, with isotopic heterogeneity in individual samples (McKibben and Eldridge, 1990). Individual samples at Conical seamount have $\delta^{34}\text{S}$ values that vary by as much as 7 per mil (Table 2). In adjacent stage 1, disseminated pyrite grains in sample 40GTVA-2 range over 4 per mil, and in sample 53GTVA-2A adjacent stage 2 sulfide grains have $\delta^{34}\text{S}$ values exceeding a range of 7 per mil. There is a wide range of $\delta^{34}\text{S}$ values within individual pyrite veins. For example sample 14-GTVA-3 has a range of over 6 per mil across the vein (Table 2). Therefore, we suggest the large variation of $\delta^{34}\text{S}$ values within pyrite is caused by boiling of the hydrothermal fluid. However, as hydrothermal fluids are not presently venting at Conical seamount there is no direct visual evidence of boiling, and no fluid inclusion investigation has been undertaken to evaluate evidence for boiling, due to the very fine grained nature of the material.

In summary, we interpret the range of $\delta^{34}\text{S}$ values in the polymetallic and pyritic stockwork mineralization (stages 1 and 2) at Conical seamount in the following way. Although the framboidal pyrite analyzed by Petersen et al. (2002) may have had an organically reduced sulfur component, we suggest that organically reduced seawater sulfate did not play a significant role in the overall sulfur budget of Conical seamount. Rather, the dominant process that produced the low $\delta^{34}\text{S}$ values in both the stage 1 and 2 sulfides was the disproportionation of magmatic SO_2 . The $\delta^{34}\text{S}$ values for the sulfides (-17.5 to $+6.1$ ‰, mean = -1.9 ‰, this study) are generally lower than the initial $\delta^{34}\text{S}$ of SO_2 (near 0‰) and values for the associated alunite (6.4–7.5‰, Petersen et al., 2002) are higher than the starting composition but lower than coeval seawater (21‰). The presence of platy alunite, associated kaolinite, aluminum phosphate minerals, and other clay minerals in stage 1 mineralization (Herzig et al., 1998b, c, 1999; Petersen et al., 2002) supports the interpretation that magmatic fluids have contributed to the hydrothermal system at Conical seamount. The mixing of magmatic fluids with inorganically reduced

seawater sulfate within Conical seamount may have produced some of the higher $\delta^{34}\text{S}$ sulfide values in stage 2 and 3 sulfides. The observed alteration (illite, montmorillonite group clays, chlorite, and adularia with minor calcite) with stage 2 mineralization (Petersen et al., 2002) suggests that interaction with seawater may have neutralized the acidity of the magmatic fluid, causing a near-neutral pH alteration assemblage to form. Boiling may have caused the large variations of $\delta^{34}\text{S}$ values within individual samples and could have been an important process in the deposition of sulfides at Conical seamount.

Ladolam deposit, Lihir Island

The magmatic-hydrothermal history at Ladolam, together with the island setting, led Carman (2003) to postulate a complex multicomponent source for the hydrothermal fluids during evolution of the deposit. Based on fluid inclusion and stable isotope evidence, Carman (2003) concluded that the stage I porphyry-style mineralization ($\delta^{34}\text{S}$ of pyrite = -1.4 to $+2.2$ ‰) was of magmatic origin. Stage II veins and breccias precipitated between 300° and 200°C , with 5 to 10 wt percent NaCl equiv due to mixing of the magmatic fluid with dilute ground water. Carman (2003) suggested that $\delta^{34}\text{S}$ values of pyrite (-7 to $+2$ ‰) and deep anhydrite (13‰) indicated a magmatic source, with no evidence of seawater input. The stage III low-sulfidation epithermal mineralization is interpreted to form from an initial magmatic brine at 230°C with 5 ± 0.5 wt percent NaCl equiv that mixed with dilute meteoric ground water to produce a hydrothermal fluid at $170^\circ \pm 20^\circ\text{C}$ and near 0 wt percent NaCl equiv. Late-stage silicic breccia ores were deposited at temperatures below 200°C as reduced fluids mixed with oxidized acid-sulfate waters of low salinity beneath an advanced argillic cap (Carman, 2003).

Our data support the conclusion by Carman (2003) that the overall light sulfur and large range of $\delta^{34}\text{S}$ values at Ladolam were initially due to magmatic fluids escaping from the crystallizing magma. It is likely that during the catastrophic collapse of a portion of the Luise volcano and unroofing of the hydrothermal system (Carman, 2003), magmatic fluids were released, likely boiled due to the rapid pressure release, and mixed with dilute ground water. These processes led to lower $\delta^{34}\text{S}$ values in the stage II transitional and stage III epithermal styles of mineralization.

New sulfur isotope data on anhydrite show that there could be two populations of $\delta^{34}\text{S}$ values, one between 8 and 14 per mil and one between 20 and 22 per mil (Fig. 6B). The high $\delta^{34}\text{S}$ values raise the possibility of the interaction with seawater, previously discounted, with magmatic fluids and ground water. The lower anhydrite $\delta^{34}\text{S}$ values are likely due to the disproportionation of magmatic SO_2 leading to enrichment of ^{34}S in the sulfate but $\delta^{34}\text{S}$ values less than coeval seawater. Two anhydrite samples with $\delta^{34}\text{S}$ values of 8.6 and 11.1 per mil (Muller et al., 2002a) have reported $^{87/86}\text{Sr}$ isotope values of 0.7040, suggesting a magmatic Sr source (Muller et al., 2002b). The higher anhydrite $\delta^{34}\text{S}$ values are the same as coeval seawater sulfate and indicate that mixing with seawater did occur at Ladolam, although the amount and extent of this mixing is unknown. There are no published Sr isotope data for the anhydrite with the higher $\delta^{34}\text{S}$ values to confirm the seawater signature. The most reasonable interpretation of the present data is that the range of sulfide and sulfate $\delta^{34}\text{S}$ values

at Ladolam is due to the complex interaction of magmatic hydrothermal fluids, meteoric water, and seawater.

The fumaroles depositing native sulfur and offshore hydrothermal vents forming pyrite have the same $\delta^{34}\text{S}$ values as the Ladolam epithermal mineralization, indicating that similar fluids are still reaching the floor of the Luise caldera. Carman (2003) interpreted that the active hydrothermal system within the Luise caldera is a remnant of the Ladolam ore-forming system.

Conclusions

The discovery of Conical seamount is a unique opportunity to examine ore-forming processes in a submarine environment, which have a number of mineralogical, chemical, and textural characteristics in common with some subaerial epithermal systems. Conical seamount has the lowest, hydrothermal sulfide (i.e., nondiagenetic) $\delta^{34}\text{S}$ values (-17.5 to $+6.1\%$) measured to date from modern sea-floor hydrothermal systems. A model by Petersen et al. (2002) for the Conical seamount hydrothermal system suggested a contribution of magmatic volatiles in the earliest stages of mineralization (stage 1), followed by a combination of sulfur leached from the underlying volcanic rocks and reduced seawater sulfate during the main base and precious metal precipitating event (stage 2). New sulfur isotope data suggest a significant input of magmatic volatiles, and possibly boiling, throughout both stage 1 and 2 mineralization. Pyrite samples from the Ladolam gold deposit have a similar range of sulfur isotope values (-12.9 to $+3.6\%$) as Conical seamount. The range of sulfide and sulfate $\delta^{34}\text{S}$ values at Ladolam is interpreted to be due to the complex interaction of magmatic hydrothermal fluids, meteoric ground water, and seawater. Active fumaroles depositing native sulfur and offshore hydrothermal vents forming pyrite have the same $\delta^{34}\text{S}$ values as the Ladolam epithermal mineralization, indicating that fluids similar to those that formed the gold deposit are still reaching the floor of the Luise caldera. Sulfur isotope data at both Conical seamount and the Ladolam deposit suggest that magmatic volatiles have contributed a significant amount of sulfur to both these gold-rich hydrothermal systems.

Acknowledgments

Principal funding for the SO-133 EDISON II cruise was provided by the German Ministry for Education and Research (BMBF grant 03G0133A to Peter Herzig). We thank Master Andresen and the officers and crew of the R/V SONNE for their expert assistance and cooperation during research activities around Lihir Island. Mark Hannington is acknowledged for providing unpublished sulfur isotope data from the Ladolam deposit and environment. JBG and RS appreciate the ARC grant obtained by Ross Large for development of the Central Science Laboratory stable isotope facilities at the University of Tasmania and the Australian Research Council's Special Research Centres Program. Sulfur isotope analyses were completed with the help of Mike Power, Sr., and Christine Cook of the Central Science Laboratory, University of Tasmania. IRJ acknowledges project support from the Mineral Resources Division of the Geological Survey of Canada. Reviews by Jeremy Richards, Minoru Kusakabe, Cornel de Ronde, Jeff Hedenquist, and

Mark Hannington have significantly improved early versions of this paper.

May 30, 2002; September 16, 2004

REFERENCES

- Arribas, Jr., A., 1995, Characteristics of high-sulfidation epithermal deposits, and their relation to magmatic fluid: Mineralogical Association of Canada Short Course Series, v. 23, p. 419–454.
- Canfield, D.E., 2001, Biogeochemistry of sulfur isotopes: Reviews in Mineralogy and Geochemistry, v. 43, p. 607–636.
- Carman, G.G., 1994, Genesis of the Ladolam gold deposit, Lihir Island, Papua New Guinea: Unpublished Ph.D. thesis, Clayton, Victoria, Australia, Monash University, 300 p.
- 2003, Geology, mineralization and hydrothermal evolution of the Ladolam gold deposit, Lihir Island, Papua New Guinea: Society of Economic Geologists Special Publication 10, p. 247–284.
- Cooke, D.R., and Simmons, S.F., 2000, Characteristics and genesis of epithermal gold deposits: Reviews in Economic Geology, v. 13, p. 221–244.
- Corbett, G.J., and Leach, T.M., 1998, Southwest Pacific Rim gold-copper systems: Structure, alteration and mineralization: Society of Economic Geologists Special Publication 6, 237 p.
- Davies, R.M., and Ballantyne, G.H., 1987, Geology of the Ladolam gold deposit: Lihir Island, Papua New Guinea: Australian Institute of Mining and Metallurgy, Pacific Rim Congress 87, Gold Coast, Australia, August 26–29, 1987, Proceedings, p. 943–949.
- de Ronde, C.E.J., 1995, Fluid chemistry and isotope characteristics of seafloor hydrothermal systems and associated VMS deposits: Potential for magmatic contributions: Mineralogical Association of Canada Short Course Series, v. 23, p. 479–509.
- de Ronde, C.E.J., Hannington, M., Stoffers, P., Wright, I., Gennerich, H.H., Browne, P., and Herzig, P., 2000, Massive sulfide mineralisation associated with a frontal arc volcano: Brothers hydrothermal system, southern Kermadec arc, New Zealand [abs.]: Hobart, Tasmania, Australia, Centre for Ore Deposit Research Special Publication 3, p. 37–38.
- Exon, N.F., Stewart, W.D., Sandy, M.J., and Tiffin, D.L., 1986, Geology and offshore petroleum prospects of the eastern New Ireland basin, northeastern Papua New Guinea: Bureau of Mineral Resources Journal of Australian Geology and Geophysics 10, p. 39–51.
- Field, C.W., and Fifarek, R.H., 1985, Light stable isotope systematics in epithermal systems: Reviews in Economic Geology, v. 2, p. 99–128.
- Gamo, T., Okamura, K., Charlou, J., Urabe, T., Auzende, J., Ishibashi, J., Shitashima, K., Chiba, H., Binns, R.A., Gena, K., Henry, K., Matsubayashi, O., Moss, R., Nagaya, Y., Naka, J., and Ruellan, E., 1997, Acidic and sulfate-rich hydrothermal fluids from the Manus back-arc basin, Papua New Guinea: Geology, v. 25, p. 139–142.
- Gemmell, J.B., and Sharpe, R., 1998, Detailed sulfur isotope investigation of the TAG hydrothermal mound and stockwork zone, 26°N, Mid-Atlantic Ridge: Proceedings of the Ocean Drilling Program, Scientific Results, v. 158, p. 71–84.
- Gemmell, J.B., Binns, R.A., and Parr, J.M., 1999, Submarine, high sulfidation alteration within DESMOS caldera, Manus basin, PNG, in C.J. Stanley et al., eds, Mineral deposits: Processes to processing, v.1, Proceedings of the 5th biennial SGA meeting and the 10th quadrennial IAGOD symposium: London, Balkema, p. 503–506.
- Goodfellow, W.D., and Franklin, J.M., 1993, Geology, mineralogy, and chemistry of sediment-hosted clastic massive sulfide in shallow cores, Middle Valley, Northern Juan de Fuca Ridge: ECONOMIC GEOLOGY, v. 88, p. 2037–2068.
- Goodfellow, W.D., Zierenberg, R.A., and the ODP Leg 169 Shipboard Science party, 1999, Genesis of massive sulfide deposits at sediment-covered spreading centers: Reviews in Economic Geology, v. 8, p. 297–324.
- Hannington, M.D., 1997, The porphyry-epithermal-VMS transition: Lessons from the Iskut River area, British Columbia, and modern island arcs: Society of Economic Geologists Newsletter 29, p. 12–13.
- Hannington, M., Poulsen, H., Thompson, J., and Sillitoe, R., 1999, Volcanogenic gold and epithermal-style mineralization in the VMS environment: Reviews in Economic Geology, v. 8, p. 325–356.
- Hedenquist, J.W., and Lowenstern, J.B., 1994, The role of magmas in the formation of hydrothermal ore deposits: Nature, v. 370, p. 519–527.
- Herzig, P.M., and Hannington, M.D., 1995a, Polymetallic massive sulfides at the modern seafloor—a review: Ore Geology Reviews, v. 10, p. 95–115.

- 1995b, Hydrothermal activity, vent fauna, and submarine gold mineralization at alkaline fore-arc seamounts near Lihir Island, Papua New Guinea: Australian Institute of Mining and Metallurgy, Pacific Rim Congress 1995, Melbourne, Australia, Proceedings, p. 279–284.
- Herzig, P., Hannington, M., McInnes, B., Stoffers, P., Villinger, H., Seifert, R., Binns, R., and Liebe, T., 1994, Submarine volcanism and hydrothermal venting studied in Papua New Guinea: EOS Transactions, v. 75, no. 44, p. 513–616.
- Herzig, P.M., Hannington, M.D., and Arribas, Jr., A., 1998a, Sulfur isotope composition of hydrothermal precipitates from the Lau back-arc: Implications for magmatic contributions to seafloor hydrothermal systems: Mineralium Deposita, v. 33, p. 226–237.
- Herzig, P., Hannington, M., Stoffers, P., and Shipboard Party, 1998b, Volcanism, hydrothermal processes and biological communities at shallow submarine volcanoes of the New Ireland fore-arc, Papua New Guinea: Freiberg, Germany, Freiberg University, Cruise Report Sonne-133, 146 p.
- 1998c, Petrology, gold mineralization, and biological communities at shallow submarine volcanoes of the New Ireland fore-arc (Papua New Guinea): Preliminary results of R/V Sonne cruise SO-133: InterRidge News, v. 7(2), p. 34–38.
- Herzig, P.M., Petersen, S. and Hannington, M.D., 1999, Epithermal-type gold mineralization at Conical seamount: A shallow submarine volcano south of Lihir Island, Papua New Guinea, in C.J. Stanley et al., eds, Mineral deposits: Processes to processing, v. 1, Proceedings of the 5th biennial SGA meeting and the 10th Quadrennial IAGOD symposium: London, Balkema, p. 527–530.
- Huston, D.L., Power, M., Gemmill, J.B., and Large, R., 1995, Design, calibration and geologic application of the first operational Australian laser ablation sulphur isotope microprobe: Australian Journal of Earth Sciences, v. 42, p. 549–555.
- Iizasa, K., Fiske, R.S., Ishizuka, O., Yuasa, M., Hashimoto, J., Ishibashi, J., Naka, J., Horii, Y., Fujiwara, Y., Imai, A., and Koyama, S., 1999, A kuroko-type polymetallic sulfide deposit in a submarine silicic caldera: Science, v. 283, p. 975–977.
- Jensen, E.P., and Barton, M.D., 2000, Gold deposits related to alkaline magmatism: Reviews in Economic Geology, v. 13, p. 279–314.
- Kennedy, A.K., Hart, S.R., and Frey, F.A., 1990, Composition and isotopic constraints on the petrogenesis of alkaline arc lavas: Lihir Island, Papua New Guinea: Journal of Geophysical Research, v. 95, p. 6929–6942.
- McInnes, B.I.A., 1992, A glimpse of ephemeral subduction zone processes from Simberi Island, Papua New Guinea: Unpublished Ph.D. thesis, Ottawa, Canada, University of Ottawa, 235 p.
- McInnes, B.I.A., and Cameron, E.M., 1994, Carbonated, alkaline metasomatic melts from a sub-arc environment: Mantle wedge samples from the Tabar-Lihir-Tanga-Feni arc, Papua New Guinea: Earth and Planetary Science Letters, v. 122, p. 125–141.
- McInnes, B.I.A., McBride, J.S., Evans, N.J., Lambert, D.D., and Andrew, A.S., 1999, Osmium isotope constraints on metal recycling in subduction zones: Science, v. 286, p. 512–516.
- McInnes, B.I.A., Gregoire, M., Binns, R.A., Herzig, P.M., and Hannington, M.D., 2001, Hydrous metasomatism of oceanic sub-arc mantle, Lihir, Papua New Guinea: Petrology and geochemistry of fluid-metasomatized mantle wedge xenoliths: Earth and Planetary Science Letters, v. 188, p. 169–183.
- McKibben, M.A., and Eldridge, C.S., 1990, Radical sulfur isotope zonation of pyrite accompanying boiling and epithermal gold deposition: A SHRIMP study of the Valles caldera, New Mexico: ECONOMIC GEOLOGY, v. 85, p. 1917–1925.
- Moyle, A.J., Doyle, B.J., Hoogvliet, H., and Ware, A.R., 1990, Ladolam gold deposit, Lihir Island: Australian Institute of Mining and Metallurgy Monograph 14, p. 1793–1805.
- Müller, D., Franz, L., Herzig, P.M., and Hunt, S., 2001, Potassic rocks from the vicinity of epithermal gold mineralization, Lihir Island, Papua New Guinea: Lithos, v. 57, p. 163–186.
- Müller, D., Herzig, P.M., Scholten, J.C., and Hunt, S., 2002a, Ladolam gold deposit, Lihir Island, Papua New Guinea: Gold mineralization hosted by alkaline rocks: Society of Economic Geologists Special Publication 9, p. 367–382.
- Müller, D., Kaminski, K., Uhlig, S., Graupner, T., Herzig, P.M., and Hunt, S., 2002b, The transition from porphyry- to epithermal-style gold mineralization at Ladolam, Lihir Island, Papua New Guinea: A reconnaissance study: Mineralium Deposita, v. 37, p. 61–74.
- Ohmoto, H., 1986, Stable isotope geochemistry of ore deposits: Reviews in Mineralogy, v. 16, p. 491–560.
- Ohmoto, H., and Lasaga, A.C., 1982, Kinetics of reactions between aqueous sulfates and sulfides in hydrothermal systems: Geochimica et Cosmochimica Acta, v. 46, p. 1727–1745.
- Ohmoto, H., and Rye, R.O., 1979, Isotopes of sulphur and carbon, in Barnes, H.L., ed., Geochemistry of hydrothermal ore deposits: New York, Wiley and Sons, p. 509–567.
- Petersen, S., Herzig, P.M., Hannington, M.D., and Jonasson, I.R., 2002, Submarine gold mineralization near Lihir Island, New Ireland fore-arc, Papua New Guinea: ECONOMIC GEOLOGY, v. 97, p. 1795–1813.
- Pichler, T., Giggenbach, W.F., McInnes, B.I.A., Buhl, D., and Duck, B., 1999, Fe sulfide formation due to seawater-gas-sediment interaction in a shallow-water hydrothermal system at Lihir Island, Papua New Guinea: ECONOMIC GEOLOGY, v. 94, p. 281–288.
- Rees, C.E., Jenkins, W.J., and Monster, J., 1978, The sulfur-isotope geochemistry of ocean water sulfate: Geochimica et Cosmochimica Acta, v. 42, p. 377–382.
- Richards, J.P., 1995, Alkalic-type epithermal gold deposits—a review: Mineralogical Association of Canada Short Course Series, v. 23, p. 367–400.
- Robinson, B.W., and Kusakabe, M., 1975, Quantitative preparation of SO₂ for ³⁴S/³²S analyses from sulfide by combustion with cuprous oxide: Analytical Chemistry, v. 7, p. 1179–1181.
- Sakai, H., Des Marais, D.J., Ueda, A., and Moore, J.G., 1984, Concentrations and isotope ratios of carbon, nitrogen and sulfur in ocean-floor basalts: Geochimica et Cosmochimica Acta, v. 48, p. 2433–2441.
- Sangster, D.F., 1968, Relative sulfur-isotope abundances of ancient seas and stratabound sulfide deposits: Geological Association of Canada Proceedings, v. 17, p. 79–91.
- Shanks, W.C., III, Bischoff, J.L., and Rosenbauer, R.J., 1981, Seawater sulfate reduction and sulfur-isotope fractionation in basaltic systems: Interactions of seawater with fayalite and magnetite at 200–350°C: Geochimica et Cosmochimica Acta, v. 45, p. 1977–1995.
- Shanks, W.C., III, Bohlke, J.K., and Seal, R.R., III, 1995, Stable isotopes in mid-ocean ridge hydrothermal systems: Interactions between fluids, minerals, and organisms: Geophysical Monograph 91, p. 194–221.
- Shipboard Scientific Party, 2002, Leg 193 summary: Proceedings of the Ocean Drilling Program Initial Reports, v. 193, p. 1–84.
- Sillitoe, R.H., Hannington, M.D., and Thompson, J.F.T., 1996, High-sulfidation deposits in the volcanogenic massive sulfide environment: ECONOMIC GEOLOGY, v. 91, p. 204–212.
- Solomon, M., Eastoe, C.J., Walshe, J.L., and Green, G.R., 1988, Mineral deposits and sulfur-isotope abundances in the Mount Read Volcanics between Que River and Mount Darwin, Tasmania: ECONOMIC GEOLOGY, v. 83, p. 1307–1328.
- Stewart, W.D., and Sandy, M.J., 1988, Geology of New Ireland and Djaul Islands, northeastern Papua New Guinea: Circum-Pacific Council for Energy and Mineral Resources, Earth Science Series 9, p. 13–30.
- Taylor, B.E., 1987, Stable isotope geochemistry of ore-forming fluids: Mineralogical Association of Canada Short Course Handbook, v. 13, p. 337–445.
- Ueda, A., and Sakai, H., 1984, Sulfur isotope study of Quaternary volcanic rocks from the Japanese islands arc: Geochimica et Cosmochimica Acta, v. 48, p. 1837–1848.
- Wallace, D.A., Johnson, R.W., Chappell, B.W., Arculus, R.J., Perfit, M.R., and Crick, I.H., 1983, Cainozoic volcanism of the Tabar, Lihir, Tanga and Feni Islands, Papua New Guinea: Geology, whole-rock analyses, and rock-forming mineral compositions: Bureau of Mineral Resources, Geology, and Geophysics Australia Report 243 (microfiche).
- Wallace, P., and Carmichael, I.S.E., 1992, Sulfur in basaltic magmas: Geochimica et Cosmochimica Acta, v. 56, p. 1863–1847.
- Woodhead, J.D., Harmon, R.S., and Fraser, D.G., 1987, O, S, Sr and Pb isotope variations in volcanic rocks from the northern Mariana Islands: Implications for crustal recycling in intra-oceanic arcs: Earth and Planetary Science Letters, v. 83, p. 39–52.
- Yang, K., and Scott, S.D., 1996, Possible contribution of a metal-rich magmatic fluid to a sea-floor hydrothermal system: Nature, v. 383, p. 420–423.

Comparison between magmatic activity and gold mineralization at Conical Seamount and Lihir Island, Papua New Guinea

**D. Müller¹, L. Franz², S. Petersen², P. M. Herzig²,
and M. D. Hannington³**

¹ Institut für Erdwissenschaften, Eidgenössische Technische Hochschule Zürich,
ETH, Zürich, Switzerland

² Institut für Mineralogie, TU Bergakademie Freiberg, Freiberg, Germany

³ Geological Survey of Canada, Ottawa, Canada

Received May 23, 2002; revised version accepted April 19, 2003

Editorial handling: E. F. Stumpf

Summary

Grab samples from the submarine Conical Seamount, located about 10 km south of the giant Ladolam gold deposit, Lihir Island, reveal the highest gold concentrations yet reported from the modern seafloor. Lavas from Conical Seamount are characterized by high K₂O contents, high K₂O/Na₂O ratios, and high Ce/Yb ratios, which are typical of high-K igneous rocks from oceanic (island) arc-settings. The primitive character of the rocks from Conical Seamount implies a magmatic evolution related to a single eruptive phase, which contrasts with the more evolved rocks forming Lihir Island. Geochemical as well as mineral chemical data suggest that the melts from both Conical Seamount and Lihir Island originate from the same magma source. In common with the samples from Lihir Island, elevated oxygen fugacities of 0.7–2.5 log units above the FMQ buffer are recorded from the Conical Seamount lavas.

There are distinct differences between the mineralization styles at Conical Seamount and at the Ladolam gold deposit, Lihir Island. While early-stage pyritic stockwork mineralization at Conical Seamount is hosted by clay-silica altered basaltic rocks with local alunite ± kaolinite alteration, main-stage Au-mineralization occurs in sericite-alkali feldspar altered polymetallic sulfide-bearing siliceous veins. By contrast, early-stage pyritic stockwork mineralization at Ladolam is restricted to biotite–magnetite ± silica-altered monzodiorite, while the main-stage bulk-tonnage mineralization occurs as auriferous pyrite-bearing hydrothermal breccias which, in places, are cut by quartz–chalcedony–illite–adularia–pyrite ± marcasite veins containing isolated bonanza gold grades.

Introduction

The Bismarck Archipelago of Papua New Guinea is well known for its metal potential including the giant (>1300 metric tons of gold) Ladolam deposit located on the island of Lihir (Moyle et al., 1990). Studies on veined peridotite xenoliths from the upper mantle beneath Lihir Island show that they are 2 to 800 times more enriched in Cu, Au, Pt, and Pd than surrounding depleted arc mantle (McInnes et al., 1999). Additionally, gold ores from Ladolam have Os isotope compositions similar to those of the underlying subduction-modified mantle peridotite, indicating that the primary source of the metals was the mantle (McInnes et al., 1999).

Conical Seamount is located about 10 km south of Lihir Island (Fig. 1). Grab samples from this seamount contain the highest concentration of gold yet reported from the modern seafloor (max. 230 ppm Au, avg. 26 ppm, n = 40) that are uniformly associated with high concentrations of Ag, As, Sb, and Hg (Petersen et al., 2002). While gold mineralization at Ladolam has evolved from a porphyry- to a low-sulfidation epithermal-style gold deposit (Carman, 1994; Müller et al., 2002a), gold mineralization at Conical Seamount shares characteristics of both low- and high-sulfidation epithermal gold deposits on land thus constituting a new type of mineralization not previously recognized on the modern seafloor (Petersen et al., 2002).

The close spatial association between Conical Seamount and Lihir Island suggests a similar genetic evolution, and this paper aims to compare the characteristic features of both mineralized systems and their host rocks in an attempt to investigate a potential genetic relationship.

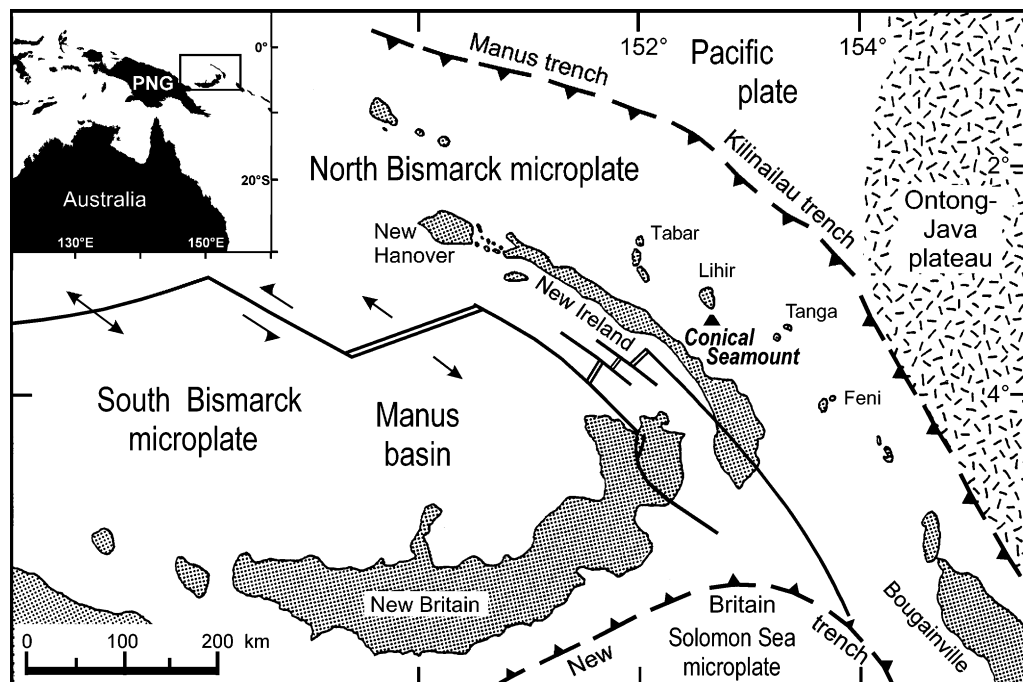


Fig. 1. Geological overview and plate tectonic setting of Conical Seamount and Lihir Island; compiled from Müller et al. (2001) and Franz et al. (2002)

Regional geological setting

The Bismarck Archipelago is located in the northeastern province of Papua New Guinea and includes the islands of New Britain, New Ireland, Bougainville and the Solomons (Fig. 1). Lihir Island is part of the Tabar-Lihir-Tanga-Feni island chain which extends for more than 260 km in the New Ireland basin to the north–east of New Ireland (Davies and Ballantyne, 1987).

The plate tectonic situation in this region during the Oligocene and Miocene was characterized by the westward subduction of the Pacific plate beneath the Melanesian arc resulting in calc-alkaline volcanism on New Ireland. About 15 million years ago, the subduction ceased due to collision of the Ontong-Java plateau with the formerly active Kilinailau trench (Coleman and Kroenke, 1981). The reconfiguration of the tectonic plates and the stress field resulted in plate rotation, subduction reversal and the formation of the presently active New Britain subduction zone (Fig. 1). At the same time volcanism at New Ireland ceased. Back-arc spreading then developed in the Manus basin and separated the Bismarck microplate into northern and southern segments (Fig. 1).

About 3.6 Ma ago volcanic activity in the New Ireland basin started on Simberi Island (Tabar Island group) and subsequently formed the volcanic islands in old fore-arc crust (Rytuba et al., 1993). The high-K calc-alkaline volcanism of the Tabar-Lihir-Tanga-Feni island chain seems to be related to north-trending extensional faults, which were either generated during the opening of the Manus back-arc basin (Taylor, 1979; Steward and Sandy, 1988) or due to a flexure in the subducting Solomon plate (Müller et al., 2002b). The partial melting of subduction-modified upper mantle was probably triggered by adiabatic decompression melting along these deep-seated extensional structures (Patterson et al., 1997).

Geology of Conical Seamount

Conical Seamount is the largest of a number of volcanic edifices that were discovered south of Lihir Island in 1994 (Herzig et al., 1994). It has a basal diameter of about 2.8 km and rises about 600 m above the seafloor to a water depth of 1050 m (Herzig et al., 1994, 1999). The seamount is characterized by a small summit plateau extending over 100 × 200 m and hosting an elongate, 100-m long E-W-oriented volcanic feature that is interpreted as an eruptive fissure (Herzig et al., 1999). Conical Seamount consists of massive lava flows, pillows, and talus breccias comprising moderately vesicular fragments and scoria. The symmetrical shape of the volcano suggests a relatively young age although its flanks are covered by pelagic sediments (Herzig et al., 1999).

Geology of Lihir Island

Lihir Island consists of Pliocene-Pleistocene lavas, volcanic breccias, and pyroclastic and epiclastic rocks derived from five volcanoes that dominate the island. These are, in chronological order, the Huniho, Wurtol, Luise, Londolovit and Kinami volcanoes (Wallace et al., 1983; Müller et al., 2001). While the Londolovit and Huniho volcanoes form the northern part of the island, the central part is

dominated by the Wurtol and Luise volcanoes and the southern part by Kinami volcano. The Pleistocene Luise stratovolcano consists of an elongate, elliptical crater, about 5.5 by 3.5 km, where the north-eastern margin has collapsed into the sea. Based on the presence of two overlapping circular demagnetized zones, the volcano probably consisted of two active centers (*Komyshan, 1999*). The southern center hosts the giant Ladolam gold deposit whereas the northern one is only partially exposed, with the largest portion now located beneath Luise Harbour. Development of the volcano has resulted in the deposition of interbedded trachyandesite and latite lavas and tuffs dipping at 20–30° away from the crater rim (*Komyshan, 1999*).

Extensive diamond drilling indicates that the Luise collapse structure does not represent a caldera, as suggested by several previous workers (e.g. *Wallace et al., 1983; Davies and Ballantyne, 1987; Moyle et al., 1990*), but instead is a partial slope failure or sector collapse of the original stratovolcano (*Carman, 1994; Sillitoe, 1994*). Failure of the north-eastern slope of Luise volcano could have either been triggered by an earthquake, by phreatic explosions, or by oversteepening of the volcano flanks during cone construction. The resulting debris avalanche slid seawards along east-striking, spoon-shaped, listric faults (*Corbett et al., 2001*). Lithostatic unloading during this process caused widespread hydraulic brecciation of the host rocks, which are healed by calcite-anhydrite veins at depth.

On a mine scale, three major structural trends are evident at Ladolam (*Corbett, 1999*). The two dominant structural trends controlling Au mineralization are the north–south oriented, near-vertical Letomazien structures and the spoon-shaped east-trending and north-dipping listric faults that result from the partial slope failure of Luise volcano. A third structural trend comprises the west-northwest-trending Huniho structures.

Based on three-dimensional modelling, the Letomazien structures are interpreted to represent the deep feeder zones of the hydrothermal gold-bearing fluid at Ladolam (*I. Treloar, pers. comm., 2000*). Importantly, Conical Seamount and the Londolovit, Luise, and Kinami volcanoes are aligned along this north–south trend. In the upper levels of the hydrothermal system at Ladolam the fluid diffused out of the Letomazien structures into the brecciated wall-rocks and along the east-trending listric faults (*Müller et al., 2002a*).

Gold mineralization at Conical Seamount

Television-guided submarine sampling at Conical Seamount recovered a series of mineralized blocks that appear to be confined to the summit of the seamount along the eruptive fissure (*Herzig et al., 1999*). Grab samples collected from the summit area include three styles of mineralization (*Petersen et al., 2002*): (1) pyritic stockwork-like material with locally intense clay-silica alteration, (2) distinctive gold-rich sulfide-bearing siliceous veins and disseminated polymetallic sulfides and (3) late-stage, fracture-filling As–Sb mineralization.

Early disseminated pyrite mineralization is related to the fracturing of the basaltic host rocks and is associated with an intense silicification of basaltic fragments (*Petersen et al., 2002*). Main stage, polymetallic sulfides occur in black siliceous veins (50–70 wt.% SiO₂) that can obtain several cm in thickness or as

minor disseminations in strongly clay-silica altered basalt. The polymetallic mineralization consists of native gold and electrum associated with sphalerite, galena, pyrite, and chalcopyrite, with minor marcasite, Pb- and As-sulfosalts, tetrahedrite, tennantite, and stibnite (*Petersen et al., 2002*).

The local presence of an alteration assemblage consisting of alunite, kaolinite, and aluminum phosphate sulfates (APS) such as woodhouseite together with early pyrite mineralization indicates the involvement of acid fluids during this stage. However, the alteration associated with the gold-rich mineralization is characterized by a near neutral pH alteration assemblage of chlorite, illite, smectite, alkali feldspar, sericite, amorphous silica, and rare carbonate.

Bonanza-grade gold concentrations of up to 230 ppm Au (avg. 25 ppm, $n = 40$) have been found in the main-stage polymetallic samples including the particularly gold-rich sulfide-bearing black siliceous veins (*Petersen et al., 2002*). The high gold contents of grab samples from various locations from the summit plateau of Conical Seamount suggest fairly widespread gold mineralization at the top of the volcano. Individual gold grains are characterized by moderate to high silver contents (10–30 wt% Ag; *Petersen et al., 2002*). Pyritic stockwork mineralization contains only minor gold concentrations (average 0.4 ppm Au) and no visible gold.

Gold mineralization at Ladolam, Lihir Island

The Ladolam gold deposit comprises four orebodies: Minifie, Lienetz, Capit, and Coastal. The two largest, Minifie and Lienetz, are currently in production by open-pit mining. The mineralization at the Minifie orebody has been documented in detail by *Carman (1994)* and *Müller et al. (2002a, b)*, and three stages of gold mineralization and alteration are distinguished: 1) an early porphyry gold system, 2) a transition between porphyry and epithermal styles, and 3) an epithermal gold mineralization event. An early-stage porphyry gold system is indicated by clasts of strongly potassic-altered monzodiorite and propylitic-altered trachyandesite that are preserved in the abundant phreatomagmatic breccias. These breccias also contain clasts of silicified and potassic-altered monzodiorite with disseminated pyrite \pm chalcopyrite and poorly developed pyrite \pm quartz stockwork veins. Additionally, deep exploration drilling under the Minifie pit area intersected monzodiorite intrusions with strong potassic alteration and andesite lavas with strong propylitic alteration (*S. Hunt, pers. comm., 2000*).

At the deeper levels of the Minifie orebody the monzodiorite and andesite lavas are brecciated and healed with calcite-anhydrite veins that are referred to as crackle breccias by *Corbett et al. (2001)*. This zone is locally called the “anhydrite seal”. The calcite-anhydrite-healed monzodiorite and andesite breccias are monolithic in composition. By contrast, the transition-stage phreatomagmatic (hydrothermal) breccias are poorly-sorted, clast-supported and heterolithic, and contain angular to subangular fragments of monzodiorite, trachyandesite, andesitic tuff, and minor laminated mudstone, as well as glassy, but devitrified, juvenile clasts. The matrix of the phreatomagmatic (hydrothermal) breccias is commonly overprinted by moderate biotite-magnetite (potassic) alteration and is strongly mineralized with fine-grained auriferous pyrite (*Corbett et al., 2001; Müller et al., 2002b*). The mineralization consists mainly of pyrite with minor marcasite and rare chalcopyrite \pm

galena \pm tetrahedrite. Pyrite (up to 20 vol%) as anhedral grains is most abundant in the breccia matrix, and to a lesser extent, disseminated in the clasts. Some pyrite is slightly anisotropic indicating a gradation to arsenian pyrite. Marcasite typically forms fibrous-bladed morphologies. Galena and tennantite generally occur as small inclusions in pyrite, whereas chalcopyrite occurs as individual grains that are restricted to the phreatomagmatic (hydrothermal) breccias. These breccias contain uniform gold grades of about 5 g/t and represent the bulk of the ore at Ladolam.

In places, the phreatomagmatic (hydrothermal) breccias are cut by late-stage grey to blue quartz–chalcedony–illite–adularia–arsenian pyrite \pm marcasite veins that contain isolated bonanza gold grades of up to 120 g/t (Müller et al., 2002a). Minerals in hydrothermal breccias near these veins are partially replaced, the biotite is altered to illite, while magnetite and chalcopyrite are replaced by pyrite. Pyrite occurs as anhedral to cubic grains intergrown with adularia, quartz, and illite in the wallrock as well as in 2- to 3-mm wide colloform aggregates rimming breccia clasts. Quartz in these late-stage veins occurs either as blue chalcedonic, fine-grained aggregates with collomorph textures or as white coarse-grained, euhedral aggregates with dog-tooth textures.

This late-stage epithermal event caused the recrystallization of earlier pyrite phases. The recrystallization event has been dated at ca. 45000 years using the $^{230}\text{Th}/^{234}\text{U}$ method on pyrite (Müller et al., 2002b). This mineralization style appears to be structurally controlled by the north-trending Letomazien faults in the deeper parts of the Minifie ore body (Corbett et al., 2001).

Geochemical characteristics and petrography of Conical Seamount compared to Lihir Island

Methods

Major and trace elements were analyzed at the Geological Survey of Canada, Freiberg University of Mining and Technology, and commercially at ACTLABS Ltd. (Canada) using a combination of XRF, ICP-ES, ICP-MS, and Instrumental Neutron Activation. Determination of ferric iron was performed by *Rudolf Naumann* at the GFZ Potsdam using the Wilson method. Mineral analyses were performed at the University of Freiberg (Germany) using a JEOL JXA-8900R electron microprobe with five spectrometers. Major and minor elements were determined at 15 kV acceleration voltage and a beam current of 20 nA with counting times of 20–30 s depending on the element. The standard sets of the Smithsonian Institute (cf. *Jarosewich et al.*, 1980) and of MACTM were used for reference. Selected microprobe analyses of the representative minerals and magmatic glass are listed in Tables 2–8. The entire dataset is available from the second author on request.

Whole-rock geochemistry and magmatic evolution

Whole-rock major and trace element data for selected samples from Conical Seamount are presented in Table 1. Geochemically, the alkaline rocks from Conical Seamount are characterized by relatively primitive compositions, as reflected by elevated MgO contents (up to 6.71 wt%), and high concentrations of the

Table 1. Major and trace element whole-rock analyses of representative volcanic rocks and magmatic glass from Conical Seamount with calculation of normative nepheline (ne%) according to the CIPW norm. Abbreviations: TB trachybasalt; TA trachyandesite; P phonolite; BTA basaltic trachyandesite; glass volcanic glass; b.d. below detection limit; n.a. not analysed. The samples were dredged during Sonne cruise SO133 in 1998. Ferric iron determined using the Wilson method except marked samples (*), for which a ferric iron content of 40% of total iron was assumed

Sample no.	07-2G	07-2G*	12-3A	12-3A*	13-4A	13-5B	13-5D	13-8A	15-2A	24*	24-1A	26-core	46-1A	47-1A	50-1C	50-1C	50-1C*	42-1C*	42-1E*	68-1A*	68-1C*																																																																																																																																																																																																																																																																																																																																																																																																																																																																																																																																																																																																																									
Rock type	TB	glass	TB	glass	TB	BTA	BTA	BTA	TB	TB	TB	TB	TB	TB	TB	TB	glass	TB	TB	TB	TB	TB																																																																																																																																																																																																																																																																																																																																																																																																																																																																																																																																																																																																																								
wt.-%																								SiO ₂	48.41	56.17	48.12	56.40	47.31	50.04	49.03	49.04	48.60	47.10	46.59	47.32	47.26	47.91	47.75	54.46	47.30	46.60	47.50	46.80			TiO ₂	0.76	0.44	0.75	0.42	0.75	0.76	0.76	0.75	0.83	0.80	0.76	0.74	0.73	0.74	0.73	0.41	0.77	0.78	0.74	0.76			Al ₂ O ₃	15.21	20.20	15.12	21.22	15.95	16.71	17.55	16.65	16.55	15.81	15.34	15.58	14.78	14.92	15.07	20.65	15.50	15.40	14.90	14.90			Fe ₂ O ₃	2.87	2.44	4.33	2.14	4.99	1.45	1.84	1.74	5.03	4.20	3.59	5.00	4.92	2.90	4.24	2.46	4.40	4.28	4.28	4.32			FeO	6.37	3.29	5.13	2.89	4.80	3.91	3.53	3.74	3.90	5.67	6.14	4.54	5.11	6.95	5.57	3.32	5.94	5.78	5.78	5.83			MnO	0.21	0.13	0.20	0.12	0.20	0.14	0.14	0.13	0.15	0.17	0.15	0.17	0.18	0.20	0.18	0.13	0.38	0.26	0.18	0.19			MgO	6.71	1.62	6.56	1.95	5.59	5.16	5.26	5.03	4.83	5.11	4.80	5.35	6.27	6.51	6.34	1.22	6.11	5.92	6.59	6.40			CaO	12.53	4.03	11.86	2.10	11.12	11.66	10.89	11.05	11.36	11.33	11.19	11.08	11.60	11.89	11.63	2.29	11.00	10.80	11.40	11.20			Na ₂ O	2.80	3.88	2.78	4.17	2.92	2.49	3.21	2.81	2.75	2.46	2.62	2.24	2.46	2.53	2.82	5.25	3.01	3.11	2.63	2.77			K ₂ O	2.85	6.47	2.77	7.90	3.28	3.10	2.91	3.30	2.77	2.40	2.31	3.31	2.93	2.98	3.03	8.16	2.70	2.81	2.76	3.00			P ₂ O ₅	0.40	b.d.	0.39	b.d.	0.55	0.55	0.61	0.57	0.45	0.46	0.43	0.42	0.39	0.40	0.38	b.d.	0.41	0.40	0.41	0.39			L.O.I.	0.60	b.d.	1.20	b.d.	1.41	2.90	3.17	3.55	1.95	3.84	3.60	2.98	1.28	1.10	1.05	b.d.	1.70	1.80	1.50	1.40			Total	99.72	98.66	99.21	99.32	98.87	98.87	98.90	98.36	99.17	99.36	97.52	98.73	97.91	99.03	98.79	98.35	99.22	97.94	98.67	97.96			ne%	8.5	2.0	6.1	5.6	7.4	1.9	5.3	4.4	2.4	1.8	2.8	2.9	4.7	6.8	7.5	16.2	6.7	8.0	5.2	7.4			mg*	71	53	75	61	73	75	77	76	74	67	64	73	74	68	72	46	70	70	72	72			ppm																								Ba	220	n.a.	240	n.a.	280	320	310	310	300	250	260	220	190	250	210	n.a.	280	250	230	260			Cu	99	n.a.	122	n.a.	215	132	105	151	127	139	150	138	114	134	105	n.a.	105	87	58	121			Co	42	n.a.	40	n.a.	34	30	23	29	33	40	37	40	34	38	37	n.a.	43	30	30	32			Hf	1.5	n.a.	1.7	n.a.	n.a.	2.0	2.1	2.0	n.a.	1.6	1.5	1.5	n.a.	n.a.	1.4	n.a.	n.a.	n.a.	n.a.	n.a.			Nb	1.3	n.a.	1.5	n.a.	n.a.	1.7	1.7	1.7	n.a.	1.5	1.5	1.4	n.a.	n.a.	1.3	n.a.	n.a.	n.a.	n.a.	n.a.			Ni	32	n.a.	33	n.a.	18	18	16	20	20	29	29	29	27	42	33	n.a.	35	25	32	27			Rb	63	n.a.	49	n.a.	55	46	45	50	60	55	51	51	56	59	60	n.a.	60	56	54	65			Sc	41	n.a.	40	n.a.	n.a.	35	35	35	n.a.	39	37	39	n.a.	n.a.	41	n.a.	35	34	39	39			Sr	910	n.a.	970	n.a.	1500	1460	1540	1470	1400	1230	1200	1050	1060	1030	940	n.a.	950	950	930	910			Ta	0.09	n.a.	0.10	n.a.	n.a.	0.11	0.11	0.11	n.a.	0.09	0.10	0.09	n.a.	n.a.	0.09	n.a.	n.a.	n.a.	n.a.	n.a.		
SiO ₂	48.41	56.17	48.12	56.40	47.31	50.04	49.03	49.04	48.60	47.10	46.59	47.32	47.26	47.91	47.75	54.46	47.30	46.60	47.50	46.80			TiO ₂	0.76	0.44	0.75	0.42	0.75	0.76	0.76	0.75	0.83	0.80	0.76	0.74	0.73	0.74	0.73	0.41	0.77	0.78	0.74	0.76			Al ₂ O ₃	15.21	20.20	15.12	21.22	15.95	16.71	17.55	16.65	16.55	15.81	15.34	15.58	14.78	14.92	15.07	20.65	15.50	15.40	14.90	14.90			Fe ₂ O ₃	2.87	2.44	4.33	2.14	4.99	1.45	1.84	1.74	5.03	4.20	3.59	5.00	4.92	2.90	4.24	2.46	4.40	4.28	4.28	4.32			FeO	6.37	3.29	5.13	2.89	4.80	3.91	3.53	3.74	3.90	5.67	6.14	4.54	5.11	6.95	5.57	3.32	5.94	5.78	5.78	5.83			MnO	0.21	0.13	0.20	0.12	0.20	0.14	0.14	0.13	0.15	0.17	0.15	0.17	0.18	0.20	0.18	0.13	0.38	0.26	0.18	0.19			MgO	6.71	1.62	6.56	1.95	5.59	5.16	5.26	5.03	4.83	5.11	4.80	5.35	6.27	6.51	6.34	1.22	6.11	5.92	6.59	6.40			CaO	12.53	4.03	11.86	2.10	11.12	11.66	10.89	11.05	11.36	11.33	11.19	11.08	11.60	11.89	11.63	2.29	11.00	10.80	11.40	11.20			Na ₂ O	2.80	3.88	2.78	4.17	2.92	2.49	3.21	2.81	2.75	2.46	2.62	2.24	2.46	2.53	2.82	5.25	3.01	3.11	2.63	2.77			K ₂ O	2.85	6.47	2.77	7.90	3.28	3.10	2.91	3.30	2.77	2.40	2.31	3.31	2.93	2.98	3.03	8.16	2.70	2.81	2.76	3.00			P ₂ O ₅	0.40	b.d.	0.39	b.d.	0.55	0.55	0.61	0.57	0.45	0.46	0.43	0.42	0.39	0.40	0.38	b.d.	0.41	0.40	0.41	0.39			L.O.I.	0.60	b.d.	1.20	b.d.	1.41	2.90	3.17	3.55	1.95	3.84	3.60	2.98	1.28	1.10	1.05	b.d.	1.70	1.80	1.50	1.40			Total	99.72	98.66	99.21	99.32	98.87	98.87	98.90	98.36	99.17	99.36	97.52	98.73	97.91	99.03	98.79	98.35	99.22	97.94	98.67	97.96			ne%	8.5	2.0	6.1	5.6	7.4	1.9	5.3	4.4	2.4	1.8	2.8	2.9	4.7	6.8	7.5	16.2	6.7	8.0	5.2	7.4			mg*	71	53	75	61	73	75	77	76	74	67	64	73	74	68	72	46	70	70	72	72			ppm																								Ba	220	n.a.	240	n.a.	280	320	310	310	300	250	260	220	190	250	210	n.a.	280	250	230	260			Cu	99	n.a.	122	n.a.	215	132	105	151	127	139	150	138	114	134	105	n.a.	105	87	58	121			Co	42	n.a.	40	n.a.	34	30	23	29	33	40	37	40	34	38	37	n.a.	43	30	30	32			Hf	1.5	n.a.	1.7	n.a.	n.a.	2.0	2.1	2.0	n.a.	1.6	1.5	1.5	n.a.	n.a.	1.4	n.a.	n.a.	n.a.	n.a.	n.a.			Nb	1.3	n.a.	1.5	n.a.	n.a.	1.7	1.7	1.7	n.a.	1.5	1.5	1.4	n.a.	n.a.	1.3	n.a.	n.a.	n.a.	n.a.	n.a.			Ni	32	n.a.	33	n.a.	18	18	16	20	20	29	29	29	27	42	33	n.a.	35	25	32	27			Rb	63	n.a.	49	n.a.	55	46	45	50	60	55	51	51	56	59	60	n.a.	60	56	54	65			Sc	41	n.a.	40	n.a.	n.a.	35	35	35	n.a.	39	37	39	n.a.	n.a.	41	n.a.	35	34	39	39			Sr	910	n.a.	970	n.a.	1500	1460	1540	1470	1400	1230	1200	1050	1060	1030	940	n.a.	950	950	930	910			Ta	0.09	n.a.	0.10	n.a.	n.a.	0.11	0.11	0.11	n.a.	0.09	0.10	0.09	n.a.	n.a.	0.09	n.a.	n.a.	n.a.	n.a.	n.a.																										
TiO ₂	0.76	0.44	0.75	0.42	0.75	0.76	0.76	0.75	0.83	0.80	0.76	0.74	0.73	0.74	0.73	0.41	0.77	0.78	0.74	0.76			Al ₂ O ₃	15.21	20.20	15.12	21.22	15.95	16.71	17.55	16.65	16.55	15.81	15.34	15.58	14.78	14.92	15.07	20.65	15.50	15.40	14.90	14.90			Fe ₂ O ₃	2.87	2.44	4.33	2.14	4.99	1.45	1.84	1.74	5.03	4.20	3.59	5.00	4.92	2.90	4.24	2.46	4.40	4.28	4.28	4.32			FeO	6.37	3.29	5.13	2.89	4.80	3.91	3.53	3.74	3.90	5.67	6.14	4.54	5.11	6.95	5.57	3.32	5.94	5.78	5.78	5.83			MnO	0.21	0.13	0.20	0.12	0.20	0.14	0.14	0.13	0.15	0.17	0.15	0.17	0.18	0.20	0.18	0.13	0.38	0.26	0.18	0.19			MgO	6.71	1.62	6.56	1.95	5.59	5.16	5.26	5.03	4.83	5.11	4.80	5.35	6.27	6.51	6.34	1.22	6.11	5.92	6.59	6.40			CaO	12.53	4.03	11.86	2.10	11.12	11.66	10.89	11.05	11.36	11.33	11.19	11.08	11.60	11.89	11.63	2.29	11.00	10.80	11.40	11.20			Na ₂ O	2.80	3.88	2.78	4.17	2.92	2.49	3.21	2.81	2.75	2.46	2.62	2.24	2.46	2.53	2.82	5.25	3.01	3.11	2.63	2.77			K ₂ O	2.85	6.47	2.77	7.90	3.28	3.10	2.91	3.30	2.77	2.40	2.31	3.31	2.93	2.98	3.03	8.16	2.70	2.81	2.76	3.00			P ₂ O ₅	0.40	b.d.	0.39	b.d.	0.55	0.55	0.61	0.57	0.45	0.46	0.43	0.42	0.39	0.40	0.38	b.d.	0.41	0.40	0.41	0.39			L.O.I.	0.60	b.d.	1.20	b.d.	1.41	2.90	3.17	3.55	1.95	3.84	3.60	2.98	1.28	1.10	1.05	b.d.	1.70	1.80	1.50	1.40			Total	99.72	98.66	99.21	99.32	98.87	98.87	98.90	98.36	99.17	99.36	97.52	98.73	97.91	99.03	98.79	98.35	99.22	97.94	98.67	97.96			ne%	8.5	2.0	6.1	5.6	7.4	1.9	5.3	4.4	2.4	1.8	2.8	2.9	4.7	6.8	7.5	16.2	6.7	8.0	5.2	7.4			mg*	71	53	75	61	73	75	77	76	74	67	64	73	74	68	72	46	70	70	72	72			ppm																								Ba	220	n.a.	240	n.a.	280	320	310	310	300	250	260	220	190	250	210	n.a.	280	250	230	260			Cu	99	n.a.	122	n.a.	215	132	105	151	127	139	150	138	114	134	105	n.a.	105	87	58	121			Co	42	n.a.	40	n.a.	34	30	23	29	33	40	37	40	34	38	37	n.a.	43	30	30	32			Hf	1.5	n.a.	1.7	n.a.	n.a.	2.0	2.1	2.0	n.a.	1.6	1.5	1.5	n.a.	n.a.	1.4	n.a.	n.a.	n.a.	n.a.	n.a.			Nb	1.3	n.a.	1.5	n.a.	n.a.	1.7	1.7	1.7	n.a.	1.5	1.5	1.4	n.a.	n.a.	1.3	n.a.	n.a.	n.a.	n.a.	n.a.			Ni	32	n.a.	33	n.a.	18	18	16	20	20	29	29	29	27	42	33	n.a.	35	25	32	27			Rb	63	n.a.	49	n.a.	55	46	45	50	60	55	51	51	56	59	60	n.a.	60	56	54	65			Sc	41	n.a.	40	n.a.	n.a.	35	35	35	n.a.	39	37	39	n.a.	n.a.	41	n.a.	35	34	39	39			Sr	910	n.a.	970	n.a.	1500	1460	1540	1470	1400	1230	1200	1050	1060	1030	940	n.a.	950	950	930	910			Ta	0.09	n.a.	0.10	n.a.	n.a.	0.11	0.11	0.11	n.a.	0.09	0.10	0.09	n.a.	n.a.	0.09	n.a.	n.a.	n.a.	n.a.	n.a.																																																	
Al ₂ O ₃	15.21	20.20	15.12	21.22	15.95	16.71	17.55	16.65	16.55	15.81	15.34	15.58	14.78	14.92	15.07	20.65	15.50	15.40	14.90	14.90			Fe ₂ O ₃	2.87	2.44	4.33	2.14	4.99	1.45	1.84	1.74	5.03	4.20	3.59	5.00	4.92	2.90	4.24	2.46	4.40	4.28	4.28	4.32			FeO	6.37	3.29	5.13	2.89	4.80	3.91	3.53	3.74	3.90	5.67	6.14	4.54	5.11	6.95	5.57	3.32	5.94	5.78	5.78	5.83			MnO	0.21	0.13	0.20	0.12	0.20	0.14	0.14	0.13	0.15	0.17	0.15	0.17	0.18	0.20	0.18	0.13	0.38	0.26	0.18	0.19			MgO	6.71	1.62	6.56	1.95	5.59	5.16	5.26	5.03	4.83	5.11	4.80	5.35	6.27	6.51	6.34	1.22	6.11	5.92	6.59	6.40			CaO	12.53	4.03	11.86	2.10	11.12	11.66	10.89	11.05	11.36	11.33	11.19	11.08	11.60	11.89	11.63	2.29	11.00	10.80	11.40	11.20			Na ₂ O	2.80	3.88	2.78	4.17	2.92	2.49	3.21	2.81	2.75	2.46	2.62	2.24	2.46	2.53	2.82	5.25	3.01	3.11	2.63	2.77			K ₂ O	2.85	6.47	2.77	7.90	3.28	3.10	2.91	3.30	2.77	2.40	2.31	3.31	2.93	2.98	3.03	8.16	2.70	2.81	2.76	3.00			P ₂ O ₅	0.40	b.d.	0.39	b.d.	0.55	0.55	0.61	0.57	0.45	0.46	0.43	0.42	0.39	0.40	0.38	b.d.	0.41	0.40	0.41	0.39			L.O.I.	0.60	b.d.	1.20	b.d.	1.41	2.90	3.17	3.55	1.95	3.84	3.60	2.98	1.28	1.10	1.05	b.d.	1.70	1.80	1.50	1.40			Total	99.72	98.66	99.21	99.32	98.87	98.87	98.90	98.36	99.17	99.36	97.52	98.73	97.91	99.03	98.79	98.35	99.22	97.94	98.67	97.96			ne%	8.5	2.0	6.1	5.6	7.4	1.9	5.3	4.4	2.4	1.8	2.8	2.9	4.7	6.8	7.5	16.2	6.7	8.0	5.2	7.4			mg*	71	53	75	61	73	75	77	76	74	67	64	73	74	68	72	46	70	70	72	72			ppm																								Ba	220	n.a.	240	n.a.	280	320	310	310	300	250	260	220	190	250	210	n.a.	280	250	230	260			Cu	99	n.a.	122	n.a.	215	132	105	151	127	139	150	138	114	134	105	n.a.	105	87	58	121			Co	42	n.a.	40	n.a.	34	30	23	29	33	40	37	40	34	38	37	n.a.	43	30	30	32			Hf	1.5	n.a.	1.7	n.a.	n.a.	2.0	2.1	2.0	n.a.	1.6	1.5	1.5	n.a.	n.a.	1.4	n.a.	n.a.	n.a.	n.a.	n.a.			Nb	1.3	n.a.	1.5	n.a.	n.a.	1.7	1.7	1.7	n.a.	1.5	1.5	1.4	n.a.	n.a.	1.3	n.a.	n.a.	n.a.	n.a.	n.a.			Ni	32	n.a.	33	n.a.	18	18	16	20	20	29	29	29	27	42	33	n.a.	35	25	32	27			Rb	63	n.a.	49	n.a.	55	46	45	50	60	55	51	51	56	59	60	n.a.	60	56	54	65			Sc	41	n.a.	40	n.a.	n.a.	35	35	35	n.a.	39	37	39	n.a.	n.a.	41	n.a.	35	34	39	39			Sr	910	n.a.	970	n.a.	1500	1460	1540	1470	1400	1230	1200	1050	1060	1030	940	n.a.	950	950	930	910			Ta	0.09	n.a.	0.10	n.a.	n.a.	0.11	0.11	0.11	n.a.	0.09	0.10	0.09	n.a.	n.a.	0.09	n.a.	n.a.	n.a.	n.a.	n.a.																																																																								
Fe ₂ O ₃	2.87	2.44	4.33	2.14	4.99	1.45	1.84	1.74	5.03	4.20	3.59	5.00	4.92	2.90	4.24	2.46	4.40	4.28	4.28	4.32			FeO	6.37	3.29	5.13	2.89	4.80	3.91	3.53	3.74	3.90	5.67	6.14	4.54	5.11	6.95	5.57	3.32	5.94	5.78	5.78	5.83			MnO	0.21	0.13	0.20	0.12	0.20	0.14	0.14	0.13	0.15	0.17	0.15	0.17	0.18	0.20	0.18	0.13	0.38	0.26	0.18	0.19			MgO	6.71	1.62	6.56	1.95	5.59	5.16	5.26	5.03	4.83	5.11	4.80	5.35	6.27	6.51	6.34	1.22	6.11	5.92	6.59	6.40			CaO	12.53	4.03	11.86	2.10	11.12	11.66	10.89	11.05	11.36	11.33	11.19	11.08	11.60	11.89	11.63	2.29	11.00	10.80	11.40	11.20			Na ₂ O	2.80	3.88	2.78	4.17	2.92	2.49	3.21	2.81	2.75	2.46	2.62	2.24	2.46	2.53	2.82	5.25	3.01	3.11	2.63	2.77			K ₂ O	2.85	6.47	2.77	7.90	3.28	3.10	2.91	3.30	2.77	2.40	2.31	3.31	2.93	2.98	3.03	8.16	2.70	2.81	2.76	3.00			P ₂ O ₅	0.40	b.d.	0.39	b.d.	0.55	0.55	0.61	0.57	0.45	0.46	0.43	0.42	0.39	0.40	0.38	b.d.	0.41	0.40	0.41	0.39			L.O.I.	0.60	b.d.	1.20	b.d.	1.41	2.90	3.17	3.55	1.95	3.84	3.60	2.98	1.28	1.10	1.05	b.d.	1.70	1.80	1.50	1.40			Total	99.72	98.66	99.21	99.32	98.87	98.87	98.90	98.36	99.17	99.36	97.52	98.73	97.91	99.03	98.79	98.35	99.22	97.94	98.67	97.96			ne%	8.5	2.0	6.1	5.6	7.4	1.9	5.3	4.4	2.4	1.8	2.8	2.9	4.7	6.8	7.5	16.2	6.7	8.0	5.2	7.4			mg*	71	53	75	61	73	75	77	76	74	67	64	73	74	68	72	46	70	70	72	72			ppm																								Ba	220	n.a.	240	n.a.	280	320	310	310	300	250	260	220	190	250	210	n.a.	280	250	230	260			Cu	99	n.a.	122	n.a.	215	132	105	151	127	139	150	138	114	134	105	n.a.	105	87	58	121			Co	42	n.a.	40	n.a.	34	30	23	29	33	40	37	40	34	38	37	n.a.	43	30	30	32			Hf	1.5	n.a.	1.7	n.a.	n.a.	2.0	2.1	2.0	n.a.	1.6	1.5	1.5	n.a.	n.a.	1.4	n.a.	n.a.	n.a.	n.a.	n.a.			Nb	1.3	n.a.	1.5	n.a.	n.a.	1.7	1.7	1.7	n.a.	1.5	1.5	1.4	n.a.	n.a.	1.3	n.a.	n.a.	n.a.	n.a.	n.a.			Ni	32	n.a.	33	n.a.	18	18	16	20	20	29	29	29	27	42	33	n.a.	35	25	32	27			Rb	63	n.a.	49	n.a.	55	46	45	50	60	55	51	51	56	59	60	n.a.	60	56	54	65			Sc	41	n.a.	40	n.a.	n.a.	35	35	35	n.a.	39	37	39	n.a.	n.a.	41	n.a.	35	34	39	39			Sr	910	n.a.	970	n.a.	1500	1460	1540	1470	1400	1230	1200	1050	1060	1030	940	n.a.	950	950	930	910			Ta	0.09	n.a.	0.10	n.a.	n.a.	0.11	0.11	0.11	n.a.	0.09	0.10	0.09	n.a.	n.a.	0.09	n.a.	n.a.	n.a.	n.a.	n.a.																																																																																															
FeO	6.37	3.29	5.13	2.89	4.80	3.91	3.53	3.74	3.90	5.67	6.14	4.54	5.11	6.95	5.57	3.32	5.94	5.78	5.78	5.83			MnO	0.21	0.13	0.20	0.12	0.20	0.14	0.14	0.13	0.15	0.17	0.15	0.17	0.18	0.20	0.18	0.13	0.38	0.26	0.18	0.19			MgO	6.71	1.62	6.56	1.95	5.59	5.16	5.26	5.03	4.83	5.11	4.80	5.35	6.27	6.51	6.34	1.22	6.11	5.92	6.59	6.40			CaO	12.53	4.03	11.86	2.10	11.12	11.66	10.89	11.05	11.36	11.33	11.19	11.08	11.60	11.89	11.63	2.29	11.00	10.80	11.40	11.20			Na ₂ O	2.80	3.88	2.78	4.17	2.92	2.49	3.21	2.81	2.75	2.46	2.62	2.24	2.46	2.53	2.82	5.25	3.01	3.11	2.63	2.77			K ₂ O	2.85	6.47	2.77	7.90	3.28	3.10	2.91	3.30	2.77	2.40	2.31	3.31	2.93	2.98	3.03	8.16	2.70	2.81	2.76	3.00			P ₂ O ₅	0.40	b.d.	0.39	b.d.	0.55	0.55	0.61	0.57	0.45	0.46	0.43	0.42	0.39	0.40	0.38	b.d.	0.41	0.40	0.41	0.39			L.O.I.	0.60	b.d.	1.20	b.d.	1.41	2.90	3.17	3.55	1.95	3.84	3.60	2.98	1.28	1.10	1.05	b.d.	1.70	1.80	1.50	1.40			Total	99.72	98.66	99.21	99.32	98.87	98.87	98.90	98.36	99.17	99.36	97.52	98.73	97.91	99.03	98.79	98.35	99.22	97.94	98.67	97.96			ne%	8.5	2.0	6.1	5.6	7.4	1.9	5.3	4.4	2.4	1.8	2.8	2.9	4.7	6.8	7.5	16.2	6.7	8.0	5.2	7.4			mg*	71	53	75	61	73	75	77	76	74	67	64	73	74	68	72	46	70	70	72	72			ppm																								Ba	220	n.a.	240	n.a.	280	320	310	310	300	250	260	220	190	250	210	n.a.	280	250	230	260			Cu	99	n.a.	122	n.a.	215	132	105	151	127	139	150	138	114	134	105	n.a.	105	87	58	121			Co	42	n.a.	40	n.a.	34	30	23	29	33	40	37	40	34	38	37	n.a.	43	30	30	32			Hf	1.5	n.a.	1.7	n.a.	n.a.	2.0	2.1	2.0	n.a.	1.6	1.5	1.5	n.a.	n.a.	1.4	n.a.	n.a.	n.a.	n.a.	n.a.			Nb	1.3	n.a.	1.5	n.a.	n.a.	1.7	1.7	1.7	n.a.	1.5	1.5	1.4	n.a.	n.a.	1.3	n.a.	n.a.	n.a.	n.a.	n.a.			Ni	32	n.a.	33	n.a.	18	18	16	20	20	29	29	29	27	42	33	n.a.	35	25	32	27			Rb	63	n.a.	49	n.a.	55	46	45	50	60	55	51	51	56	59	60	n.a.	60	56	54	65			Sc	41	n.a.	40	n.a.	n.a.	35	35	35	n.a.	39	37	39	n.a.	n.a.	41	n.a.	35	34	39	39			Sr	910	n.a.	970	n.a.	1500	1460	1540	1470	1400	1230	1200	1050	1060	1030	940	n.a.	950	950	930	910			Ta	0.09	n.a.	0.10	n.a.	n.a.	0.11	0.11	0.11	n.a.	0.09	0.10	0.09	n.a.	n.a.	0.09	n.a.	n.a.	n.a.	n.a.	n.a.																																																																																																																						
MnO	0.21	0.13	0.20	0.12	0.20	0.14	0.14	0.13	0.15	0.17	0.15	0.17	0.18	0.20	0.18	0.13	0.38	0.26	0.18	0.19			MgO	6.71	1.62	6.56	1.95	5.59	5.16	5.26	5.03	4.83	5.11	4.80	5.35	6.27	6.51	6.34	1.22	6.11	5.92	6.59	6.40			CaO	12.53	4.03	11.86	2.10	11.12	11.66	10.89	11.05	11.36	11.33	11.19	11.08	11.60	11.89	11.63	2.29	11.00	10.80	11.40	11.20			Na ₂ O	2.80	3.88	2.78	4.17	2.92	2.49	3.21	2.81	2.75	2.46	2.62	2.24	2.46	2.53	2.82	5.25	3.01	3.11	2.63	2.77			K ₂ O	2.85	6.47	2.77	7.90	3.28	3.10	2.91	3.30	2.77	2.40	2.31	3.31	2.93	2.98	3.03	8.16	2.70	2.81	2.76	3.00			P ₂ O ₅	0.40	b.d.	0.39	b.d.	0.55	0.55	0.61	0.57	0.45	0.46	0.43	0.42	0.39	0.40	0.38	b.d.	0.41	0.40	0.41	0.39			L.O.I.	0.60	b.d.	1.20	b.d.	1.41	2.90	3.17	3.55	1.95	3.84	3.60	2.98	1.28	1.10	1.05	b.d.	1.70	1.80	1.50	1.40			Total	99.72	98.66	99.21	99.32	98.87	98.87	98.90	98.36	99.17	99.36	97.52	98.73	97.91	99.03	98.79	98.35	99.22	97.94	98.67	97.96			ne%	8.5	2.0	6.1	5.6	7.4	1.9	5.3	4.4	2.4	1.8	2.8	2.9	4.7	6.8	7.5	16.2	6.7	8.0	5.2	7.4			mg*	71	53	75	61	73	75	77	76	74	67	64	73	74	68	72	46	70	70	72	72			ppm																								Ba	220	n.a.	240	n.a.	280	320	310	310	300	250	260	220	190	250	210	n.a.	280	250	230	260			Cu	99	n.a.	122	n.a.	215	132	105	151	127	139	150	138	114	134	105	n.a.	105	87	58	121			Co	42	n.a.	40	n.a.	34	30	23	29	33	40	37	40	34	38	37	n.a.	43	30	30	32			Hf	1.5	n.a.	1.7	n.a.	n.a.	2.0	2.1	2.0	n.a.	1.6	1.5	1.5	n.a.	n.a.	1.4	n.a.	n.a.	n.a.	n.a.	n.a.			Nb	1.3	n.a.	1.5	n.a.	n.a.	1.7	1.7	1.7	n.a.	1.5	1.5	1.4	n.a.	n.a.	1.3	n.a.	n.a.	n.a.	n.a.	n.a.			Ni	32	n.a.	33	n.a.	18	18	16	20	20	29	29	29	27	42	33	n.a.	35	25	32	27			Rb	63	n.a.	49	n.a.	55	46	45	50	60	55	51	51	56	59	60	n.a.	60	56	54	65			Sc	41	n.a.	40	n.a.	n.a.	35	35	35	n.a.	39	37	39	n.a.	n.a.	41	n.a.	35	34	39	39			Sr	910	n.a.	970	n.a.	1500	1460	1540	1470	1400	1230	1200	1050	1060	1030	940	n.a.	950	950	930	910			Ta	0.09	n.a.	0.10	n.a.	n.a.	0.11	0.11	0.11	n.a.	0.09	0.10	0.09	n.a.	n.a.	0.09	n.a.	n.a.	n.a.	n.a.	n.a.																																																																																																																																													
MgO	6.71	1.62	6.56	1.95	5.59	5.16	5.26	5.03	4.83	5.11	4.80	5.35	6.27	6.51	6.34	1.22	6.11	5.92	6.59	6.40			CaO	12.53	4.03	11.86	2.10	11.12	11.66	10.89	11.05	11.36	11.33	11.19	11.08	11.60	11.89	11.63	2.29	11.00	10.80	11.40	11.20			Na ₂ O	2.80	3.88	2.78	4.17	2.92	2.49	3.21	2.81	2.75	2.46	2.62	2.24	2.46	2.53	2.82	5.25	3.01	3.11	2.63	2.77			K ₂ O	2.85	6.47	2.77	7.90	3.28	3.10	2.91	3.30	2.77	2.40	2.31	3.31	2.93	2.98	3.03	8.16	2.70	2.81	2.76	3.00			P ₂ O ₅	0.40	b.d.	0.39	b.d.	0.55	0.55	0.61	0.57	0.45	0.46	0.43	0.42	0.39	0.40	0.38	b.d.	0.41	0.40	0.41	0.39			L.O.I.	0.60	b.d.	1.20	b.d.	1.41	2.90	3.17	3.55	1.95	3.84	3.60	2.98	1.28	1.10	1.05	b.d.	1.70	1.80	1.50	1.40			Total	99.72	98.66	99.21	99.32	98.87	98.87	98.90	98.36	99.17	99.36	97.52	98.73	97.91	99.03	98.79	98.35	99.22	97.94	98.67	97.96			ne%	8.5	2.0	6.1	5.6	7.4	1.9	5.3	4.4	2.4	1.8	2.8	2.9	4.7	6.8	7.5	16.2	6.7	8.0	5.2	7.4			mg*	71	53	75	61	73	75	77	76	74	67	64	73	74	68	72	46	70	70	72	72			ppm																								Ba	220	n.a.	240	n.a.	280	320	310	310	300	250	260	220	190	250	210	n.a.	280	250	230	260			Cu	99	n.a.	122	n.a.	215	132	105	151	127	139	150	138	114	134	105	n.a.	105	87	58	121			Co	42	n.a.	40	n.a.	34	30	23	29	33	40	37	40	34	38	37	n.a.	43	30	30	32			Hf	1.5	n.a.	1.7	n.a.	n.a.	2.0	2.1	2.0	n.a.	1.6	1.5	1.5	n.a.	n.a.	1.4	n.a.	n.a.	n.a.	n.a.	n.a.			Nb	1.3	n.a.	1.5	n.a.	n.a.	1.7	1.7	1.7	n.a.	1.5	1.5	1.4	n.a.	n.a.	1.3	n.a.	n.a.	n.a.	n.a.	n.a.			Ni	32	n.a.	33	n.a.	18	18	16	20	20	29	29	29	27	42	33	n.a.	35	25	32	27			Rb	63	n.a.	49	n.a.	55	46	45	50	60	55	51	51	56	59	60	n.a.	60	56	54	65			Sc	41	n.a.	40	n.a.	n.a.	35	35	35	n.a.	39	37	39	n.a.	n.a.	41	n.a.	35	34	39	39			Sr	910	n.a.	970	n.a.	1500	1460	1540	1470	1400	1230	1200	1050	1060	1030	940	n.a.	950	950	930	910			Ta	0.09	n.a.	0.10	n.a.	n.a.	0.11	0.11	0.11	n.a.	0.09	0.10	0.09	n.a.	n.a.	0.09	n.a.	n.a.	n.a.	n.a.	n.a.																																																																																																																																																																				
CaO	12.53	4.03	11.86	2.10	11.12	11.66	10.89	11.05	11.36	11.33	11.19	11.08	11.60	11.89	11.63	2.29	11.00	10.80	11.40	11.20			Na ₂ O	2.80	3.88	2.78	4.17	2.92	2.49	3.21	2.81	2.75	2.46	2.62	2.24	2.46	2.53	2.82	5.25	3.01	3.11	2.63	2.77			K ₂ O	2.85	6.47	2.77	7.90	3.28	3.10	2.91	3.30	2.77	2.40	2.31	3.31	2.93	2.98	3.03	8.16	2.70	2.81	2.76	3.00			P ₂ O ₅	0.40	b.d.	0.39	b.d.	0.55	0.55	0.61	0.57	0.45	0.46	0.43	0.42	0.39	0.40	0.38	b.d.	0.41	0.40	0.41	0.39			L.O.I.	0.60	b.d.	1.20	b.d.	1.41	2.90	3.17	3.55	1.95	3.84	3.60	2.98	1.28	1.10	1.05	b.d.	1.70	1.80	1.50	1.40			Total	99.72	98.66	99.21	99.32	98.87	98.87	98.90	98.36	99.17	99.36	97.52	98.73	97.91	99.03	98.79	98.35	99.22	97.94	98.67	97.96			ne%	8.5	2.0	6.1	5.6	7.4	1.9	5.3	4.4	2.4	1.8	2.8	2.9	4.7	6.8	7.5	16.2	6.7	8.0	5.2	7.4			mg*	71	53	75	61	73	75	77	76	74	67	64	73	74	68	72	46	70	70	72	72			ppm																								Ba	220	n.a.	240	n.a.	280	320	310	310	300	250	260	220	190	250	210	n.a.	280	250	230	260			Cu	99	n.a.	122	n.a.	215	132	105	151	127	139	150	138	114	134	105	n.a.	105	87	58	121			Co	42	n.a.	40	n.a.	34	30	23	29	33	40	37	40	34	38	37	n.a.	43	30	30	32			Hf	1.5	n.a.	1.7	n.a.	n.a.	2.0	2.1	2.0	n.a.	1.6	1.5	1.5	n.a.	n.a.	1.4	n.a.	n.a.	n.a.	n.a.	n.a.			Nb	1.3	n.a.	1.5	n.a.	n.a.	1.7	1.7	1.7	n.a.	1.5	1.5	1.4	n.a.	n.a.	1.3	n.a.	n.a.	n.a.	n.a.	n.a.			Ni	32	n.a.	33	n.a.	18	18	16	20	20	29	29	29	27	42	33	n.a.	35	25	32	27			Rb	63	n.a.	49	n.a.	55	46	45	50	60	55	51	51	56	59	60	n.a.	60	56	54	65			Sc	41	n.a.	40	n.a.	n.a.	35	35	35	n.a.	39	37	39	n.a.	n.a.	41	n.a.	35	34	39	39			Sr	910	n.a.	970	n.a.	1500	1460	1540	1470	1400	1230	1200	1050	1060	1030	940	n.a.	950	950	930	910			Ta	0.09	n.a.	0.10	n.a.	n.a.	0.11	0.11	0.11	n.a.	0.09	0.10	0.09	n.a.	n.a.	0.09	n.a.	n.a.	n.a.	n.a.	n.a.																																																																																																																																																																																											
Na ₂ O	2.80	3.88	2.78	4.17	2.92	2.49	3.21	2.81	2.75	2.46	2.62	2.24	2.46	2.53	2.82	5.25	3.01	3.11	2.63	2.77			K ₂ O	2.85	6.47	2.77	7.90	3.28	3.10	2.91	3.30	2.77	2.40	2.31	3.31	2.93	2.98	3.03	8.16	2.70	2.81	2.76	3.00			P ₂ O ₅	0.40	b.d.	0.39	b.d.	0.55	0.55	0.61	0.57	0.45	0.46	0.43	0.42	0.39	0.40	0.38	b.d.	0.41	0.40	0.41	0.39			L.O.I.	0.60	b.d.	1.20	b.d.	1.41	2.90	3.17	3.55	1.95	3.84	3.60	2.98	1.28	1.10	1.05	b.d.	1.70	1.80	1.50	1.40			Total	99.72	98.66	99.21	99.32	98.87	98.87	98.90	98.36	99.17	99.36	97.52	98.73	97.91	99.03	98.79	98.35	99.22	97.94	98.67	97.96			ne%	8.5	2.0	6.1	5.6	7.4	1.9	5.3	4.4	2.4	1.8	2.8	2.9	4.7	6.8	7.5	16.2	6.7	8.0	5.2	7.4			mg*	71	53	75	61	73	75	77	76	74	67	64	73	74	68	72	46	70	70	72	72			ppm																								Ba	220	n.a.	240	n.a.	280	320	310	310	300	250	260	220	190	250	210	n.a.	280	250	230	260			Cu	99	n.a.	122	n.a.	215	132	105	151	127	139	150	138	114	134	105	n.a.	105	87	58	121			Co	42	n.a.	40	n.a.	34	30	23	29	33	40	37	40	34	38	37	n.a.	43	30	30	32			Hf	1.5	n.a.	1.7	n.a.	n.a.	2.0	2.1	2.0	n.a.	1.6	1.5	1.5	n.a.	n.a.	1.4	n.a.	n.a.	n.a.	n.a.	n.a.			Nb	1.3	n.a.	1.5	n.a.	n.a.	1.7	1.7	1.7	n.a.	1.5	1.5	1.4	n.a.	n.a.	1.3	n.a.	n.a.	n.a.	n.a.	n.a.			Ni	32	n.a.	33	n.a.	18	18	16	20	20	29	29	29	27	42	33	n.a.	35	25	32	27			Rb	63	n.a.	49	n.a.	55	46	45	50	60	55	51	51	56	59	60	n.a.	60	56	54	65			Sc	41	n.a.	40	n.a.	n.a.	35	35	35	n.a.	39	37	39	n.a.	n.a.	41	n.a.	35	34	39	39			Sr	910	n.a.	970	n.a.	1500	1460	1540	1470	1400	1230	1200	1050	1060	1030	940	n.a.	950	950	930	910			Ta	0.09	n.a.	0.10	n.a.	n.a.	0.11	0.11	0.11	n.a.	0.09	0.10	0.09	n.a.	n.a.	0.09	n.a.	n.a.	n.a.	n.a.	n.a.																																																																																																																																																																																																																		
K ₂ O	2.85	6.47	2.77	7.90	3.28	3.10	2.91	3.30	2.77	2.40	2.31	3.31	2.93	2.98	3.03	8.16	2.70	2.81	2.76	3.00			P ₂ O ₅	0.40	b.d.	0.39	b.d.	0.55	0.55	0.61	0.57	0.45	0.46	0.43	0.42	0.39	0.40	0.38	b.d.	0.41	0.40	0.41	0.39			L.O.I.	0.60	b.d.	1.20	b.d.	1.41	2.90	3.17	3.55	1.95	3.84	3.60	2.98	1.28	1.10	1.05	b.d.	1.70	1.80	1.50	1.40			Total	99.72	98.66	99.21	99.32	98.87	98.87	98.90	98.36	99.17	99.36	97.52	98.73	97.91	99.03	98.79	98.35	99.22	97.94	98.67	97.96			ne%	8.5	2.0	6.1	5.6	7.4	1.9	5.3	4.4	2.4	1.8	2.8	2.9	4.7	6.8	7.5	16.2	6.7	8.0	5.2	7.4			mg*	71	53	75	61	73	75	77	76	74	67	64	73	74	68	72	46	70	70	72	72			ppm																								Ba	220	n.a.	240	n.a.	280	320	310	310	300	250	260	220	190	250	210	n.a.	280	250	230	260			Cu	99	n.a.	122	n.a.	215	132	105	151	127	139	150	138	114	134	105	n.a.	105	87	58	121			Co	42	n.a.	40	n.a.	34	30	23	29	33	40	37	40	34	38	37	n.a.	43	30	30	32			Hf	1.5	n.a.	1.7	n.a.	n.a.	2.0	2.1	2.0	n.a.	1.6	1.5	1.5	n.a.	n.a.	1.4	n.a.	n.a.	n.a.	n.a.	n.a.			Nb	1.3	n.a.	1.5	n.a.	n.a.	1.7	1.7	1.7	n.a.	1.5	1.5	1.4	n.a.	n.a.	1.3	n.a.	n.a.	n.a.	n.a.	n.a.			Ni	32	n.a.	33	n.a.	18	18	16	20	20	29	29	29	27	42	33	n.a.	35	25	32	27			Rb	63	n.a.	49	n.a.	55	46	45	50	60	55	51	51	56	59	60	n.a.	60	56	54	65			Sc	41	n.a.	40	n.a.	n.a.	35	35	35	n.a.	39	37	39	n.a.	n.a.	41	n.a.	35	34	39	39			Sr	910	n.a.	970	n.a.	1500	1460	1540	1470	1400	1230	1200	1050	1060	1030	940	n.a.	950	950	930	910			Ta	0.09	n.a.	0.10	n.a.	n.a.	0.11	0.11	0.11	n.a.	0.09	0.10	0.09	n.a.	n.a.	0.09	n.a.	n.a.	n.a.	n.a.	n.a.																																																																																																																																																																																																																																									
P ₂ O ₅	0.40	b.d.	0.39	b.d.	0.55	0.55	0.61	0.57	0.45	0.46	0.43	0.42	0.39	0.40	0.38	b.d.	0.41	0.40	0.41	0.39			L.O.I.	0.60	b.d.	1.20	b.d.	1.41	2.90	3.17	3.55	1.95	3.84	3.60	2.98	1.28	1.10	1.05	b.d.	1.70	1.80	1.50	1.40			Total	99.72	98.66	99.21	99.32	98.87	98.87	98.90	98.36	99.17	99.36	97.52	98.73	97.91	99.03	98.79	98.35	99.22	97.94	98.67	97.96			ne%	8.5	2.0	6.1	5.6	7.4	1.9	5.3	4.4	2.4	1.8	2.8	2.9	4.7	6.8	7.5	16.2	6.7	8.0	5.2	7.4			mg*	71	53	75	61	73	75	77	76	74	67	64	73	74	68	72	46	70	70	72	72			ppm																								Ba	220	n.a.	240	n.a.	280	320	310	310	300	250	260	220	190	250	210	n.a.	280	250	230	260			Cu	99	n.a.	122	n.a.	215	132	105	151	127	139	150	138	114	134	105	n.a.	105	87	58	121			Co	42	n.a.	40	n.a.	34	30	23	29	33	40	37	40	34	38	37	n.a.	43	30	30	32			Hf	1.5	n.a.	1.7	n.a.	n.a.	2.0	2.1	2.0	n.a.	1.6	1.5	1.5	n.a.	n.a.	1.4	n.a.	n.a.	n.a.	n.a.	n.a.			Nb	1.3	n.a.	1.5	n.a.	n.a.	1.7	1.7	1.7	n.a.	1.5	1.5	1.4	n.a.	n.a.	1.3	n.a.	n.a.	n.a.	n.a.	n.a.			Ni	32	n.a.	33	n.a.	18	18	16	20	20	29	29	29	27	42	33	n.a.	35	25	32	27			Rb	63	n.a.	49	n.a.	55	46	45	50	60	55	51	51	56	59	60	n.a.	60	56	54	65			Sc	41	n.a.	40	n.a.	n.a.	35	35	35	n.a.	39	37	39	n.a.	n.a.	41	n.a.	35	34	39	39			Sr	910	n.a.	970	n.a.	1500	1460	1540	1470	1400	1230	1200	1050	1060	1030	940	n.a.	950	950	930	910			Ta	0.09	n.a.	0.10	n.a.	n.a.	0.11	0.11	0.11	n.a.	0.09	0.10	0.09	n.a.	n.a.	0.09	n.a.	n.a.	n.a.	n.a.	n.a.																																																																																																																																																																																																																																																																
L.O.I.	0.60	b.d.	1.20	b.d.	1.41	2.90	3.17	3.55	1.95	3.84	3.60	2.98	1.28	1.10	1.05	b.d.	1.70	1.80	1.50	1.40			Total	99.72	98.66	99.21	99.32	98.87	98.87	98.90	98.36	99.17	99.36	97.52	98.73	97.91	99.03	98.79	98.35	99.22	97.94	98.67	97.96			ne%	8.5	2.0	6.1	5.6	7.4	1.9	5.3	4.4	2.4	1.8	2.8	2.9	4.7	6.8	7.5	16.2	6.7	8.0	5.2	7.4			mg*	71	53	75	61	73	75	77	76	74	67	64	73	74	68	72	46	70	70	72	72			ppm																								Ba	220	n.a.	240	n.a.	280	320	310	310	300	250	260	220	190	250	210	n.a.	280	250	230	260			Cu	99	n.a.	122	n.a.	215	132	105	151	127	139	150	138	114	134	105	n.a.	105	87	58	121			Co	42	n.a.	40	n.a.	34	30	23	29	33	40	37	40	34	38	37	n.a.	43	30	30	32			Hf	1.5	n.a.	1.7	n.a.	n.a.	2.0	2.1	2.0	n.a.	1.6	1.5	1.5	n.a.	n.a.	1.4	n.a.	n.a.	n.a.	n.a.	n.a.			Nb	1.3	n.a.	1.5	n.a.	n.a.	1.7	1.7	1.7	n.a.	1.5	1.5	1.4	n.a.	n.a.	1.3	n.a.	n.a.	n.a.	n.a.	n.a.			Ni	32	n.a.	33	n.a.	18	18	16	20	20	29	29	29	27	42	33	n.a.	35	25	32	27			Rb	63	n.a.	49	n.a.	55	46	45	50	60	55	51	51	56	59	60	n.a.	60	56	54	65			Sc	41	n.a.	40	n.a.	n.a.	35	35	35	n.a.	39	37	39	n.a.	n.a.	41	n.a.	35	34	39	39			Sr	910	n.a.	970	n.a.	1500	1460	1540	1470	1400	1230	1200	1050	1060	1030	940	n.a.	950	950	930	910			Ta	0.09	n.a.	0.10	n.a.	n.a.	0.11	0.11	0.11	n.a.	0.09	0.10	0.09	n.a.	n.a.	0.09	n.a.	n.a.	n.a.	n.a.	n.a.																																																																																																																																																																																																																																																																																							
Total	99.72	98.66	99.21	99.32	98.87	98.87	98.90	98.36	99.17	99.36	97.52	98.73	97.91	99.03	98.79	98.35	99.22	97.94	98.67	97.96			ne%	8.5	2.0	6.1	5.6	7.4	1.9	5.3	4.4	2.4	1.8	2.8	2.9	4.7	6.8	7.5	16.2	6.7	8.0	5.2	7.4			mg*	71	53	75	61	73	75	77	76	74	67	64	73	74	68	72	46	70	70	72	72			ppm																								Ba	220	n.a.	240	n.a.	280	320	310	310	300	250	260	220	190	250	210	n.a.	280	250	230	260			Cu	99	n.a.	122	n.a.	215	132	105	151	127	139	150	138	114	134	105	n.a.	105	87	58	121			Co	42	n.a.	40	n.a.	34	30	23	29	33	40	37	40	34	38	37	n.a.	43	30	30	32			Hf	1.5	n.a.	1.7	n.a.	n.a.	2.0	2.1	2.0	n.a.	1.6	1.5	1.5	n.a.	n.a.	1.4	n.a.	n.a.	n.a.	n.a.	n.a.			Nb	1.3	n.a.	1.5	n.a.	n.a.	1.7	1.7	1.7	n.a.	1.5	1.5	1.4	n.a.	n.a.	1.3	n.a.	n.a.	n.a.	n.a.	n.a.			Ni	32	n.a.	33	n.a.	18	18	16	20	20	29	29	29	27	42	33	n.a.	35	25	32	27			Rb	63	n.a.	49	n.a.	55	46	45	50	60	55	51	51	56	59	60	n.a.	60	56	54	65			Sc	41	n.a.	40	n.a.	n.a.	35	35	35	n.a.	39	37	39	n.a.	n.a.	41	n.a.	35	34	39	39			Sr	910	n.a.	970	n.a.	1500	1460	1540	1470	1400	1230	1200	1050	1060	1030	940	n.a.	950	950	930	910			Ta	0.09	n.a.	0.10	n.a.	n.a.	0.11	0.11	0.11	n.a.	0.09	0.10	0.09	n.a.	n.a.	0.09	n.a.	n.a.	n.a.	n.a.	n.a.																																																																																																																																																																																																																																																																																																														
ne%	8.5	2.0	6.1	5.6	7.4	1.9	5.3	4.4	2.4	1.8	2.8	2.9	4.7	6.8	7.5	16.2	6.7	8.0	5.2	7.4			mg*	71	53	75	61	73	75	77	76	74	67	64	73	74	68	72	46	70	70	72	72			ppm																								Ba	220	n.a.	240	n.a.	280	320	310	310	300	250	260	220	190	250	210	n.a.	280	250	230	260			Cu	99	n.a.	122	n.a.	215	132	105	151	127	139	150	138	114	134	105	n.a.	105	87	58	121			Co	42	n.a.	40	n.a.	34	30	23	29	33	40	37	40	34	38	37	n.a.	43	30	30	32			Hf	1.5	n.a.	1.7	n.a.	n.a.	2.0	2.1	2.0	n.a.	1.6	1.5	1.5	n.a.	n.a.	1.4	n.a.	n.a.	n.a.	n.a.	n.a.			Nb	1.3	n.a.	1.5	n.a.	n.a.	1.7	1.7	1.7	n.a.	1.5	1.5	1.4	n.a.	n.a.	1.3	n.a.	n.a.	n.a.	n.a.	n.a.			Ni	32	n.a.	33	n.a.	18	18	16	20	20	29	29	29	27	42	33	n.a.	35	25	32	27			Rb	63	n.a.	49	n.a.	55	46	45	50	60	55	51	51	56	59	60	n.a.	60	56	54	65			Sc	41	n.a.	40	n.a.	n.a.	35	35	35	n.a.	39	37	39	n.a.	n.a.	41	n.a.	35	34	39	39			Sr	910	n.a.	970	n.a.	1500	1460	1540	1470	1400	1230	1200	1050	1060	1030	940	n.a.	950	950	930	910			Ta	0.09	n.a.	0.10	n.a.	n.a.	0.11	0.11	0.11	n.a.	0.09	0.10	0.09	n.a.	n.a.	0.09	n.a.	n.a.	n.a.	n.a.	n.a.																																																																																																																																																																																																																																																																																																																																					
mg*	71	53	75	61	73	75	77	76	74	67	64	73	74	68	72	46	70	70	72	72			ppm																								Ba	220	n.a.	240	n.a.	280	320	310	310	300	250	260	220	190	250	210	n.a.	280	250	230	260			Cu	99	n.a.	122	n.a.	215	132	105	151	127	139	150	138	114	134	105	n.a.	105	87	58	121			Co	42	n.a.	40	n.a.	34	30	23	29	33	40	37	40	34	38	37	n.a.	43	30	30	32			Hf	1.5	n.a.	1.7	n.a.	n.a.	2.0	2.1	2.0	n.a.	1.6	1.5	1.5	n.a.	n.a.	1.4	n.a.	n.a.	n.a.	n.a.	n.a.			Nb	1.3	n.a.	1.5	n.a.	n.a.	1.7	1.7	1.7	n.a.	1.5	1.5	1.4	n.a.	n.a.	1.3	n.a.	n.a.	n.a.	n.a.	n.a.			Ni	32	n.a.	33	n.a.	18	18	16	20	20	29	29	29	27	42	33	n.a.	35	25	32	27			Rb	63	n.a.	49	n.a.	55	46	45	50	60	55	51	51	56	59	60	n.a.	60	56	54	65			Sc	41	n.a.	40	n.a.	n.a.	35	35	35	n.a.	39	37	39	n.a.	n.a.	41	n.a.	35	34	39	39			Sr	910	n.a.	970	n.a.	1500	1460	1540	1470	1400	1230	1200	1050	1060	1030	940	n.a.	950	950	930	910			Ta	0.09	n.a.	0.10	n.a.	n.a.	0.11	0.11	0.11	n.a.	0.09	0.10	0.09	n.a.	n.a.	0.09	n.a.	n.a.	n.a.	n.a.	n.a.																																																																																																																																																																																																																																																																																																																																																												
ppm																								Ba	220	n.a.	240	n.a.	280	320	310	310	300	250	260	220	190	250	210	n.a.	280	250	230	260			Cu	99	n.a.	122	n.a.	215	132	105	151	127	139	150	138	114	134	105	n.a.	105	87	58	121			Co	42	n.a.	40	n.a.	34	30	23	29	33	40	37	40	34	38	37	n.a.	43	30	30	32			Hf	1.5	n.a.	1.7	n.a.	n.a.	2.0	2.1	2.0	n.a.	1.6	1.5	1.5	n.a.	n.a.	1.4	n.a.	n.a.	n.a.	n.a.	n.a.			Nb	1.3	n.a.	1.5	n.a.	n.a.	1.7	1.7	1.7	n.a.	1.5	1.5	1.4	n.a.	n.a.	1.3	n.a.	n.a.	n.a.	n.a.	n.a.			Ni	32	n.a.	33	n.a.	18	18	16	20	20	29	29	29	27	42	33	n.a.	35	25	32	27			Rb	63	n.a.	49	n.a.	55	46	45	50	60	55	51	51	56	59	60	n.a.	60	56	54	65			Sc	41	n.a.	40	n.a.	n.a.	35	35	35	n.a.	39	37	39	n.a.	n.a.	41	n.a.	35	34	39	39			Sr	910	n.a.	970	n.a.	1500	1460	1540	1470	1400	1230	1200	1050	1060	1030	940	n.a.	950	950	930	910			Ta	0.09	n.a.	0.10	n.a.	n.a.	0.11	0.11	0.11	n.a.	0.09	0.10	0.09	n.a.	n.a.	0.09	n.a.	n.a.	n.a.	n.a.	n.a.																																																																																																																																																																																																																																																																																																																																																																																			
Ba	220	n.a.	240	n.a.	280	320	310	310	300	250	260	220	190	250	210	n.a.	280	250	230	260			Cu	99	n.a.	122	n.a.	215	132	105	151	127	139	150	138	114	134	105	n.a.	105	87	58	121			Co	42	n.a.	40	n.a.	34	30	23	29	33	40	37	40	34	38	37	n.a.	43	30	30	32			Hf	1.5	n.a.	1.7	n.a.	n.a.	2.0	2.1	2.0	n.a.	1.6	1.5	1.5	n.a.	n.a.	1.4	n.a.	n.a.	n.a.	n.a.	n.a.			Nb	1.3	n.a.	1.5	n.a.	n.a.	1.7	1.7	1.7	n.a.	1.5	1.5	1.4	n.a.	n.a.	1.3	n.a.	n.a.	n.a.	n.a.	n.a.			Ni	32	n.a.	33	n.a.	18	18	16	20	20	29	29	29	27	42	33	n.a.	35	25	32	27			Rb	63	n.a.	49	n.a.	55	46	45	50	60	55	51	51	56	59	60	n.a.	60	56	54	65			Sc	41	n.a.	40	n.a.	n.a.	35	35	35	n.a.	39	37	39	n.a.	n.a.	41	n.a.	35	34	39	39			Sr	910	n.a.	970	n.a.	1500	1460	1540	1470	1400	1230	1200	1050	1060	1030	940	n.a.	950	950	930	910			Ta	0.09	n.a.	0.10	n.a.	n.a.	0.11	0.11	0.11	n.a.	0.09	0.10	0.09	n.a.	n.a.	0.09	n.a.	n.a.	n.a.	n.a.	n.a.																																																																																																																																																																																																																																																																																																																																																																																																											
Cu	99	n.a.	122	n.a.	215	132	105	151	127	139	150	138	114	134	105	n.a.	105	87	58	121			Co	42	n.a.	40	n.a.	34	30	23	29	33	40	37	40	34	38	37	n.a.	43	30	30	32			Hf	1.5	n.a.	1.7	n.a.	n.a.	2.0	2.1	2.0	n.a.	1.6	1.5	1.5	n.a.	n.a.	1.4	n.a.	n.a.	n.a.	n.a.	n.a.			Nb	1.3	n.a.	1.5	n.a.	n.a.	1.7	1.7	1.7	n.a.	1.5	1.5	1.4	n.a.	n.a.	1.3	n.a.	n.a.	n.a.	n.a.	n.a.			Ni	32	n.a.	33	n.a.	18	18	16	20	20	29	29	29	27	42	33	n.a.	35	25	32	27			Rb	63	n.a.	49	n.a.	55	46	45	50	60	55	51	51	56	59	60	n.a.	60	56	54	65			Sc	41	n.a.	40	n.a.	n.a.	35	35	35	n.a.	39	37	39	n.a.	n.a.	41	n.a.	35	34	39	39			Sr	910	n.a.	970	n.a.	1500	1460	1540	1470	1400	1230	1200	1050	1060	1030	940	n.a.	950	950	930	910			Ta	0.09	n.a.	0.10	n.a.	n.a.	0.11	0.11	0.11	n.a.	0.09	0.10	0.09	n.a.	n.a.	0.09	n.a.	n.a.	n.a.	n.a.	n.a.																																																																																																																																																																																																																																																																																																																																																																																																																																		
Co	42	n.a.	40	n.a.	34	30	23	29	33	40	37	40	34	38	37	n.a.	43	30	30	32			Hf	1.5	n.a.	1.7	n.a.	n.a.	2.0	2.1	2.0	n.a.	1.6	1.5	1.5	n.a.	n.a.	1.4	n.a.	n.a.	n.a.	n.a.	n.a.			Nb	1.3	n.a.	1.5	n.a.	n.a.	1.7	1.7	1.7	n.a.	1.5	1.5	1.4	n.a.	n.a.	1.3	n.a.	n.a.	n.a.	n.a.	n.a.			Ni	32	n.a.	33	n.a.	18	18	16	20	20	29	29	29	27	42	33	n.a.	35	25	32	27			Rb	63	n.a.	49	n.a.	55	46	45	50	60	55	51	51	56	59	60	n.a.	60	56	54	65			Sc	41	n.a.	40	n.a.	n.a.	35	35	35	n.a.	39	37	39	n.a.	n.a.	41	n.a.	35	34	39	39			Sr	910	n.a.	970	n.a.	1500	1460	1540	1470	1400	1230	1200	1050	1060	1030	940	n.a.	950	950	930	910			Ta	0.09	n.a.	0.10	n.a.	n.a.	0.11	0.11	0.11	n.a.	0.09	0.10	0.09	n.a.	n.a.	0.09	n.a.	n.a.	n.a.	n.a.	n.a.																																																																																																																																																																																																																																																																																																																																																																																																																																																									
Hf	1.5	n.a.	1.7	n.a.	n.a.	2.0	2.1	2.0	n.a.	1.6	1.5	1.5	n.a.	n.a.	1.4	n.a.	n.a.	n.a.	n.a.	n.a.			Nb	1.3	n.a.	1.5	n.a.	n.a.	1.7	1.7	1.7	n.a.	1.5	1.5	1.4	n.a.	n.a.	1.3	n.a.	n.a.	n.a.	n.a.	n.a.			Ni	32	n.a.	33	n.a.	18	18	16	20	20	29	29	29	27	42	33	n.a.	35	25	32	27			Rb	63	n.a.	49	n.a.	55	46	45	50	60	55	51	51	56	59	60	n.a.	60	56	54	65			Sc	41	n.a.	40	n.a.	n.a.	35	35	35	n.a.	39	37	39	n.a.	n.a.	41	n.a.	35	34	39	39			Sr	910	n.a.	970	n.a.	1500	1460	1540	1470	1400	1230	1200	1050	1060	1030	940	n.a.	950	950	930	910			Ta	0.09	n.a.	0.10	n.a.	n.a.	0.11	0.11	0.11	n.a.	0.09	0.10	0.09	n.a.	n.a.	0.09	n.a.	n.a.	n.a.	n.a.	n.a.																																																																																																																																																																																																																																																																																																																																																																																																																																																																																
Nb	1.3	n.a.	1.5	n.a.	n.a.	1.7	1.7	1.7	n.a.	1.5	1.5	1.4	n.a.	n.a.	1.3	n.a.	n.a.	n.a.	n.a.	n.a.			Ni	32	n.a.	33	n.a.	18	18	16	20	20	29	29	29	27	42	33	n.a.	35	25	32	27			Rb	63	n.a.	49	n.a.	55	46	45	50	60	55	51	51	56	59	60	n.a.	60	56	54	65			Sc	41	n.a.	40	n.a.	n.a.	35	35	35	n.a.	39	37	39	n.a.	n.a.	41	n.a.	35	34	39	39			Sr	910	n.a.	970	n.a.	1500	1460	1540	1470	1400	1230	1200	1050	1060	1030	940	n.a.	950	950	930	910			Ta	0.09	n.a.	0.10	n.a.	n.a.	0.11	0.11	0.11	n.a.	0.09	0.10	0.09	n.a.	n.a.	0.09	n.a.	n.a.	n.a.	n.a.	n.a.																																																																																																																																																																																																																																																																																																																																																																																																																																																																																																							
Ni	32	n.a.	33	n.a.	18	18	16	20	20	29	29	29	27	42	33	n.a.	35	25	32	27			Rb	63	n.a.	49	n.a.	55	46	45	50	60	55	51	51	56	59	60	n.a.	60	56	54	65			Sc	41	n.a.	40	n.a.	n.a.	35	35	35	n.a.	39	37	39	n.a.	n.a.	41	n.a.	35	34	39	39			Sr	910	n.a.	970	n.a.	1500	1460	1540	1470	1400	1230	1200	1050	1060	1030	940	n.a.	950	950	930	910			Ta	0.09	n.a.	0.10	n.a.	n.a.	0.11	0.11	0.11	n.a.	0.09	0.10	0.09	n.a.	n.a.	0.09	n.a.	n.a.	n.a.	n.a.	n.a.																																																																																																																																																																																																																																																																																																																																																																																																																																																																																																																														
Rb	63	n.a.	49	n.a.	55	46	45	50	60	55	51	51	56	59	60	n.a.	60	56	54	65			Sc	41	n.a.	40	n.a.	n.a.	35	35	35	n.a.	39	37	39	n.a.	n.a.	41	n.a.	35	34	39	39			Sr	910	n.a.	970	n.a.	1500	1460	1540	1470	1400	1230	1200	1050	1060	1030	940	n.a.	950	950	930	910			Ta	0.09	n.a.	0.10	n.a.	n.a.	0.11	0.11	0.11	n.a.	0.09	0.10	0.09	n.a.	n.a.	0.09	n.a.	n.a.	n.a.	n.a.	n.a.																																																																																																																																																																																																																																																																																																																																																																																																																																																																																																																																																					
Sc	41	n.a.	40	n.a.	n.a.	35	35	35	n.a.	39	37	39	n.a.	n.a.	41	n.a.	35	34	39	39			Sr	910	n.a.	970	n.a.	1500	1460	1540	1470	1400	1230	1200	1050	1060	1030	940	n.a.	950	950	930	910			Ta	0.09	n.a.	0.10	n.a.	n.a.	0.11	0.11	0.11	n.a.	0.09	0.10	0.09	n.a.	n.a.	0.09	n.a.	n.a.	n.a.	n.a.	n.a.																																																																																																																																																																																																																																																																																																																																																																																																																																																																																																																																																																												
Sr	910	n.a.	970	n.a.	1500	1460	1540	1470	1400	1230	1200	1050	1060	1030	940	n.a.	950	950	930	910			Ta	0.09	n.a.	0.10	n.a.	n.a.	0.11	0.11	0.11	n.a.	0.09	0.10	0.09	n.a.	n.a.	0.09	n.a.	n.a.	n.a.	n.a.	n.a.																																																																																																																																																																																																																																																																																																																																																																																																																																																																																																																																																																																																			
Ta	0.09	n.a.	0.10	n.a.	n.a.	0.11	0.11	0.11	n.a.	0.09	0.10	0.09	n.a.	n.a.	0.09	n.a.	n.a.	n.a.	n.a.	n.a.																																																																																																																																																																																																																																																																																																																																																																																																																																																																																																																																																																																																																										

(continued)

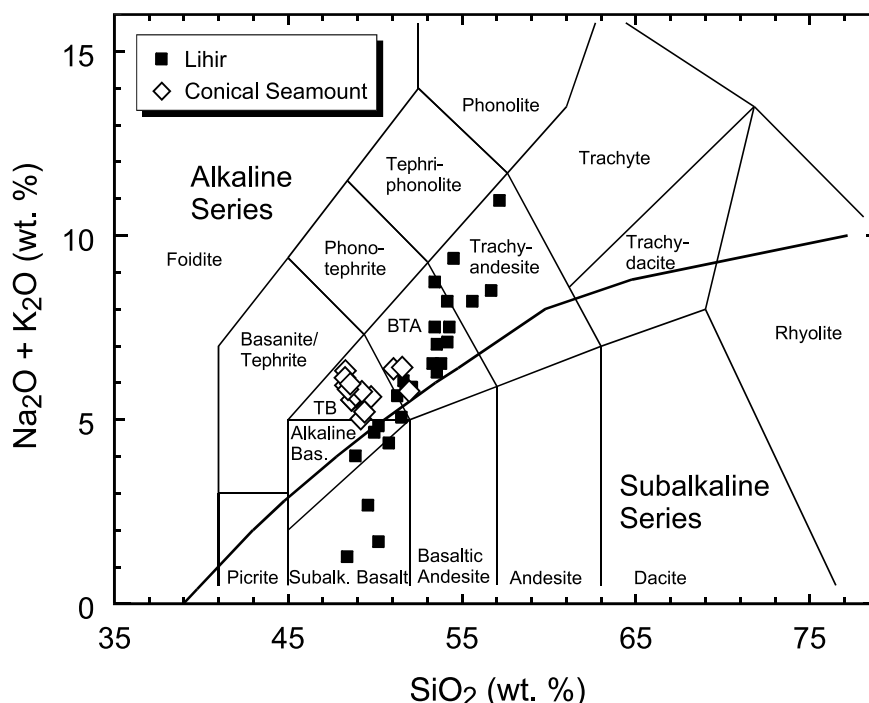


Fig. 2. Total alkali versus silica (TAS) plot showing rocks from Conical Seamount (white diamonds) and Lihir Island (dark squares). Composition of magmatic glass is not displayed. Note that the three samples from Lihir Island plotting in the field for subalkaline basalts are olivine-clinopyroxene cumulates. Rock abbreviations: *TB* trachybasalt; *BTA* basaltic trachyandesite

mantle-compatible elements (V, Ni, and Co up to 320, 42, and 43 ppm, respectively). These data are consistent with moderate to high mg# (46–77). An elevated oxygen fugacity is revealed by the Wilson method indicating an average of about 40% Fe^{3+} of total Fe for most of the samples. The rocks (Fig. 2) are characterized by high K_2O contents (up to 3.31 wt%), high average $\text{K}_2\text{O}/\text{Na}_2\text{O}$ ratios (1.19), and high average Ce/Yb ratios (13.0), which are typical of high-K igneous rocks transitional to shoshonites (Pearce, 1982). The elevated LILE (e.g. Rb, Sr, Ba up to 65, 1540, and 320 ppm, respectively), low LREE (e.g. La <15.0 ppm, Ce <33.0 ppm), and very low HFSE concentrations (e.g. TiO_2 <0.83 wt%, Zr <75 ppm, Nb <1.7 ppm, Hf <2.1 ppm) are typical for potassic igneous rocks from oceanic (island) arc settings (Müller and Groves, 2000).

Petrography and chemistry of magmatic minerals and glass

Most volcanic rocks of Conical Seamount are vesicular trachybasalts with porphyritic or glomerophytic textures. The phenocrysts mainly consist of clinopyroxene (20–25 vol%), plagioclase (5 vol%), olivine (1–3 vol%) and phlogopite (<2 vol.-%). The groundmass of the samples consists of glass with microcrysts (<15 μm) of plagioclase, clinopyroxene and spinel as well as small accessory prisms of apatite. The vesicles comprise about 10–15 vol% of the rock and vary

in size from small rounded (<1 mm) to elongate bubbles with a length of up to 10 mm; they are not filled by hydrothermal phases. Clinopyroxene forms idiomorphic prismatic crystals with distinct oscillatory zoning and a length of up to 5 mm. They often include small olivine and spinel crystals and also contain irregularly shaped melt inclusions. Lath-shaped plagioclase phenocrysts with sizes of up to 1 mm display distinct optical zoning, which is also true for tablets of phlogopite with similar sizes. One sample (13DR-5D) contains euhedral, up to 2 mm long, prisms of brownish clinoamphibole. Olivine often yields tiny inclusions of spinel phenocrysts with diameters of >0.2 mm.

Four typical pristine samples from Conical Seamount were chosen for the analysis of the primary magmatic minerals; the results are compared with samples from Lihir Island.

Table 2. Representative microprobe analyses of clinopyroxene from Conical Seamount samples. End member calculation after Lindsley (1983). Calculation of ferric iron following Droop (1987)

Clinopyroxene wt.-%	7DR-2G Cpx core	7DR-2G Cpx rim	12DR-3A Cpx core	12DR-3A Cpx rim	13DR-5D Cpx core	13DR-5D Cpx rim	50DR-1C Cpx core	50DR-1C Cpx rim
SiO ₂	49.42	46.87	52.12	48.75	50.29	48.11	50.89	48.42
TiO ₂	0.38	0.71	0.25	0.53	0.45	0.59	0.48	0.68
Al ₂ O ₃	4.36	7.05	2.89	5.24	4.12	5.80	4.07	7.01
Cr ₂ O ₃	0.32	0.00	0.08	0.00	0.04	0.00	0.02	0.03
Fe ₂ O ₃	4.14	6.14	2.21	4.29	3.46	5.56	1.29	2.27
MgO	14.47	12.32	15.89	13.75	13.34	12.51	13.71	12.31
CaO	23.16	22.29	23.43	22.39	23.31	23.24	21.83	21.71
MnO	0.06	0.23	0.09	0.21	0.30	0.27	0.24	0.20
FeO	2.54	3.23	2.98	3.83	4.57	3.36	6.59	6.28
Na ₂ O	0.29	0.58	0.24	0.33	0.44	0.50	0.43	0.48
K ₂ O	0.00	0.01	0.01	0.00	0.00	0.01	0.01	0.02
Total	99.14	99.43	100.18	99.30	100.32	99.94	99.58	99.42
Cations (O = 6)								
Si	1.842	1.759	1.908	1.822	1.864	1.796	1.895	1.812
Ti	0.011	0.020	0.007	0.015	0.013	0.017	0.014	0.019
Al	0.192	0.312	0.125	0.231	0.180	0.255	0.179	0.309
Fe ³⁺	0.116	0.173	0.061	0.120	0.097	0.156	0.036	0.064
Cr	0.009	0.000	0.002	0.000	0.001	0.000	0.001	0.001
Mg	0.804	0.689	0.867	0.766	0.737	0.696	0.761	0.686
Ca	0.925	0.896	0.919	0.896	0.926	0.930	0.871	0.870
Mn	0.002	0.007	0.003	0.007	0.009	0.009	0.008	0.006
Fe ²⁺	0.079	0.101	0.091	0.120	0.142	0.105	0.205	0.197
Na	0.021	0.042	0.017	0.024	0.031	0.037	0.031	0.035
K	0.000	0.000	0.001	0.000	0.000	0.000	0.000	0.001
Total	4.000	4.000	4.000	4.000	4.000	4.000	4.000	4.000
Endmembers								
Wo	40.4	36.8	42.8	38.6	42.3	39.8	41.2	37.7
En	54.3	55.1	51.7	53.1	48.4	52.3	46.3	48.4
Fs	5.3	8.1	5.4	8.3	9.3	7.9	12.5	13.9

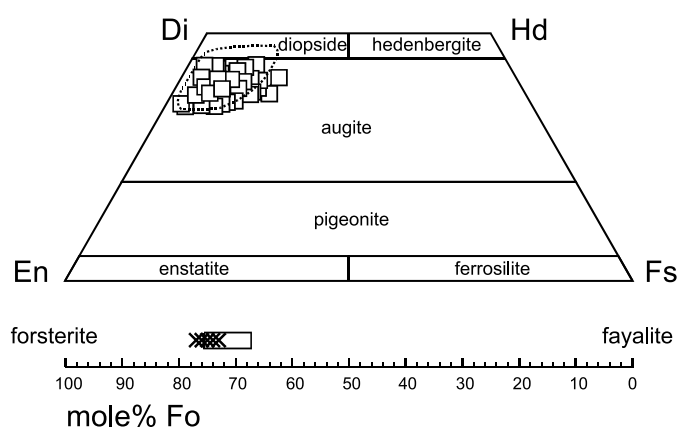


Fig. 3. Pyroxene quadrilateral showing the composition of pyroxene phenocrysts from Conical Seamount (squares) and the composition field of pyroxenes from Lihir (dotted line). Composition of olivine phenocrysts from Conical Seamount (crosses) and Lihir (box) is displayed below

Table 3. *Representative microprobe analyses of olivine from Conical Seamount samples*

Olivine wt.-%	7DR-2G Ol core	7DR-2G Ol rim	12DR-3A Ol core	12DR-3A Ol rim	50DR-1C Ol core	50DR-1C Ol rim
SiO ₂	38.58	37.88	38.39	38.00	38.28	37.69
TiO ₂	0.01	0.02	0.01	0.00	0.00	0.00
Al ₂ O ₃	0.04	0.03	0.02	0.04	0.03	0.05
Cr ₂ O ₃	0.01	0.02	0.00	0.01	0.00	0.04
MgO	37.79	39.24	39.54	39.94	38.40	37.74
CaO	0.27	0.26	0.28	0.29	0.26	0.34
MnO	0.58	0.53	0.47	0.48	0.54	0.62
FeO	23.04	21.91	21.46	20.67	22.70	23.31
NiO	0.02	0.00	0.03	0.00	0.00	0.00
Total	100.34	99.90	100.19	99.43	100.21	99.79
Cations (O = 4)						
Si	1.004	0.988	0.994	0.989	0.997	0.991
Ti	0.000	0.000	0.000	0.000	0.000	0.000
Al	0.001	0.001	0.001	0.001	0.001	0.001
Cr	0.000	0.000	0.000	0.000	0.000	0.001
Mg	1.466	1.525	1.527	1.550	1.491	1.479
Ca	0.007	0.007	0.008	0.008	0.007	0.009
Mn	0.013	0.012	0.010	0.011	0.012	0.014
Fe	0.502	0.478	0.465	0.450	0.494	0.512
Ni	0.000	0.000	0.001	0.000	0.000	0.000
Total	2.995	3.011	3.005	3.010	3.002	3.008
Endmembers						
Mg ₂ SiO ₄	73.74	75.44	75.95	76.78	74.38	73.41
Fe ₂ SiO ₄	25.22	23.62	23.13	22.29	24.66	25.43
Ca ₂ SiO ₄	0.37	0.36	0.38	0.40	0.36	0.47
Ni ₂ SiO ₄	0.02	0.00	0.03	0.00	0.00	0.00
Mn ₂ SiO ₄	0.65	0.58	0.51	0.53	0.59	0.69

Clinopyroxene has a slightly variable composition with Wo_{35-44} , En_{45-58} and Fs_{3-17} (calculation of endmembers after *Lindsley*, 1983; see also Table 2) and, according to charge balance constraints, yields prominent amounts of ferric iron (28–99% of total iron). Zonation patterns are similar in all samples with decreasing *Wo*- and increasing *En*- and *Fs*- as well as *Al*, *Ti* and *Na*-contents from core to rim. The compositions match well with those of the clinopyroxene phenocrysts from Lihir Island samples (Fig. 3).

Olivine phenocrysts as well as tiny matrix olivine grains (Table 3) yield forsterite components of 73–77 mole-% and *CaO*-contents of up to 0.37%, which is quite similar to Lihir olivine (Fig. 3; cf. *Müller et al.*, 2001). The crystals show increasing *Ca*- and *Mg*-contents towards the rim but in part also display irregular zonation patterns.

Clinoamphibole from Conical Seamount is pargasite and minor *Mg*-hastingsite (classification of *Leake et al.*, 1997), which yield elevated amounts of ferric iron (20–43% of the total iron using the maximum- Fe^{3+} calculation of *Schumacher*,

Table 4. Representative microprobe analyses of core, intermediate (*im.*) and rim sections of clinoamphibole from Conical Seamount. Calculation of ferric iron after *Schumacher* (1997)

Clinoamphibole wt.-%	13DR-5D	13DR-5D	13DR-5D	13DR-5D	13DR-5D	13DR-5D
	Hbl1 core	Hbl1 im	Hbl1 rim	Hbl2 core	Hbl2 im.	Hbl2 rim
SiO ₂	40.16	40.92	39.81	40.45	39.52	40.29
TiO ₂	1.53	1.66	1.79	2.10	2.25	1.99
Al ₂ O ₃	13.95	13.33	14.18	13.79	14.07	14.08
Fe ₂ O ₃	4.58	3.53	4.79	3.11	5.35	4.55
Cr ₂ O ₃	0.02	0.00	0.00	0.00	0.02	0.01
MgO	12.54	12.43	13.26	12.70	12.86	12.91
CaO	11.91	11.84	11.96	11.84	11.65	11.79
MnO	0.24	0.27	0.26	0.25	0.23	0.23
FeO	8.76	9.77	7.33	9.36	7.69	8.13
Na ₂ O	2.03	2.24	2.07	2.17	2.19	2.06
K ₂ O	1.98	1.67	1.94	1.95	1.99	2.00
Total	97.71	97.66	97.40	97.71	97.82	98.03
Cations (O = 23)						
Si	5.971	6.082	5.909	6.004	5.863	5.950
Ti	0.172	0.185	0.200	0.235	0.251	0.221
Al	2.444	2.335	2.480	2.413	2.461	2.450
Fe ³⁺	0.512	0.394	0.535	0.347	0.597	0.506
Cr	0.003	0.000	0.000	0.000	0.003	0.001
Mg	2.780	2.754	2.934	2.810	2.843	2.842
Ca	1.897	1.886	1.901	1.884	1.853	1.866
Mn	0.030	0.034	0.032	0.031	0.029	0.029
Fe ²⁺	1.089	1.215	0.910	1.161	0.954	1.004
Na	0.585	0.647	0.596	0.625	0.629	0.590
K	0.375	0.317	0.368	0.368	0.376	0.376
Total	15.858	15.850	15.866	15.878	15.858	15.834

1997) and shows irregular, oscillatory zoning of Ti, Al and Na (Table 4). According to microprobe analyses, clinoamphibole from Conical Seamount is almost free of F and Cl (i.e. <0.1 wt%).

Phlogopite displays a zoning with decreasing X_{Mg} -values ($=Mg/(Mg + Fe^{2+})$) and decreasing Ti-contents from core to rim, which is especially prominent in sample 7DR-2G (e.g., X_{Mg} core: 0.79; X_{Mg} rim: 0.83; cf. Table 5). The phlogopite phenocrysts from Conical Seamount are poor in Ba (<0.13 wt%) and only yield

Table 5. Representative microprobe analyses of phlogopite phenocrysts from Conical Seamount lavas. Calculation of H_2O by iteration

Phlogopite wt.-%	7DR-2G Phl1 core	7DR-2G Phl1 rim	7DR-2G Phl2 core	7DR-2G Phl2 rim	13DR-5D Phl1 core	13DR-5D Phl1 rim	13DR-5D Phl2 core	13DR-5D Phl2 rim
SiO ₂	38.09	38.22	36.88	37.25	37.77	39.46	38.18	38.05
TiO ₂	1.70	1.36	2.93	1.99	2.57	1.77	2.67	2.29
Al ₂ O ₃	16.53	16.36	17.02	17.13	16.70	15.87	16.59	17.25
Cr ₂ O ₃	0.10	0.18	0.00	0.07	0.04	0.08	0.01	0.03
MgO	18.61	20.82	16.59	18.56	17.93	18.87	18.24	17.56
CaO	0.16	0.05	0.02	0.02	0.01	0.01	0.02	0.06
MnO	0.06	0.04	0.12	0.06	0.10	0.11	0.09	0.12
FeO	9.07	7.82	12.26	10.47	10.79	10.17	10.44	10.77
BaO	0.03	0.00	0.02	0.05	0.13	0.01	0.08	0.12
Na ₂ O	0.68	0.54	0.72	0.65	0.73	0.74	0.76	0.80
K ₂ O	9.56	9.73	9.67	9.79	9.60	9.61	9.61	9.20
H ₂ O ⁻	4.01	4.10	4.02	3.99	4.04	4.08	4.06	4.06
F ⁻	0.17	0.09	0.14	0.27	0.17	0.19	0.20	0.15
Cl ⁻	0.02	0.01	0.04	0.02	0.05	0.04	0.04	0.05
Total	98.72	99.27	100.37	100.20	100.57	100.92	100.90	100.43
Ions (O = 12)								
Si	2.786	2.766	2.700	2.709	2.738	2.831	2.752	2.752
Ti	0.094	0.074	0.162	0.109	0.140	0.095	0.145	0.124
Al	1.425	1.395	1.469	1.468	1.427	1.342	1.409	1.470
Cr	0.006	0.010	0.000	0.004	0.002	0.005	0.001	0.002
Mg	2.029	2.246	1.811	2.012	1.938	2.018	1.959	1.893
Ca	0.013	0.004	0.001	0.001	0.001	0.000	0.001	0.004
Mn	0.003	0.002	0.007	0.004	0.006	0.007	0.006	0.007
Fe	0.555	0.474	0.751	0.637	0.654	0.610	0.629	0.652
Ba	0.001	0.000	0.001	0.002	0.004	0.000	0.002	0.003
Na	0.096	0.076	0.102	0.092	0.103	0.103	0.106	0.112
K	0.892	0.898	0.904	0.909	0.888	0.879	0.884	0.849
Total Cations	7.899	7.945	7.907	7.946	7.902	7.892	7.894	7.868
OH	1.958	1.978	1.962	1.937	1.960	1.950	1.950	1.960
F	0.040	0.021	0.033	0.061	0.040	0.040	0.040	0.030
Cl	0.003	0.001	0.005	0.002	0.010	0.010	0.000	0.010
Total Anions	2.000	2.000	2.000	2.000	2.000	2.000	2.000	2.000
X_{Mg}	0.79	0.83	0.71	0.76	0.75	0.77	0.76	0.74

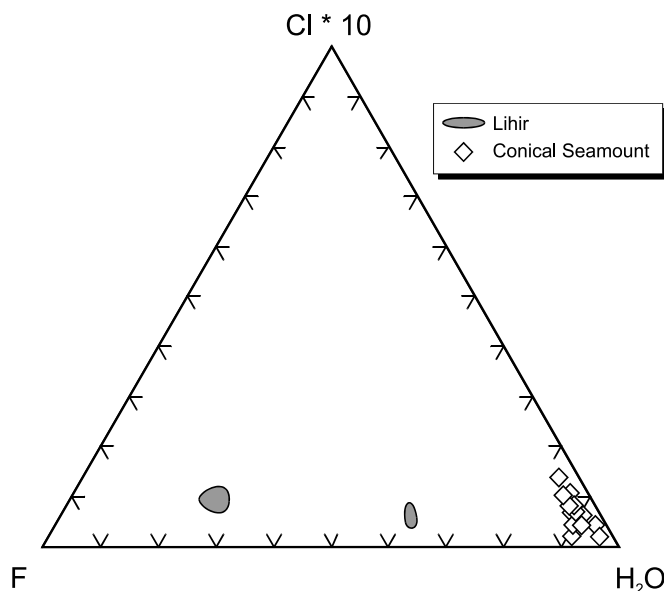


Fig. 4. Chlorine*10-F-H₂O triangular diagram showing compositions of phlogopite phenocrysts from Conical Seamount and Lihir Island

low concentrations of F and Cl (<0.3 wt% F and <0.05 wt% Cl) pointing to very high H₂O contents (up to 4.2 wt%) as shown on the Clx10-F-H₂O triangular plot (Fig. 4). Phlogopite phenocrysts from the Lihir magmatites are unzoned, yield somewhat higher X_{Mg} -values (0.83–0.86) and contain distinctly higher amounts of F (4.7–5.4 wt%; Müller et al., 2001).

Plagioclase phenocrysts from Conical Seamount (Table 6) always show normal zonation patterns with An_{85–80} (core) to An_{67–55} (rim) and minor amounts of orthoclase component (up to 5 mole-%). This is quite similar to the plagioclase phenocrysts from Lihir Island (i.e. core: An_{83–72}; rim: An_{63–44}; cf. Müller et al., 2001).

Spinel phenocrysts are virtually unzoned magnetites with a considerable amount of hercynite (up to 29 mol%) and TiO₂ contents of 3.4–4.8 wt% (Table 7), thus yielding the same composition as the small spinel inclusions in olivine. Spinel from Lihir Island shows somewhat lower X_{Mg} -values (0.07–0.14 for Lihir vs. 0.19–0.26 for Conical) and considerably more TiO₂ (6.2–9.2 wt%) than the spinel phenocrysts from Conical Seamount (Müller et al., 2001).

Glass constitutes part of the groundmass of the Conical Seamount volcanic rocks and is also commonly found as inclusions in clinopyroxene and plagioclase phenocrysts. Glass in samples 7DR-2G, 12DR-3A and 50DR-1G is potassic and alkali-rich with a basic to intermediate composition (Tables 1 and 8). According to CIPW-norm calculations, the glass contains variable amounts of normative nepheline and has a composition ranging from tephriphonolite and phonolite (samples 12DR-3a and 50DR-1C) to trachyandesite (sample 7DR-2G).

Thermobarometry

Magmatic temperatures for the olivine-bearing samples were estimated using the geothermometer of Ballhaus et al. (1991), which is based on the Fe–Mg

Table 6. Representative microprobe analyses of plagioclase phenocrysts from Conical Seamount lavas

Plagioclase wt.-%	7DR-2G Pl core	7DR-2G Pl rim	12DR-3A Pl core	12DR-3A Pl rim	13DR-5D Pl core	13DR-5D Pl rim	50DR-1C Pl core	50DR-1C Pl rim
SiO ₂	46.84	50.40	46.38	50.98	47.33	53.23	47.39	51.50
Al ₂ O ₃	33.45	30.81	33.40	30.25	33.74	29.87	33.23	30.62
MgO	0.03	0.09	0.00	0.09	0.01	0.02	0.03	0.05
CaO	16.35	13.32	16.80	12.97	16.41	12.03	16.47	13.31
MnO	0.01	0.00	0.00	0.00	0.03	0.00	0.03	0.01
FeO	0.52	0.64	0.62	0.62	0.59	0.48	0.56	0.60
BaO	0.01	0.03	0.00	0.07	0.00	0.02	0.01	0.03
Na ₂ O	1.80	3.28	1.63	3.68	1.84	4.04	1.70	3.26
K ₂ O	0.25	0.62	0.20	0.68	0.17	0.59	0.22	0.57
Total	99.26	99.19	99.03	99.34	100.12	100.29	99.64	99.94
Cations (O = 8)								
Si	2.169	2.320	2.157	2.344	2.172	2.407	2.185	2.347
Al	1.826	1.671	1.830	1.639	1.825	1.592	1.806	1.645
Mg	0.002	0.006	0.000	0.006	0.001	0.001	0.002	0.004
Ca	0.811	0.657	0.837	0.639	0.807	0.583	0.814	0.650
Mn	0.000	0.000	0.000	0.000	0.001	0.000	0.001	0.000
Fe	0.020	0.025	0.024	0.024	0.023	0.018	0.021	0.023
Ba	0.000	0.001	0.000	0.001	0.000	0.000	0.000	0.001
Na	0.162	0.293	0.147	0.328	0.164	0.355	0.152	0.288
K	0.015	0.036	0.012	0.040	0.010	0.034	0.013	0.033
Total	5.006	5.009	5.008	5.021	5.002	4.991	4.994	4.991
Endmembers								
Anorthite	82.14	66.58	84.05	63.38	82.28	59.96	83.12	66.92
Albite	16.37	29.67	14.77	32.54	16.70	36.49	15.53	29.63
Orthoclase	1.47	3.69	1.19	3.96	1.02	3.51	1.32	3.39
Celsian	0.02	0.05	0.00	0.13	0.00	0.04	0.02	0.06

exchange between coexisting olivine and spinel. Temperatures of 1000–1082 °C (± 30 °C) were calculated for either olivine and spinel phenocrysts as well as olivine phenocrysts and spinel inclusions. Average temperatures for the trachybasalt samples 7DR-2G and 12DR-3A are 1037 °C and 1031 °C, respectively, and 1026 °C for sample 50DR-1C (Table 9). Compared to the olivine-spinel geothermometer, thermometry based on the Fe–Mg-exchange between olivine and melt often leads to somewhat lower temperatures, which may be due to late cooling processes. Using the method of *Roeder* (1974; T Mg algorithm), temperatures of about 920–980 °C are estimated for samples 7DR-2G and 12DR-3A. The application of the T Fe algorithm of *Roeder* (1974) usually leads to distinctly higher temperatures, which may be due to prominent amounts of ferric iron (i.e. 29–35% of total iron) in the glass. This coincides well with the results of the Fe³⁺-determination on the magmatites (cf. Table 1). In sample 50DR-1C, variable composition of the glass results in a distinct scatter of the olivine-melt

Table 7. Representative microprobe analyses of spinel phenocrysts (P) and spinel inclusions in olivine (I) from Conical Seamount samples. Calculation of ferric iron following Droop (1987)

Spinel wt.-%	7DR-2G		7DR-2G		7DR-2G		12DR-3A		12DR-3A		13DR-5D		13DR-5D		50DR-1C		50DR-1C	
	Spl P core	Spl P rim	Spl I core	Spl I rim	Spl P core	Spl P rim	Spl P core	Spl P rim	Spl P core	Spl P rim	Spl P core	Spl P rim	Spl P core	Spl P rim	Spl P core	Spl P rim	Spl P core	Spl P rim
SiO ₂	0.12	0.13	0.11	0.16	0.11	0.11	0.11	0.11	0.10	0.10	0.09	0.09	0.13	0.08	0.13	0.08	0.13	0.08
TiO ₂	4.68	4.57	4.29	4.31	4.30	4.26	4.30	4.26	3.44	3.44	3.47	3.47	4.76	4.64	4.76	4.64	4.76	4.64
Al ₂ O ₃	9.21	8.91	10.79	10.14	10.47	9.57	10.47	9.57	6.23	6.23	6.21	6.21	10.05	9.29	10.05	9.29	10.05	9.29
Cr ₂ O ₃	0.19	0.17	0.23	0.23	0.20	0.26	0.20	0.26	0.04	0.04	0.06	0.06	0.25	0.20	0.25	0.20	0.25	0.20
Fe ₂ O ₃	51.06	51.93	50.55	50.86	50.19	51.52	50.19	51.52	57.66	57.66	57.54	57.54	50.20	51.05	50.20	51.05	50.20	51.05
MgO	5.01	5.00	5.13	4.97	5.43	5.05	5.43	5.05	3.96	3.96	3.90	3.90	5.00	4.89	5.00	4.89	5.00	4.89
CaO	0.01	0.03	0.02	0.03	0.02	0.04	0.02	0.04	0.27	0.27	0.14	0.14	0.01	0.03	0.01	0.03	0.01	0.03
MnO	0.42	0.39	0.41	0.40	0.40	0.43	0.40	0.43	0.50	0.50	0.55	0.55	0.40	0.44	0.40	0.44	0.40	0.44
FeO	28.87	28.83	28.70	28.89	27.81	28.44	27.81	28.44	28.79	28.79	29.05	29.05	29.28	28.87	29.28	28.87	29.28	28.87
ZnO	0.00	0.02	0.10	0.08	0.09	0.00	0.09	0.00	0.09	0.09	0.00	0.00	0.00	0.08	0.00	0.08	0.00	0.08
NiO	0.01	0.07	0.08	0.03	0.06	0.02	0.06	0.02	0.00	0.00	0.00	0.00	0.04	0.00	0.04	0.00	0.04	0.00
Total	99.60	100.03	100.42	100.10	99.07	99.71	99.07	99.71	101.07	101.07	101.01	101.01	100.12	99.58	100.12	99.58	100.12	99.58
Cations (O = 4)																		
Si	0.004	0.005	0.004	0.006	0.004	0.004	0.004	0.004	0.003	0.003	0.003	0.003	0.004	0.003	0.004	0.003	0.004	0.003
Ti	0.124	0.121	0.112	0.113	0.114	0.113	0.114	0.113	0.092	0.092	0.093	0.093	0.125	0.123	0.125	0.123	0.125	0.123
Al	0.383	0.369	0.441	0.418	0.433	0.396	0.433	0.396	0.262	0.262	0.261	0.261	0.414	0.387	0.414	0.387	0.414	0.387
Cr	0.005	0.005	0.006	0.006	0.006	0.007	0.006	0.007	0.001	0.001	0.002	0.002	0.007	0.006	0.007	0.006	0.007	0.006
Fe ³⁺	1.355	1.375	1.320	1.338	1.326	1.363	1.326	1.363	1.546	1.546	1.545	1.545	1.320	1.356	1.320	1.356	1.320	1.356
Mg	0.264	0.262	0.266	0.259	0.284	0.265	0.284	0.265	0.210	0.210	0.208	0.208	0.261	0.257	0.261	0.257	0.261	0.257
Ca	0.001	0.001	0.001	0.001	0.001	0.002	0.001	0.002	0.010	0.010	0.005	0.005	0.000	0.001	0.000	0.001	0.000	0.001
Mn	0.013	0.012	0.012	0.012	0.012	0.013	0.012	0.013	0.015	0.015	0.016	0.016	0.012	0.013	0.012	0.013	0.012	0.013
Fe ²⁺	0.851	0.848	0.833	0.844	0.817	0.836	0.817	0.836	0.858	0.858	0.867	0.867	0.856	0.852	0.856	0.852	0.856	0.852
Zn	0.000	0.000	0.002	0.002	0.002	0.000	0.002	0.000	0.002	0.002	0.000	0.000	0.000	0.002	0.000	0.002	0.000	0.002

(continued)

Table 7 (continued)

Spinel wt.-%	7DR-2G Spl P core	7DR-2G Spl P rim	7DR-2G Spl I core	7DR-2G Spl I rim	12DR-3A Spl P core	12DR-3A Spl P rim	13DR-5D Spl P core	13DR-5D Spl P rim	50DR-1C Spl P core	50DR-1C Spl P rim
Ni	0.000	0.002	0.002	0.001	0.002	0.001	0.000	0.000	0.001	0.000
Total	3.000	3.000	3.000	3.000	3.000	3.000	3.000	3.000	3.000	3.000
X _{Mg}	0.24	0.24	0.24	0.23	0.26	0.24	0.20	0.19	0.23	0.23
Endmembers										
Fe ₂ TiO ₄	12.35	12.04	11.16	11.26	11.32	11.22	9.20	9.29	12.46	12.29
FeCr ₂ O ₄	0.27	0.23	0.32	0.32	0.28	0.36	0.05	0.09	0.34	0.28
Fe ₃ O ₄	59.80	60.13	60.33	61.11	58.44	60.53	67.06	67.75	59.94	60.12
MgFe ₂ O ₄	26.24	26.10	26.46	25.75	28.30	26.38	20.96	20.70	25.94	25.66
CaAl ₂ O ₄	0.05	0.10	0.08	0.09	0.08	0.16	1.01	0.53	0.03	0.12
MnAl ₂ O ₄	1.26	1.16	1.19	1.18	1.18	1.29	1.50	1.64	1.18	1.32
ZnAl ₂ O ₄	0.00	0.05	0.25	0.21	0.23	0.00	0.23	0.00	0.00	0.20
NiAl ₂ O ₄	0.03	0.20	0.22	0.08	0.17	0.07	0.00	0.00	0.12	0.00

Table 8. Representative microprobe analyses of magmatic glass from Conical Seamount lavas (avg. = average values) with calculation of normative nepheline (ne%) according to the CIPW norm. According to the geochemical data, ferric iron contents of 40% of total iron were assumed. TP tephriphonolite, other rock abbreviations see Table 1

Glass Type	7DR-2G TA	7DR-2G TA	7DR-2G TA	12DR-3A TP	12DR-3A P	12DR-3A P	50DR-1C P	50DR-1C P	50DR-1C P
wt.-%	F3 3-1	F3 3-3	avg. (n = 26)	xt 8	6	avg. (n = 8)	F6 1-9	F6 2-17	avg. (n = 28)
SiO ₂	55.54	56.83	56.17	55.21	55.36	56.40	54.74	53.47	54.46
TiO ₂	0.41	0.41	0.44	0.35	0.34	0.42	0.41	0.32	0.41
Al ₂ O ₃	19.80	20.72	20.20	22.45	20.86	21.22	20.95	20.97	20.65
Cr ₂ O ₃	0.00	0.00	0.01	0.04	0.00	0.02	0.00	0.00	0.01
Fe ₂ O ₃	2.70	2.30	2.43	2.77	2.17	2.14	3.09	2.08	2.46
MgO	1.97	1.24	1.62	2.22	1.86	1.95	1.61	0.65	1.22
CaO	4.83	2.98	4.03	1.98	1.75	2.10	1.79	1.93	2.29
MnO	0.14	0.11	0.13	0.10	0.12	0.12	0.12	0.12	0.13
FeO	3.64	3.10	3.29	2.50	2.93	2.89	4.17	2.81	3.32
NiO	0.00	0.00	0.00	0.00	0.00	0.00	0.00	0.00	0.00
Na ₂ O	3.55	4.35	3.88	3.97	4.46	4.17	4.54	6.40	5.25
K ₂ O	6.26	7.16	6.47	7.96	8.12	7.90	8.60	8.34	8.16
Total	98.84	99.19	98.66	99.55	97.98	99.31	100.02	97.08	98.36
ne%	1.1	4.0	1.5	5.8	8.2	4.9	11.9	23.6	15.7

Fe–Mg-exchange temperatures although temperatures calculated for glass in direct contact with olivine are quite close to the results of the olivine-spinel geothermometry (Table 9).

Two of the investigated samples contain phlogopite in contact with magmatic glass, which allows the application of the geothermometer of *Righter and Carmichael* (1996). This geothermometer is based on the Ti-exchange between phlogopite and coexisting melt and has an error of $\pm 50^\circ\text{C}$. Chemical equilibrium was assumed for the Ti-rich rim section of phlogopite and the adjacent glass, which resulted in remarkably constant temperatures of 1021–1063 $^\circ\text{C}$ for different phlogopite phenocrysts. These temperatures are in accord with the results of the olivine-spinel geothermometer of *Ballhaus et al.* (1991) indicating that partitioning of Ti had taken place.

Distinctly lower temperatures were estimated for the hornblende-bearing basaltic trachyandesite sample 13DR-5D. The geothermometer of *Colombi* (1988), which is based on the titanium content of Ca-amphibole, yields temperatures of up to 850 $^\circ\text{C}$ for the core and 750–770 $^\circ\text{C}$ for the rim section of the hornblende. The error of the method is $\pm 30^\circ\text{C}$. These results coincide with the temperatures calculated using the semi-quantitative geothermometer of *Ernst and Liu* (1998), which also permits an estimate of the crystallization depth of the hornblende based on its Al-content. For the core sections of the hornblende crystals, pressures of 10–14 kbar were estimated, pointing to an early crystallization of hornblende in the course of magma ascent. The crystallization of clinopyroxene took place at a rather

Table 9. *P-T estimates for analyses of magmatic minerals and coexisting glass from Conical Seamount. T BBG olivine-spinel geothermometer of Ballhaus et al. (1991); T Roeder olivine-melt geothermometer of Roeder (1974); T R&C phlogopite-melt geothermometer of Righter and Carmichael (1996); T Colombi Ti in hornblende geothermometer of Colombi (1988); P E&L semiquantitative hornblende geobarometer of Ernst and Liu (1998); P Nimis clinopyroxene geobarometer of Nimis (1995); $\Delta\log(f_{O_2})^{FMQ}$ values determined with the QUILF program of Andersen et al. (1993). Rock abbreviations see Table 1*

Sample	Rock type	T BBG (°C)	T Roeder (°C)	T R&C (°C)	T Colombi (°C)	P E&L (kbar)	P Nimis (kbar)	$\Delta\log_{f_{O_2}}^{FMQ}$
7DR-2G	TB	1006–1069	950–980	1021–1063	–	–	0–3.6	0.66–1.68
12DR-3A	TB	1001–1083	922–983	–	–	–	0–4.1	2.17–2.39
13DR-5D	BTA	–	–	–	781–846*	10.0–14.0*	0–1.6	–
50DR-1C	TB	1005–1047	695–1017	–	–	–	0.2–4.5	2.35–2.46

* Core analyses of amphibole

late stage of magma ascent, as indicated by numerous inclusions of matrix minerals as well as glass. This is supported by the pressures of 0–4.5 (± 2) kbar calculated using the clinopyroxene barometry of *Nimis* (1995), based on crystal structure modelling of the clinopyroxene.

A quantification of the oxygen fugacity is possible using the QUILF-program of *Andersen et al.* (1993), which uses the composition of coexisting olivine and spinel phenocrysts. For the samples from Conical Seamount, $\Delta\log(f_{O_2})$ -values of 0.7 to 2.5 above the fayalite-magnetite-quartz oxygen buffer (FMQ) were determined. The high oxygen fugacity of these magmatites may be the consequence of mantle metasomatism by a water-bearing silicate melt or more likely for a solute-rich hydrous fluid emerging from an underlying, subducted slab as postulated by *Parkinson and Arculus* (1999). This type of metasomatism was found in mantle xenoliths from the neighbouring TUBAF Seamount, which formed during the same magmatic event. The xenoliths reveal distinct modal metasomatism (i.e. metasomatic mineral assemblages on veins or penetrative metasomatic alteration) from a hydrous fluid with similarly high $\Delta\log(f_{O_2})^{FMQ}$ -values (*Franz et al.*, 2002).

Discussion and conclusions

The close spatial association between the mineralization at Conical Seamount and on Lihir Island suggests a similar genetic evolution. Alkaline rocks from Conical Seamount and from Lihir Island plot along a common fractionation trend (Fig. 5) suggesting that the melts from Conical Seamount and Lihir Island are derived from the same parental magma chamber (cf. *Kennedy et al.*, 1990; *Müller et al.*, 2001). This interpretation is confirmed by very similar chondrite-normalized trace element patterns of unmineralized samples from both localities (Fig. 6). The primitive character (< 49 wt% SiO_2) of the rocks from Conical Seamount, when compared to the more evolved and, hence, compositionally more diverse range of samples from Lihir Island, implies a magmatic evolution related to only a single eruptive event. By contrast, the volcanoes from Lihir Island were probably the products of multiple eruptions.

Mineral parageneses and the composition of magmatic phases from Conical Seamount and Lihir Island and the sequence of crystallization are overall very similar pointing to a common magma source. Geothermometry on coexisting spinel and olivine phenocrysts delivers somewhat lower temperatures for the Lihir magmatites compared to Conical Seamount (i.e. 800–965 °C for Lihir vs. 1000–1082 °C for Conical Seamount). This suggests cooling of the Lihir magma in the shallow hypabyssic intrusive level and/or during ascent. The marked differentiation of the Lihir magma, as indicated by their geochemistry, indicates a longer lithospheric ascent when compared to the lavas at Conical Seamount. Minor differences occur for the chemical composition of phlogopite phenocrysts. Phlogopite from Conical Seamount (Fig. 4) contains low F and Cl concentrations (< 0.3 wt% F and < 0.05 wt% Cl), but high H_2O contents (up to 4.1 wt%). This contrasts with primary, high F (up to 5.4 wt% F) phlogopite phenocrysts from Lihir Island, which may be explained by the more evolved compositions of their host rocks (*Müller et al.*, 2001; Fig. 5).

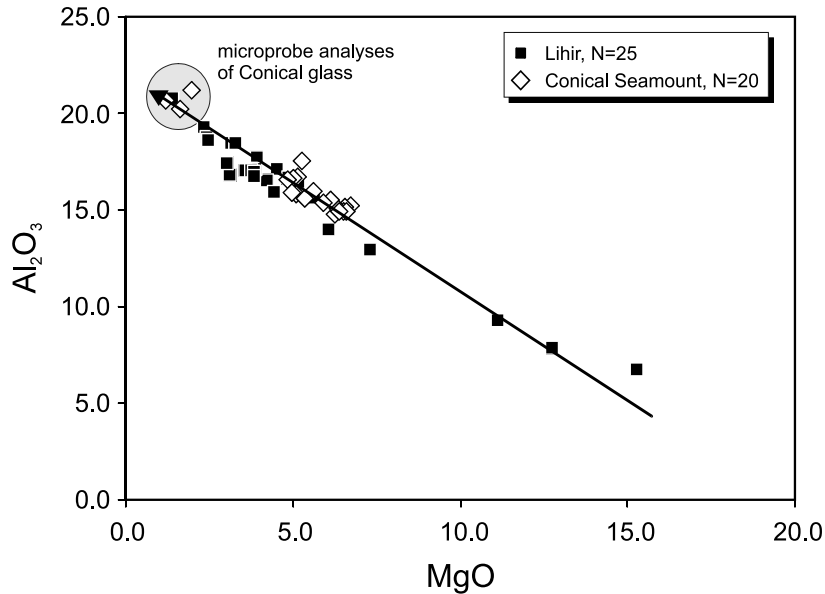


Fig. 5. MgO versus Al₂O₃ biaxial diagram showing one single fractionation trend for the rocks from Conical Seamount and Lihir Island

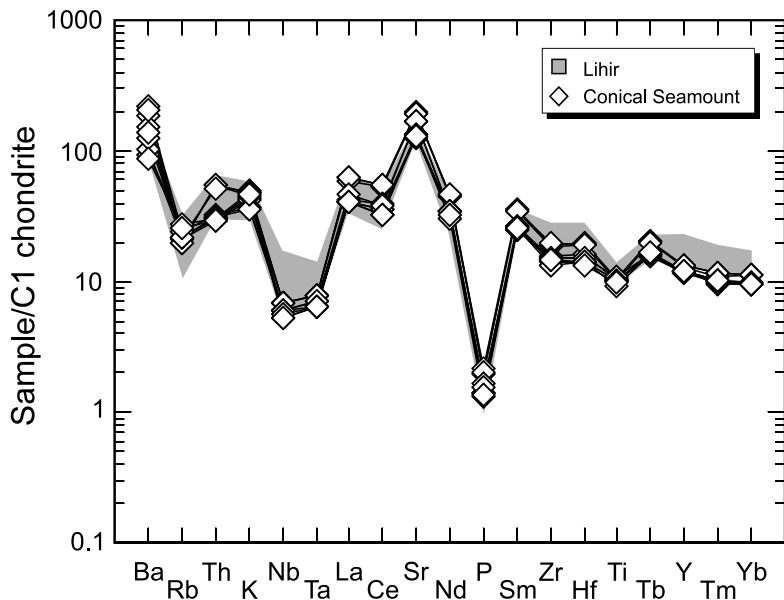


Fig. 6. Chondrite-normalized trace element abundance pattern of igneous rocks from Conical Seamount (diamonds) and Lihir Island (shaded area). Normalizing values after *Thompson* (1982). Their similar patterns are interpreted to reflect their derivation from a common parental magma chamber at depth

There are distinct differences between the mineralization styles at Conical Seamount and Lihir Island that may in part be related to the greater abundance of seawater at Conical Seamount. Pyritic stockwork mineralization at Conical

Seamount is hosted by strongly silicified and clay-altered basaltic rocks (*Petersen et al., 2002*), while at Ladolam pyritic stockwork mineralization is restricted to biotite-magnetite \pm silica altered monzodiorite (*Müller et al., 2002a*).

Both the acidic alunite-kaolinite-bearing alteration locally accompanying early-stage pyrite mineralization and the main-stage polymetallic sulfide mineralization occurring in black sericite-alkali feldspar-bearing siliceous veins at Conical Seamount have not been observed at Ladolam. Instead, the bulk ore at Minifie, the largest and best exposed orebody at Ladolam, consists of biotite-magnetite altered phreatomagmatic (hydrothermal) breccias overprinted by fine-grained auriferous pyrite, minor marcasite and rare chalcopyrite \pm galena \pm tetrahedrite (*Müller et al., 2002b*). In places, these hydrothermal breccias are cut by late-stage grey to blue quartz-chalcedony-illite-adularia-pyrite \pm marcasite veins that contain isolated bonanza gold grades (*Müller et al., 2002a*). The late-stage, fracture-filling As-Sb mineralization observed at Conical Seamount has also not been documented in ores from the Ladolam gold deposit.

The sulfur isotopic composition of sulfide separates and bulk samples from Conical Seamount ranges from +2.0 to -13.9‰ $\delta^{34}\text{S}$ (mean = -3.1‰ $\delta^{34}\text{S}$, $n=28$) with characteristic values for different stages of the mineralization (*Petersen et al., 2002*). The negative sulfur isotopic ratios for sulfides from Conical Seamount and differences in sulfur isotopic ratios between coexisting sulfides and alunite are unusual for modern seafloor hydrothermal systems (*Herzig et al., 1998*). This, in combination with the platy nature of the alteration mineral alunite and the presence of aluminum phosphate sulfates has been used to suggest a contribution of magmatic fluids or gases to the mineralizing fluid at Conical Seamount (*Arribas et al., 1995; Petersen et al., 2002*). By contrast, sulfur isotopic data from Ladolam suggest a fractionated magmatic sulfur source, although they do not provide evidence for the interaction with seawater sulfate (*Müller et al., 2002b*).

Elevated oxygen fugacities of 0.7–2.5 log units above the FMQ buffer are recorded for lavas from Conical Seamount, which is quite similar to samples from Lihir Island ($\Delta\log(f_{\text{O}_2})^{\text{FMQ}} = 1.4$ to 4.8; cf. *Müller et al., 2001*). This high magma f_{O_2} , as commonly also indicated by abundant igneous magnetite (>5 vol%), seems to be a prerequisite for the enrichment of large quantities of Au in arc magmas (*Sillitoe, 1979; Mungall, 2002*). An increase in f_{O_2} at any given temperature will decrease the concentration of dissolved sulfide in the melt and will therefore hamper the segregation of Cu and Au into a sulfide melt (*Carmichael and Ghiorso, 1986; Candela, 1992*). Thus, Au and Cu will remain in the volatile-enriched upper part of the magma chamber. Once volatile saturation occurs during secondary boiling, the magma chamber releases pulses of metal- and volatile-enriched melts. The high f_{O_2} of the rocks from both Conical Seamount and Lihir Island is thus an indicator of their high potential for gold mineralization.

Acknowledgments

Thanks are due to *N. Vielreicher* (Perth), *E. Stumpfl* (Leoben) and an anonymous reviewer for critical and constructive comments to the manuscript. *R. Naumann* and *J. Erzinger* (both GFZ Potsdam) are thanked for the determination of ferric iron. We gratefully acknowledge the support and inspiring comments of *S. Hunt* (Lihir Gold) during the field

work of the first author on Lihir Island. This study has been financially supported by the German Research Foundation (DFG grant MU1619-2 to *D. Müller*), the German Federal Ministry for Education and Science (BMBF grants 03G0094A and 03G0133A) and the Leibniz Award of the German Research Foundation to *P. Herzig*, and by Lihir Gold Limited.

References

- Andersen DJ, Lindsley DH, Davidson PM* (1993) QUILF: a pascal program to assess equilibria among Fe–Mg–Mn–Ti oxides, pyroxenes, olivine, and quartz. *Comput Geosci* 19: 1333–1350
- Arribas A, Cunningham CG, Rytuba JJ, Rye RO, Kelly WC, Podwysocki MH, McKee EH, Tosdal RM* (1995) Geology, geochronology, fluid inclusions, and isotope geochemistry of the Rodalquilar gold alunite deposit, Spain. *Econ Geol* 90: 795–822
- Ballhaus C, Berry RF, Green DH* (1991) High pressure experimental calibration of the olivine-orthopyroxene-spinel oxygen geobarometer: implications for the oxidation state of the upper mantle. *Contrib Mineral Petrol* 107: 27–40
- Candela PA* (1992) Controls on ore metal ratios in granite-related ore systems: an experimental and computational approach. *Transact Roy Soc Edinburgh, Earth Sci* 83: 317–326
- Carman GD* (1994) Genesis of the Ladolam gold deposit, Lihir Island, Papua New Guinea. Thesis, Monash University, Melbourne, Australia, 263 pp (unpublished)
- Carmichael ISE, Ghiorso MS* (1986) Oxidation-reduction relations in basic magma: a case for homogeneous equilibria. *Earth Planet Sci Lett* 78: 200–210
- Coleman PJ, Kroenke LW* (1981) Subduction without volcanism in the Solomon Island arc. *Geo-Marine Lett* 1: 129–134
- Colombi A* (1988) Métamorphisme et géochimie des roches mafiques des Alpes ouest-centrales (géoprofil Viège-Domodossola-Locarno). Thesis, University of Lausanne, Switzerland, 216 pp (unpublished)
- Corbett G* (1999) Comments on the structural controls and styles of gold mineralization in the Minifie pit, Lihir Island. Report to Lihir Management Company, 15 pp (unpublished)
- Corbett G, Hunt S, Cook A, Tamaduk P, Leach T* (2001) Geology of the Ladolam gold deposit, Lihir Island, from exposures in the Minifie open pit. PNG Geology, Exploration and Mining Conference, Port Moresby, pp 69–77
- Davies RM, Ballantyne GH* (1987) Geology of the Ladolam gold deposit, Lihir Island, Papua New Guinea. *PacRim Congress* 87, Melbourne, pp 943–949
- Droop GTB* (1987) A general equation for estimating Fe³⁺ concentrations in ferromagnesian silicates and oxides from microprobe analyses, using stoichiometric criteria. *Min Mag* 51: 431–435
- Ernst WG, Liu J* (1998) Experimental phase equilibrium study of Al- and Ti-contents of calcic amphibole in MORB – a semiquantitative thermobarometer. *Am Mineral* 83: 952–969
- Franz L, Becker KP, Kramer W, Herzig PM* (2002) Veined mantle xenoliths from the metasomatic fore-arc wedge of the Bismarck Microplate (Papua New Guinea) – petrological and geochemical consequences and extent of slab-induced hydrous metasomatism. *J Petrol* 43: 315–343
- Herzig PM, Hannington MD, McInnes B, Stoffers P, Villinger H, Seifert R, Binns R, Liebe T, Scientific party R/V SONNE CRUISE SO-94* (1994) Submarine volcanism and hydrothermal venting studied in Papua, New Guinea. *Eos, Transact Am Geophys Union* 75: 513–516

- Herzig PM, Hannington MD, Arribas A* (1998) Sulfur isotope composition of hydrothermal precipitates from the Lau back-arc: implications for magmatic contributions to seafloor hydrothermal systems. *Mineral Deposita* 33: 226–237
- Herzig PM, Petersen S, Hannington MD* (1999) Epithermal-type gold mineralization at Conical Seamount: a shallow submarine volcano south of Lihir Island, Papua New Guinea. In: *Stanley et al.* (eds) *Proceedings SGA-IAGOD Meeting London*. Balkema, Rotterdam, pp 527–530
- Jarosevich E, Nelen JA, Norberg JA* (1980) Reference samples for electron microprobe analysis. *Geostand Newslett* 4: 43–47
- Kennedy AK, Grove TL, Johnson RW* (1990) Experimental and major element constraints on the evolution of lavas from Lihir Island, Papua New Guinea. *Contrib Mineral Petrol* 104: 722–734
- Komyshan P* (1999) Geological interpretations of Lihir Island. CSA Report R8.99, Melbourne, 40 pp (unpublished)
- Leake BW, Wooley AR, Arps CES, Birch WD, Gilbert MC, Grice JD, Hawthorne FC, Kato A, Kisch HJ, Krivovichev VG, Linthout K, Laird J, Mandarino J, Maresch WV, Nickel EH, Rock NMS, Schumacher JC, Smith DC, Stephenson NCN, Ungaretti L, Whittaker EJW, Youzhi G* (1997) Nomenclature of amphiboles. Report of the subcommittee on amphiboles of the International Mineralogical Association Commission on new minerals and mineral names. *Eur J Mineral* 9: 623–651
- Lindsley DH* (1983) Pyroxene thermometry. *Am Mineral* 68: 477–493
- McInnes BIA, McBride JS, Evans NJ, Lambert DD, Andrew AS* (1999) Osmium isotope constraints on ore metal recycling in subduction zones. *Science* 286: 512–516
- Moyle AJ, Doyle BJ, Hoogvliet H, Ware AR* (1990) Ladolam gold deposit, Lihir Island. In: *Hughes FE* (ed) *Geology of the mineral deposits of Australia and Papua New Guinea*. Australasian Inst Min Metall: 1793–1805
- Müller D, Groves DI* (2000) Potassic igneous rocks and associated gold-copper mineralization, 3rd ed. Springer, Berlin Heidelberg New York Tokyo, 252 pp
- Müller D, Franz L, Herzig PM, Hunt S* (2001) Potassic igneous rocks from the vicinity of epithermal gold mineralization at Lihir Island, Papua New Guinea. *Lithos* 57: 163–186
- Müller D, Kaminski K, Uhlig S, Graupner T, Herzig PM, Hunt S* (2002a) The transition from porphyry- to epithermal-style gold mineralization at Ladolam, Lihir Island, Papua New Guinea. *Mineral Deposita* 37: 61–74
- Müller D, Herzig PM, Scholten J, Hunt S* (2002b) The Ladolam gold deposit: gold mineralization hosted by alkaline rocks. *Econ Geol Spec Publ* 9: 367–382
- Mungall JE* (2002) Roasting the mantle: slab melting and the genesis of major Au and Au-rich Cu deposits. *Geology* 30: 915–918
- Nimis P* (1995) A clinopyroxene geobarometer for basaltic systems based on crystal-structure modeling. *Contrib Mineral Petrol* 121: 115–125
- Parkinson IJ, Arculus RJ* (1999) The redox state of subduction zones: insights from arc-peridotites. *Chem Geol* 160: 409–423
- Patterson DB, Farley KA, McInnes BIA* (1997) Helium isotopic composition of the Tabar-Lihir-Tanga-Feni island arc, Papua New Guinea. *Geochim Cosmochim Acta* 61: 2485–2496
- Pearce JA* (1982) Trace element characteristics of lavas from destructive plate boundaries. In: *Thorpe RS* (ed) *Andesites*. Wiley, New York, pp 525–548
- Petersen S, Herzig PM, Hannington MD, Jonasson IR, Arribas A* (2002) Submarine vein-type gold mineralization near Lihir Island, New Ireland Fore-arc, Papua New Guinea. *Econ Geol* 97: 1795–1813

- Richter, Carmichael* (1996) Phase equilibria of phlogopite lamprophyres from western Mexico: biotite-liquid equilibria and P-T estimates for biotite-bearing igneous rocks. *Contrib Mineral Petrol* 123: 1–21
- Roeder* (1974) Activity of iron and olivine solubility in basaltic liquids. *Earth Planet Sci Lett* 23: 397–410
- Rytuba JJ, McKee EH, Cox D* (1993) Geochronology and geochemistry of the Ladolam gold deposit, Lihir island, and gold deposits and volcanoes of Tabar and Tatau, Papua New Guinea. *US Geol Surv Bull* 2039: 119–126
- Schumacher JC* (1997) The estimation of ferric iron in electron microprobe analyses of amphiboles. *Eur J Mineral* 9: 643–651
- Sillitoe RH* (1979) Some thoughts on gold-rich porphyry copper deposits. *Mineral Deposita* 14: 161–174
- Sillitoe RH* (1994) Erosion and collapse of volcanoes: causes of telescoping in intrusion-centered ore deposits. *Geology* 22: 945–948
- Steward WD, Sandy MJ* (1988) Geology of New Ireland and Djaul Islands, northeast Papua New Guinea. In: *Marlow MS, Dadisman SV, Exton NF* (eds) *Geology and offshore resources of Pacific island arcs – New Ireland and Manus region, Papua New Guinea*. Circum-Pacific Council for Energy and Mineral Resources, Earth Science Series 9: 12–30
- Taylor B* (1979) Bismarck Sea: evolution of a back arc basin. *Geology* 7: 171–174
- Thompson RN* (1982) Magmatism of the British Tertiary Volcanic Province. *Scott J Geol* 18: 50–107
- Wallace DA, Johnson RW, Chappell BW, Arculus RJ, Perfit MR, Crick IH* (1983) Cainozoic volcanism of the Tabar, Lihir, Tanga, and Feni islands, Papua New Guinea: geology, whole-rock analyses, and rock-forming mineral compositions. Bureau of Mineral Resources, Australia, BMR Report 243

Authors' addresses: *D. Müller* (corresponding author), Institute for Isotope Geology and Mineral Resources, Department of Earth Sciences, Swiss Federal Institute of Technology, ETH-Zentrum NO, F63, CH-8092 Zürich, Switzerland, e-mail: dan.muller@erdw.ethz.ch; *L. Franz, S. Petersen, P. M. Herzig*, Institut für Mineralogie, TU Bergakademie Freiberg, Brennhausgasse 14, D-09596 Freiberg, Germany; *M. D. Hannington*, Geological Survey of Canada, 601 Booth Street, Ottawa, Ontario K1A 0E8, Canada